Lecture Notes in Mechanical Engineering

Mohamed Haddar
Lotfi Romdhane
Jamel Louati
Abdelmajid Ben Amara *Editors*

Design and Modeling of Mechanical Systems

Proceedings of the Fifth International Conference on Design and Modeling of Mechanical Systems, CMSM'2013 Djerba, Tunisia, March 25–27, 2013

Springer

Lecture Notes in Mechanical Engineering

For further volumes:
http://www.springer.com/series/11236

Mohamed Haddar, Lotfi Romdhane,
Jamel Louati, and Abdelmajid Ben Amara (Eds.)

Design and Modeling of Mechanical Systems

Proceedings of the Fifth International Conference on Design and Modeling of Mechanical Systems, CMSM'2013, Djerba, Tunisia, March 25–27, 2013

Springer

Editors
Professor Mohamed Haddar
National School of Engineers of Sfax
Sfax
Tunisia

Professor Jamel Louati
National School of Engineers of Sfax
Sfax
Tunisia

Professor Lotfi Romdhane
National School of Engineers of Sousse
Sousse Erriadh
Tunisia

Professor Abdelmajid Ben Amara
National School of Engineers of Monastir
Monastir
Tunisia

ISSN 2195-4356 ISSN 2195-4364 (electronic)
ISBN 978-3-642-37142-4 ISBN 978-3-642-37143-1 (eBook)
DOI 10.1007/978-3-642-37143-1
Springer Heidelberg New York Dordrecht London

Library of Congress Control Number: 2013933303

Printed on acid-free paper

Springer is part of Springer Science+Business Media (www.springer.com)

Introduction

The International Congress on Design and Modeling of Mechanical Systems (CMSM) brings together the international scientific community to discuss various topics in the field of mechanical engineering in its broadest aspect. The first four editions have contributed to a considerable progress in research done by different teams through the exchange of information and skills generated during those meetings.

Organized in Djerba, Tunisia, on March 25-27, 2013, the fifth edition of the congress (CMSM'2013) was characterized by a greater international influence with respect to the past. The close collaboration between the Unit of Mechanics, Modeling and Manufacturing (U2MP) of the National School of Engineers of Sfax, the Mechanical Engineering Laboratory (MBL) of the National School of Engineers of Monastir and Mechanics Laboratory of Sousse (LMS) of the National School of Engineers of Sousse brought together nearly 300 participants to expose their work and provide a forum to debate the following topics:

1. Mechatronics and Robotics
2. Dynamics of mechanical systems
3. Fluid structure interaction and vibroacoustics
4. Modeling and analysis of materials and structures
5. Design and manufacturing of mechanical systems

The scientific committee of CMSM'2013 has selected high quality contributions exposed during various sessions of the congress and collected them in this proceedings book, which provides, by its original articles, an overview of recent research advancements in the field of mechanical engineering.

Contents

Part I: Mechatronics and Robotics

Part II: Dynamics of Mechanical Systems

Part I
Mechatronics and Robotics

Optimization of the Combustion in Large Marine Diesel Engine by Controlling the Exhaust Gas

Sabri Bechir

U.R. Automatique et Robotique Marine (ARM),
Académie Navale,
7050 Menzel Bourguiba Tunisia
Sabri.bechir@yahoo.fr

Abstract. The diesel engine performance and emissions are strongly linked to the air-fuel mix which is a function of the oxygen content in the exhaust gases. It is possible to regulate the air-fuel mixture in a diesel engine, by controlling the turbocharger speed through a bypass valve by a regulator whose reference is the oxygen content in the exhaust gas. For the execution of this work we have taken as a model a marine diesel engine type Wartsila NSD 12 ZAV 40S with 8200 Kw nominal power, using the engine shop trials data. Engine manufacturers provide charts on relationships gas flow, power etc. The work is based on these curves for modeling the control system**.** Simulation is carried out using Matlab and Simulink and simulation results are presented to illustrate the performances of this approach.

Keywords: exhaust gas pollution, marine diesel engine, test bench, optimization, simulation.

1 Introduction

Diesel engines provide the major power sources for marine transportation and contribute to the prosperity of the worldwide economy. However, the emissions from diesel engines also seriously threaten the environment and are considered one of the major sources of air pollution. The pollutants emitted from marine vessels are confirmed to cause the ecological environmental problems such as the ozone layer destruction, enhancement of the greenhouse effect (Jaroslaw and Tadeusz 2011).

Diesels engine operate with an air excess ratio. Engine power, specific fuel consumption, and emissions relate closely to air ratio among all the engine variables. Air ratio is also called lambda. It indicates the amount that the actual available air-fuel ratio mixture differs from the stoichiometric air-fuel ratio of the fuel being used.

The regulation of the oxygen amount in exhaust gas according to the signal supplied by the lambda probe wideband**,** is better suited for the efficiency test of a

M. Haddar et al. (Eds.): *Design and Modeling of Mechanical Systems*, LNME, pp. 3–10.
DOI: 10.1007/978-3-642-37143-1_1

combustion process because oxygen and excess air are almost independent of the fuel type. The normal engine operation is between 60% and 100% load of the rated power and the study is conducted on this basis.

2 Excess Air as a Function of the Power

One of equations used to determine air-fuel ratio λ:

$$\lambda = Q_{mair} / (\alpha_0 \; Q_{mc}) \tag{1}$$

Where α_0 is the theoretical coefficient of excess air (kg of air per kg of fuel), α is real coefficient of excess air , Q_{mc} the fuel mass flow rate (kg/h), Q_{mair} the mass air flow rate (kg /h.), λ is the ratio between real and the theoretical coefficient.

$$\lambda = \alpha / \alpha_0 \tag{2}$$

The function of the air coefficient lambda power function (based on fuel consumption curve) is given by the following expression.

$$\lambda = 0{,}0067 \; (P_{n\%}) + 2.2939 \tag{3}$$

Where P_n is the nominal engine power (8200 Kw) and $P_{n\%}$ the percentage of rated power without unity.

2.1 The Sensor Transmitter Position of the Fuel Setting

The characteristic function of the variation of power as a function of the fuel setting according to the curve can be expressed by the following equation (Robert 1996, Wartsila 1998).

$$P_{n\%} = 21{,}25 \; C_r - 60 \tag{4}$$

Where C_r is the fuel setting (from 0 to 10)**.**

On the other hand, the output of the transmitter sensor given by the relationship.

$$I_c = C_r / 0.05 \tag{5}$$

Where I_c output current of fuel setting sensor.

2.2 The Lambda Sensor

We will use a lambda sensor (Antonio and al 2012) whose characteristics give the function dependent current air ratio lambda by the equation (Delphi 2009).

$$I_L = 0{,}1537\lambda^6 + 2{,}5546\lambda^5 - 17{,}113\lambda^4 + 59{,}083\lambda^3 - 111{,}09\lambda^2 + 109{,}5\lambda - 42{,}695 \tag{6}$$

Where I_L the output current of the lambda sensor.

3 Relationship between the Operating Engine Parameters

3.1 The Turbocharger

The turbocharger is characterized by a series of curves compressor air pressure and flow, turbocharger speed. In the following the equations between the differents parameters (Robert 1996, Wartsila 1998).

$$V_{TC} = -1.7927\,(P_{n\%})^2 + 389.37(P_{n\%}) + 788.31 \tag{7}$$

$$P_{air} = -2\ 10^{-6}\ (P_{n\%})^2 + 0{,}0318\ (P_{n\%}) + 0{,}3922 \tag{8}$$

$$P_{air} = 0{,}0002\ \ (V_{TC}) - 0{,}6113 \tag{9}$$

$$Q_{vair} = 1{,}4323\,(V_{TC}) - 1084 \tag{10}$$

$$T_{air} = 0.0011\,(P_{n\%})^2 + 0.0704 \text{ x } (P_{n\%}) + 25.101 \tag{11}$$

$$Q_{mair} = Q_{vair}\ \rho_0\ X\,273/(273 + T_{air})\,(101300 + P_{air})/101300 \tag{12}$$

$$Q_{mgaz} = 2\ 10^{-5}\,(P_{n\%})^3 - 0.0041(P_{n\%})^2 + 0.4936\,(P_{n\%}) - 7.5518 \tag{13}$$

$$V_{TC} = 0.951\,(Q_{mts})^3 - 81.908\,(Q_{mts})^2 + 2332.9\,(Q_{mts}) + 247.02 \tag{14}$$

Where V_{TC} is the turbocharger speed in rev/min, P_{air} the air compressor pressure output in bar, P the pressure in actual operating conditions, Q_{vair} the volume air flow rate in m^3/h, T_{air} the intake air temperature in °C, T the temperature in actual operating conditions in °C, Q_{mgaz}, the engine output gas mass flow (Kg/s), ρ_0 the density of the air at 0°C and at atmospheric pressure at sea level.

3.2 The Engine

From the fuel consumption curve the hourly fuel consumption is expressed as (Robert 1996, Wartsila 1998):

$$C_h = 0.001\,(P_{n\%})^3 - 0.1807\,(P_{n\%})^2 + 25.556\,(P_{n\%}) - 111.13 \tag{15}$$

Where C_h is the hourly fuel consumption in Kg/h.

$$Q_{mgt} = Q_{mair} + C_h \tag{16}$$

Where Q_{mair} and Q_{mgt} are the mass gas flow in Kg/h.

$$\lambda = Q_{mair}(C_h \text{ x } \alpha_0) \tag{17}$$

4 The By-Pass Valve for Controlling the Air Flow

4.1 Valve Position

Valve is mounted in parallel with the turbocharger figure 1. Where Q_{mgv} is valve input mass gas flow, Q_{mgTC} is input mass gas flow in Kg/s. and I_V the control current of the valve (Eric and Claes 2005).

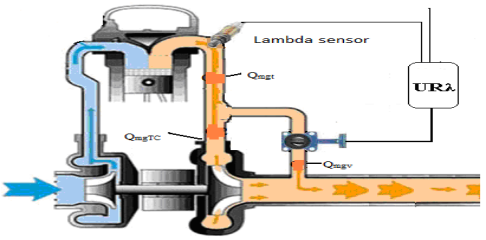

Fig. 1 Schematic diagram of our supercharged engine

4.2 Selection Valve

To simplify the calculation we will use a proportional valve with linear flow characteristic current. It is controlled by a current. The flow rate of gas leaving the valve is given by the following formula:

$$Q_{mgV} = Q_{mgt} - Q_{mgTC} \tag{18}$$

5 The Controller System

The aim of the controller for the bypass valve is to avoid surge and to minimize the time the bypass valve is being held open, the following expression given the PI controller. At each step of fuel that is a fraction of the nominal power $P_{n\%}$ corresponds to a value of λ. Which is the desired form of a current (I_L)

$$H(s) = K_p + \frac{K_i}{s} \tag{19}$$

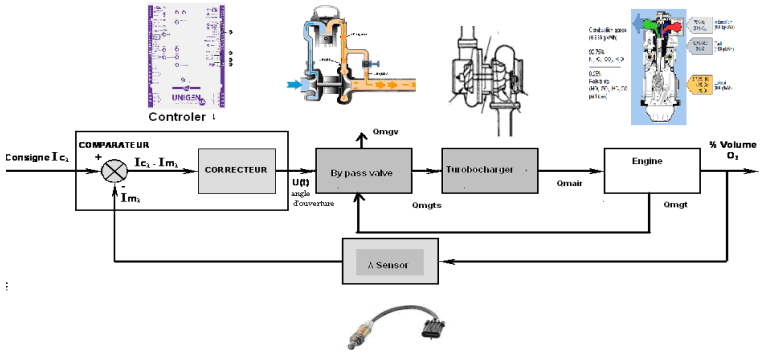

Fig. 2 Synoptic of the control Loop

6 Numerical Simulation

The first simulation figure 4 improve the function of the bypass valve, the opening of the valve according the power just for making sure that the model is working, fig. 5 the response of the valve in case of perturbation.

The second simulation figure 6 shows the variation of λ according to the engine power. From Figure 7 we observe that the controller corrects the disturbance effect. The third simulation, Figure 8 shows the step response of the system by varying the power of 60 to 100% can be seen in the response exceeded because the parameters of the controller are poorly chosen; the excess disappears in Figure 9 with appropriate parameters.

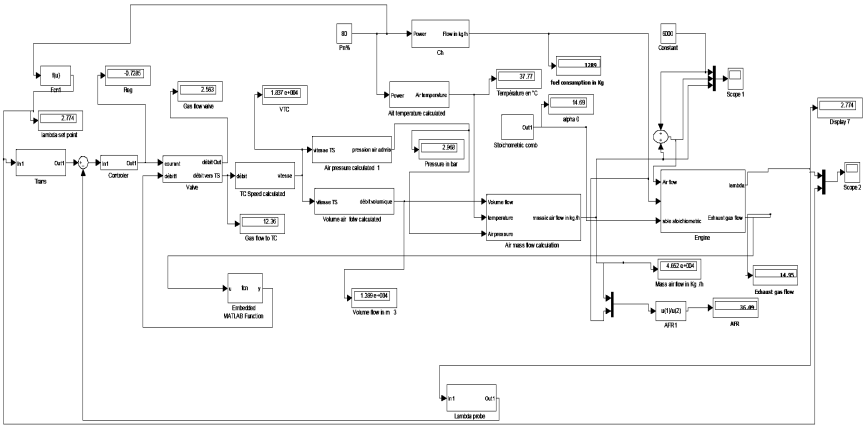

Fig. 3 The control Loop

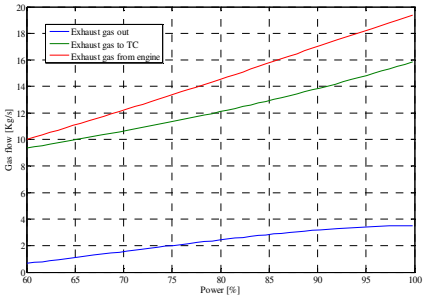

Fig. 4 Exhaust gas flow without perturbation

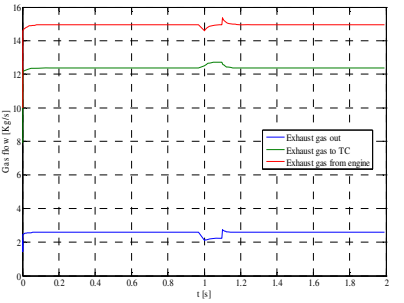

Fig. 5 Exhaust gas flow with perturbation

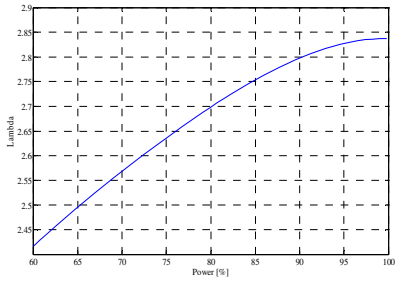

Fig. 6 λ VS Pn% without perturbation

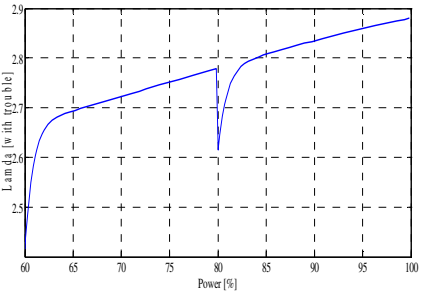

Fig. 7 λ VS Pn% with perturbation

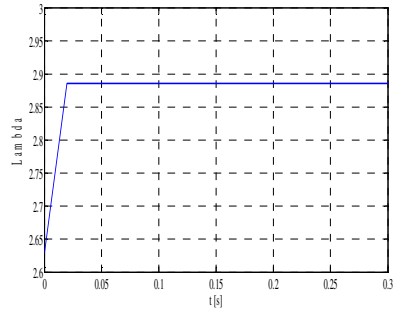

Fig. 8 System response with arbitrary parameters

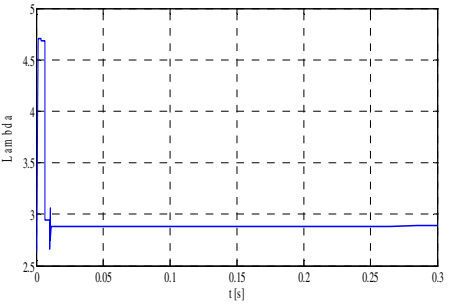

Fig. 9 System response with optimized parameters

7 Conclusion

The effect of optimizing the air flow clearly shows the respect the constraint of air / fuel imposed. Thus we can see the need for continuous information on the flow of air to manage correctly pollution levels.

Based on performance curves on test benches provided by manufacturers for modeling the system, the control system is capable for adjusting the intake air of the engine by the control of a valve connected in parallel with the turbocharger.

The control of a variable in a closed loop is designed to follow a predetermined reference value. We viewed our system tool SIMULINK of MATLAB software.

By controlling the amount of oxygen in exhaust gas in a marine diesel engine we contribute to environmental protection. The optimization procedure provides the flow and pressure of air which is ideal to use. The practical realization of the control can ensure this operation is an important issue to consider in the future.

References

Journal Article

Jaroslaw, M., Tadeusz, B.: Marine engine exhaust gas emission after treatment system concept maritime. Journal of Kones Power Train and Transport 18(4) (2011)

Eric, W., Claes, F.: Bypass valve modeling and surge control for turbocharged si engines. Master's thesis performed in vehicular systems, reg nr: lith-isy-ex-3712 (2005)

Jerzy, K.: Laboratory study on influence of air duct throttling on exhaust gas composition in marine four-stroke diesel engine. Journal of Kones Power Train and Transport 19(1) (2012)

Antonio, S., Francisco, S., Cavalcante, J., Lutero, C.: Monitoring Industrial Combustion through Automotive Oxygen Sensor. International Transaction Journal of Engineering, Management, & Applied Sciences & Technologies (2012)

Lin, C.Y., Huang, J.C.: An oxygenating additive for improving the performance and emission characteristics of marine diesel engines. Ocean Engineering 30 1699–1715 (2002, 2003)

Rakopoulos, C.D., Giakoumis, E.G.: Review of Thermodynamic Diesel Engine Simulations under Transient Operating Conditions. School of Mechanical Engineering, National Technical University of Athens 2006-01-0884 Copyright ©SAE International (2006)

Jerzy, H.: Emissions from marine engines versus imo certification and requirements of tier 3. Journal of Kones Powertrain and Transport 18(2) (2011)

Dimitrios, T.: Prediction of marine diesel engine performance under fault conditions. Applied Thermal Engineering 20 (2000)

Dissertation

Test bench diesel Engine Wartsila 12ZA40S (Technical Documents) Grandi Motori trieste (September 14, 1998)

Schieman, R.: Technical information. Turbo Magazine VTR 354 TC Map (1992-1996)

ABB Turbocharger Technical Documents

Delphi, Wide Range Oxygen Sensor (2009)

Sebastien, A.: Simulation of the ECU of an Internal Combustion Engine (2011)

Annex

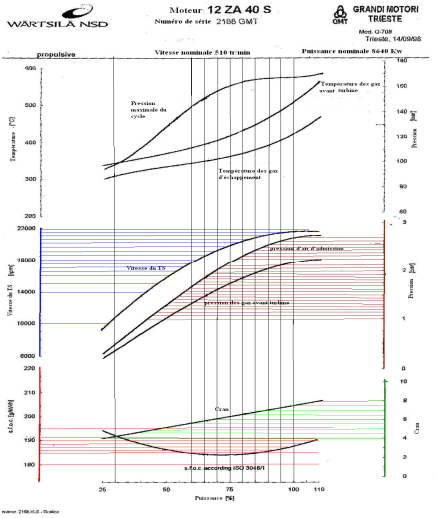

Fig. 1 Test bench of 12 ZAV Engine

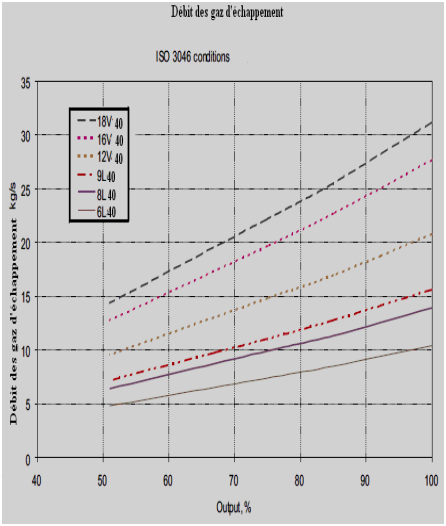

Fig. 2 Flow gas VS $P_{n\%}$ 12ZAV 40 S

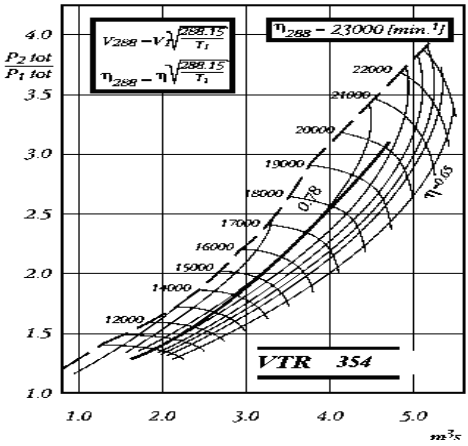

Fig. 3 VTR 354 TC map

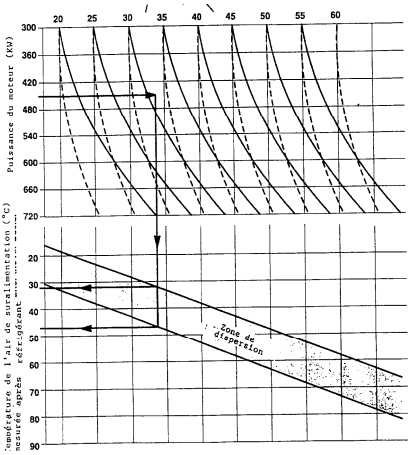

Fig. 4 Air temperature VS Power

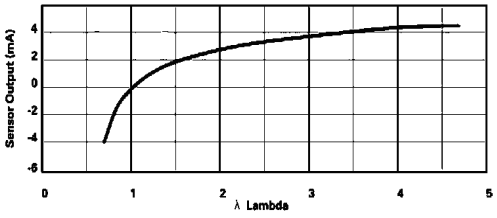

Fig. 5 Lambda probe characteristic curve

Dynamic in Path Planning of a Cable Driven Robot

Mourad Ismail[1], Lahouar Samir[2], and Lotfi Romdhane[1]

[1] Laboratoire de Mécanique de Sousse (LMS)
Ecole Nationale d'Ingénieurs de Sousse,
Université de Sousse, Tunisia
{mourad.smail,lotfi.romdhane}@gmail.com
[2] Laboratoire de Génie Mécanique (LGM)
Ecole Nationale d'Ingénieurs de Monastir,
Université de Monastir, Tunisia
samirlahouar@gmail.com

Abstract. Robot path planning problem is well studied in the literature, whereas the dynamics problem is not so addressed. Indeed, most of the path-planning algorithms are limited to formulate the problem as a geometrical problem. In high acceleration, robots undergo important inertia forces that the path planner has to take into account. The goal of this work is to design a trajectory planner able to take into account the high accelerations to which the cable robot is submitted. The dynamic problem can be formulated as to maintain cable tensions in a well-defined interval that is to say between 0 and 200N in our case. This means that restrictions must be made on the maximum and minimum values of the accelerations and decelerations that limit the maximum speed to be reached by the robot. The planner is composed of three phases. The first consists of finding the path that leads the robot from the initial position to final position while avoiding obstacles, without addressing the dynamic problem. In the second phase the planner interpolates the trajectory as a Spline in order to guarantee the continuity and the derivability of the required velocities. The third phase will then treat the dynamic problem.

Keywords: Under constrained cable-driven robots, Passive serial support, Dynamics modeling, Trajectory planning, Velocity and acceleration constrains.

1 Introduction

Cable-driven robots have recently attracted great interest for many applications due to their promising design. As reported in [1], Albus and his team has suggested the use of wire robots to realize a crane in the Robocrane project [2]. The use of cables gives this robot the possibility to control both translation and rotation. Other robots can be listed as the parallel crane used for shipping trade and proposed by August in [3].Cable robots are usually simple in form and can be classified according to many criteria. The most known classification is based on

M. Haddar et al. (Eds.): *Design and Modeling of Mechanical Systems*, LNME, pp. 11–18.
DOI: 10.1007/978-3-642-37143-1_2

the degree to which the cables determine the pose of the manipulator, so cable robots can be considered as fully constrained or under constrained [4].

In this work we will study a hybrid cable driven robot with a passive serial support. The use of a serial link is proposed by Trevisani in [5] and [6], and we adopted this configuration in order to get more accuracy by adding encoders to the passive arm. In fact, two major issues yet to be solved: the path planning with collision avoidance, and the control of cable tensions so it remains positive and bounded.

Traditionally, path planning methods have been classified into three types of methods that are global methods, local methods and mixed methods. Global methods [7] assume a complete knowledge of the environment. The major drawbacks of such methods are: incapability to deal with dynamic environments, high computational time cost. To overcome these problems, local methods have been proposed. One of the most popular of these methods is the potential field method proposed by Khatib [8] and the method of constraints proposed by B-Faverjon and Tournassoud [9].Mixed methods are a combination of both global and local methods. Other methods have also been proposed, such as the use of neural network proposed by S-Yang [10].

In the next section a dynamic model of the cable robot is given. Then we present the method proposed for collision avoidance. To keep positive bounded cable tensions we have adopted the technique proposed by Trevisani [5] which limits the maximum and the minimum values of the accelerations and decelerations. The original method only considers straight or circular trajectory, in this work it is extended to deal with any trajectory. The generated trajectory and the accelerations and decelerations will be used by the controller to drive the robot toward the goal position and finally we give some results.

2 System Description

Fig. 1 shows hybrid parallel/serial architecture of a cable driven robot that we will introduce in this work.

The end-effector is supported in parallel by two cables that winds around two separate pulleys, and are forced to pass through the two fixed vertices at the top of the base polygon. The end-effector is manipulated by two tensioning actuators that can extend or retract the cables so it can translate in a planar rectangular subset of the workspace. The end-effector is connected to the free end of a passive two-link planar two-degree-of-freedom serial manipulator by means of a revolute joint at the end point.

3 Cable Driven Robot Dynamics Modeling

The model developed in this section ignores Coulomb friction and assumes that the links are rigid and the cables are mass less and perfectly stiff (i.e. the cables inertias and spring stiffness are neglected).

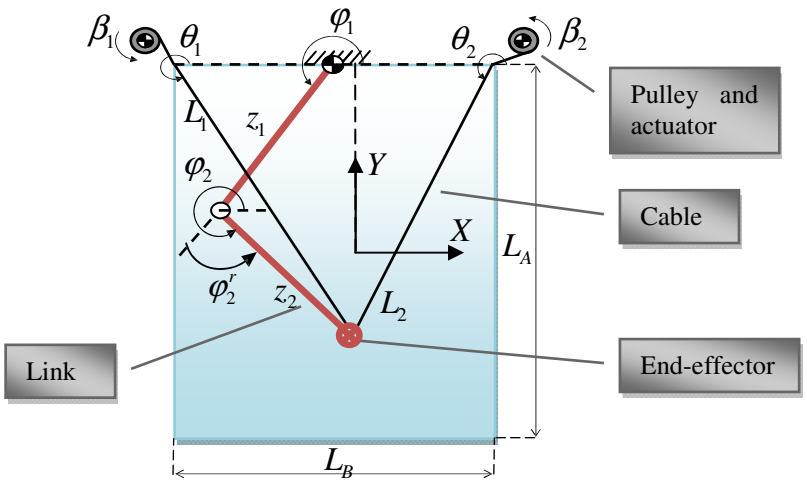

Fig. 1 Cable driven robot with passive serial-link support

The overall system dynamic model is obtained by combining the equations of motion of the three cable driven robot sub-systems: the end-effector, the actuators, and the serial manipulator.

Dynamics Modeling of the End Effectors

$$F_T + F_S - P_e = m\ddot{X} \tag{1}$$

The force F_T exerted by the cables on the end-effector can be computed through the expression:

$$F_T = \begin{Bmatrix} F_{Tx} \\ F_{Ty} \end{Bmatrix} = \begin{bmatrix} -\cos\theta_1 & -\cos\theta_2 \\ -\sin\theta_1 & -\sin\theta_2 \end{bmatrix} \begin{Bmatrix} t_1 \\ t_2 \end{Bmatrix} := ST \tag{2}$$

Dynamics Modeling of the ith Actuator

If a Linear model is adopted for friction; the actuator dynamic equations are expressed by the following matrix relationship:

$$\tau - J\ddot{\beta} - C\dot{\beta} = rT \tag{3}$$

By combining Eq. (1) – (3), the following equation can be obtained:

$$S\tau = rm\ddot{X} + SJ\ddot{\beta} + SC\dot{\beta} - rF_S + rP_e \tag{4}$$

Dynamics Modeling of the Serial Manipulator

The force F_S exerted by the serial manipulator on the end-effectors can be computed by direct application of the Newton–Euler's laws to the two links comprising the serial manipulator.

$$F_S = M_S \ddot{X}_{G2} + I_{NS}\ddot{\phi} + P_m \tag{5}$$

The use of these relations allows getting to the following expression for F_S:

$$F_S = \left(M_S F + I_{NS}\right) J_k^{-1} \ddot{X} + \left[M_S G - \left(M_S F + I_{NS}\right) W\right] \left(J_k^{-1} \dot{X}\right)^2 + P_m \tag{6}$$

The Overall System Equation Can Be Obtained by Combining Eq (4) - (6)

$$S(X)\tau = M_{eqX}(X)\ddot{X} + N_X(X, \dot{X}) + P_X(X) \tag{7}$$

4 Path Planning

In this section we are interested in finding a secure path that takes the robot from the initial position to a desired final position in a minimum time. It means that the robot must evolve toward its goal far from any obstacle, accelerate and decelerate and always maintain positive and bounded cable tensions.

4.1 Collision Avoidance

This method is based on the alternation of two searching modes [11]. The first one is a depth search mode, which is active when the robot is far from the obstacle. The second one is a width search mode, which is active when the robot is near an

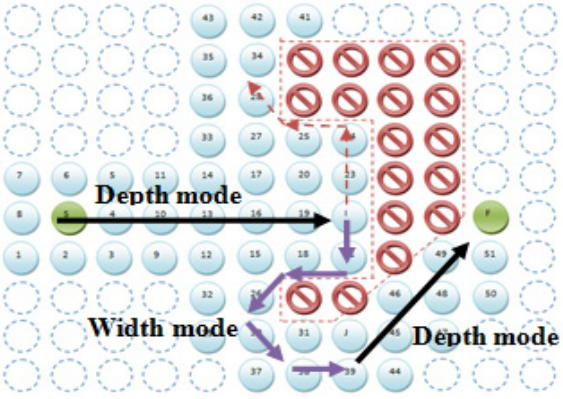

Fig. 2 Generated free collision path from S to F

obstacle and permits to find the best way to avoid an obstacle. Although a grid is needed, it is not necessary to construct it before beginning path-planning. Collision is cheeked only for those nodes in the search path.

We explain the method by using a point robot evolving in a plan with the presence of obstacles.

To achieve smooth trajectory planning, we will use cubic Spline interpolation based trajectory planning method, which is aiming to give us smoother trajectory.

4.2 Dynamic Issues in Path Planning

The cable driven robot dynamic model presented above allows translating these constraints into intuitive limits on the end-effectors path velocity and acceleration. The compact expression of cable can be found by combining Eqs. (1) And (2)

$$T = Z\ddot{X} - K(J_k^{-1}\dot{X})^2 + D \tag{8}$$

In order to get positive and bounded cable tensions, it is necessary that the chosen trajectory always satisfies this inequality:

$$0 \le Z\ddot{X} - K(J_k^{-1}\dot{X})^2 + D \le T_{\max} \tag{9}$$

A useful simplification of the inequality structure can be obtained by explicitly considering the magnitude and the direction of the velocity vector, which is tangent to the path. Let v and a be the magnitude and the direction of the velocity vector, then $\dot{X} = \begin{Bmatrix} v\cos\alpha \\ v\sin\alpha \end{Bmatrix}$ and $\ddot{X} = \begin{Bmatrix} a\cos\alpha - \frac{v^2}{\gamma}\sin\alpha & a\sin\alpha + \frac{v^2}{\gamma}\cos\alpha \end{Bmatrix}^T$.

Depending on the position of the end effector, the radius γ of the path curvature has to be updated. This allows the controller be able to instantaneously compensate the Coriolis forces effects.

5 Trajectory Planning

In this section the trajectories adopted are the ones most employed in industry: those with trapezoidal velocity profile. The desired path is clearly an input of the trajectory planning procedure.

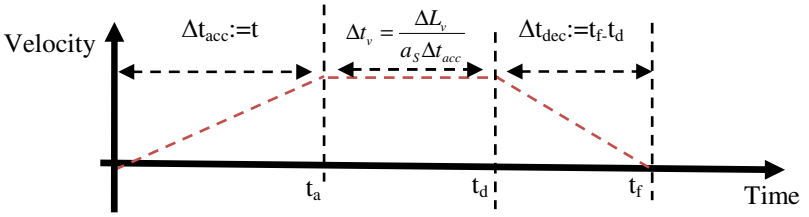

Fig. 3 Trapezoidal velocity profile

The traversal time t_f takes the form:

$$t_f = \Delta t_{acc} + \Delta t_v + \Delta t_{dec} = \frac{L_t + \Delta L_{acc} + \Delta L_{dec}}{\sqrt{2\Delta L_{acc} a_S}} \tag{10}$$

The forces $S(X)\tau$ that the cable has to exert on the end-effector are calculated according to the path generated by the geometric planning algorithm.

For more robust control over the system, the following nonlinear control law is adopted:

$$S(X)\tau = M_{eqX}(X)\left(\ddot{X}_{ref} + K_d \dot{e} + K_p e\right) + N_X(X, \dot{X}) + P_X(X) \tag{11}$$

K_p And K_d are diagonal matrices of the proportional and the derivative gain.

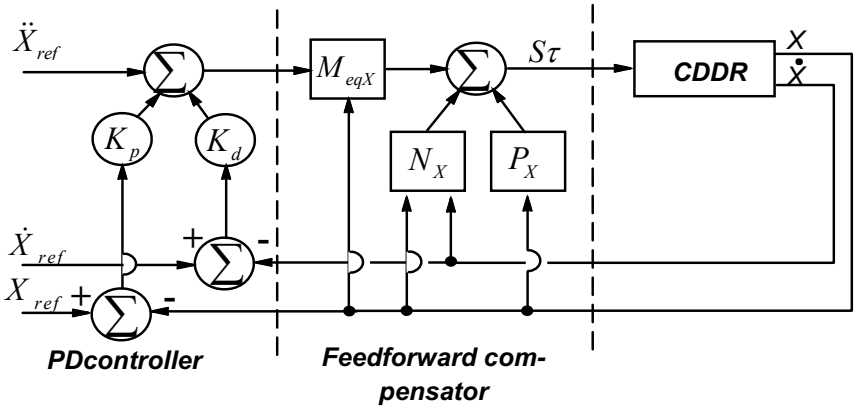

Fig. 4 Feedforward Dynamic Controller

6 Results and Simulations

The coordinate of the starting point and of the target point are, respectively:

[-0.31, 0.41] and [0.2,-0.4]

The coordinate, geometries and dimensions of the obstacles are:

Obstacle1: circle: The radius=0.20m Coordinates of the center: [0.3m, 0.0m].
Obstacle2: circle: The radius=0.20m Coordinates of the center: [0.0m, 0.2m].

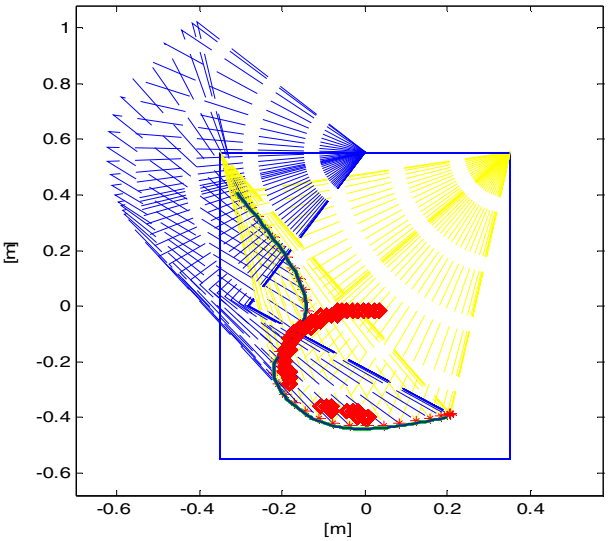

Fig. 5 Spline interpolated free collision path

For the dynamic simulation the acceleration and deceleration are set as follow: as=6.5m/s^2, ai=5m/s^2, Vim= 0.9m/s

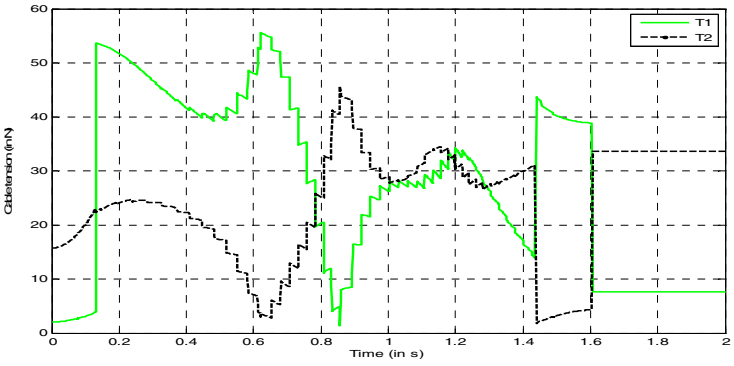

Fig. 6 Cables tensions [in N]

After simulation we get a traversal time t_f: tf= 1.533644s while all cable tensions remains positive and blow 200N. The maximum velocity reachable by the cable driven robot depends in the minimum of the path curvature.

7 Conclusion

In this paper we have demonstrated that it is possible to apply the dynamic approach to complex paths such as the trajectory obtained by the geometric path planning algorithm. So it's possible to maximize the acceleration and deceleration phases. In this case, we can minimize the transversal time needed by the robot to reach its finale position (the goal position).

References

[1] Merlet, J.-P.: Parallel Robots, 2nd edn. Kluwer, Dordrecht (2005)
[2] Albus, J., Bostelman, R., Dagalakis, N.: The Nist Robocrane. J. of Robotic Systems 10(5), 709–724 (1993)
[3] Schoenflies, A.: Beweis eines Satzes über Bewegungsgruppen. Nachrichten von der Königl. Gesellschaft der Wissenschaften und der Georg (15), 495–501 (August 1886)
[4] Ming, A., Higuchi, T.: Study on multiple degree-of-freedom positioning mechanism using wires (part 1) - concept, design and control. International 179 Journal of the Japanese Society for Precision Engineering 28, 131–138 (1994)
[5] Trevisani, A.: Underconstrained planar cable-direct-driven robots: A trajectory planning method ensuring positive and bounded cable tensions. Mechatronics 20(1), 113–127 (2010)
[6] Trevisani, A., Gallina, P., Williams II, R.L.: Cable-Direct-Driven Robot (CDDR) with Passive SCARA Support: Theory and Simulation. Journal of Intelligent & Robotic Systems 46(1), 73–94, doi:10.1007/s10846-006-9043-7
[7] Paden, B., Mess, A., Fisher, M.: Path planning using a jacobian-based free space generation algorithm. In: Proceedings of IEEE International Conference on Robotics and Automation, Scottsdale, Arizona, pp. 1732–1737 (1989)
[8] Khatib, O.: Real-time obstacle avoidance for manipulators and mobile robots. The International Journal of Robotics Research 5(1), 90–99 (1986)
[9] Faverjonet, B., Touranssoud, P.: A local based approach for path planning of manipulators with a high number of degrees of freedom. In: Proceedings of IEEE International Conference on Robotics and Automation, Raleigh, pp. 1152–1159 (Mars 1987)
[10] Yang, S.: Dans le livre, Biologically inspired neural network approaches to real-time collision free robot motion planning. In: Biologically Inspired Robot Behavior Engineering, pp. 143–172. Springer (2003) ISBN 3790815136
[11] Lahouar, S., Ottaviano, E., Zeghoul, S., Romdhane, L., Ceccarelli, M.: Collision free path-planning for cable-driven parallel robots. Robotics and Autonomous Systems 57(11) (November 2009)

Integrating Radial Basis Functions with Modelica for Mechatronic Design

Moncef Hammadi[1], Jean-Yves Choley[1], Alain Riviere[1], and Mohamed Haddar[2]

[1] LISMMA, Supméca, 3 rue Fernand Hainaut 93407 Saint-Ouen, France
moncef.hammadi@supmeca.fr
[2] U2MP, ENIS - University of Sfax, route de Soukra, B.P. 1173, 3038, Sfax, Tunisia
mohamed.haddar@enis.rnu.tn

Abstract. Multi-domain modeling language Modelica is well suited for modeling and simulation of mechatronic systems. However, there are limitations when dealing with mechatronic components, taking into account the coupling between geometry and multi-physics behavior, because Modelica does not support solving of partial differential equations (PDEs). In this paper we present an approach that integrates radial basis functions with Modelica, for solving problems modeled with PDEs. An application of the method to a case of 1D thermal modeling and by comparing results to the finite element method, it is shown that this approach guarantees both fast simulation and accurate results.

Keywords: Radial Basis Functions, PDE, Thermal modeling, Modelica, Mechatronics.

1 Introduction

Mechatronics is a synergistic integration of mechanics, electronics, and information technologies. The main goal of mechatronic design approach is to develop complex systems with a high level of spatial and functional integration of mechatronic subsystems (Janschek 2012). The objective of spatial and functional integration is to minimize space, mass and cost, and in the same time to maximize the number of mechatronic system functions. The development of many mechatronic products is today facing this challenge.

In the automotive field for instance, the obligation to reduce emissions, fuel consumption and cost, on one side, and to integrate more functions for safety, performance and comfort, on the other side, impose to design new integrated complex mechatronic systems such as new powertrains, power modules, micro-electromechanical systems (MEMS) or piezoelectric transducers.

Designers of these complex systems are today facing problems of their optimization, because they have to take into account the interaction between the control system and the multi-physics coupling with geometry of mechatronic components.

M. Haddar et al. (Eds.): *Design and Modeling of Mechanical Systems*, LNME, pp. 19–25.
DOI: 10.1007/978-3-642-37143-1_3

To accomplish successfully this task, new integrated methods and tools are required for fast and accurate simulation of mechatronic design.

Multi-domain modeling softwares, such as those based on Modelica language, are the most common tools for mechatronic modeling and simulation (Tiller 2001). Despite their possibilities to simulate complex systems modeled with differential algebraic equation (DAE), the drawback of these tools, however, is the limitation in resolving partial differential equations (PDE). Other tools such as those based on finite element method (FEM) have better accuracy to design mechatronic components modeled with PDE. Nevertheless, the latter are also limited in mechatronic design. First FEM tools are time consuming mainly when dealing with a mechatronic system with a big number of components. The second limitation is that FEM tools are not supporting control design, which is required in mechatronic design. Consequently new approaches for elaborating accurate models with multi-domain modeling tools are required for mechatronic design.

A new mesh free method for resolving partial differential equations based on Radial Basis Functions (RBF) is currently undergoing fantastic results in many engineering fields, such as fluid dynamics (Kansa1990) or linear and nonlinear mechanics (Tiago and Leitão 2006). The objective of this method is to eliminate the mesh and approximate the solution with a set of random points.

In this paper we present an approach integrating RBF with Modelica language for elaborating compact models for fast and accurate simulation in mechatronic design.

After this introduction, the basic concepts required for integrating RBF with Modelica are presented. Then, an application for integrating Multiquadric RBF with Modelica for thermal modeling is detailed. After that, results are discussed and the paper ends with a conclusion.

2 Basic Concepts of RBF

A radial basis function ϕ is a continuous spline defined as:

$$\Re^+ \to \Re^+, \left\|\vec{x}-\vec{\mu}\right\| \to \phi\left\|\vec{x}-\vec{\mu}\right\|, \tag{1}$$

$\vec{\mu}$ is a set of nodes $(\vec{\mu}_j \in \Sigma,\ j=1,2,...,N;\ \Sigma \subset \Re^d)$, d is the dimension of vectors $\vec{x}$ and $\vec{\mu}$.

ϕ depends upon the distance $r=\left\|\vec{x}-\vec{\mu}\right\|$ separating $\vec{x}$ of the set of nodes $\vec{\mu}$. The distance r is commonly measured using the Euclidean norm.

An approximation function g can be defined by:

$$g(x)=\sum_{j=1}^{N}\lambda_j.\phi\left\|\vec{x}-\vec{\mu}_j\right\|, \vec{x}\in\Re^d, \lambda_j\in\Re \tag{2}$$

A real-valued function $f(\vec{x})$ can be approximated by $g(\vec{x})$ by determining the coefficients λ of the approximation. These coefficients are determined by satisfying the limit conditions together with interpolation conditions which are given by:

$$g(\mu_i) = f(\mu_i), i = 1,...,N \tag{3}$$

To apply RBF for resolving partial differential equations (PDEs), an example will be treated in the next paragraph for solving one-dimensional heat conduction equation.

3 Integrating Radial Basis Functions with Modelica for Thermal Modeling

Considering the one-dimensional heat conduction equation

$$\rho.C_p.\frac{\partial T(z,t)}{\partial t} = k.\frac{\partial^2 T(z,t)}{\partial z^2} \tag{4}$$

Where $\rho[kg/m^3]$ is the mass density of the material, $C_p[J.kg^{-1}.K^{-1}]$ is the specific heat capacity and $k[W.m^{-1}.K^{-1}]$ the thermal conductivity.
With two limit conditions:

$$k.\frac{\partial T(z,t)}{\partial z} = -\frac{P}{A},\ for\ z = L_z \tag{5}$$

and

$$T(0,t) = T_0, \tag{6}$$

and an initial condition

$$T(z,0) = T_i, \tag{7}$$

Where $P[W]$ is the heat flow imposed to one limit ($z=L_z$), $A\ [m^2]$ the surface to which P is applied, $T_0[K]$ is a temperature imposed to the other limit ($z=0$) and $T_i[K]$ is the initial temperature of the material.
The Multiquadric RBF is expressed as:

$$\phi(\| z - \mu_j \|) = \sqrt{(z-\mu_j)^2 + c^2} \tag{8}$$

Parameter c is a positive constant called shape parameter.

The derivatives of ϕ can be easily determined as:

$$\frac{\partial \phi}{\partial z} = \frac{(z-\mu_j)}{\sqrt{(z-\mu_j)^2 + c^2}} \tag{9}$$

$$\frac{\partial^2 \phi}{\partial z^2} = \frac{1}{\sqrt{(z-\mu_j)^2 + c^2}} - \frac{(z-\mu_j)^2}{(\sqrt{(z-\mu_j)^2 + c^2})^3} \tag{10}$$

We can propose an approximation for the temperature:

$$T(z,t) = \sum_{j=1}^{N} \lambda_j(t).\phi(\| z - \eta_j \|) \tag{11}$$

By applying the derivatives to (11) the problem can be easily coded and solved with Modelica language.

4 Results and Discussion

To validate our approach, we consider a simple plate with dimensions (10 mm x 10 mm x 1 mm). The finite element method with Ansys software has been chosen to validate the results generated. A comparison between the thermal model developed using RBF approach (RBF-Modelica) and a default thermal model made using the standard components of Modelica library (Default-Modelica).

Figure 1 shows the finite element model developed for validation. This model is composed of 8804 nodes and 1656 elements. The material considered in this study is copper with the following parameters: ρ= *8960 kg/m3*, *k=384 W/m/K*, *Cp=384 J/kg/K, A=*$10^{-4}m^2$.

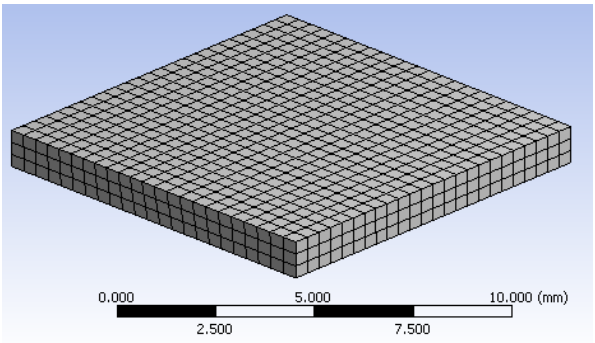

Fig. 1 FEM model with Ansys Workbench

A heat flow rate *P=400 W* is applied to the top face of the plate and a fixed temperature T_0=*30°C* is applied to the bottom face. The initial temperature is T_i=*30°C* and the transient regime is taken into consideration. The FEM simulation is performed over an interval of time of 0.02 second with a step of 2.10^{-4} second, using Ansys WorkBench software. The time of simulation on a normal personal computer is 1min 45 seconds.

Figure 2 shows a comparison of the evolution of temperature on the top face of the plate for the RBF-Modelica model, the Default-Modelica model and the FEM model. The number of nodes used for the RBF-Modelica model is N=10 and the shape parameter is c=0.001.

The figure 2 shows that there is a good correlation between the FEM simulation and the RBF-Modelica simulation. However, the default-Modelica model shows a result of simulation far from the two other simulations.

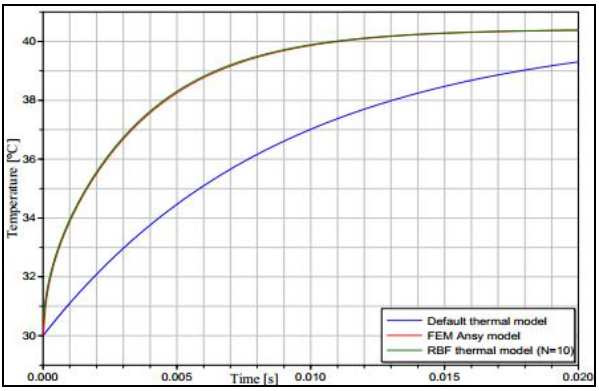

Fig. 2 Comparison of temperature variation: RBF (N=10, c=0.001), Default and FEM

Figure 3 shows the relative error for the default-Modelica and RBF-Modelica (c=0.001) models for different number of nodes N, by comparison to FEM simulation. The figure indicates that the Default-Modelica model has a maximum relative error of 10%, while it is 4% for the RBF model with N=3, the error is less than 1% for RBF (N=5) and only 0.4% for RBF (N=10).

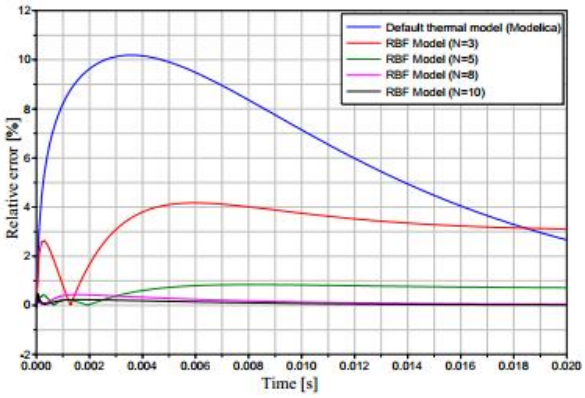

Fig. 3 Relative error depending on number of nodes N

Taking N=10, figure 4 shows the relative error for different shape parameters c. The maximum relative error reaches 1.4% for c=0.0005, 0.4% for c=0.001 and 0.2% for c between 0.0015 and 0.002.

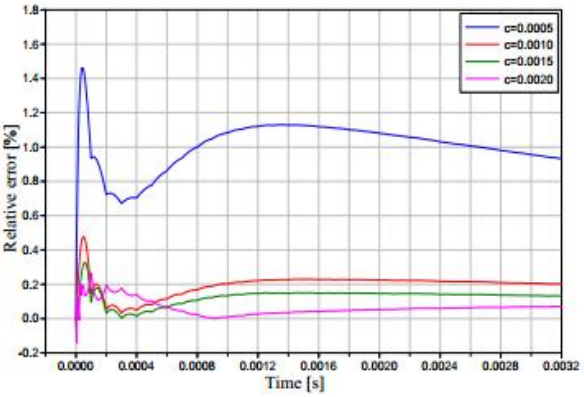

Fig. 4 Relative error depending on shape parameter c

The different results of simulation performed in this study has demonstrated the good accuracy of RBF models integrated with Modelica even for a low number of nodes (N=5).

It should be mentioned that the time of simulation for RBF-Modelica models is only 9 seconds. Therefore, the approach integrating RBF with Modelica guarantees accurate models with fast simulation.

5 Conclusion

An approach integrating RBF with Modelica language has been presented in this paper. Even only the thermal aspect has been considered in this presentation, the proposed approach can be easily applied to other mechatronic components modeled with PDE.

By comparing the proposed approach to finite element method, results show a good trade between accuracy and fast simulation. Therefore the proposed approach can be very important for mechatronic design.

In next works other components will be modeling using this approach taking into account the multi-physics coupling.

Acknowledgements. This work is partially supported by research laboratories LISMMA and U2MP. The authors also gratefully acknowledge the helpful comments and suggestions of the reviewers, which have improved the presentation.

References

Janschek, K.: Mecatronic System Design, Methods, Models, Concepts (2012) ISBN 978-3-642-17530-5, Translated by Kristof Richmond

Tiller, M.M.: Introduction to physical modeling with Modelica. Springer (2001)

Kansa, E.J.: Multiquadric - A scattered data approximation scheme with applications to computational fluid dynamics: II. Solutions to parabolic, hyperbolic, and elliptic partial differential equations. Computers Math. Applic. 19(6-8), 147–161 (1990)

Tiago, C.M., Leitão, V.M.A.: Application of radial basis functions to linear and nonlinear structural analysis problems. Computers & Mathematics with Applications 51(8), 1311–1334 (2006), ISSN 0898-1221, doi:10.1016/j.camwa.2006.04.008

Biomechanical Model of the Knee to Estimate the Musculotendinous Forces during an Isometric Extension

Sami Bennour[1], Nidhal Zarrouk[2], Mohamed Dogui[2],
Lotfi Romdhane[1], and Jean-Pierre Merlet[3]

[1] Laboratoire de Mécanique de Sousse (LR11ES36),
École Nationale d'Ingénieurs de Sousse,
Université de Sousse 4054 Tunisia
{sami.bennour,lotfi.romdhane}@gmail.com
[2] U.R Neurophysiologie de la Vigilance, de l'Attention et des Performances,
Service d'Explorations Fonctionnelles du Système Nerveux,
CHU Sahloul, Sousse, 4051 Tunisia
nidhal.zarrouk@yahoo, mohamed.dogui@rns.tn
[3] Equipe de Recherche COPRIN, INRIA,
Sophia Antipolis 06902 France
Jean-Pierre.Merlet@sophia.inria.fr

Abstract. In this work, we present an improved biomechanical model of the knee and the muscle group involved to ensure the movement of extension of the knee joint, under an external load. The problem of redundancy is solved by presenting the problem as an optimization procedure. In order to identify the best objective function to be optimized, we carried out some experimental tests during which measurements of some tendon forces were performed using EMG sensors.

Keywords: Biomechanical knee model, Extension, Musculotendinous forces, Electromyography, Optimization.

1 Introduction

The determination of musculotendinous forces generated in the joints during a person daily activity has been investigated by several researchers (An et al 1984, Harding et al 1993, Jinha et al 2006). This biomechanical study has several applications in many fields such as medicine, ergonomics and rehabilitation.

Modeling the human joint musculotendinous apparatus can help prevent the onset of diseases, improving the ergonomics of work tools, or preventing the risk of injury associated with movements or sports techniques. To determine these forces, it is possible to make a direct measurement (in vivo) of muscle forces. These techniques were tested on animals (Walmsley et al 1978, Herzog and Leonard 1991), however, they are not widespread in humans (Dennerlein et al 1998, Kursa et al 2005). These experiments are indeed heavy and they require surgery. Most of the research in this field relies on models based on Hill's model presented in 1938

M. Haddar et al. (Eds.): *Design and Modeling of Mechanical Systems*, LNME, pp. 27–35.
DOI: 10.1007/978-3-642-37143-1_4

(Hill 1938, Scott and Winter 1991). These models usually involve three parameters: muscle fiber length, velocity of contraction and muscle activation. The muscle activation may be correlated with the electromyography (EMG) recording (Valero-Cuevas et al 1998).

In this work, we are interested in estimating the level of musculotendinous forces in the knee using an optimization technique along with an experimental validation. In Section 2, we present the adopted biomechanical model of the knee and the muscle groups involved to ensure the movement of extension of the knee joint. The optimization technique to solve this problem is also presented. Sections 3 and 4 present the experimental setup along with the obtained results, which were then confronted with those obtained by simulation. Some concluding remarks are presented in Section 5.

2 Biomechanical Model

For extension the isometric force recovered at the instep is the result of an eccentric contraction of 4 extrinsic flexors: Vastus intermedius (VASINT), Vastus lateralis (VASLAT), Vastus medialis (VASMED) and Rectus femoris (RECFEM).

To determine the musculotendinous forces for different muscles recruited during the extension, we constructed a biomechanical model of the knee involving the skeletal structure and the different muscle groups performing the movements of this joint.

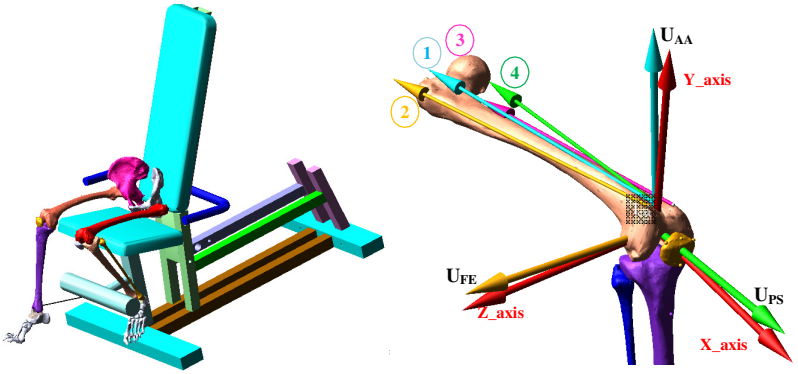

Fig. 1 Different muscles for the extension motion from knee

Different muscles recruited to perform the movements of extension of the knee, are shown by their insert points on different segments of the skeleton model (Fig. 1). The coordinates of the different points of insertions for the muscles and the points of application of external forces are given in a global reference coordinate system (Table 1).

Table 1 Insertion points of the muscle force and external force providing the movements of the knee

N°	Muscle (part)	Symbol	Insertion point (I_i)		
			x (mm)	y (mm)	z (mm)
1	Vastus intermedius	VASINT	-4,33	32,64	0,76
2	Vastus lateralis	VASLAT	2,25	38,58	12,93
3	Vastus medialis	VASMED	5,29	29,86	-16,19
4	Rectus femoris	RECFEM	-4,33	32,64	0,76
			Application point (I_{ext})		
External force			135,20	-316,66	30,00

In this work, an external force is applied at the tip of the tibia and its effect on the different muscles actuating the joint is studied.

The equilibrium of the knee joint under an external force applied at the tip of the tibia yields 3 equations representing the equilibrium of the moments around the three axe x, y and z.

In our case, the musculoskeletal model of the knee is made of 4 flexor muscles for a single degree of freedom in rotation. Therefore, there are an infinite number of combinations of musculotendinous efforts to counterbalance the external force.

Mathematically, one needs to solve three scalar equations with 4 unknowns in case of extension, which yields an infinite number of solutions. Therefore, we will apply an optimization technique to find a solution that minimizes a physiologically meaningful objective function.

Given the redundant nature of the problem, the model will therefore be solved by an optimization technique to find an optimal solution to the problem.

In general, the optimization technique aims to calculate musculotendinous forces that ensure the dynamic equilibrium, while minimizing a given objective function. The objective function aims to identify the way human body recruits the muscle fibers to produce a given task. Several optimization criteria have been devised for this problem. The most common ones are:

$$f_1 = \sum_{i=1}^{4} (F_i)^p \ , \quad f_2 = \sum_{i=1}^{4} \left(\frac{F_i}{A_i} \right)^p \ , \quad f_3 = \sum_{i=1}^{4} \left(\frac{F_i}{(F_i)_{\max}} \right)^p \tag{1}$$

Where the objective functions to be minimized are:

- f_1 is the sum of muscular effort, (Sereig and Arvikar 1989).
- f_2 is the sum of stresses in the muscles, (Crowninschield and Brand 1981).
- f_3 is the normalized sum of muscular effort, (Pedotti et al 1978).

And:

- F_i is the musculotendinous strength of the ith muscle.
- A_i and $(F_i)_{\max}$, are, respectively, the PCSA (The physiologic cross-sectional area) and the maximum force of the ith muscle.
- p, represents the exponent of the objective function: $p=1$ linear, $p=2$ quadratic, $p=3$ cubic, ….

3 Experimental Set-Up

The objective of this experiment is to load the knee of a person and measure simultaneously the external force, using a load cell, and the activity of some muscles, using EMG measurements. Therefore, the physiological data used in this study A_i and $(F_i)_{\max}$, were taken from Table 2 which is relative to a person with a height of $170 \pm 9\ cm$ and weight $80 \pm 15\ kg$ (Edith et al 2010).

Table 2 Physiological properties of the knee's muscles, (Edith et al 2010)

N°	Muscle (part)	symbol	A_i (cm^2)	$(F_i)_{\max}$ (N)
1	Vastus intermedius	VASINT	16.8	1024.2
2	Vastus lateralis	VASLAT	37.0	2255.4
3	Vastus medialis	VASMED	23.7	1443.7
4	Rectus femoris	RECFEM	13.9	848.8

The person was seated comfortably on an experimental chair (Fig. 2). The hip was positioned at 90° of flexion. A leather ankle cuff was placed around the dominant leg just proximal to the malleoli and tightly attached to a load cell (range 0-2500 N; Globus Ergometer, Globus, Codogne, Italy) by an adjustable chain. The chain was adjusted in length so that when the subject performed knee extension, the knee remained in 90° of flexion (0° corresponding to full knee extension). Positions of the hip and knee were confirmed using an universal goniometer.

During the experimental test, the person is asked to push or pull using his knee to get a maximum contraction of the muscles during 5 seconds.

The external force is recorded during each test. The test carried out, aims to assess isometric forces (dynamic equilibrium), where the muscle generated contracts, but maintains its length unchanged.

The signal from the load cell was amplified using a Globus amplifier (Tesys 400, Globus, Codogne, Italy) and fed through an analog-to-digital converter (12 bit) and stored on computer with a sampling frequency of $1000\ Hz$.

Surface EMG activity was recorded in the VASLAT muscle of the dominant thigh during the isometric test by using bipolar surface electrodes (Delsys DE-2.1, Delsys® Inc, Boston, USA) in accordance with the European Recommendations

for Surface Electromyography (Hermens et al 2000). Electromyographic signals were amplified (Common Mode Rejection Ratio, CMRR = 92 dB; input impedance > $10^{15}\Omega$; gain = 1000) using a differential amplifier (Bagnoli-4 EMG System, DelSys Inc., Boston, USA) and filtered to a bandwidth between 20 Hz and 450 Hz, using a band-pass second order Butterworth filter. The signals were analogue-to-digital converted (with 16-bit accuracy in the signal range ± 5 V; Bagnoli-4 EMG System, DelSys Inc., Boston, USA) at a sampling rate of 1000 Hz and stored in a personal computer for subsequent analysis (EMGworks 3.0 DelSys Analysis software, Boston, USA).

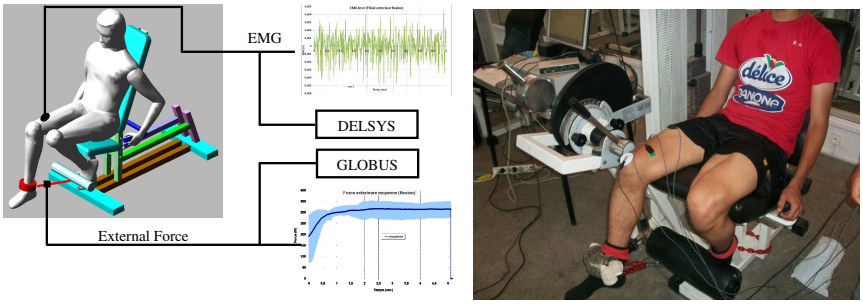

Fig. 2 Experimental set-up. The recording of EMG VASLAT, symbolized here by a black square, was made using the DVR station DELSYS. The recording of force signals was achieved using the acquisition system GLOBUS.

Fig. 3 shows the recorded external force during the test.

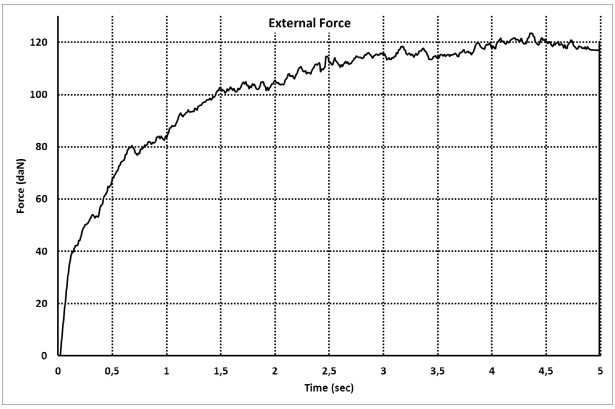

Fig. 3 External force measured during test of isometric extension of the knee

The measured EMG signals were processed by the RMS function (Root Mean Square) given by:

$$EMG_i^{RMS} = \left(\left(1/T \right) \cdot \int_{t-\frac{T}{2}}^{t+\frac{T}{2}} \left(EMG_i^{MAV}(t) \right)^2 \cdot dt \right)^{1/2} \quad (2)$$

$EMG_i^{MAV}(t)$ is the mean absolute value (MAV) of EMG crude signal of the muscle as a function of time. T is the time interval of the processing window.

The measured activity of the muscles can be translated into forces generated by the muscles. The model given by (Louis and Gorce 2009) can be used to convert the above signals into forces in the muscles. This model is given by:

$$F_i = (F_i)_{\max} \cdot (a(t))_i \quad \text{where} \quad (a(t))_i = EMG_i^{RMS} \Big/ \left(EMG_i^{RMS} \right)_{\max} \quad (3)$$

Where:

- EMG_i^{RMS} The RMS from EMG signal for muscle «i» during the test,
- $\left(EMG_i^{RMS} \right)_{\max}$ The maximum of the EMG_i^{RMS} signal for muscle «i».
- $(a(t))_i$ Is the activation of muscle «i».

4 Validation of the Model

Fig. 4 illustrates the musculotendinous forces obtained experimentally by integrating the EMG^{RMS} signals and the forces given by solving the optimization problem using different objective functions.

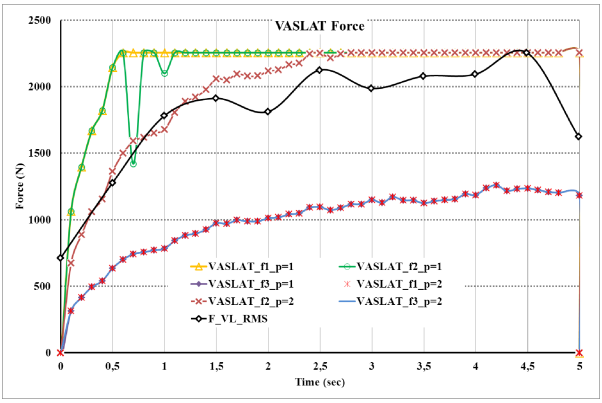

Fig. 4 Muscle force of VASLAT obtained through measured EMG^{RMS} signal in comparison with those obtained by optimization

$$\left(f_1 = \sum_{i=1}^{4} (F_i)^p \; ; f_2 = \sum_{i=1}^{4} \left(\frac{F_i}{A_i} \right)^p \; ; f_3 = \sum_{i=1}^{4} \left(\frac{F_i}{(F_i)_{\max}} \right)^p \right)$$

Comparing the results obtained by simulation to those calculated using the measured EMG^{RMS} signals, for the VASLAT muscle, shows clearly that the linear optimization methods (p = 1), produces forces that are not comparable to those obtained experimentally (Fig. 4). Using the quadratic objective function (p = 2), however, yields better results that are closer to the experimental results. Still, among the three functions tested (Eq.1), only the function « $\sum \left(\frac{F_i}{(A_i)_{\max}} \right)^2$ » yields an acceptable value of the muscular effort of VASLAT, in the case of extension. In conclusion, the three objective functions were tested with a linear ($p = 1$) and nonlinear ($p = 2$) (Pedotti et al 1978, Herzog and Binding 1987) exponents, yielding the following remarks:

The use of linear criteria does not give satisfactory results because they favor muscle activity with the largest PCSA or maximum force (Challis 1997). The activation of another muscle is obtained only when the muscle reaches its physiological limit ($(F_i)_{\max}$). This result is obtained in the extension phase of the knee.

The use of nonlinear criteria yields VASLAT muscle forces (Fig. 4) that are close to the experimentally obtained values.

Therefore, the objective function that will be used to find all the forces in all the muscles is $f_2 = \sum \left(\frac{F_i}{(A_i)_{\max}} \right)^2$.

Fig. 5 shows the values of the musculotendinous forces of the VASINT, VASLAT, VASMED and RECFUM in the case of extension of the knee.

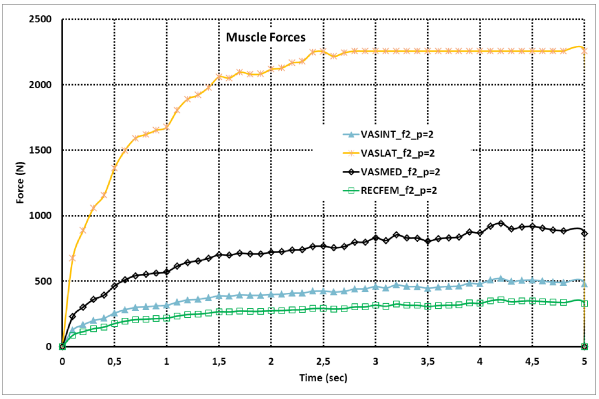

Fig. 5 musculotendinous forces obtained by simulation for extension test by $f_2 = \sum_{i=1}^{4} \left(\frac{F_i}{A_i} \right)^2$

In the case of the extension, four muscles are involved (Fig. 5). In this case also, there is one muscle that is the most active with forces around $2250\ N$, i.e., the Vastus lateralis (VASLAT). A second muscle, Vastus medialis (VASMED), has forces around $900\ N$ (Fig 5). The third is the Vastus intermedius (VASINT), which develops a force of $500\ N$. The last muscle, i.e., Rectus femoris (RECFEM) is developing a force of only $300\ N$.

This analysis shows the role of each muscle in balancing an external force on the tibia.

5 Conclusion

An improved biomechanical model of the knee and the muscle groups involved to ensure the balancing of the extension of the knee joint under an external load. Due to the high number of muscles involved in the knee joint, the problem of solving for the muscle forces was presented as an optimization problem. Several objective functions were tested and an experimental procedure was required to identify the best one. This experimental procedure was limited to the measurement of only one muscle, due to the problem of accessibility. The built biomechanical model, however, allowed us to quantify the forces in all 4 muscles involved in the extension of the knee.

References

An, K.N., Kwak, B.M., Chao, E.Y., Morrey, B.F.: Determination of muscle and joint forces: a new technique to solve the indeterminate problem. Journal of Biomechanical Engineering 106, 364–367 (1984)

Jinha, A., Ait-Haddou, R., Herzog, W.: Predictions of co-contraction depend critically on degrees of freedom in the musculoskeletal model. Journal of Biomechanics 39(6), 1145–1152 (2006)

Walmsley, B., Hodgson, J., Burke, R.: Forces produced by medial gastroenemius and soleus muscles during locomotion in freely moving cats. Journal of Neurophysiology 41, 1203–1216 (1978)

Herzog, W., Leonard, T.: Validation of optimization models that estimate the forces exerted by synergistic muscles. Journal of Biomechanics 24, 31–39 (1991)

Dennerlein, J.T., Diao, E., Mote, C.D., Rempel, D.M.: Tensions of the flexor digitorum superficialis are higher than a current model predicts. Journal of Biomechanics 31, 295–301 (1998)

Kursa, K., Diao, E., Lattanza, L., Rempel, D.: In vivo forces generated by finger flexor muscles do not depend on the rate of fingertip loading during an isometric task. Journal of Biomechanics 38(11), 2288–2293 (2005)

Hill, A.V.: The heat of shortening and the dynamic constants of muscle. Proceedings of the Royal Society of London. Series B, Biological Sciences 126(843), 136–195 (1938)

Scott, S.H., Winter, D.A.: A comparison of three muscle pennation assumptions and their effect on isometric and isotonic force. Journal of Biomechanics 24, 163–167 (1991)

Valero-Cuevas, F.J., Zajac, F.E., Burgar, C.G.: Large indexfingertip forces are produced by subject-independent patterns of muscle excitation. Journal of Biomechanics 31, 693–703 (1998)

Sereig, A., Arvikar, R.: Biomechanical analysis of the musculoskeletal structure for medicine and sports, 1st edn. Hemisphere Publishing Corporation, New York (1989)

Crowninschield, R.D., Brand, R.A.: A physiologically based criterion of muscle force prediction in locomotion. Journal of Biomechanics 14, 793–801 (1981)

Pedotti, A., Krishnan, V.V., Stark, L.: Optimization of muscle-force sequencing in human locomotion. Mathematical Biosciences 38, 57–76 (1978)

Hermens, H.J., Freriks, B., Disselhorst-Klug, C., Rau, G.: Development of recommendations for SEMG sensors and sensor placement procedures. J. Electromyogr. Kinesiol. 10, 361–374 (1999)

Edith, M.A., Samuel, R.W., Richard, L.L., Scott, L.D.: A Model of the Lower Limb for Analysis of Human Movement. Ann. Biomed. Eng. 38(2), 269–279 (2010), doi:10.1007/s10439-009-9852-5

Louis, N., Gorce, P.: Upper limb muscle forces during a simple reach-to-grasp movement: a comparative study. Med. Biol. Eng. Comput. 47, 1173–1179 (2009)

Challis, J.H.: Producing physiologically realistic individual muscle force estimations by imposing constraints when using optimization techniques. Medical Engineering and Physics 19, 253–261 (1997)

Development of Co-simulation Environment with ADAMS/Simulink to Study Maneuvers of a Scooter

Aymen Khadr[1], Ajmi Houidi[2], and Lotfi Romdhane[1]

[1] Laboratory of Mechanics Sousse (LMS),
National Engineering School of Sousse, University of Sousse
khadr.aymen@yahoo.fr, lotfi.romdhane@gmail.com
[2] LMS, Higher Institute of Applied Sciences and Technology of Sousse,
University of Sousse
ajmi.houidi@issatso.rnu.tn

Abstract. To properly assess the dynamic behavior of a two-wheeled vehicle with simulation, it is necessary to stabilize lateral movement by replicating the control actions of a human driver during each integration step. The aim of this work is to develop an environment of co-simulation that consists of a multi-body scooter in interaction with the road using ADAMS and a virtual PID controller implemented in Simulink to mimic the actions of the driver. The driver interacts with the scooter by means of a steering torque applied to the handlebar. The idea is to develop a scheme of a closed loop control capable of generating a steering torque based on the error between the measured scooter-driver system roll angle and the reference roll angle. Simulation examples are presented in this paper to evaluate the performance of the virtual driver developed during a « U »turn maneuver and a lane change maneuver.

Keywords: Scooter, Driver, Multibody Simulation, Dynamic, Control.

1 Introduction

Simulation of multibody systems is an important tool for the design of two-wheeled vehicles, especially in the early stages of the process to evaluate its dynamic behavior while reducing development costs. To simulate the dynamics of a motorcycle, it is necessary not only to develop a model of the bike, but also to define a virtual driver. In fact, the two-wheeled vehicles are inherently unstable and it is not possible to simulate open loop maneuvers as the case of cars.

There are several simulation tools of multibody systems. In this work, in order to design a co-simulation environment for a two-wheeled vehicle, we used the ADAMS software to develop a model of a scooter-driver system interacting with the road. The model of a virtual driver is also designed using Simulink software to replicate the actions of a human driver during maneuvers.

M. Haddar et al. (Eds.): *Design and Modeling of Mechanical Systems*, LNME, pp. 37–43.
DOI: 10.1007/978-3-642-37143-1_5

2 Multibody Model of a Scooter–Driver System

Compared to vehicle modeling, literature in modeling motorcycles is less common. Early models were made of only two rigid bodies (Sharp 1971), recent models, however, can have up to seven bodies (Sharp and Limebeer2001). Complexity is usually necessary for the study of specific behaviors during acceleration, braking, etc ... (Sharp 1976), (Sharp 1994), (Sharp 2001). The model used in this study (Fig. 1a) is composed of seven articulated rigid bodies: the front wheel, the rear wheel, the upper part of the fork including the handlebars, the lower part of the fork, the frame including the lower part of the driver, the swing-arm and the upper part of the driver. The suspensions are taken into account in this model: telescopic fork for the front suspension and swing-arm for the rear suspension.

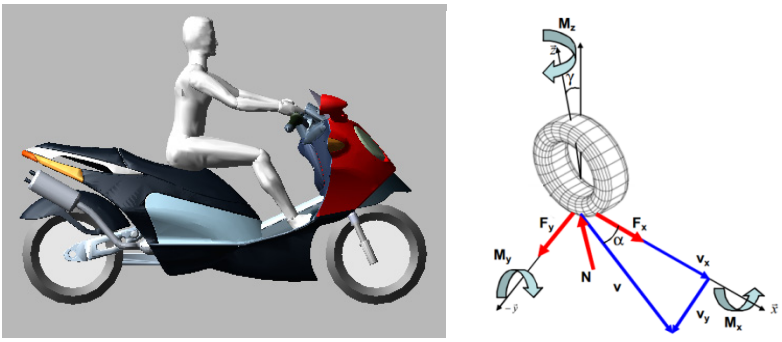

(a) (b)

Fig. 1 (a): Multibody model of scooter-driver (b): Representation of forces and moments due to the contact wheel-ground (Lamri 2008)

In this work, the contact between the tire and the road is modeled by the PAC-MC tire model of ADAMS based on magic-formula (Document ADAMS/Tire). This model calculates the forces Fx and Fy and moments Mx, My and Mz in the point of contact wheel-road (Fig.1b) as a function of: N, longitudinal and lateral slip and angle of inclination with the road.

3 Virtual Driver Model

3.1 State of the Art

Driving from one place to another can be considered as a combination of three tasks: planning the path, follow the planned trajectory and keep the vehicle in a stable condition. Modeling driver was discussed in different ways. There are three interesting approaches in the literature (Hamid 2012), the first is to use PID controllers, the second uses models based on fuzzy logic and neural networks and the

latter approach is the use of hybrid models based on construction of realistic human behavior while driving .

The human driver has the possibility of controlling the two-wheeled vehicle by turning the handlebar, by moving the upper body relative to the seat and by acting on the brake and / or accelerator pedal (Lot et al 2007). It is very difficult to translate these human skills in a virtual driver, which is much simpler. This problem is the subject of several research projects which lead to the conclusion that the stabilization of lateral movement of motorized two-wheelers is essentially ensured by the inclination of the upper part of the driver and the steering torque. In fact, the latter has the most important control input (Cossalter and Lot 2006).

3.2 Stabilization of Roll Motion

In a corner the driver must be able to balance the centrifugal forces acting on the scooter with his weight by leaning inward turn with a roll angle ϕ, as shown in Fig. 2. In a maneuver containing turns, the roll angle is taken as the primary reference for the driver to follow a reference trajectory. This angle is calculated in steady state cornering by the following relationship (1):

$$\phi_{reference} = \arctan\left(\frac{Ma_y}{Mg}\right) = \arctan\left(\frac{u^2 K(s)}{g}\right) \tag{1}$$

Where u is the longitudinal speed of the scooter and K is the curvature of the reference trajectory.

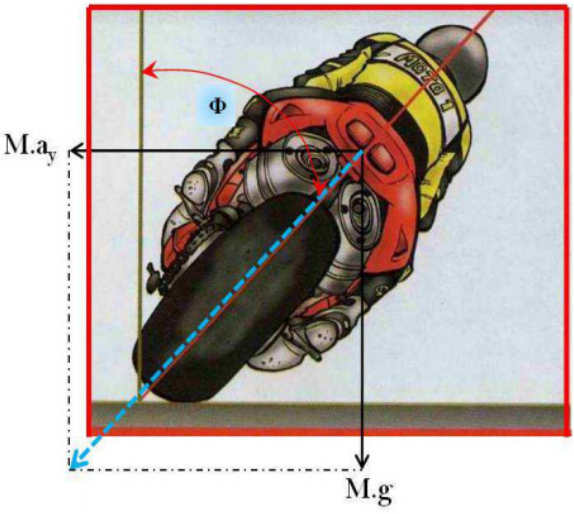

Fig. 2 Equilibrium roll in turns (Hamid 2012)

3.3 Driver Model

In this study the simplifying assumption is that the main scooter is controlled only by means of a steering torque applied on handlebars while the movements of the upper body of the driver relative to the frame are neglected (Cossalter and Lot 2006).In this case, the model scooter-driver is reduced to six rigid bodies by attaching the upper part of the human to the frame. The steering torque τ_B to be applied on the handlebar is calculated with a PID controller, based on the error of the roll angle according to the relationship (2):

$$\tau_B = K_P\left(\phi_{reference} - \phi(t)\right) + K_I\int\left(\phi_{reference} - \phi(t)\right)dt + K_D\frac{d\phi(t)}{dt} \qquad (2)$$

4 Co-simulation ADAMS/Simulink

4.1 Utility

Simulink toolbox of Matlab, offers the possibility of designing any control strategy, both for linear and nonlinear systems (Pulles 2003). In this study, an interaction is made between ADAMS and Simulink. In fact, Simulink is used to simulate the virtual driver as a simple PID controller, which aims the control of the scooter-driver multibody model during driving maneuvers.

4.2 Steps of Implementation

Co-simulation ADAMS / Simulink is developed according to the following steps:

- Establish the multibody model scooter-driver with ADAMS (Fig. 1).
- Identify inputs and outputs for the model. The studied model has a single input which is the steering torque and a single output, which is the roll angle as mentioned in Section 3.
- Export the ADAMS model in Simulink. The result is a block named **adams_sub** (Fig. 3) that contains the complete dynamics of the scooter-driver model with its inputs and outputs.

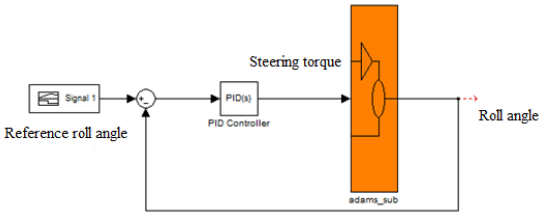

Fig. 3 Control scheme in Simulink

- Build the control scheme using the Simulink block **adams_sub**. The complete control scheme implemented in Simulink is shown in Fig. 3.
- Simulate the model and analyze the results.

5 Simulations and Results

In this section we will present the results of the simulations during two standard maneuvers: the first is a path in the shape of "U" and the second is a simple lane change. The two maneuvers are done with a constant velocity.

5.1 First Maneuver: "U"Turn

This maneuver performed with a constant velocity (15.6 m/s) with a radius of curvature of 50 m. It's done in three phases: Entering into the corner; the desired roll angle increases from 0 rad to the desired roll angle and it remains constant and finally when exiting the turn, the desired roll angle decreases to return 0rad.

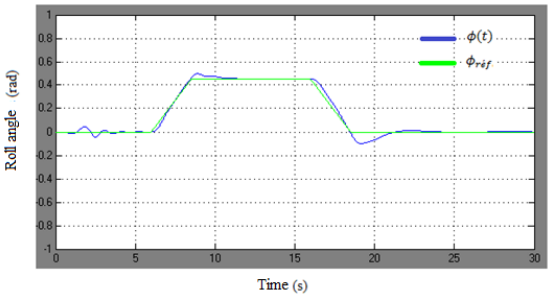

Fig. 4 Evolution of the roll angle of the scooter-driver system in comparison with the reference roll angle during the "U" turn

Fig. 4 shows the evolution of the roll angle of the scooter-driver system compared to the reference roll angle, which defines the trajectory of maneuver to follow. There is a good coincidence between the two curves. This proves that the PID controller could control the scooter with the steering torque applied to the handlebars. During the crossing of the right turn, a steering torque50N.cm is applied on the handlebar as shown in Fig. 5a. We may also note on Fig. 5b that the steering angle increases from 0rad to 0.03rad during the turn. This allows us to say that these parameters are in agreement during the path following of the trajectory.

5.2 Second Maneuver : Lane Change

In this type of maneuvers the driver leans to one side, then quickly straightens the scooter and leans immediately on the other side and always keeping a constant velocity (15.6 m/s). It consists essentially in imposing a sinusoidal roll motion.

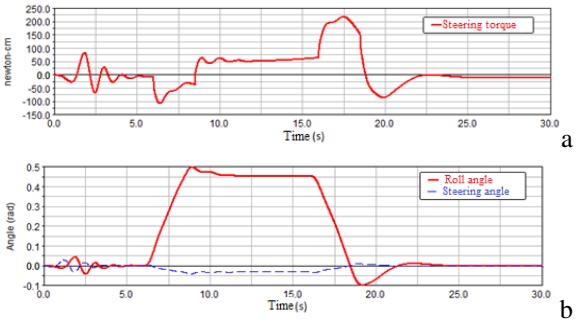

Fig. 5 (a): Steering torque (b): Evolution of the roll angle and the steering angle during the "U" turn

By examining the curves of the reference roll angle and the simulated one, on Fig. 6, we can conclude that the lane change maneuver is performed successfully. The virtual controller developed was able to follow the desired trajectory. We can check the progress of maneuver noticing changes in the steering angle that goes

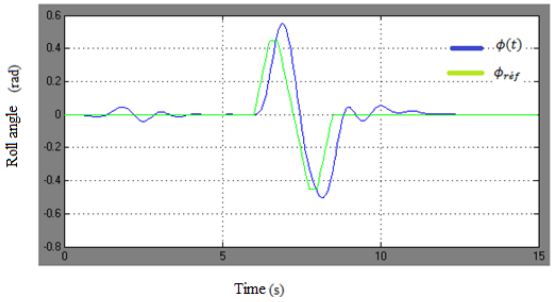

Fig. 6 Evolution of the roll angle of the scooter-driver system in comparison with the reference roll angle during the lane change

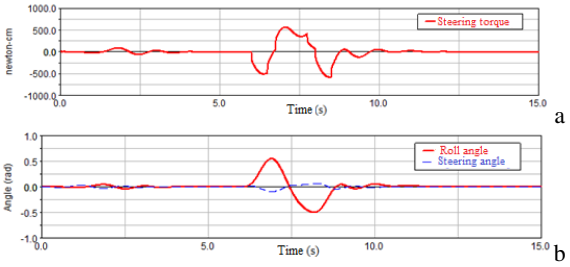

Fig. 7 (a): Steering torque (b): Evolution of the roll angle and the steering angle during the lane change

from 0rad to -0.1rad for the first inclination to the right and a steering torque of 500N.cm (Fig. 7). Similarly for the second phase (left inclination) the steering angle takes a positive value of 0.1rad with a steering torque applied to 500N.cm in the other direction (left).

6 Conclusions and Perspectives

In this paper, an environment of co-simulation has been proposed, consisting of a scooter-driver multibody system developed in ADAMS and a virtual driver model implemented in Simulink. This is in the form of a simple PID controller and aims to stabilize the scooter-driver and follow a desired trajectory. In this study the driver interacts with the scooter by means of the steering torque calculated with the closed loop PID controller based on the error in the roll angle. "U" turn and a lane change were simulated successfully proving that the driver model (PID) can stabilize the scooter and make it follow a predefined trajectory with reduced error.

Taking this study as a starting point, it is necessary to study more complex controllers. The development of a multibody model of a driver fully active will be an interesting area of research. In this case not only the steering torque exerted on the handlebar will be modeled while driving a two-wheeled vehicle, but also the natural movement of the human body and the various interactions with the two-wheeled vehicle.

References

Sharp, R.S.: The stability and control of motorcycles. Jour. Mech. Eng. Sci. 13(5), 316–329 (1971)

Sharp, R.S., Limebeer, D.J.N.: A motorcycle model for stability and control analysis. Multibody System Dynamics 6(2), 123–142 (2001)

Sharp, R.S.: Stability, control and steering responses of motorcycles. Vehicle System Dynamics 35(4-5), 291–318, 334–342 (2001)

Sharp, R.S.: The stability of motorcycles in acceleration and deceleration. In: Inst. Mech. Eng. Conference Proceedings on “Braking of Road Vehicles”, London, pp. 45–50 (1976)

Sharp, R.S.: Vibrational modes of motorcycles and their design parameter sensitivities. In: Vehicle NVH and Refinement. Proc. Int. Conf. Mech. Eng., pp. 107–121. Birmingham, London (1994)

Document ADAMS /Tire, Tire Models

Lamri, N.: Design and implementation of a mechatronic platform dedicated to the simulation of vehicle driving motorized two-wheelers. Ph.D. Thesis Speciaty"Robotics", University of Evry-Val d’Essonne (2008)

Hamid, S.: System for Assistance to Conduct Two-wheeled vehicles Motorized. Ph.D. Thesis, University of Evry-Val d’Essonne (2012)

Lot, R., et al.: Advanced Motorcycle Virtual Rider. In: 20th International Symposium: Dynamics of Vehicles on Roads and Tracks, Berkeley, California, pp. 13–17 (2007)

Cossalter, V., Lot, R.: A non linear rider model for motorcycles. In: FISITA 2006, World Automotive Congress, Yokohama, Japan, October 22–27, Paper n° F20006V075 (2006)

Pulles, R.J.: Controller design for ADAMS models using Matlab/SIMULINK interaction. DCT report 2003.029

Kinematics, Workspace and Singularities Analysis of the 3-UPU Wrist Manipulator

Ahmed Hachem Chebbi[1], Zouhaier Affi[2], and Lotfi Romdhane[3]

[1] Laboratoire de génie mécanique, IPEIG, Sousse, Tunisia
ahmed.h.chebbi@gmail.com
[2] Laboratoire de génie mécanique, ENIM, Sousse, Tunisia
zouhaier.affi@enim.rnu.tn
[3] Laboratoire de mécanique, ENISo, Sousse, Tunisia
lotfi.romdhane@enim.rnu.tn

Abstract. This work deals with the kinematics and singularity of the spherical 3-UPU parallel manipulator. Firstly the structure of the spherical 3-UPU robot is presented. Then the forward kinematic model is developed where the roll, pitch and yaw angles describing the orientation of the mobile platform are given in a closed form. We prove that the forward kinematic problem has eight solutions. Based on the developed model, the singularity of the manipulator is analyzed and we show that the workspace of the spherical 3-UPU manipulator is free of singularity. To illustrate this study some simulations are given for a given 3-UPU architecture.

Keywords: Parallel manipulator, Kinematics, workspace, singularity.

1 Introduction

Parallel manipulators (PMs) have focused a great attention in the last decades for their complementary characteristics with respect to the serial manipulators. Indeed, they exhibit high rigidity, high payload/weight ratio, high dynamic performance but a limited workspace and a low dexterous manipulability. Six degrees of freedom (DOF) PMs have been widely studied. Moreover, recently great attention has been devoted to less than 6-DOF PMs since many applications do not necessarily need six DOFs and they have a relatively simple model. In particular, three DOF robots have been proposed in the literature, which provide pure rotational, pure translational, and a mixed rotational translational motion of the end effector (platform) with respect to the base (Gosselin and Angeles 1989, Hervè and Sparacino 1991, Yang et al. 1995, Tsai 1996, Di Gregorio 2003, Di Gregorio 2004).

This paper focuses on the orientation workspace and the singularity of the 3-UPU spherical parallel manipulator (Di Gregorio 2003).

The paper is organized as follows. In Section 2, the kinematic modeling of the 3-UPU wrist is treated where the pitch and yaw angles presenting the orientation of the moving platform are presented in closed form. Section 3 presents the

M. Haddar et al. (Eds.): *Design and Modeling of Mechanical Systems*, LNME, pp. 45–52.
DOI: 10.1007/978-3-642-37143-1_6

singularity analysis of the manipulator. Section 4 presents a case study of 3-UPU wrist manipulator where we solve the kinematic model and present its work space on joint and operational spaces.

2 Kinematics of the 3-UPU Wrist Manipulator

The 3-UPU spherical wrist manipulator proposed by (Di Gregorio 2003), which features a spherical moving platform connected to a fixed base by three extensible legs of type UPU, where U and P are respectively for universal and actuated prismatic pair (Fig. 1). The universal pair U comprises two revolute pairs with intersecting and perpendicular axes, centered at point B_i, i=1,2,3 in the base and at point A_i, i=1,2,3 in the platform.

In order to have a pure rotation motion of the platform, two conditions have to be fulfilled (Di Gregorio 2003):

- The first three revolute pair axes fixed in the platform (base) must converge at a fixed point.
- In each leg, the intermediate revolute pair axes must be parallel to each other and perpendicular to the leg axis which is the line through the universal joints centers.

The architecture of the manipulator proposed in this paper is shown in Fig. 1. The first revolute joints connected to the base (platform) are orthogonal and intersect at point *P*. Let $\mathbf{S_b}(P,\mathbf{x_b},\mathbf{y_b},\mathbf{z_b})$ and $\mathbf{S_p}(P,\mathbf{x_p},\mathbf{y_p},\mathbf{z_p})$ two reference frames fixed on the base and the platform, respectively (Fig. 1).The $\mathbf{x_b}$, $\mathbf{y_b}$ and $\mathbf{z_b}$ axes ($\mathbf{x_p}$, $\mathbf{y_p}$ and $\mathbf{z_p}$) are along the line PB_i, i=1,2,3, respectively (PA_i).

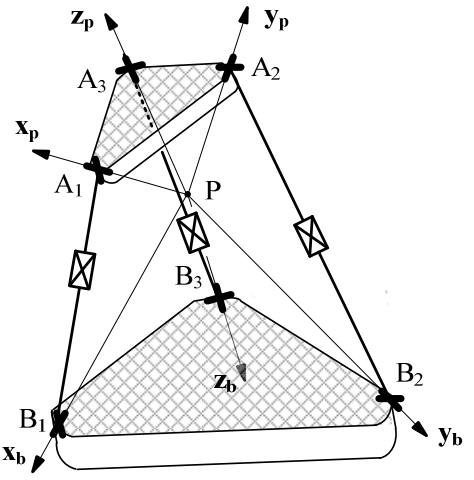

Fig. 1 The 3-UPU spherical wrist manipulator

The loop closure equation of (PB_iA_iP), can be written as follows:

$$\mathbf{PB_i + B_iA_i + A_iP = 0} \tag{1}$$

Let:

$$\mathbf{b_i} = \left[\mathbf{PB_i}\right]_{S_b} \tag{2}$$

$$\mathbf{l_i} = \left[\mathbf{B_iA_i}\right]_{S_b} \tag{3}$$

$$\mathbf{p_i} = \left[\mathbf{PA_i}\right]_{S_p} \tag{4}$$

where $\mathbf{b_i}$ and $\mathbf{l_i}$ are two vectors expressed in the fixed reference frame $\mathbf{S_b}$ and $\mathbf{p_i}$ is expressed in the frame $\mathbf{S_p}$.

Let $\mathbf{Q}$ be the rotation matrix that takes $\mathbf{S_p}$ into $\mathbf{S_b}$, which can be written as:

$$\mathbf{Q} = \begin{bmatrix} c\theta\, c\psi & -c\varphi\, s\psi + s\varphi\, s\theta\, c\psi & s\psi\, s\varphi + c\psi\, s\theta\, c\varphi \\ c\theta\, s\psi & c\psi\, c\varphi + s\psi\, s\theta\, s\varphi & -s\varphi\, c\psi + c\varphi\, s\theta\, s\psi \\ -s\theta & s\varphi\, c\theta & c\varphi\, c\theta \end{bmatrix}_{S_b} \tag{5}$$

where:

c and s are the cosine and the sine of the corresponding angle respectively.
φ,θ and ψ are the rotation angles around $\mathbf{x_b}$, $\mathbf{y_b}$ and $\mathbf{z_b}$ axes respectively (roll pitch and yaw)

Thus, the expression of the vector $\mathbf{p_i}$, i=1,2,3, expressed in the fixed frame $\mathbf{S_b}$ is given by:

$$\left[\mathbf{p_i}\right]_{S_b} = \mathbf{Qp_i} \qquad i=1,2,3 \tag{6}$$

In this case, Eq. (1) yields:

$$\mathbf{l_i} = -\mathbf{b_i} + \mathbf{Qp_i} \qquad i=1,2,3 \tag{7}$$

The vectors $\mathbf{b_i}$ and $\mathbf{p_i}$ contain the geometric parameters of the base and the platform in the local references systems respectively. The vector $\mathbf{l_i}$ is a variable vector, which represents the length and the orientation of the i-th leg.

Squaring both sides of Eq. (7), yields:

$$l_i^2 = b_i^2 + p_i^2 - \mathbf{2b_i^T Qp_i} \qquad i=1,2,3 \tag{8}$$

where l_i, b_i and p_i are the norm of the vectors $\mathbf{l_i}$, $\mathbf{b_i}$ and $\mathbf{p_i}$ respectively.

Replacing the expression of the rotation matrix **Q** in Eq. (8), the following system can be obtained:

$$\begin{cases} -c\varphi\, s\psi + s\varphi\, s\theta\, c\psi = \dfrac{l_1^2 - p_1^2 - b_1^2}{2b_1 p_1} \\ -s\varphi\, c\psi + c\varphi\, s\theta\, s\psi = \dfrac{l_2^2 - p_2^2 - b_2^2}{2b_2 p_2} \\ -s\theta = \dfrac{l_3^2 - p_3^2 - b_3^2}{2b_3 p_3} \end{cases} \tag{9}$$

By solving the third equation of the system (9) given above, two solutions for the angle θ, can be obtained:

$$\begin{cases} \theta = -\arcsin\left(\dfrac{l_3^2 - p_3^2 - b_3^2}{2b_3 p_3}\right) \\ \text{or} \\ \theta = -\pi + \arcsin\left(\dfrac{l_3^2 - p_3^2 - b_3^2}{2b_3 p_3}\right) \end{cases} \tag{10}$$

These solutions can exist, if the following condition is fulfilled:

$$\left|b_3 - p_3\right| \le l_3 \le b_3 + p_3 \tag{11}$$

According to the solutions obtained for the angle θ, the first two equations of equation (9) can be solved:

$$\sin(\psi - \varphi) = \frac{c_1 - c_2}{c_3 - 1} \tag{12.a}$$

$$\sin(\psi + \varphi) = -\frac{c_1 + c_2}{c_3 + 1} \tag{12.b}$$

where c_i, i=1,2,3 are given:

$$c_i = \frac{l_i^2 - p_i^2 - b_i^2}{2p_i b_i} \qquad i=1,2,3 \tag{13}$$

The solution of the set of equations (12), which derived from the two solutions of the angle θ is given by:

$$
\begin{cases} \psi = \dfrac{1}{2}\left(\arcsin\left(-\dfrac{c_1+c_2}{c_3+1} \right) + \arcsin\left(\dfrac{c_1-c_2}{c_3-1} \right) \right) \\ \varphi = \dfrac{1}{2}\left(\arcsin\left(-\dfrac{c_1+c_2}{c_3+1} \right) - \arcsin\left(\dfrac{c_1-c_2}{c_3-1} \right) \right) \end{cases}
$$

$$
\begin{cases} \psi = \pi - \dfrac{1}{2}\left(\arcsin\left(-\dfrac{c_1+c_2}{c_3+1} \right) + \arcsin\left(\dfrac{c_1-c_2}{c_3-1} \right) \right) \\ \varphi = \dfrac{1}{2}\left(-\arcsin\left(-\dfrac{c_1+c_2}{c_3+1} \right) - \arcsin\left(\dfrac{c_1-c_2}{c_3-1} \right) \right) \end{cases}
$$

$$
\begin{cases} \psi = \dfrac{\pi}{2} + \dfrac{1}{2}\left(-\arcsin\left(-\dfrac{c_1+c_2}{c_3+1} \right) + \arcsin\left(\dfrac{c_1-c_2}{c_3-1} \right) \right) \\ \varphi = \dfrac{\pi}{2} - \dfrac{1}{2}\left(\arcsin\left(-\dfrac{c_1+c_2}{c_3+1} \right) - \arcsin\left(\dfrac{c_1-c_2}{c_3-1} \right) \right) \end{cases}
$$

$$
\begin{cases} \psi = \dfrac{\pi}{2} + \dfrac{1}{2}\left(\arcsin\left(-\dfrac{c_1+c_2}{c_3+1} \right) - \arcsin\left(\dfrac{c_1-c_2}{c_3-1} \right) \right) \\ \varphi = -\dfrac{\pi}{2} + \dfrac{1}{2}\left(\arcsin\left(-\dfrac{c_1+c_2}{c_3+1} \right) + \arcsin\left(\dfrac{c_1-c_2}{c_3-1} \right) \right) \end{cases} \tag{14}
$$

Thus, eight solutions exist for one given set of li's.

These solutions can exist, if the following conditions are fulfilled:

$$
-1 \le \frac{c_1+c_2}{c_3+1} \le 1 \;\; ; \;\; -1 \le \frac{c_1-c_2}{c_3-1} \le 1 \;\; ; \; c_3 \neq \pm 1 \tag{15}
$$

3 Singularity of the 3-UPU Spherical Manipulator

In this section, the singularity of the manipulator is analyzed. The Jacobean matrix relates the angular velocity of the moving platform to the velocities of the actuators. Singularities occur when the Jacobean matrix becomes singular. Taking advantage from the closed form of the developed kinematic model of the wrist 3-UPU manipulator, the Jacobean matrix is given by:

$$
\mathbf{J} = \begin{pmatrix} -\dfrac{l_1}{2p_1b_1}(A+B) & -\dfrac{l_2}{2p_2b_2}(A-B) & \dfrac{l_3}{2p_3b_3}(C+D) \\ 0 & 0 & -\dfrac{2l_3}{\sqrt{4b_3^2p_3^2-\left(l_3^2-p_3^2-b_3^2\right)^2}} \\ -\dfrac{l_1}{2p_1b_1}(A-B) & -\dfrac{l_2}{2p_2b_2}(A+B) & \dfrac{l_3}{2p_3b_3}(C-D) \end{pmatrix} \tag{16}
$$

where A, B, C and D are given by:

$$\begin{cases} A=\dfrac{1}{(c_3+1)\sqrt{1-\dfrac{c_1+c_2}{(c_3+1)^2}}} \\ B=\dfrac{1}{(c_3-1)\sqrt{1-\dfrac{c_1-c_2}{(c_3-1)^2}}} \\ C=\dfrac{c_1+c_2}{(c_3+1)^2\sqrt{1-\dfrac{c_1+c_2}{(c_3+1)^2}}} \\ D=\dfrac{c_1-c_2}{(c_3-1)^2\sqrt{1-\dfrac{c_1-c_2}{(c_3-1)^2}}} \end{cases} \tag{17}$$

The determinant of the Jacobean matrix is given by:

$$\det(\mathbf{J})=\frac{2l_1 l_2 l_3 A B}{p_1 b_1 p_2 b_2 \sqrt{4b_3^2 p_3^2-\left(l_3^2-p_3^2-b_3^2\right)^2}} \tag{18}$$

According to Eq. (18), the manipulator is far from singularity in the permissible domain of the length of the three legs.

4 Case Study

In this section, an example of application of the method detailed in the previous section is presented. The given data are the following: The radius of the circle through points B_i, which define the base of the manipulator r_b=100 mm (b_i=122.47 mm); The platform is defined by the coordinates of points A_i, i=1,2,3 (p_i = 80 mm): $[\mathbf{p_1}]_{\mathbf{Sp}} = p_1\,[0\ -1\ 0]^T$; $[\mathbf{p_2}]_{\mathbf{Sp}} = p_2\,[0\ 0\ -1]^T$; $[\mathbf{p_3}]_{\mathbf{Sp}} = p_3\,[-1\ 0\ 0]^T$.

For the given actuators lengths l_1= 150 mm, l_2= 105 mm, l_3= 130 mm, the possible solutions of the kinematic model are shown in Fig. 2. Based to the mounting condition, there are only two solutions can be accepted (solutions 1 and 3).

By satisfying the condition of existence solution for a set of given l_i's (Eqs.(11,15)), the permissible domain of the length of the three legs is determined and shown in Fig. 3. In this permissible domain of the length of the three legs, the workspace of the manipulator is free from singularity. Thus, for each set of l_i, i=1,2,3, the pitch and yaw angles which represent the orientation of the platform with respect to the base is determined and shown in Fig. 4.

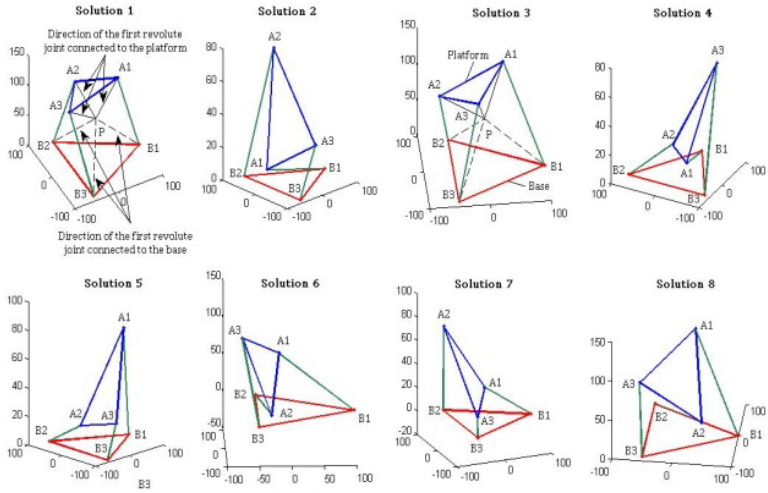

Fig. 2 Different solutions of the orientation of the platform

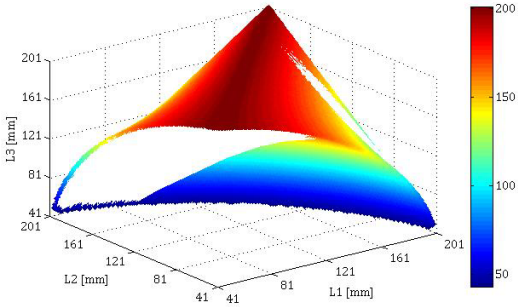

Fig. 3 The permissible domain of the length of the three legs

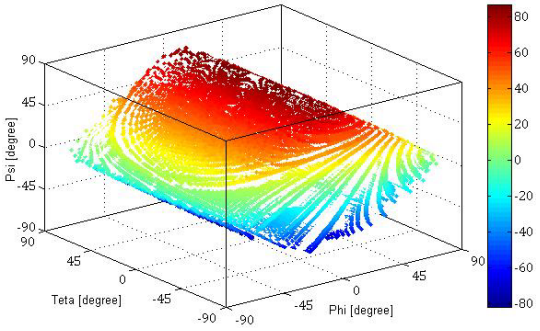

Fig. 4 Pitch and yaw angles for the permissible domain

5 Conclusion

The forward geometric model was derived for the 3-UPU spherical parallel manipulator. We showed that there are eight solutions for the forward geometric model. We also showed that the workspace of the 3-UPU spherical manipulator is free from singularity. A case study shows the efficiency of the method.

References

Gosselin, C., Angeles, J.: The optimum kinematic design of a spherical three degree of freedom parallel manipulator. ASME Journal of Mechanisms, Transmission and Automation in Design, 202–207 (1989)

Hervè, J.M., Sparacino, F.: Structural synthesis of parallel robots generating spatial translation. In: Fifth ICAR International Conference on Advanced Robotics, pp. 808–813 (1991)

Yang, P.H., Waldron, K., Orin, D.E.: Kinematic of a three degree of freedom motion platform for a low-cost driving simulator. Advances in Robot Kinematics, 89–98 (1996)

Tsai, L.W.: Kinematics of three-degrees of freedom platform with three extensible limbs. In: Recent Advances in Robot Kinematics, pp. 401–410. Kluwer, Dordrecht (1996)

Di Gregorio, R.: Kinematics of the 3-UPU wrist. Mech. and Mach. Theory, 253–263 (2003)

Di Gregorio, R.: Statics and Singularity Loci of the 3-UPU Wrist. IEEE Transactions on Robotics 20, 630–635 (2004)

Romdhane, L.: Design and analysis of a hybrid serial-parallel manipulator. Mechanism and Machine Theory 34, 1037–1055 (1999)

On the Kinematics of Spherical Parallel Manipulators for Real Time Applications

Abdelbadia Chaker[1], Abdelfattah Mlika[1],
Med Amine Laribi[2], Lotfi Romdhane[1], and Said Zeghloul[2]

[1] Laboratoire de Mcanique, Université de Sousse-
Ecole Nationale d'Ingnieurs de Sousse, BP 264 Sousse-Erriadh, TUNISIA
{abdelbadi3,abdelfattah.mlika,lotfi.romdhane}@gmail.com
[2] Institut PPRIME, UPR 3346, CNRS - Université de Poitiers - ENSMA,
Bd Pierre et Marie Curie BP 30179, 86962 FUTUROSCOPE CHASSENEUIL, France
{med.amine.laribi,said.zeghloul}@univ-poitiers.fr

Abstract. This paper deals with the computation of the forward and inverse kinematic model of a 3-RRR spherical parallel mechanism (SPM) for a teleoperation solution. The context of real time application is aimed; thus, the determination of the desired solution out of several possibilities, is crucial to guarantee motion continuity. The SPM structure kinematics is then detailed and a strategy, based on Newton Raphson method, is proposed to solve these models. Experimental results are presented to validate the proposed approach.

Keywords: Spherical parallel manipulator, kinematics, real time,teleoperation system, Newton raphson.

1 Introduction

The spherical parallel architecture represents an interesting alternative for applications with a fixed center of motion. The platform of the mechanism is moving over a spherical surface which center coincides with the base reference origin; Different varieties of this mechanism have been studied before. These studies covered a wide range of characteristics such as workspace (Bulca et al., 1999), kinematic analysis (Gosselin and Lavoie, 1993), design parameters optimization (Chaker et al., 2012), singularity (Wang and Gosselin, 2004) and dexterity (Merlet, 2006). However, being a parallel structure, the forward displacement, which calls for the position and orientation of the platform when the actives joints are given, is a difficult problem for which no general procedure has been determined yet. Bai et al. (2009) presented a strategy based on the input-output equation of spherical four bar linkages which yields the eight solutions of SPM model. This method makes possible the identification of all the solution when the mechanism is in a fixed position. In the same context, Bombin et al. (2001) took advantage of the subdivision and convex hull properties of polynomials in Bernstein form to propose a procedure to solve the forward kinematics of the SPM. But this method is not reliable since it depends on the intuition of the researcher when simplifying equations. The presented strategies do

M. Haddar et al. (Eds.): *Design and Modeling of Mechanical Systems*, LNME, pp. 53–60.
DOI: 10.1007/978-3-642-37143-1_7

not consider real time constraints such as the resolution time and the determination of the exact one of the eight solutions in order to guarantee the continuity of the platform movement. In fact, such constraints are very important when passing from theoritical study to practical realisation. In this paper, the problem of the SPM is revisited with the aim of finding a robust method that takes in consideration real time and teleoperation applications constraints . The method is applicable for both forward and inverse displacement of the mechanism. The solution is based on the Newton Raphson method (NRM) that solves the model with consideration of the initial position of the platform. Thus we can guarantee a continuous solution when platform is moving and a reduced time of computation.

2 Teleoperation Context

The context of this work is a teleoperation system for minimally invasive surgery. The expert site is compose by an experimented operator and a haptic device based on a spherical parallel architecture that controls a slave robots operating on the patient. Fig. 1 describes the principle of teleportation. The main constraint of this system is the real time exchange of information related to the position and orientation of every mechanism. Thus, computing these parameters have to be very accurate and respects time conditions.

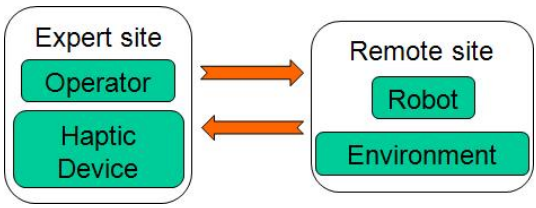

Fig. 1 Teleoperation system

The parallel structure of the haptic device (Fig. 6) presents a complicated kinematic models. In the case of the forward one, one has to solve a nonlinear system. The respect of a predifined time period of 10ms is imposed by the real time constraint. The inverse kinematics presents also the risk of losing the continuity of motion when the problem admits multiple solutions.

3 Kinematics of the SPM

Figure 2.a presents the 3-RRR architecture of the proposed SPM. Three identical legs *A*, *B* and *C* relate the base to the platform. Each leg of the SPM is made out of two links and three revolute joints.The three actuated revolute joints with the base have orthogonal axes $\mathbf{Z}_{1k}$ *(k= A,B and C)*. All the axes of the joints are intersecting in point *O*, the center of motion of the platform $\mathbf{Z}_E$.

Each link is characterized by a constant angle between the axes of its two joints that represents its dimension. Figure 2.b shows the geometric parameters of one leg. The angles α,β, γ are respectively between the first two joint axes, the second and the third one , and between the third joint axis and platform axis .

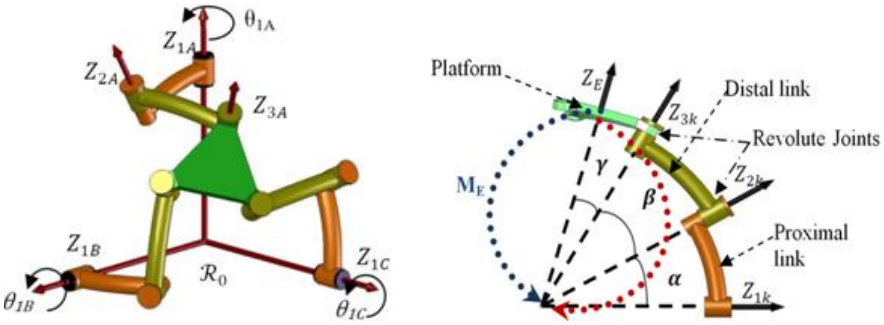

(a) SPM architucture (b) One leg parameters

Fig. 2 Architecture and parameters of the SPM

The three legs of the SPM are identical and the actuated joint axes are located along the base frame axes **X**, **Y**and **Z**, respectively. The workspace of the platform is then the intersection of the workspaces of three legs considered each as a spherical serial kinematic chain.

The motion of the SPM is generated by only revolute joints. The kinematics of the mechanism can be described by the following relation:

$$\mathbf{Z}_{2k} \cdot \mathbf{Z}_{3k} = cos(\beta) \tag{1}$$

Where $\mathbf{Z}_{2k}$ and $\mathbf{Z}_{3k}$ are respectively the axes of the second and the third joint of each leg and detailed as:

$$\mathbf{Z}_{2k} = Rot(\mathbf{Z}_{1k}, \theta_{1k}).Rot(\mathbf{X}_{2k}, \alpha).\mathbf{Z}_{1k} \tag{2}$$

$$\mathbf{Z}_{3k} = Rot(\mathbf{Z}_{1k}, \psi).Rot(\mathbf{X}, \theta).Rot(\mathbf{Z}_E, \varphi).Rot^{-1}(\mathbf{X}_{3k}, -\gamma).\mathbf{Z}_{1k} \tag{3}$$

The $\mathbf{Z}_E$ platform axis is described by the three ZXZ-Euler angles, ψ, θ and φ. θ_{1k} and θ_{2k} are, respectively, the joint variables of the revolute joint and the cylindrical intermediate joint of leg k (k= A,B and C) .The axes $\mathbf{X}_{2k}$ and $\mathbf{X}_{3k}$ are given respectively by $\mathbf{X}_{2k} = \mathbf{Z}_{1k} \times \mathbf{Z}_{2k}$ and $\mathbf{X}_{3k} = \mathbf{Z}_{2k} \times \mathbf{Z}_{3k}$.

The system of three equations **F** resulting from applying equation (1) for the three legs of the mechanism can be exploited for both forward and inverse displacement.

3.1 Forward Kinematics

The forward displacement determines the posture of the platform defined by the Euler angles when knowing the active joints parameters θ_{1k}. The operational vector of parameters $V = [\psi, \theta, \phi]^T$, are the three ZXZ-Euler angles of the platform, representing the orientation of the platform with respect to the base.

Applying the equation 1, the forward kinematics consists on solving the following system:

$$\mathbf{V} = f(\mathbf{q}) -> \begin{cases} \psi = f_1(\theta_{1A}, \theta_{1B}, \theta_{1C}) \\ \theta = f_2(\theta_{1A}, \theta_{1B}, \theta_{1C}) \\ \varphi = f_3(\theta_{1A}, \theta_{1B}, \theta_{1C}) \end{cases} \tag{4}$$

As for all parallel mechanisms,this forward kinematics is a non linar system combining polynomial trigonometric parameters. This make very difficult the resolution of the system and the determination of the platform position. Usual methods are not efficient in this case even with a powerful computing capacity.

3.2 Inverse Kinematics

The inverse model of the SPM is easier to obtain, it yields the actuators angles on the base $[\theta_{1A}, \theta_{1B}, \theta_{1C}]$ corresponding to a given platform position.

$$\begin{cases} A_1 cos(\theta_{1A}) + B_1 sin(\theta_{1A}) + C_1 = 0 \\ A_2 cos(\theta_{1B}) + B_2 sin(\theta_{1B}) + C_2 = 0 \\ A_3 cos(\theta_{1C}) + B_3 sin(\theta_{1C}) + C_3 = 0 \end{cases} \tag{5}$$

The inverse kinematics seems to be easier to solve than the forward one. Equations (6) can also be written by using the trigonometric tan-half identities. Which yields a polynomial problem that can be computed easily.

$$\begin{cases} A'_1 T_1^2 + B'_1 T_1^2 + C'_1 = 0 \\ A'_2 T_2^2 + B'_2 T_3^2 + C'_2 = 0 \\ A'_3 T_3^2 + B'_3 T_3^2 + C'_3 = 0 \end{cases} \tag{6}$$

where T_i are respectively $tan(\frac{\theta_{1k}}{2}), i = (A, B, C)$

However, this system admits eight possible solutions. The difficulty is in identifying the correct configuration that ensures no change in the aspect and the continuity of movement.

3.3 Jacobian Matrix

The jacobian matrix can be obtained by differentiating Eq. (1) with respect to time. The obtained equation can be written as:

$$\dot{\mathbf{Z}}_{2k}\mathbf{Z}_{3k} + \mathbf{Z}_{2k}\dot{\mathbf{Z}}_{3k} = 0 \tag{7}$$

with $\dot{\mathbf{Z}}_{2k} = \theta_{1k}\mathbf{Z}_{1k} \times \mathbf{Z}_{2k}$ et $\dot{\mathbf{Z}}_{\mathbf{3k}} = \boldsymbol{\omega} \times \mathbf{Z}_{3k}$

$\boldsymbol{\omega}$ is the angular velocity of the end effector..

For the whole manipulator and in a matrix form, we can write:

$$\boldsymbol{\omega} = \mathbf{J}\dot{\mathbf{q}} = \mathbf{A}^{-1}\mathbf{B}\dot{\mathbf{q}} \tag{8}$$

where $\mathbf{J}$ is the jacobian matrix and $\mathbf{B}$ a 3×3 diagonal matrix:

$$\mathbf{B} = Diag\left[\mathbf{Z}_{1A} \times \mathbf{Z}_{2A} \cdot \mathbf{Z}_{3A}, \mathbf{Z}_{1B} \times \mathbf{Z}_{2B} \cdot \mathbf{Z}_{3A}, \mathbf{Z}_{1C} \times \mathbf{Z}_{2C} \cdot \mathbf{Z}_{3C}\right] \tag{9}$$

And

$$\dot{\mathbf{q}} = \left[\dot{\theta}_{1A}, \dot{\theta}_{1B}, \dot{\theta}_{1C}\right]^T \tag{10}$$

$$\mathbf{A} = \left[(\mathbf{Z}_{3k} \times \mathbf{Z}_{2k})^T\right] \tag{11}$$

4 Proposed Algorithm

The proposed algorithm is based on NRM (Galantai, 2000) for solving equations numerically. It is based on the simple idea of linear approximation. he solution of the problem is sought in the neighborhood of an initial gess designed by the user. In the case of SPM kinematics and for our real time teleoperation, this strategy can ensure a rapid convergence to the desired solution especially for a nonlinear system of equations such as the ones obtained for forward displacement problem of the parallel structure. In fact, the forward displacement will be solve in a limited number of iterations since the initial guess meets with the last orientation (ψ, θ, ϕ) of the platform. In the case of the inverse kinematics, this strategy helps to avoid the multiple solution problem by choosing the nearest posture to the initial one. The figure 3 presents the flow chart of the algorithm. Depending on the treated problem (direct or inverse), the algorithm is initialized with the known parameters. The system F describing the kinematics is generated and the Jacobian matrix is computed. A loop calculation is then launched whith an initial gess vector $\mathbf{S_0}$ corresponding to

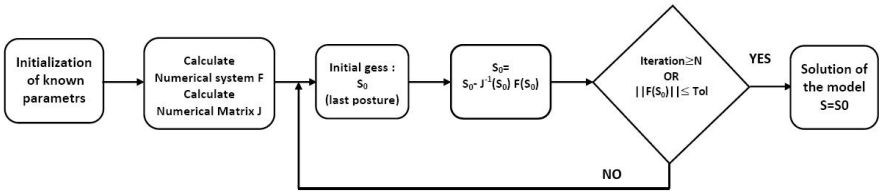

Fig. 3 Newton raphson flow chart

the last position of the mechanism. For every i^{th} loop, the initial gess is set to taking the value of the $i^{th} - 1$ loop solution. The final solution **S** is retained if a maxima of iterations N is reached or it satisfies a predifined precision **Tol** fixed in our case to 10^{-4} which represents the quadratic error of the solution.

5 Results

The implementation of the NRM to solve both forward and inverse kinematics of the SPM, made possible the determine precisely and in a continuous way the motion of the SPM . as an example to validate the algorithm we have chosen an arbitrary trajectory for every active joint illustrated in the Fig. 4. The aim is to evaluate the ability of the algorithm to manipulate real time movements and its response time caracterized by the number of iterations needed touconverge to a solution.

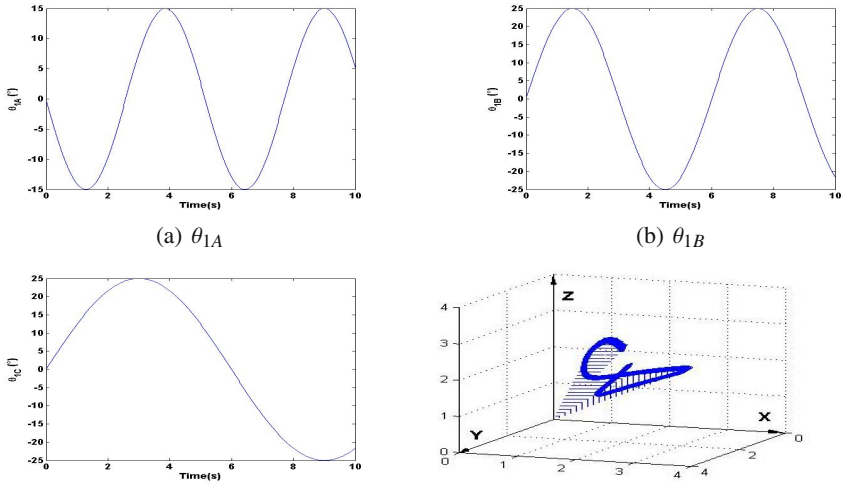

(a) θ_{1A} (b) θ_{1B}

(c) θ_{1C} (d) Trajectory

Fig. 4 Actuator Joints angles injected to the algorithm (a,b,c) and the trajectory generated(d)

Fig. 5 represent the results of the Euler angles describing the platform orientation. The profile of each is continuous which confirms the performance of the strategy in preserving the aspect of the movement. Fig. 5.d shows that a maximum of two iterations was needed to solve the system. This means that the trajectory is followed instantly while keeping the imposed precision of 10^{-4} degree for every parameter.

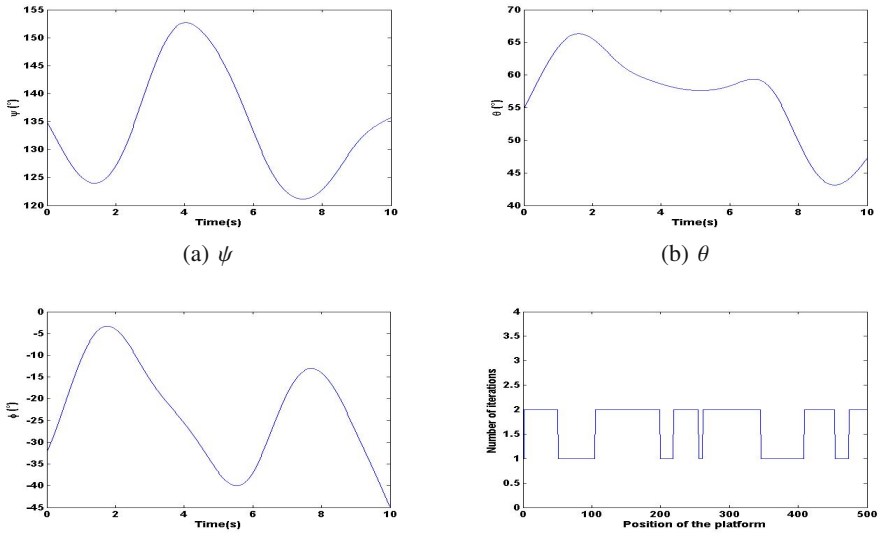

(a) ψ (b) θ

(c) φ (d) Number of iterations

Fig. 5 Resulting Euler angles from the algorithm (a,b,c) and the number of iterations(d)

Fig. 6 First prototype of the SPM

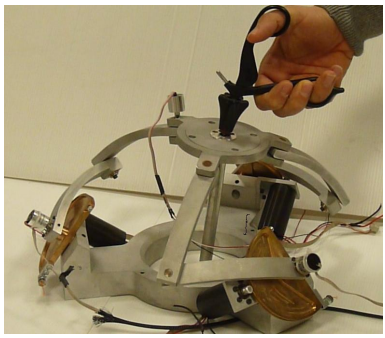

6 Conclusion

An algorithm based on the NRM used to solve kinematics of an SPM is presented. The strategy is well suited for teleoperation context since it is applicable for both forward and inverse kinematics with similar performance. This makes intersesting its implementation for a telesurgery haptic device (Fig. 6. The kinematics of the SPM was then revisited and a formulation of the strategy was proposed. The results on an arbitrary trajectory of the manipulator confirmed its capacities to determine the exact solution over the eight possibilities. The respect of the real time constraint is garanteed. The performances of this method are also validated on the prototype of the haptic device realized on lab.

References

Bai, S., Hansen, M.R., Angeles, J.: A robust forward-displacement analysis of spherical parallel robots. Mechanism and Machine Theory 44(12), 2204–2216 (2009)

Bombin, C., Ros, L., Thomas, F.: On the computation of the direct kinematics of parallel spherical mechanisms using bernstein polynomials. In: Proceedings of IEEE International Conference on Robotics and Automation, ICRA, vol. 4, pp. 3332–3337 (2001)

Bulca, F., Angeles, J., Zsombor-Murray, P.: On the workspace determination of spherical serial and platform mechanisms. Mechanism and Machine Theory 34(3) (1999)

Chaker, A., Mlika, A., Laribi, M.A., Romdhane, L., Zeghloul, S.: Synthesis of spherical parallel manipulator for dexterous medical task. Frontiers of Mechanical Engineering 7(2), 150–162 (2012)

Galantai, A.: The theory of newton's method. Journal of Computational and Applied Mathematics 124(12), 25–44 (2000)

Gosselin, C.M., Lavoie, E.: On the kinematic design of spherical three-degree-of-freedom parallel manipulators. The International Journal of Robotics Research 12(4), 394–402 (1993)

Merlet, J.P.: Jacobian, manipulability, condition number, and accuracy of parallel robots. Journal of Mechanical Design 128(1), 199 (2006)

Wang, J., Gosselin, C.M.: Singularity loci of a special class of spherical 3-DOF parallel mechanisms with prismatic actuators. Journal of Mechanical Design 126(2), 319 (2004)

Towards the Integration of Safety Analysis in a Model-Based System Engineering Approach with SysML

Faïda Mhenni[1], Nga Nguyen[2], and Jean-Yves Choley[1]

[1] LISMMA – SUPMECA, 3 rue Fernand Hainaut,
93400 Saint-Ouen, France
{faida.mhenni,jean-yves.choley}@supmeca.fr
[2] Laris – Eisti, Avenue du Parc,
95000 Cergy Pontoise, France
nn@eisti.eu

Abstract. Mechatronic systems are complex systems involving knowledge from various disciplines such as computer science, mechanics, electronics and control. Model-based system engineering is an efficient approach to cope with the increasing system complexity. It covers specifying, designing, simulating and validating systems and is very useful for the design of complex systems since it helps better manage the complexity while enhancing consistency and coherence. This approach allows errors to be detected as soon as possible in the design process, and thus reduces the overall cost of the product. Integrating safety concerns from early design stages, within the MBSE approach helps the designer to consider safety aspect during system architecture synthesis and reduce the number of iterations and design changes. This paper presents a step towards the integration of safety within the MBSE approach. SysML is chosen as a modeling language because it offers unified communication semantics to the multidisciplinary collaborating team involved in the design of complex systems. A case study illustrates the proposed approach.

Keywords: safety analysis, SysML, MBSE.

1 Introduction

Nowadays manmade systems are getting more complex, achieving more functions and thus involving an increasing number of components and new technologies. Components of different disciplines such as actuators, sensors, software are interacting together in a synergic way. In such interactively complex systems, there are many branching paths among components making the interactions unpredictable to system designers and users. Therefore, complex systems are error prone and safety critical since errors could lead to accidents with potentially catastrophic effects. Normal Accident Theory (NAT) explains that, when a technology becomes sufficiently complex and tightly coupled, accidents become inevitable and therefore in a sense they become 'normal' (Perrow 1981).

M. Haddar et al. (Eds.): *Design and Modeling of Mechanical Systems*, LNME, pp. 61–68.
DOI: 10.1007/978-3-642-37143-1_8

Consequently, the design of such systems is challenging. Firstly, the increasing complexity of manufactured systems makes their development and safety analysis more difficult and big efforts are required to manage the complexity, maintaining coherence and consistency through the development, and deal with numerous requirements relevant to multiple domains. Moreover, safety critical systems must be certified according to continuously more rigorous safety regulations before commercialization. In addition, sharp industrial competitiveness obliges industrials to shorten time to market and reduce development costs. Communication among the engineering team working together is also challenging. In fact, engineers from different fields and with different technological backgrounds cooperate together during the design process. This usually leads to misunderstanding and confusion.

Model-Based System Engineering (MBSE) approach is required to manage the complexity, enhance consistency and allow modeling and simulation of the whole system. A unified language to model and specify the system will remedy to the communication problem; SysML, the semi-formal systems modeling language seems very appropriate for us and is adapted in our work.

2 Related Work

As manufactured systems began to be more widely used, an as manmade system cannot be perfect and are subject to different kind of malfunction, – caused either by design errors, human errors, component failure or any other direct cause or combination of contributing events – many research works focused on system safety. The first efforts were noted in the military domain leading for instance to the military standards (MIL-STD-1629A , MIL-STD-882D). The aim of such standards is to help designers in identifying potential hazards and the appropriate corrective actions. Safety analysis techniques can be split into two categories: qualitative and quantitative approaches. Qualitative methods try to find the causal dependencies between a hazard on system level and failures of individual components, while quantitative methods aim at providing estimations about probabilities, rates and severity of consequences. Many techniques are proposed for this purpose and are extensively described in (Ericson 2005). These safety analyses are usually performed separately with independent tools. Consequently, they occur late in the design process when the design is already finalized and thus, miss the opportunity to influence design choices and decisions (Sharvia and Papadopoulos 2010).

The purpose of our work is to provide a methodology to integrate safety analysis early in the design stage, when the first design models are available. The proposed methodology is based on pertinent semi-formal models built using SysML. The end goal of this work is to automate parts of the safety analysis process and, consequently, both reduce the time and cost and improve the quality of the

system safety studies. The methodology allows system engineers to perform early validation of system safety requirements in the design process. In the scope of this paper, the preliminary work of identifying relevant information from design models and then using it to perform safety analysis is presented.

Dubois (Dubois 2008) proposed to directly include safety requirements in the design process with SysML. To respect safety standards, the triplet requirement models, solution models and validation and verification (V&V) models are isolated. For this purpose, a SysML profile respecting safety standards called RPM (Requirement Profile for MeMVaTEX) was developed. The requirement stereotype of SysML is replaced by the MeMVaTEX requirement, by adding various properties such as "*verifiable*", "*verification type*", "*derived from*", "*satisfied by*", "*refined by*", "*traced to*", etc. In this work, traceability is assured between requirement models, between requirement and solution models, and between requirement and V&V models by using these properties. However, only the integration of safety requirements is considered in this work but safety analysis techniques (from which safety requirements are derived) are performed separately.

Another attempt more complete is proposed by P. David et al. (David 2009, Cressent et al. 2010, David et al. 2010) work on the generation of an FMEA report from system functional behaviors written in SysML models, and on the construction of dysfunctional models by using the AltaRica language in order to compute reliability indicators. In their methodology called MéDISIS, they start with the automatic computation of a preliminary FMEA. The structural diagrams, namely Block Definition Diagram (BDD) and Internal Block Diagram (IBD), and the behavioral diagrams such as Sequence Diagram (SD) and Activity Diagram (AD) are analyzed in detail to give an exhaustive list of failure modes for each component and each function, with their possible causes and effects. Then the final FMEA report is created with help from experts in the safety domain. To facilitate a deductive and iterative method like MéDISIS, a database of dysfunctional behaviors is kept updated in order to rapidly identify failure modes in different analysis phases. The next step of their work is the mapping between SysML models and AltaRica data flow language, so that existing tools to quantify reliability indicators such as the global failure rate, the mean time to failure, etc. can be used directly on the failure modes identified in the previous step.

The work of David and his team is currently one of the most advanced research works about the integration of SysML and safety analyses.

3 Safety Analysis Integration in an MBSE Approach with SysML

System engineering approach aims at realizing a system that satisfies customer needs. It focuses on defining customer needs and required functionality and then proceeds with design synthesis and system validation (INCOSE). To support systems engineering approach a tool must be able to model system requirements,

behavior and structure and ensure consistency between these different views. SysML can represent the different aspects of systems (Friedenthal et al. 2009):

- Requirements and their relationships to other requirements and to other modeling elements like components, test cases etc.
- Function-based, message-based (scenarios) and state-based behavior.
- Structure by modeling composition, and interconnection and interactions between components.
- Constraints on the physical and performance properties.

It also supports allocations between these different aspects, enhancing consistency and coherence between element models and making change impact evaluation easier.

The rich modeling capabilities of SysML made it a good candidate to support MBSE approach. This OMG standard is being widely used in both industrial and academic projects (a few examples can be found in (Wölkl and Shea 2009, Cressent et al. 2011, Piques and Adrianarison 2012) because it provides a consistent, well-defined, and well-understood language to communicate the requirements and corresponding designs among engineers. The system model performed with SysML contains relevant information to support safety engineers in performing safety analyses from the early design phases.

Usually a design process begins with requirement definition and analysis. In this phase, the already known safety requirements are captured in the SysML model. In the second phase, system functions are identified from functional requirements and one or more functional architectures are defined and compared. Once a list of functions is available, functional hazard assessment can be performed in order to identify failure modes of each function and then the effects of each failure. Functions are thus classified according to their criticality and safety requirements are derived in order to eliminate risks or bring them to an acceptable level. These requirements specify allowable failure rates such as failures resulting in catastrophic effects are unlikely to occur. The requirements model is then updated and the whole process iterates until a satisfactory functional model is established. Then components are allocated to functions to define the physical structure of the system. These components shall satisfy the safety requirements derived from the functional hazard analysis. Component based safety analysis techniques, like Fault Tree Analysis, can then be applied based on the system architecture performed in SysML. Fault propagation cans then be deduced and allowed failure probabilities are distributed on different components in order to satisfy quantitative safety requirements. The requirements are accordingly updated with new safety requirements and new induced functions may be added. The whole process shall be iterated again to assess system safety with the new changes and evaluate their impact on both performance and behavior of the system. The whole process can be summarized in Fig. 1.

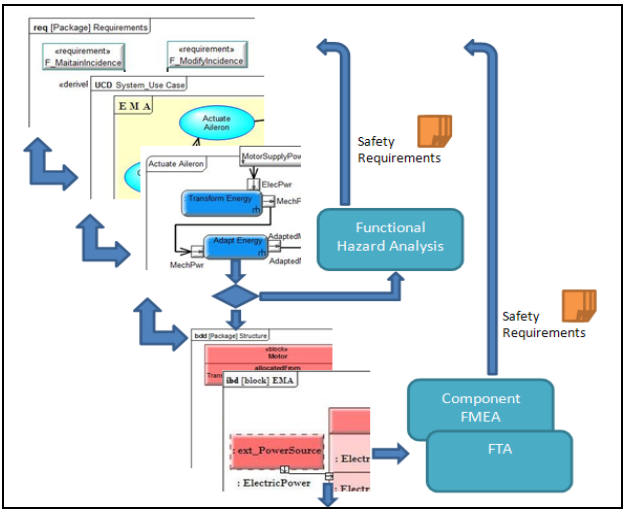

Fig. 1 Integration of safety analysis techniques in a SysML based MBSE Process

4 A Case Study

In this section, it will be shown how SysML model can be used for safety analysis in order to improve consistency and take safety aspects in consideration from the early design stages. The case study addressed in our paper is the wheel brake system of a fictitious aircraft described in the ARP 4761 standard – Appendix L (SAE-ARP 4761-1996).

First, requirements are captured within SysML. Then, functions are derived from functional requirements and captured within the SysML model. Main functions are then decomposed in sub-functions. An extract of the brake down of the aircraft functions is given in Fig. 2. At this early stage, safety analysis can already begin with analyzing functions. SysML functions model gives a list of functions that is helpful for safety engineers. In our example, an aircraft Functional Hazard Analysis (FHA) is performed to identify safety critical functions. The "Decelerate Aircraft on Ground" is identified as being safety critical since its failure could lead to catastrophic effects like the aircraft leaving the runway or crashing the buildings or equipment on the airport (SAE-ARP 4761-1996). "Decelerate Aircraft on Ground" function is broken down into sub-functions and is achieved by a number of aircraft sub-systems. Among these subsystems, the wheel brake system, which is the subject of our study, is the most influencing in decelerating the aircraft.

Safety requirements are derived to bring the effects of identified failure modes to acceptable levels. These requirements shall be satisfied by the physical system being developed. The choice of the system components and architecture is influenced by safety aspects resulting in less iteration and design changes.

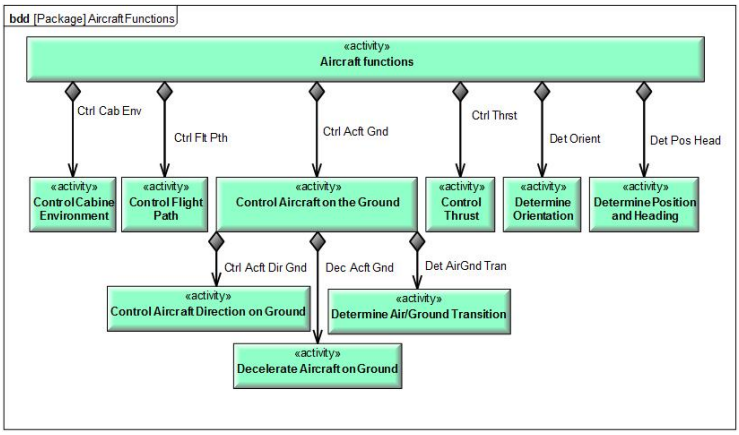

Fig. 2 Extract of aircraft level functions brake down

The wheel brake systems shall satisfy the following requirement: "*The wheel-braking system shall be able to stop the aircraft safely in the landing phase, at high speeds and on different runway surfaces and climate conditions*".

Thus, the architecture of the wheel brake system must be reliable and fault tolerant to minimize the risk of failure. Thus the wheel braking system is designed with redundant components: it is composed of two redundant hydraulic lines, a normal line that is first activated and an alternate one that is activated when the normal chain is inoperative. Each of the two systems has an independent power source. A supplementary power source, an accumulator, is added as an emergency power source (mandatory for the wheel-brake system in aircraft (Moir and Seabridge 2001)). It provides the braking system with hydraulic power when all the other power sources are inoperative.

The different flow exchanges between components are given in Fig. 3 via a SysML Internal Block Diagram. For the sake of simplicity, the selection valve is not shown in this diagram. The selection valve is inserted across the two lines and checks the availability of power, i.e. hydraulic pressure above the threshold, on each of the two lines. The annunciating system feeds back the BSCU system with the state of the hydraulic lines. The BSCU system itself feeds back the high level control unit with the state of the entire wheel brake system.

Analyzing the interactions among system components, the failure propagation among components can be easily deduced and the Fault Tree built. The fault Tree detailing the "unannunciated loss of all wheel brakes" is given in Fig. 4.

Fault tree is used to analyze fault propagation through components. It can also be used for a quantitative analysis by allocating probabilities to different events.

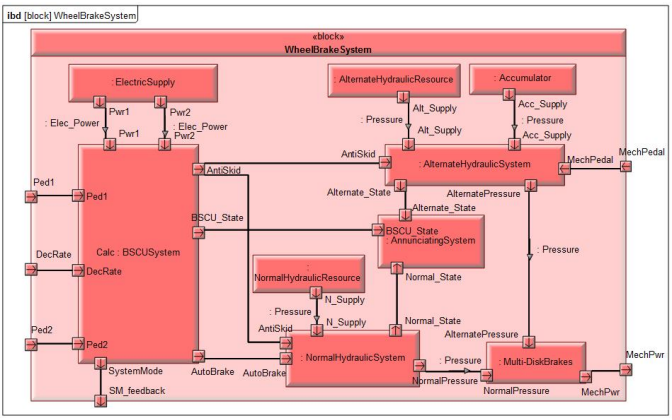

Fig. 3 Internal model of the wheel brake system

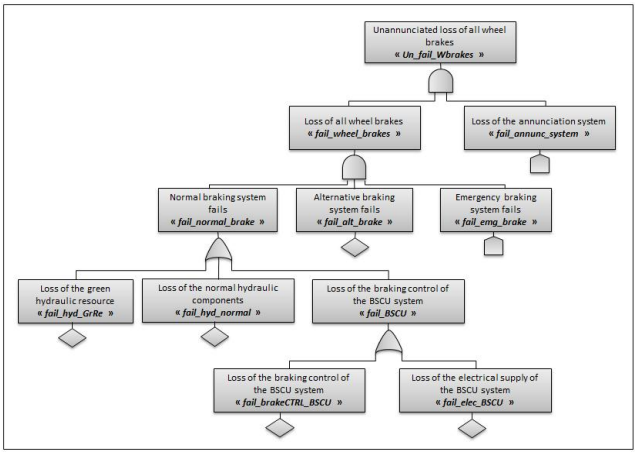

Fig. 4 Fault Tree for "unannunciated loss of all wheel brakes" failure

5 Conclusion

This work is a contribution to the integration of safety analysis within SysML based MBSE approach. It was shown how SysML models can help in performing safety analysis by providing the information needed in a structured way. A case study was presented to illustrate the proposed approach.

In future works, the extension of SysML to support automatic generation of safety analysis datasheets will be considered. Automatic generation helps enhancing coherence and reduces gaps in the design process consequently reducing design errors as well as time and cost.

References

MIL-STD-1629A, Procedure for performing a failure mode, effects and criticality analysis (1980)

MIL-STD-882D, Standard practice for system safety (2000)

Cressent, R., David, P., Idasiak, V., Kratz, F.: Increasing reliability of embedded systems in a SysML centered MBSE process: Application to LEA project. In: Workshop on Model Based Engineering for Embedded Systems Design, M-BED, vol. (1) (2010)

Cressent, R., Idasiak, V., Kratz, F.: Prise en compte des analyses de la sûreté de fonctionnement dans l'ingénierie de système dirigée par les modèles SysML. Génie Logiciel, 33–39 (2011)

David, P.: Contribution à l'analyse de sûreté de fonctionnement des systèmes complexes en phase de conception: application à l'évaluation des missions d'un réseau de capteurs de présence humaine. PhD thesis, Université d'Orléans (2009)

David, P., Idasiak, V., Kratz, F.: Reliability study of complex physical systems using SysML. Reliability Engineering and System Safety 95(4), 431–450 (2010)

Dubois, H.: Gestion des exigences de sûreté de fonctionnement dans une approche IDM. Journées Neptune (5) (2008)

Ericson, C.A.: Hazard Analysis Techniques for System Safety. John Wiley & sons (2005)

Friedenthal, S., Moore, A., Steiner, R.: A practical Guide to SysML. The Systems Modeling Langage. Morgan Kaufmann Publishers (2009)

Moir, I., Seabridge, A.: Aircraft Systems, Mechanical Electrical and Avionics Subsystems Integration, 2nd edn. Professionnal Engineering Publishing (2001)

Perrow, C.: Normal accident at Three Mile Island. Society 18(5), 17–26 (1981)

Piques, J.-D., Adrianarison, E.: SysML for embedded automotive systems: lessons learned. In: Embedded Real Time Software and Systems ERTS, Toulouse, France (2012)

SAE-ARP 4761-1996 Guidelines and methods for conducting the safety assessment process on civil airborne systems and equipment. ARP-4761

Sharvia, S., Papadopoulos, Y.: Integrating compositional safety analysis and formal verification. In: Petratos, P., Sarrafzadeh, M. (eds.) Strategic Advantage of Computing Information Systems in Enterprise Management, pp. 181–201 (2010)

Wölkl, S., Shea, K.: A computational product model for conceptual design using SysML. In: Proceedings of the ASME 2009 International Design Engineering Technical Conferences & Computers and Information in Engineering Conference (2009)

Modeling and Simulation of Micro EDM Process

Maher Barkallah, Hichem Hassine, Jamel Louati, and Mohamed Haddar

Mechanics Modelling and Production Research Unit (U2MP)
University of Sfax, Sfax Engineering School (E.N.I.S.),
B.P. 1173-3038-Sfax – Tunisia
bark_maher@yahoo.fr

Abstract. In contrast to Robust Design applications, the simulation of a mechatronic system including both mechanical and electrical parts requires a different strategy for the investigation of its robustness. Differences mainly results from interactions between the mechanical and the electrical part of the mechatronic system. Micro Electrical Discharge Machining (μEDM) is good example for mechatronics application. This paper presents an approach to evaluate robustness of mechatronic comfort systems. At the outset, this study revolves around modeling of the various constitutive blocs of the machine through the appliance of the 'Matlab/Simulink' as well as analyzing the strength of this model by resorting to the same software programme of simulation . Having gone through the phase of simulation, the main outcomes of this experience where noticed at the level of the parameters defining the drilling such as the gap and the position of the electrode.

Keywords: Micro-EDM process, Electro Discharge Machining, simulation, robustness, mechatronic system.

1 Introduction

There is a vast demand in the production of microstructures by non-traditional method such us micro-electroerosion (Micro -EDM). Micro-EDM process is based on the thermoelectric energy generated the workpiece and an electrode. It is an efficient machining process to obtain micro-metal hole with various advantages resulting from its characteristics of non-contact and thermal process. Pulse discharges occur in a small gap between the work piece and the electrode and between the removing the unwanted material from the parent metal through the process of melting and vaporization.

Despite the fact that the electro erosion process has not taken definite shape in the previous researches that have been conducted so far, we can affirm that both production and quality of the surface have always been one of the major arenas of investigation for researchers .Nevertheless, the study of the strength as well as the fiability of the machine may give rise to a wide range of findings and innovations. Since this study has been conducted through the application of a mechatronic

M. Haddar et al. (Eds.): *Design and Modeling of Mechanical Systems*, LNME, pp. 69–77.
DOI: 10.1007/978-3-642-37143-1_9

system, the µEDM has figured out a variety of shortcomings for the mastering control and optimatisation purposes.

Studies conducted in this context have laid the emphasis upon these four major issues of improvement which are respectively:

- The etincelle aspect: certain works which have taken into account of the energy of the impulsion are at the basis of the µEDM.
- Passive dynamics (Imai and al.) these works take into account all sorts of dynamics and certain erosion conditions.
- Active dynamics (Osenbruggen and al.): is the domain that has been covered the least as it require an electronic back ground and algorithms of adapted regulation and adjusted parameters. Thus, constructors tend to keep secrets about at the level of the core of the machine.
- The precision aspect (Masaki and al.)

This study intends to propose some of the improvement for commanding the µEDM procedure through analyzing the strength of the represented via a mecatronic model gathering both electronic and mechanic features.

This paper is structured as following a modeling of the µEDM: is first presented followed by a simulation that will lead us ultimately to a host of results that will be investigated and a range of perspectives that are sprung from the experiences and applications conducted.

2 Modeling

To understand and analyze the phenomena occurring in micro-EDM, a model desorbing the behavior of an EDM machine is developed. This model will help analyzing the robustness of the mechatronic system to fully exploit the material removal by EDM in the case of micro-drilling.

In this section we first describe the model and its implementation in Matlab Simulink. Next, we present a simulation of the parameters involved in micro-EDM. From this configuration, we different parameters are varied by simulations and explain their influence in the process is investigated.

2.1 Description of the Model

The global model consists of four blocks shown in Figure 1. The symbols used in the block diagrams, are the standards used by the simulation software Matlab-Simulink. The reference machining is drilling. We therefore modeled the process based on this type of machining. In the following, the main blotches are defined:

- Block **"Servo"**

This block represented in Figure 2 transmits position setpoints, for adjusting the distance of the gap as a function of the voltage part -electrode. The Compr which varies between 0 and 255 V whose role is to adjust the gap. The higher this value

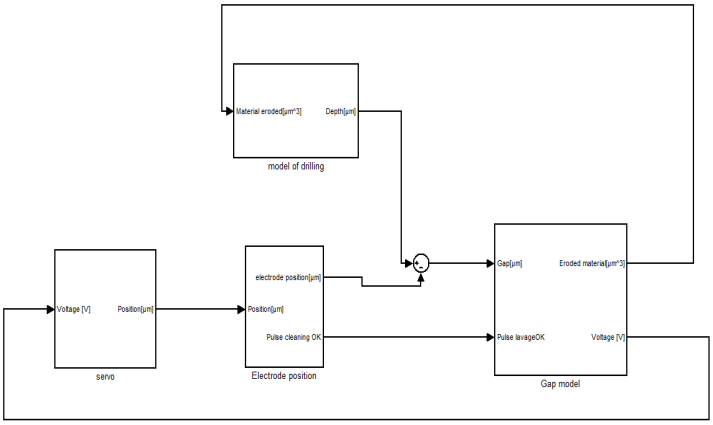

Fig. 1 Bloc scheme of the modeling process µEDM

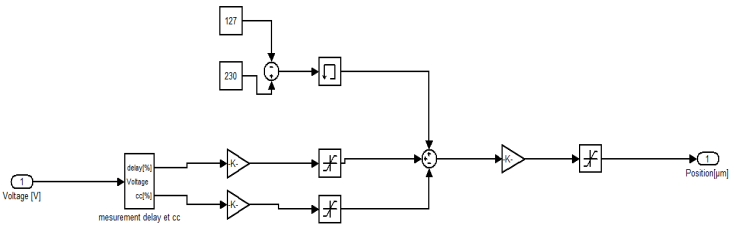

Fig. 2 Block "Servo"

is small over the electrode approaches the workpiece. The gain is a parameter that defines the nervousness of the enslavement of the gap. The last block, ' set Transmission' allows the transmission of results from an interpolator.

- Block **"positioning of the electrode"**

The block represented in Figure 3, is responsible for positioning the electrode. It includes the transfer function of the robot and the position controller. To ensure cleaning of the gap zone, a backward movement of the electrode of a magnitude greater than 2µm generates a pulse wash: the signal "Pulse Cleaning Ok". This signal resets the variable of contamination which is the percentage of eroded material found in the zone of the gap.

- The block **"model of the gap"**

Figure 4 shows the modeling process µEDM. The block "generator breakdown and" simulates the pulse generator and conditions allowing a spark erosion. The latter depend on the Gap and contamination of the dielectric Pulse Contam. The two values calculated by this block are the volume of material eroded and the gap voltage.

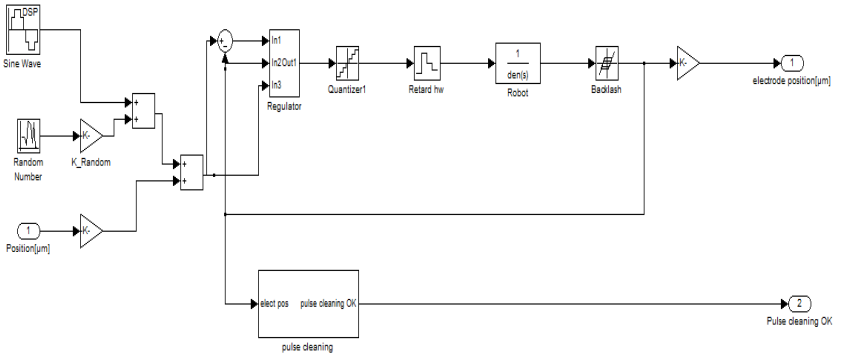

Fig. 3 Block "positioning of the electrode"

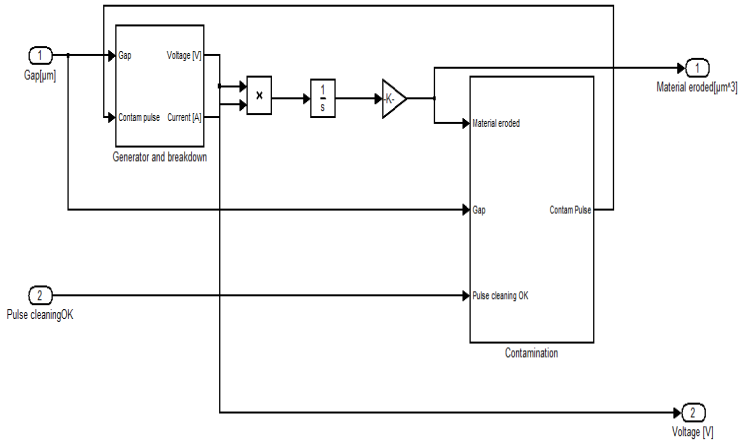

Fig. 4 Model of the gap

The block "contamination" determines the percentage of the eroded material in the volume of dielectric between the electrode and workpiece (Fig. 5). This percentage depends on the washing and speed, and the material torn during discharge.

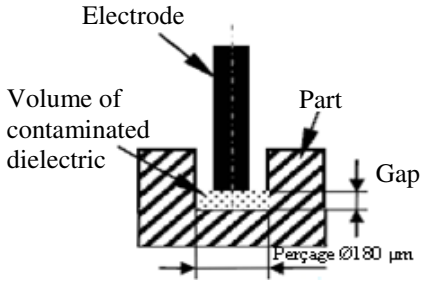

Fig. 5 Representation of the volume of contaminated dielectric during a drilling

- The block **"model of drilling"**

Transforms the volume of eroded material into a vertical displacement of the drill diameter dependent.

3 Simulations

In this section we present some simulations from the model described above, different parameters are varied successively to show their influence on the process. The reference machining for our work is micro-drilling with a diameter of about 180µm. Therefore the process is simulated based on this type of machining. The electrode which is responsible of this task is made of tungsten with a diameter of 149µm. The relaxation generator is modeled by an RC circuit for the charging and discharging of a capacitor. Using an oscillator, we can vary the pulse time and the standing time noted.

The simulation of this generator was carried out under the following conditions: The pulse energy is set by the energy contained in the capacitor C = 5nF. The discharge of capacitor occurs when the electrode-part distance corresponds to the distance of claque. The resistance Rd = 10Ω is the channel resistance during the erosive discharge. Using an oscillator, it is possible to vary the pulse on-time t_e as the pulse off-time noted t_{off} through a resistor Rc = 40Ω and with a signal voltage of 250 V square amplitude (Figure 6).

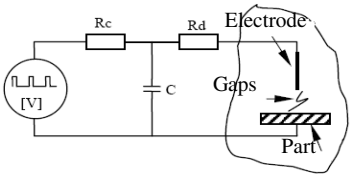

Fig. 6 Generator relaxation

The graphs in Figures 7 and 8, represent the voltage and current simulated by the model as a function of time. This current increases to a constant value (5.25 A), and then there is a reset to 0 to ensure the cleanup phase. This rotation depends on the pulse duration and dead times are controlled from the oscillator providing the ignition voltage.

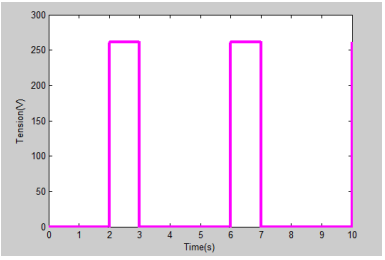

Fig. 7 Evolution of the voltage u=f(t)

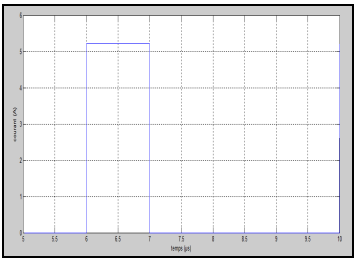

Fig. 8 Evolution of the current i= f(t)

The tearing of the material depends on the movement of the electrode relative by to the workpiece. We present this movement in figure 9:

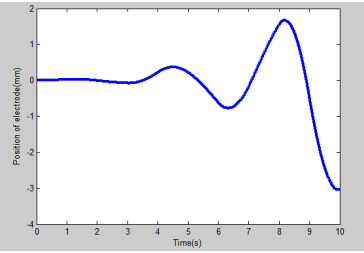

Fig. 9 Evolution of the electrode position

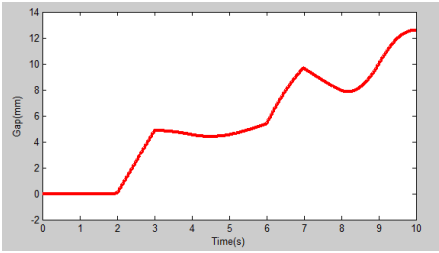

Fig. 10 Gap Variation

Drilling depends essentially on the position of the electrode which is in motion during drilling or during cleaning of the dielectric and the gap. From recoil allows the electrode cleaning circuit ejects the eroded material. The drilling operation depends primarily upon the position of the electrode which is in motion during both the drilling operations and the cleaning of the dielectric and the gap. Through a withdrawal movement, the electrode allows the cleaning circuit to eject the eroded material. On the basis of the simulation algorithms, a retreat of more than 2µm sets into motion the cleaning circuit and hence ends the operation of perforation.

As far as the disposition of the electrode is concerned, the positive direction is that which allows the piece to get nearer. Thus, this perforation type requires one machine axiom which is the perforation axe. The disposition of the graphic chart (fig.10) stands in accordance with the status of the impulsions transmitted during the removal of the materiel since the electrode gets nearer to the piece during the process of the erosion of the material but gets away as soon as the cleaning or the dielectric renewal phase starts to take place.

4 Robustness Analysis

The EDM is controlled by the technological parameters: voltage, current, gap, pulse duration, etc. It is in this sense that a parametric is presented analysis to control the adjustment of these parameters.

4.1 Parametric Robustness

4.1.1 Parameters of Servo Bloc

This bloc is characterized by certain parameters, we will focus on the influence of the Compr, which is a parameter that allows adjusting the gap. The bigger the gap, the less significant the distance between the electrode and the part becomes.

This parameter ranges from 0 to 255 V. During the simulation, an attempt has been made to fix this value at the level of 230 V but for our analysis of the strength aspect the results are represented with Compr = 100

The main Remarque that could be derived from the previous studies is that the mere variation of the variable Compr will cause a mild or light variation at the level of the gap but without bringing about any disturbances in the process of as the perforation speed remains practically unchanged as long as the performances are kept.

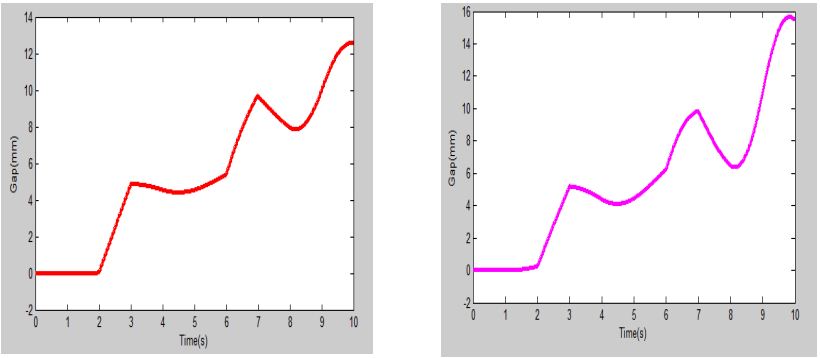

Fig. 11 Gap Variation

4.1.2 Parameters of the Electrode Positioning

For the parametric study conducted on this bloc, a special attention was accorded to the robot. For this component, the prime transfer function of the entity into a motion which will be subject to variation in order to test and measure the influence on this parameter upon this entire operation.

In the following part we will present the results for an entity in movement of motors for the robot m=70g, that is to say, we have divided this value into (Imai and al. 1996) in comparison with the earlier stage of this work.

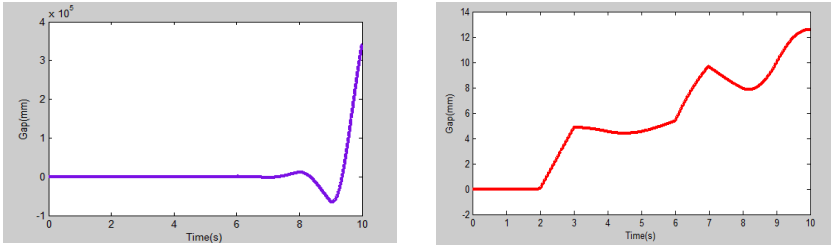

m=70g m=350g

Fig. 12 Robot's mass m = 70g

The decrease of the entity into motion for robot allows increasing the swinging movement back and forth at the level of the electrode, consequently the contamination decreases and the cleaning process takes advantage of that.

Concerning the performances of the procedure of perforation, the calculation of the speed shows that there will be a light rise in order to pass to 60µm/s.

This study lays the emphasis upon the electronic band passing from the robot which is dependent upon other parameters which are respectively: the constant of the motors couples and the raider of cols. The main conclusion that can be derived is that this parameter may improve the electro erosion since this latter is linked to the balance existing between the materiel manufactured and the one evacuated. This equilibrium depends upon the flux of the dielectric procedure in charge of the cleaning of the zone of the work and the evacuation of the eroded material.

4.2 Robustness Analysis of the Change in the Model

Our focal point consists in commanding the robot where we have used for the simulation the regulator as a counter reaction of the status. In this case we will be conducting the robot via the regulator PID which is frequently used in the industrial arena. Each robot articulation is carried out by a PID control of a constant gain. The PID control is the most used one in the industrial field for this range of reasons including its minimal cost in terms of time and the easiness of its implementation.

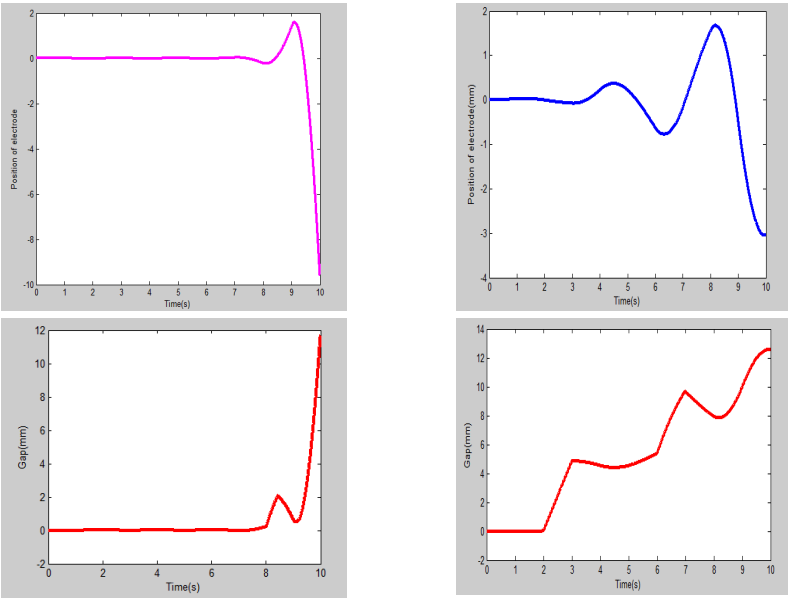

Fig. 13 Variation of gap

The PID control may satisfy the stability of the model but it is limited in terms of performances. For the robots with high precision which are systems with complex dynamics, the time answer varies in accordance with time in terms of its configuration, consequently error pursuit increases, especially in the case of quick movements where it produces data transfer. The PID control is not so efficient in these sorts of applications.

5 Conclusion

In the present study, In order to understand and analyze the phenomena occurring in micro EDM, we developed a model to simulate the behavior of an EDM machine. From this model, we varied different parameters, to explain their influences by simulations at the robustness of the process of material removal by EDM in the case of micro-drilling.

References

Imai, et al.: Improvement of EDM machining Speed by Using High Frequency response Actuator. International Journal of Electrical Machining (1) (January 1996)

Osenbruggen, C.V., Luimes, G., Dijck, A.V., Siekman, J.: Micro spark erosion as a technique in microminiaturization. In: IFAC-IFIP Symposium on Microminiaturization (1965)

Masaki, T., Kawata, K., Mizutani, T., Yonemochi, K., Shibuya, A., Masuzawa, T.: Micro Electro-Discharge Machining. In: Proceedings of International Symposium for Electro-Machining (ISEM 1989), pp. 26–29 (1989)

Zhang, J.H., Lee, T.C., Lau, W.S., Ai, X.: Spark erosion with ultrasonic frequency. Journal of Materials Processing Technology 68, 83 (1997)

Bleys, P., Kruth, J.-P., Lauwers, B., Zryd, A., Delpretti, R., Tiricarico, C.: Real-time Tool Wear Compensation in Milling EDM. Annals of the CIRP 51(1), 157 (2002)

Jean-Philippe, B.: Conception de robots de très haute précision à articulations flexibles: interaction dynamique-commande, Thèse N0 2907, Faculté des sciences et techniques de l'ingénieur, EPFL, Suisse (2003)

Clavel, R.: Conception d'un robot parallèle rapide à 4 degrés de liberté, Thèse N0 925, Département de microtechnique, EPFL, Suisse (1991)

Paul, F., Sameer, M., Jonathan, H.: Best Practices for Establishing a Model-Based Design Culture, SAE Paper 2007-01-0777

Jeff, T., Larry, K., Siva, N.: Caterpillar Automatic Code Generation, SAE Paper 2004-01-0894 (2004)

Clarence, W.: Mechatronics: An Integrated Approach. CRC Press (2005) ISBN 0849312744

Part II
Dynamics of Mechanical Systems

Integration of Drill Torsional-Axial Coupling in a Global Spindle-Self Vibratory Drilling Head Model

Mousavi Said G., Gagnol Vincent, and Ray Pascal

Clermont Université, Institut Pascal,
UBP-CNRS-IFMA, Campus des Cézeaux
24 Avenue des Landais,
63177 AUBIERE Cedex, France
{Said.Mousavi,Vincent.Gagnol,Pascal.Ray}@ifma.fr

Abstract. The drilling of deep holes with small diameters remains an unsatisfactory technology, since its productivity is rather limited. The main limit to an increase in productivity is directly related to the poor chip evacuation, which induces frequent tool breakage and poor surface quality. Retreat cycles and lubrication are common industrial solutions, but they induce productivity and environmental drawbacks. An alternative response to the chip evacuation problem is the use of a vibratory drilling head, which enables the chips to be fragmented thanks to the axial self-excited vibration. Contrary to conventional machining processes, axial drilling instability is sought, thanks to an adjustment of head design parameters and appropriate conditions of use. In this paper, self-vibratory cutting conditions are established through a specific stability lobes diagram. A dynamic high-speed spindle / drilling head / tool system model is elaborated on the basis of rotor dynamics predictions. The model-based tool tip FRF is integrated into an analytical stability approach. The torsional-axial coupling of the twist drill is investigated and consequences on drilling instability are established.

Keywords: Self-vibratory drilling, Machine tool dynamics, Stability prediction, Chatter analysis.

1 Introduction

The drilling of deep, small-diameter holes is an unsatisfactory machining operation that results in poor surface quality and low productivity. These drawbacks are mainly related to difficulties in evacuating the chips through the drill flute during the cut. Non-productive retreat cycles and the use of high-pressure lubrication are the current industrial solutions used to evacuate chips, but present respectively productivity and environmental problems. New drilling techniques have emerged, based on the tool's axial vibration, in order to fragment the chips and enhance their evacuation without the need for lubricants and retreat cycles. The two major technologies are:

M. Haddar et al. (Eds.): *Design and Modeling of Mechanical Systems*, LNME, pp. 81–88.
DOI: 10.1007/978-3-642-37143-1_10

- Vibration-assisted drilling technologies, based on forced excitations generated by a specific system implemented in the tool-holder.
- Self-vibratory drilling technology, which uses the cutting energy to generate tool axial vibration (Guibert et al. 2008). A specific Self-Vibratory Drilling Head (SVDH) excites low-energy chatter vibration for specific process parameters by using a combination of a low-rigidity axial spring and an additional mass located between the spindle and the tool. The self-excited vibrations must be tuned and controlled in order to have a magnitude greater than the feed per tooth, which enables the fragmentation of the chips without external adjunction of energy.

In this paper an original approach to establishing accurate stability lobes diagram in self-excited drilling operations is proposed. The predicted speed-dependent transfer function of the overall system, composed of spindle-SVDH-twist drill, is then integrated into an analytical chatter vibration stability approach to calculate the associated dynamic stability lobes diagram.

In the second section, the spindle-SVDH rotor dynamics model is presented. A special rotor-beam element, developed in a co-rotational reference frame (Gagnol et al. 2007) is implemented. The rolling bearing stiffness matrices are calculated around a static function point on the basis of T.C Lim's formulation (Lim T.C. and Singh 1990) and then integrated into the global finite element model. The rotating system is derived using *Timoshenko* beam theory. The identification of contact dynamics in tool-SVDH-spindle assemblies is carried out using the receptance coupling method on the basis of experimental substructure characterization (Forestier et al. 2011). The identified models are then integrated into the global spindle-SVDH-tool model.

In section 3, a generic accurate drilling force model is developed by taking into account the drill geometry, cutting parameters and effect of torsion on the thrust force. Section 4 is dedicated to the prediction of adequate drilling conditions based on controlled self-excited drill vibration. A specific instability lobes diagram is elaborated by integrating into an analytical stability analysis the overall structural model-based tool tip FRF of the system associated with the proposed drilling force model. Investigations are focused on the drill's torsional-axial coupling role on instability predictions. Finally, a conclusion is presented.

2 Model Building

The vibratory drilling system is composed of a SVDH body clamped to the spindle by a standard HSK63A tool-holder interface. A SVDH vibrating subsystem is jointed to the SVDH body using a specific spring, and axially guided by a ball retainer. Finally, a long drill is held in the SVDH vibrating subsystem with a standard ER25 collet chuck. The SVDH system is mounted on a spindle capable of speeds up to 15500 rpm. The spindle has four angular bearings in overall back-to-back configuration (Figure 1).The spindle-SVDH-tool system is composed of four structural subsystems: the drill, the SVDH vibrating subsystem, the SVDH body and the spindle.

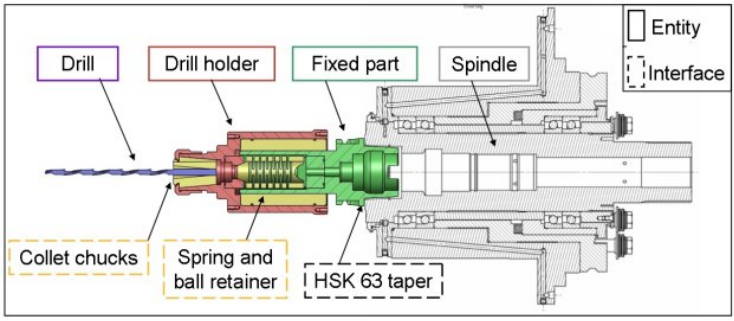

Fig. 1 The spindle-SVDH-tool system

2.1 Structural Elements

The model for the spindle-SVDH-tool system is restricted to the rotating structure composed of the spindle shaft, the SVDH and the drill. This hypothesis was established by an experimental modal identification procedure carried out on spindle substructure elements (Gagnol et al. 2007). Dynamic equations were obtained using *Lagrange* formulation associated with a finite element method. Due to the size of the rotor sections, shear deformations had to be taken into account. Then the rotating substructure was built using *Timoshenko* beam theory. The relevant shape functions were cubic in order to avoid shear-locking. A special three-dimensional rotor-beam element with two nodes and six degrees of freedom per node was developed in the co-rotational reference frame. The damping model used draws on *Rayleigh* viscous equivalent damping, which makes it possible to regard the damping matrix **D** as a linear combination of the mass matrix **M** and the spindle rigidity matrix **K**:

$$\mathbf{D} = \alpha\mathbf{K} + \beta\mathbf{M} \tag{1}$$

Where α and β are damping coefficients. The set of differential equations can be written as:

$$\mathbf{M}\ \ddot{\mathbf{q}}_N + (2\Omega\mathbf{G} + \mathbf{D})\dot{\mathbf{q}}_N + \left(\mathbf{K} - \Omega^2\mathbf{N}\right)\mathbf{q}_N = \mathbf{F}(t) \tag{2}$$

Where **M** and **K** are the mass and stiffness matrices, **D** is the viscous equivalent damping matrix, $\mathbf{q}_N$ and $\mathbf{F}(t)$ are the nodal displacement and force vectors. **G** and **N** are respectively representative of gyroscopic and spin softening effects. Ω is the rotor's angular velocity.

2.2 Modelling of Spindle-SVDH-Tool Interfaces

The dynamic behaviour of the interfaces represented by the HSK63 taper, spring and ball retainer, and collet chuck are taken into account (Fig.2).

The identification procedure of the interface models was carried out by Forestier (Forestier et al. 2011) based on the receptance coupling method and then integrated into the model as illustrated in figure 2.

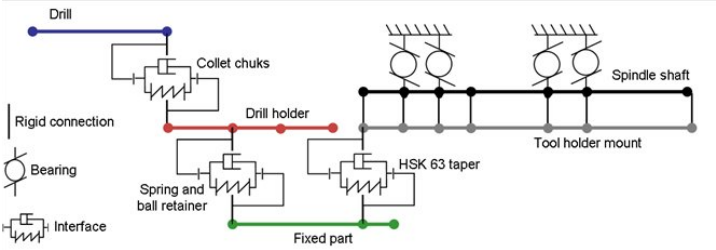

Fig. 2 The spindle-SVDH-tool System Finite Element Model

3 Drilling Force Model

The energy required to maintain the self-excited vibration is provided by the cutting forces. These excite both the SVDH and the flexible low-diameter drill. The combination of rigid body motion and dynamic displacements of the drill induces mainly torsional and axial vibrations.

Several force models have been proposed in the literature for the primary cutting edge presented in figure 3 in zone 1. Both geometrical parameters and cutting pressures change greatly along the cutting lip of the twist drill (Roukema et al. 2006). Each cutting lip can be thought of as being composed of a number of small differential segments. The elementary tangential force dFt is perpendicular to the cutting edge and the axial force dFz is in the drill axial direction. The cutting forces, axial forces and torque applied to the drill are evaluated by summing the elementary forces and torques acting on the basic elements of the edge of the drill and are expressed as a function of chip thickness h and width b .

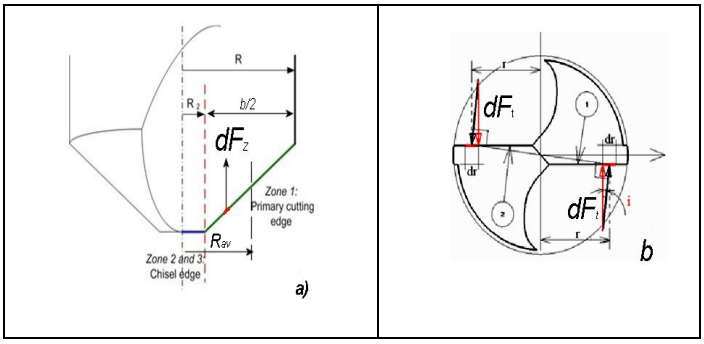

Fig. 3 Drill geometry, elementary forces

Following Tlusty (Tlusty 1985) and Stephenson and Agapiou (Stephenson and Agapiou 1992), the net variations in the time-varying part of tangential and thrust forces at the drill tip are assumed to be proportional to the chip area. The influence of the ploughing effect and the effect of the chisel edge are not taken into account in the proposed cutting force model. Hence, the thrust force, the axial force and the torque at the tool tip are respectively:

$$F_t = \sum_i dF_t = -K_t bh$$
$$F_Z = \sum_i dF_Z = -K_Z bh \quad (3)$$
$$M_Z = 2\sum dF_t \cdot r(z) = -K_t bhR_{av}$$

Where R_{av} is the average radius of the cutting force, h is the chip thickness and b is the radial depth of cut (drill diameter minus pilot hole diameter if there is a pilot hole). K_z and K_t are the average cutting pressures in the axial and tangential directions respectively.

Torsional-Axial Coupling

The development of a torsional-axial vibration model (Bayly and Metzer 2001) was a major milestone in understanding chatter in machining using a twist drill. The torsional-axial theory of Bayly is based on the fact that when a twist drill "untwists", it extends in length (figure 4).

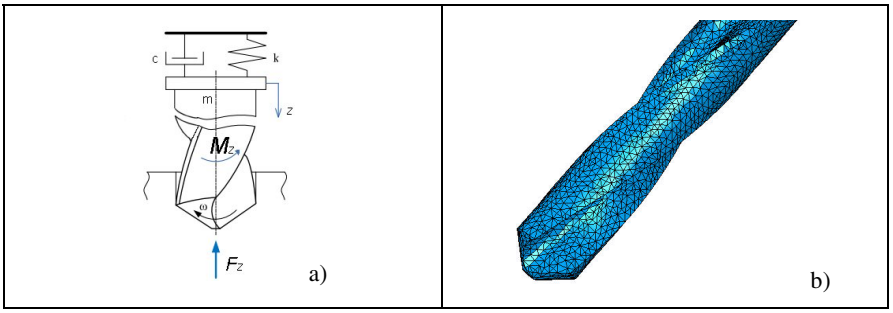

Fig. 4 a) Dynamic model of drill bit b) Finite element model of the drill

Twisting and axial deformations are coupled. Accordingly, the second member of equation (2) becomes:

$$F(t)\cdot \vec{z} = -F_z(t) - (\theta)M_Z(t) \quad (4)$$

The θ term represents a torsional-axial coupling parameter, since it relates the applied torque to drill axial excitation. It is determined by FEM analysis (fig. 4b). The coupling is negative, since when the drill twists in -z resulting from the

negative cutting torque it also extends in +z which results in a negative axial force contribution. According to equation (3), equation (4) can be rewritten

$$F(t)\cdot\vec{z} = h\cdot b\cdot K_t\cdot\alpha \quad \text{with} \quad \alpha = \frac{K_Z}{K_t} + R_{av}\cdot\theta \tag{5}$$

K_z and K_t are identified through experimental drilling characterization (Guibert and al. 2008), and the coupling term $R_{av}\theta$ by finite element modelling of the drill. In our case, using a carbide drill of 5 mm diameter, the helix angle is 30° and the material to be machined is 35MnV7. The identification of terms $R_{av}\theta$ and α is respectively 0.45 and 0.39.

4 Stability Prediction

Torsional-axial coupling in the drill and SVDH vibration provide a mechanism for torsional-axial chatter. The torsional vibrations lead to the shortening and lengthening of the drill, which results in a wavy surface of the bottom of the hole. The main difficulty of vibratory drilling is to foresee the cutting conditions that will generate regular vibrations able to induce interrupted cutting. In this study, the drilling operation is considered as having one degree of freedom in thrust force, taking into account the torsion effect in this direction. The analytical method allows the stability of system to be investigated from the study of the chip thickness (Fig 5.a). The regenerative chatter of system can be presented by the block diagram shown in fig 5.b.

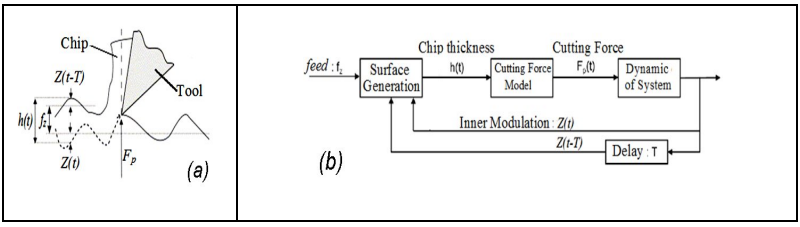

Fig. 5 a) dynamic chip thickness b) block diagram of chatter dynamics

The cutting forces and coupling term, equation 5, are substituted into equation (2) for motion in the drill's axial direction:

$$\left(\mathbf{M}\ \ddot{\mathbf{q}}_N + (2\Omega\mathbf{G}+\mathbf{D})\dot{\mathbf{q}}_N + \left(\mathbf{K}-\Omega^2\mathbf{N}\right)\mathbf{q}_N\right)\cdot\vec{z} = \alpha K_t b\left(Z(t)-Z(t-\tau)\right) \tag{6}$$

The stability limit, integrating drill torsional-axial vibration, can be established:

$$D_{\lim} = \frac{-1}{\alpha\cdot K_t\cdot 2\cdot G(\omega)} \tag{7}$$

Where $G(\omega)$ is the real part of the global system (Spindle-SVDH-drill) transfer function. α is the torsional-axial coupling term (eq. 5). The stiffness and mobile mass of the SVDH are adjustable and require tuning to optimize the process. The stability lobes in a drilling operation can be established.

Figure 6a represents the computed stability diagrams in the plane of spindle speed and SVDH stiffness. It can be noticed that the torsional-axial coupling effect influences the instability of the process, depending on SVDH rigidity. Figure 6b represents stability predictions in the plane of spindle speed and drill diameter. It is established for SVDH rigidity of up to 1.2e7 Nm, where the operating domain representative of self-excited vibrations is increased. For a drilling operation with a 5 mm diameter drill, the maximum spindle speed is increased from 16800 rpm to 19500 rpm by taking into account the torsional-axial coupling of the drill.

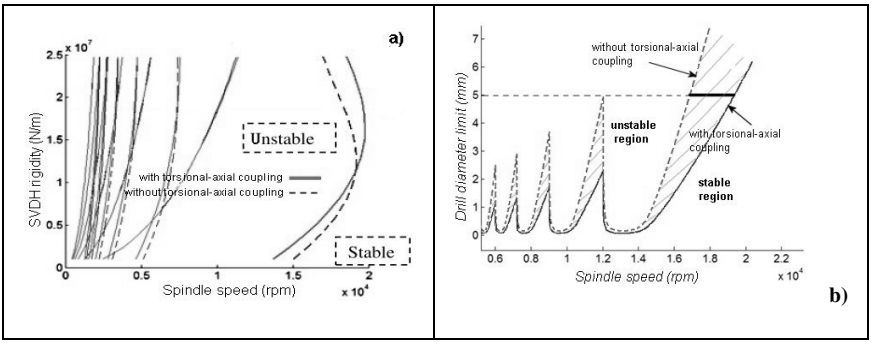

Fig. 6 Stability lobes with and without torsional-axial coupling

5 Conclusion

In this work, an original approach to establishing an accurate stability lobes diagram in a self-excited drilling operation is proposed. The torsional-axial coupling of the twist drill is modelled based on Bayly's approach and integrated into the overall system dynamics in order to investigate drilling stability. The stability lobes established indicate a significant modification of self-excited operating zones, allowing increased drilling operation productivity.

References

Guibert, N., Paris, H., Rech, J.: A numerical simulator to predict the dynamical behavior of the self vibratory drilling head. International Journal of Machine Tools and Manufacture 48, 644–655 (2008)

Gagnol, V., Bouzgarrou, C.B., Ray, P., Barra, C.: Model-based chatter stability prediction for high-speed spindles. International Journal of Machine Tools and Manufacture 47, 1176–1186 (2007)

Lim, T.C., Singh, R.: Vibration transmission throught rolling element bearings, Part I to Part III. Journal of Sound and Vibrations 139, 179–199, 201–225 (1990)

Forestier, F., Gagnol, V., Ray, P., Paris, H.: Model-based operating recommendations for high-speed spindles equipped with a self-vibratory drilling head. Journal of Mechanism and Machine Theory 46, 1610–1622 (2011)

Gagnol, V., Bouzgarrou, B.C., Ray, P., Barra, C.: Rotor dynamics based chatter prediction in milling and spindle design optimization. ASME Journal of Manufacturing Science and Engineering 129, 407–415 (2007)

Roukema, J.C., Altintas, Y.: Generalized modeling of drilling vibration, Part I: Time domain model of drilling kinematics, dynamics and hole formation. International Journal of Machine Tools & Manufacture 46, 2073–2085 (2006)

Tlusty, J.: Machine Dynamics. In: King, R.I. (ed.) Handbook of High-Speed Machining Technology. Chapman and Hall, New York (1985)

Stephenson, D.A., Agapiou, J.S.: Calculation of main cutting edge forces and torque for drills with arbitrary point geometries. International Journal of Machine Tools and Manufacture 32, 52–538 (1992)

Bayly, P.V., Metzler, S.A.: Theory of Torsional Chatter in Twist Drills: Model, Stability Analysis and composition to test. Journal of Manufacturing Science and Engineering 123, 552–561 (2001)

A Discrete Model for Transverse Vibration of a Cantilever Beam Carrying Multi Lumped Masses: Analogy with the Continuous Model

Ahmed Eddanguir and Rhali Benamar

University Mohammed V – Agdal,
LERSIM, Ecole Mohammadia d'Ingénieurs,
Rabat, Maroc.
eahmed66@hotmail.com,
rbenamar@emi.ac.ma

Abstract. The purpose of the present paper is to make the analogy between a physically discrete model and a continuous model for non-constrained linear transverse vibrations of cantilever beams carrying multi lumped masses. The discrete model is an N-degree of freedom system made of N masses placed at the ends of solid bars connected with spiral springs. Calculations are made based on the classical vibration model involving the mass matrix $[m_{ij}]$ and the linear rigidity matrix $[k_{ij}]$. The boundary conditions at the free ends are taken into account using the fact that no flexural rigidity is present at the bar located at the free end. The clamped end condition is taken into account using a spiral spring with a very high rigidity. The numerical results show a good convergence of the first and second linear frequencies obtained by the discrete model and those obtained via the Dunkerley second formula.

Keywords: Transverse vibration, cantilever beam, discrete model, lumped masses, continuous model.

1 Introduction

A cantilever is a beam clamped at only one end and often used in many constructions, principally in cantilever bridges balconies. The cantilever beam can also be used in fixed-wing airplane. The objective of this work is to make the analogy between the classical model of a cantilever beam carrying multi lumped masses and the discrete model (Eddanguir et al 2011), leading to the expressions for the equivalent spiral and axial stiffness, in terms of the continuous beam geometrical and mechanical characteristics. Some numerical results are given and compared to those obtained via the Dunkerley second formula.

M. Haddar et al. (Eds.): *Design and Modeling of Mechanical Systems*, LNME, pp. 89–96.
DOI: 10.1007/978-3-642-37143-1_11

2 General Theory

2.1 Presentation of the Discrete System for Transverse Vibration

The discrete system shown in figure 1 is a multi-degree-of-freedom system (*N*-dof) made of *N* masses and *N+2* spiral springs, with C_r being the linear rigidities of the r^{th} spiral spring. The springs are attached by identical bars of length l , which are supposed to be massless, not infinitely rigid, and made of an elastic material which may be slightly deformed. The momentum M_r in the r^{th} spiral spring is given by: $M_r = -C_r^l \theta$ (Eddanguir 2012)

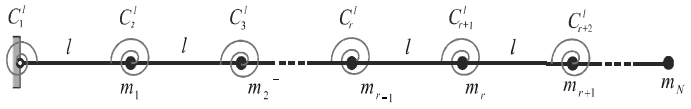

Fig. 1 The multi degree of freedom discrete system

The linear potential energy stored in the *N* spiral springs, subjected to the rotations shown in Figure 1, can be written as:

$$V_l = \frac{1}{2}\sum_{i=1}^{N} C_i^l (\theta_i - \theta_{i-1})^2 \tag{1}$$

2.2 Presentation of the Continuous Model for Transverse Vibration of Beams

Consider transverse vibrations of the cantilever beam shown in Figure 2 and having the following characteristics; *E*, Young's modulus; *L*, length of beam; *S*, area of the cross section; *I*, second moment of area of cross section; $y(x,t)$, transverse displacement $y(x,t) = y(x)\sin \omega t$.

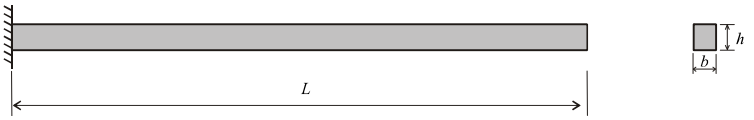

Fig. 2 The clamped-free uniform beam

The linear potential energy due to the bending of a continuous beam is given by:

$$V_l = \frac{1}{2} EI \int_0^L \left(\frac{d^2 y}{dx^2} \right)^2 dx \tag{2}$$

Using the following finite difference technique:

$$\left.\frac{d^2y}{dx^2}\right|_i = \frac{\left.\frac{dy}{dx}\right|_i - \left.\frac{dy}{dx}\right|_{i-1}}{l} = \frac{\theta_i - \theta_{i-1}}{l} \tag{3}$$

by substituting equation (3) in equation (2), we get:

$$V_l = \frac{1}{2}\frac{EI}{l}\sum_{i=1}^{N}(\theta_i - \theta_{i-1})^2 \tag{4}$$

by identification of equations (1) and (4), we get:

$$C_i^l = \frac{EI}{l} = \frac{N}{L}EI \qquad (2 \le i \le N+1) \tag{5}$$

2.3 Calculation of the Coefficients k_{ij} of the Stiffness Matrix[K_{ij}]

In order to express the linear rigidity matrix k_{ij} in terms of the beam characteristics, we recall the following expressions established in ref (Eddanguir et al. 2012) and equation (5).

$$\begin{aligned}
k_{rr} &= \frac{1}{l^2}(C_r^l + 4C_{r+1}^l + C_{r+2}^l) = \frac{I}{l^3}(E_r + 4E_{r+1} + E_{r+2}) \quad r = 1,..,N \\
k_{rr+1} &= -\frac{2}{l^2}(C_{r+1}^l + C_{r+2}^l) = -\frac{2I}{l^3}(E_{r+1} + E_{r+2}) \qquad r = 1,...,N-1 \\
k_{rr+2} &= \frac{C_{r+2}^l}{l^2} = \frac{E_{r+2}I}{l^3} \qquad r = 1,...,N-2
\end{aligned} \tag{6}$$

The mass matrix [M_{ij}] and the rigidity matrix [K_{ij}] of this clamped-free beam are given by:

$$\left[M_{ij}\right] = \frac{\rho SL}{N}\left[m_{ij}\right] \tag{7}$$

and

$$\left[K_{ij}\right] = \frac{N^3 EI}{L^3}\left[k_{ij}\right] \tag{8}$$

To obtain the linear stiffness matrix of the clamped-free beam we should have:

$C_1 = 3C_i$ *and* $C_{N+2} = 0$, $m_i = m$ *for* $(1 \le i \le N-1)$ and $m_N = 0{,}5m$ with $m = \rho SL/N$.

The eigen value problem describing the linear system is given by:

$$\left[K_{ij}\right]\{X\} = \omega_n^2\left[M_{ij}\right]\{X\} \tag{9}$$

Replacing equations (7) and (8) into equation (9) leads to:

$$\left[k_{ij}\right]\{X\} = \omega_n^2 \frac{\rho S L^4}{EI\, N^4}\left[m_{ij}\right]\{X\} \tag{10}$$

Note that:

$$\lambda_n = \omega_n^2 \frac{\rho S L^4}{EI\, N^4} \tag{11}$$

For the uniform beams we have (Thomson and Dahleh 1997):

$$\beta_n^4 = \rho S \frac{\omega_n^2}{EI} \tag{12}$$

Equations (11) and (12) lead to:

$$(L\beta_n)^4 = \lambda_n N^4 \tag{13}$$

with:

$$\left[K_{ij}\right] = \frac{N^3 EI}{L^3}\begin{bmatrix} 8 & -4 & 1 & 0 & \cdots & \cdots & 0 \\ -4 & 6 & -4 & 1 & 0 & & \vdots \\ 1 & -4 & 6 & -4 & \ddots & \ddots & \vdots \\ 0 & 1 & \ddots & \ddots & \ddots & 1 & 0 \\ \vdots & \ddots & \ddots & -4 & 6 & -4 & 1 \\ \vdots & & \ddots & 1 & -4 & 5 & -2 \\ 0 & \cdots & \cdots & 0 & 1 & -2 & 1 \end{bmatrix} \quad \text{and} \quad \left[M_{ij}\right] = \frac{\rho S L}{N}\begin{bmatrix} 1 & 0 & & \cdots & 0 \\ 0 & 1 & \ddots & & \vdots \\ & \ddots & \ddots & \ddots & \\ \vdots & & \ddots & 1 & 0 \\ 0 & & \cdots & 0 & 0{,}5 \end{bmatrix} \tag{14}$$

$$1 \le i, j \le N$$

The numerical results obtained for different values of *N*-dof are summarized in Table 1. The comparison of the frequency parameters of modes 1 and 2 of the clamped-free beam obtained using 20, 30 and 40 degrees of freedom with the corresponding continuous model is given in figure 3 showing a good convergence of the discrete model to the continuous uniform beam model (Thomson and Dahleh 1997).

Table 1 Comparison of the frequency parameters of modes 1, 2 and 3 of the continuous clamped-free beam with the corresponding discrete model

Mode		dof	$\omega_i^2 * N^4$	$(\beta_i l)^4$	*Error%*	$\omega\,(\mathrm{mod}\,el)$	$\omega_{(theory)}$	*Error%*
	1	20	12,73	12,36	3,00	104,90	103,36	1,49
		30	12,62		2,08	104,43		1,03
		40	12,56		1,59	104,18		0,79
	2	20	491,79	485,52	1,29	651,92	647,75	0,64
		30	491,96		1,33	652,03		0,66
		40	491,18		1,17	651,52		0,58

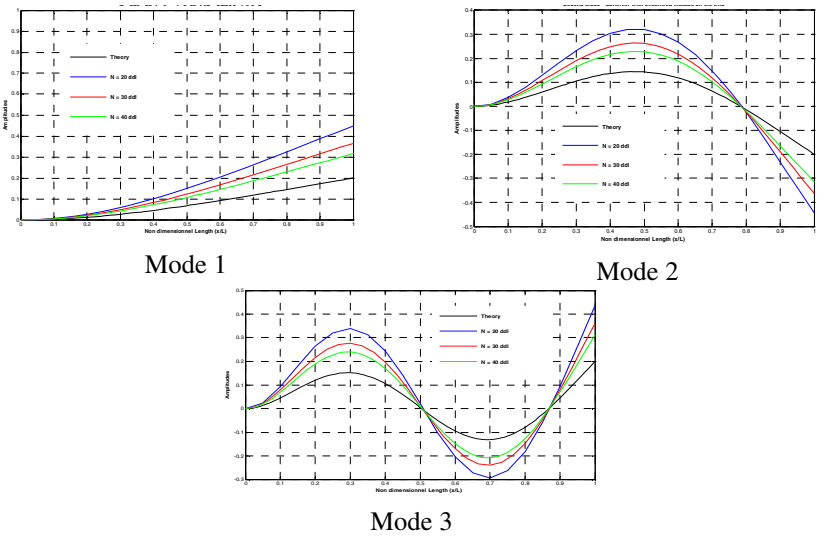

Fig. 3 Convergence of first three mode shapes of the discrete system to the continuous clamped-free uniform beam

2.4 *General Terms of the Mass Matrix [Mij] for the Uniform Cantilever Beam Carrying Multi Lumped Masses*

Consider now a cantilever beam carrying multi lumped masses M_1, M_2,…M_P as shown in figure 4.

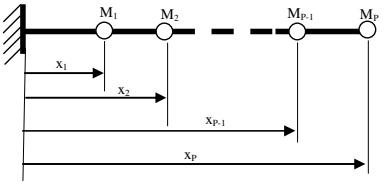

Fig. 4 Cantilever beam carrying multi lumped masses

The expression for the Dunkerley second formula gives the first and second frequencies of vibration of the system shown in figure 4, as follows (Igora and Olga 2004):

$$\omega_{1r}^2 = 1/\sum_{i=1}^{i=P} \delta_{ii} M_i \qquad \text{for the first mode} \tag{15}$$

$$\omega_{2r}^2 = \left(\sum_{i=1}^{i=P} \delta_{ii} M_i\right) / \left(\sum_{i=2}^{i=P} \begin{vmatrix} \delta_{i-1i-1} M_{i-1} & \delta_{i-1i} M_i \\ \delta_{ii-1} M_{i-1} & \delta_{ii} M_i \end{vmatrix}\right) \qquad \text{for the second mode} \tag{16}$$

with: $\delta_{ij} = (3x_i^2 x_j - x_i^3)/6EI$ $for\ x_j > x_i$ and $\delta_{ij} = \delta_{ji}$ $for\ \ i, j = 1,2,...,P$

δ_{ij} is the unit displacement indicating the displacement along the i^{th} direction due to the unit load (force or moment) acting in the j^{th} direction.

The first and the second linear frequencies of the cantilever beam without lumped masses (i.e. $M_1=M_2=.....=M_P=0$) are given by (Thomson and Dahleh 1997):

$\omega_{01}^2 = \frac{1,87510^4}{L^4}\frac{EI}{\rho S}$ for the first mode , $\omega_{02}^2 = \frac{4,69409^4}{L^4}\frac{EI}{\rho S}$ for the second mode.

The square of the first and second frequencies of vibration for the given real system can be calculated using the expression: $\omega_i^2 = \omega_{0i}^2\omega_{ir}^2/(\omega_{0i}^2 + \omega_{ir}^2)\ \ (i = 1,2)$.

To obtain the linear stiffness matrix of the clumped-free beams carrying multi lumped masses, we should change the correspondent matrix element i.e. $m_{pp} = (1 + N\alpha_p)\rho SL/N \quad for\ p \neq N$ and $m_{NN} = m(0,5 + N\alpha_p)$ if M_P is on the end of the free beam; with: $(\alpha_i = M_i/\rho SL \ \ (i = 1,2,....,P)$.

3 Application to a Cantilever Beam Carrying Three Lumped Masses

Consider now a cantilever beam carrying three lumped masses M_1, M_2 and M_3 (for $P=3$) as shown in figure 5-a, and let's apply the second Dankerley formula (Igora and Olga 2004) for modeling an airplane wing (figure 5-b), as a three degrees of freedom lumped mass system, (EI = constant).

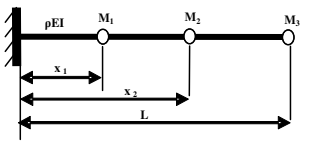

(a)

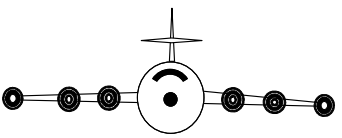

(b)

Fig. 5 Cantilever beam carrying three lumped masses M1, M2 and M3 (a) and the corresponding airplane wing (b)

The general characteristics of the cantilever beam (figure 5-a) are given in table 2:

Table 2 Characteristics of the cantilever beam made of aluminum

L (m)	x_1=L/3	x_2=2L/3	S (m^2)	I (m^4)	ρ (kg/m^3)	E (N/m^2)	M_T (kg)
5	5/3	10/3	0,25	1/192	2700	7.1010	3375

The symmetric matrix of the unit displacements of the correspondent cantilever beam (figure 5-a) is given by:

$$\delta_{ij} = \frac{1}{EI}\begin{bmatrix} 1,54321 & 3,85802 & 6,17284 \\ 3,85802 & 12,34568 & 21,60494 \\ 6,17284 & 21,60494 & 41,66667 \end{bmatrix}$$

The comparison between the linear frequencies of the first and second linear mode shapes calculated with the discrete model (Ndof=60) and the expressions for the Dunkerley second formula shows a good convergence (Table 3).

Also, the comparison of modes 1 and 2 of the clamped-free beam obtained with: $\alpha_1 = \alpha_2 = \alpha_3 = 0$, $\alpha_1 = \alpha_2 = \alpha_3 = 0,1$ and $\alpha_1 = \alpha_2 = \alpha_3 = 0,5$ is given in figure 6 and shows the influence of the ration α_i of lumped masses M_i on the mode the continuous uniform beam model.

Table 3 Comparison between the numerical and Dunkerley formulas frequencies

Mode	$\omega(\mathrm{mod}\,el)$	$\omega(Dun\,\mathrm{ker}\,ley)$	$Erreur\%$
1	101,2596	100,6330	0,618
2	631,7625	636,3332	0,723

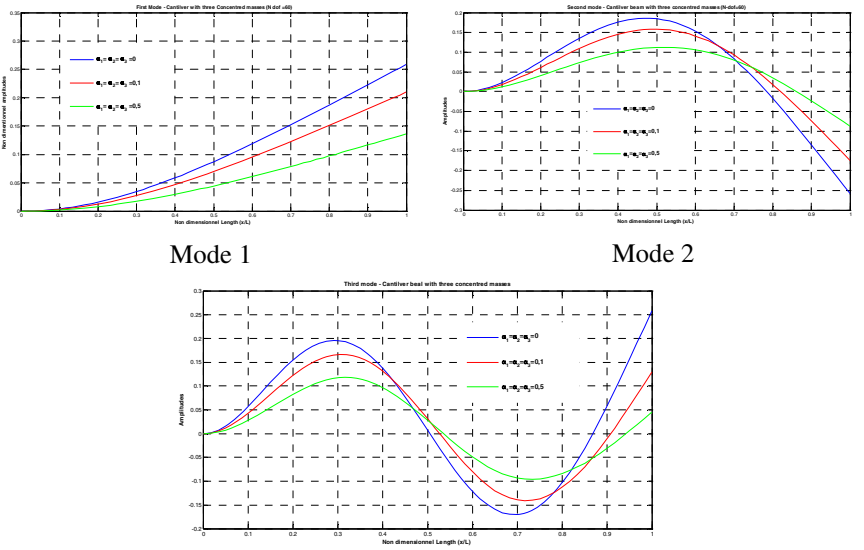

Mode 1 Mode 2

Mode 3

Fig. 6 Convergence of the three first mode shapes of the discrete system to those of the continuous clamped-free uniform beam carrying three lumped masses

4 Conclusion

A physical discrete model for linear transverse vibrations of beams has been used with the objective to present a cantilever beam carrying multi masses. The model proposed in reference [Eddanguir 2012] has been valued using the analogy between the discrete system and its equivalent continuous model. The results obtained for the frequency of the linear discrete system compare well with those based on Dunkerley formulas frequencies theory (Igora and Olga 2004). Moreover, the model proposed in this work may be representative of the bending vibration of a cantilever beam with many concentred masses and different types of discontinuities.

References

Eddanguir, A., Beidouri, Z., Benamar, R.: Nonlinear transverse steady-state periodic forced vibration of 2-dof systems with cubic nonlinearities. Europeen Journal of Computation Mechanics 20(1-4), 143–166 (2011)

Eddanguir, A.: Contribution à une théorie d'analyse modale non linéaire: Application aux vibrations transversales libres et forcées à non linéarités localisées des systèmes discrets à deux et à plusieurs degrés de liberté Thèse de doctorat, Université Mohammed V Agdal, Ecole Mohammadia d'Ingénieurs, Rabat, Morocco (Juillet 2012)

Eddanguir, A., Beidouri, Z., Benamar, R.: Geometrically nonlinear transverse steady-state periodic forced vibration of multi-degree-of-freedom (N-dof) systems with a distributed nonlinearity. Ain Shams Engineering Journal Elsevier 3(3), 191–207 (2012)

Igora, K., Olga, I.L.: Book Formulas for Structural Dynamics: Tables, Graphs and Solutions. McGraw-Hill Companies (2004)

Thomson, W.T., Dahleh, M.D.: Theory of Vibration with Applications, 5th edn. (1997) (Hardcover)

Numerical Continuation of Equilibrium Point and Limit Cycles of a Rigid Rotor Supported by Floating Ring Bearings

Amira Amamou and Mnaouar Chouchane

Laboratory of Mechanical Engineering,
National Engineering School of Monastir,
University of Monastir, Tunisia
Amira.amamou@mailpost.tn,
mnaouar.chouchane@enim.rnu.tn

Abstract. Today, floating ring bearings are commonly used in rotors of high-speed turbochargers because of their low cost and their vibration suppressing capability. Nevertheless, and similar to conventional hydrodynamic bearings, floating ring bearings may exhibit self-excited vibrations and become unstable above the instability threshold speed. In this paper, a nonlinear dynamic model of a perfectly balanced rigid rotor supported by two identical floating ring bearings is used to determine the rotor vibration behavior. The hydrodynamic forces are modeled by applying the short bearing theory and the half Sommerfeld conditions for both fluid films. Numerical continuation is applied to determine stable or unstable limit cycles bifurcating from the equilibrium point at the Hopf bifurcation. This paper shows that the stable limit cycles undergo a single limit point bifurcation however no bifurcation is predicted for the unstable limit cycles.

Keywords: Floating ring bearing, Nonlinear stability analysis, bifurcations of limit cycles, Numerical continuation.

1 Introduction

Floating ring bearings commonly used in machines operating at high angular speeds. This type of hydrodynamic bearings has a ring inserted freely between the journal and the fixed bush. In a hydrodynamic regime, an internal oil film is formed between the journal and the floating ring and an external oil film is formed between the floating ring and the fixed bush. Similar to other hydrodynamic bearings, a floating ring bearing may become unstable if stability threshold speed is exceeded. This instability is due to the hydrodynamic forces generated in the lubricating oil film and if not controlled, it may lead to a premature bearing failure.

Tanaka and Hori (Tanaka and Hori 1972) have developed an analytical dynamic model of a symmetric, balanced rotor supported by two identical floating ring bearings. The model is linearized about the equilibrium position and bearing stability curves are determined. Experimental investigation and numerical

M. Haddar et al. (Eds.): *Design and Modeling of Mechanical Systems*, LNME, pp. 97–103.
DOI: 10.1007/978-3-642-37143-1_12

simulation have been used to prove the validity of the predicted stability charts. Similar stability limit curves have also been published by Li (Li 1982). These stability charts only predict the stability boundaries using linearized dynamic equations. Nonlinear analysis is required to predict the bifurcations of the equilibrium points of journal bearing and floating ring centers in the neighborhood of the stability threshold rotating speed. Boyaci et al. (Boyaci et al 2008) applied the Hopf bifurcation theory to separate the stability boundary curves published in (Tanaka and Hori 1972) into border segments with supercritical stable limit cycles and segments with unstable subcritical limit cycles. Amamou and Chouchane (Amamou and Chouchane 2011) published a similar investigation on the floating ring bearing using analytical and numerical methods.

Although continuation approach has been applied to investigate the bifurcation behavior of rotors with single oil film bearings (e.g. Chouchane and Amamou 2011), very few researches provides an accurate prediction for the detection of bifurcations of the equilibrium point and limit cycles of floating ring bearings. In an application to a flexible turbocharger rotor supported by floating bearings, Boyaci et al (Boyaci et al 2011) have focused on the bifurcation analysis and the determination of large amplitude limit cycle oscillations of turbocharger rotor.

However, in this paper, numerical continuation analysis is used to predict the bifurcation behavior of a perfectly balanced rigid rotor in floating ring bearings after undergoing a Hopf bifurcation and to determine the speed range beyond which limit cycles may no longer exist or may themselves encounter some form of bifurcation.

2 Dynamic Model

Consider a rigid perfectly balanced symmetric rotor supported by two identical floating ring bearings. A cross section of the hydrodynamic floating ring bearing bearing is shown in Fig. 1 (a).

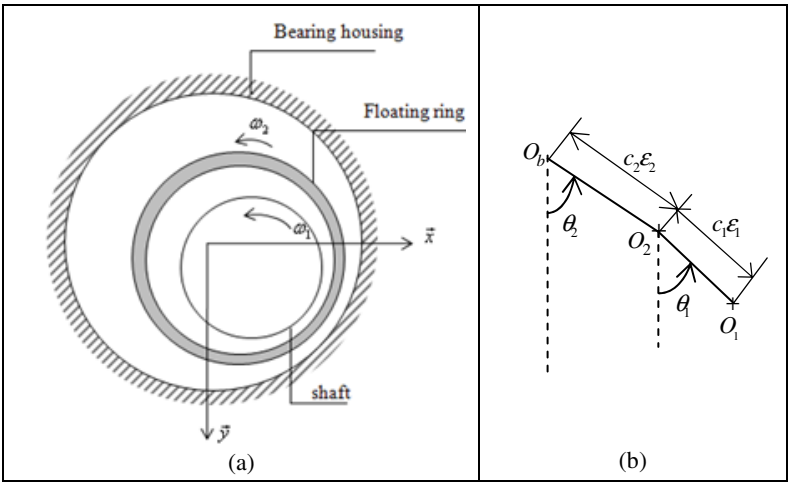

Fig. 1 (a) A cross section of a floating ring bearing; (b) Journal and floating ring positions in polar coordinates

While the shaft which has a constant radius R_1 rotates with constant angular speed ω_1, the floating ring of an internal radius R_2 and an external radius R_3 rotates at an angular velocity $\omega_2 < \omega_1$. The hydrodynamic forces for the two films are obtained by applying the short bearing approximation and using the half Sommerfeld boundary conditions. The quantities associated with the inner film are identified by subscript 1 and subscript 2 refers to the outer film.

In a hydrodynamic lubrication regime, the system's equations of motion may be given in dimensionless form as (Amamou and Chouchane 2011):

$$\begin{cases} \ddot{\varepsilon}_1 = \varepsilon_1\dot{\theta}_1^2 + \dfrac{\Gamma}{\varpi_1\sigma} f_{\varepsilon_1}\left(\varepsilon_1,\dot{\varepsilon}_1,\theta_1,\dot{\theta}_1,\varepsilon_2,\dot{\varepsilon}_2,\theta_2,\dot{\theta}_2\right) \\ \ddot{\theta}_1 = \dfrac{-2\dot{\varepsilon}_1\dot{\theta}_1}{\varepsilon_1} + \dfrac{\Gamma}{\varepsilon_1\varpi_1\sigma} f_{\theta_1}\left(\varepsilon_1,\dot{\varepsilon}_1,\theta_1,\dot{\theta}_1,\varepsilon_2,\dot{\varepsilon}_2,\theta_2,\dot{\theta}_2\right) \\ \ddot{\varepsilon}_2 = \varepsilon_2\dot{\theta}_2^2 - \dfrac{\Gamma}{\varpi_1\sigma\gamma} f_{\varepsilon_2}\left(\varepsilon_1,\dot{\varepsilon}_1,\theta_1,\dot{\theta}_1,\varepsilon_2,\dot{\varepsilon}_2,\theta_2,\dot{\theta}_2\right) + \dfrac{\cos\theta_2}{\gamma\varpi_1^2} \\ \ddot{\theta}_2 = \dfrac{-2\dot{\varepsilon}_2\dot{\theta}_2}{\varepsilon_2} - \dfrac{\Gamma}{\varepsilon_2\varpi_1\sigma\gamma} f_{\theta_2}\left(\varepsilon_1,\dot{\varepsilon}_1,\theta_1,\dot{\theta}_1,\varepsilon_2,\dot{\varepsilon}_2,\theta_2,\dot{\theta}_2\right) - \dfrac{\sin\theta_2}{\varepsilon_2\gamma\varpi_1^2} \end{cases} \tag{1}$$

$\dot{(\,)}$ denotes the derivatives with respect to nondimensional time $\tau = \omega_1 t$. $f_{\varepsilon_1}, f_{\theta_1}, f_{\varepsilon_2}$ and f_{θ_2} are nonlinear functions of the position and velocity of the journal center and the floating ring center. ε_1, ε_2 are the eccentricity ratios and θ_1, θ_2 are the attitude angles as defined in Fig. 1 (b). $\gamma = \dfrac{c_2}{c_1}$ and $\delta = \dfrac{R_3}{R_2}$ are respectively the clearance ratio and the ratio between the external and internal radius of the floating $\sigma = \dfrac{W_2}{W_1}$ is the weight ratio. $\Gamma = \dfrac{\mu R_1 L^3}{2M_1 c_1^{2.5} g^{0.5}}$ is the dimensionless bearing modulus and $\varpi_1 = \omega_1\sqrt{\dfrac{c_1}{g}}$ is the dimensionless journal speed.

3 Bifurcation of Equilibrium Point and Limit Cycles

The nonlinear dynamic behavior of rotors supported by floating ring bearings includes by several phenomena observed experimentally and cannot be predicted by basic analytical methods. Thereby, numerical continuation is essential to determine the branch of the journal equilibrium point, the Hopf bifurcation point and the bifurcating stable or unstable limit cycles so that significant insights into oil whirl, jumping and hysteresis phenomena are appropriately predicted.

The continuation algorithm typically detects any bifurcation appearing as a single control parameter is varied. This type of bifurcation is called codimension one bifurcation. The first step of the bifurcation analysis is to determine branches of

equilibrium point solutions of the system of equations (1) for a selected set of bearing modulus Γ. Stable equilibrium points exist for rotating speeds less than the threshold speed ϖ_c at the Hopf point, designated by "H", and unstable equilibrium points exist for $\varpi > \varpi_c$. At the Hopf point, the branch of equilibrium point bifurcates into limit cycles. The system has either stable limit cycles for $\varpi > \varpi_c$ or unstable limit cycles for $\varpi < \varpi_c$. Limit cycles may themselves undergo bifurcations particularly through a limit point of cycles (LPC) also called a folding bifurcation or a saddle node bifurcation. At this bifurcation, a branch of stable limit cycles and a branch of unstable limit cycles collide together and disappear. Continuation may be proceeded from the LPC point to find another branch of stable or unstable limit cycles as long as the bearing clearance limit is not reached.

The computation of equilibrium and periodic solutions are carried out in this paper by the numerical continuation software package MATCONT providing methods for continuation of branches of equilibrium point and the limit cycle solutions and detection of their bifurcations.

4 Results and Discussion

For typical values of bearing parameters, curves representing the variation of ε_{1s} with ϖ_1 are represented for a set of selected journal modulus Γ as shown in Fig. 2.

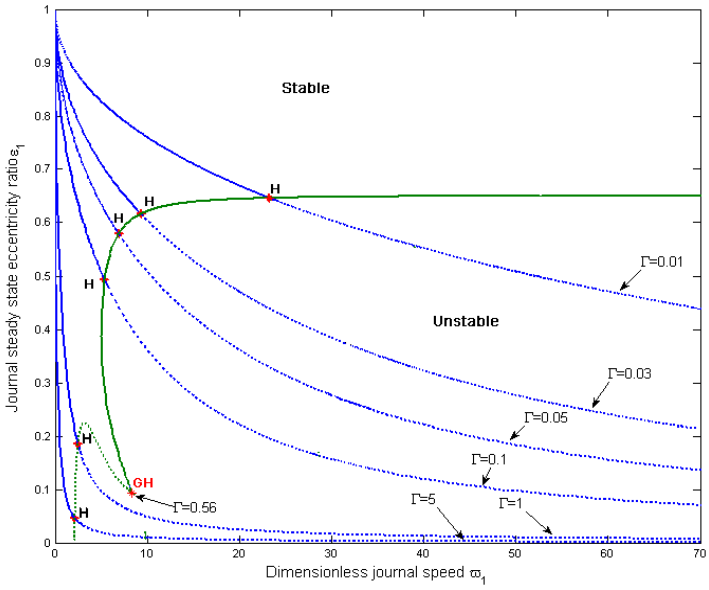

Fig. 2 Branches of the equilibrium point eccentricity of the journal center for a selected set of bearing modulus Γ and for bearing parameters $\delta = 1.32$, $\sigma = 0.043$ and $\gamma = 1$

The Hopf point H separates each equilibrium point branch into a stable and an unstable equilibrium branches segments. Stable equilibrium branch is shown in solid line and unstable equilibrium branch is shown in dashed line. Hopf bifurcation points of different of equilibrium branches of the journal center are joined to form a stability threshold curve in the plane $(\varpi_1, \varepsilon_1)$. We precisely determined this stability curve using Γ and ϖ_1 as two bifurcation parameters in a two parameter continuation. Along this curve, a Generalized Hopf bifurcation point (GH) has been found indicating a transition from one type of bifurcation to another. Hopf bifurcation is supercritical for $\Gamma < 0.56$ and subcritical for $\Gamma > 0.56$. The stability boundary is shown in solid line for the former case and in dashed line for the latter. The stability boundary obtained by a codimension two continuation is identical to that derived from linear modeling.

Once a Hopf bifurcation is detected for any of the ε_{1s} versus ϖ_1 curves in Fig. 2, numerical continuation of limit cycles is applied using the Hopf point as initial point and ϖ_1 as a control parameter to determine the branch of limit cycles. The supercritical bifurcation profiles of journal center for a selected set of bearing modulud Γ are shown in Fig. 3.

For a balanced floating ring bearing, limit cycles are only expected to undergo a single Limit Point of Cycles bifurcation (LPC) as long as the eccentricity ratio limit, $\varepsilon_1 = 0$ or $\varepsilon_1 = 1$ is not reached since the system of equation of motion (1) is not be defined for these two values of ε_1. At an LPC bifurcation shown in

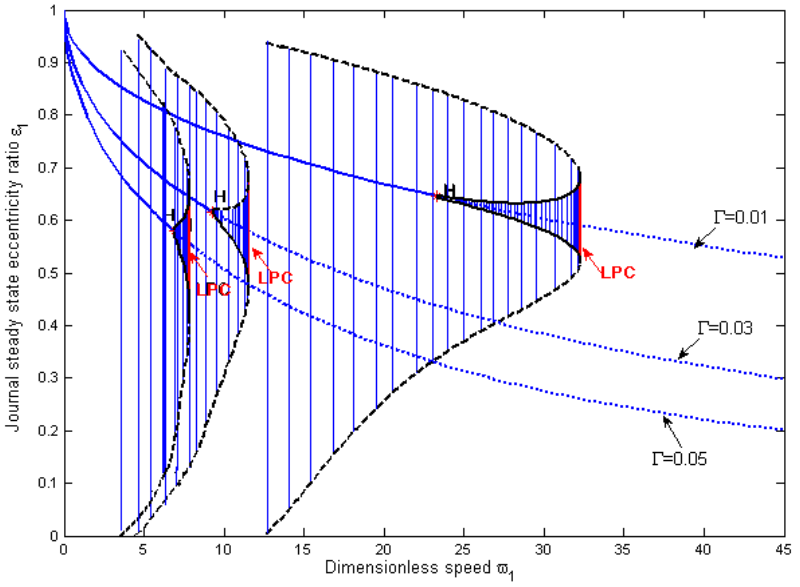

Fig. 3 Stable supercritical branches of limit cycles and their bifurcations for the journal center for three selected bearing modulus $\Gamma = 0.01, 0.03, 0.05$ and for bearing parameters $\delta = 1.32$, $\sigma = 0.043$ and $\gamma = 1$

Fig. 3, a branch of stable limit cycles bifurcates into a branch of unstable limit cycles. The contours of stable cycles are represented by solid line and those of unstable cycles are represented by dashed lines. The amplitude of the supercritical stable limit cycles gradually increases with rotor speed ϖ_1 up to the bifurcation point ϖ_{1LPC}. The size of limit cycles increases at a higher rate for higher bearing modulus Γ. At this rotor speed ϖ_{1LPC}, the stable limit cycle changes its stability by a saddle node bifurcation and unstable limit cycles appear with much higher amplitudes at $\varpi < \varpi_{1LPC}$. This branch of periodic solutions ends when the eccentricity limit, $\varepsilon_1 = 0$, is reached. The $(\varpi_{1c}, \varpi_{1LPC})$ speed range varies with Γ and defines the domain of attraction of stable limit cycles. The unstable limit cycles define the basin of attraction of the stable equilibrium point or limit cycles. A large disturbance of the equilibrium point in this rotor speed range, due to a choc or an earthquake for example, may cause the rotor to leave this basin of attraction which may be the reason for destructive vibrations.

For bearing modulus $\Gamma > 0.56$, the journal center undergoes unstable limit cycles of decreasing size with rotor speed ϖ_1 until the journal eccentricity limit $(\varepsilon_1 = 0)$ is reached and before an LPC bifurcation is encountered. The subcritical bifurcation profiles are shown in Fig. 4.

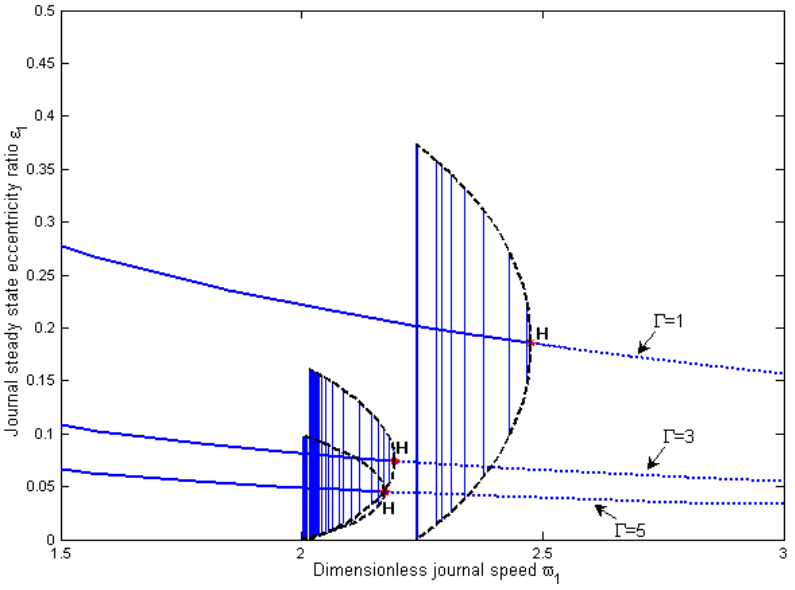

Fig. 4 Unstable subcritical branches of limit cycles for the journal center for three selected bearing modulus $\Gamma = 1, 3, 5$ and for bearing parameters $\delta = 1.32$, $\sigma = 0.043$ and $\gamma = 1$

No jumping or hysteresis phenomenon is expected in this case. Therefore, with regard to practical applications the behavior of the floating ring bearing is more critical because the only stable solution is the equilibrium point before the bifurcation takes place. The basin of attraction given by the unstable limit cycle is too small for high bearing modulus compared to perturbations from operation.

It should be noted that similar curves to those determined by numerical continuation for the journal center, shown previously, may be drawn for the floating ring center.

5 Conclusion

A nonlinear dynamic investigation of the floating ring bearing has been presented in this paper. A four degree of freedom model in polar coordinates has been used. For typical bearing design, the model depends only on two parameters: the non-dimensional rotor speed and the bearing modulus.

Numerical continuation is applied to determine the onset of instability due to a Hopf bifurcation of the equilibrium point and to predict the limit cycles and their bifurcations. The system is shown to undergo a Limit Point of Cycle bifurcation for the supercritical region. For the subcritical bifurcation, no bifurcation of limit cycles is predicted. To further reveal the complex behavior of the system, codimension-two numerical continuation is employed to predict Hopf bifurcation boundaries in a two-parameter space.

References

Tanaka, M., Hori, Y.: Stability characteristics of floating bush bearing. ASME Journal of Lubrication Technology 94, 248–259 (1972)

Li, C.: Dynamics of rotor bearing systems supported by floating ring bearings. ASME Journal of Lubrication Technology 104, 469–477 (1982)

Boyaci, A., Hetzler, H., Seemann, W., Wauer, J., Proppe, C.: Analytical bifurcation analysis of a rotor supported by floating ring bearings. Nonlinear Dynamics 57, 497–507 (2008)

Amamou, A., Chouchane, M.: Non-linear stability analysis of floating ring bearings. Proc. IMechE Part C: J. Mechanical Engineering Science 225, 2804–2818 (2011)

Chouchane, M., Amamou, A.: Bifurcation of Limit Cycles in Fluid Film Bearings. International Journal of Non-Linear Mechanics 46, 1258–1264 (2011)

Boyaci, A., Seemann, W., Proppe, C.: Bifurcation analysis of a turbocharger rotor supported by floating ring bearings. In: Gupta, K. (ed.) IUTAM Symposium on Emerging Trends in Rotor Dynamics. IUTAM Book series, vol. 25 (2011), doi:10.1007/978-94-007-0020-8829

Prediction Life of Horizontal Rotors by Natural Frequency Evolution

Sami Lecheb[1], Abdelkader Nour[1], Ahmed Chellil[1], Saad Sam[1], Dalila Belmiloud[1], and Houcin Kebir[2]

[1] Laboratoire Dynamique des Moteurs et Vibroacoustique,
Université de Boumerdès,
(LDMV-UMBB) Algerie
samir_lecheb@yahoo.fr
[2] Laboratoire Roberval,
Université de Technologie de Compiègne,
UTC, France

Abstract. Detection of crack shaft in a rotating machine is one of the most challenging problems in equipment predictive maintenance. In the available literature, various crack detection methods have been applied to study the dynamic behavior of a cracked shaft. This study concerned with the dynamic behavior of the rotor. We have also studied the different types of transverse cracks and the different methods that have been applied for shaft crack diagnosis. We have also studied the forces applied to the rotor and the movement in order to determine the stress, strain and mode shapes. Was also addressed in this note to study the issues of cracks in three-dimensional in solid objects by using ABAQUS software which based to finite element to give the results. The six first natural frequencies of rotor were decreased after cracking in the shaft critical zone, and this reduce is nonlinear; however the corresponding displacements were increased. Also the stress and strain increased with crack initiation. This reduces of mode shapes frequencies can be used indicator for diagnostic and predicted the life time of rotor.

Keywords: horizontal rotor, dynamic, frequencies, crack initiation, fatigue life.

1 Introduction

P The vibration behavior of a rotating shaft with a transverse crack has been studied since the late 1960's [01]. The approaches for detecting cracked shafts during the operation of equipment were initiated about fifty years ago in response to a systems failure. [02] Are ongoing the cause of shaft cracks. Cracks may be caused by mechanical stress raisers, abrupt cross-sectional changes, heavy shrink fits, dents and grooves, or factors such as fretting or metallurgical factors [03]. Transverse cracks (Fig.1), this type of crack is perpendicular to the shaft axis. They reduce the shaft cross-sectional area and result in significant damages to rotors. These have been extensively studied by the most past and current researchers ([04], [05], [06] and [07]).

M. Haddar et al. (Eds.): *Design and Modeling of Mechanical Systems*, LNME, pp. 105–110.
DOI: 10.1007/978-3-642-37143-1_13

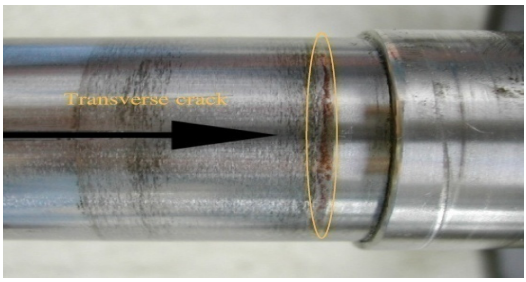

Fig. 1 A transverse crack [4]

Some of the excellent review papers that have appeared include [08], who reviewed the dynamics of a cracked rotor, and developed detection methods for diagnosing fracture damage. [09] Reviewed vibration-based condition, the two common vibration analysis techniques, for structural damage or degradation, were based on natural frequencies or mode shape. A crack present in the shaft could be predicted. The stiffness of a shaft is reduced by a crack. Measuring these changes can help with identifying an early stage crack [10]. In [03] review, the emphasis was on crack detection in shafts by using vibration-based, modal testing and genetic algorithms. [11] The field experience support the conclusion that a transverse crack modifies the dynamic behavior of the rotor. [12] Presented the basic method by comparing the contour graph of the first two structural natural frequencies to analyze the crack depth and location.

[13] Have presented a signal-based method through analysis of the Dynamic Response of a cracked shaft. [14] Studied the open crack of a static state rotor through vibration analysis using a continuous model. [15] Have reported a harmonic excitation method for "detection of a rotor crack based on nonlinear vibration diagnosis. During each revolution, the crack opens and closes gradually, in other words, it breathes during shaft rotation. Crack breathing is one of the popular approaches for studying the dynamics of a cracked shaft by many researchers [16].

The aim of this study is to determine the field of displacement, strain, stress concentration and mode shapes. We also study the fatigue crack initiation of the horizontal rotor due to the initiation of cracks in its shaft.

2 Numerical Simulation of the Crack Initiation

In this case, we simulate the rotor on two fixed supports bearing by ABAQUS software, we give the distribution of the stress, strain and field of the displacement under aerodynamical and centrifuge loads, and visualization of the mode shapes (determine the six first naturals frequencies) and we will see the dynamic behavior of the rotor with crack. In first we should locate the critical zone:

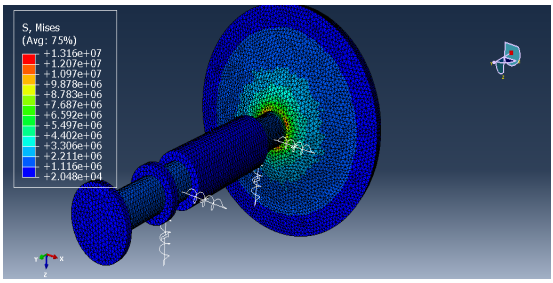

Fig. 2 Von Mises Stress of the LP rotor of a gas turbine 5002

The stress concentration is located in link between disk and shaft.
The six first modes shapes of rotor uncracking are shown:

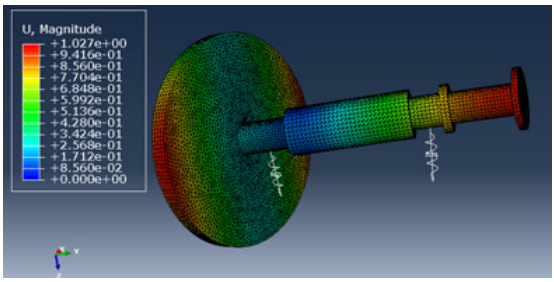

Fig. 3 4th mode-tensile-bending (U_{max}=1.027mm f=2.844 Hz)

About the dynamic behavior of rotor cracking, we will create the crack in the stress concentration zone of the rotor:

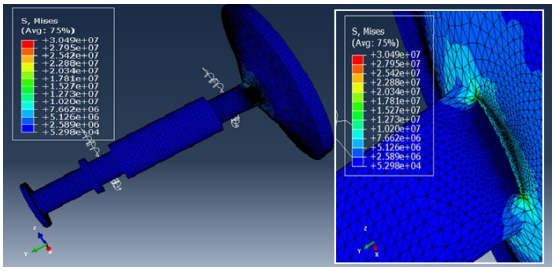

Fig. 4 Von Misses stress of cracking shaft

We have stress concentration in the level crack tip. The 2nd mode shape of rotor cracking shown below:

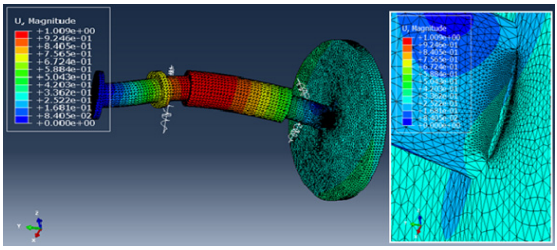

Fig. 5 2nd mode shape (f= 0.827 HZ, U_{max} = 1.009 mm)

The comparison between two cases has shown in the (Tab.1) below:

Table 1 Comparison of the (natural frequencies, maximal displacement) with and without crack

	Without crack		With crack	
Mode 1	f(Hz)	1.304	f(Hz)	0.748
	u_{max}(	1.000	u_{max}(	1.001
Mode2	f(Hz)	2.068	f(Hz)	0.827
	u_{max}(	1.006	u_{max}(	1.009
Mode 3	f(Hz)	2.213	f(Hz)	0.878
	u_{max}(	1.041	u_{max}(	1.224
Mode 4	f(Hz)	2.844	f(Hz)	1.649
	u_{max}(	1.027	u_{max}(	1.137
Mode 5	f(Hz)	4.758	f(Hz)	1.713
	u_{max}(	1.003	u_{max}(	1.010
Mode 6	f(Hz)	4.762	f(Hz)	2.816
	u_{max}(	1.202	u_{max}(	1.215

Note it on the tablet the natural frequencies decrease after the initiation crack in the shaft. And this reduce is nonlinear.

Table 2 Comparison of maximum strain and stress under loadings, without and with crack

	Max stress (MPa)	Max Strain
Plate without crack	1.316E+01	6.965E+01
Plate with crack	3.049E+01	1.454E+02

The table above that the strain max augments and the stress takes a very important increase because we have stress concentration at crack-tip.

3 Conclusion

We conclude when we have a defect form such as cracks, the maximum strain and displacement increased under loads, also we see that the stresses are concentrated around the crack tip and it is very higher. We can deduce also the crack is related to the decrease in natural frequencies observed and modified the vibration in mode shapes of the structure. So, it has a great effect in the damage of the rotor. The nonlinear reduce to natural frequencies can be used as a residual indicator of damage to the crack initiation, and thus highlight the life of the component. So the depictive and diagnostic of defects predict the life of the rotor.

References

[1] Dimarogonas, A.D., Papadopoulos, C.A.: Vibration of cracked shafts in bending. Journal of Sound and Vibration 91(4), 583–593 (1983)
[2] Dimarogonas, A.D.: Vibration of cracked structures: A state of the art review. Engineering Fracture Mechanics 55(5), 831–857 (1996)
[3] Sabnavis, G., Kirk, R.G., Kasarda, M., Quinn, D.: Cracked Shaft Detection and Diagnostics: A Literature Review. The Shock and Vibration Digest 36(4), 287–296 (2004)
[4] Gasch, R.: A Survey of the Dynamic Behavior of a Simple Rotating Shaft with a Transverse Crack. Journal of Sound and Vibration 160(2), 313–332 (1993)
[5] Dirr, B.O., Popp, K., Rothkegel, W.: Detection and simulation of small transverse cracks in rotating shafts. Archive of Applied Mechanics 64(3), 206–222 (1994)
[6] Han, D.J.: Vibration analysis of periodically time-varying rotor system with transverse crack. Mechanical Systems and Signal Processing 21(7), 2857–2879 (2007)
[7] Al-Shudeifat, M.A., Butcher, E.A.: New breathing functions for the transverse breathing crack of the cracked rotor system: Approach for critical and subcritical harmonic analysis. Journal of Sound and Vibration 330(3), 526–544 (2011)
[8] Wauer, J.: On the Dynamics of Cracked Rotors: A Literature Survey. Applied Mechanics Reviews 43(1), 13–17 (1990)
[9] Carden, E.P., Fanning, P.: Vibration Based Condition Monitoring: A Review. Structural Health Monitoring 3, 355–377 (2004)

[10] Sekhar, A.S., Prabhu, B.S.: Crack detection and vibration characteristics of cracked shafts. Journal of Sound and Vibration 157(2), 375–381 (1992)
[11] Bachschmid, N., Pennacchi, P., Tanzi, E., Vania, A.: Identification of transverse crack position and depth in Rotor Systems. Meccanica 35(6), 563–582 (2000)
[12] Lee, Y.-S., Chung, M.-J.: A study on crack detection using eigenfrequency test data. Computers & Structures 77(3), 327–342 (2000)
[13] Mohiuddin, M.A., Khulief, Y.A.: Dynamic Response Analysis of Rotor-Bearing Systems With Cracked Shaft. Journal of Mechanical Design 124(4), 690–696 (2002)
[14] Dong, G.M., Chen, J., Zou, J.: Parameter identification of a rotor with an open crack. European Journal of Mechanics - A/Solids 23(2), 325–333 (2004)
[15] Ishida, Y., Inoue, T.: Detection of a Rotor Crack Using a Harmonic Excitation and Nonlinear Vibration Analysis. Journal of vibration and Acoustics 128(6), 741–749 (2006)
[16] Sekhar, A.S.: Identification of unbalance and crack acting simultaneously in a rotor system: Modal expansion versus reduced basis dynamic expansion. Journal of Vibration and Control 11(9), 1125–1145 (2005)

Defect Detection through Stochastic Wave Finite Element Method

Faker Bouchoucha[1], Mohamed Najib Ichchou[2], and Mohamed Haddar[1]

[1] Unit of Dynamics of the Mechanical Systems (UDSM),
National School of Engineers of Sfax. BP. W3038 Sfax – Tunisia
fakersbouchoucha@yahoo.fr, mohamed.haddar@enis.rnu.tn
[2] Laboratory of Tribology and Dynamics of Systems (LTDS),
Ecole Centrale de Lyon – 36 Avenue Guy de Collongues 69130 Ecully. France
Mohamed.Ichchou@ec-lyon.fr

Abstract. In this paper, the authors present a numerical approach to study Defect detection through Stochastic Wave Finite Element Method. The uncertain material properties are modeled as a set of random fields. The structure is presented considering two waveguides connected through a stochastic coupling element, simulated as the defect (crack). Diffusion matrix for uncertain media through stochastic wave finite element method is studied in this paper. The forced response following a vibratory excitation is computed to investigate the defect detection. The computational efficiency of the method is demonstrated by comparison with MC simulation.

Keywords: Stochastic wave finite element, uncertain waveguide, diffusion matrix, forced response, defect.

1 Introduction

Many researchers proposed some structural health monitoring (SHM) techniques in order to carry out the monitoring and the diagnosis of the risks (Alleyne et al.1998, Bouchoucha et al. 2010). SHM is among the fields of application of guided wave propagation. Wave finite element method (WFEM) can be used for wave propagation predictions and wave scattering estimations. The WFEM regards the waveguide structure as a periodic system assembled by identical substructures, the dispersion curves and the mode shapes are among the primary properties to be given (Mencik and Ichchou 2005, Duhamel et al. 2006).

In the literature, however, most of founded numerical issues of wave propagation simulations are mainly limited to deterministic media. Numerical guided wave techniques characterization in spatially homogeneous random media is investigated in this paper. The uncertainties are often present in geometric properties, material characteristics and boundary conditions of the model. These variables are taken into account in models according to the both parametric (Pellissetti et al. 2008) and non-parametric (Soize 1999) approaches. (Ichchou et al 2011) considered the wave propagation features in random guided elastic media through

M. Haddar et al. (Eds.): *Design and Modeling of Mechanical Systems*, LNME, pp. 111–118.
DOI: 10.1007/978-3-642-37143-1_14

the Stochastic Wave Finite Element Method (S.W.F.E.M) using a parametric probabilistic technique.

(Bouchoucha et al 2013) presented in their paper a numerical approach to study the guided elastic wave propagation in uncertain elastic media. Stochastic Wave Finite Element Method (S.W.F.E.M) formulation with consideration of spatial variability of material and geometrical properties is developed for probabilistic analysis of structures. They extended their work in (Bouchoucha et al 2013) to the diffusion matrix for uncertain media through stochastic wave finite element method (SWFEM). The stochastic diffusion relationship allows evaluating the statistics of reflection and transmission coefficients under structural uncertainty.

This paper will extends mentioned works in order to provide a full numerical description of the stochastic problem of the wave propagation in uncertain damaged structure. The main contribution of this paper seems the calculation of the stochastic forced response of the uncertain waveguide with defect.

The paper contains 5 sections. In section 2, the formulation of the wave propagation in uncertain waveguide is presented through state vector representation. Section 3 provides the stochastic diffusion matrix formulation. Section 4 gives mainly guided wave propagation in uncertain elastic media through stochastic diffusion matrix. Numerical results and discussions are presented in section 5. A conclusion together with a description of the work in progress is ultimately given.

2 Wave Propagation in Uncertain Periodic Waveguide

In this section, we use the SWFE formulation to study the guided wave propagation in uncertain undamaged structure (figure 1). We calculate the stochastic displacement of any substructure k $\left(k \in \{1...N\}\right)$ through the modal decomposition and the polynomial chaos projection (Bouchoucha et al 2013).

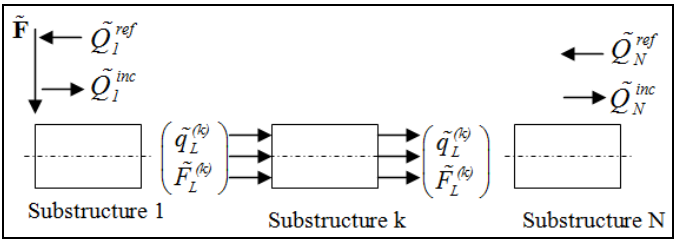

Fig. 1 An illustration of the periodic waveguide

The stochastic kinematic variables, displacements $\tilde{q}$ and forces $\tilde{F}$ are represented through stochastic state vectors: $\tilde{u}_L = (\tilde{q}_L^{\,T} - \tilde{F}_L^{\,T})^T$ and $\tilde{u}_R = (\tilde{q}_R^{\,T}\ \tilde{F}_R^{\,T})^T$. In this way, it can be shown that state vectors $\tilde{u}_L$ and $\tilde{u}_R$ are related by the stochastic transfer matrix $\tilde{\mathbf{S}}$.

$$\tilde{u}_R = \tilde{\mathbf{S}}.\tilde{u}_L \tag{1}$$

Using a modal decomposition, the stochastic state vectors can be projected on the wave mode base:

$$\tilde{u}_L^{(k)} = \tilde{\varphi}\tilde{Q}^{(k)}, \tilde{u}_R^{(k)} = \tilde{\varphi}\tilde{Q}^{(k+1)} \quad \text{where } \tilde{\varphi} = \begin{pmatrix} \tilde{\varphi}_q^{inc} & \tilde{\varphi}_q^{ref} \\ \tilde{\varphi}_F^{inc} & \tilde{\varphi}_F^{ref} \end{pmatrix}, \tilde{Q}^{(k)} = \begin{pmatrix} \tilde{Q}^{inc} \\ \tilde{Q}^{ref} \end{pmatrix}^{(k)} \tag{2}$$

$\tilde{\varphi}$ is the matrix of the stochastic eigenvectors which is independent from the considered substructure, $\tilde{Q}^{(k)}$ represents the vector of the stochastic wave mode amplitude evaluated for the substructure k. The generalized coordinates $\tilde{Q}^{(k)}$ and $\tilde{Q}^{(k-1)}$ evaluated for the k^{th} and $(k-1)^{th}$ substructures, respectively, can be related in this way:

$$\tilde{Q}^{(k)} = \tilde{\lambda}\tilde{Q}^{(k-1)} = \begin{pmatrix} \tilde{\lambda}^{inc} & 0 \\ 0 & \tilde{\lambda}^{ref} \end{pmatrix}\tilde{Q}^{(k-1)} \tag{3}$$

Where $\tilde{\lambda}$ is a diagonal stochastic eigenvalue matrix.

Then, we can establish the following recurrence relationship:

$$\tilde{Q}^{(k)} = \tilde{\lambda}^{k-1}\tilde{Q}^{(1)} \tag{4}$$

The stochastic state vectors of the k^{th} substructure can be written through the modal decomposition as:

$$\tilde{u}_L^{(k)} = \begin{pmatrix} \tilde{\varphi}_q^{inc} & \tilde{\varphi}_q^{ref} \\ \tilde{\varphi}_F^{inc} & \tilde{\varphi}_F^{ref} \end{pmatrix}\begin{pmatrix} \tilde{\lambda}^{inc} & 0 \\ 0 & \tilde{\lambda}^{ref} \end{pmatrix}^{k-1}\begin{pmatrix} \tilde{Q}^{inc} \\ \tilde{Q}^{ref} \end{pmatrix}^{(1)} \tag{5}$$

The polynomial chaos projection of the stochastic state vector $\tilde{u}_L^{(k)}$ is formulated in the following Gaussian form:

$$\tilde{u}_L^{(k)} = \bar{u}_L^{(k)} + \sigma_{u_L^{(k)}}\varepsilon \tag{6}$$

Where $\bar{u}_L^{(k)} = \begin{pmatrix} \bar{q}_L^{(k)} \\ -\bar{F}_L^{(k)} \end{pmatrix} = \bar{\varphi}\bar{\lambda}^{(k-1)}\bar{Q}^{(1)}$

And $\sigma_{u_L^{(k)}} = \begin{pmatrix} \sigma_{q_L^{(k)}} \\ -\sigma_{F_L^{(k)}} \end{pmatrix} = (k-1)\bar{\varphi}\bar{\lambda}^{(k-2)}\sigma_\lambda\bar{Q}^{(1)} + \sigma_\varphi\bar{\lambda}^{(k-1)}\bar{Q}^{(1)} + \bar{\varphi}\bar{\lambda}^{(k-1)}\sigma_{Q^{(1)}}$

In this paragraph, we established the mean and the standard deviation of the state vectors of any substructure k following an uncertainty introduced in the system parameters. We can extract the stochastic displacement using the appropriate boundary conditions.

3 Stochastic Diffusion Matrix Formulation

In this section, we use the SWFE formulation to study the stochastic diffusion matrix which represents the wave/defect interaction (Bouchoucha et al 2013).

For the waveguide 1 (figure 2), the kinematic variables of the N^{th} cell can be written through the modal decomposition:

$$\tilde{q}_R^{1,N} = \tilde{\varphi}_q^{inc}\tilde{\lambda}^{inc}\tilde{Q}_{1,N}^{inc} + \tilde{\varphi}_q^{ref}\tilde{\lambda}^{ref}\tilde{Q}_{1,N}^{ref} \quad \text{and} \quad \tilde{F}_R^{1,N} = \tilde{\varphi}_F^{inc}\tilde{\lambda}^{inc}\tilde{Q}_{1,N}^{inc} + \tilde{\varphi}_F^{ref}\tilde{\lambda}^{ref}\tilde{Q}_{1,N}^{ref} \tag{7}$$

And for the waveguide 2 (figure 2), the kinematic variables of the 1^{st} cell can be expressed as:

$$\tilde{q}_L^{2,1} = \tilde{\varphi}_q^{inc}\tilde{Q}_{2,1}^{inc} + \tilde{\varphi}_q^{ref}\tilde{Q}_{2,1}^{ref} \quad \text{and} \quad -\tilde{F}_L^{2,1} = \tilde{\varphi}_F^{inc}\tilde{Q}_{2,1}^{inc} + \tilde{\varphi}_F^{ref}\tilde{Q}_{2,1}^{ref} \tag{8}$$

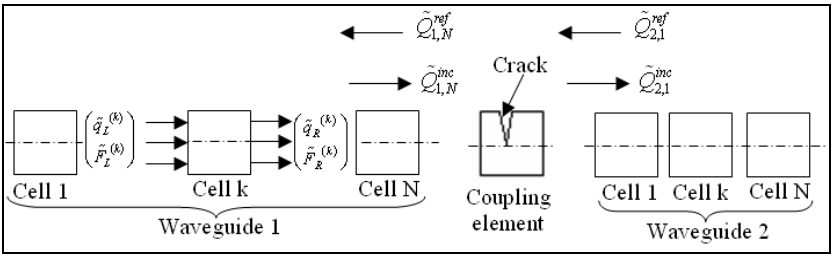

Fig. 2 An illustration of the damaged structure

In the next paragraph, we will use the kinematic variable expresses to study the defect/wave interaction through the diffusion matrix. The modelling of the waveguide with defect is presented in Figure 2; the crack is modelled by a coupling element. The dynamical equilibrium of the stochastic coupling element can be formulated in this way:

$$\tilde{D}^c.\tilde{q}^c = \begin{pmatrix} \tilde{D}_{LL}^c & \tilde{D}_{LR}^c \\ \tilde{D}_{RL}^c & \tilde{D}_{RR}^c \end{pmatrix}\begin{pmatrix} \tilde{q}_L^c \\ \tilde{q}_R^c \end{pmatrix} = \tilde{F}^c = \begin{pmatrix} \tilde{F}_L^c \\ \tilde{F}_R^c \end{pmatrix} \tag{9}$$

Where $\tilde{q}^c$ and $\tilde{F}^c$ represent the stochastic kinematic variables, displacements and forces defined on the dof's on the left and right boundaries of the coupling element. $\tilde{\mathbf{D}}^{\mathbf{c}}$ represents the stochastic dynamic stiffness matrix of the coupling element condensed on the dof's on the left and right boundaries:

The continuity of displacement and force fields can be written as:

$$\tilde{q}_L^c = \tilde{q}_R^{1,N}, \quad \tilde{q}_R^c = \tilde{q}_L^{2,1}, \quad \tilde{F}_L^c = -\tilde{F}_R^{1,N} \quad \text{and} \quad \tilde{F}_R^c = -\tilde{F}_L^{2,1} \tag{10}$$

The dynamical equilibrium will be written in this way:

$$\tilde{D}^c\begin{pmatrix} \tilde{q}_R^{1,N} & \tilde{q}_L^{2,1} \end{pmatrix}^T = -\begin{pmatrix} \tilde{F}_R^{1,N} & \tilde{F}_L^{2,1} \end{pmatrix}^T \tag{11}$$

By introducing equations (7) and (8) in equation (11) and after some analytical treatments, we have:

$$\begin{pmatrix} \tilde{D}^c_{LR}\tilde{\varphi}^{inc}_q & \tilde{D}^c_{LR}\tilde{\varphi}^{ref}_q \\ \tilde{D}^c_{RR}\tilde{\varphi}^{inc}_q - \tilde{\varphi}^{inc}_F & \tilde{D}^c_{RR}\tilde{\varphi}^{ref}_q - \tilde{\varphi}^{ref}_F \end{pmatrix} \begin{pmatrix} \tilde{Q}^{inc}_{2,1} \\ \tilde{Q}^{ref}_{2,1} \end{pmatrix} = - \begin{pmatrix} \tilde{D}^c_{LL}\tilde{\varphi}^{inc}_q\tilde{\lambda}^{inc} + \tilde{\varphi}^{inc}_F\tilde{\lambda}^{inc} & \tilde{D}^c_{LL}\tilde{\varphi}^{ref}_q\tilde{\lambda}^{ref} + \tilde{\varphi}^{ref}_F\tilde{\lambda}^{ref} \\ \tilde{D}^c_{RL}\tilde{\varphi}^{inc}_q\tilde{\lambda}^{inc} & \tilde{D}^c_{RL}\tilde{\varphi}^{ref}_q\tilde{\lambda}^{ref} \end{pmatrix} \begin{pmatrix} \tilde{Q}^{inc}_{1,N} \\ \tilde{Q}^{ref}_{1,N} \end{pmatrix} \tag{12}$$

4 Guided Wave Propagation in Uncertain Elastic Media through Stochastic Diffusion Matrix

According to the stochastic diffusion matrix, we can establish a relationship between the stochastic kinematic variables at the left and the right borders of the coupling element (figure 2). Using the polynomial chaos projection of the equation (12), we can extract the relationship between the means of the stochastic kinematic variables at the left and the right borders of the coupling element as follows:

$$\left(\bar{Q}^{inc}_{2,1} \quad \bar{Q}^{ref}_{2,1}\right)^T = \left(\bar{b}\right)^{-1}\bar{a}\left(\bar{Q}^{inc}_{1,N} \quad \bar{Q}^{ref}_{1,N}\right)^T \tag{13}$$

Where $\bar{b} = \begin{pmatrix} -\bar{D}^c_{LR}\bar{\varphi}^{inc}_q & -\bar{D}^c_{LL}\bar{\varphi}^{ref}_q \\ -\bar{D}^c_{RR}\bar{\varphi}^{inc}_q + \bar{\varphi}^{inc}_F & -\bar{D}^c_{RR}\bar{\varphi}^{ref}_q - \bar{\varphi}^{ref}_F \end{pmatrix}$

And $\bar{a} = \begin{pmatrix} \bar{\varphi}^{inc}_F\left(\bar{\lambda}^{inc}\right) + \bar{D}^c_{LL}\bar{\varphi}^{inc}_q\left(\bar{\lambda}^{inc}\right) & \bar{D}^c_{LL}\bar{\varphi}^{ref}_q\left(\bar{\lambda}^{ref}\right) + \bar{\varphi}^{ref}_F\left(\bar{\lambda}^{ref}\right) \\ \bar{D}^c_{RL}\bar{\varphi}^{inc}_q\left(\bar{\lambda}^{inc}\right) & \bar{D}^c_{RL}\bar{\varphi}^{ref}_q\left(\bar{\lambda}^{ref}\right) \end{pmatrix}$

The relationship between the standard deviations of the stochastic kinematic variables at the left and the right borders of the coupling element can be written as follows:

$$\begin{pmatrix} \sigma_{Q^{inc}_{2,1}} \\ \sigma_{Q^{ref}_{2,1}} \end{pmatrix} = \left(\bar{b}\right)^{-1}\bar{a}\begin{pmatrix} \sigma_{Q^{inc}_{1,N}} \\ \sigma_{Q^{ref}_{1,N}} \end{pmatrix} + \left(\left(\bar{b}\right)^{-1}\begin{pmatrix} \sigma_{a11} & \sigma_{a12} \\ \sigma_{a21} & \sigma_{a22} \end{pmatrix} - \left(\bar{b}\right)^{-1}\begin{pmatrix} \sigma_{b11} & \sigma_{b12} \\ \sigma_{b21} & \sigma_{b22} \end{pmatrix}\left(\bar{b}\right)^{-1}\bar{a}\right)\begin{pmatrix} \bar{Q}^{inc}_{1,N} \\ \bar{Q}^{ref}_{1,N} \end{pmatrix} \tag{14}$$

Where $\sigma_{a11} = \sigma_{\varphi^{inc}_F}\left(\bar{\lambda}^{inc}\right) + \bar{\varphi}^{inc}_F\left(\sigma_{\lambda^{inc}}\right) + \sigma_{D^c_{LL}}\bar{\varphi}^{inc}_q\left(\bar{\lambda}^{inc}\right) + \bar{D}^c_{LL}\sigma_{\varphi^{inc}_q}\left(\bar{\lambda}^{inc}\right) + \bar{D}^c_{LL}\bar{\varphi}^{inc}_q\left(\sigma_{\lambda^{inc}}\right)$

$\sigma_{a12} = \sigma_{\varphi^{ref}_F}\left(\bar{\lambda}^{ref}\right) + \bar{\varphi}^{ref}_F\left(\sigma_{\lambda^{ref}}\right) + \sigma_{D^c_{LL}}\bar{\varphi}^{ref}_q\left(\bar{\lambda}^{ref}\right) + \bar{D}^c_{LL}\sigma_{\varphi^{ref}_q}\left(\bar{\lambda}^{ref}\right) + \bar{D}^c_{LL}\bar{\varphi}^{ref}_q\left(\sigma_{\lambda^{ref}}\right)$

$\sigma_{a21} = \sigma_{D^c_{RL}}\bar{\varphi}^{inc}_q\left(\bar{\lambda}^{inc}\right) + \bar{D}^c_{RL}\sigma_{\varphi^{inc}_q}\left(\bar{\lambda}^{inc}\right) + \bar{D}^c_{RL}\bar{\varphi}^{inc}_q\left(\sigma_{\lambda^{inc}}\right)$

$\sigma_{a22} = \sigma_{D^c_{RL}}\bar{\varphi}^{ref}_q\left(\bar{\lambda}^{ref}\right) + \bar{D}^c_{RL}\sigma_{\varphi^{ref}_q}\left(\bar{\lambda}^{ref}\right) + \bar{D}^c_{RL}\bar{\varphi}^{ref}_q\left(\sigma_{\lambda^{ref}}\right)$,

$\sigma_{b11} = -\sigma_{D^c_{LR}}\bar{\varphi}^{inc}_q - \bar{D}^c_{LR}\sigma_{\varphi^{inc}_q}$, $\sigma_{b12} = -\sigma_{D^c_{LR}}\bar{\varphi}^{ref}_q - \bar{D}^c_{LR}\sigma_{\varphi^{ref}_q}$, $\sigma_{b21} = -\sigma_{D^c_{RR}}\bar{\varphi}^{inc}_q - \bar{D}^c_{RR}\sigma_{\varphi^{inc}_q} + \sigma_{\varphi^{inc}_F}$,

$\sigma_{b22} = -\sigma_{D^c_{RR}}\bar{\varphi}^{ref}_q - \bar{D}^c_{RR}\sigma_{\varphi^{ref}_q} + \sigma_{\bar{\varphi}^{ref}_F}$

This development allows to report the propagation study to the waveguide1 at the left of the coupling element through the stochastic diffusion matrix.

The stochastic displacement $\tilde{q}_L^{(k)}$ can be calculated only in function of $\tilde{Q}^{(1)}$ according to the following equation:

$$\tilde{q}_L^{(k)} = \tilde{\varphi}_q^{inc} \left(\tilde{\lambda}^{inc}\right)^{(k-1)} \tilde{Q}^{inc(1)} + \tilde{\varphi}_q^{ref} \left(\tilde{\lambda}^{ref}\right)^{(k-1)} \tilde{Q}^{ref(1)} \tag{15}$$

5 Numerical Results and Discussion

In this section, we study the longitudinal vibration of the structure in order to validate the SWFEM. We consider the following boundary conditions:

$$\tilde{F}_L^{(1)} = \tilde{F}\,(\text{excitation}) \text{ and } \tilde{F}_R^{(N)} = 0\ (\text{free end}) \tag{16}$$

The boundary conditions are used to evaluate the vector of the stochastic wave mode amplitude evaluated for the first substructure $\tilde{Q}^{(1)}$ through equations (4) and (12). The excitation has a Gaussian distribution $\tilde{F} = \overline{F} + \sigma_F.\varepsilon$ when $\sigma_F = 0.05.\overline{F}$.

We introduce the uncertainty in the structural parameters to study their effects on the wave propagation. These parameters were a Gaussian distribution $(\text{standard deviation} = 0.05.\text{mean})$.

We study the forced response of the structure with defect for the longitudinal mode. According to the equation (15), we can calculate the stochastic longitudinal forced displacement. The polynomial chaos projection of $\tilde{q}_L^{(k)}$ leads to extract the mean and the standard deviation of the forced longitudinal vibration.

Monte Carlo simulations are used to validate the SWFEM results. The mean of the stochastic forced response with defect is presented in figure 3. The effect of the structural parameter perturbations in presence of defect is presented in figure 4. In figure 5, we present the mean and the standard deviation of the forced response with defect following uncertainty introduced in Young modulus in order to demonstrate the efficiency of the proposed method. In fact, the wave propagation isn't affected by the perturbation of the structural parameters. Figure 6 illustrates the competence of the SWFEM as a tool for the defect detection through the comparison between the forced response with and without defect.

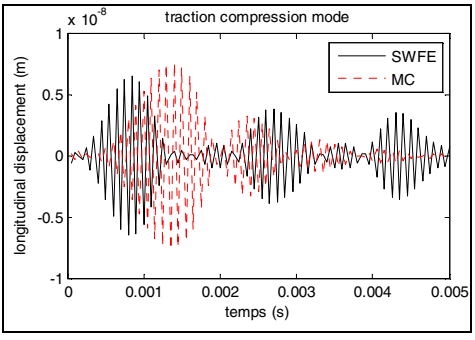

Fig. 3 Mean of the forced response of the waveguide with defect

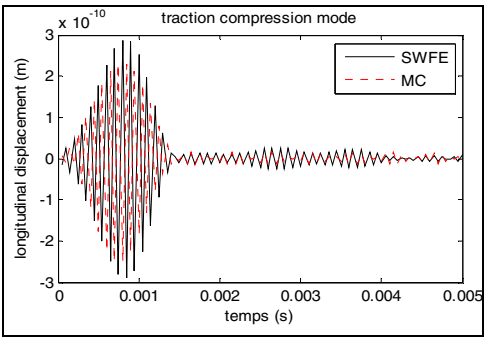

Fig. 4 Standard deviation with defect (E stochastic)

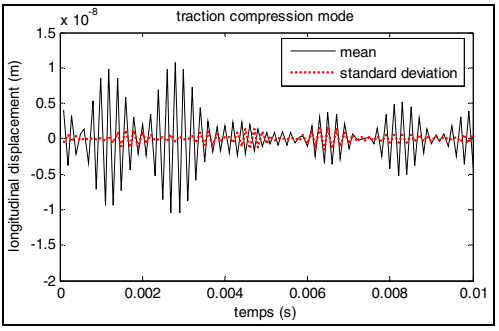

Fig. 5 The forced response with defect (E stochastic)

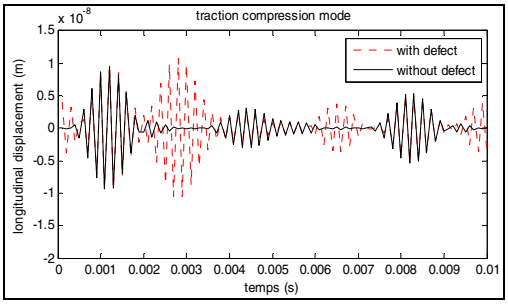

Fig. 6 The defect detection for the traction compression mode

6 Conclusion

In this paper, the subject of forced response in uncertain structure with defect was dealt with. The structure is presented considering two waveguides connected through a stochastic coupling element, simulated as the defect (crack), the stochastic diffusion relationship is used to study the wave/defect interaction

following an uncertainty introduced in the structure parameters. The stochastic wave finite element method is used for the defect detection in uncertain structure. The main paper finding can be extracted as follows:

1. Stochastic forced response associated to stochastic wave propagation is given.
2. Stochastic diffusion matrix associated to damage front is given. This paper provides a numerical investigation of guided waves and defect interaction.
3. The defect detection in uncertain structure is offered.

The SWFE offers some interesting research perspectives. The use of SWFE for energy issues in complex wave guide is an important task. Among the investigations in progress, the mid and high frequencies behavior is the main target in this case. Further investigations are under progress in order to use such numerical methods in the context of smart materials and structures.

References

Alleyne, D.N., Lowe, M.J.S., Cawley, P.: The reflection of guided waves from circumferential notches in pipes. Journal of Applied Mechanics 65, 635–641 (1998)

Bouchoucha, F., Akrout, M., Fakhfakh, T., Ichchou, M.N., Haddar, M.: Detection of the defects in cylindrical pipes: Application to the Wave Finite Element Method. International Journal of Modeling, Identification and Control (IJMIC) 9(4), 336–349 (2010)

Bouchoucha, F., Ichchou, M.N., Haddar, M.: Guided wave propagation in uncertain elastic media. Ultrasonics 53, 303–312 (2013)

Bouchoucha, F., Ichchou, M.N., Haddar, M.: Diffusion matrix through stochastic wave finite element method. Finite Elements in Analysis and Design 64, 97–107 (2013)

Duhamel, D., Mace, B.R., Brennan, M.J.: Finite element analysis of the vibrations of waveguides and periodic structures. Journal of Sound and Vibration 294, 205–220 (2006)

Ichchou, M.N., Bouchoucha, F., Ben Souf, M.A., Haddar, M., Dessombz, O.: Stochastic wave finite element for random periodic media through first-order perturbation. Computer Methods in Applied Mechanics and Engineering 200, 2805–2813 (2011)

Mencik, J.M., Ichchou, M.N.: Multi mode propagation and diffusion in structures through finite element. European Journal of Mechanics/ A: Solid 24(5), 877–898 (2005)

Pellissetti, M., Capiez-Lernout, E., Pradlwater, H., Soize, C., Schueller, G.I.: Reliability analysis of a satellite structure with a parametric and a non-parametric probabilistic model. Comput. Methods appl. Mech. Engrg. 198, 344–357 (2008)

Soize, C.: A nonparametric model of random uncertainties in linear structural dynamics (1999) ISBN 152: 109-138

Reduction Method Applied to Viscoelastically Damped Finite Element Models

Souhir Zghal[1,2], Mohamed Lamjed Bouazizi[2], Rchid Nasri[1], and Noureddine Bouhaddi[3]

[1] Ecole Nationale d'Ingénieurs de Tunis, Université de Tunis El Manar, BP 37, 1002 Tunis Belvédère, Tunisie
souhirzghal@yahoo.fr, Rachid.Nasri@enit.rnu.tn
[2] Institut Préparatoire aux Etudes d'Ingénieurs de Nabeul, Université de Carthage, 8000 M'rezga, Nabeul-Tunisie
lamjed.bouazizi@ipein.rnu.tn
[3] Institut FEMTO ST UMR 6174, Département Mécanique Appliquée R.Chaléat, Université de Franche-Comté, 24 chemin de l'épitaphe 25000 Besançon-France
noreddine.bouhaddi@univ.fcomte.fr

Abstract. This paper is devoted to procedures for finite element modelling of structures incorporating viscoelastic materials, with emphasis placed on reduction methods intended for the reduction of the order of the finite elements matrices of the damped systems. This work focuses the use of Guyan reduction method. To account the frequency-dependant behaviour of viscoelastic materials, the Golla-Hughes-Mc-Tavish (GHM) model is used. The paper is organized as follows: introductory comments are first presented regarding the use of viscoelastic models and the procedures for their inclusion in the finite element structural matrices. Next, the studied Guyan reduction method is developed. Numerical simulations applied to beam and plate structures are presented to illustrate the use of Guyan reduction method applied to GHM damped finite element models. These examples will highlight the domain of validity of the proposed method, its performance and practical interest in the dynamic analysis of viscoelastically damped structures.

Keywords: sandwich, viscoelastic materials, finite element modelling, Guyan reduction.

1 Introduction

Viscoelastic sandwich materials offer advantages in term of high specific stiffness and strength values. Furthermore, they are corrosion resistant, have good anti-vibrations and anti-noise properties and this make them suitable for a variety of structural engineering applications. So, sandwich structures have been the subject of many investigations. To model the dynamic behavior of these structures incorporating viscoelastic dampers, finite element procedures have been combined with models intended to describe the frequency dependence of mechanical properties of

M. Haddar et al. (Eds.): *Design and Modeling of Mechanical Systems*, LNME, pp. 119–126.
DOI: 10.1007/978-3-642-37143-1_15

viscoelastic materials. An important class of such models is based on the addition of internal or dissipative variables to account for the viscoelastic behavior which the most useful and effective approach is the Hughes-Golla-Mc Tavish (GHM) model [1, 2]. Unfortunately, the inclusion of internal variables leads to global systems of equations of motion whose numbers of degrees-of-freedom (dofs) largely exceeds the order of the associated undamped system. As a result, the numerical resolution of such equation can requires prohibitive computational effort. To remedy this situation and reduce the order of the finite elements matrices, model reduction techniques are adopted. One effective and popular model reduction method is the "Guyan condensation method" [3, 4] according to which reduction is achieved by partitioning the equations of motion in term of master and slaves coordinates. By neglecting the inertia associated to the salve coordinates, only the master coordinates are kept in the model. Thereby, this method removes some of the physical coordinates and produces a reduced order model with coordinates are a subset of the original coordinates system; The obtained reduced model preserves the dynamic properties of original GHM model and leads to a drastic reduction of the dofs in the whole finite element model without loss of precision in the low frequency band.

2 GHM Finite Element Model

The GHM model was introduced by Golla Hughes (1985) [1] and modified by Golla McTavish (1993) [2]. According to this model, the modulus function in the Laplace domain is expressed as:

$$G(s) = G_0\left(1 + \sum_{i=1}^{N_G} \alpha_i \frac{s^2 + 2\xi_i\omega_i s}{s^2 + 2\xi_i\omega_i s + \omega_i^2}\right) \tag{1}$$

Where: G_0 is the static modulus; α_i , ξ_i , ω_i are the parameters of the i mini-oscillator, and N_G is the number of mini-oscillators.

Consider the finite element equation of motion of a structure containing N degree-of-freedom:

$$[M]\{\ddot{q}\} + [K]\{q\} = \{f\} \tag{2}$$

Where $[M] \in \mathbb{R}^{N\times N}$ is the mass matrix (symetric and positive definite), $[K] \in \mathbb{R}^{N\times N}$ is the stiffness matrix (symmetric and nonnegative), $\{q\} \in \mathbb{R}^N$ is the vector displacements and $\{f\} \in \mathbb{R}^N$ is the loading vector.

It is assumed that the structure contains both elastic and viscoelastic elements, so that the stiffness matrix can be decomposed as follows:

$$[K] = [K_e] + [K_V(s)] \tag{3}$$

$[K_e]$ is the stiffness matrix corresponding to the purely elastic substructure and $[K_V(s)]$ is the stiffness matrix associated to the viscoelastic substructure.

The inclusion of the frequency-dependent behavior of the viscoelastic material can be made as follows:

$$[K_V(s)] = G(s)[\bar{K}_V] \tag{4}$$

A series of dissipative coordinates can be defined as follows:

$$\{z_i(s)\} = \left\{ \frac{\omega_i^2}{s^2 + 2\xi_i\omega_i s + \omega_i^2} \right\} \{q(s)\} \tag{5}$$

Then, by combining equations (3) and (4) with (2), introducing equation (5) in the formulation and after some manipulations and back to time domain, the following coupled system of equation for **one mini-oscillator** is obtained:

$$\left\{ s^2 \begin{bmatrix} [M] & [0] \\ [0] & [M_z] \end{bmatrix} + s \begin{bmatrix} [0] & [0] \\ [0] & [D_z] \end{bmatrix} + \begin{bmatrix} [K_q] & [K_{qz}] \\ [K_{qz}]^T & [K_z] \end{bmatrix} \right\} \begin{Bmatrix} q(s) \\ z(s) \end{Bmatrix} = \begin{Bmatrix} f(s) \\ 0 \end{Bmatrix} \tag{6}$$

Or in compact form:

$$\left\{ s^2[M_G] + s[D_G] + [K_G] \right\} \{q_G(s)\} = \{f_G(s)\} \tag{7}$$

The equation of motion in time domain can be expressed in matrix form as follows:

$$[M_G]\{\ddot{q}_G\} + [D_G]\{\dot{q}_G\} + [K_G]\{q_G\} = \{F_G\} \tag{8}$$

Where:

$$[M_G] = \begin{bmatrix} [M] & 0 & \cdots & 0 \\ 0 & \frac{\alpha_1}{\omega_1^2}[K_V^0] & 0 & \vdots \\ \vdots & 0 & \ddots & 0 \\ 0 & \cdots & 0 & \frac{\alpha_{N_G}}{\omega_{N_G}^2}[K_V^0] \end{bmatrix}; \quad [D_G] = \begin{bmatrix} 0 & 0 & \cdots & 0 \\ 0 & \frac{2\alpha_1\xi_1}{\omega_1}[K_V^0] & 0 & \vdots \\ \vdots & 0 & \ddots & 0 \\ 0 & \cdots & 0 & \frac{2\alpha_{N_G}\xi_{N_G}}{\omega_{N_G}}[K_V^0] \end{bmatrix}$$

$$[K_G] = \begin{bmatrix} [K_e] + [K_V^\infty] & -\alpha_1[K_V^0] & \cdots & -\alpha_{N_G}[K_V^0] \\ -\alpha_1[K_V^0]^T & \alpha_1[K_V^0] & 0 & \vdots \\ \vdots & 0 & \ddots & 0 \\ -\alpha_{N_G}[K_V^0]^T & \cdots\cdots & 0 & \alpha_{N_G}[K_V^0] \end{bmatrix}; \qquad [K_V^0] = G_0[\bar{K}_V]; [K_V^\infty] = [K_V^0]\left(1 + \sum_{i=1}^{N_G} \alpha_i\right)$$

Consequently, the inclusion of dissipative coordinates increases the order of the differential equation of motion such that the structural degrees-of-freedom are least doubled. This increases the computational time of the system and motivates the use of reduction methods.

3 Guyan Reduction Method

Guyan reduction [3, 4] is based to divide the displacements vector $\{q\}$ into two sub-vectors: a sub-vector of master dofs $\{q^m\}$ and sub-vector of slave dofs $\{q^s\}$ as follows:

$$\{q\} = \begin{Bmatrix} q^m \\ q^s \end{Bmatrix} \tag{9}$$

By neglecting the inertia and the external load associated to the first equation of equation of motion (6) writing in time domain and partitioning it in master and slaves dofs leads to follows system of equations:

$$\begin{bmatrix} K_q^{mm} & K_q^{ms} \\ K_q^{sm} & K_q^{ss} \end{bmatrix} \begin{Bmatrix} q^m \\ q^s \end{Bmatrix} = -\begin{bmatrix} K_{qz}^{mm} & K_{qz}^{ms} \\ K_{qz}^{sm} & K_{qz}^{ss} \end{bmatrix} \{z\} \tag{10}$$

Where:

m and s are, respectively, the index of master dofs contribution and slaves dofs contribution.

Consider the esclave part of equation (10), the global vector of the viscoelastic vector can be expressed in function of master dofs and dissipative dofs as follows:

$$\begin{Bmatrix} q^m \\ q^s \\ z \end{Bmatrix} = [T] \begin{Bmatrix} q^m \\ z \end{Bmatrix} \tag{11}$$

Where:

[T] is the Guyan matrix transformation as form:

$$[T] = \begin{bmatrix} I_1 & 0 \\ t_1 & t_2 \\ 0 & I_2 \end{bmatrix} \tag{12}$$

$$[t_1] = -[K_q^{ss}]^{-1} [K_q^{sm}] \tag{13.1}$$

$$\left[t_2\right] = -\left[K_q^{ss}\right]^{-1}\left[K_{qz}^{sm} \quad K_{qz}^{ss}\right] \tag{13.2}$$

Consequently, the reduced equation of motion corresponding to Guyan condensation is expressed such that:

$$\left[M_c\right]\{\ddot{q}\} + \left[D_c\right]\{\dot{q}\} + \left[K_c\right]\{q\} = \{f_c\} \tag{14}$$

Where: $\left[M_c\right]$; $\left[D_c\right]$ and $\left[K_c\right]$ are respectively the mass, the stiffness and the damping condensed matrices.

4 Numerical Simulations

Numerical examples are presented to illustrate the use of the model previously described to evaluate the damping performance of the viscoelastic materials and Guyan reduction method as applied to beam and plate structures. Hence, the viscoelastic beam and plate are constituted by two elastic layers (faces) in Aluminum and a viscoelastic layer (core) of the nuance ISD112. All the calculations are developed using the software MATLAB®. The material and geometrical characteristics of both beam and plate structures are shown in Table 1. The values of the parameters of the viscoelastic commercially available ISD112, manufactured by3M™ used at 27°C for one mini-oscillator are presented in Table 2.

Table 1 Material and geometrical properties of the used sandwich structures [5]

Elastic Layers	Shear modulus: $G_f = 9{,}6 \times 10^{10}$Pa
	Poisson ratio: $\upsilon_f = 0{,}3$
	Density :$\rho_f = 2766\text{Kg.m}^{-3}$
	Thickness: $h_f = 1{,}524\text{mm}$
Viscoelastic layer	Shear modulus: GHM modulus (1)
	Poisson ratio: $\upsilon_c = 0{,}49$
	Density :$\rho_c = 1600\text{Kg.m}^{-3}$
	Thickness: $h_c = 0{,}127\text{mm}$
Beam	Length: L=177,8mm Width: l=12,7mm
Rectangular plate	Length: L=177,8mm Width: l=88,9mm

Table 2 Parameters of the GHM viscoelastic model identified for material ISD112 3M™ for one mini-oscillator

Model GHM (i=1)	Value
α_i	4.8278
ω_i	28045
ξ_i	22.013
G_0 [MPa]	4.8278

Case 1: Viscoelastic Beam

The used FE mesh of the beam involves one element through the width and 20 elements along the length. The excitation point and the response point are selected at the extremity of the beam. The response curves of the full and the reduced GHM model are presented in figure 1.

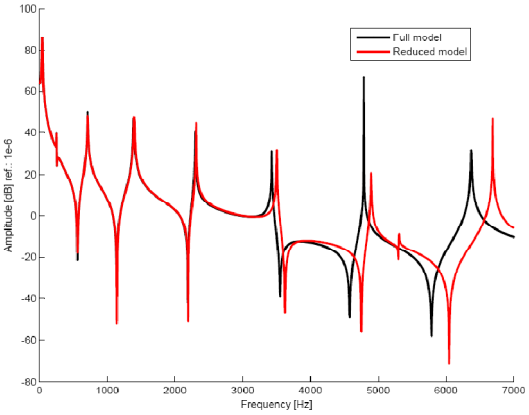

Fig. 1 FRFs for the full and reduced system-Guyan method of the viscoelastic beam

Figure 1 shows the frequency response functions of the beam for the Guyan reduced model compared with those of full model. As can be seen, FRFs of the two models stick to the first three modes of vibration in the study frequency band [0-7000] Hz and taking off from a certain frequency called the cutoff frequency which is around 4000 Hz. This cutoff frequency defines the utility field of the Guyan condensation method from which the results are not acceptable. So, this reduction method is a viable method of modeling the parameters of a viscoelastic material and leads to drastic reduction of the dofs in the whole finite element model without loss of precision in the low frequency band.

Case 2: Viscoelastic Plate

For the finite element model, a mesh of 50 elements is carry out with 10 × 5 elements are discretized in the directions of the length and width respectively. The following figure shows the FRFs response of the full and reduced GHM plate.

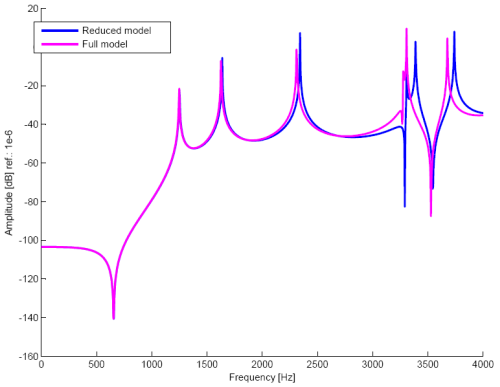

Fig. 2 FRFs for the full and reduced system-Guyan method of the Viscoelastic plate

For the viscoelastic sandwich plate, the FRFs function responses for full and Guyan reduced models are combined for the first three vibration modes. Beyond the 3000 Hz value, defining the cutoff frequency, the response curves do not stick. This cutoff frequency defines the domain of validity of this method in which the results are accuracy and valid.

5 Conclusions

Finite element procedures of structures incorporating viscoelastic materials that are able to reproduce the FRFs before and after reduction was implemented, with emphasis placed on the incorporation of models to account the frequency-dependant behavior of viscoelastic materials by the GHM model and the implementation of the Guyan reduction method.

The numerical simulations presented in this paper enabled to illustrate the application of reduction order procedures as a tool to evaluate the damping, natural frequencies of the reduction viscoelastically structures as a dynamic representation of the larger order systems, reduction the time for processing the data and the analysis and enable to reduce the CPU time while preserving the dynamic properties of original GHM model. This method is so efficient for the damping systems which contain a large number of dofs leading to reduced system which is a subset of original system without loss of precision in the low frequency band.

References

[1] Mc-Tavish, D.J., Hughes, P.C.: Dynamics of viscoelastic structure-a time domain, finite element formulation. ASME, Int. J. Applied Mechanics 52, 897–906 (1985)

[2] Mc-Tavish, D.J., Hughes, P.C.: Modeling of linear viscoelastic space structures. ASME, Int. J. Vibration and Acoustics of Applied Mechanics 52, 103–113 (1993)

[3] Guyan, R.J.: Reduction of Stiffness and Mass Matrices. AIAA Journal 3(2), 38 (1965)
[4] Park, C.H., Inman, D.J., Lam, M.J.: Model reduction of Viscoelastic finite element models. Int. J. Sound and Vibration 219, 619–637 (1999)
[5] Bilasse, B., Daya, E.M.: Modélisation numérique des vibrations linéaires et non linéaires des structures sandwiches à âme viscoélastique. Thèse présentée à l'université de Metz France (2010)

Coupled Finite Element-Boundary Element Formulation for Noise and Vibration Attenuation Using Shunt Piezoelectric Materials

Walid Larbi, Jean-François Deü, and Roger Ohayon

Structural Mechanics and Coupled Systems Laboratory,
Conservatoire National des Arts et Métiers,
292, rue Saint-Martin,
75141 Paris Cedex 03, France
{walid.larbi,jean-francois.deu,roger.ohayon}@cnam.fr

Abstract. In this paper, we present a coupled finite element/boundary element method (FE/BE) for control of noise radiation and sound transmission of vibrating structure by active piezoelectric techniques. The system consists of an elastic structure (with surface mounted piezoelectric patches) coupled to external/internal acoustic domains. The passive shunt damping strategy is employed for vibration attenuation in the low frequency range.

Keywords: finite element method, boundary element method, vibroacoustics, piezoelectric patches, shunt damping technique, noise and vibration attenuation.

1 Introduction

During the last two decades there has been an accelerating level of interest in the control of noise radiation and sound transmission from vibrating structures by active piezoelectric techniques in the low frequency range. In this context, resonant shunt damping techniques have been recently used for interior structural-acoustic problems [1, 2]. The present work concerns the extension of this technique to internal/external vibroacoustic problems using a finite-element/boundary-element method (FEM/BEM) for the numerical resolution of the fully coupled electromechanical-acoustic system.

First, a finite element formulation of an elastic structure with surface-mounted piezoelectric patches and subjected to pressure load due to the presence of an external fluid is derived from a variational principle involving structural displacement, electrical voltage of piezoelectric elements and acoustic pressure at the fluid-structure interface. This formulation, with only one couple of electric variables per patch, is well adapted to practical applications since realistic electrical boundary conditions, such that equipotentiality on the electrodes and prescribed global electric charges, naturally appear. The global charge/voltage variables are intrinsically adapted to include any external electrical circuit into the electromechanical problem and to simulate the effect of resistive or resonant shunt techniques.

M. Haddar et al. (Eds.): *Design and Modeling of Mechanical Systems*, LNME, pp. 127–134.
DOI: 10.1007/978-3-642-37143-1_16

In the second part of this work, the direct boundary element method is used for modeling the scattering/radiation of sound by the structure coupled to an acoustic domain. The BEM is derived from Helmholtz integral equation involving the surface pressure and normal acoustic velocity at the boundary of the acoustic domain. The coupled FE-BE model is obtained by using a compatible mesh at the fluid-structure interface. The present coupling procedure is quite general and suitable for modeling any three-dimensional geometry for bounded or unbounded structural-acoustic radiation problems.

2 Finite Element Formulation of Elastic Structure with Piezoelectric Shunt Systems

2.1 Harmonic Equations

An elastic structure occupying the domain Ω_E is equipped with P piezoelectric patches and coupled to an inviscid linear acoustic fluid occupying the domain Ω_F (figure 1). Each piezoelectric patch has the shape of a plate with its upper and lower surfaces covered with a very thin layer electrodes. The pth patch, $p \in \{1, \cdots, P\}$, occupies a domain $\Omega^{(p)}$ such that $(\Omega_E, \Omega^{(1)}, \cdots, \Omega^{(P)})$ is a partition of the all structure domain Ω_S. In order to reduce the vibration amplitudes of the coupled problem, a resonant shunt circuit made up of a resistance $R^{(p)}$ and an inductance $L^{(p)}$ in series is connected to each patch [3, 1, 4].

We denote by Σ the fluid-structure interface and by $\mathbf{n}^S$ and $\mathbf{n}^F$ the unit normal external to Ω_S and Ω_F, respectively. Moreover, the structure is clamped on a part Γ_u and subjected (i) to a given surface force density $\mathbf{F}^d$ on the complementary part Γ_σ of its external boundary and (ii) to a pressure field p due to the presence of the fluid on its boundary Σ. The electric boundary condition for the pth patch is defined by a prescribed surface density of electric charge Q^d on $\Gamma_D^{(p)}$.

The linearized deformation tensor is $\boldsymbol{\varepsilon} = \frac{1}{2}\left(\nabla \mathbf{u} + \nabla^T \mathbf{u}\right)$ and the stress tensor is denoted by $\boldsymbol{\sigma}$. Moreover, $\mathbf{D}$ denotes the electric displacement and $\mathbf{E}$ the electric

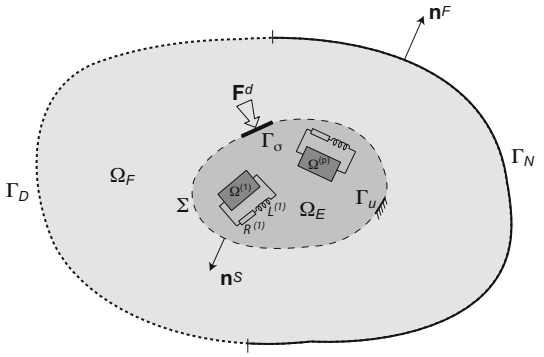

Fig. 1 Vibrating structure with piezoelectric shunt systems coupled to an acoustic domain

field such that $\mathbf{E} = -\nabla\psi$ where ψ is the electric potential. ρ_S is the mass density of the structure. The linear piezoelectric constitutive equations write:

$$\boldsymbol{\sigma} = \mathbf{c}\,\boldsymbol{\varepsilon} - \mathbf{e}^T\,\mathbf{E} \tag{1}$$

$$\mathbf{D} = \mathbf{e}\,\boldsymbol{\varepsilon} + \boldsymbol{\epsilon}\,\mathbf{E} \tag{2}$$

where $\mathbf{c}$ denotes the elastic moduli at constant electric field, $\mathbf{e}$ denotes the piezoelectric constants, and $\boldsymbol{\epsilon}$ denotes the dielectric permittivities at constant strain.

The local equations of elastic structure with piezoelectric patches and submitted to an acoustic pressure are [5]

$$\operatorname{div}\boldsymbol{\sigma} + \omega^2\rho_S\mathbf{u} = \mathbf{0} \qquad \text{in } \Omega_S \tag{3a}$$

$$\boldsymbol{\sigma}\,\mathbf{n}^S = \mathbf{F}^d \qquad \text{on } \Gamma_\sigma \tag{3b}$$

$$\mathbf{u} = \mathbf{0} \qquad \text{on } \Gamma_u \tag{3c}$$

$$\boldsymbol{\sigma}\,\mathbf{n}^S = p\,\mathbf{n} \qquad \text{on } \Sigma \tag{3d}$$

$$\operatorname{div}\mathbf{D} = 0 \qquad \text{in } \Omega^{(p)} \tag{4a}$$

$$\mathbf{D}\cdot\mathbf{n}^S = Q^d \qquad \text{on } \Gamma_D^{(p)} \tag{4b}$$

where ω is the angular frequency.

For each piezoelectric patch, a set of hypotheses, which can be applied to a wide spectrum of practical applications, are formulated [1, 4].

Under those assumptions, the electric field vector $\mathbf{E}^{(p)}$ can be considered normal to the electrodes and uniform in the piezoelectric patch [6], so that for all $p \in \{1, \cdots, P\}$:

$$\mathbf{E}^{(p)} = -\frac{V^{(p)}}{h^{(p)}}\mathbf{n}^{(p)} \quad \text{in} \quad \Omega^{(p)} \tag{5}$$

where $V^{(p)}$ is the potential difference between the upper and the lower electrode surfaces of the pth patch which is constant over $\Omega^{(p)}$ and where $\mathbf{n}^{(p)}$ is the normal unit vector to the surface of the electrodes.

2.2 Finite Element Formulation

After applying variational formulation to Eqs. (3) and (4) (see [1]) and discretization by finite element method and using the following additional relation between electrical potential differences and electric charges due to the shunt circuits:

$$-\omega^2\mathbf{L}\mathbf{Q} - i\omega\mathbf{R}\mathbf{Q} + \mathbf{V} = \mathbf{0} \tag{6}$$

we find the following matrix equation:

$$\begin{bmatrix} \mathbf{K}_u + \mathbf{C}_{uV}\mathbf{K}_V^{-1}\mathbf{C}_{uV}^T & \mathbf{C}_{uV}\mathbf{K}_V^{-1} & -\mathbf{C}_{up} \\ \mathbf{K}_V^{-1}\mathbf{C}_{uV}^T & \mathbf{K}_V^{-1} & \mathbf{0} \end{bmatrix} \begin{bmatrix} \mathbf{U} \\ \mathbf{Q} \\ \mathbf{P}_\Sigma \end{bmatrix} - i\omega \begin{bmatrix} \mathbf{0} & \mathbf{0} & \mathbf{0} \\ \mathbf{0} & \mathbf{R} & \mathbf{0} \end{bmatrix} \begin{bmatrix} \mathbf{U} \\ \mathbf{Q} \\ \mathbf{P}_\Sigma \end{bmatrix} + - \omega^2 \begin{bmatrix} \mathbf{M}_u & \mathbf{0} & \mathbf{0} \\ \mathbf{0} & \mathbf{L} & \mathbf{0} \end{bmatrix} \begin{bmatrix} \mathbf{U} \\ \mathbf{Q} \\ \mathbf{P}_\Sigma \end{bmatrix} = \begin{bmatrix} \mathbf{F} \\ \mathbf{0} \end{bmatrix} \quad (7)$$

where $\mathbf{Q} = (Q^{(1)}\, Q^{(2)} \cdots Q^{(P)})^T$ and $\mathbf{V} = (V^{(1)}\, V^{(2)} \cdots V^{(P)})^T$ are the column vectors of electric charges and potential differences; $\mathbf{R} = \text{diag}\left(R^{(1)}\, R^{(2)} \cdots R^{(P)}\right)$ and $\mathbf{L} = \text{diag}\left(L^{(1)}\, L^{(2)} \cdots L^{(P)}\right)$ are the diagonal marices of the resistances and inductances of the patches; $\mathbf{U}$ and $\mathbf{P}_\Sigma$ are the vectors of nodal values of $\mathbf{u}$ and p; $\mathbf{M}_u$ and $\mathbf{K}_u$ are the mass and stiffness matrices of the structure (elastic structure with piezoelectric patches); $\mathbf{C}_{uV}$ is the electric mechanical coupled stiffness matrix; $\mathbf{K}_V = \text{diag}\left(C^{(1)}\, C^{(2)} \cdots C^{(P)}\right)$ is a diagonal matrix filled with the P capacitances of the piezoelectric patches; $\mathbf{C}_{up}$ is the fluid-structure coupled matrix; $\mathbf{F}$ is the applied mechanical force vector.

3 Boundary Element Formulation for External/Internal Acoustic Fluid

3.1 Harmonic Equations

In this section, the direct boundary element method for exterior/interior acoustic domain is presented. The governing equations of the acoustic fluid are [7, 8]

$$\Delta p + k^2 p = 0 \qquad \text{in } \Omega_F \quad (8a)$$

$$\frac{\partial p}{\partial n} = 0 \qquad \text{on } \Gamma_D \quad (8b)$$

$$\frac{\partial p}{\partial n} = \rho_F \omega^2 \mathbf{u} \cdot \mathbf{n} \qquad \text{on } \Sigma \quad (8c)$$

$$\frac{\partial p}{\partial r} + ikp = \theta(\frac{1}{r}) \qquad \text{for } r \to \infty \quad (8d)$$

Eq. (8a) represents the Helmholtz equation where $k = \omega/c$ is the wave number, i.e. the ration of the circular frequency ω and the sound velocity c; Eq. (8b) is the rigid boundary condition on Γ_D; Eq. (8c) is the kinematic interface fluid-structure condition on Σ; Eq. (8d) represents the Summerfield condition at infinity.

3.2 Boundary Element Formulation

The boundary element formulation for acoustic problems can be used for the interior and exterior problems. The Helmholtz equation is valid for the pressure p at the arbitrary collocation point $\mathbf{x}$ within the acoustic domain Ω_F. A weak form of this equation is obtained by weighting with the fundamental solution:

$$G(\mathbf{x},\mathbf{y}) = \frac{e^{ik|\mathbf{x}-\mathbf{y}|}}{4\pi|\mathbf{x}-\mathbf{y}|} \tag{9}$$

where $|\mathbf{x}-\mathbf{y}|$ denotes the distance between the arbitrary point $\mathbf{x}$ and the load source point $\mathbf{y}$.

Applying Green's second theorem, the Helmholtz equation can be transformed into a boundary integral equation, which can be expressed as follows

$$c(\mathbf{x})p(\mathbf{x}) = \int_{\partial\Omega_F} p(\mathbf{y})\frac{\partial G(\mathbf{x},\mathbf{y})}{\partial n_y}\mathrm{d}S - \int_{\partial\Omega_F}\frac{\partial p(\mathbf{y})}{\partial n_y}G(\mathbf{x},\mathbf{y})\mathrm{d}S \tag{10}$$

where $c(\mathbf{x})$ is the corner coefficient.

The fluid boundary is divided into N quadrilateral elements ($\partial\Omega_F = \sum_{j=1}^{N} S_j$) and Eq. (10) is discretized. After using the relation between the acoustic pressure and the fluid normal velocity $\frac{\partial p}{\partial n} = -i\rho_F\omega v$ (where $v = \mathbf{v}^F \cdot \mathbf{n}$) and numerical evaluation, the discrete Helmholtz equation can be written in the following matrix form:

$$\mathbf{HP} = i\rho_F\omega\mathbf{G}\mathbf{v} \tag{11}$$

where $\mathbf{P}$ and $\mathbf{v}$ are the vectors with sound pressure and velocity in the normal direction to the boundary surface at the nodal position of the boundary element mesh.

4 FE/BE Formulation for the Fluid-Structure with Shunt Systems Coupled Problem

The fluid boundary domain $\partial\Omega_F$ is divided into two parts including Γ_D (where the rigid boundary condition is applied) and the interface Σ (for the fluid-structure interface) such as $\partial\Omega_F = \Gamma_D \cup \Sigma$ and $\Gamma_D \cap \Sigma = \emptyset$. The boundary conditions given in Eqs. (8b) and (8c) can be expressed in discretized form

$$\mathbf{v}_D = \mathbf{0} \qquad \text{on } \Gamma_D \tag{12a}$$

$$\mathbf{v}_\Sigma = i\omega\mathbf{T}\mathbf{U} \quad \text{on } \Sigma \tag{12b}$$

where $\mathbf{T}$ is the global coupling matrix that transforms the nodal normal displacement of the structure to the normal velocity of the acoustic fluid at the interface. Substituting Eqs. (12) into the BE matrix expression (Eq. (11)) yields

$$\begin{bmatrix}\mathbf{H}_{11} & \mathbf{H}_{12}\\ \mathbf{H}_{21} & \mathbf{H}_{22}\end{bmatrix}\begin{bmatrix}\mathbf{P}_\Sigma\\ \mathbf{P}_D\end{bmatrix} = \begin{bmatrix}\mathbf{G}_{11} & \mathbf{G}_{12}\\ \mathbf{G}_{21} & \mathbf{G}_{22}\end{bmatrix}\begin{bmatrix}i\rho_F\omega^2\mathbf{T}\mathbf{U}\\ \mathbf{0}\end{bmatrix} \tag{13}$$

By combining Eq. (7) with Eq. (13), we find the following coupled FE/BE matrix equation

$$\begin{bmatrix} \mathbf{K}_u + \mathbf{C}_{uV}\mathbf{K}_V^{-1}\mathbf{C}_{uV}^T - \omega^2\mathbf{M}_u & \mathbf{C}_{uV}\mathbf{K}_V^{-1} & -\mathbf{C}_{up} & \mathbf{0} \\ \mathbf{K}_V^{-1}\mathbf{C}_{uV}^T & \mathbf{K}_V^{-1} - i\omega\mathbf{R} - \omega^2\mathbf{L} & \mathbf{0} & \mathbf{0} \\ i\rho_F\omega^2\mathbf{G}_{11}\mathbf{T} & \mathbf{0} & \mathbf{H}_{11} & \mathbf{H}_{12} \\ i\rho_F\omega^2\mathbf{G}_{21}\mathbf{T} & \mathbf{0} & \mathbf{H}_{21} & \mathbf{H}_{22} \end{bmatrix} \begin{bmatrix} \mathbf{U} \\ \mathbf{Q} \\ \mathbf{P}_\Sigma \\ \mathbf{P}_D \end{bmatrix} = \begin{bmatrix} \mathbf{F} \\ \mathbf{0} \\ \mathbf{0} \\ \mathbf{0} \end{bmatrix} \quad (14)$$

5 Numerical Example

We consider a 3D hexaedric acoustic cavity of size A= 0.3048 m, B=0.1524 m and C=0.1524 m along the directions x, y, and z, respectively. The cavity is completely filled with air (density ρ= 1.2 kg/m^3 and speed of sound c=340 m/s). The cavity walls are rigid except the top one, which is a flexible aluminum plate of thickness 1 mm. The density of the plate is 2690 kg/m^3, the Youngs modulus is 70 GPa and Poisson ratio 0.3. On the top surface of the plate, a PIC 151 patch is bonded, whose in plane dimensions are 0.0762×0.0508 m^2 along x and y and 0.5 mm thick (see figure 2). The mechanical characteristics of the piezoelectric material PIC 151 are given in [2].

The plate is excited by an unit distributed time harmonic pressure load. The coupled FEM/BEM results are compared with those obtained from a FEM/FEM analysis. As can be seen in figure 3, the sound pressure level is calculated on the plate center. The results for the two methods are very similar at sound level peaks

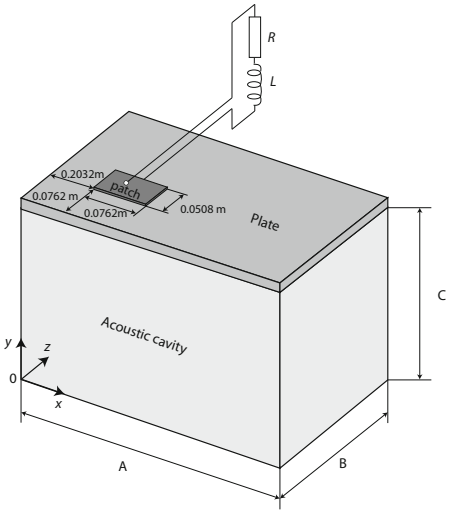

Fig. 2 Electromechanical-acoustic coupled system: geometrical data

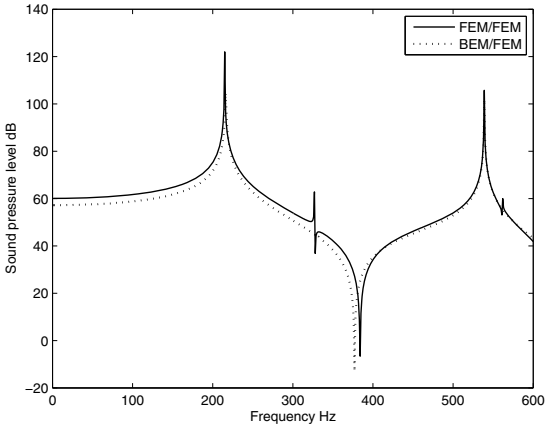

Fig. 3 Sound pressure level on plate center: comparison between FEM/FEM and FEM/BEM approaches

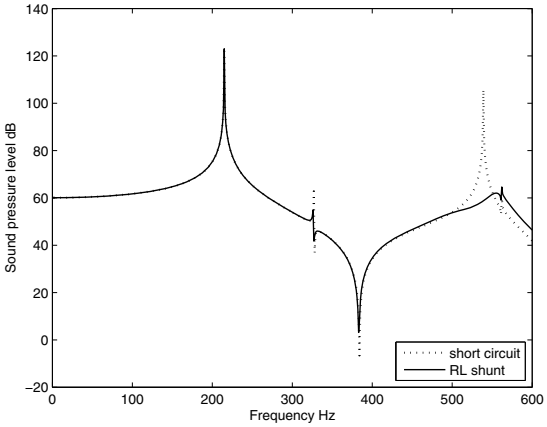

Fig. 4 Sound pressure level on plate center with and without shunt system

(resonance frequencies) which enable us to check the validity of the proposed FEM/BEM coupled formulation.

In order to achieve maximum vibration dissipation of the third coupled mode, the patch is tuned now to an RL shunt circuit. The optimal values of the shunt electrical circuit are taken R=348 Ω and L=0.61 H. The system vibratory response is obtained with the proposed BEM/FEM approach. Figure 4 presents the sound pressure level on plate center with and without shunt system. This figure shows that the resonant magnitude for the third mode has been significantly reduced due to the shunt effect. In fact, the strain energy present in the piezoelectric material is

converted into electrical energy and hence dissipated into heat using the RL shunt device.

6 Conclusions

In this work, a coupled finite element/boundary element method (FEM/BEM) for control of noise radiation and sound transmission of vibrating structure by active piezoelectric techniques is presented. The passive shunt damping strategy is employed for vibration attenuation in the low frequency range. Work in progress concerns the optimization of piezoelectric patches positioning and form.

References

1. Larbi, W., Deü, J.-F., Ciminello, M., Ohayon, R.: Structural-acoustic vibration reduction using switched shunt piezoelectric patches: A finite element analysis. Journal of Vibration and Acoustics 132(5), 051006 (9 pages) (2010)
2. Larbi, W., Deü, J.-F., Ohayon, R.: Finite element formulation of smart piezoelectric composite plates coupled with acoustic fluid. Composite Structures 94(2), 501–509 (2012)
3. Hagood, N., Von Flotow, A.: Damping of structural vibrations with piezoelectric materials and passive electrical network. Journal of Sound and Vibration 146(2), 243–268 (1991)
4. Deü, J.-F., Larbi, W., Ohayon, R.: Structural-acoustic vibration reduction using piezoelectric shunt techniques: FE formulation and reduced order model. In: Proc. of the 3rd International Conference on Computational Methods in Structural Dynamics and Earthquake Engineerin, COMPDYN 2011, Corfu, Greece, May 25-28 (2011)
5. Deü, J.-F., Larbi, W., Ohayon, R.: Piezoelectric structural acoustic problems: Symmetric variational formulations and finite element results. Computer Methods in Applied Mechanics and Engineering 197(19-20), 1715–1724 (2008)
6. Thomas, O., Deü, J.-F., Ducarne, J.: Vibrations of an elastic structure with shunted piezoelectric patches: Efficient finite element formulation and electromechanical coupling coefficients. International Journal for Numerical Methods in Engineering 80(2), 235–268 (2009)
7. Walker, S.: Boundary elements in fluid-structure interaction problems rotational shells. Applied Mathematical Modelling 4, 345–350 (1980)
8. Rajakumar, C., Ali, A.: Boundary Element-Finite Element Coupled Eigenanalysis of Fluid-Structure Systems. International Journal for Numerical Methods in Engineering 39(10), 1625–1634 (1996)

A TMD Parameters Optimization with Uncertain Bounded Structural Parameters

Elyes Mrabet[1], Samir Ghanmi[1], Mohamed Guedri[1], and Mohamed Ichchou[2]

[1] Unité de Recherche en Dynamique des Structures, Modélisation et Ingénierie des Systèmes Multi-physiques, Institut Préparatoire aux Etudes d'Ingénieur de Nabeul, Campus Universitaire El Mrazka Nabeul 8000, Tunisie
elyes.mrabet@yahoo.fr, samir.ghanmi@ipein.rnu.tn, mohamed.guedri@isetn.rnu.tn

[2] LTDS UMR5513 Ecole Centrale de Lyon, 36 Avenue Guy de Collongue, 69134 Ecully, France
mohamed.ichchou@ec-lyon.fr

Abstract. The purpose of the present work is to present and discuss a technique for optimizing the parameters of a vibration absorber in the presence of structural uncertain but bounded parameters. The technique used in the optimization is an interval extension based on a Taylor expansion of the objective function. The technique allows transforming the problem, initially stochastic, into two independents deterministic sub-problems. Two kinds of problems are considered: the Stochastic Structural Optimization (SSO) and the Reliability Based Optimization (RBO). It has been demonstrated through a Tuned mass Damper optimisation problem that the technique is valid for the structural optimization problem, even for high levels of uncertainties and is less suitable for the reliability based optimization, especially when considering high levels of uncertainties.

Keywords: Uncertainties/ Bounded parameters, Stochastic Structural Optimization, Reliability Based Optimization, Taylor expansion, Interval extension.

1 Introduction

Probabilistic methods are very powerful for the study of vibration control problems in the presence of uncertainties in design parameters, these methods cannot be applied when the statistical parameters are insufficient. In many practical cases, parameters are only described by their extreme and mean values and they are called uncertain but bounded parameters. To solve this kind of problem, a technique based on a Taylor expansion and interval extension (Subrata and Bijian 2011) is investigated in this work and it will be applied on two kinds of optimization problems.

M. Haddar et al. (Eds.): *Design and Modeling of Mechanical Systems*, LNME, pp. 135–142.
DOI: 10.1007/978-3-642-37143-1_17

2 Structural Model and the State Space Equation

Figure 1 shows an idealized mechanical model of a TMD described by $\omega_T = \sqrt{k_T/m_T}$ and $\xi_T = c_T/2\sqrt{k_T m_T}$, attached with a single degree of freedom primary system described with $\omega_s = \sqrt{k_s/m_s}$ and $\xi_s = c_s/2\sqrt{k_s m_s}$. The system is excited by a base acceleration $\ddot{y}_b$ due to seismic motion which is modeled by the Kanai-Tajimi stationary stochastic process (Subrata and Bijian 2011).

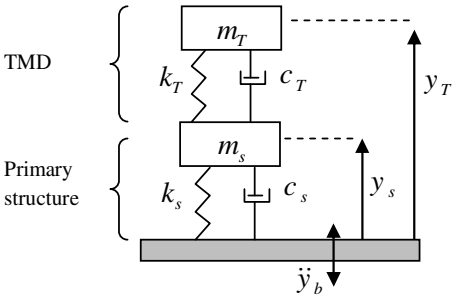

Fig. 1 The primary structure, TMD system

Considering the mass ratio $\lambda = m_T/m_s$, the system equations written in the state space form are deduced from the characteristic system matrices A and B:

$$A = \begin{pmatrix} 0 & 0 & 1 & 0 & 0 & 0 \\ 0 & 0 & 0 & 1 & 1 & 0 \\ 0 & 0 & 0 & 0 & 0 & 1 \\ -\omega_T^2 & \omega_T^2 & \omega_f^2 & -2\xi_T\omega & 2\xi_T\omega_T & 2\xi_f\omega_f \\ \lambda\omega_T^2 & -(\lambda\omega_T^2+\omega_s^2) & \omega_f^2 & 2\lambda\xi_T\omega_T & -2(\xi_s\omega_s+\lambda\xi_T\omega_T) & 2\xi_f\omega_f \\ 0 & 0 & -\omega_f^2 & 0 & 0 & -2\xi_f\omega_f \end{pmatrix},$$

$$B = 2\pi S_0 \begin{pmatrix} 0 & \cdots & 0 \\ \vdots & \ddots & \vdots \\ 0 & \cdots & 1 \end{pmatrix}$$

ξ_f, ω_f and y_f are the damping ratio, the natural frequency and the relative response (with respect to the ground) of the elastic filter (Subrata and Bijian 2011). The global space state vector is then $Y = (y_T, y_s, y_f, \dot{y}_T, \dot{y}_s, \dot{y}_f)^T$ and S_0 is the intensity of the stationary Gaussian zero means white noise process applied at the bed rock (Subrata and Bijian 2011). The stochastic response of the system is completely known by the space state covariance matrix $R \in \mathbf{R}^{6\times6}$ which is the solution of the Lyapunov equation:

$$AR + RA^T + B = 0 \tag{1}$$

The root mean square displacement (rmsd) of the primary system and the root mean square velocity (rmsv) are $\sigma_{y_s} = \sqrt{R(2,2)}$ and $\sigma_{\dot{y}_s} = \sqrt{R(5,5)}$, respectively.

3 Uncertain But Bounded Parameters and Response Model

When Structure parameters $\mathbf{x} = (x_1, x_2, ..., x_n)$ are Uncertain But Bounded (UBB), it is natural to describe them using intervals. Let $X = [X_1, X_2, ..., X_n]$ be the corresponding box then for every $x_i \in \mathbf{x}$ the corresponding interval is $X_i = [\underline{x}_i, \bar{x}_i]$. Introducing the mean value μ_i of X_i and the maximum deviation Δx_i from the mean, the uncertain but bounded parameter can be written as:

$$X_i = [\underline{x}_i, \bar{x}_i] = [\mu_i - \Delta x_i, \mu_i + \Delta x_i] = \mu_i + \Delta x_i e_\Delta \quad \text{where } e_\Delta = [-1, 1] \tag{2}$$

Then, the *i*th such interval variable can be defined as (Subrata and Bijian 2011), $x_i = \mu_i + \delta x_i$ where $|\delta x_i| \le \Delta x_i$, $i = 1, ..., n$.

Any response variable $f(\mathbf{x})$ that depends on UBB parameter $\mathbf{x}$ is also UBB response. Assuming that the level of uncertainties is small, the response can be expanded in the Taylor series about the mean value $\mu = (\mu_1, ..., \mu_n)$ in the first order terms of $\delta x_i \in [-\Delta x_i, \Delta x_i]$ as:

$$f(\mathbf{x}) = f(\mu) + \sum_{i=1}^{n} \left. \frac{\partial f}{\partial x_i} \right|_{x_i = \mu_i} \delta x_i + ... \tag{3}$$

For presentation convenience, all derivatives $\partial f / \partial x_i$ are evaluated at the mean value of the associated uncertain parameter.

By making use of the interval extension in interval mathematics and adopting the monotonic assumption (Rama et *al.* 2011), the interval region of the function involving the UBB parameters can be separated out to the upper and lower bound function as:

$$\bar{f}(X) = f(\mu) + \sum_{i=1}^{n} \left| \frac{\partial f}{\partial x_i} \right| \Delta x_i \quad \text{and} \quad \underline{f}(X) = f(\mu) - \sum_{i=1}^{n} \left| \frac{\partial f}{\partial x_i} \right| \Delta x_i \tag{4}$$

4 Taylor Expansion of the System Matrices

As the system matrices *A* and *B* involve UBB parameters, the associated response covariance matrix *R* will also involve these parameters. The system matrices can be approximated using Taylor expansion and written in the form of (Eq.3).

Neglecting the higher order term and equating the equal order term, for *i*th UBB parameter, we obtain:

$$A(\mu)R(\mu) + R(\mu)A(\mu)^T + B(\mu) = 0 \qquad \text{and} \tag{5}$$

$$A(\mu)\frac{\partial R}{\partial x_i} + \frac{\partial R}{\partial x_i}A(\mu)^T + B^u = 0 \quad \text{where} \quad B^u = \frac{\partial A}{\partial x_i}R(\mu) + R(\mu)\frac{\partial A}{\partial x_i}^T \tag{6}$$

5 Uncertain But Bounded Parameters and TMD Optimization

The stochastic structural optimization (SSO) can be formulated as follows (Rama et *al.* 2011):

$$\text{Find} \quad d = (\omega_T, \xi_T) \quad \text{To minimize} \quad OF_1 = \sigma_{y_s} \tag{7}$$

The objective function OF_1 is function of UBB parameters and it can be approximated then extended considering (Eq.3) and (Eq.4) as follows:

$$\overline{\sigma}_{y_s}(X) = \sigma_{y_s}(\mu) + \sum_{i=1}^{n}\left|\frac{\partial \sigma_{y_s}}{\partial x_i}\right|\Delta x_i \quad \text{and} \qquad \underline{\sigma}_{y_s}(X) = \sigma_{y_s}(\mu) - \sum_{i=1}^{n}\left|\frac{\partial \sigma_{y_s}}{\partial x_i}\right|\Delta x_i \tag{8}$$

$\sigma_{y_s}(\mu)$ can be obtained from (Eq.5) and the sensitivity of rmsd can be obtained as:

$$\frac{\partial \sigma_{y_s}}{\partial x_i} = \frac{1}{2}\left(\frac{\partial R(2,2)}{\partial x_i} \Big/ \sqrt{R(2,2)}\right) \tag{9}$$

In which the sensitivity of R is obtained by solving (Eq.6) and the sensitivity of A is performed using finite difference method.

Thus, the initial SSO problem is now split into two independent sub-problems yielding the lower and the upper bound solutions.

In the RBO, the optimal criterion proposed for a mechanical system with a TMD is the minimization of the probability of failure of the primary system defined as the exceedance of the displacement y_s to a given threshold value β in a given period [*0,T*]. The failure probability can be approximated by the classical Rice's formula based on the Poisson assumption (Subrata and Bijian 2011) as:

$$P_f(\mathbf{x}) = 1 - \exp\left(-\upsilon_\beta(\mathbf{x})T\right) \text{ where } \upsilon_\beta(\mathbf{x}) = \frac{\sigma_{\dot{y}_s}(\mathbf{x})}{\pi\sigma_{y_s}(\mathbf{x})}\exp\left(\frac{-\beta^2}{2\sigma_{y_s}^2(\mathbf{x})}\right) \tag{10}$$

Thus, the optimization problem can be formulated as:

$$\text{Find} \quad d = (\omega_T, \xi_T) \quad \text{To minimize} \quad OF_2 = P_f(\mathbf{x}) \tag{11}$$

The objective function OF_2 is function of UBB parameters and it can be approximated then extended considering (Eq.3) and (Eq.4) as follows:

$$\overline{P}_f(X) = P_f(\mu) + \sum_{i=1}^{n} \left| \frac{\partial P_f}{\partial x_i} \right| \Delta x_i \quad \text{and} \quad \underline{P}_f(X) = P_f(\mu) - \sum_{i=1}^{n} \left| \frac{\partial P_f}{\partial x_i} \right| \Delta x_i \tag{12}$$

The derivative $\partial P_f / \partial x_i$ can be obtained by direct differentiation as follows:

$$\partial P_f / \partial x_i = \exp\left[-T \left\{ \frac{\sigma_{\dot{y}_s}}{\pi \sigma_{y_s}} \exp\left(\frac{-\beta^2}{2\sigma_{y_s}^2} \right) \right\} - \frac{\beta^2}{2\sigma_{y_s}^2} \right] \times \left[\frac{T\beta^2 \sigma_{\dot{y}_s}}{\pi \sigma_{y_s}^4} \frac{\partial \sigma_{y_s}}{\partial x_i} + \frac{T}{\pi \sigma_{y_s}^2} \left(\sigma_{y_s} \frac{\partial \sigma_{\dot{y}_s}}{\partial x_i} - \sigma_{\dot{y}_s} \frac{\partial \sigma_{y_s}}{\partial x_i} \right) \right]; \quad \frac{\partial \sigma_{\dot{y}_s}}{\partial x_i} = \frac{1}{2} \left(\frac{\partial R(5,5)}{\partial x_i} \Big/ \sqrt{R(5,5)} \right) \tag{13}$$

Thus, the initial RBO problem is now split into two independent sub-problems yielding the lower and the upper bound solutions.

6 Numerical Study

For the numerical study, the UBB parameters are chosen $\mathbf{x} = (\omega_f, \xi_f, \omega_s, \xi_s, S_0)$.

The nominal values are assumed $\mu = (9\pi; 0.4; 8.4\pi; 0.03; 0.03)$, $\lambda = 0.02$, $T = 20$ and $\beta = 0.045$. The optimization is performed using the genetic algorithm available with Matlab global optimization toolbox. The optimization results for the SSO are given in (fig.2-4), for the RBO they are shown in (fig.5-7).

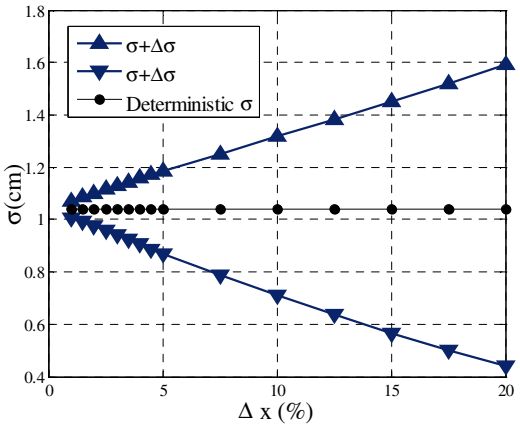

Fig. 2 Optimized root mean square displacement (SSO)

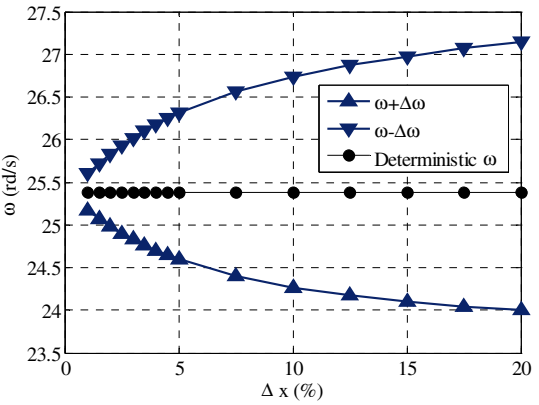

Fig. 3 Optimized natural frequencies (SSO)

The inspection of (fig.2) shows that the lower and upper bounds of the optimized rmsd are linear function of the uncertainties and they are perfectly symmetric with respect to the deterministic value. These results are predictable considering (Eq.8) where rmsd is linear function of uncertainties. The same remarks can be done for (fig.3) in spite of the fact that the corresponding lower and upper bounds frequencies are linear function only over a small range of uncertainties ($\Delta x \leq 5\%$). It can be noted that in (Zhiping and Xiaojun 2009) the authors propose a level of uncertainty less than 5% for comparison of regions replies given by the "Vertex" solution and the interval analysis.

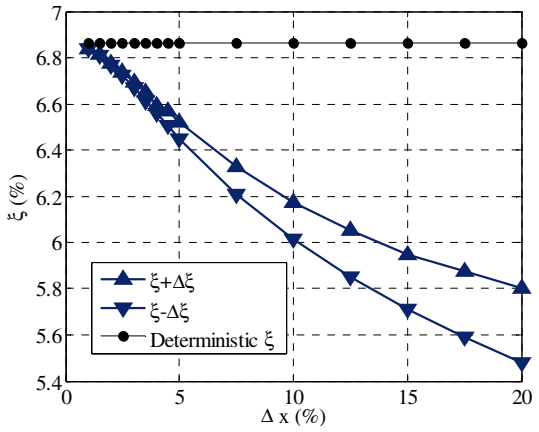

Fig. 4 Optimized damping ratio (SSO)

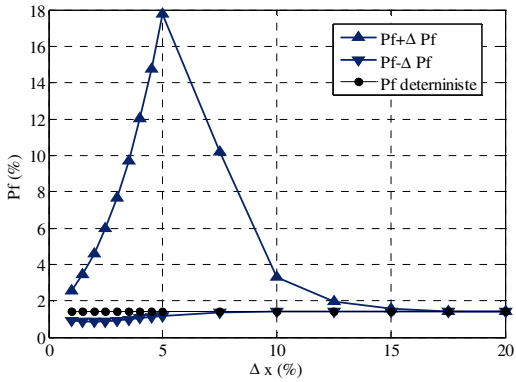

Fig. 5 Optimized failure probability (RBO)

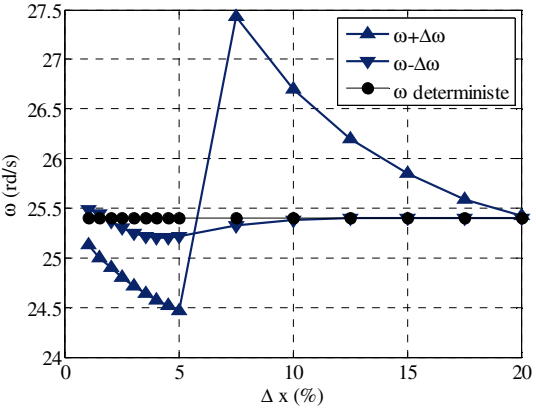

Fig. 6 Optimized natural frequencies (RBO)

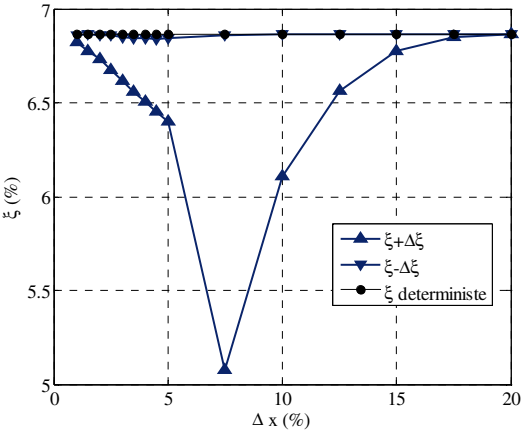

Fig. 7 Optimized damping ratio (RBO)

The inspection of (fig.5) shows that the optimized lower and upper failure probabilities are only linear over a small range of uncertainties. The some remark can be done for (fig.6) and (fig.7). Furthermore, the upper bound of P_f in (fig.5) became decreasing function of uncertainties which is not coherent with (Eq.12). This fact is probably because of the non satisfaction of the monotonic assumption.

7 Conclusion

According to the results, we conclude that the technique based on a Taylor expansion followed by an extension to intervals is well suited for the stochastic structural optimization when it is less for the reliability based optimization. This is probably because in the SSO, the monotonicity assumption is satisfied by the objective function whereas in RBO, the hypothesis is only valid for low levels of uncertainty. For RBO, other techniques must be considered and they will be the perspectives of this work.

References

Debbarma, R., Chakraborty, S., Ghosh, S.K.: Optimum design of tuned column dampers under stochastic earthquake load considering uncertain bounded system parameters. Mechanical Sciences 33, 136–144 (2011), doi:10.1016/j.ijmecsci.2010.07.004

Chakraborty, S., Roy, B.K.: Reliability based design optimum design of tuned mass damper in seismic vibration control of structures with bounded uncertain parameters. Probabilistic Engineering Mechanics 26, 215–221 (2011), doi:10.1016/j.probengmech.2010.07.007

Qiu, Z., Wang, X.: Vertex solution theorem for the upper and lower bounds on the dynamic response of structures with uncertain-but-bounded parameters. Acta Mech. Sin. 25, 367–379 (2009), doi:10.1007/s10409-008-0223-5

Influence of Temperature and Rotational Speed on the Properties of Magnetorheological Brake

Bajkowski Jerzy[1] and Bajkowski Jacek Mateusz[2]

[1] Warsaw University of Technology, Institute of Machine Design Fundamentals, Narbutta 84, 02-524, Warsaw, Poland
jba@simr.pw.edu.pl
[2] Warsaw University of Technology, Institute of Vehicles, Narbutta, 84, 02-524, Warsaw, Poland
jm.bajkowski@gmail.com

Abstract. The paper concerns the comprehensive research of the influence of temperature and rotational speed on the properties of the rotary brake, filled with magnetorheological fluid. The results were obtained for the specially designed device, manufactured at the Institute of Machine Design Fundamentals of the Warsaw University of Technology. Extensive results of the research are presented, along with the equation of motion and heat transfer.

Keywords: magnetorheological brake, temperature, rotational speed, dissipation.

1 Introduction

One of the groups of smart materials is classified as the controllable fluids. They can change their properties under the influence of the external physical fields. For magnetic or electric fluids, it is possible to control their unusual mechanical properties by changing the values of magnetic or electric field surrounding the fluid.

When exposed to a magnetic field, magnetorheological fluid (MRF) changes state from a free-flowing, Newtonian like, to a semi-solid state called the active one. In active state particles of the MRF align along the magnetic flux lines in a chain-like combination. As a consequence of the particles rearrangement, the yield strength of the fluid increases and can be controlled by adjusting the magnetic field, generated in a gap by an electric coil. The switch between free-flowing and active state is very quick (several ms), and reversible process.

Polarized, ferromagnetic, carbonyl particles are the main component of the typical MR fluid. Their diameter ranges from 0,1 μm up to 2,5 μm The carbonyl particles are coated by a layer of an active, anti-oxidation agent, which also prevents clustering and settlement of the particles. The diameter of the coated particle of MR fluid is up to 10 μm (Sapinski, 2006). The coated particles are dispersed in a non-magnetic carrier fluid, which is usually oil, glycol, liquid hydrocarbon, hydrofluoric, water, or other type of complex substances. In (Milecki, 2010), the

M. Haddar et al. (Eds.): *Design and Modeling of Mechanical Systems*, LNME, pp. 143–149.
DOI: 10.1007/978-3-642-37143-1_18

value of the yield stress for modern MR fluids ranges from 25 kPa up to 100 kPa, which requires generation of the magnetic field of intensity 150 kA/m and 250 kA/m.

However, the major disadvantage of the fluids consisting of ferro particles is their natural tendency to settle, as a consequence of the difference in density of the carrier fluid and the micro-magnet particles. This effect is minimized in the rotary devices, which provide constant mixing of the fluid. Despite the issues, MRFs are used in many devices, especial in all kind of dashpots, clutches and brakes.

2 Purpose and Scope of the Research

The presented study deals with the research of the manufactured prototype, rotary MR break, which is intended to be used in a heavy, military vehicle of special purpose. The study focuses on determining the influence of the rotary speed on the temperature of the device. The dependency between the temperature and efficiency of the brake, i.e., the braking torque was determined as well. The dependencies were determined for different values of coil current which induces the magnetic field inside the gap of the device.

When designing the MR brake, several simplifications were crucial to compute the brake's parameters. The direct-shear mode of the fluid's flow was assumed. Parameters and dimensions of the brake were computed according to an algorithm presented in (Milecki, 2010). The construction and cross-section of the device is presented in fig. 1

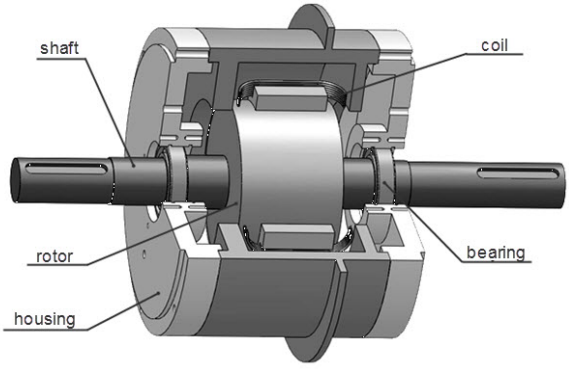

Fig. 1 Cross-section of the rotary magnetorheological brake

The MRF - 132DG fluid produced by Lord Co., was used in the prototype of the brake. The fluid is a suspension of a 10 μm diameter sized, magnetically susceptible particles, in a carrier, hydrocarbon fluid. The density of the liquid is 3 g/cm^3 and viscosity 0,09 Pa·s. The maximum yield stress value is 50 kPa for the magnetic induction 1,5 T.

The shear stress of a liquid in the narrow gap is controlled by the changes in the magnetic field whose vector is normal to the direction of the flow. The magnetic

field intensity can be changed by adjusting the current in the coil winding. The construction of the solenoid, which enables a step change in the value of the magnetic field acting on the fluid, was patented.

Special laboratory stand, presented in fig. 2 allowed studying extensively the efficiency of the device. The stand also allows examining the rotary devices working in a clutch and break configuration as a torque transmission system. The experiments were conducted using the high accuracy, measuring devices: torque sensors, thermocouple sensors, infrared camera, frequency inverter and PCI analog card. The main shaft was driven by the electro servo motor of 20 kW power. The coil current was controlled by the stabilized, programmable, laboratory power supply.

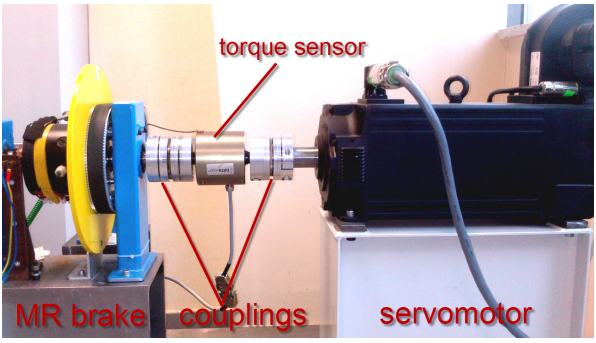

Fig. 2 Laboratory stand with serwomotor and MR brake

In order to examine the temperature, preferably would be to record the temperature of the MR fluid inside the gap of the device. That type of measurement would require using a thermocouple sensor placed inside the housing, which would be hard to achieve. However the thermocouple sensors have high thermal inertia and provide the measure with some time delay, which was in that case unacceptable.

In order to overcome the problem, separate experiments were conducted, using thermo-camera to measure the temperature of the housing and thermocouple sensors placed inside the test sample. The difference between the temperature of the surface of the brake and the temperature of the fluid, for different coil currents, was measured. This allowed to define the correction coefficient of temperature measurement.

3 Model of the System

The model of the system (Bajkowski et al., 2008), used for the MR rotational brake research is presented in fig. 3.

The mass moment of inertia of the engine is I_s The driving moment is denoted M_s. Mass moment of inertia of the couplings is I_W, and the mass moment of inertia of the brake's rotor is I_H. The frictional moment is denoted M_H, while the damping coefficient of is η. Torque sensor was installed between couplings.

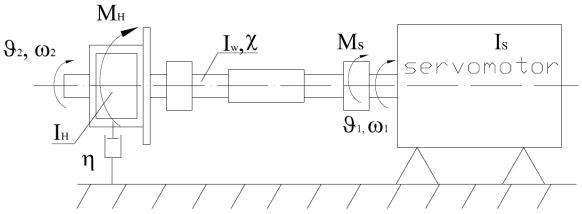

Fig. 3 Model of the laboratory stand, used in the magnetorheological rotary brake tests

The equation of motion takes the following form:

$$\begin{cases} I_s\ddot{\vartheta}_1 + \chi(\vartheta_1 - \vartheta_2) + \eta(\dot{\vartheta}_1 - \dot{\vartheta}_2) = M_s \\ I_H\ddot{\vartheta}_2 + \chi(\vartheta_2 - \vartheta_1) + \eta(\dot{\vartheta}_2 - \dot{\vartheta}_1) = M_H \end{cases} \tag{1}$$

Assuming the modified rheological model of the fluid by Filisko, the heat balance equation can be denoted as (Bajkowski, 2006):

$$\dot{\theta}(t) = \begin{cases} \dfrac{M_s(t) - \tau(t)M_T(\theta(t))}{C_p(\theta(t))} \\ \dfrac{1}{C_p}\left\{\dfrac{1}{C_R}\left[\begin{array}{l} I^2R + M_s^2(t) - 2\tau(t)M_s(t)M_{H0}\theta(t) + \\ +\tau^2(t)M_{H0}^2\theta^2(t) + \tau(t)M_{H0}M_s(t) + \\ -\tau^2(t)M_{H0}^2(\theta(t)) \end{array}\right]\right\} - \kappa\theta(t) \end{cases} \tag{2}$$

$$\tau = \begin{cases} sign\,\dot{\vartheta} & for \quad \dot{\vartheta} \neq 0 \\ [-1, +1] & for \quad \dot{\vartheta} = 0 \end{cases} \tag{3}$$

where:

C_p – specific heat of the MR fluid,
$C_R(\theta(t))\dot{\vartheta}(t)$ – energy dissipation function,
$\tau(t)M_T(\theta(t))\dot{\vartheta}(t)$ – heat energy due to friction,
κ – coefficient of thermal conductivity,
$\kappa\theta(t)$ – energy change function,
$\theta = \theta(t)$ – temperature function,
ϑ – rotation angle,
I – coil current,
R – resistance.

4 Results

The fig. 4 presents the braking torque value over time, for rotational speed of 3 rot/min. As the speed is low, the temperature remains constant, as the process of breaking the particle chains is evaluating slowly. The braking torque also does not change in time.

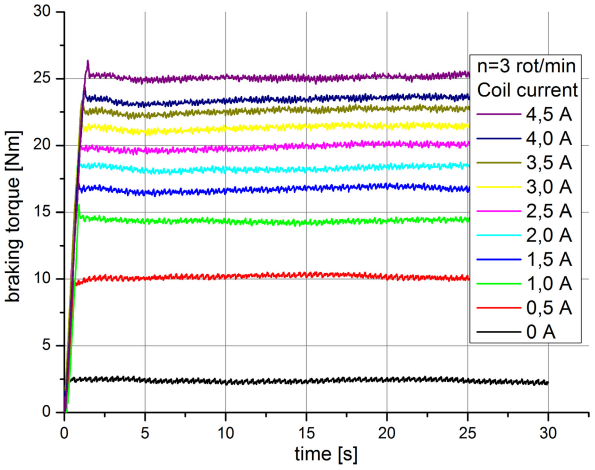

Fig. 4 Evolution of the braking torque over time for rotation speed 3 rot/min – temperature remain constant

The relations between the braking torque and rotational speed, for different values of coil current and higher speed are presented in fig. 5. The measurements were taken at constant temperature of the device which was 21°C

The braking torque is increasing with the coil current. For 0,5 A the average torque vale was 10 Nm, while for 2,0 A torque value was 25 Nm. While increasing the coil current over 2,0 A, just a minor increase in braking torque is observed. This is due to the fact that the MRF-132DG fluid reaches saturation for magnetic field strength 300 kA/m (around for 2,1 A). If the rotation speed increases, the braking torque value grows respectively. Although, for higher currents than 0,5 A the effect is negligible.

Considering the influence of temperature on the torque, presented in fig. 6, we find that as the temperature is increasing, the torque is decreasing regardless of the value of the intensity of the magnetic field strength.

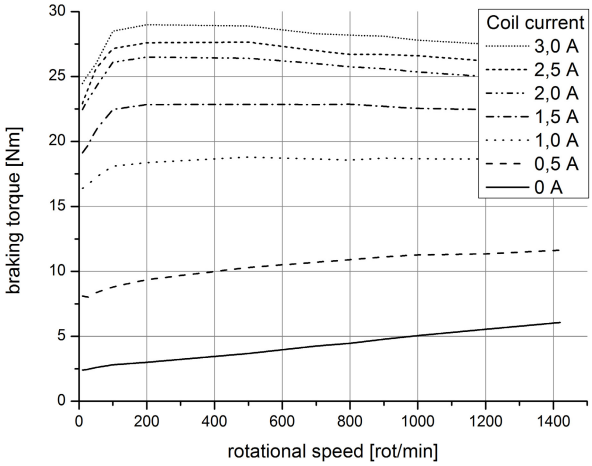

Fig. 5 Braking torque as a function of rotational speed, for different values of coil current

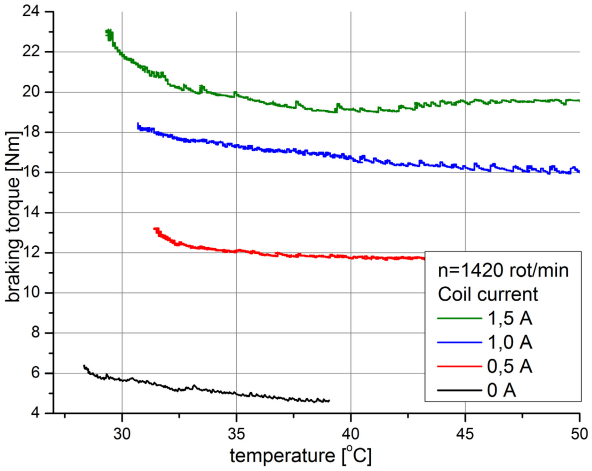

Fig. 6 Decrease of the braking torque as a function of the temperature of the device for constant rotational speed

As the shaft rotational speed increases, a significant temperature raise of the device is observed, due to the disintegration of the MR fluid particle chains, formed in the magnetic field. This leads to an uncontrolled reduction of the yield point of the non-Newtonian liquid, and thus the braking torque noticeably declines.

The overheating is dangerous as the high temperature may melt the coils insulation, and the MRF changes its properties. The overheating of the device is 35°C of the surface of the housing, which is around 70°C of the temperature of the fluid inside the device. Taking into consideration the time dependencies (fig. 7), it can be

stated that the MR brake can work efficiently for periods of 100 s for speed up to 500 rot/min. For 1420 rot/min, the device can work continuously only for short periods of 60 s, without overheating.

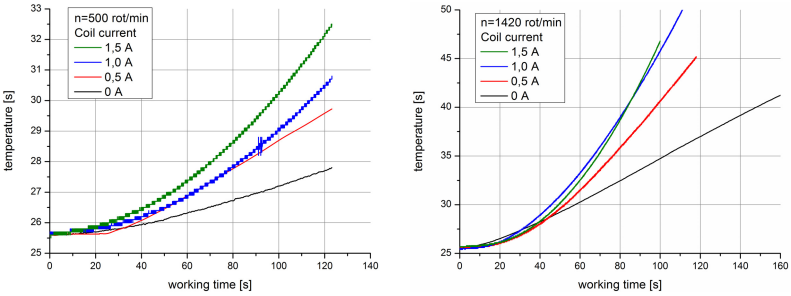

Fig. 7 Comparison of the temperature of the device over working time, obtained for 500 rot/min and 140 rot/min

5 Conclusions

The experiment allowed to carefully examine the response of the MR brake for different magnetic field strength's, taking into consideration parameters important for real-life applications: rotational speed, temperature and exploitation time. The comprehensive experimental research was supported by formulating the model of the system, motion and heat balance equation. The collected material will help to improve the design of the MR brakes and clutches and to increase the efficiency of such devices.

References

Sapiński, B.: Magnetorheological Dampers in Vibration Control, 1st edn. AGH University Press, Cracow (2006)

Milecki, A.: Ciecze elektro- i magnetoreologiczne oraz ich zastosowania w technice. Wydawnictwo Politechnika Poznanska, Poznan (2010)

Bajkowski, J., Nachman, J., Shillor, M., Sofonea, M.: A model for a Magnetorheological Damper. Mathematical and Computer Modeling 48(1-2), 56–68 (2008)

Bajkowski, M.: Analiza wpływu wybranych charakterystyk tłumika MR na zmiany właściwości dynamicznych modelu obiektu specjalnego. Dissertation. Politechnika Warszawska (2006)

Fault Detection of Nonlinear Systems Using Multi-model Structure: Application to a Ship Propulsion System

Dallagi Habib

U.R Automatique et Robotique Marine (ARM), Académie Navale,
7050 Menzel Bourguiba Tunisia
Habib.dallagi@ept.rnu.tn

Abstract. This paper presents a design of a residual generator in order to detect faults of ship propulsion system. The obtained system's model belongs to the polynomial system class. Following some results in linear systems, a residual generator design method is developed, guaranteeing fault detection. The simulation result shows how a fault detectability procedure can be made on the ship propulsion system.

Keywords: Fault detection, ship propulsion system, modeling multi-model, residual generator, numerical simulation.

1 Introduction

Diagnosis and fault detection mobilized to date many researchers in this area, causing the development of groups of researchers on modeling and diagnosis. For more than a twenty years of studies and research have been conducted on how we could detecting a failure, and failure of the causal relationship between events. Thus, we could improve the reliability the ship propulsion system, thus increasing the duration of life. This work is to develop a method diagnosis based on the observation of the state vector for the detection and isolation of failure electrical and/or mechanical. As a key component in ship, the reliable operation of ship propulsion system is a primary concern for the entire ship system. Fault detection and diagnosis of ship propulsion system, is critical for the improvement of system reliability (Svrd 2009, Toscano 2005, Kumamaru and al 2002, Bonivento and al 2002).

2 Fault Detection Based Linear Observer

The main idea generation methods residual vector is based observers estimating some or all of the variables the state vector of the system being monitored from measurable quantities and system inputs. The residual is generated by forming the difference (optionally filtered) and between the outputs estimated the actual outputs. The observer finally returns a model with a parallel system against reaction which weights the output gap. This principle is illustrated in figure 1.

M. Haddar et al. (Eds.): *Design and Modeling of Mechanical Systems*, LNME, pp. 151–158.
DOI: 10.1007/978-3-642-37143-1_19

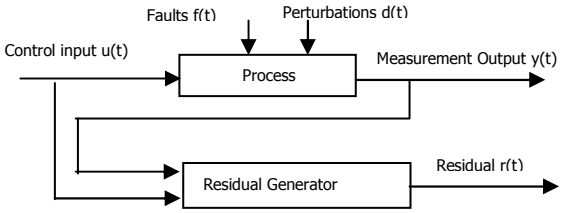

Fig. 1 Residual generator approach scheme

2.1 Design of the Unknown Input Residual Generator

Consider the linear continuous system affine in the control inputs unknowns (Aiping and Qinghua 2001, Akhenak and al 2004):

$$\begin{cases} \dot{x}(t) = A\,x(t) + B\,u(t) + R\,d(t) + F\,f(t) \\ y(t) = C\,x(t) \end{cases} \tag{1}$$

Where $x \in \Re^n$ is the state vector, $u \in \Re^m$ is the control vector, $y \in \Re^p$ is the vector of measured outputs, $d \in \Re^q$ is the vector of immeasurable disturbances (q <p) is the fault vector in the system. Matrix A, B, C, F and R are known and of suitable size. R is the vector which characterizes the disturbances acting on the system. F is the vector characterizing the fault affecting the system. The waste generator is governed by the equations (2).

$$\dot{z}(t) = \hat{A}\,z(t) + E\,y(t) + J\,u(t) \tag{2a}$$

$$r(t) = R_1\,z(t) + R_2\,y(t) \tag{2b}$$

Where: $z \in \Re^j$ ($j \leq n$) is the state vector of the observer, $r(t) \in \Re$ is the residual generated. Matrixes $\hat{A}$, *E, J, R1* and *R2, E, J* are to be determined. The waste generator (2) must be sensitive to faults f (t) while being insensitive to unknown input d(t) obeys the following definition:

Definition: The system described by equations (2) is a residual generator of unknown input linear system (1) if and only if, for any u (t) and d(t) we have:

1. $\lim_{t\to\infty} r(t) = 0$ if $f(t) = 0 \quad \forall \quad t>0$
2. There is a matrix T such that for all u (t) and f (t) = 0, we have $z = T\,x \;\forall\; t>0$
3. For $z_0 = T\,x_0 \;\forall$ u (t) and f(*t*) $\neq$ 0 we have r(t) $\neq$ 0

The condition (1) allows us to have a residual r(t)=0 in the absence of default regardless of unknown inputs, the condition (2) provides an estimate of the system state in the presence of disturbances and condition (3) ensures that the residual is non-zero in the presence of defects.

The observation error is given by:

$$e = z - T\,x \tag{3}$$

With is a matrix of appropriate size.

$$\dot{e} = \dot{z} - T\ \dot{x} \tag{4}$$

The dynamics of the observation error is then given by:

$$\dot{e} = \hat{A}\ e + (\hat{A}T - TA + EC)\ x + (J - TB)\ u - TRd - TFf \tag{5}$$

Using equations (2a) and (2b) the residual can be put in the form (6):

$$r(t) = R_1 z(t) + R_2 y(t) = R_1 (z(t) - Tx) + R_1 Tx + R_2 Cx$$
$$r(t) = R_1 e + (R_1 T + R_2 C)x \tag{6}$$

According to the conditions (1), (2) and (3) of the definition, the system (2) is a residual of generator system (1) if and only if:

$$\hat{A}(t) - TA + EC = 0 \tag{7}$$

$$TR = 0 \tag{8}$$

$$J = TB \tag{9}$$

$\hat{A}$ is stable.

For r(t) converges to zero for all entries, known and unknown, the following relation must be satisfied:

$$R_1 T + R_2 C = 0 \tag{10}$$

The synthesis of this generator requires therefore the determination of the parameters, $\hat{A}$, E, J, R_1 and R_2 the system (2) taking into account the constraints (7) to (10).

3 Block Diagram of the System Studied

Designs of military ships need to consider frequent operations under hostile environments. Healthy and safe operations of devices onboard are extremely important because any unexpected fault or shutdown may result in loss of a ship and human lives. As a key component in the ship propulsion system, the reliable operation of propulsion system is a primary concern for the entire ship system (Kumamaru and al 2002, Bonivento and al 2002, Svrd 2009). Fault detection and diagnosis of propulsion system is critical for the improvement of system reliability.

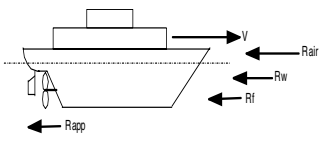

Fig. 2 Ship movement

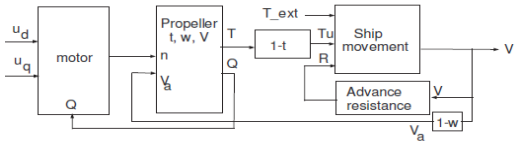

Fig. 3 Block diagram of the ship propulsion system

The advance total resistance (Boudrigua and al 2011) is given: $R = R_w + R_f + R_{app} + R_{air}$

Where: R: advance total resistance, R_f: friction resistance, R_W: waves resistance, R_{app}: appendices resistance, R_{air}: air resistance.

The Model characterizing the ship electric propulsion system (Dallagi 2010, Dallagi and all 2007, Dallagi and Nejim 2005), is given by the equations 11.

$$\begin{cases} \dot{i}_d = -\dfrac{R_s}{L_d} i_d + p\,\Omega\,\dfrac{L_q}{L_d}\,i_q + \dfrac{1}{L_d} u_d \\ \dot{i}_q = -p\,\Omega\,\dfrac{L_d}{L_q}\,i_d - \dfrac{R_s}{L_q}\,i_q - \dfrac{p\varphi_f}{L_q}\Omega + \dfrac{1}{L_q} u_q \\ \dot{\Omega} = \dfrac{1}{I_m}\left[\left(p(L_d - L_q)\,i_d i_q + p\,\varphi_f i_q\right) - \dfrac{1}{4\pi^2}\left(\rho\Omega^2 D^5 s_1\right) - \dfrac{1}{2\pi}\left(\rho\Omega D^4 s_2(1-w)V\right) - Q_f\right] \\ \dot{V} = \dfrac{1}{m}\left[-aV^2 + \dfrac{1}{4\pi^2}(1-t)\eta\rho D^4\Omega^2 + \dfrac{1}{2\pi}(1-t)(1-w)r_2\rho D^3\Omega V - T_{ext}\right] \end{cases} \tag{11}$$

We obtain the multi variable non-linear system of fourth order as follows:

$$\begin{cases} \dot{x} = f(x) + g(x)u \\ y = h(x) \end{cases}$$

With: $x \in \Re^n$:The state vector, $u \in \Re^m$:The control vector, $y \in \Re^p$:The output vector given by $y = [i_d \quad V]^T$, Ω: propeller speed, Q_f: fiction shaft, V: ship speed, T_{ext}: applied strength by the outside environment on the ship, V: ship speed (m/s), φ_f : inductor flux, u_d: stator voltage longitudinal component, u_q: stator voltage transverse component, i_d: stator current longitudinal component, i_q: stator current transverse component, I_m: shaft inertia.

The parameters of the propulsion system are: water Density: ρ=1025 kg/m^3, Propeller diameter: D=5m, Ship weight: m=23282000, Resistance coefficient: a=1.5 10^5, Torque coefficient: s_1=0.075; s_2=0.1375, shaft inertia I_m=250 , Thrust coefficient: r_1=0.5, r_2=1:1, Coefficient de suction: t=0.178, φ_f=1,Wake fraction: w=0.2304, stators Resistance: Rs=0.0148, Inductance longitudinal: L_d=0.0060, Inductance transversal: L_q=0.0059, Pairs number of poles: p=2, Motor power: S=5MVA,Voltage: U=4.160KV.

The model of the propulsion system is complex and unusable for this reason we define a set of local models linearize the system around its operating points most representative. In this section, we presented modeling approach multi-model. The process is represented in continuous domain by the non-linear form as follows (Orjuela and al 2007, Akhenak and al 2004, Orjuela 2008).

$$\begin{cases} \dot{x}(t) = f\left(x(t), u(t)\right) \\ y(t) = g\left(x(t), u(t)\right) \end{cases} \tag{12}$$

The linearization of the nonlinear system about an operating point $(x_i, u_i) \in \Re^n \times \Re^p$ allows developing the model (Mi), whose structure is written:

$$(\mathrm{M_i}) \quad \begin{cases} \dot{x}_i(t) = A_i\left(x(t) - x_i(t)\right) + B_i\left(u(t) - u_i(t)\right) + f\left(x_i(t), u_i(t)\right) \\ y_i(t) = C_i\left(x(t) - x_i(t)\right) + g\left(x_i(t), u_i(t)\right) \end{cases} \tag{13}$$

While this model is written following local form:

$$(\mathrm{M_i}) \quad \begin{cases} \dot{x}_i(t) = A_i x(t) B_i u(t) + d_i \\ y_i(t) = C_i x(t) + e_i \end{cases} \tag{14}$$

d_i and e_i are the constants of linearization, which is calculated as follows:

$$\begin{cases} d_i = f\left(x_i, u_i\right) - A_i x_i - B_i u_i \\ e_i = g\left(x_i, u_i\right) - C_i x_i \end{cases} \tag{15}$$

Thus, the overall model on the process considered, with operating points can be written according to the multilayer structure model below:

$$\begin{cases} \dot{x}(t) = \sum_{i=1}^{n} v_i(t)\left(A_i x(t) + B_i u(t) + d_i\right) \\ y(t) = \sum_{i=1}^{n} v_i\left(C_i x(t) + e_i\right) \end{cases} \tag{16}$$

Where: $t \in \Re^+$ is the time variable, $x_i(t) \in \Re^n, u_i(t) \in \Re^p$ and $y_i(t) \in \Re^q$ are respectively the status, the command and the output of the process to the model (Mi), $x(t) \in \Re^n, u(t) \in \Re^p$ and $y(t) \in \Re^q$ are respectively the state vector, the vector and the vector control process output, $v_i(t)$ is the coefficient of relevance relative to the model (Mi), called validity.

3.1 The Approach of Residual

In this context, we can adopt as default, the remoteness of the area of validity. And can be regarded as the residual error between the actual value of the output of the process and its value calculated on the basis of each model:

$r_i(t) = \left\| y(t) - y_i(t) \right\|$; $i \in \{1, ...M\}$, where M is the number of models and $\left\| . \right\|$ is standard. y (t): the output of the system, yi(t): the output of the model Mi. The residual can be normalized to sum model:

$$r'_i(t) = \frac{\left\| y(t) - y_i(t) \right\|}{\sum_{j=1}^{M} \left\| y(t) - y_j(t) \right\|}; \quad \forall i = 1, ..., M \tag{17}$$

So they move in the interval [0, 1] and they satisfy the property of convex sum:

$$\begin{cases} \sum_{i=1}^{M} r'_i(t) = 1 \\ 0 \le r'_i(t) \le 1 \end{cases} \tag{18}$$

3.2 Calculation Validities

The validity coefficients based models are estimated online during the evolution process based on residual, which represent the errors between the behavior of the latter and behavior patterns as indicated by the expressions below:

$$r_i(t) = \frac{\|x(t) - x_i(t)\|}{\sum_{j=1}^{n} \|x(t) - x_j(t)\|}; \forall i = 1,...,n \qquad r_i(t) = \frac{\|y(t) - y_i(t)\|}{\sum_{j=1}^{n} \|y(t) - y_j(t)\|}; \forall i = 1,...,n \tag{19}$$

Then the validity, to be inversely proportional to the residual, can be calculated according to the relation:

$$v_i(t) = \frac{1 - r_i(t)}{\sum_{j=1}^{n} (1 - r_j(t))}; \forall i = 1,\ldots,n \tag{20}$$

Such that the validity $v_i(t)$ of the model, $r_i(t)$ and the residual (Mi) satisfy the property of the sum $\sum_{i=1}^{n} v_i(t) = 1$ and convex $v_i^{renf}(t) = v_i(t) \prod_{j=1, j\neq i}^{n} (1 - v_i(t)) \forall i = 1,...,n$

4 Simulation Results

To validate our approach, we use two linear models obtained for two operating points. The two linear models are designed and used for the construction of two linear observers. We will generate some faults on the propulsion system and observe the generator behavior.

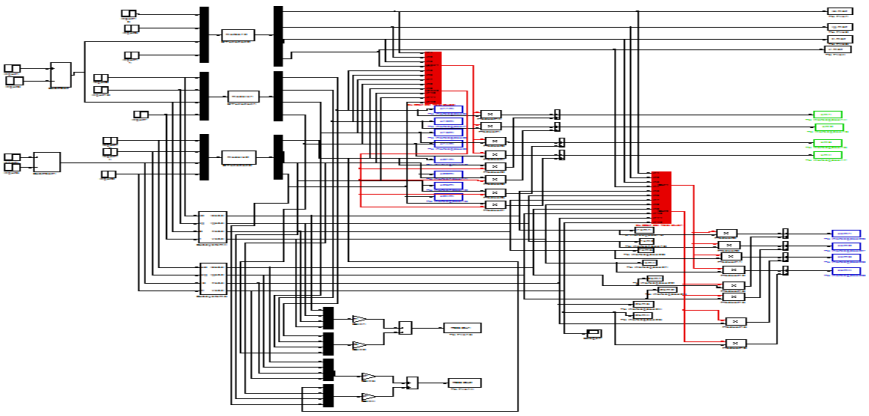

Fig. 4 Block diagram of the detection system

We will apply two faults on the ship propulsion system and observe the effects of faults of the system and its behavior for detecting faults. Apply two faults f1 (friction torque Fault) and f2 (propeller Fault).

Fault of friction torque on the shaft: We provoked a on the shaft a friction torque of intensity 400NM, within the time interval [300s 500s]. We remark that the residual generator detects the fault on the time interval [300s 500s] where the fault has been occurred figure 9.

Fault on the propeller: We have applied a fault of intensity 1000N between time t=700s and t=900s in the propeller. Consequently it has generated residual r_2 between t=700s and t=900s. The residual signal increase in magnitude considerably, when the fault occur between t=700s and t=900s figure 10. Thus, we can verify that the proposed residual generator is effective to detect faults. The simulation results are shown in figures 5 to 10.

For fault Isolation, the system is affected by two inputs. To detect for these two faults, we will design two observers: one observer detects the first (fault 1) and considers the second (default 2) as an unknown input and therefore it will generate an r_1. The second detect the second (fault 2) and consider the first (fault 1) as an unknown input and therefore it will generate a residue r_2. We have illustrated the case where two faults occur on the system.

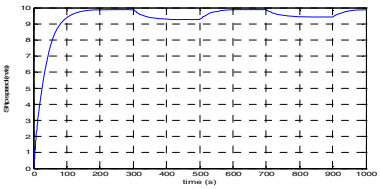

Fig. 5 Ship speed

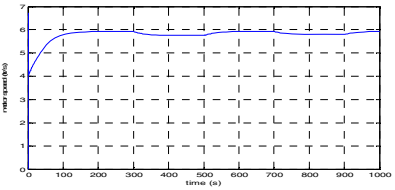

Fig. 6 Motor speed

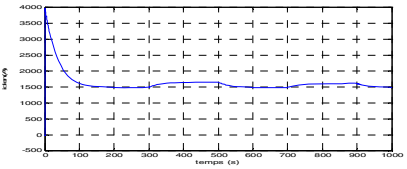

Fig. 7 Current id

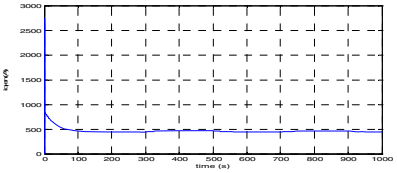

Fig. 8 Current iq

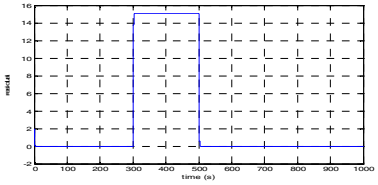

Fig. 9 Residual r1

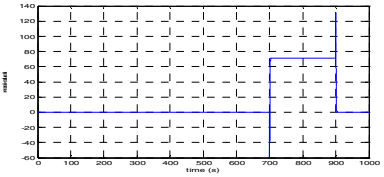

Fig. 10 Residual r2

5 Conclusion

We proposed and developed a method for fault detection based on modeling and multi-model linear observers. To detect and localize defects in a nonlinear system, we used the approach of multi-input observer unknown. Each observer is designed to estimate the states of a local model. This detection method can therefore be distributed in three stages; multi-model modeling, simulation and comparison of measures. Numerical simulations of the propulsion system have validated this approach and shown that residual generators allow well de-signed to fault detect.

References

Toscano, R.: Commande et diagnostic des systèmes dynamiques. Elipses, Paris (2005)

Jakubek, S., Jorgl, H.P.: Fault-diagnosis and Fault-Compensation for Nonlinear Systems. In: American Control Conference (2000)

Dallagi, H., Nejim, S.: Modelisation and Simulationof an Electric Drive for a Two Propeller Ship. In: 17me Congrs Mondial IMACS, Calcul Scientifique, Mathmatiques Appliques et Simulation, Paris, France (2005)

Dallagi, H.: Mathematical modeling of electric propulsion systems for marine vessels. In: 6th International Conference on Electrical Systems and Automatic Control, Hammamet, Tunisia (2010)

Bonivento, C., Paoli, A., Marconi, L.: Fault-tolerant control of the ship propulsion system benchmark. Control Engineering Practice (2002)

Svrd, C.: Residual Generation Methods for Fault Diagnosis with Automotive Applications. Thesis Department of Electrical Engineering Linkpings universitet, Linkping, Sweden (2009)

Dallagi, H., Tlili, A., Nejim, S.: Observer Based Optimal Control of Ship Electric Propulsion System. In: 4th International Conference on Informatics in Control, Automation and Robotics, ICINCO 2007, Angers, France, May 9-12 (2007)

Boudrigua, K., Dallagi, H., Sabri, B.: Estimation et optimisation de la résistance totale d'une carène et de la puissance propulsive des navires. In: 4th International Congress Conception Design and Modeling of Mechanical Systems, CMSM 2011, Sousse, Tunisia (2011)

Orjuela, R., Marx, B., Maquin, D., Ragot, J.: Estimation d'état des systèmes non linéaires par une approche multi-modèle découplé. In: 2ème Journées Doctorales– Journées Nationales MACS, JD-JN-MACS, Reims, France (2007)

Kumamaru, K., Kamata, H., Inoue, K.: Fault diagnosis of dynamics systems by using a quick dentification method and its application to ship propulsion system. In: 15th Triennial World Congress. IFAC, Barcelona (2002)

Gasso, K.: Identification des systèmes dynamiques non-linéaires: approche multi-modèle. PhD thesis, Institut National Polytechnique de Lorraine (2000)

Akhenak, A., Chadli, M., Ragot, J., Maquin, D.: Estimation of state and unknown inputs of a nonlinear system represented by a multiple model. In: 11th IFAC Symposium on Automation in Mineral and Metal Processing, Nancy, France (2004)

Aiping, X., Qinghua, Z.: Residual Generation for Fault Detection and Isolation in Linear Time Varying Systems. CDC France (2001)

Orjuela, R.: Contribution à l'estimation d'état et au diagnostic des systèmes représentés par des multi-modèles. thèse, Nancy (2008), `http://pegase.scd.inplnancy.fr/theses/`

Nonlinear Forced Vibrations of Rotating Composite Beams with Internal Combination Resonance

Ferhat Bekhoucha[1], Saïd Rechak[1], Laëtitia Duigou[2], and Jean-Marc Cadou[2]

[1] Mechanical Engineering and Development,
Ecole Nationale Polytechnique,
Avenue Hassen Badi, El-Harrach,
16200, Algiers, Algeria
[2] Laboratoire d'Ingénierie des MATériaux de Bretagne,
Université de Bretagne Sud,
Rue de Saint-Maudé,
BP 92116, 56321, Lorient Cedex, France
ferhat.bekhoucha@g.enp.edu.dz

Abstract. This work deals with forced vibration of nonlinear rotating composite beams with uniform cross-section. Coupling the Galerkin method with the balance harmonic method, the nonlinear intrinsic and geometrical exact equations of motion for anisotropic beams are converted into a static formulation, which is treated with the continuation method; the asymptotic numerical method, where power series expansions and Padé approximants are used to represent the generalized vector of displacement and the frequency. Response curves are obtained and the nonlinearity is studied for various angular speed. Internal resonance flexion-flexion is found and the angular speed effect on the coupling between modes is investigated.

Keywords: Nonlinear vibration of rotating beams, Galerkin method, Harmonic balance method, Asymptotic Numerical Method, internal resonance.

1 Introduction

Composite rotating beams may encountered in varied structural applications, like a wind turbine and helicopter blades and robot arms. To understand their behavior and have a better design, many geometrically exact formulation for the nonlinear dynamics were developed, that can be used for vibration studies (Borri and Mantegazza 1985) and (Bauchau and Kang 1993). These theories are displacement-based formulations, i.e. the displacements and finite rotations must be defined and the solution, usually by using the FEM, needs a large number of variables.

This study is based on the intrinsic formulation developed by Hodges, (Hodges 1990) and (Hodges 2003), which covers the anisotropic beams with large deformations and small strains. It takes advantage of the one-dimensional characteristic

M. Haddar et al. (Eds.): *Design and Modeling of Mechanical Systems*, LNME, pp. 159–166.
DOI: 10.1007/978-3-642-37143-1_20

of a beam, does not require variable definitions of displacement and rotation, and thus it is less expensive than using (3D) finite-element methods (FEM).

The Hodge's model includes both geometric and inertia nonlinearities, which often exhibit strong behavior when their natural frequencies are commensurable, i.e. when the system has an internal or parametric resonance. The response is multimodal with interaction between modes conducted by an energy exchange between excited mode, and others modes, not directly excited, involved in this internal resonance. The internal resonance in multi-degree-of-freedom and elastic structures is well explained in (Nayfeh and Pai 2004).

Internal combination resonance of the form $\omega_i = \omega_j \pm \omega_k$ is studied for nonlinear systems in many papers.(Nayfeh et al. 1992) summarized the investigations on the response of a three-degree-of freedom system with the combination internal resonance, they found that the system exhibits an energy exchange between modes and the excitation of the third mode can induce large responses of the two other modes. (Zaretzky and Crespo da Silva 1994) investigated flexural-flexural-torsional responses of cantilever beams with the in-plane bending mode being excited at primary resonance. They found that the out-of-plane bending and torsional modes are related by a constant and the directly excited in-plane bending mode presents pseudo-saturation.

In this work, the nonlinear response of a rotating composite beam to harmonic excitation is studied. This composite beam is governed by a nonlinear quadratic system and presents a sum type combination internal resonance, and hence the effect of the angular speed on the internal combination resonance is investigated. A Galerkin approximation is applied to this model, where the weighting functions are chosen to be used for the same functions modes, leading to an energy balance and consequently, provide a better numerical approximation of the solution of these nonlinear equations (Patil and Althoff 2010). Hence, the initial partial differential equations are reduced to one differential equation, which by using the harmonic balance method, is converted again to a nonlinear algebraic equation.

As a continuation method, the asymptotic numerical method (ANM) is applied and the solutions are presented in the frequency domain. The ANM has been successfully used to solve nonlinear problems such as nonlinear elasticity and nonlinear vibrations (Boumediene et al. 2009) (Cochelin et al. 1994), and in fluid mechanics (Cadou et al. 2008). It is often introduced in the elementary step of discretization using finite-element method. The main advantage of the ANM lies in the analytical form of the solution due to the polynomial approximation or Padé approximants instead of the point by point solution that can be obtained by other continuation methods, the pseudo-arclength or shooting methods.

The aim of this paper is to firstly apply the ANM to a nonlinear system after discretization and to secondly explore the effect of the angular speed on both the nonlinearity of the response curves of a selected composite beam and on the interaction between modes in combination resonance conducted by the energy exchange.

2 Mathematical Formulation

2.1 Nonlinear Intrinsic Equations

Based on Timoshenko beam model, the Euler-Lagrange nonlinear equations of motion derived from Hamilton's principle are (Hodges 1990)

$$F' + \tilde{K}F + f = \dot{P} + \tilde{\Omega}P \tag{1}$$

$$M' + \tilde{K}M + (\tilde{e}_1 + \tilde{\gamma})F + m = \dot{H} + \tilde{\Omega}H + \tilde{V}P \tag{2}$$

where ($\bullet'$) denotes the derivative with respect to the undeformed beam reference line x_1 as illustrated in Fig. 1, ($\dot{\bullet}$) denotes the absolute time derivative and ($\tilde{a}$) is the antisymmetric matrix associated with a vector ($\vec{a}$). F is the internal force vector, composed of an axial force and two shear forces. M is the internal moment, composed of a twisting moment and two bending moments. They are related to generalized strains, beam strains and curvatures, and ($\kappa = K - k$) by:

$$\begin{Bmatrix} F \\ M \end{Bmatrix} = \begin{bmatrix} \mathbb{U} & \mathbb{V} \\ \mathbb{V}^T & \mathbb{W} \end{bmatrix} \begin{Bmatrix} \gamma \\ \kappa \end{Bmatrix} = S \begin{Bmatrix} \gamma \\ \kappa \end{Bmatrix} \tag{3}$$

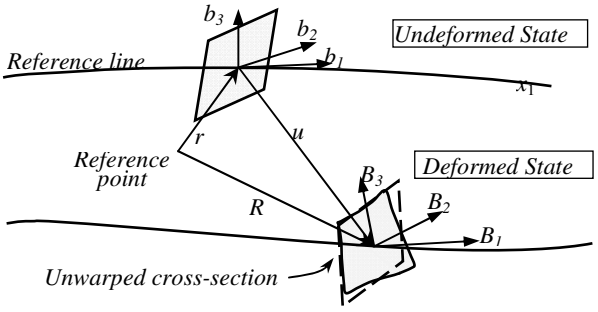

Fig. 1 Schematic of beam model, frames and reference line

$\mathbb{U}$, $\mathbb{V}$ and $\mathbb{W}$ are matrices (3x3) and represent the components of the stiffness matrix S (6x6). For complex cross section and anisotropic beams, a 2-D FEM analysis is required to determine the stiffness matrix S, as in (Yu et al. 2002), in which the results are obtained by using VABS code based on the variational asymptotic method developed by Berdichevsky (Yu et al. 2002).

In Equations (1) and (2), P and H are the linear and angular momentums vectors, related to V and Ω, the linear and angular velocities vectors by the equation,

$$\begin{Bmatrix} P \\ H \end{Bmatrix} = \begin{bmatrix} \mu\Delta & -\mu\tilde{\bar{x}} \\ \mu\tilde{\bar{x}} & \mathbb{I} \end{bmatrix} \begin{Bmatrix} V \\ \Omega \end{Bmatrix} \tag{4}$$

where μ is the mass per unit length, $\tilde{\bar{x}}$ is the antisymmetric matrix associated with $\bar{x} = [\,0\ \bar{x}_2\ \bar{x}_3\,]$, the offset from the reference line of the cross-sectional mass center, and $\mathbb{I}$ is composed of cross-sectional mass moments and product of inertia.

The nonlinear intrinsic equations of motion (1) and (2), are solved along with two other nonlinear kinematical equations (Hodges 2003),

$$V' + \tilde{K}\,V + (\tilde{e}_1 + \tilde{\gamma})\Omega = \dot{\gamma} \tag{5}$$

$$\Omega' + \tilde{K}\Omega = \dot{\Omega} \tag{6}$$

The partial differential equations (1), (2), (5) and (6) with the algebraic equations (3) and (4) represent the system of nonlinear intrinsic equations for the dynamics of a general beams undergoing small local strains and large deformations.

2.2 Galerkin Approximation

The Galerkin approximation with shifted Legendre polynomials used as trial functions, result in (Patil and Althoff 2010), that the system of equations is reduced in one differential equation in time. The variables $\Omega(x,t)$, $F(x,t)$ and $M(x,t)$ are approximated similarly to $V(x,t)$ as: $V(x,t) = \sum_{i=1}^{nf} \Phi_i(x) v_i(t)$ where (nf) is the number of trial functions used, $v_i(t)$ is three component vector and hence a new generalized vector (q) is defined:

$$q = [q_1\ \ q_2\ \ \ldots\ q_{nf}] \text{ with } q_i = [v_i(t)\ \ \varpi_i(t)\ \ f_i(t)\ \ m_i(t)]^T \tag{7}$$

Based on the energy consistent weighting principle, the above system is reduced to one differential equation of motion in time as (Patil and Althoff 2010):

$$A_{ki}\dot{q} + B_{ki}q + C_{kij}q.q + D_k + f_k + m_k = 0 \tag{8}$$

The natural frequencies are obtained from a linearization of equation (8) around a steady state solution ($\dot{q} = 0, q = q_0$), with no disturbance ($f_k = 0, m_k = 0$) and inserting a solution $q = Xe^{\omega t}$ (X is the eigenvector, ω is the natural frequency):

$$\hat{A}_{ki}\dot{q} + \hat{B}_{ki}q = 0 \text{ with, } \hat{A}_{ki} = A_{ki} \text{ and } \hat{B}_{ki} = B_{ki} + (C_{kij} + C_{kji})q_0 \tag{9}$$

2.3 Solution

To resolve the differential equation (8) in the frequency domain, first, it is converted to an algebraic equation by using the harmonic balance method, and then the continuation method; the ANM, is applied. In the following, a clamped beam harmonically exited at the tip is considered with no distributed forces nor moments. The excitation force computed in the vector D_k is assumed to be: $F^L(t) = F_0 \cos \omega t$, and hence the response of the beam can be given as:

$$q(t) = \sum_{j=0}^{H-1} (qc_j \cos \omega t + qs_j \sin \omega t) \tag{10}$$

New vector ($\overline{q}$ is introduced, containing all harmonics. By inserting series equation (10) and using the harmonic balance method, the governing equation (8) is rewritten in the frequency domain:

$$R(\overline{q}, \omega) = \omega \overline{A}\,\overline{q} + \overline{B}\,\overline{q} + \overline{C}\,\overline{q}.\overline{q} + \overline{D} = 0 \tag{11}$$

where matrices $\overline{A}$, $\overline{B}$, $\overline{C}$ and $\overline{D}$ are derived from matrices A_{ki}, B_{ki}, C_{kij} and D_k The aim is to apply the ANM to this quadratic algebraic equation, with the unknowns; vector $\overline{q}$ and the frequency ω that can be developed in a power series with respect to path parameter 'a' in the vicinity of a regular solution ($\overline{q}_0$, ω_0):

$$\overline{q}(a) = \overline{q}_0 + \sum_{j=1}^{n} a^j \overline{q}_j , \quad \omega(a) = \omega_0 + \Sigma_{j=1}^{n} a^j \omega_j \tag{12}$$

$\overline{q}_j$ and ω_j are the new unknowns which have to be computed and the path parameter 'a' can be defined as the projection of the increments of $\overline{q}$ and ω on the tangent vector ($\overline{q}_1$, ω_1):

$$a = (\overline{q} - \overline{q}_0)^T \overline{q}_1 + (\omega - \omega_0)\omega_1 \tag{13}$$

Introducing the polynomial developments equation (12) into (11) and (13) and equating like powers of 'a', one obtains the following set of linear systems:

$$\textbf{Order 1} \begin{cases} R_{\overline{q}}.\overline{q}_1 = -\omega_1 \overline{A}\,\overline{q}_0 \\ \overline{q}_1^T.\overline{q}_1 + \omega_1^2 = 1 \end{cases} \tag{14}$$

$$\textbf{Order p} \begin{cases} R_{\overline{q}}.\overline{q}_p = D_p \\ \overline{q}_1^T.\overline{q}_p + \omega_1 \omega_p = 0 \end{cases} \tag{15}$$

With $D_p = -\omega_p \overline{A}\,\overline{q}_0 - \sum_{i=1}^{p-1} \omega_{p-i} \overline{A}\,\overline{q}_i + \overline{C}\,\overline{q}_i \overline{q}_{p-i}$ and $R_{\overline{q}}$, is the jacobian which is regular at q_0 and is defined by: $R_{\overline{q}} = \partial R / \partial \overline{q} = \omega_0 \overline{A} + \overline{B} + 2\overline{C} q_0$. Generally ω_0 is taken zero, thus q_0 corresponds to the steady state solution and can be obtained by a Newton-Raphson method. The polynomial solution equation (12) agree well in the zone of validity $[0 \;\; a_{ms}]$ and diverge out of this zone. The limit a_{ms} is computed automatically using a simple criterion proposed in (Cochelin et al. 1994) conditioned by a tolerance η_s . This algorithm can be improved by replacing the polynomial representation by rational fractions named a Padé approximants.

3 Application

The model of composite beam studied here is the Active Twist Rotor (ATR) blade developed for an articulated rotor and presented with their structural parameters in (Althoff et al. 2012). It has a span 1.397m, an airfoil NACA 0012 and is made of E-glass, S-glass and Active Fiber Composite (AFC). The actuation forces are not considered. Details of ATR blade can be found in (Traugott et al. 2006).

Based on the previous studies (Boumediene et al. 2009) and (Althoff et al. 2012), the Numerical applications were performed with the optimal parameters: the number of function in Galerkin approximation $nf = 10$ modes, the number of harmonic $H = 3$, the truncation order $n = 15$, and the tolerance $\eta_s = 10^{-4}$.

Table 1 presents the first four natural frequencies (bending modes) with and without the angular speed. It can be observed that all modes increase with increasing angular speed and for these cases: $\omega_{2/z} \approx \omega_{1/z} + \omega_{1/y}$, which is defined as an internal combination resonance of flexural-flexural type. While the beam is excited at the vicinity of the out-of-plane mode $\omega_{1/z}$ (first mode), the interaction between this mode and the in-plane mode $\omega_{1/y}$ is investigated. (Patil et al. 2010) show that the natural frequencies determined by using Galerkin approximation are more precise than those obtained using the FEM (Traugott et al. 2006).

Table 1 The lowest four natural frequencies of the ATR for static and rotating cases

Modes	$\Omega_3 = 0$ rad/s		$\Omega_3 = 10$ rad/s	$\Omega_3 = 20$ rad/s
	Traugott et al. 2006	Present	Present	Present
1st/z	13.68	13.64	17.44	25.53
1st/y	70.76	70.60	70.73	71.10
2nd/z	86.71	84.40	88.13	98.47
3rd/z	248.8	232.0	235.5	246.5

Figures 2(a, b) show the out-of-plane response curves for $\Omega_3 = 0$ rad/s and $\Omega_3 = 20$ rad/s. One can observe the distortion of the response curve (2b) caused by the angular speed and hence the hardening system is transformed to softening at the beginning and later on to a hardening system. At the turning point when the maximum amplitude is reached a drop is happen for a small gap and recovered immediately after. Figures 2(c, d) show the corresponding in-plane response curves that prove the internal resonance. The curve relative to zero angular speed is similar to the results of (Zaretzky and C. Da Silva 1994) dealing with isotropic beams.

One can observe that the maximum of the in-plane amplitude is reached at the minimum of the out-of-plane amplitude explained by a partial exchange of energy.

In figure 2(d), a decrease of the amplitude of the in-plane response due to the increase in stiffness is noticed. Figure 3 shows the zone of interactions at ω≈18.8 rad/s. One can observe that the exchange of energy is intermittently in this gap described by the opposite direction of the arrows placed on the curves.

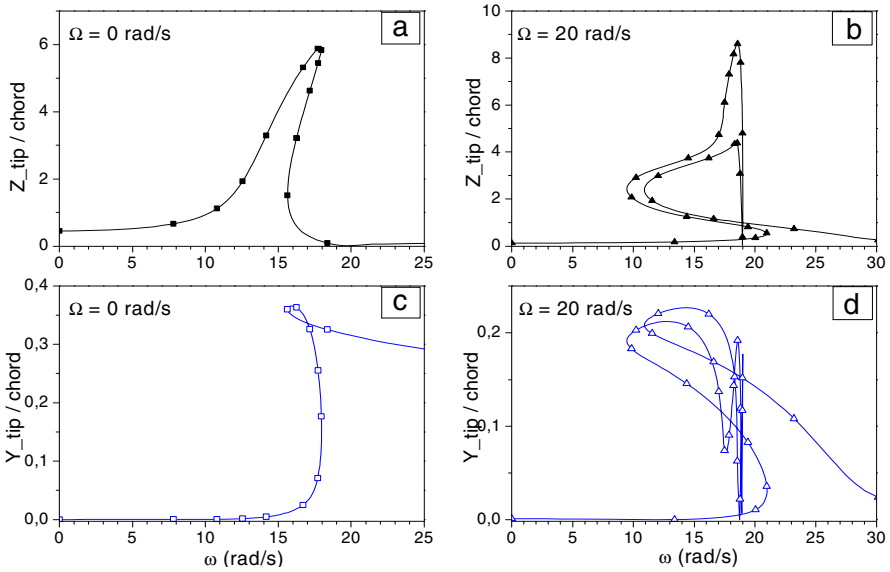

Fig. 2 In-plane and out-of-plane response curves for cases: (Ω_3=0, Ω_3=20 rad/s). Point symbols indicate the initial points of the ANM steps.

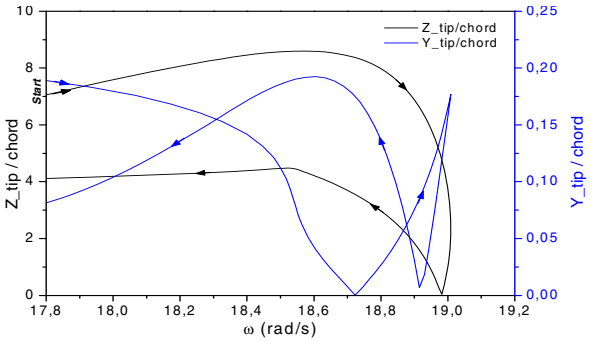

Fig. 3 Response curves and internal resonance in rotating case (Ω_3=20 rad/s)

4 Conclusion

In this paper, a fluxural-fluxural interaction in rotating composite beam subjected to harmonic excitation is studied. This beam presents an internal combination resonance in both cases without and with moderate angular speed. The response curves are distorted with the application of angular speed with some singularities explained by the internal resonance and the interchange of energy between two flexural modes involved, in-plane and out-of-plane. This interaction becomes more complex in the nonzero angular speed case, and the exchange of energy comes to be intermittent.

References

Althoff, M., Patil, M.J., Traugott, J.P.: Nonlinear modeling and control design of active helicopter blades. J. Amer. Helic. Sty. 57, 1–11 (2012)

Bauchau, O.A., Kang, N.K.: A multibody formulation for helicopter structural dynamic analysis. J. Amer. Helic. Sty. 38, 3–14 (1993)

Borri, M., Mantegazza, P.: Some contributions on structural and dynamic modeling of helicopter rotor blades. l'Aerotecnica Miss e Spazio 64, 143–154 (1985)

Boumediene, F., et al.: Nonlinear forced vibration of damped plates by an asymptotic numerical method. Comput. Struct. 87, 1508–1515 (2009)

Cadou, J.M., et al.: Convergence acceleration of iterative algorithms. Applications to thin shell analysis and Navier–Stokes equations. Comput. Mech. 43, 253–264 (2008)

Cochelin, B., et al.: Asymptotic numerical methods and Padé approximants for non-linear elastic structures. Int. J. Numer. Method Eng. 37, 187–213 (1994)

Hodges, D.H.: A mixed variational formulation based on exact intrinsic equations for dynamics of moving beams. Int. J. Solids Struct. 26, 1253–1273 (1990)

Hodges, D.H.: Geometrically exact intrinsic theory for dynamics of curved and twisted anisotropic beams. AIAA J. 41, 1131–1137 (2003)

Nayfeh, A.H., Pai, P.F.: Linear and nonlinear structural mechanics. Wiley-VCH (2004)

Nayfeh, T.A., et al.: Three-mode interaction in harmonically excited systems with quadratic nonlinearities. Nonlinear Dynam. 3, 385–410 (1992)

Patil, M.J., Althoff, M.: Energy-consistent, Galerkin approach for the nonline-ar dynamics of beams using intrinsic equations. J. Vibrat. Cont. 17, 1748–1758 (2010)

Traugott, J.P., Patil, M.J., Holzapfl, F.: Nonlinear modeling of integrally actuated beams. Aero. Sci. Tech. 10, 509–518 (2006)

Yu, W., et al.: On Timoshenko-like modeling of initially curved and twisted composite beams. Int. J. Solids Struct. 39, 5101–5121 (2002)

Zaretzky, C.L., Crespo Da Silva, M.R.M.: Nonlinear flexural-flexural-torsional interactions in beams including the effect of torsional dynamics.II: combination resonance. Nonlinear Dynam. 5, 161–180 (1994)

Behavior of Single-Lap Bolted Joint Subjected to Dynamic Transverse Load

Olfa Ksentini[1,2,*], Bertrand Combes[2], Mohamed Slim Abbes[1], Alain Daidie[2], and Mohamed Haddar[1]

[1] Unité de Mécanique, Modélisation et Production,
Ecole Nationale d'Ingénieurs de Sfax,
Université de Sfax, Tunisie
Olfa.ing@gmail.com,
{slim.abbes,mohamed.haddar}@enis.rnu.tn
[2] Institut Clément Ader,
Institut National des Sciences Appliquées de Toulouse,
Université de Toulouse, France
{bcombes,alain.daidie}@insa-toulouse.fr

Abstract. Bolted joints used in aeronautical structures are subject to vibrations, which can result in critical damage either from self-loosening or from fatigue. This study is devoted to the examination of the dynamic behavior of a simple bolted joint assembly subjected to quickly varying transverse load, which induces bending of the jointed plates. The adopted approach is based on finite element method, with a coupled bolt model and a penalty friction model, and implicit time simulation. Numerical result sets are presented and discussed.

Keywords: bolted joint, dynamic study, finite element model, friction, transverse shear load, coupled bolt model.

1 Introduction

Bolted joints present an essential element of mechanical structures. They are widely used in aerospace, railway and automobile construction. Their role is to create, from isolated elements, consistent and robust construction. Mounting of a bolted joint usually consists of application of relative rotation between screw and nut until installation of desired preload, which will maintain the integrity of the assembly. Self-loosening of bolted joints is one of the problems encountered in aeronautical structures, resulting from both vibration process and inadequate knowledge of contact phenomenon. Our ultimate aim is to study bolted joints self-loosening, when subjected to the transverse shear stresses resulting from vibrations, within the framework of aeronautical applications.

* Corresponding author.

M. Haddar et al. (Eds.): *Design and Modeling of Mechanical Systems*, LNME, pp. 167–174.
DOI: 10.1007/978-3-642-37143-1_21

R.A Ibrahim (R.A. Ibrahim and C.L. Pettit ,2005) focused on the bolt relaxation resulting from vibration. L. Champaney (L. Champaney et al, 2008) developed strategy for the analysis of contact problems.

Different methods can be used to model the bolted assembly, either by solid bolt model or by coupled bolt model. Many papers discussed the first method. Zhang (Zhang et al, 2007) developed a three-dimensional finite element (FE) model, taking into consideration the helix angle of the threads to simulate self-loosening. Other authors (G. Dinger and C. Friedrich, 2011) (D. Koch et al, 2012) presented a three dimensional finite element model to reveal the self-loosening process, taking into account friction between the nut and the screw and in all the contact areas. All these papers have focused on the self-loosening process but they are limited to the quasi-static case.

J. Kim (J. Kim et al, 2006) presented four kinds of finite element models intended to analysis of bolted joints: solid bolt model, coupled bolt model, spider bolt model and no-bolt model. The solid bolt model uses three-dimensional finite elements. In the coupled model, the bolt shaft is approximately modeled by a beam element, and the nodes corresponding to the head and the nut are connected to the contact surfaces under the nut and the head through deformable coupling elements. The spider bolt model is similar to the coupled model except it is modeled with rigid elements instead of coupling elements. The last model is the no-bolt one, in which a pressure corresponding to the bolt clamping force is imposed on the washer surface to reproduce the pretension effect. J. Montgomery in (J. Montgomery, 2002) presented other models in addition to those previously cited.

The objective of the present study is the analysis of the dynamic behavior of an elementary assembly of two plates connected by a single simplified bolt, without taking into account the threaded connection between screw and nut.

In this paper, we shall first describe the finite element model. Dynamic study requires huge computational time, so the coupled bolt model will be adopted to reduce the number of elements and the time of simulation, and a penalty method will be used to simulate friction between the different parts. Then an analysis of dynamic behavior will be carried out, including slip and displacements induced by vibration under the effect of quickly varying load.

2 Model Presentation

The finite element analysis software Abaqus\Standard 6.11-2 has been used to model an assembled bolted joint. As shown in figure 1 the model is composed of two plates which are 38 mm wide, 89 mm long and 6.35 mm thick, joined by M6.35 bolt. The geometry is simplified: due to the model symmetry, only half of the structure is modeled, and the bolt is modeled by a beam element. Reduced integrated hexahedral eight node elements (C3D8R) are used for the plates meshing. Young's modulus and Poisson's ratio are respectively 210 GPa and 0.3 for the whole steel structure.

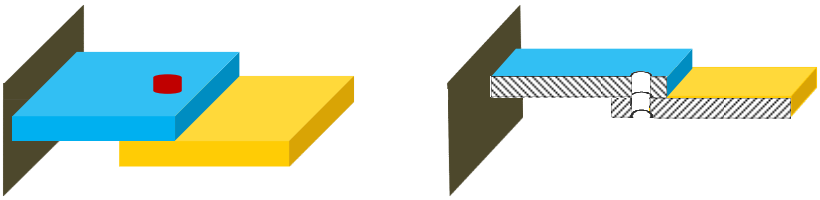

(a) (b)

Fig. 1 Complete geometric model (a), Simplified geometric model (b)

The adopted coupling model, which is called "distributed constraint" in Abaqus software, is shown in figure 2. The bolt is modeled by a beam element, of which each end node is tied to the nodes of the nut-plate or head-plate contact surface by a coupling element. This coupling method constrains the translational and rotational degrees of freedom of the control point and the constrained area.

A contact interface is established on the plane surface between the plates, but we do not allow any contact between the bolt shaft and the corresponding hole.

Modeling of contact carries a great importance due to the effects associated with stick-slip during contact. It can lead to divergence problems if not correctly introduced. Two friction enforcement methods are implemented in Abaqus: the penalty and Lagrange multiplier methods. The penalty method is chosen in this case; it allows some relative elastic penetration of slave surface in the master one to avoid the divergence problems.

This penalty method also uses a transversal stiffness that allows some relative motion of the surfaces (elastic slip) when they should be sticking. Coulomb friction is the standard friction model implemented in Abaqus: the critical stress is proportional to the normal contact pressure. In this case the adopted friction coefficient is equal to 0.1.

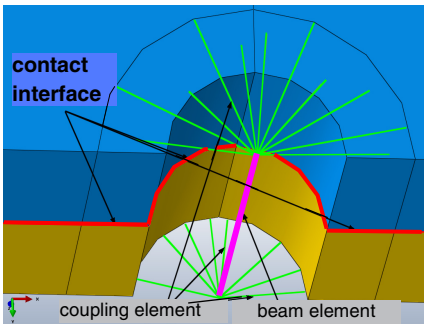

Fig. 2 Bolt model with distributed constraint

The preload Fp is restricted to 7 kN in the bolt element, the maximum normal stress in the bolt shaft is equal to 212 MPa. The boundary conditions are shown in figure 3. The left plate is clamped at its left end whereas the other plate is subject to harmonic load F(t) in the x direction at its right end. The excitation frequency

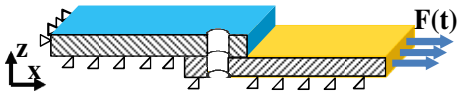

Fig. 3 Boundary conditions

will be chosen close to that of the first Eigenmode, in order to maximize the dynamic effects. To meet the symmetry requirement, rotation in the x direction, translation and rotation in the z direction of faces in the XZ plane are inhibited.

The following flowchart shows the different steps of calculation. In the first one the bolt preload is established in the beam. In the next step, the length of bolt shaft is adjusted to reproduce the initial preload, and to allow subsequent stresses changes in the bolt. Then the external load is applied at the previously cited frequency, and the movement and behavior of the structure is simulated through an implicit dynamic analysis. The implicit method of resolution is based on the full Newton iterative method with an increment strategy. This algorithm for implicit dynamic approach is presented by Hilber (H.M. Hilber et al, 1978). A 5% modal damping is used.

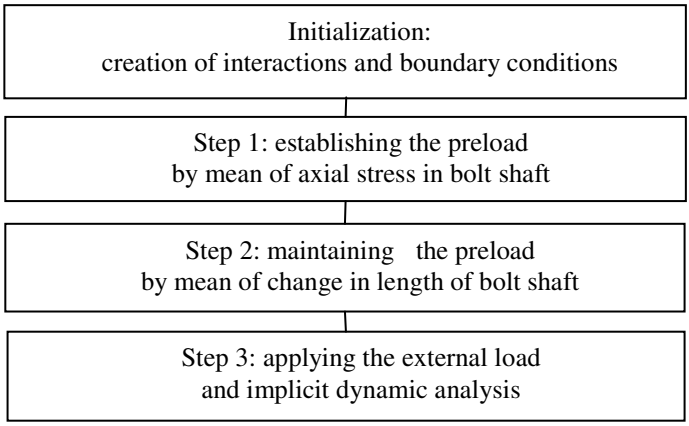

Fig. 4 Flowchart of successive steps

3 Results and Discussion

The different results obtained from the dynamic analysis are presented in this section. The contact areas variation and the extension of sliding zones will be presented; the influence of friction on the transversal displacement will be exposed. Finally the influence of the load amplitude on the displacement behavior is revealed.

Figure 5 shows the first three Eigenfrequencies and the shapes of Eigenmodes. These shapes correspond to the bending in the XZ plane of a beam with a constant section. The excitation frequency will be set to 250 Hz.

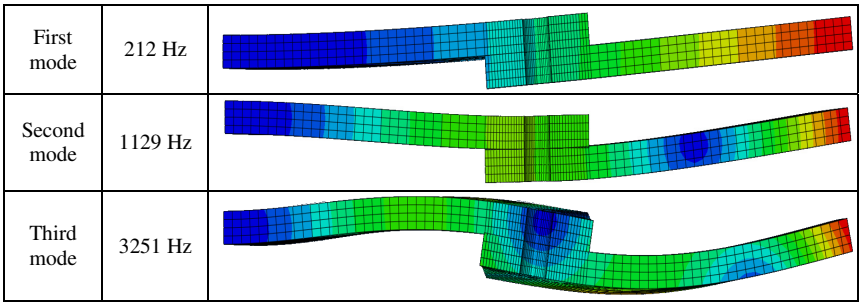

Fig. 5 First three Eigenmodes: The colors depend on magnitude of displacement

A sinusoidal load ranging between 0 and 2000 N is now applied. Figure 6 shows the evolution of contact status between the plates at different times of the load cycle. The red color corresponds to the sticking area and the green color to the sliding area, while the blue color denotes a lack of contact.

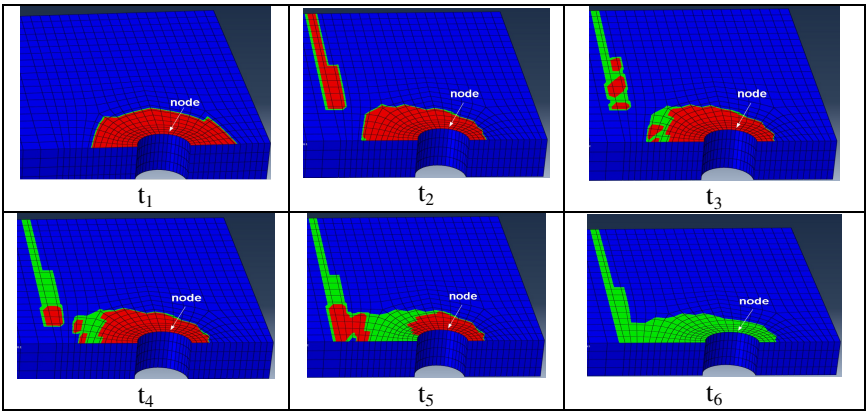

Fig. 6 Contact status between plates: Time is increasing from t1 to t6, and transverse load also increases

At time t_1, there is no relative slipping between the assembled plates, and the contact area spreads only under the bolt head. At t_2, a new contact zone appears at the end of the overlapping plate, due to the bending of joint. Then the transversal load increases, and sliding appears at t_3, starting far from the bolt, and progressing toward it at t_4 and t5. Finally at t6, the transverse load is sufficient to bring the whole contact area into slipping. From this time, there is a global displacement between the plates, until the transversal load decreases and sticking appears again. Figure 7 shows the dynamic response of the structure. Displacements and slipping are evaluated at node indicated in figure 6.

The first two calculation steps take place during the first 2 milliseconds, without any displacement of the node. Then the transversal load appears (figure 7a) and initiates the movement. The displacement in direction x is approximately sinusoidal, while the displacement in direction z (figure 7b) shows a beat phenomenon. This one is due to summation of two sinusoids with close frequencies:

- the linear response of the structure to the sinusoidal excitation force, at 250 Hz, induces a sinusoidal movement at the same frequency;
- the transient response of the first mode to the initial excitation step induces an approximately sinusoidal bending movement at the first Eigenfrequency 212 Hz.

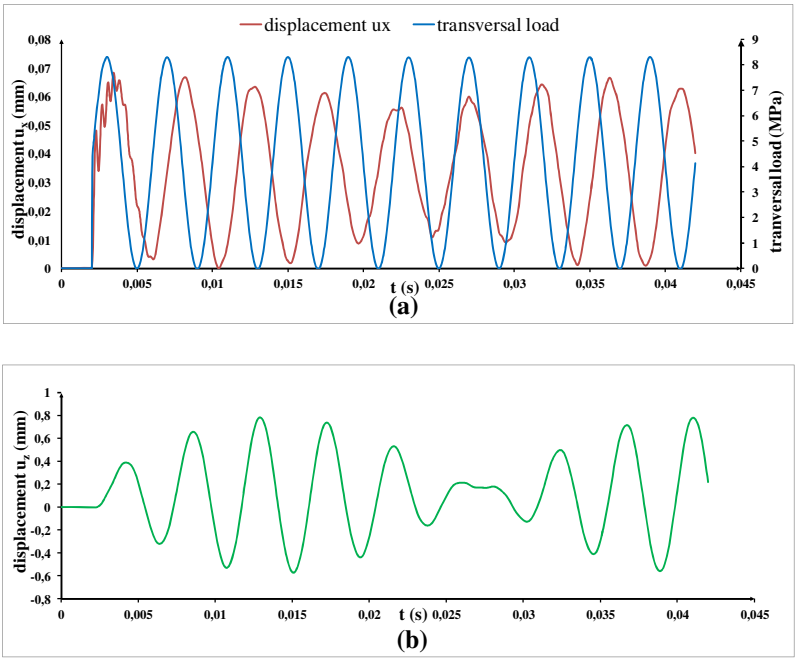

Fig. 7: Responses to transversal load: (a) Transverse load and displacement in x (b) Displacement in z

Figure 8 focuses on the very first cycles of movement. We can see the initial discontinuity in transverse load at time t=2 ms, which causes a strong excitation of the Eigenmodes of the structure. The oscillations being present until t=6ms are caused by the transient response of the third mode, at its Eigenfrequency 3251 Hz. During these oscillations, the contact status at the node of interest toggles between sticking and slipping. Then these oscillations vanish, and a more regular operation comes: the slipping appears when the transverse load approaches its extreme value, and disappears when it reverses direction. The slipping time results in slight irregularity in the displacement curve.

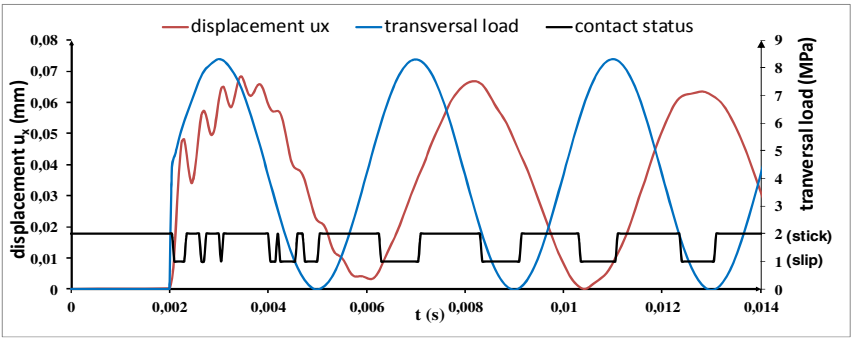

Fig. 8 Beginning of the response to transversal load

Figure 9 shows the influence of amplitude of transversal load, passing from 2000 N to 3000 N. When this amplitude increases, the slipping phenomenon becomes more significant and affects the displacement in the x direction, which becomes more irregular.

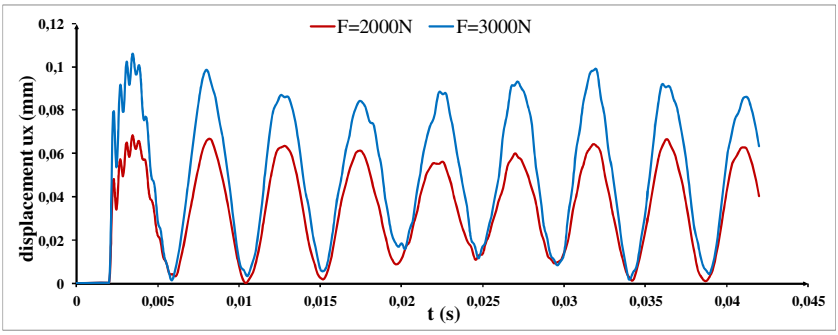

Fig. 9 Influence of load amplitude on the x displacement

4 Conclusion

In this paper, the coupled bolt model is used to simulate the dynamic behavior of a bolted joint assembly. Penalty approach is used to model the contact between the assembled plates. The results of the dynamic behavior under a quickly varying load are presented.

The adopted approach for modeling of bolted joints presents some advantages in order to study their dynamic behavior: it is reliable, and it doesn't need large computational time. However, this method presents some drawbacks, as it does not reproduce the rotational effects in the bolt. In fact, for modeling the self-loosening of bolts, it will be necessary to introduce the helix angle of the threads and friction between the screw and nut. This will be the subject of our next work.

References

Champaney, L., Boucard, P.-A., Guinard, S.: Adaptive multi-analysis strategy for contact problems with friction: Application to aerospace bolted joints. Comput. Mech. 42, 305–315 (2008), doi:10.1007/s00466-007-0213-7

Dinger, G., Friedrich, C.: Avoiding self-loosening failure of bolted joints with numerical assessment of local contact state. Engineering Failure Analysis 18, 2188–2200 (2011), doi:10.1016/j.engfailanal.2011.07.012

Guillot, J.: Calcul des assemblages vissés : Assemblages de pièces planes de faibles épaisseurs. Partie 1, Techniques de l'Ingénieur, BM5564, pp. 1–20 (2010)

Guillot, J.: Calcul des assemblages vissés : Assemblages de pièces planes de faibles épaisseurs. Partie 2, Techniques de l'Ingénieur, BM5565, pp. 1–16 (2011)

Hilber, H.M., Hughes, T.J.R.: Dissipation and 'overshoot' for time integration schemes in structural dynamics. Earthquake Eng. Struct. Dyn. 6(1), 99–117 (1978), doi:10.1002/eqe.4290060111

Ibrahim, R.A., Pettit, C.L.: Uncertainties and dynamic problems of bolted joints and other fasteners. Journal of Sound and Vibration 279, 857–936 (2005), doi:10.1016/j.jsv.2003.11.064

Kim, J., Yoon, J.C., Kang, B.S.: Finite element analysis and modeling of structure with bolted joints. Applied Mathematical Modeling 31(5), 895–911 (2006), doi:10.1016/j.apm.2006.03.020

Koch, D., Friedrich, C., Dinger, G.: Simulation of rotational self-loosening of bolted joints. NAFEMS Seminar - FEM Idealisation of Joints, 157 pages REF : R0103, pp. 115–127 (2012)

Montgomery, J.: Methods for modeling bolts in the bolted joint. In: ANSYS world Users Conference (2002)

Sun, J.S., Lee, K.H., Lee, H.P.: Comparison of implicit and explicit finite element methods for dynamic problems. Journal of Materials Processing Technology 105(1-2), 110–118 (2000), doi:10.1016/S0924-0136(00)00580-X

Zhang, M., Jiang, Y.Y., Lee, C.H.: Finite Element Modeling of Self-Loosening of Bolted Joints. Journal of Mechanical Design 129(2), 218–226 (2007), doi:10.1115/1.2406092

Numerical Stress and Fatigue Behavior of a Helicopter Blade by Modal Analysis

Ahmed Chellil[1], Abdelkader Nour[1], Samir Lecheb[1], Mohamed Chibani[1], and Houcine Kebir[2]

[1] Motor dynamic and Vibroacoustic Laboratory, University of Boumerdès, Algeria
cchellil@yahoo.fr
[2] Laboratoire Roberval, Université de Technologie de Compiègne, UTC, France

Abstract. The objective of this research task is to implement a model to make it possible to simulate the fatigue behavior of a helicopter blade by modal analysis. A study of the aerodynamics of the helicopters was made though the determination of the aerodynamics loads applied to the main blade of helicopter and extract their frequencies and eigen modes with crack and without crack. The expressions of the different energies and virtual work from elements of the blade are developed. A finite element model was defined in order to study the vibratory phenomena. This model makes it possible to extract the Eigen frequencies and modes shapes of the blade, and to calculate the stresses which act on the structure.

The Eigen frequencies of helicopter blade were decreased after cracking in the critical zone, and this reduce is nonlinear; however the stress increased with crack propagation. Therefore the modal analysis is an important factor for the detection of fatigue in aircraft structures.

Keywords: helicopter blade, dynamics, finite element, numerical, fatigue.

1 Introduction

A helicopter is defined as an aircraft, which uses rotating blades. This allows the helicopter to hover relative to the ground without vertical and horizontal flight velocities. One of the earliest investigations of flap-lag-torsion stability of elastic hingeless blades was the work of Hodges and Ormiston [1], where their equations for the stability analysis of a uniform, untwisted rotor blade.

Particularly, Hodges and Coworkers [2] have developed a beam model that accounts for all of the non-classical effects mentioned above, while requiring significantly less computational effort than a direct three dimensional (3D) solution based on a nonlinear finite element discretization of the structure. Clearly, it is desirable to upgrade the blade model in the Friedmann and Al.[3] analysis code with VABS. Although VABS was designed to be used with the geometrically exact formulation described in Hodges, it has been used to calculate the cross-sectional properties needed as inputs for other rotorcraft analysis codes (Hodges et al., [4]). In VABS,

M. Haddar et al. (Eds.): *Design and Modeling of Mechanical Systems*, LNME, pp. 175–180.
DOI: 10.1007/978-3-642-37143-1_22

the in-plane stresses are not neglected since it has been shown that the uniaxial stress assumption can lead to significant errors in the torsional rigidity for some composite cross-sections (Yu et al., 2002b)[5].The research discussed above typically modeled damage in helicopter blades using the frequency domain. Brinker et al. [6] introduced a new frequency domain technique for the modal identification of output-only systems, i.e. in the case where the modal parameters must be estimated without knowing the input exciting the system. Badewi and Kung [7] also studied the effect of fatigue on the modal properties of composite structures. They mention that the idea of using modal properties can be used as a real time indicator of damage in structures, in the present paper; a composite helicopter rotor blade is modeled as a thin walled composite beam using the Chandra and Chopra [8] approach. A progressive damage model which includes the key damage modes in composite such as matrix cracking using by M. pawar[9], this study is to simulate helicopter blade with crack and without crack by appropriate criteria the frequencies and the modes shapes of a helicopter blade .

2 Formulation of the Dynamic Problem

The differential equations governing the nonlinear lead-lag, flapping and torsion of composite rotor blade are:

Lead-lag equation:

$$-\frac{m\Omega^2}{2}\left[v'(R^2-x^2)\right]' - 2m\Omega\left(v'\int_x^R \dot{v}\,dx\right)' + \left[EI_{z'} - (EI_{z'} - EI_{y'})\sin^2(\Re\theta)\right]v'''' + (EI_{z'} - EI_{y'})\frac{\sin(2\Re\theta)}{2}w''' + (EI_{z'} - EI_{y'})\left[-\sin(2\Re\theta)(\phi v'')' + \cos(2\Re\theta)(\phi w'')'\right] - 2m\Omega\beta_{pc}\dot{w} - 2m\Omega\int_0^x (v'\dot{v}' + w'\dot{w}')\,dx + m(\ddot{v} - \Omega^2 v) = L_v \tag{1}$$

Flap equation:

$$-\frac{m\Omega^2}{2}\left[w'(R^2-x^2)\right]' - 2m\Omega\left(w'\int_x^R \dot{v}\,dx\right)' + \left[EI_{y'} + (EI_{z'} - EI_{y'})\sin^2(\Re\theta)\right]w'''' + (EI_{z'} - EI_{y'})\frac{\sin(2\Re\theta)}{2}v''' + (EI_{z'} - EI_{y'})\left[\cos(2\Re\theta)(\phi v'')' + \sin(2\Re\theta)(\phi w'')'\right] + 2m\Omega\beta_{pc}\dot{v} + m\ddot{w} = L_w - m\Omega^2\beta_{pc}x \tag{2}$$

Torsion equation:

$$-\frac{m\Omega^2}{2}k_A^{\,2}\left[\phi'(R^2-x^2)\right]' - GJ\phi'' + mk_m^{\,2}\ddot{\phi} + m\Omega^2(k_{m2}^{\,2} - k_{m1}^{\,2})\phi\cos(2\theta) + (EI_{z'} - EI_{y'})\left[(w''^2 - v''^2)\frac{\sin 2\Re\theta}{2} + v''w''\cos 2\Re\theta\right] = M_\phi - m\Omega^2(k_{m2}^{\,2} - k_{m1}^{\,2})\frac{\sin 2\theta}{2} \tag{3}$$

2.1 Numerical Solutions

The equations of motion are solved by the Galerkin method. The solution in lead-lag flapping and twisting are expressed in dimensionless form in terms of series, based on generalized coordinates and mode shape functions are given by:

$$\bar{v} = \sum_{J=1}^{N} V_J(\psi)\Psi_J(\bar{x}), \quad \bar{w} = \sum_{J=1}^{N} W_J(\psi)\Psi_J(\bar{x}) \quad , \quad \phi = \sum_{J=1}^{N} \phi_J(\psi)\Theta_J(\bar{x}) \tag{4}$$

Where $\psi = \Omega t$, $\bar{x} = x/R$ and N is the number of modes; $\Psi_J(\bar{x})$ and $\Theta_J(\bar{x})$ are the mode shapes for the bending and torsion of the cantilever beam.

$$\begin{aligned} \Psi_J(\bar{x}) &= \cosh(\beta_J \bar{x}) - \cos(\beta_J \bar{x}) - \alpha_J\left[\sinh(\beta_J \bar{x}) - \sin(\beta_J \bar{x})\right] \\ \Theta_J(\bar{x}) &= \sqrt{2}\sin(\gamma_J \bar{x}) \end{aligned} \tag{5}$$

By employing the technology, Eq. (4) is substituted into Eq. (1) to (3). The equations of motion for the orthotropic composite blade can be rearranged in matrix form as:

$$[M]\{\ddot{X}\} + [C]\{\dot{X}\} + [K]\{X\} = \{0\} \tag{6}$$

The coefficients $[M]$, $[C]$ and $[K]$ represent the mass, damping and stiffness matrices are given as functions of the equilibrium solution, V_{0j} , W_{0j} et ϕ_{0j}

3 Modelling of the Blade

3.1 Cross-Section of the Blade

An investigated helicopter rotor blade (Fig. 1) is equipped with NACA23012 airfoil with active part radius 8.56 m and chord length 0.421 m. This rotor blade consists of D-spar made of unidirectional GFRP (Glas Fiber Reinforced Polymer), skin made of $+45^0/-45^0$ GFRP, foam core, MFC actuators and balance weight. The thickness of skin GFRP layer is 0.125 mm and thickness of MFC layer is 0.3 mm. The material properties of the rotor blade components are as follows:

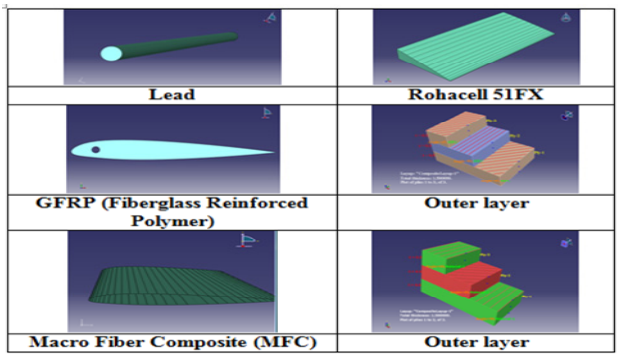

Fig. 1 Helicopter blade material

We study simulate the following blade which represent in the figure

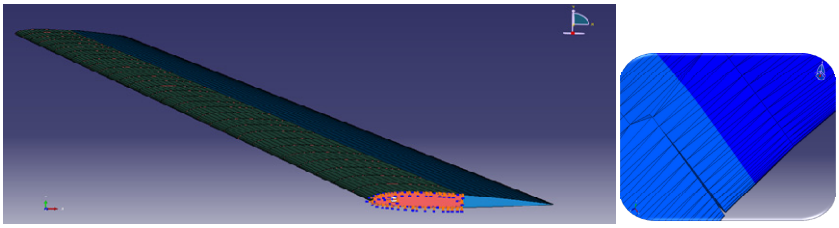

Fig. 2 Helicopter blade model with crack

To identify the response of the structure, the Von Mises equivalent stress is represented for the blade with crack and without crack.

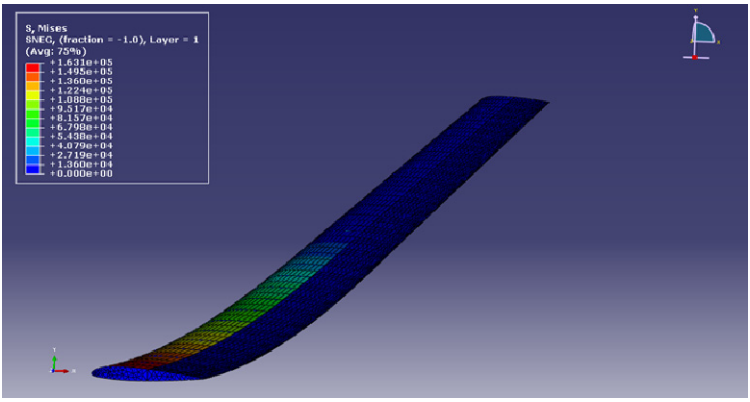

Fig. 3 Von Mises equivalent stress for blade without crack

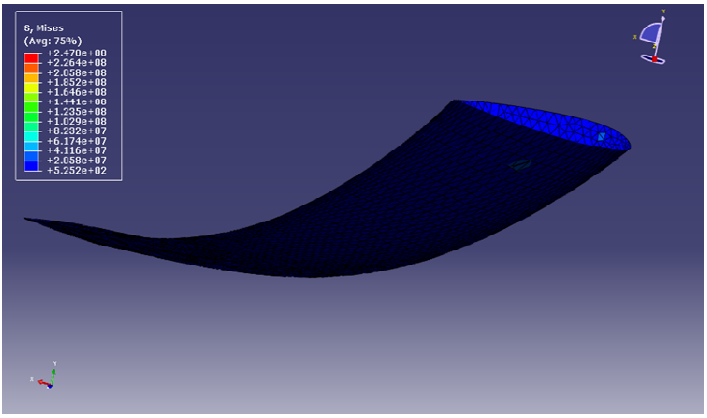

Fig. 4 Von Mises equivalent stress for blade with crack

We remark notice that the max .principal stress of the blade without crack is situated at the fixed end the maximum value equal to 8.28 E+07 Pa.

In case (cracked blade), we note the tension is the very higher at the end the party Crack .This is equal to (2.47 E +08 Pa). So it's an increase this represents the concentration of stress.

We'll comparison between blade with crack and without crack we get this result in flowing table:

Table 1 Strain, von mises and tresca Stress distribution

	Von-Mises stress(MPa)	Tresca stress (MPa)	Stain
Without crack	82.8	94.8	$6.58\ 10^{-4}$
With crack	247	263	$4.11\ 10^{-3}$

Table 2 Eigen frequencies for blade with crack and without crack

Frequency [Hz]	Mode 1	Mode 2	Mode 3	Mode 4	Mode 5	Mode 6
Without crack	0.84	1.85	5.37	11.96	15.37	29.33
With crack	0.49	1.00	2.95	6.11	8.12	16.01

In this section is to locate the distribution of pressure and stress of composite blade, yet force application with drawn perpendicular to the blade, then we create a crack in the blade simple in fixed side and conclude various stresses and strain. the frequencies in the blade without crack are very high comparison with the blade with crack

4 Conclusion

The work is based on modeling by finite element method the helicopter blade. To realize this modeling we have used the so called a numerical simulation by the ABAQUS software to analyze the aerodynamic forces of the helicopter blade; it calculates the frequencies and Eigen values, stress, strain and the displacement, as well as we noticed after the simulation of the blade without crack and with crack; the frequencies in the blade without crack are very high comparison with the blade with crack and stress and displacement of the blade with crack are very large comparison with the blade without crack.

References

[1] Hodges, D.H., Ormiston, R.A.: Stability of Elastic Bending and Torsion of Uniform Cantilevered Rotor Blades in I-lover. In: Structures, Structural Dynamics, and Material Conference, Williamsburg, Virginia. AIAA Paper 73-105 (March 1973)

[2] Hodges, D.H., Saberi, H., Ormiston, R.A.: Development of non linear beam elements forrotorcraft comprehensive analyses. Journal of the American Helicopter Society 52(1), 36–48 (2007)
[3] Friedmann, P.P., Glaz, B., Rafael Palacios, A.: Moderate deflection composite helicopter rotor blade model with an improved cross-sectional analysis. International Journal of Solids and Structures 46(10), 2186–2200 (2009)
[4] Hodges, D.H., Yu, W.: A rigorous, engineer-friendly approach for modeling realistic, composite rotor blades. Wind Energy 10, 179–193 (2007)
[5] Yu, W., Volovoi, V.V., Hodges, D.H., Hong, X.: Validation of the variational asymptotic beam sectional analysis. AIAA Journal 40(10), 2105–2112 (2002)
[6] Rew, K.H., Kim, S., Lee, I., Park, Y.: Real time estimation of multi-modal frequencies for smart structures. Smart Materials and Structures 11, 36–47 (2002)
[7] Bedewi, N.E., Kung, D.N.: Effect of fatigue loading on the modal properties of composite structures and its utilization for prediction of residual life. Composite Structures 37, 357–371 (1997)
[8] Chandra, R., Chopra, I.: Structural response of composite beams and blades with elastic couplings. Compos. Eng. 2(5-6), 347–374 (1992)
[9] Pawar, P.M., Ganguli, R.: On the effect of progressive damage on composite helicopter rotor system behaviour. Composite Structures 78, 410–423 (2007)

Detection of Gear Tooth Pitting Based on Transmission Error Measurements

Feki Nabih, Cavoret Jérôme, Ville Fabrice, and Velex Philippe

Université de Lyon – INSA Lyon – LaMCoS - UMR CNRS 5259,
Bâtiment Jean d'Alembert – 20,
Avenue Albert Einstein – 69621
Villeurbanne Cedex – France
{Nabih.Feki,Philippe.Velex}@insa-lyon.fr

Abstract. This paper deals with the experimental validation of the dynamic model of a single stage geared system representative of a back-to-back test rig. The validation relies on loaded transmission error (TE) measurements by using optical encoders which are compared with simulation results. The influence of tooth pitting on TE is highlighted and it is demonstrated that a simple pit model can reproduce the actual vibrations generated by such surface failures.

Keywords: Gear, transmission error, tooth pitting, experimental.

1 Introduction

The dynamic behavior of gears has been widely studied over the last 30 years based on, first, single torsional degree of freedom models and, progressively, more sophisticated three-dimensional representations accounting for the couplings between torsion, bending, traction and compression. To date, non-linear dynamic models with variable mesh stiffness make it possible to simulate critical frequencies, the influence of geometrical errors and assembly defect, the occurrence of contact losses between the teeth, etc. It is widely accepted that transmission error (TE) represents an indicator of the vibration and noise performance of gears. TE is classically defined as the difference between the actual and theoretical gear angular positions and its time variations are representative of the mesh dynamic excitations, (Velex and Ajmi 2006).

The numerical gear dynamic model under consideration is based on that introduced by Velex and Maatar (1996) with the pinion-gear pair being assimilated to two rigid cylinders connected by a series of time-varying, non-linear springs representing the mesh stiffness function. Shafts are simulated by classic two-node elements and bearings are represented by additional lumped stiffness elements. Gear tooth pitting can be simulated anywhere on the active tooth flanks via some suitable localized distributions of normal deviations with respect to ideal tooth flanks (Feki et al., 2012).

M. Haddar et al. (Eds.): *Design and Modeling of Mechanical Systems*, LNME, pp. 181–188.
DOI: 10.1007/978-3-642-37143-1_23

In this paper, experimental investigations have been conducted using a standard power circulating FZG fatigue test rig in order to generate real pitting failures on tooth flanks. The test-rig was instrumented by optical encoders to continuously measure transmission error under load and appraise the influence of pits on mesh excitations. The first section of the paper is devoted to the description of the experimental set-up along with the measurement principles and methodology. Then, a number of spectral analyses are presented in order to compare the experimental and simulated transmission error signals. A reasonable agreement is observed in terms of critical frequencies and amplitudes thus validating the gear dynamic model with tooth pitting.

2 Experimental Set-Up

2.1 Description of the FZG Gear Test Rig

The FZG gear test rig was originally developed at the Forschungsstelle für Zahnräder und Getriebebau (FZG) of the Technical University of Munich. It is an electromechanical system composed of an asynchronous motor with a speed controller (100 to 3000 rpm) and a back-to-back rig consisting in test and slave gears connected by two shafts (Fig. 1). The secondary shaft is divided in two parts with the load clutch. This device is fixed on one side to the foundation by means of a locking pin. On the other side, the half shaft is twisted with the lever and weights in order to apply a static load torque. This torsion torque is kept constant during the operation of the test bench after bolting the clutch, removing the weights and lever, and unlocking the shaft.

This machine was specifically designed for testing highly-loaded gears and the related fatigue issues (contact and root stresses). High powers can be reached thanks to the power circulation and the capability to impose a torque by elastic deformation independently of the speed imposed by the electric motor.

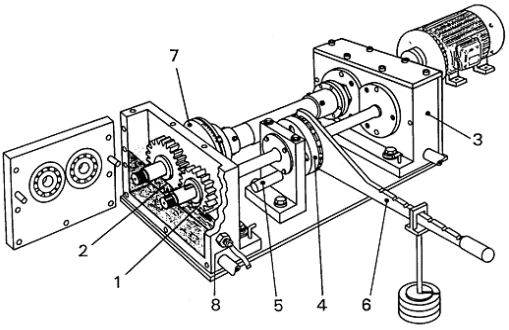

1 Test pinion
2 Test wheel
3 Slave gear
4 Load clutch
5 Locking pin
6 Load lever and weights
7 Torque measuring clutch
8 Temperature sensor

Fig. 1 FZG back-to-back gear test rig (Höhn 2008)

2.2 Measurement Principle

From an experimental point of view, transmission error can be measured by systems based on accelerometers or high-resolution optical encoders. In the present case, TE was derived from the data of two optical encoders mounted on the free-ends of either shafts of the gear system as illustrated in Figure 2.

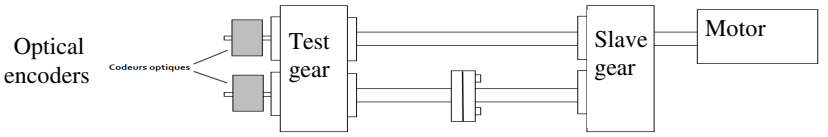

Fig. 2 Optical encoders mounting positions on FZG back-to-back gear test rig

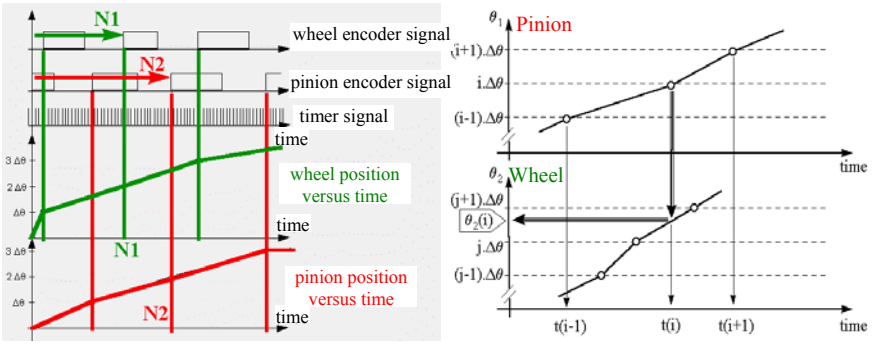

(a) pinion and wheel angular positions versus time

(b) way of processing transmission error from encoder signals

Fig. 3 Measurement principle (De Vaujany et al., 2005)

The optical encoders were mounted very close to the test pinion and gear in order to make transmission error measurements more representative of the gear behavior. The measurement principle relies on counting the number of pulses from a timer signal with a very high frequency (80 MHz here) between two rising edges of the optical encoder signal (Remond 1998). Having a common reference (same timer and counter), the counting can be simultaneously performed on the two channels. Figure 3.a shows a simplified scheme leading to the reconstruction of the time variations of the pinion and gear angular positions (De Vaujany et al., 2005) in relation to the number of encoder pulses per revolution (here, 2500 pulses).

2.3 Experimental Transmission Error (TE) Calculation

Having stored the measured time lengths between successive rising edges from both encoders, transmission error can be deduced by using several methods. According to Remond and Play, the so-called "angular methods" seem to be more

representative of physical phenomena than asynchronous methods (Remond and Play, 1999). In fact, the use of angular methods leads to bring out the dynamic effects of gear geometry, eccentricity, tooth meshing and especially gear tooth faults. This method consists in sampling the gear angular position with reference to the pinion angular position (Fig. 3.b). Then, the new gear angular position $\theta_2(i)$ is resolved by linear interpolation at times corresponding to the number of timer pulses between two consecutive rising edges of the pinion encoder. The TE formula can then be numerically reconstructed by taking into account the speed ratio leading to an expression of the form:

$$TE(i) = \theta_1(i) - \frac{Z_2}{Z_1}\theta_2(i) = i \cdot \Delta\theta_1 - \frac{Z_2}{Z_1}\theta_2(i) \quad (1)$$

3 Results and Discussions

All the following results have been obtained for a test spur gear whose characteristics are detailed in Table 1 (Höhn, 2008).

Table 1 Main geometrical characteristics of test spur gear (C-type)

	pinion	gear
centre distance (mm)		91.5
number of teeth	16	24
Module (mm)		4.5
pressure angle (°)	20	20
face width (mm)	14	14
pitch diameter (mm)	73.2	109.8
profile shift coefficient	0.1817	0.1715

3.1 Generation of Actual Pitting

In order to investigate the vibration behavior of a spur gear in the presence of pitting, a fatigue test was performed to generate a "natural" gear tooth pitting. The test conditions, taken from DGMK Information Sheet (2006), are intended to lead to pitting (short duration test pitting). In short, it consist in applying very important loading levels (levels 9 and 10 in Table 2) at a constant rotational speed while controlling the oil temperature in the gearbox (90 ± 3 ° C (DGMK Information Sheet, 2006)). The torque applied to the output shaft causes a force distribution on the tooth contact surfaces resulting in local Hertzian pressure distributions (a maximal local Hertzian contact stress of 2069 N/mm² for loading level 9 (DGMK Information Sheet, 2006)). This type of fatigue test is mainly used to determine the influence of lubricants on pitting resistance.

Table 2 Loading levels

Loading levels	4	5	6	7	8	9	10
Load torque (N.m)	60.75	94.1	135.3	183.35	239.25	302	372.7
Input torque (N.m)	91.12	141.15	202.95	275.02	358.87	453	559.05

Under these conditions, the test was performed by cooling the test gear box to allow a continuous use of the FZG machine. A single pit was found on one pinion tooth after 13 million cycles. Figure 4 shows the actual shape of the obtained pit on a C-type tooth.

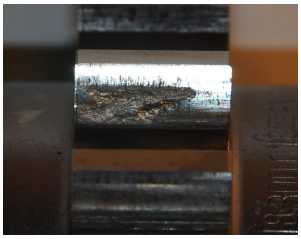

Fig. 4 Actual gear tooth pitting

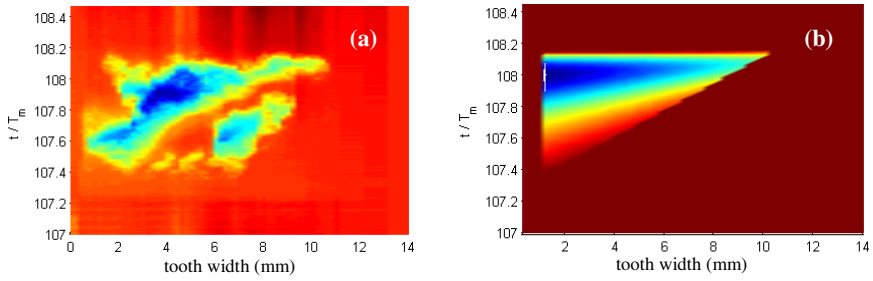

Fig. 5 (a) Actual and (b) simulated tooth pitting

The dimensions of the actual pitting failure on the tooth are plotted in Figure 5.a where t / T_m (T_m is the mesh period) represents a dimensionless time but also the position in the profile direction. The defect is characterized by a triangular shape on the tooth surface and a maximum depth around 380 µm.

In order to compare the numerical and experimental results, the tooth pitting is simulated by a hole on one pinion tooth based on the measured size and shape as illustrated in Figure 5.b.

3.2 Comparison between Measured and Simulated Transmission Error Spectra

Figures 6 to 9 show the spectra of the experimental and theoretical (simulated) transmission error (TE) signals of the test gear with and without the presence of a

pit in one tooth of the pinion. The TE signals have been obtained for a rotational speed of 30 Hz on the input shaft and under loading level 7 (as defined in Table 2). All the presented spectra have been calculated using a Blackman window in order to obtain narrow and distinctive peaks. Their amplitudes are divided by their maximum amplitude in each case.

For the same operating conditions, it can be noticed that the spectra of the experimental and simulated signals (with or without tooth pitting) look similar. In all the cases, significant amplitude is reported at the fifth harmonic of the mesh frequency. According to the simulation results, this frequency corresponds to a critical frequency of the mechanical system (test gear, shafts and bearing) with a very large contribution of the gear element (84.19 %) to the total modal strain energy.

In the presence of one tooth pit, the spectra exhibit modulation sidebands between the different gear mesh harmonics mainly around the first and fifth harmonics. However, these sidebands are not present in the transmission error spectra of healthy gears. For example, between harmonics 4 and 5 or 5 and 6, 16 peaks emerge in the TE spectra with pitting (Fig. 7 and Fig. 9). These peaks are separated by the pinion rotational frequency and their number (between two harmonics) corresponds to the number of pinion teeth. This explains that, in the presence of a fault, the frequency modulation is controlled by the rotational frequency of the defective wheel (pinion in our case).

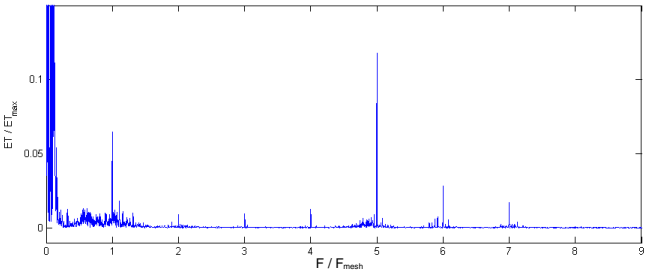

Fig. 6 Spectrum of the experimental TE signal without gear tooth pitting

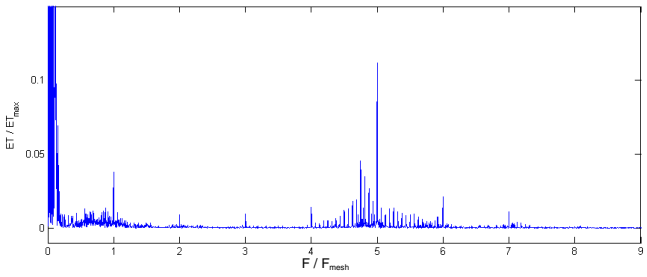

Fig. 7 Spectrum of the experimental TE signal in the presence of a tooth pit

It is also noticed that the TE spectra with pitting reveal an asymmetry in the sideband distributions which indicates a modulation both in amplitude and frequency. The main reasons for this asymmetry are, a) the dynamic effects caused by the vicinity of these sidebands and the resonance zone (critical frequencies), (Inalpolat and Kahraman 2009, McFadden and Smith 1985) and, b) the effect of the carrier frequency of the pinion rotation on the modulation sidebands (Inalpolat and Kahraman 2009).

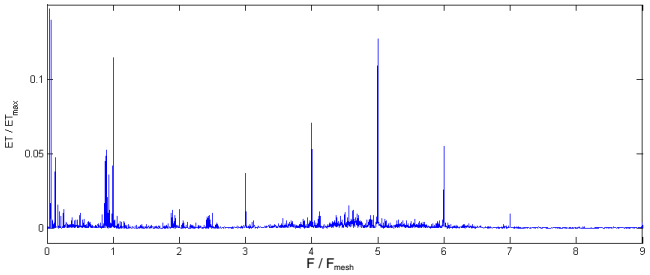

Fig. 8 Spectrum of the simulated TE signal without gear tooth pitting

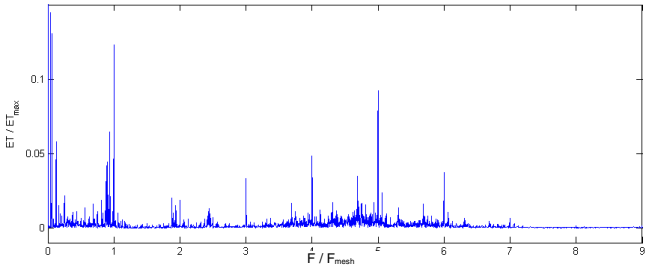

Fig. 9 Spectrum of the simulated TE signal in the presence of a tooth pit

4 Conclusion

In conclusion of these comparisons between experimental and numerical results, a good qualitative agreement in terms of response spectra is observed. By comparing the spectral representations of the TE signals with and without pitting, it can be concluded that the presence of pitting on the teeth modifies the spectral image of transmission error, hence suggesting a possibility of early detection by vibration monitoring. These observations also validate the gear dynamic model and its extension to implementing a pitting model.

References

Velex, P., Ajmi, M.: On the modeling of excitations in geared systems by transmission errors. J. Sound Vib. 290, 882–909 (2006)

Velex, P., Maatar, M.: A mathematical model for analyzing the influence of shape deviations and mounting errors on gear dynamic behaviour. J. Sound Vib. 191, 629–660 (1996)

Feki, N., Clerc, G., Velex, P.: An integrated electro-mechanical model of motor-gear units - Applications to tooth fault detection by electric measurements. Mechanical Systems and Signal Processing 29, 377–390 (2012)

Remond, D.: Practical performances of high-speed measurement of gear Transmission Error or torsional vibrations with optical encoders. Measurement Science & Technology 9, 347–353 (1998)

Remond, D., Play, D.: Advantages and perspectives of gear Transmission Error measurement with optical encoders. In: Congrès Mondial des Engrenages et Transmissions, Paris, France (1999)

De Vaujany, J.-P., Remond, D., Guingand, M.: Simulation numéque et mesure de l'erreur de transmission d'engrenage spiro-conique aéronautique. In: Congrès Français de Mécanique (2005)

Höhn, B.-R., Oster, P., Tobie, T., Michaelis, K.: Test methods for gear lubricants. Goriva i Maziva 47, 129–152 (2008)

DGMK Information Sheet, Short Test Procedure to investigate the Lubricant Influence on the Pitting Carrying Capacity of Gears (2006)

Inalpolat, M., Kahraman, A.: A theoretical and experimental investigation of modulation sidebands of planetary gear sets. J. of Sound and Vibration 323, 677–696 (2009)

McFadden, P.D., Smith, J.D.: An explanation for the asymmetry of the modulation sidebands about the tooth meshing frequency in epicyclic gear vibration. Proceedings of the Institution of Mechanical Engineers 199, 65–70 (1985)

Multi-objective Optimization of Gear Tooth Profile Modifications

Ghribi Dhafer[1,2], Bruyère Jérôme[2], Velex Philippe[2], Octrue Michel[1], and Haddar Mohamed[3]

[1] CETIM, Pôle d'Activités Mécatronique, Transmissions et Capteurs (MEC), Senlis, France
Dhafer.Ghribi@cetim.fr
[2] Université de Lyon, INSA Lyon, LaMCoS, UMR CNRS 5259, France
Philippe.Velex@insa-lyon.fr
[3] Université de Sfax, Ecole Nationale d'Ingénieurs de Sfax, U2MP, Tunisie

Abstract. In a context of permanent technological progress to produce ever more reliable and efficient industrial products, modern gears are increasingly subject to strict requirements in terms of load capacity, performance, noise generation, etc. The definition of tooth modifications in order to improve performance criteria such as transmission error fluctuations, efficiency, wear resistance, etc. is a challenging problem for designers because these criteria often evolve in a contradictory manner. This paper deals with the multi-objective optimization of tooth profile modifications and its main purpose is to propose an approach to help design tooth corrections in order to simultaneously optimize several objective functions. An optimization technique based on a specific algorithm (NSGA-II) is presented and its effectiveness in terms of multi-criterion optimization in the sense of Pareto optimal is analyzed based on a number of case studies.

Keywords: gear, profile tooth modifications, multi-objective optimization, robustness.

1 Introduction

The performance of a gear system is plural and multidimensional (depends on several variables). Ideally, the design process should identify the solution leading to the best compromise between the various criteria defining the quality of the system. However, the difficulties of implementation are significant and such a process is rarely possible. The main objective of this study is to explore the approaches that achieve design optimization with respect to several simultaneous criteria. After presenting the proposed approach based on the Pareto method, an appropriate algorithm is introduced to optimize a number of criteria via some suited tooth profile modifications.

M. Haddar et al. (Eds.): *Design and Modeling of Mechanical Systems*, LNME, pp. 189–197.
DOI: 10.1007/978-3-642-37143-1_24

2 Multi-objective Optimization

2.1 Overview

Most of the time, there is no solution to the multi-objective optimization problem (including that defined in Equation 1) which simultaneously optimizes all the criteria and it is therefore necessary to develop acceptable compromises between the different objectives.

$$\begin{aligned} &\text{minimize} \quad f_i(X) \quad \text{for } i=1,\ldots,p \quad \text{with } X(x_1,x_2,..) \in D \\ &\text{subjected to:} \quad \begin{cases} g_j(X) \le 0 & \text{for } j=1,\ldots \\ h_k(X)=0 & \text{for } k=1,\ldots \end{cases} \end{aligned} \tag{1}$$

Two approaches can be found in the literature (Miettinen 1999). The first strategy consists in transforming the original multi-objective problem into a single objective formulation (one objective function) by linearly combining all the criteria. The trade-off is thus fixed a priori by weighted terms associated with each criterion.

$$\begin{cases} F(X)=\sum_{i=1}^{N} w_i f_i(X) \\ \text{With } 0 \le w_i \le 1 \quad \text{and} \quad \sum_{i=1}^{N} w_i = 1 \end{cases} \tag{2}$$

The value taken by the weighting terms (w_i) reflects the importance (relative weight) of the associated objective function. Solutions (2) can be derived using conventional techniques such as gradient methods, genetic algorithms, etc. This formulation has the advantage of being simple to understand but presents the major drawback of relying strongly on weighting terms, often determined subjectively, whose influence on the results is considerable. Moreover, whenever designers wish to change these values, a new search has to be completed. The second methodology found in the literature is based on the Pareto method in which a solution is defined as a Pareto optimal if it is not dominated by another solution in the same space. In general, the Pareto optimum is not unique but comprises a set of solutions constituting the so-called Pareto front (see Figure1).

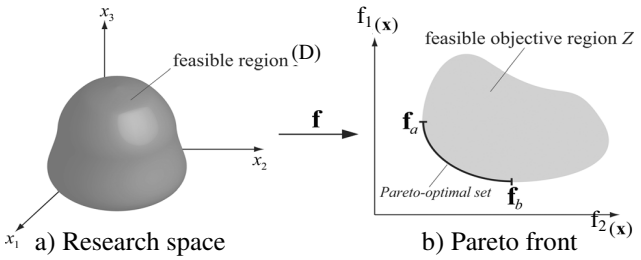

Fig. 1 Definition of Pareto front (Artoni et al. 2011)

2.2 Optimization Based on Genetic Algorithms

Based on the concept described above, the goal of an optimization algorithm for multi-objective problem is to determine its Pareto front which is the set of solutions optimizing all the criterion linear combinations. By so doing, designers can refine the criteria in order to make an appropriate choice of parameters. Genetic algorithms are highly robust optimization techniques which are also adapted to multi-criterion problems (Zitzler et al. 2000 and Deb et al. 2002). The basic principle consists in taking a population of solutions and transforming it by several operations (cross-over, mutation...) in order to determine the Pareto front. Several methods are proposed in the literature, which differ mainly by their results in terms of solution distributions on the Pareto front and convergence speed. An updated state of the art can be found in (Zitzler et al. 2000 and Deb et al. 2002). Deb et al. have proposed an optimization algorithm "NSGA-II" (Non-Dominated Sorting Genetic Algorithm-II) considered as more efficient and faster than its predecessors. Its elitist approach makes it possible to store the best solutions found in the previous generations and NSGA-II does not require any parameter calibration. The dual convergence-diversity objective is achieved, firstly, by the use of a sorting procedure (the calculation of the performance) that promotes non-dominated solutions and, secondly, by the introduction of a technique for measuring density (crowding) solutions of the non-dominated front. The general principle of selection is summarized as follows: for two solutions with different ranks, that with the lowest rank is preferred (rank here characterizes the non-dominance of the solution). For solutions localized on the same front, the solutions in the region where the density is lower are chosen, which corresponds to the highest crowding distance. An illustration of the operating principles of this algorithm is shown in Figure 2.

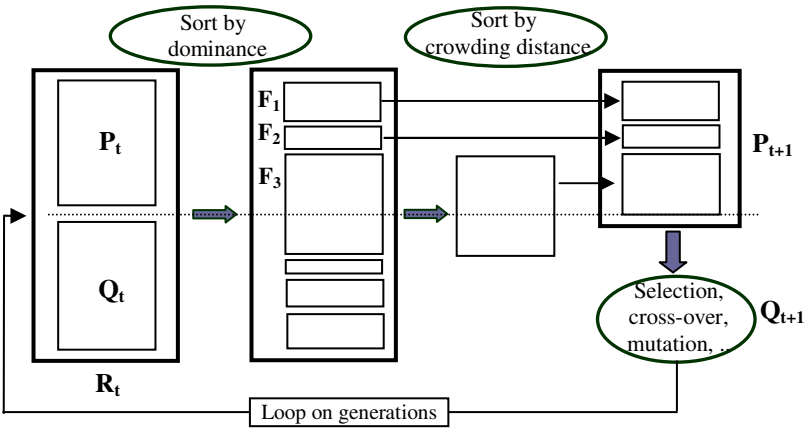

Fig. 2 Evolution procedure of the NSGA-II algorithm

3 Gear Tooth Modifications: Multi-objective Optimization

3.1 Design Variables

Tooth flank modifications are mostly used to ensure quasi-uniform motion transfer and avoid corner contacts at engagement (Maatar and Velex 1997). They consist in the introduction of voluntary tooth geometry changes in the profile direction with respect to perfect tooth flanks which are often characterized by a depth E at tooth tips and an extent of modification $L_c = \Gamma\varepsilon_\alpha Pb_a$ (Figure 3). In what follows, the relief amplitude E is normalised with respect to δ_m: the average static mesh deflection for a perfect gear (further denoted E*).

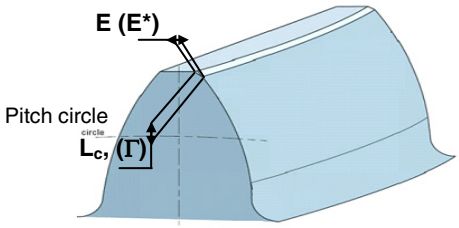

Fig. 3 Tooth profile modifications (parameters to be optimized)

3.2 Optimization Targets

Like any other design process, gear design is in constant evolution to meet the demands and expectations of customers on the final product. Due to the increasingly requirements on energy saving, many studies focus on efficiency, weight and footprint reduction while keeping acceptable contact and root resistance, wear and temperature rises. In addition, for a number of applications (such as automotive industry), gear noise and vibration have become key-issues which should also be addressed in optimal profile design. Based on these considerations, the following performance criteria have been considered in this paper:

a) The fluctuations of the quasi-static transmission error (RMS(TEs): Root Mean Square) representative of vibration and noise excitations (Velex et al. 2011).
b) The power losses by tooth friction using the loss factor (Λp) defined in (Velex and Ville 2009).
c) The maximum value of the pV (pressure * sliding velocity) product which, to some extent, is an indicator of the possible occurrence of wear and scuffing (Osman and Velex 2010).

3.3 Applications

In this section, the NSGA-II algorithm is combined with a numerical gear model with the objective of defining the profile tooth modifications leading to the best

compromise with regard to a number of criteria representing the gear performance. The helical gear example defined in Table 1 is treated and the optimization variables are the dimensionless depth (E*) and extent (Γ) of profile modification. The profile corrections are supposed to be linear, symmetric tip relief on the pinion and gear teeth. In what follows, bi- and tri-objective problems are successively considered.

Table 1 Gear data for multi-objective optimization

---	**Pinion/ Gear**	---	**Pinion/ Gear**
Tooth Number	28/56	Normal pressure angle (deg)	20
Face width (mm)	40/40	Profile contact ratio	1.48
Addendum coeffi-	1/1	Overlap contact ratio	1.34
Dedendum coeffi-	1.4/1.4	Helix angle (deg)	25
Module(mm)	4	Center distance (m)	No backlash
Pinion torque (Nm)	850	δ_m, average static mesh deflection	20μm

3.3.1 Bi-objective Problems

- **Problem 1**

Figure 4.a represents the Pareto front obtained when simultaneously considering the loss factor (Λp) and the fluctuations of the quasi-static transmission error (RMS(TEs)). The antagonistic variations of these two criteria are clearly visible but, moreover, additional information on the criterion levels that can be simultaneously achieved is available. Figure 4.b shows the combinations of profile modifications corresponding to the Pareto front in the previous figure using a colour correspondence between the two graphs. The results agree with those of Velex and Ville 2009 who have found that larger profile modifications tend to reduce tooth friction losses. Turning to transmission error fluctuations, the NSGA-II algorithm converges on the characteristic optimal area similar to that obtained by the authors using several analytical and numerical methods (Velex et al. 2011) and (Ghribi et al. 2012). From these figures, it can be concluded that the solutions circled in

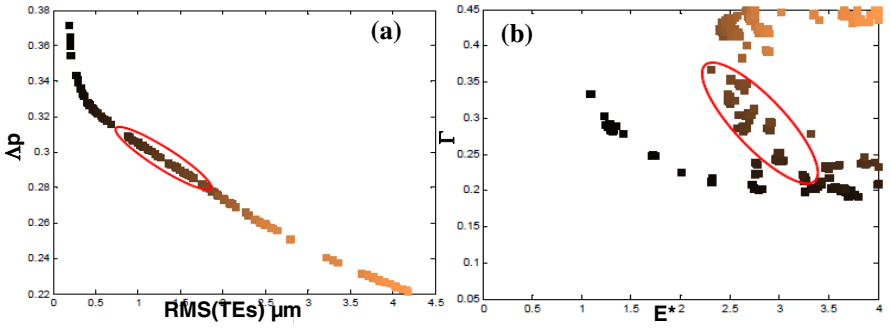

Fig. 4 NSGA-II results: RMS(TEs)_ Λp

red are reasonable compromises between efficiency and noise. These profile modifications are characterized by dimensionless extents ranging between 0.2 - 0.35 and large dimensionless depths (2.5 <E* <3.5).

- **Problem 2**

In this section, the simultaneous optimization of the maximum value of the pV product (max (pV)) and RMS (TEs) is tackled. The corresponding results are plotted in Figure 5. The NSGA-II algorithm leads to a Pareto front whose shape resembles that found in the previous example. As for problem 1, a compromise can be reached by considering the set of profile modifications circled in red in both Figures 5.a and 5.b. characterized by a significant dimensionless length (Γ) and a smaller range of variation for the dimensionless depth (1.5 <E* <2).

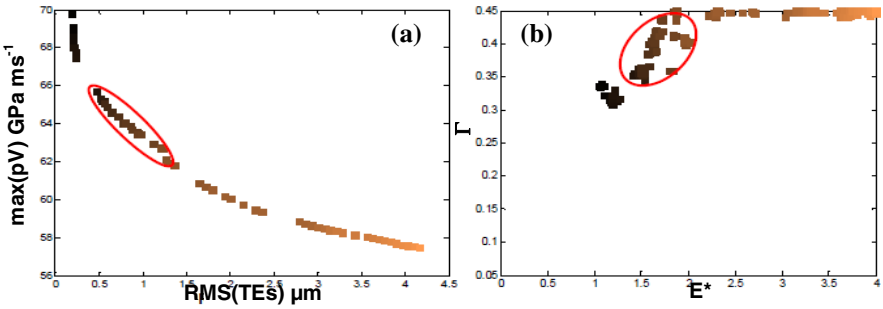

Fig. 5 NSGA-II results: RMS(TEs)_ max(pV)

It can be observed that significant depths of modification combined with long relief tend to reduce the max(pV) criterion. Concerning the modifications minimizing RMS(TEs), only a fraction of the previous characteristic optimum area in Fig. 4 ('master curve' according to the terminology in (Ghribi et al. 2012) has been found which is defined by the cluster of darker points. This reduction is mainly due to the evolution of the objective function (max (pV)) versus the parameters of profile modification: all the points in the vicinity of the master curve optimize RMS(TEs) but, among them, only those with a greater extent (Γ) minimize max(pV).

- **Problem 3**

Conventional optimization procedures minimize objective functions by considering the nominal values of the design parameters only whereas their inevitable and partly uncontrollable variability is neglected. This third problem is aimed at introducing such variations at the early design stage in order to propose robust profile modifications. Robust design can be defined as seeking design variables that make the system able to maintain its level of performance despite the variability of its parameters and its environment. For a performance (Y), this approach involves two statistical parameters namely: the mean (μ_Y) and standard deviation (σ_Y).

In this section, the simultaneous optimization of these two statistical parameters related to the performance (RMS (TEs)) is proposed. A Gaussian Quadrature (GQ) method is employed to estimate their values for a normal distribution associated with a quality grade of 7 (Ghribi et al. 2012). The Pareto solutions obtained are plotted in Figure 6.a and the corresponding combinations (E*, Γ) are given in Figure 6.b.

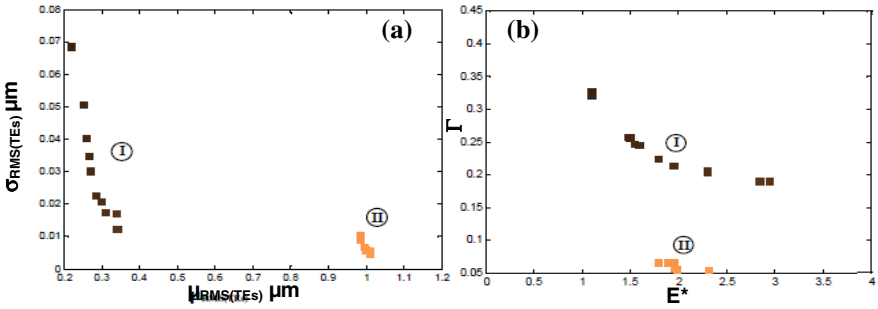

Fig. 6 NSGA-II results: $\mu_{RMS(TEs)}$_$\sigma_{RMS(TEs)}$ (in µm)

The results indicate that the Pareto front is composed of two main parts (sub-fronts):

a) Part I appears as the most interesting fraction of the front because the dispersion factor $\sigma_{RMS(TEs)}$ can be significantly decreased without increasing the mean value $\mu_{RMS(TEs)}$.
b) Part II allows obtaining significant reductions in standard deviation but the corresponding profile modifications downgrade the performance in terms of average value.

This finding is consistent with the results obtained by the authors (Velex et al. 2011) with a robustness function defined as a weighted sum. It can be noticed that, for all the simulations, the robust solutions are located very close to the master curve that defines the parameters of profile modifications minimizing RMS (TEs) (Velex et al. 2011) and (Ghribi et al. 2012).

3.3.2 Tri-objective Problem

Finally, the search for the Pareto area in the case of a three-objective optimization problem is presented. The objective functions are: RMS (TEs), max(pV) and the loss factor (Λp). For the sake of clarity, the representation of three-dimensional Pareto has been replaced by two planar projections of the cloud of points as found by the NSGA-II algorithm (see figure 7). These points correspond to non-dominated solutions for this problem.

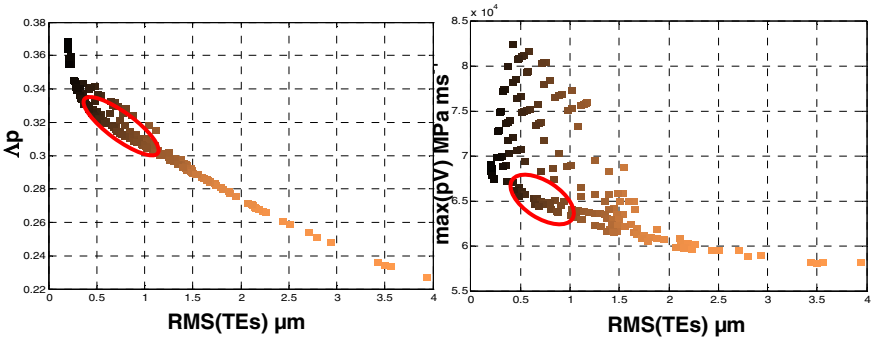

Fig. 7 Projections of NSGA-II results: RMS(TEs)_ Λp_max(pV)

An interesting optimization area corresponds to the profile modifications circled in red in Figure 7 which are characterized by tip relief amplitude such that (E*) lies between 1.4 and 2.1 and (Γ), the dimensionless length of modification, between 0.29 and 0.37.

4 Conclusion

The design of gear tooth modifications is an example of optimization problems relying on several criteria. To solve this problem, the NSGA-II algorithm (Non-Dominated Sorting Genetic Algorithm II) has been used as optimization method. It is a variant of genetic algorithms which is combined with the Pareto method (principle of dominance). This method is then applied to conduct multi-criterion optimization of tooth modification parameters. The results show the ability of this method to find Pareto fronts which, for designers, are useful guidelines for the selection of optimal combinations of modifications leading to the best trade-off.

References

Miettinen, K.: Nonlinear multiobjective optimization. Springer, Berlin (1999)

Artoni, A., Gabiccini, M., Guiggiani, M., Kahraman, A.: Multi-objective ease-off optimization of hypoid gears for their efficiency, noise and durability performances. ASME, J. Mech. Des. 133, 121007 (2011)

Deb, K., Pratap, A., Agarwal, S., Meyarivan, T.: A fast and elitist multiobjective genetic algorithm: NSGA-II. IEEE Transactions on Evolutionary Computation 6(2), 182–197 (2002)

Zitzler, E., Deb, K., Thiele, L.: Comparison of Multiobjective Evolutionary Algorithms: Empirical Results. Evolutionary Computation 8(2), 173–195 (2000)

Maatar, M., Velex, P.: Quasi-Static and Dynamic Analysis of Narrow-Faced Helical Gears With Profile and Lead Modifications. ASME, J. Mech. Des. 119(4), 474–480 (1997)

Velex, P., Bruyere, J., Houser, D.R.: Some Analytical Results on Transmission Errors in Narrow-Faced Spur and HelicalGears: Influence of Profile Modifications. J. Mech. Des. 133(3), 031010-1–031010-11 (2011)

Velex, P., Ville, F.: An analytical approach to tooth friction losses in spur and helical gears – Influence of profile modifications. ASME, J. Mech. Des. 131(10), 10 pages (2009)

Osman, T., Velex, P.: Static and dynamic simulations of mild abrasive wear in wide-faced spur and helical gears. Mechanism and Machine Theory 45, 911–924 (2010)

Ghribi, D., Bruyère, J., Velex, P., Octrue, M., Haddar, M.: A Contribution to the Design of Robust Profile Modifications in Spur and Helical Gears by Combining Analytical Results and Numerical Simulations. ASME, J. Mech. Des. 134, 061011-1–031010-9 (2012)

Dhafer, G., Jérôme, B., Philippe, V., Michel, O., Haddar, M.: Robust Optimization of Gear Tooth Modifications Using a Genetic Algorithm. In: Fakhfakh, T., Bartelmus, W., Chaari, F., Zimroz, R., Haddar, M. (eds.) CMMNO 2012, Part V, vol. 110, pp. 589–597. Springer, Heidelberg (2012)

An Experimental Investigation of the Dynamic Behavior of Planetary Gear Set

Maha Karray[1], Fakher Chaari[1], Alfonso Fernandez Del Rincon[2], Fernando Viadero[2], and Mohamed Haddar[1]

[1] Dynamics of Mechanical Systems Research Unit,
National School of Engineers of sfax, BP1173 – 3038 – Sfax – Tunisia
maha-karray@hotmail.fr,
fakher.chaari@gmail.com,
mohamed.haddar@enis.rnu.tn
[2] Department of Structural and Mechanical Engineering,
University of Cantabria, Spain
{viaderof,fernandra}@unican.es

Abstract. In this paper an experimental planetary gear set rig is developed for dynamic analysis purposes. This bench is composed by two identical planetary gears connected by a common shaft. Two tri axial accelerometers are mounted in both rings. Series of mmeasurements were achieved to study the influence of speeds as well as loads on the dynamic behaviour of the system. Time histories are characterized by a periodic fluctuation. Spectra showed sidebands around the mesh frequency and its harmonics. In order to identify the natural frequencies of the bench, series of run up are done. Influence of load on natural frequencies values is also investigated.

Keywords: planetary gears, dynamic behaviour, natural frequencies, load, sidebands, experimental studies.

1 Introduction

Planetary gear sets are used commonly in many industrial applications such as automobiles, helicopters, aircraft engines, heavy machinery and marine vehicles. Noise and vibration remain one of the main concerns in these applications. Mesh and bearing forces are the primary sources of such behavior. The study of planetary gear dynamics was performed over the last 30 years. Two approaches were adopted model based and experimental analysis. Analytical models should include multiple mesh contacts, detailed kinematics, mesh stiffness variation, transmission error excitation.. which explains the few works dedicated to analytical and experimental analysis of planetary gears.

Major analytical studies proposed lumped-parameter models to predict free and forced vibration characteristics of planetary gear sets where the gears are rigid bodies interconnected by springs representing teeth in mesh and support bearings.

M. Haddar et al. (Eds.): *Design and Modeling of Mechanical Systems*, LNME, pp. 199–206.
DOI: 10.1007/978-3-642-37143-1_25

It is possible to find models going from purely torsional to finite elements models (Kahraman 1994, Lin and Parker 1999-2002).

Experimental studies on planetary gear vibrations are scarce due to the complexity of the transmission with difficult access to the internal gears. (Hidaka and Terauchi 1976-1979) and (Hidaka et al 1979) studied the static and dynamic load sharing behavior of planetary gear set. (Kahraman 1999) developed a generalized model to predict load sharing of planets under quasi-static conditions and validated the model with experiments. (Ligata 2007) investigated with experimental and theoretical approaches the influence of several system level factors in gear stress. (Inalpolat and Kahraman 2009) presented a theoretical and experimental investigation on modulation sidebands phenomena observed in planetary gear sets. (Botman 1980) presented measurement results on the planetary gear of a PT6 aircraft engine which showed some peculiar behavior of planetary gear vibration concerning load sharing, response due to gear errors, and dynamic instability. Few experimental researches were dedicated to two stage planetary gear and this can be explained by the complexity of this transmission.

The study presented in this paper is expected to provide the understanding by experimental approach the behavior of a two stages planetary gear by achieving modal analysis and measuring dynamic response.

2 Description of the Bench

The bench is based on the ‘‘back-to-back’’ concept power circulation. It was developed at the University of Cantabria in Spain. It consists of two identical planetary gear sets (a test gear set and a reaction gear set) as shown in Figure 1. In this arrangement, the sun gears of both planetary gear sets are connected to each other through a common shaft. Likewise, the carrier of the test gear set is connected to the carrier of the reaction gear set via a rigid hollow shaft. The ring of the test gear set is held stationary while an external torque is applied mechanically to the ring of the reaction gear set giving rise to a closed power loop. A motor is connected to the shaft of the sun gear driving both gear sets while the gearmeshes carry the load imposed by the torque trapped in the closed loop through the external torque applied to the reaction ring gear.

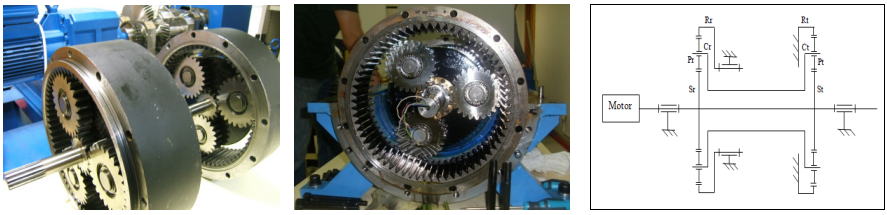

Fig. 1 Back to back planetary gear set rig

3 Instrumentation, Data Analysis

In each ring, two tri axial accelerometers (type ISOTRON) are mounted. The rotational speed of the carrier is measured with an encoder.

Vibration signals are recorded in LMS SCADAS and the data is processed with LMS Test.Lab software to obtain the acceleration spectra. Time histories were collected and averaged. An autopower is then used to obtain frequency spectra corresponding to each averaged time history.

4 Experimental Results

The characteristics of the gear system are giving in table 1.

Table 1 Planetary gear characteristics

	Carrier	Ring	Sun	Planet
Number of teeth	-	65	16	24
Moment of inertia (kgm²)	0.0021	0.697	0.0003	0.002
Base diameter (mm)	57.55	249.38	61.38	92.08

In order to study the effect of the variation of the speed and the influence of load, several tests using different load at different speed of the carrier were carried out. Series of run up are done to identify and characterize natural frequencies of the bench.

4.1 Time Varying Acceleration

The system was runned with 2 input speeds 300rpm and at 480rpm. In the two cases the system was loaded and then unloaded.

Figure 2 shows the time evolution of the acceleration measured on the ring and the corresponding spectrum for an unloaded system and at 300rpm. At this speed the mesh frequency is 325Hz.

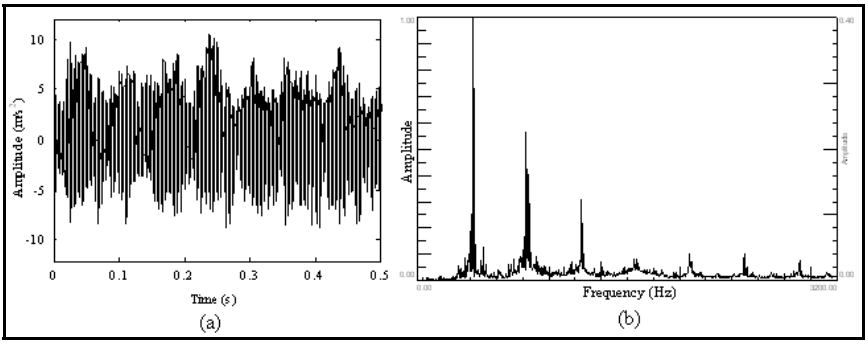

Fig. 2 (a) Evolution of the acceleration on the ring (b) the corresponding spectrum (unloaded system at 300rpm)

Another test was made for 300 rpm but with a loaded system by mass. The corresponding acceleration and the spectra are shown in figure 3.

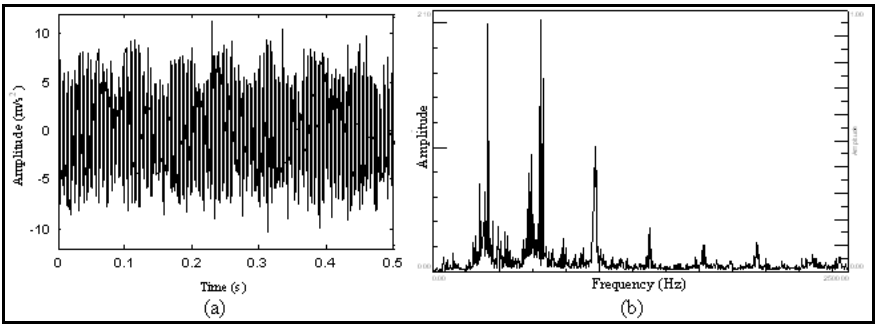

Fig. 3 (a) Evolution of the acceleration on the ring (b) the corresponding spectrum (loaded system at 300rpm)

For the second chosen speed 480rpm, figure 4 presents the time evolution of the acceleration and its spectrum for the unloaded case and figure 5 presents the same descriptors for the same speed but for a loaded case.

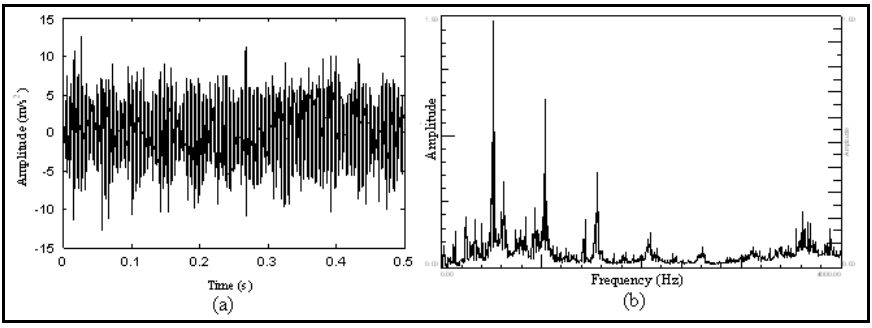

Fig. 4 (a) Evolution of the acceleration on the ring (b) the corresponding spectrum (unloaded system at 480rpm)

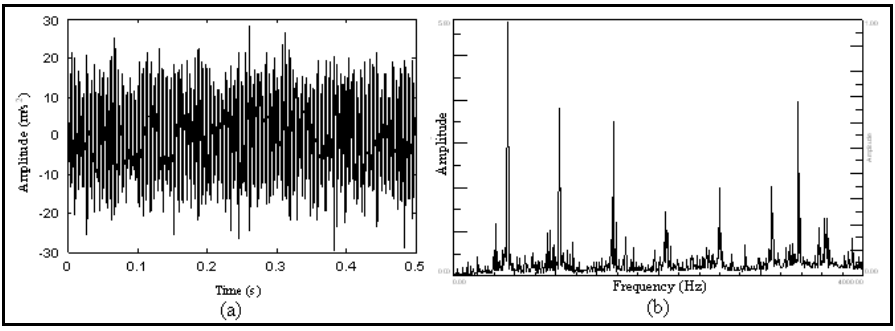

Fig. 5 (a) Evolution of the acceleration on the ring (b) the corresponding spectrum (loaded system at 480rpm)

As we increase the speed of the system the amplitude of the vibration increases for loaded and unloaded cases.

Time histories acceleration show periodic fluctuation in vibration levels.

The ring is fixed and the accelerometer indicates a periodic fluctuation in vibration amplitudes as planets pass close to this transducer. This fact leads to the apparition of an amplitude modulation of vibration in time histories which results in amplitude modulation with sidebands around mesh frequencies and harmonics. Other source of these sidebands can be manufacturing errors. Results were obtained for such transmissions by (Inalpolat and Kahraman 2009).

When the system is loaded the amplitude of the acceleration increase with more sidebands around the mesh components.

4.2 Run Up Tests

The objective of this experimental study is to characterize the natural frequencies of the bench. When the motor is initially started, a sudden torque is applied to the system which can excite torsional natural frequencies of the system.

Two methods were used to load the system:

-Hydraulic jack as a spring attached to the free ring (figure 6).

-Mass attached to the free ring by an arm (figure 7).

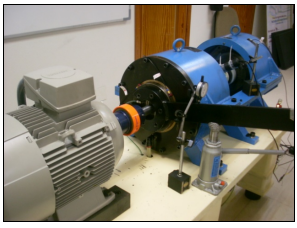

Fig. 6 System loaded by a jack

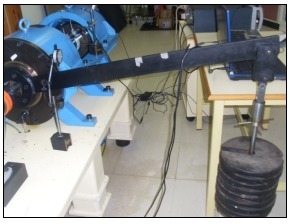

Fig. 7 System loaded by mass

A waterfall plot is created by stacking multiple frequency spectra at 10 rpm speed increments. Frequency in Hertz is shown on the horizontal axis and motor speed is shown on the vertical axis. Order lines or multiples of running speed appear as diagonal lines.

The simulated first natural frequency was found to be 27Hz.

We start by loading the system by mass in order to study the influence of adding more and more mass to the free ring on the value of the first natural frequency.

Figure 8(a) shows the waterfall spectra for a run up for with an unloaded system. The first natural frequency was identified during this test equal to 23.71Hz.

After adding 4 mass to the arm (half of total load) a second run up is done. For this case the first natural frequency change and it is founded near to 18.74Hz (figure 8(b)).

Now the system is completely loaded. Figure 8(c) shows the waterfall corresponding to this test. First natural frequency changes to 18.52Hz. The decrease of the natural frequency value is expected since the increase of mass will decrease the value of the first natural frequency.

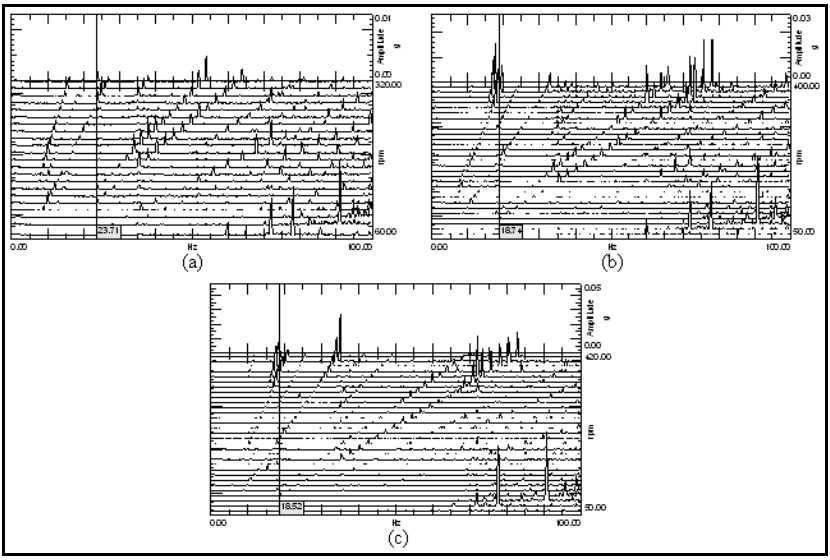

Fig. 8 Waterfall plot of the ring of a system loaded by mass during a run up

In order to load the system without introducing additional masses, a hydraulic jack is used. It will produce the same load effect as for the case of added masses.

In this case the jack will act as a spring with high rigidity.

For an unloaded system the first natural frequency is found to be near to 27.82Hz (figure 9(a)).

Than the system is loaded by a jack as we add 8 mass to the attached arm. It is noticed that the first natural frequency is unchangeable. It is within 3 percent of the calculated computed frequency.

The simulated second natural frequency is predicted to be 134Hz while the third is about 454Hz.

Figure 9(b) and (c) show that the second measured natural frequency is to be 137.6Hz and the third natural frequency is about 460Hz. So the second one is within 2.6 percent of the calculated frequency and the third one is within 1.3 percent. There is no effect when using the mass or the jack to load the system.

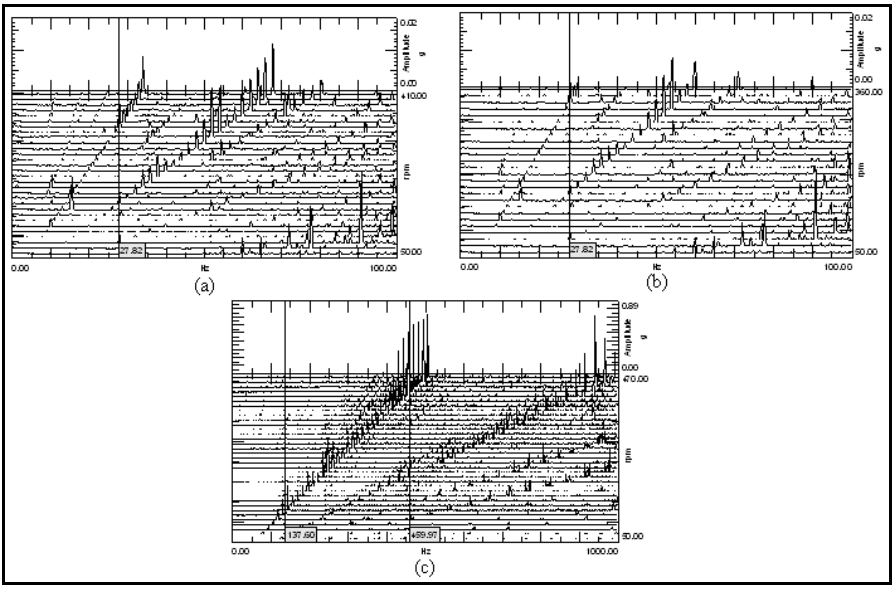

Fig. 9 Waterfall plot of the ring of a system loaded by jack during a run up

5 Conclusion

In this work an experimental study of "back to back" power circulation is developed. The bench is composed by two identical planetary gears, with three planets, connected together by a common shaft. Measurements are taken by accelerometer attached to the ring. Several tests are made to characterize the bench and study its dynamic behaviour. A series of tests in stationary conditions are done to show the influence of the speed and the load on the dynamic behaviour of the system. It is noticed apparition of sidebands in frequency domain. Resonance is studied by doing a run up in order to identify natural frequency.

Acknowledgements. This work is supported by the Tunisian-Spanish Joint Project no A1/037038/11.

References

Kahraman, A.: Natural modes of planetary gear trains. J. Soud. Vib. 173, 125–130 (1994a)

Kahraman, A.: Load sharing characteristics of planetary transmissions. Mech. Mach. The. 29, 1151–1165 (1994b)

Kahraman, A.: Planetary Gear Train Dynamics. ASME J. Mechl. Des. 116(3), 713–720 (1994c)

Lin, J., Parker, R.G.: Analytical characterization of the unique properties of planetary gear free vibration. Transaction of ASME. J. Vib. Acou. 121, 316–321 (1999)

Lin, J., Parker, R.G.: Planetary gear parametric instability caused by mesh stiffness variation. J. Soud. Vib. 249, 129–145 (2002)

Hidaka, T., Terauchi, Y.: Dynamic behavior of planetary gear-1st Report, Load distribution in planetary gear. Bulletin of the JSME 19, 678–690 (1976)

Hidaka, T., Terauchi, Y., Dohi, K.: On the relation between the run out errors and the motion of the center of sun gear in stoeckicht planetary gear. Bulletin of the JSME 22, 748–754 (1979)

Hidaka, T., Terauchi, Y.: Dynamic behavior of planetary gear-7th Report, Influence of the thickness of ring gear. Bulletin of the JSME 22, 1142–1149 (1979)

Kahraman, A.: Static Load Sharing Characteristics of Transmission Planetary Gear Sets: Model and Experiment. In: Transmission and Driveline Systems Symposium. SAE paper 01-1050 (1999)

Ligata, H.: Impact of system-level factors on planetary gear set behaviour. Dissertation, The Ohio State University (2007)

Inalpolat, M., Kahraman, A.: A theoretical and experimental investigation of modulation sidebands of planetary gear sets. J. Soud. Vib. 323, 677–696 (2009)

Botman, M.: Vibration Measurements on Planetary Gears of Aircraft Turbine Engines. AIAA Journal 17, 351–357 (1980)

Identification of the Unconstrained Modes of 3D Axisymmetric Structures from Measurements under Constraining Support Conditions

José Antunes, Vincent Debut, and Miguel Carvalho

Applied Dynamics Laboratory, Campus Tecnologico e Nuclear,
Instituto Superior Técnico/Universidade Técnica de Lisboa,
Estrada Nacional 10, 2695-066 Bobadela LRS, Portugal
vincentdebut@itn.pt

Abstract. An inverse method for extracting the unconstrained modal parameters of 3D axisymmetric structures from measurements performed under constrained configurations is proposed. The work was originally motivated by the need of knowing the tuning of large historical carillon bells which now lie on reinforcement fixtures, implying a quite different response of the bells from their original suspended state. In this paper, we extend to three-dimensional bodies the identification technique recently developed by the authors for a case of study consisting on a simple discrete mass-spring circular ring. Considering a modal model of a free cylinder as a first approximation of a bell, we present the identification strategy and then illustrate the efficiency of the technique by providing identification results for the original system modal frequencies from the constrained system. By operating directly on the constrained transfer functions measured at the constraint locations, the technique is not prone to modal identification nor to truncation errors, and therefore appears particularly convenient for modal testing on real structures.

Keywords: Structural modification techniques, inverse problems, modal identification, cylindrical shells.

1 Introduction

Structural modification is usually referred to as a technique to analyze the effects of additional local physical elements on the vibrational properties of a structure. For a practical configuration, the problem can be addressed by using a direct or an inverse formulation. The direct problem aims to predict the dynamical property changes once the physical parameters of the system have been modified, whereas the inverse problem aims to determine the necessary structural changes that would result in a desired dynamic behaviour. Although less frequent, the *reverse* problem can also be of interest: it consists of recovering the unconstrained modes of a structure from the dynamical information measured (or computed) under constrained configuration.

The motivation for this work stems from an interest in knowing the tuning of large historical carillon bells, which had to be provisionally supported using scaffolds, constraining the bell rim at several locations. In that form, the difficulties created

M. Haddar et al. (Eds.): *Design and Modeling of Mechanical Systems*, LNME, pp. 207–215.
DOI: 10.1007/978-3-642-37143-1_26

by the additional anchoring of the bells appeared as an opportunity to formulate the dynamical problem in terms of structural modification techniques which might enable us to produce (more or less crude) estimations of the original bell modes, before installation of the constraining supports.

Following such an objective, the present authors recently described a method for recovering the free modes of axisymmetric systems from frequency response data (FRFs) stemming from a constrained configuration [1]. Instead of solving an eigenvalue problem, the proposed approach, developed along the lines of Li and He [2], involves a set of linear equations with readily available solutions. The method, applied for a conceptual system of discrete mass-stiffness elements arranged in a ring shape, seems promising. One central feature is to impose some specific properties of axisymmetric bodies during the inversion, which also allows to identifiy simultaneously both mass and stiffness local constraints.

In this paper, we extend to three-dimensional structures the method of identification presented in [1] by considering a free cylinder as a first approximation for a carillon bell. We start by briefly presenting the relevant formulations of structural modifications and then describe the identification technique for recovering the unconstrained modes as well as the constraint parameters from constrained measurements. The inversion procedure for the case of three-dimensional axi-symmetric structure is then detailed and finally, numerical examples are provided to demonstrate the feasibility of the method developed for the given system.

2 Basic Modelling Approach for Structural Modifications

The dynamics of a (conservative) structure is generally modeled mathematically in terms of a mass matrix $[\mathbf{M}_u]$ and a stiffness matrix $[\mathbf{K}_u]$ which can be written as:

$$[\mathbf{M}_u]\{\ddot{Y}(t)\} + [\mathbf{K}_u]\{Y(t)\} = \{F(t)\} \tag{1}$$

If local structural modifications are applied by means of additional mass m_p and stiffness k_p at locations $p = 1, \ldots, P$, then the dynamical equations of the constrained system can be written as:

$$[\mathbf{M}_c]\{\ddot{Y}(t)\} + [\mathbf{K}_c]\{Y(t)\} = \{F(t)\} \tag{2}$$

where matrices $[\mathbf{M}_c] = [\mathbf{M}_u] + [\mathcal{M}_c]$ and $[\mathbf{K}_c] = [\mathbf{K}_c] + [\mathcal{K}_c]$ now contain the effects of the modifications m_p and k_p, which can be assumed diagonal for simplicity. To analyse the effects of the modifications on a structure, several techniques have been proposed, involving either modal parameter or frequency response data. However, the use of FRFs is particularly attractive for real structures since only the FRFs at the constrained locations are needed in practice [2]. By definition, the transfer function is related to the mass and stiffness matrices by a simple inversion, given by:

$$\begin{aligned} &\textit{Free configuration} && [\mathbf{H}_u(\omega)] = \left[-\omega^2[\mathbf{M}_u] + [\mathbf{K}_u]\right]^{-1} \\ &\textit{Constrained configuration} && [\mathbf{H}_c(\omega)] = \left[-\omega^2[\mathbf{M}_c] + [\mathbf{K}_c]\right]^{-1} \end{aligned} \tag{3}$$

Other advantage of the FRFs technique lies in the fact that it is neither prone to modal truncation or modal identifications errors, offering robustness to the identification results. Of pratical interest is that one can derive the constrained transfer functions directly from the unconstrained ones through the relation [3]:

$$[\mathbf{H}_c(\omega)] = \Big[\, [I] + [\mathbf{H}_u(\omega)](-\omega^2[\mathcal{M}_c] + [\mathcal{K}_c]\,)\Big]^{-1}\,[\mathbf{H}_u(\omega)] \tag{4}$$

or, conversely:

$$[\mathbf{H}_u(\omega)] = \Big[\, [I] + [\mathbf{H}_c(\omega)](\omega^2[\mathcal{M}_c] - [\mathcal{K}_c]\,)\Big]^{-1}\,[\mathbf{H}_c(\omega)] \tag{5}$$

Once known the modification matrices, this offers to deduce the transfer functions of the free system from computed or measured FRFs.

3 Inverse Identification Procedure

When we now turn to consider the given problem, it seems attractive to reformulate the dynamics of the original system in terms of the constrained configuration:

$$(\,[\mathbf{M}_c] - [\mathcal{M}_c]\,)\{\ddot{Y}_u(t)\} + (\,[\mathbf{K}_c] - [\mathcal{K}_c]\,)\{Y_u(t)\} = \{F(t)\} \tag{6}$$

Assuming an external harmonic excitation, the free system executes an harmonic oscillation at a given frequency, satisfying the following equation:

$$\Big(-\omega^2[\mathbf{M}_c] + [\mathbf{K}_c]\Big)\{Y_u(\omega)\} - \Big(-\omega^2[\mathcal{M}_c] + [\mathcal{K}_c]\Big)\{Y_u(\omega)\} = \{F(\omega)\} \tag{7}$$

which can be recasted into the form, by using Eq.(3):

$$\Big([I] - [\mathbf{H}_c(\omega)][-\omega^2[\mathcal{M}_c] + [\mathcal{K}_c]\,]\Big)\{Y_u(\omega)\} = [\mathbf{H}_c(\omega)]\{F(\omega)\} \tag{8}$$

An interesting feature in Eq.(8) is that, under no external excitation, it represents an eigenvalue problem

$$\{Y_u(\omega)\} = \Big[\, [\mathbf{H}_c(\omega)]\Big(-\omega^2[\mathcal{M}_c] + [\mathcal{K}_c]\Big)\Big]\{Y_u(\omega)\} \tag{9}$$

from which the modal frequencies ω_{un} and modeshapes $\{\phi_{un}\}$ of the free system can be computed. Based on this relation, the modal properties of the free system can be related with the data obtained from the constrained configuration since

$$\{\phi_{un}\} = \Big[\, [\mathbf{H}_c(\omega_{un})]\Big(-\omega_{un}^2[\mathcal{M}_c] + [\mathcal{K}_c]\Big)\Big]\{\phi_{un}\} \tag{10}$$

At this point, it should be recalled that structural modification is carried out locally so that only the FRFs information at the modifications points are needed. In practice, this approach, originally presented by Li and He [2], allows to determine either mass or stiffness modifications to score a desired modal behaviour. As noted in [2], the matrices $[\mathcal{M}_c]$ and $[\mathcal{K}_c]$ may commute with $\{\phi_{un}\}$ so that,

$$\{\phi^*_{un}\} = [\mathbf{H}^*_c(\omega_{un})][\phi^*_{un}]\left(-\omega^2_{un}\{\mathsf{m}_c\} + \{\mathsf{k}_c\}\right) \tag{11}$$

where $[\mathbf{H}^*_c(\omega_{un})]$ is a fully populated matrice, $[\phi^*_{un}]$ is a diagonal matrix built from the terms of $\{\phi^*_{un}\}$, $\{\mathsf{m}_c\}$ and $\{\mathsf{k}_c\}$ are vectors containing the terms of the diagonal constraints matrices $[\mathcal{M}_c]$ and $[\mathcal{K}_c]$, and * denotes quantities at the constraint coordinates. In the form of Eq.(11), given a target modal behaviour ω_{un} and $\{\phi_{un}\}$, the problem does not involve to solve the original eigenvalue problem (9) but only a set of linear equations. If only mass modifications are carried out, Eq.(11) gives:

$$\{\mathsf{m}_c\} = -\frac{1}{\omega^2_{un}}\left[[\mathbf{H}^*_c(\omega_{un})][\phi^*_{un}]\right]^{-1}\{\phi^*_{un}\} \tag{12}$$

Similarly, if only stiffness modifications are considered, then Eq.(11) leads to:

$$\{\mathsf{k}_c\} = \left[[\mathbf{H}^*_c(\omega_{un})][\phi^*_{un}]\right]^{-1}\{\phi^*_{un}\} \tag{13}$$

4 Application to Perfect 3D Axi-symmetric Structures

4.1 Dynamical Modelling of Cylindrical Shell

Shell vibration generally involves a combination of longitudinal and transverse motions. The normal modes $u(x, \theta, t)$ of the shell wall in the transverse direction can be described as the product of a beam function in the axial direction $U_m(x)$ (with appropriate boundary conditions), with a circumferential function $\varphi_n(\theta)$ in the horizontal plane, taking the form:

$$\overrightarrow{u}(x, \theta) = A_{mn}U_m(x)\overrightarrow{\varphi}_n(\theta) \tag{14}$$

where A_{mn} is an amplitude coefficient, and m and n relate to the number of nodal meridians extending over the top of the shell and the number of nodal circles respectively. To be more accurate, circumferential motions present both normal and tangential displacements since an excitation along one direction is able to excite motions in both directions, so that:

$$\overrightarrow{\varphi}_n(\theta) = \varphi^r_n(\theta)\overrightarrow{e}_r + \varphi^t_n(\theta)\overrightarrow{e}_t \quad \text{with} \quad \begin{vmatrix}\varphi^r_n(\theta) = \cos(n\theta)\\ \varphi^t_n(\theta) = -\sin(n\theta)/n\end{vmatrix} \tag{15}$$

One must also remind that perfectly axi-symmetrical structures exhibit normal modes occurring in degenerate pairs, which become non-degenerate when slight alteration of the symmetry is introduced. Of course, these two orthogonal modal families are an important aspect of the modelling for the correct dynamical description of axisymmetric bodies. Assuming of maximum of M nodal lines in the axial direction and N nodal lines in the circumferential plane, the size of the modal basis is therefore $M \times 2N$.

In what follows, the original structure considered is a free cylinder, open on the lower end and fitted with a clamped cover on the upper end, for which a modal model is considered. The original structure is then constrained at several locations

of the open end, using point masses and stiffnesses. For both constrained and unconstrained configurations, the useful transfer functions $[\mathbf{H}(\omega)]$ are computed from:

$$[\mathbf{H}(\omega)] = [\mathbb{U}] \left[-\omega^2[\mathbb{M}] + [\mathbb{K}]\right]^{-1} [\mathbb{U}]^T \tag{16}$$

where $[\mathbb{M}]$ and $[\mathbb{K}]$ are diagonal matrices of the modal parameters and $[\mathbb{U}]$ is the modal matrix of the corresponding modeshapes. Approximations of the natural frequencies and modeshapes used in the simulations, solutions of the Donnel-Mushtari-Vlasov equations, are found in [4]. Examples of computed modeshapes of the free structure are presented in Figure 1 (see Section 5 for detail).

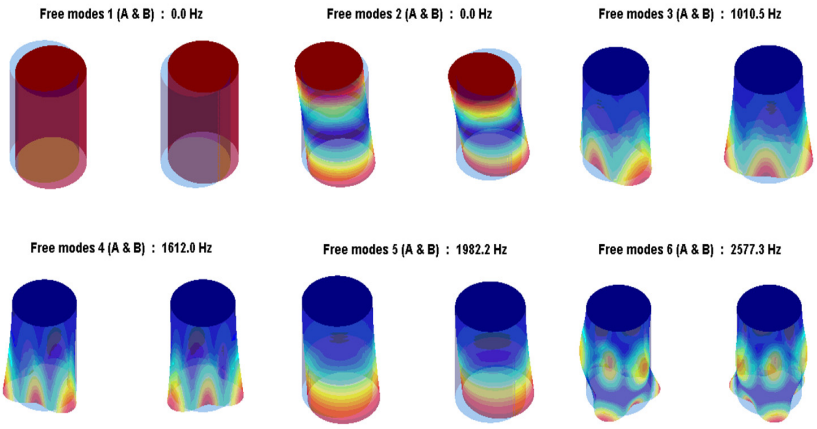

Fig. 1 Natural modes of the unconstrained system

4.2 Identification of the Unconstrained Modes and Constraints

Based on the ideas developed in section 3, Debut et al. [1] recently demonstrated the feasibility of such an approach for 2D axi-symmetric discrete structures. Interestingly, by enforcing essential properties of all perfect axisymmetric unconstrained bodies during the inversion, identification of the local constraints and modal properties of the free system, can be achieved. Indeed, implicit in the technique is the fact that all free axisymmetric structures display rigid-body modes, as well as modal doublets, with known similar mode shapes and near-identical frequencies.

For the given problem, it should be obvious by now that an important aspect of the modelling is to account for both radial and tangential motions of the structure and also to include the two orthogonal families of modes in the modal basis. In particular, this requires to account for a set of FRFs functions relating all constraint coordinates in accordance with each possible type of excitation and motion. It thus leads to consider *radial-to-radial*, *radial-to-tangential*, *tangential-to-radial* as well as *tangential-to-tangential* point-to-point transfer functions, each family of FRFs having the generic form:

$$H_{ij}^{pq}(\omega) = \sum_n \frac{\varphi_n^p(\theta_i)\varphi_n^q(\theta_j)}{m_n(\omega_n^2 - \omega^2)} \tag{17}$$

where H_{ij}^{pq} is the frequency response of the structure measured at point θ_j in the direction $\overrightarrow{e_q}$ considering an excitation at point θ_i in the direction $\overrightarrow{e_p}$, with p,q=r or t.

The identification scheme can now be further generalized by writing Eq.(9) in the expanded form:

$$\begin{Bmatrix} \{\phi_{un}^{r*}\} \\ \{\phi_{un}^{t*}\} \end{Bmatrix} = \begin{bmatrix} \mathbf{H}_c^{rr*}(\omega) & \mathbf{H}_c^{rt*}(\omega) \\ \mathbf{H}_c^{tr*}(\omega) & \mathbf{H}_c^{tt*}(\omega) \end{bmatrix} \begin{bmatrix} \boldsymbol{\Phi}_{un}^{r*} & 0 \\ 0 & \boldsymbol{\Phi}_{un}^{t*} \end{bmatrix} \left(-\omega^2 \begin{Bmatrix} \{\mathsf{m}_c^r\} \\ \{\mathsf{m}_c^t\} \end{Bmatrix} + \begin{Bmatrix} \{\mathsf{k}_c^r\} \\ \{\mathsf{k}_c^t\} \end{Bmatrix} \right) \tag{18}$$

where $\mathbf{H}_c^{pq*}$ is a submatrice of FRFs relating the responses of the constrained structure in the q-direction with the excitations in the p-direction, between all constraint coordinates, $\boldsymbol{\Phi}_{un}^{r*}$ and $\boldsymbol{\Phi}_{un}^{t*}$ are diagonal matrices built from the terms of $\{\phi_{un}^{r*}\}$ and $\{\phi_{un}^{t*}\}$ respectively, while $\{\mathsf{m}_c^r\}$, $\{\mathsf{m}_c^r\}$, $\{\mathsf{k}_c^r\}$ and $\{\mathsf{k}_c^t\}$ are the mass and stiffness modifications in the radial and tangential directions. The inversion now proceeds as follows:

1. In view of the fact that the free system displays at least one rigid-body mode (for n=1), an estimation of the stiffness modifications is given by applying Eq.(18):

$$\begin{Bmatrix} \{\mathsf{k}_c^r\} \\ \{\mathsf{k}_c^t\} \end{Bmatrix} = \left(\begin{bmatrix} \mathbf{H}_c^{rr*}(\omega) & \mathbf{H}_c^{rt*}(\omega) \\ \mathbf{H}_c^{tr*}(\omega) & \mathbf{H}_c^{tt*}(\omega) \end{bmatrix}_{\omega \to 0} \begin{bmatrix} \boldsymbol{\Phi}_{u1}^{r*} & 0 \\ 0 & \boldsymbol{\Phi}_{u1}^{t*} \end{bmatrix} \right)^{-1} \begin{Bmatrix} \{\phi_{u1}^{r*}\} \\ \{\phi_{u1}^{t*}\} \end{Bmatrix} \tag{19}$$

2. Then, to identify the mass modifications, one considers two similar orthogonal modeshapes of near-identical modal frequencies of the unconstrained system (e.g $\omega_{un} \approx \omega_{u(n+1)}$) and write Eq.(18) for each chosen mode. By applying a compatibility condition between these two estimations, one finally obtains:

$$\begin{aligned} &\left(\begin{bmatrix} \mathbf{H}_c^{rr*}(\omega_{u(n+1)}) & \mathbf{H}_c^{rt*}(\omega_{u(n+1)}) \\ \mathbf{H}_c^{tr*}(\omega_{u(n+1)}) & \mathbf{H}_c^{tt*}(\omega_{u(n+1)}) \end{bmatrix} \begin{bmatrix} \boldsymbol{\Phi}_{u(n+1)}^{r*} & 0 \\ 0 & \boldsymbol{\Phi}_{u(n+1)}^{t*} \end{bmatrix} \right)^{-1} \begin{Bmatrix} \{\phi_{u(n+1)}^{r*}\} \\ \{\phi_{u(n+1)}^{t*}\} \end{Bmatrix} - \\ &\left(\begin{bmatrix} \mathbf{H}_c^{rr*}(\omega_{un}) & \mathbf{H}_c^{rt*}(\omega_{un}) \\ \mathbf{H}_c^{tr*}(\omega_{un}) & \mathbf{H}_c^{tt*}(\omega_{un}) \end{bmatrix} \begin{bmatrix} \boldsymbol{\Phi}_{un}^{r*} & 0 \\ 0 & \boldsymbol{\Phi}_{un}^{t*} \end{bmatrix} \right)^{-1} \begin{Bmatrix} \{\phi_{un}^{r*}\} \\ \{\phi_{un}^{t*}\} \end{Bmatrix} = \{0\} \end{aligned} \tag{20}$$

which is a nonlinear problem but can be solved for ω_{un} through a systematic frequency sweep. Once determined the unconstrained modal frequency ω_{un}, the inertial modifications are estimated from Eq.(18) using the assumed given modeshapes. Notice that, for free axisymmetric structures, the modeshape functions at the interface where constraints will be applied can always be safely assumed following Eq.(15).

Actually, one useful aspect of the above-described procedure is the possibility to specify arbitrarily the unconstrained modeshape to consider for the determination of the inertial constraints. Actually, Eq.(20) is valid for any pair of modes and one can perform several estimations of the inertial modifications to ensure the reliability of the results. Furthermore, other advantage is that it does not imply any modal

parameter identification of the constrained system. Actually, some errors always occur from either a faulty modal data acquisition procedure or a bias in the numerical algorithm, which may consequently have perverse effects on the identification results. Also related to the modelling aspect, a third advantage is that the method is not prone to truncation error as common for modal-based approach identification technique [5].

5 Illustrative Computations and Conclusion

The system considered consists on a closed clamped-free circular shell with geometrical and physical data: mean radius 0.1m, height 0.25m, thickness 0.01m, module Young 10^{11} N.m^{-2}, density 8500 kg.m^{-3} and Poisson coefficient 0.3. The cylinder has been divided into 64 locations in the circumferential plane, and mass and stiffness constraints have been applied in both radial and tangential directions, at locations 1, 16, 32, and 48. For illustration, Figure 2 displays some of the first modes of the constrained system, which gives evidence of all the significant differences displayed by the computed modes (compare with Figure 1). In Figure 3 are shown the absolute values of radial-to-radial and tangential-to-tangential FRFs collected at node 1 by appling an excitation at the same node, for both the unconstrained and constrained configurations. Finally, Figure 4 displays the superposition of the computed and identified radial-to-radial and tangentiel-to-tangential transfer functions measured in the same conditions. Obviously, the results in Figure 4, based on simulated data, are over-impressive when compared with what can be reasonably expected from experimental data. Although such analysis may appear overambitious for real situations, the results presented in this paper are quite encouraging for using experimental data measured on a laboratory setup.

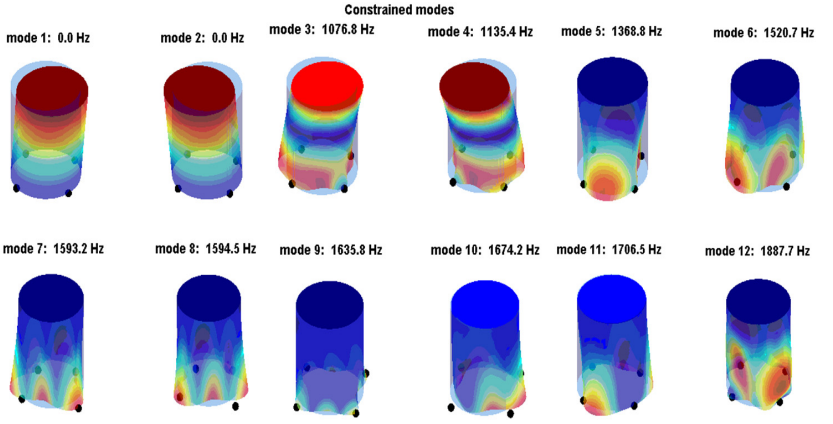

Fig. 2 Natural modes of the constrained system. Constraint locations appears as large black circles. $m_1^r = m_3^r$=10 Kg, $m_2^r = m_4^r$=10 Kg, $m_1^t = m_3^t$=5 Kg, $m_2^t = m_4^t$=2.5 Kg, $k_1^r = k_3^r$=10^9 N.m^{-1}, $k_2^r = k_4^r$=0.5×10^9 N.m^{-1} and $k_1^t = k_3^t$=0.5×10^9 N.m^{-1}, $k_2^t = k_4^t$=0.25×10^9 N.m^{-1}.

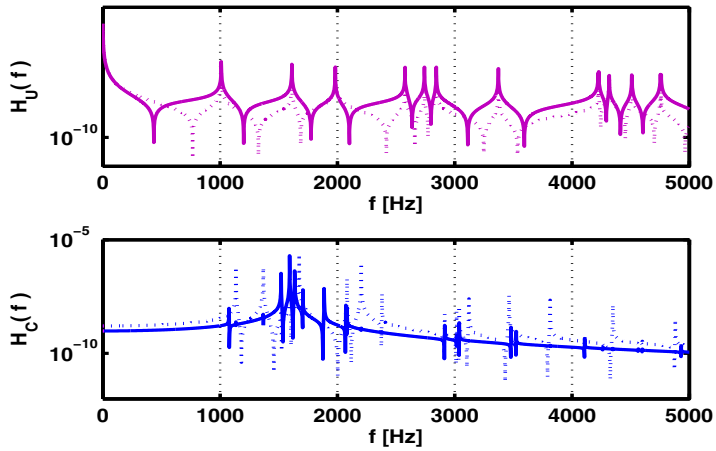

Fig. 3 Computed radial-to-radial (solid) and tangential-to-tangential (dot) transfer functions of the unconstrained (up) and constrained (down) systems. $x_i = 1$, $x_j = 1$. Note that a small amount of modal damping has been added artificially for display.

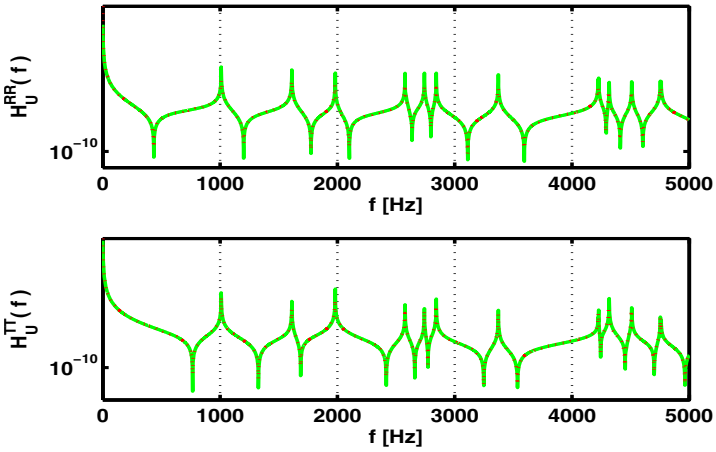

Fig. 4 Computed (green) and identified (red) radial-to-radial (up) and tangential-to-tangential (down) transfer functions of the unconstrained system. $x_i = 1$, $x_j = 1$

Acknowledgements. This work was supported by the Portuguese FCT, research project PTDC/EAT-MMU/104255/2008.

References

1. Debut, V., Carvalho, M., Antunes, J.: Recovering the unconstrained modes of axisymmetric structures from measurements under constrained condition. In: Proceeding of the 19th International Congress on Sound and Vibration, Vilnius, Lithuania (2012)
2. Li, T., He, J.: Local structural modification using mass and stiffness changes. Engineering Structures 21, 1028–1037 (1999)
3. Ozguven, H.N.: Structural modifications using frequency response functions. Mechanical Systems and Signal Processing 4, 53–63 (1990)
4. Soedel, W.: Shells. Encyclopedia of Vibrations. Elsevier (2001)
5. Avitabile, P.: Twenty years of structural dynamic modification: a review. Sound and Vibration 37, 14–25 (2003)

Dynamic Modeling of Rail Vehicle Traveling at High Speed

Nejlaoui Mohamed[1], Houidi Ajmi[2], Affi Zouhir[3], and Romdhane Lotfi[4]

[1] L M S, Ecole Nationale d'Ingénieurs de Monastir, Tunisia
nejlaouimohamed@gmail.com
[2] LMS, Institut Supérieur des Sciences Appliquées et de Technologie de Sousse, Tunisie
ajmi.houidi@issatso.rnu.tn
[3] LGM, Ecole Nationale d'Ingénieurs de Monastir, Tunisia
zouhaier.affi@enim.rnu.tn
[4] LMS, Ecole Nationale d'Ingénieurs de Sousse, Tunisie
lotfi.romdhane@enim.rnu.tn

Abstract. This work deals with dynamic modeling of rail vehicles traveling at high speed. We will develop a three-dimensional analytical dynamic model of a rail vehicle with 34 degree of freedom. This model considers the elasticity of the wheel-rail contact and the rail contact surface irregularity. The developed model is solved by using the Rung-Kutta method and validated by experimental results from the literature. The developed model can be used to quantify the comfort of the rail vehicle passengers.

Keywords: Dynamic modeling, rail vehicle, high speed, rail irregularities.

Nomenclature

i,j,k	Index of wheelset, wheel and bogie respectively	$\varphi_{ki}, \varphi_k, \overline{\varphi}$	Pitch motion of the wheelsets, the bogies and the carbody respectively
$X_{ki}, X_k, \overline{X}$	longitudinal displacement of the wheelsets, the bogies and the carbody respectively	e_0	Half of the track gauge
$Y_{ki}, Y_k, \overline{Y}$	Lateral displacement of the wheelsets, the bogies and the carbody respectively	Cij	Coefficients of Kalker
$Z_{ki}, Z_k, \overline{Z}$	Vertical displacement of the wheelsets, the bogies and the carbody respectively	F_{xij}	Longitudinal creep forces
$\alpha_{ki}, \alpha_k, \overline{\alpha}$	Yaw motion of the wheelsets, the bogies and the carbody respectively	F_{yij}	Lateral creep forces
$\theta_{ki}, \theta_k, \overline{\theta}$	Roll motion of the wheelsets, the bogies and the carbody respectively	M_{zij}	The creep moment acting in vertical direction

M. Haddar et al. (Eds.): *Design and Modeling of Mechanical Systems*, LNME, pp. 217–224.
DOI: 10.1007/978-3-642-37143-1_27

1 Introduction

Dynamic modeling of railway vehicles (RV) is a complex task. The complexity is caused by several factors such as the condition of the wheel-rail contact, the number of the vehicle solids and the degrees of freedom. Such model is needed for predicting safety and comfort of the RV passengers. At high speeds, the rails irregularities can cause not only mechanical anomalies that affect the safety but also the comfort of passengers.

In this context, several studies have investigated the behavior of RV through the analysis of wheel-rail interaction with presence of irregularities. Bowe et al (2005) presented a mathematical model for predicting the vibrations of a rail excited by a moving wheel. They model the irregularity of the wheel and the rail by a linear spring.

Other work considers the RV as mass, spring and damper system. Mastinu et al (2001) and J. Real et al (2004) considered the RV as 2 degrees of freedom (DOF). But the 2 DOF model, cannot be used to represent exactly the real system (Di Mino 2007).

Di Mino (2007) developed a two-dimensional model of a vehicle with 10 DOF to study the vehicle-rail interaction. The author considered the vertical displacement of the different vehicle components and pitching motion of the carbody and bogies. This model focused only on the vertical dynamic motion.

Until now there are a limited number of three-dimensional models of rail vehicle developed in bibliographic (Xia et al. 2005; Majka et al. 2008). In the Xia et al. 2005 and Majka et al. 2008 models, the wheel is supposed always in direct contact with the rail and without elastic deformations. However, in presence of rail irregularities, the wheel-rail contact area is deformable (Bowe et al. 2005).

In this work, we develop a three-dimensional analytical model of RV with 34 DOF. This model is useful for the analysis of the dynamic behavior of vehicle-track interaction at high speed. In this model the wheel rail contact area is considered deformable and the rail surface present irregularities. Thus, in Section 2 we present the vehicle model and the dynamic modeling of RV system. The resolution and validation of the developed model will be presented in Section 3. Section 4 presents conclusions and possible perspectives.

2 The Rail Vehicle System Model

2.1 The Vehicle Model

The railway vehicle is composed of a body, two bogies and four axles as shown in Figure 1. The wheelsets are connected to the bogies through primary suspensions. The bogies are connected to the carbody through secondary suspensions. Each suspension is made by a spring and a damper, connected in parallel, working in three directions (Nejlaoui et al. 2009; Nejlaoui et al.2013).

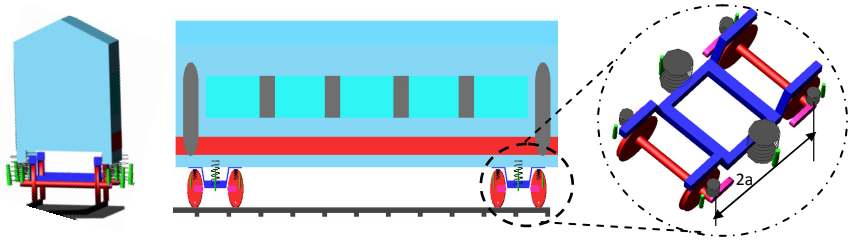

Fig. 1 Model of the RV system

Each component of the RV system is defined by six DOF (fig. 2). At constant speed, we have neglected the wheelsets pitching motion. On the other hand, it has been shown that the lateral displacement depends on the rolling motion of a wheelsets (cheng et al, 2009).

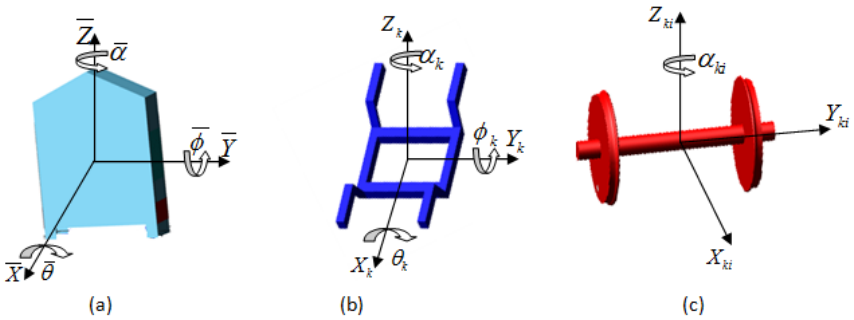

Fig. 2 DOF of vehicle components (a) Carbody (b) bogie (c) wheelset

The generalized coordinate vector **q** of the vehicle at 34 DOF is given by:

$$\mathbf{q} = \left[\overline{X}, \overline{Y}, \overline{Z}, \overline{\alpha}, \overline{\theta}, \overline{\phi}, X_k, Y_k, Z_k, \alpha_k, \theta_k, \varphi_k X_{ki}, Y_{ki}, Z_{ki}, \alpha_{ki} \right]^T \ (k, i = 1, 2) \tag{1}$$

2.2 The Wheel-Rail Contact Model

To model the elastic deformation in the wheel-rail contact area, we adopt the model of Hertz. This model contains a spring with a vertical rigidity K_H (Fig. 3). On the other hand, the contact forces depend on the longitudinal, the lateral creep forces and the creep moment. These forces of wheel-rail contact are modeled by using the linear theory of Kalker given by (Sezer et al. 2011):

$$F_{xij} = -C_{33}\left(e_0 \frac{\dot{\alpha}_{ij}}{V} \right) \tag{2}$$

$$F_{yij} = \left[C_{11} \left(\frac{\dot{Y}_{ij}}{V} - \alpha_{ij} \right) + C_{12} \left(\frac{\dot{\alpha}_{ij}}{V} \right) \right] \tag{3}$$

$$M_{zij} = \left[C_{12} \left(-\frac{\dot{Y}_{ij}}{V} + \alpha_{ij} \right) + C_{22} \left(\frac{\dot{\alpha}_{ij}}{V} \right) \right] \tag{4}$$

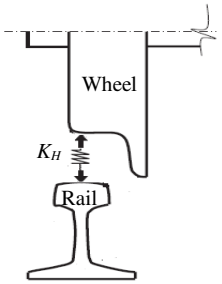

Fig. 3 The model of Hertz

In this work, we suppose that the rail present irregularities on the upper surfaces.

2.3 Dynamic Modeling of the RV System

The dynamic model of the RV system is obtained based on the Lagrange formalism given by:

$$\frac{d}{dt}\left(\frac{\partial T}{\partial \dot{q}_i}\right) - \frac{\partial T}{\partial q_i} + \frac{\partial D}{\partial \dot{q}_i} + \frac{\partial V}{\partial q_i} = Q_i \tag{5}$$

Where :

T : the kinetic energy of the RV system
V : the kinetic energy of the RV system
D : the kinetic function of the RV system
Q_i : the generalized forces associated to generalized coordinate q_i

The equations of motion of the railway vehicle system, derived by using the Lagrange formalism, are developed and expressed in linear form given simply by:

$$[\mathbf{M}]\ddot{\mathbf{q}} + [\mathbf{C}]\dot{\mathbf{q}} + [\mathbf{K}]\mathbf{q} = \mathbf{F} \tag{6}$$

$[\mathbf{M}],[\mathbf{C}],[\mathbf{K}]$ et $\mathbf{F}$ are respectively the mass, dissipation, rigidities matrix and the vector forces external to the system.

3 Resolution and Validation of the Developed Model

3.1 Resolution Method of the Developed Model

To solve the obtained dynamic model, we have used Rung-Kutta method. This method is applicable for solving differential equations of first order. To achieve this goal, we have used the change of variables in the differential equations of the dynamic model in order to replace the second order differential equation to the first order one as follow:

$$\ddot{X} = f(t,x,y) \Rightarrow \begin{cases} Y = \dot{X} = f(t,x,y) \\ et \\ \dot{Y} = \ddot{X} = f(t,x,y) \end{cases} \tag{7}$$

Hence at each time $t \in [a,b]$, the different values of displacement, speed and acceleration of the RV system can be determined. The advantage of this method is that does not use the calculation of the derivatives compared to other numerical methods (Nocedal et al.1999) which avoid the premature convergence.

3.2 Validation of the Developed Model

The rail surface irregularity distribution is given experimentally by Xia et al (2005) (fig. 4). This irregularity is the input that excites the RV system.

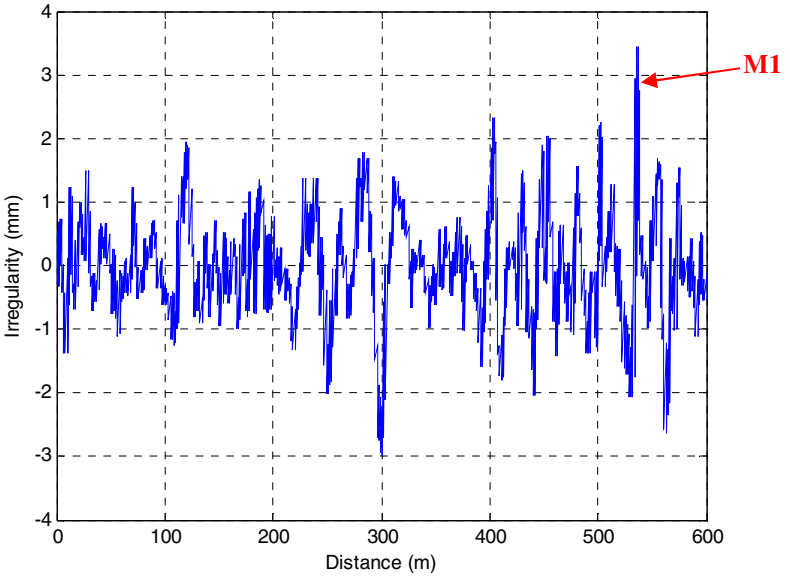

Fig. 4 Experimental rail surface irregularity

The system responses to this input irregularity are given by the carbody vertical acceleration. Figure 5 and figure 6 represent respectively the evolution of carbody vertical acceleration at the speed 180Km/h and at 240km/h.

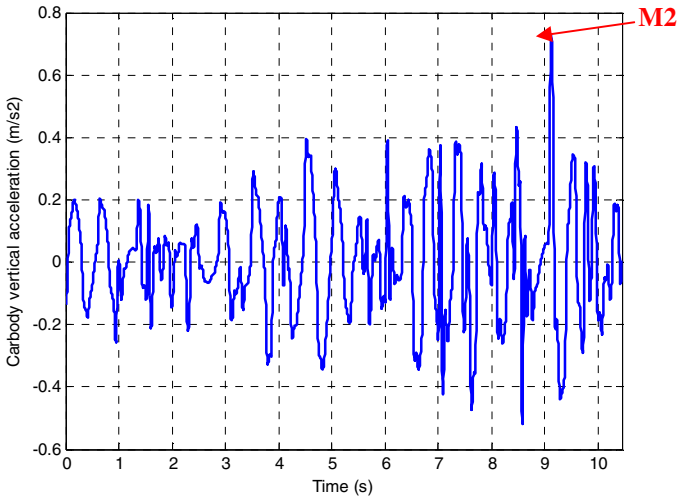

Fig. 5 Carbody vertical acceleration at 180 Km/h

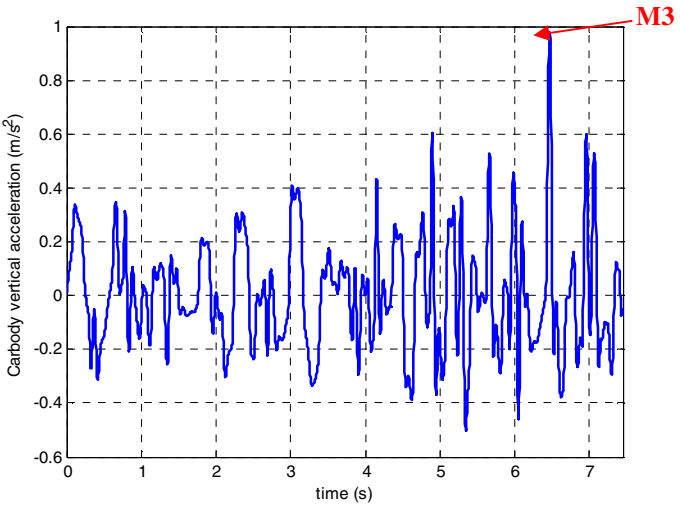

Fig. 6 Carbody vertical acceleration at 240 Km/h

At each speed, we can note that the maximum of carbody acceleration (point M2 and M3 in fig. 5 and 6). The maximum of acceleration corresponds to an upper limit of irregularity (point M1 in fig. 4)

The validation of the developed model is performed by comparing the simulation results to the one given experimentally by Xia et al (2005). Therefore, we show in fig. 7 the evolution of carbody acceleration as a function of the RV speed in the range of 180Km/h to 330Km/h. Fig. 7 gives both the results given by our model and the experimental one given by Xia, 2005.

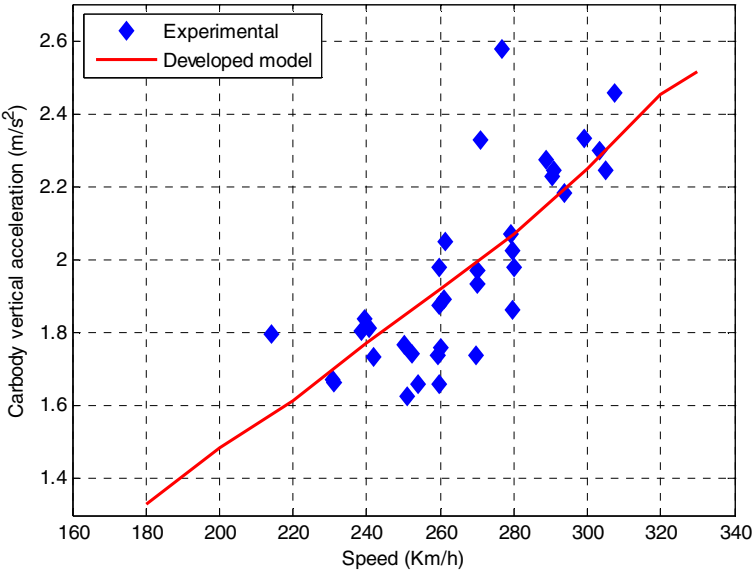

Fig. 7 Carbody vertical acceleration vs RV speed

One can note that the carbody vertical acceleration increases with speed. In fact the increase of speed increases the degree of instability of the RV system. It can be noticed from fig. 7 that the results developed by our model are in concordance with experimental results both in amplitudes and in distribution tendencies.

4 Conclusion

This work deals with the dynamic modeling of rail vehicles traveling at a high speed. We have developed a three-dimensional analytical dynamic model of a rail vehicle with 34 degrees of freedom. This model considers the elasticity of the wheel-rail contact and the rail contact surface irregularity. The developed model is solved by using the Rung-Kutta method and validated with experimental results from the literature. This model can be used to quantify the rail vehicles passenger comfort.

References

Bowe, C.J., Mullarkey, T.P.: Wheel-rail contact elements incorporating irregularities. Advances in Engineering Software 36, 827–837 (2005)

Cheng, Y.-C., Lee, S.-Y., Chen, H.-H.: Modeling and nonlinear hunting stability analysis of high-speed railway vehicle moving on curved tracks. Journal of Sound and Vibration 324, 139–160 (2009)

Di Mino, G.: A model of dynamic interaction between a train vehicle and a rail track. In: 4th International Congress PALERMO, Italy, September 12-14 (2007)

Real, J., Salvador, P., Montalbán, L., Bueno, M.: Determination of rail vertical profile through inertial methods. Proceedings of the Institution of Mechanical Engineers, Part F: Journal of Rail and Rapid Transit 225, 14 (2004)

Majka, M., Hartnett, M.: Effects of speed, load and damping on the dynamic response of railway bridges and vehicles. Computers and Structures 86, 556–572 (2008)

Mastinu, G.R.M., Gobbi, M., Pace, G.D.: Analytical formulae for the design of a railway vehicle suspension system, proceedings of the Institution of Mechanical Engineers. Part C: Journal of Mechanical Engineering Science 215, 683 (2001)

Nejlaoui, M., Affi, Z., Houidi, A., Romdhane, L.: Analytical modeling of rail vehicle safety and comfort in short radius curved tracks. C. R. Mecanique 337, 303–311 (2009)

Nejlaoui, M., Houid, A., Affi, Z., Romdhane, L.: Multiobjective robust design optimization of rail vehicle moving in short radius curved tracks based on the safety and comfort criteria. Simulation Modelling Practice and Theory 30, 21–34 (2013)

Nocedal, J., Wright, S.J.: Numerical Optimization. Springer, New York (1999)

Sezer, S., Atalay, A.E.: Dynamic modeling and fuzzy logic control of vibrations of a railway vehicle for different track irregularities. Simulation Modelling Practice and Theory 19, 1873–1894 (2011)

He, X., Zhang, N.: Dynamic analysis of railway bridge under high-speed trains. Computers and Structures 83, 1891–1901 (2005)

Early Detection of Mechanical Defects by Neural Networks "Spectral Analysis"

Bouzouane Bélaid[1] and Hamzaoui Nacer[2]

[1] Laboratoire de Mécanique Avancée (LMA),
Université des Sciences et de la Technologie
Houari Boumédiène, BP 32, El Alia,
16111 Bab Ezzouar, Alger Algérie
bbouzouane@yahoo.fr
[2] Laboratoire de Vibrations Acoustique (LVA),
INSA de Lyon, Bât. Antoine de Saint Exupéry,
25 bis, Avenue Jean Capelle, 69621 Villeurbanne Cedex, France
nacer.hamzaoui@insa-lyon.fr

Abstract. Various methods are implemented to identify the nature of a defect on a rotating machine, by using vibratory measures; they differ in their precision, simplicity of implementation and their sensitivity to errors measurement. The identification of several defects combination is still difficult to implement by conventional signal processing, as the vibration signal that emerges is disturbed, thus making any identification so hard.

Spectrum is sometimes difficult to interpret, especially in the case of combined defects. is proposed in this paper to use neural networks to ascend to defects sought. the basis of learning outcomes will consist of spectra measured signals.

In this study, we proposed a method based on the neural networks to identify one defect or several combinations of mechanical defects. Thus we propose the neuronal method: the Radial Basis Function (RBF). We highlight their capacity to detect the defect and their sensibility with regard to a signal noise characterizing the other independent sources to the defects. This evaluation will be done with measurement will be carried out on a housing bearing and test bench made up of a toothed gearing on two floors, and without lubrication. Some provoked defects will be analyzed in this study.

Keywords: Neural Network, Radial Basis Function, Back Propagation, Diagnosis Bearings defaults, Diagnosis gears defaults, Signal processing.

1 Introduction

Awareness in industry of the importance of conditional maintenance dawned early, and account was taken of the significant role played by vibration when diagnosing defects in rotating machines. Indeed, changes in the vibratory signature of rotating machines are often the first physical manifestation of an anomaly, potential causes of damage and or faults.

M. Haddar et al. (Eds.): *Design and Modeling of Mechanical Systems*, LNME, pp. 225–234.
DOI: 10.1007/978-3-642-37143-1_28

Moreover, the global parameters resulting from this signature are good indicators for monitoring the condition of rotating machine and mention can be made of a global vibratory velocities ranging from 10 to 1000 Hz, the crest factor and kurtosis.

However, diagnoses also call on other investigation techniques, such as spectral analysis [1], though this is often insufficient in particular when the signal results from a defect generated by defective bearings and gears. Cepstral analysis, Envelope analysis, Short-Time Fourier Transform [2] and [3] and wavelet transforms [4] and [5] can be used to solve such problems. Nevertheless, few systems make use of these techniques and monitoring remains the responsibility of a specialist. Furthermore, detecting defects is more painstaking as a signal generated by a bearing may be masked by noise or other defects.

The more complex mechanical systems and rotating machines, in particular become, the more difficult it is to maintain them. Also, as machines are becoming increasingly automated, a new type of maintenance is being implemented, based on condition monitoring maintenance using neural networks. Mention can be made of the Wenlung Li's [6] experimental study of an expert system that uses a neural network based on acoustical signals to diagnose unbalance on a rotating machine. It relies on a Back propagation Neural network (BPN) with one hidden layer.

The article by Lay Wuxing [7] is interesting when approaching this type of problem. Indeed, each tooth in a gear is engaged in alternation thus the load conditions are also alternated. Moreover, Gaussian type noise is generated leading to measurements that make detecting gear defects very difficult.

The works of Samanta and ... [8] have shown the effectiveness of neural networks for diagnosis of bearing defects. The network used, is with two hidden layers with a binary output characterizing the state of the machine: normal or default bearing. The vibration signals are not used directly at the entrance of the network but are subject a prior treatment. Three methods were used: detecting the envelope (demodulation), filtering and the wavelet transform.

Neural networks are widely used in fault detection of rotating machinery, the article by Czeslaw and ... [9] deals with problems of diagnosis in an induction motor in the case of the rotor, stator and bearing defects. Two types of networks have been used: multilayer perceptron and the Kohonen map organizer [10]. The method gave satisfactory results; however, the efficiency is better for the detection of faults on the stator and rotor than the bearing.

This paper proposes an approach for classifying gear defects in order to achieve good identification, by using two step-treatments: the "cumulative" method and "Radial Basis Networks". The first is used to minimize Gaussian noise and the second is a network that allows rapid convergence of the network. The Radial Basis Network is then used as a classifier for the different states of the gearing cycle, i.e. different normal or defective conditions. The results showed that this method of classification based on the combination of "cumulative" and Radial Basis Networks is very promising and provides better precision.

Here, we use Radial Basis Networks in order to identify gear and bearing defects simultaneously. The purpose of this work is to provide additional analysis for

defect identification by using the neuronal approach. A demonstration is presented of the capacity of this technique to identify the defect to be diagnosed.

A study was conducted by using neural networks as a basis for learning the signals measured after injection of defects of bearings and gears [11]. The results were very satisfactory as to the ability of the method to trace the fault.

2 Theorical Study

2.1 Neural Networks

An elementary neuron is a programmable controller composed of several inputs X_i, one output (see Fig. 1), and a transfer function between the neuron's inputs and its output.

f is the activation function, the parameters wi and b are respectively the weight and the bias that are the unknowns of the problem, allowing the network to adapt to the desired output.

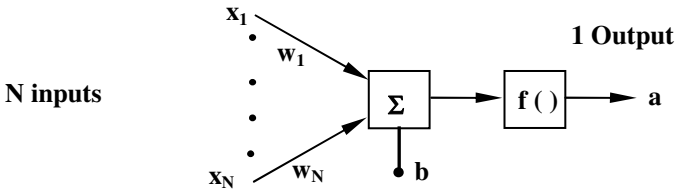

Fig. 1 Formal neuron

Output ***a*** is given by the expression:

$$a = f\left(\sum_{1}^{N} a_i + b\right) \tag{1}$$

The generalization of the neuron to a larger system in order to solve more complex problems leads to forming neural networks. This requires the introduction of multiple outputs and at least one intermediate layer called hidden layer with several neurons (see Fig. 2).

Each neuron is adjustable, by changing the weights ***wi*** and bias ***bi*** to adapt the network from the input vector X to the output vector A.

$$X = (x_1, \ldots\ldots, x_N) \text{ and } A = (a_1, \ldots\ldots, a_m).$$

To achieve this, we use a learning base containing a set of vectors ***Xj*** and ***Ann***, ***nn*** being the number of training sets. For each set the training consists in evaluating parameters w_i and b_i in order to minimize the total error between the desired output and the output calculated by the network.

The final stage of the network is its application. The network is presented with a non trained set ***X*** and by interpolation: if ***X*** resembles ***Xj***, it will have the label ***Aj***.

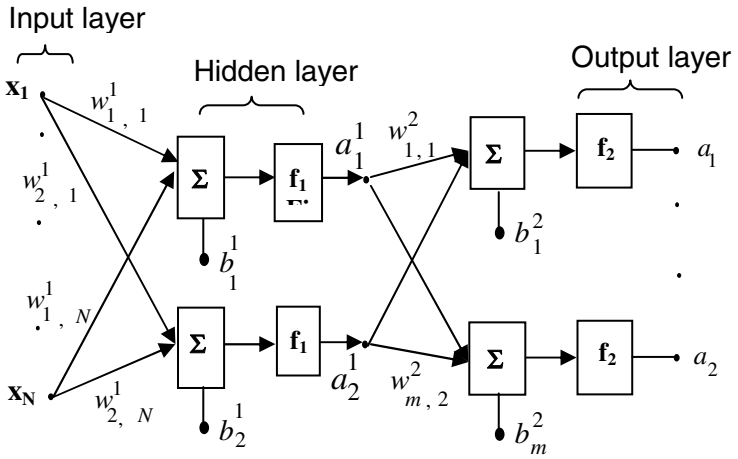

Fig. 2 Neural networks

Outputs a_i are given by :

$$a_m = f_2\,(a_1^1\, w_{m,1}^2 + a_2^1\, w_{m,2}^2 + b_m^2) \tag{2}$$

where :

$$\begin{aligned} a_2^1 &= f_1\,(x_1\, w_{2,1}^1 + \ldots\ldots + x_N\, w_{2,N}^2 + b_2^1) \\ a_1^1 &= f_1\,(x_1\, w_{1,1}^1 + \ldots\ldots + x_N\, w_{1,N}^2 + b_1^1) \end{aligned} \tag{3}$$

2.2 Radial Basis Network

This network is a network with error back-propagation whose hidden layer activation function is a Gaussian function:

$$f_1(x) = \exp\left[-\frac{(x - c_j)^T\,(x - c_j)}{2\sigma_j^{\,2}}\right], \qquad j = 1, \ldots\ldots, N_c \tag{4}$$

N_c is the number of neurons on the hidden layer.

$2\sigma_j^2$: Characterizes the Gaussian flatness

c_j designates the center of the activation function of the radial neuron, usually taken as equal to w_i .

thus we obtain :

$$f_1(x) = \exp\left[-\frac{\left\| x_i - w_{ij} \right\|}{2\sigma_j^{\,2}} \right], \qquad j = 1, ..., N_c \quad \text{et} \quad i = 1, ..., N \tag{5}$$

$\| \ \|$ frames the Euclidian norm and N represents the number of neurons in the input layer.

Contrary to the sigmoid neurons, the radial neurons work locally, thereby considerably reducing the size of the calculations and thus treating the problem with one input of the network containing several neurons.

2.3 Spectral Analysis and Spectrum

The frequency representation for access to the spectral components of a signal is given by:

$$S_X(f) = \int_{-\infty}^{+\infty} x(t).\exp(-j2\pi ft)\, dt \tag{6}$$

Where f is the frequency and and represents the amplitude spectrum. In discrete formulation we obtain:

$$X(f) = \sum_{k=0}^{N-1} x(k.Te)\exp(-2j\pi fTe) \tag{7}$$

Where Te is the sampling period

And N the number of samples corresponding to the duration of the signal to be analyzed.

2.4 Description of the Test Bench and Experimental Protocol

The test bench consists of a two stage toothed gear and a bearing housing (see Fig. 3) both hooded by a structure made of steel plate, of which the lid and one side were made of Plexiglas to allow vibrometer measurements.

The four pinions had straight teeth with a modulus of 2mm. The number of teeth were Z_1 = 45, Z_2 = 65, Z_3 = 50 and Z_4 = 42 respectively. Bearings with one line of balls (SKF 6002 type) were assembled on the six housings.

In order to generate the different series of training sets and the sets to test the network, we simulated tooth defects in the form of scratch on one tooth on pinions 1 and 3. Three types of degradation were imposed on wheel 1: moderate, accentuated and very accentuated. Two types of degradation were imposed on pinion 3: moderate and accentuated. Similarly, on the bearing of housing P2 defects were simulated on the inner ring and the outer ring in the form of scratches. Two types of degradation were employed for each ring: moderate and accentuated.

When running the motor at N = 1800 rpm, the combination of these various defects enabled us to generate 60 different series (including the signal generated by the machine in its new state) in the form of signals collected at a sampling rate of 48000 Hz with an acquisition time of 10s. Fifty series were chosen for the training and ten were chosen to test the network. The accelerometer allowing acquisition was placed on bearing housing P2. The signals and the series used to test the network were taken between the higher and lower limits of the series chosen for training the interpolation network. Measurements were performed in the lubricated case.

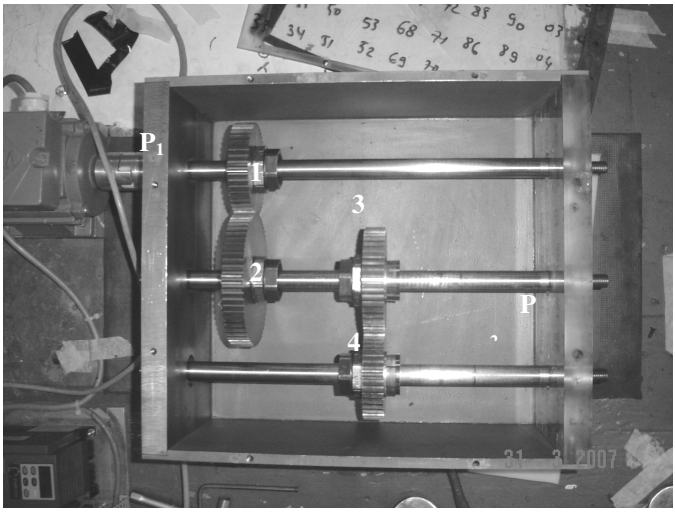

Fig. 3 Test bench (two stage speed reduction gear)

A Radial Basis Function network was used as a very high sampling rate was applied for the signals used for the training, Fe = 48 000 Hz during acquisition time T = 10s. Moreover, this type of network is better adapted to the signals in the presence of a strong noise, which is the case in reality, as shown previously.

During training, we presented the amplitudes of the sampled signal to the network. The output is binary: **1** if there is defect and **0** otherwise. The position of the activated neuron depends on the type of defect (see Table 2).

Table 1 Simulated defects

Simulated Defects
Gear 1 : 03 degradations (moderate, accentuated, aggravated)
Gear 3 : 02 degradations (moderate, accentuated)
Bearing : housing P2 Defect on external ring : 02 degradations (moderate, accentuated)

Table 2 Training series and their corresponding outputs

	Neurons of the output layer
Normal (without defects)	(**1** ; 0 ; 0 ; 0 ; 0)
Gear defect 1	(0 ; **1** ; 0 ; 0 ; 0)
Gear defect 3	(0 ; 0 ; **1** ; 0 ; 0)
External ring bearing defect	(0 ; 0 ; 0 ; **1** ; 0)
Gear defect 1 and external ring bearing defect	(0 ; 0 ; 0 ; 0 ; **1**)

2.5 Determination of the Natural Frequencies of the Structure

Fig. 4 shows the spectrum of the gear defect on pinion 1. We noted spectral emergences around 750 Hz and 3000 Hz. Measurements were taken on the housing P2 (see Fig.3).

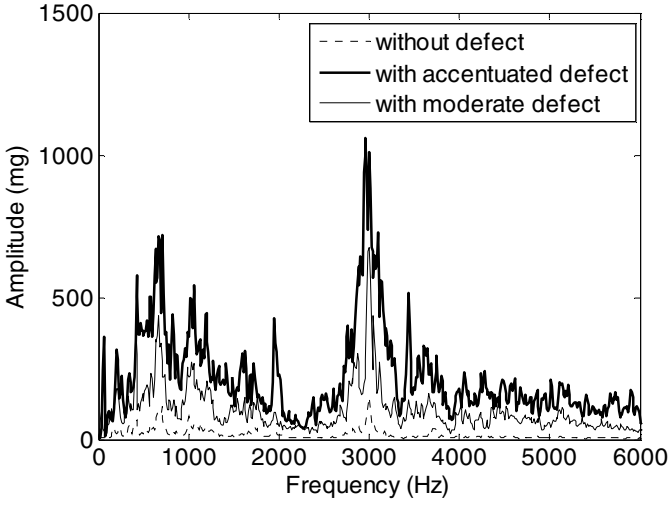

Fig. 4 Spectrum of defects on the wheel N°1 at N = 1800 rpm

This spectrum shows the full difficulty of diagnosis in the presence of frequencies of higher amplitude related to the vibratory response of the main structure. The amplitudes of these frequencies increase with the aggravation of the defect that acts like a loading force. We carried out an experimental modal analysis to identify the frequencies and natural modes of the structure encasing the speed reduction gear. These frequencies correspond to the natural frequencies of this structure.

Fig. 5, shows the four natural modes placed under stress during our vibratory measurements. These modes were obtained by experimental modal analysis (vibratory measurements at several points of the envelope of the speed reduction gear), the excitation point is a pulse on the steel plate close to the bearing housing P2.

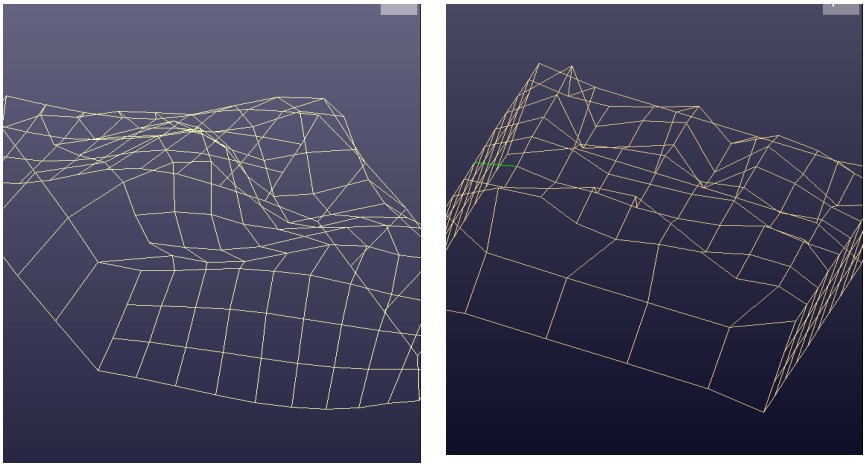

(a) 752 Hz (b) 3000 Hz

Fig. 5 Vibration modes of the structure encasing the speed reduction gear

The advantage of the neuronal approach is that during training it integrates these different types of information related to the proper frequencies of the structure or to a specific background noise, so as to take into account new events such as the emergence or aggravation of a mechanical defect in the detection.

2.6 Results

Table 3 shows the results obtained by transmitting signals of non learned defects to the network. Neuron1, which corresponds to the normal case (without defect), is activated whereas the others are not, thereby demonstrating efficient identification. The results presented in this paper concern the lubricated case.

Table 3 The example tested and their corresponding output neurons

Generalization	Neuron 1	Neuron 2	Neuron 3	Neuron 4	Neuron 5
Normal	**0.9314**	-0.1054	0.1052	0.1151	0.1109
Gear 1	0.1223	**0.9017**	- 0.1117	0.1239	0.1109
Gear 3	0.1198	-0.1235	**0.9700**	0.1287	0.1184
Gear 3	-0.0101	0.0238	**0.9512**	0.0601	0.0001
Bearing BE moderate	**0.7617**	0.0277	- 0.0063	**0.4125**	0.0150
Bearing BE	0.1188	0.2275	- 0.1191	**0.8954**	0.1024
Bearing BE	0.1077	-0.2254	- 0.0081	**0.8912**	-0.1877
Gear 1+ Bearing BE	-0.0912	*-0.3912*	- 0.1046	0.0991	**0.7204**
Gear 1+ Bearing BE	0.1702	*0.4702*	0.1113	0.1209	**0.5913**
Gear 1+ Bearing BE moderate	-0.0208	**0.6651**	- 0.0106	0.0219	**0.4500**

We obtained the same results for the other types of defects: gear1, gear 3 and bearing. The neuron matching the defect was activated each time. However, when introducing a moderate bearing defect alone or combined with a gear defect (gear 1 in this case), the network tented to detect no defect for the first case and a gear defect for the second case.

3 Conclusion

The study enabled us to show that the Radial Basis Function network adapted for detecting and identifying defects, with regard to background noise signal sampling. The implementation of this network enabled us to systematically identify the type of defect. However, identification is more difficult in the case of combined bearing and gear defects than a gear defect alone.

The results showed that identification becomes tedious and erroneous in the presence of noise, corresponding to a non lubricated case in a real situation. It is therefore necessary to process the signals measured.

Taking this work further, it would be interesting to consider the neuronal method in combination with the wavelet method and filtring in a non lubricated case.

References

[1] Sid Ahmed, M.: Traitement du signal pour détecter de manière précoce les défaillances des machines. Forum FIST 1991, Orléans (1991)

[2] Randall, R.B.: Developments in Digital Analysis Techniques for Diagnostics of Bearings and Gears. In: Fifth International Congress on Sound and Vibration, Adelaide, South Australia, December 15-18, pp. 300–309 (1997)

[3] Randall, R.: Detection and diagnosis of incipient bearing failure in helicopter gearbox. Engineering Failure Analysis 11(2), 177–190 (2004)

[4] James, C., Li, Ma, J.: Wavelet decomposition of vibrations for detection of bearing-localised defects. NDT&E International 30(3), 143–149 (1997)
[5] Purushotham, V., Narayanan, S., Prasod, S.A.N.: Multi-faults diagnosis of rolling bearing element using wavelet analysis and hidden Markov model based fault recognition. NDT&E International 38(8), 654–664 (2005)
[6] Wenlung, L., Tsai, Y.P., Chiu, C.L.: The experimental study of the expert system for diagnosing unbalances by ANN and acoustic signals. Journal of Sound and Vibration 272(1+2), 69–83 (2004)
[7] Wuxing, L., Tse, P.W., Guicai, Z., Tielin, S.: Classification of gear fault using cumulants and the radial basis function network. Mechanical Systems and Signal Processing 18(2), 381–389 (2004)
[8] Samanta, B., Al-Balushi, K.R.: Artificial neural network based fault diagnosis of rolling element bearings using time – domain features. Mechanical Systems and Signal Processing 17(2), 317–328 (2003)
[9] Kowalski, C.T., Orlowska-Kowalska, T.: Neural networks application for induction motor faults diagnosis. Mathematical and Computers in Simulation 63(3-5), 435–448 (2003)
[10] Bouzouane, B., Hamzaoui, N.: Détection mechanical defects by neural networks. Experimental analysis. Applied Mechanics and Materials 232, 674–681 (2012)

Part III
Fluid Structure Interaction and Vibroacoustics

PIV Study of the Down-Pitched Blade Turbine Hydrodynamic Structure

Bilel Ben Amira, Zied Driss, Sarhan Karray, and Mohamed Salah Abid

Laboratory of Electromechanical Systems (LASEM),
National School of Engineers of Sfax (ENIS),
University of Sfax,
B.P. 1173, Rte Soukra 3038 Sfax, Tunisia
benamira.bilel@yahoo.fr,
{Zied.Driss,MohamedSalah.Abid}@enis.rnu.tn

Abstract. The aim of this study is to investigate the blade inclination effect in the flow generated by three different down-pitched blade turbines in a stirred tank. Particle image velocimetry (PIV) technique is used to predict the velocity fields and the turbulent characteristics. This technique consist on a 532 nm Nd:YAG laser, a CCD camera and a mini-synchronizer. In this study, it has been noted that the velocity increases with increasing the blade inclination.

Keywords: down-pitched blade turbines, flow, stirred tank, blade inclination, PIV.

1 Introduction

Turbine blade configuration is one of the most important characteristics in stirred tank. Therefore, several researches are established to enhance the turbine configuration. Xuereb and Bertrand (1996) used the computational Fluid Dynamics (CFD) to analyze the fields of velocity components and local energy dissipation. Therefore, they used a low viscosity becoming highly viscous Newtonian and then pseudo-plastic fluids in a stirred vessel generated by two propellers settled. Alcamo et al. (2005) used the Smagorinsky model in the large-eddy simulation (LES) to model the unresolved, or sub-grid, scales. The numerical approach is investigated to compute the turbulent flow field generated in an unbaffled stirred tank by a Rushton turbine. Hollander et al. (2003) used the Large Eddy flow simulations to obtain an accurate numerical description on the scale-up behavior of the turbulent flow encountered in stirred vessels equipped with either a Rushton or a pitched blade turbine. Kchaou et al. (2008) used a computational fluid dynamic model to investigate the hydrodynamic behaviors induced by a flat-blade turbine and a pitched-blade turbine in a stirred vessel. Driss et al. (2009) used Naviers-Stokes equations to study the blade number effect in the turbulent flow in a closed stirred vessel generated with pitched blade turbine. Karray et al. (2011) used a coupling algorithm between the computational fluid dynamics and the computational

M. Haddar et al. (Eds.): *Design and Modeling of Mechanical Systems*, LNME, pp. 237–244.
DOI: 10.1007/978-3-642-37143-1_29

structure dynamics to compute the equilibrium of a flexible anchor impeller in a stirred vessel**.** Ammar et al. (2011) used Naviere Stokes equation in conjunction with the Renormalization Group of the k-ε turbulent model. This model is used to study the hydrodynamic behavior induced by six flat blades turbine, the Rushton turbine and the pitched blades turbine generated in stirred tanks. Gabriele et al. (2009) used angle resolved particle image velocimetry to analyze the turbulent flow characteristics of an up-pumping pitched blade turbines and to be compared with their down-pumping equivalent. Hassan et al. (2009) used an experimental apparatus to characterize an unbaffled vessel equipped with four nozzle spargers generated with anchor turbine in terms of power consumption and gas-liquid mass transfer. Doulgerakis et al. (2009) used Proper Orthogonal Decomposition (POD) analysis to identify and to characterize particle image velocimetry (PIV) data of the different flow structures in reactors stirred by radial impellers. Hill et al. (2000) used three dimension particle image velocimetry to measure the flow around a Rushton turbine. Halla et al. (2005) used a particle image velocimetry (PIV) to investigate the macroscopic hydrodynamic performance of a miniaturised unbaffled stirred vessel equipped with an eccentric six-blade up-pumping pitched blade turbine. Kumaresan and Joshi (2006) used the impeller blade angle, number of blades, blade width, blade twist, blade thickness, pumping direction and interaction of flow with the vessel wall to characterize the flow generated by different impeller geometries numerically. Feng et al. (2012) used an explicit algebraic stress model (EASM) to simulate anisotropic turbulent flows in baffled stirred tanks equipped with a standard Rushton turbine. Cheng et al. (2012) used Rushton disk turbine (RDT), half circle blade disk turbine (HCDT), 45° pitched blade turbine down flow (PBTD) and 45° pitched blade turbine up flow (PBTU) to calculate an experimental data. In fact, this data was studied on the mixing time of the continuous phase and power consumption of Gas – liquid – liquid dispersions in a mechanically agitated baffled tank.

In this study, we are interested in analyzing the hydrodynamic structure of the turbulent flow for three down-pumping pitched six-blade turbines, whose blade inclinations are equal to 45°, 60° and 75°.

2 Materials

Figure 1 shows the different turbines which are used in this study. In addition, figure 2 shows the cylindrical tank which is fixed inside a squared tank. Moreover, the water height is settled to be equal to the cylindrical tank diameter (H = D = 300 mm). The vessel is mounted with particle image velocimetry (PIV). The PIV system is equipped with Nd:YAG laser working in 2x30 mJ and 532 nm wavelength. The laser sheet propagated along the centerline of the tank and vertically along the shaft. Furthermore, the acquisition is achieved with a CCD camera with 1600 x 1200 pixels as resolution. A mini-synchronizer system is used to provide the synchronization between the different PIV compartments. The interrogation windows area is settled to be equal to 32x32 pixels.

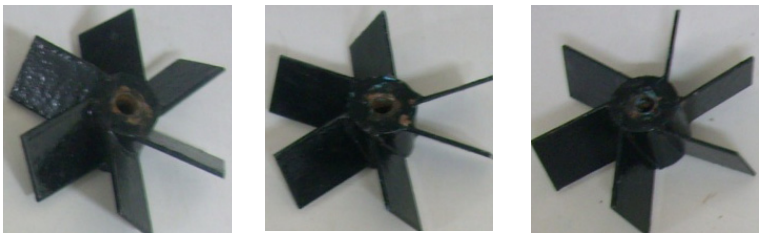

(a) 45 D (b) 60 D (c) 75 D

Fig. 1 Turbines

Fig. 2 PIV system

3 Results

3.1 Flow Field

Figure 3 shows the velocity field for three down-pumping pitched six-blade turbines. According to these results, one main circulation loop is presented in the inferior region of the impeller for the three down-pumping configurations. The mean recirculation loops are localized close to the bottom of the vessel and near the vessel wall. In addition, the velocity increases as the fluid accelerates from the

upward to the downward direction. In fact, an oblique velocity direction appears close to the impeller. Then, it becomes horizontal in the bottom and becomes vertical upward along the side wall. Furthermore, a dead zone appears in upper region of the vessel.

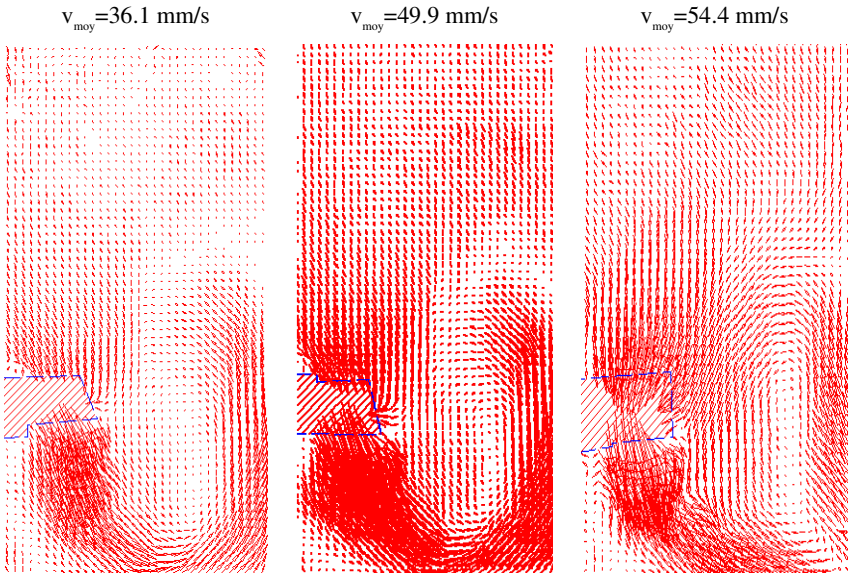

Fig. 3 Velocity field

3.2 Vorticity

Figure 4 shows the distribution of the vorticity generated by the three configurations. According to these results, the maximum values were observed in two locations corresponding to the highest values and the lowest values for all configurations. Consequently, the highest and the lowest local vortices values were found close the impeller level. Then, they became medium moving both upward and downward from this level. Hence, the maximum vorticity values become larger and more diffused in the bulk of the discharge flow. Furthermore, the areas of the lowest values are larger than that of the highest values. Moreover, the highest value areas become more distinct and localized into narrowed areas at the inferior region of the impeller. In fact, the highest value areas are localized at the end of the blade, and the lowest one are presented near the shaft. As a result, the lowest vorticity values decrease with increasing of the blade inclination angle.

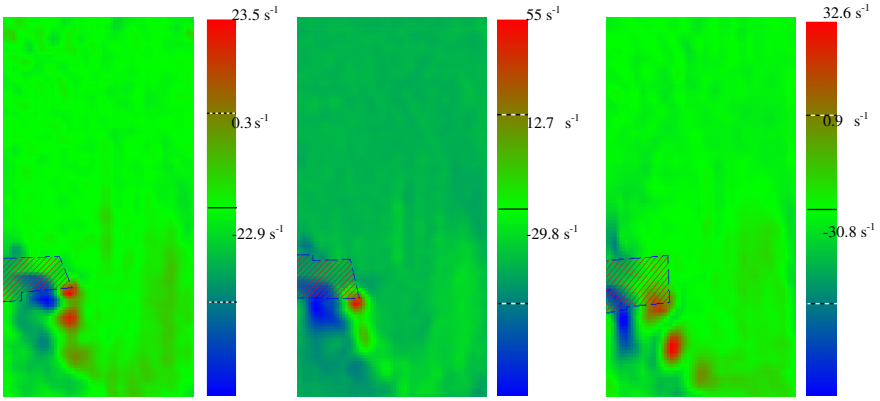

(a) 45 D (b) 60 D (c) 75 D

Fig. 4 Vortices

3.3 Turbulent Kinetic Energy

Figure 5 shows the distribution of the turbulent kinetic energy generated by the three configurations. According to these results, the areas of the maximum characteristics of turbulent kinetic energy are overlapped, whereas, they become larger and more diffuse in the bulk of the discharge flow. Moreover, the faraway region is localized in the same direction of the velocity acceleration. The rest of the bulk region of the tank is described with the lowest values of the turbulent kinetic energy. The highest value area is localized near the blade in the inferior region of the blade.

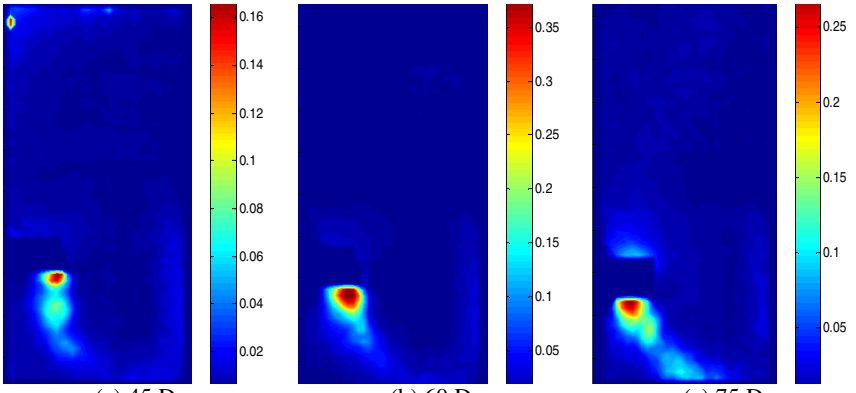

(a) 45 D (b) 60 D (c) 75 D

Fig. 5 Turbulent kinetics energy

3.4 *Turbulent Viscosity*

Figure 6 shows the distribution of the turbulent viscosity generated by the three configurations. Similar observations may be made as the turbulent kinetics energy. In fact, for all the configurations, the areas of the maximum characteristics of turbulent viscosity are overlapped. Whereas, they become more large and more diffuse in the region of the discharge flow. Moreover, the faraway region is localized in the same direction of the velocity acceleration. The rest of the bulk region of the tank is described with the lowest values of the turbulent viscosity. The highest value area is localized near the blade in the inferior region of the blade.

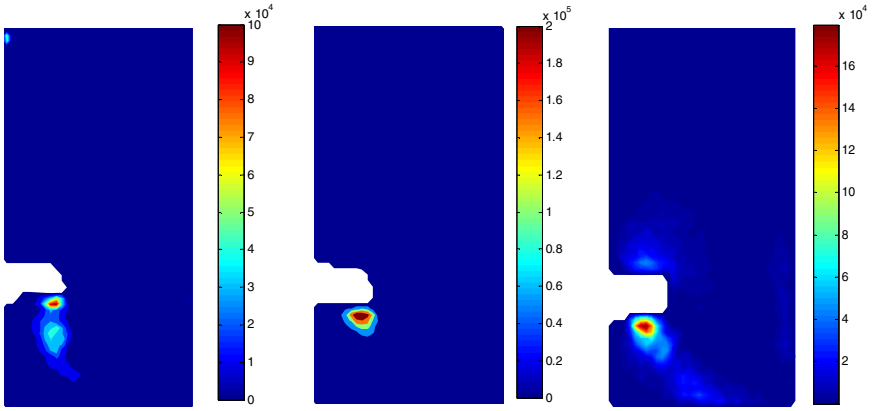

Fig. 6 Turbulent viscosity

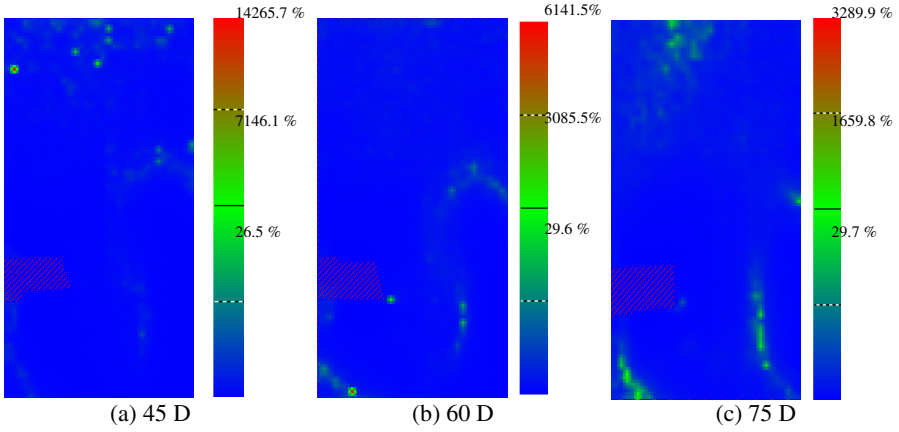

Fig. 7 Turbulent intensity

3.5 Turbulent Intensity

Figure 7 shows the distribution of the turbulent intensity generated by the three configurations. For all these configurations, the areas of the maximum characteristics of turbulent intensity were overlapped. Moreover, the bulk region of the tank is described with the lowest values of the turbulent intensity. The highest value areas are distinct and spread in the whole region of the tank.

4 Conclusion

In this paper, an experimental study was achieved to investigate the blade inclination effect in the hydrodynamics structure of the flow. In fact, in this study we are foxed to study three down-pitched blade turbines as well as 75°, 60° and 45°. Therefore, one main circulation loop is presented in all the configurations. Moreover, the velocity values increase with increasing the blade inclination.

References

Xuereb, C., Bertrand, J.: 3-d hydrodynamics in a tank stirred by a double-propeller system and filled with a liquid having evolving rheological properties. Chemical Engineering Science 51, 1725–1734 (1996)

Alcamo, R., Micale, G., Grisafi, F., Brucato, A., Ciofalo, M.: Large-eddy simulation of turbulent flowin an unbaffled stirred tank driven by a Rushton turbine. Chemical Engineering Science 60, 2303–2316 (2005)

Hollander, E.D., Derksen, J.J., Kramer, H.M.J., Van Rosmalen, G.M., Van den Akker, H.E.A.: A numerical study on orthokinetic agglomeration in stirred tanks. Powder Technology 130, 169–173 (2003)

Kchaou, H., Driss, Z., Bouzgarrou, G., Chtourou, W., Abid, M.S.: Numerical Investigation of Internal Turbulent Flow Generated By A Flat-Blade Turbine and A Pitched-Blade Turbine in A Vessel Tank. International Review of Mechanical Engineering (I.RE.M.E.) 2(3) (2008)

Driss, Z., Bouzgarrou, G., Chtourou, W., Kchaou, H., Abid, M.S.: Simulation numérique de l'écoulement turbulent généré par des turbines à différents nombre de pales inclinées. In: Récents Progrès en Génie des Procédés, Numéro 98–2-910239-72-1. SFGP, Paris (2009)

Driss, Z., Bouzgarrou, G., Chtourou, W., Kchaou, H., Abid, M.S.: Computational studies of the pitched blade turbines design effect on the stirred tank flow characteristics. European Journal of Mechanics B/Fluids 29, 236–245 (2010)

Karray, S., Driss, Z., Kchaou, H., Abid, M.S.: Numerical simulation of fluid-structure interaction in a stirred vessel equipped with an anchor impeller. Journal of Mechanical Science and Technology 25, 1749–1760 (2011)

Ammar, M., Chtourou, W., Driss, Z., Abid, M.S.: Numerical investigation of turbulent flow generated in baffled stirred vessels equipped with three different turbines in one and two-stage system. Energy 36, 5081–5093 (2011)

Gabriele, A., Nienow, A.W., Simmons, M.J.H.: Use of angle resolved PIV to estimate local specific energy dissipation rates for up- and down-pumping pitched blade agitators in a stirred tank. Chemical Engineering Science 64, 126–143 (2009)

Hassan, R., Loubiere, K., Legrand, J.: Power consumption and mass transfer in an unbaffled stirred tank for autothermal thermophilic digestion of sludge. In: Récents Progrès en Génie des Procédés. Numéro 98 –2-910239-72-1. SFGP, Paris (2009)

Doulgerakis, Z., Yianneskis, M., Ducci, A.: On the interaction of trailing and macro-instability vortices in a stirred vessel - enhanced energy levels and improved mixing potential. In: 13th European Conference on Mixing London, April 14-17 (2009)

Hill, D.F., Sharp, K.V., Adrian, R.J.: Stereoscopic particle image velocimetry measurements of the flow around a Rushton turbine. Experiments in Fluids 29, 478–485 (2000)

Halla, J.F., Barigoua, M., Simmonsa, M.J.H., Stittb, E.H.: APIV study of hydrodynamics in gas–liquid high throughput experimentation (HTE) reactors with eccentric impeller configurations. Chemical Engineering Science 60, 6403–6413 (2005)

Kumaresan, T., Joshi, J.B.: Effect of impeller design on the flow pattern and mixing in stirred tanks. Chemical Engineering Journal 115, 173–193 (2006)

Feng, X., Cheng, J., Li, X., Yang, C., Mao, Z.S.: Numerical simulation of turbulent flow in a baffled stirred tank with an explicit algebraic stress model. Chemical Engineering Science 69, 30–44 (2012)

Cheng, D., Cheng, J., Li, X., Wang, X., Yang, C., ShaMao, Z.: Experimental study on gas–liquid–liquid macro-mixing in a stirred tank. Chemical Engineering Science 75, 256–266 (2012)

Modeling and Analysis of the Hydrodynamic Structure around a Vertical Axis Water Turbine

Zied Driss*, Mohamed Ali Jemni, Amin Chelly, and Mohamed Salah Abid

Laboratory of Electro-Mechanic Systems (LASEM),
National School of Engineers of Sfax (ENIS),
Univrsity of Sfax, B.P. 1173,
Road Soukra km 3.5, 3038 Sfax, Tunisia
Zied.Driss@enis.rnu.tn

Abstract. Numerical investigation was carried out to study the hydrodynamic structure flow around a vertical axis water turbine. The CFD code "Flow Simulation" has been used to present the local characteristics in different longitudinal section planes of the considered control volume. The numerical model is based on the resolution of the Navier-Stokes equations in conjunction with the standard k-ε turbulence model. These equations were solved by a finite volume discretization method.

Keywords: Water turbine, hydrodynamic structure, modeling, control volume.

1 Introduction

The renewable energies are a real opportunity to meet some of our energy needs while respecting environmental imperatives, social, economic, strategic and ethical (Evans et al. 2009), Jebaraj and Iniyan 2006). The use of renewable energies is obviously not new. But, with the advent of industrial revolution, they were marginalized in favor of other energy sources that were thought most promising. In recent decades, however, air pollution, global warming and the risks of nuclear power have raised awareness of the need for organization of society that respects the environment in which we live (Skoglund et al. 2010, Vine 2008). Hydroelectricity, as a technology, started in the last decade of the 19th century, and pre-dates by many years the increasing public awareness of environmental issues (Strupczewskim 2003). The researches in hydrodynamics are directed towards local knowledge of hydrodynamic phenomena around turbines. In fact, knowledge of local hydrodynamic structures allows analyzing the performance of water turbines for the development of optimum operating conditions and the improvement of the quality of the flow in different compartments. Face of this information request, the numerical simulations implements modeling techniques to calculate the various parameters of the flow in any configuration.

* Corresponding author.

M. Haddar et al. (Eds.): *Design and Modeling of Mechanical Systems*, LNME, pp. 245–252.
DOI: 10.1007/978-3-642-37143-1_30

In this paper, numerical simulation provided by the computational fluid dynamic code "Flow Simulation" was investigated around a vertical axis water turbine. Specifically, we are interested in characterizing the hydrodynamic structure of the turbulent flow in different planes of the considered control volume.

2 Numerical Model

The system under investigation is defined by a test section equipped by a vertical axis water turbine (figure 1). The CFD code "Flow Simulation" has been used. The numerical model is based on the resolution of the Navier-Stokes equations in conjunction with the standard k-ε turbulence model. These equations were solved by a finite volume discretization method (Driss et al. 2012). The boundary conditions are presented in figure 2. In the present study, the inlet velocity is equal to V=4.45 m.s^{-1} and the outlet pressure is equal to p=101325 Pa. The compartment in the vicinity of the turbine presents a rotation area defined by Ω=4 rad. s^{-1}. Figure 3 and table 1 illustrate all information about meshing.

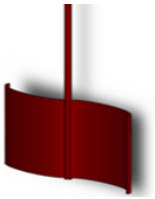

Fig. 1 Vertical axis water turbine

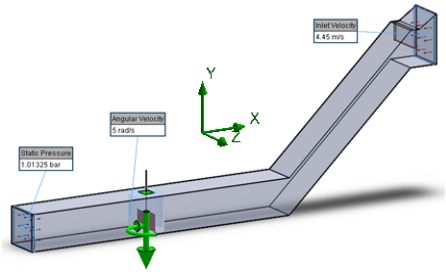

Fig. 2 Boundary conditions

Table 1 Meshing parameters

Basic mesh dimensions		Number of cells	
Cells number in X direction	42	Fluid cells	4436
Cells number in Y direction	17	Solid cells	4686
Cells number in Z direction	17	Partial cells	6614

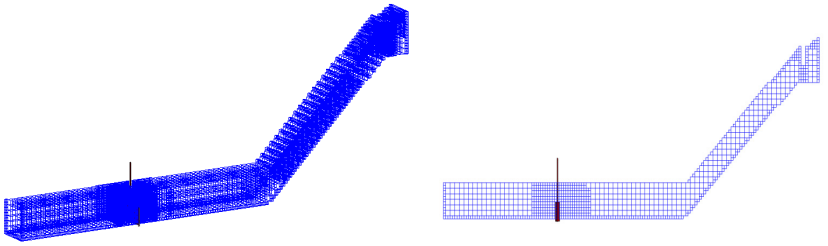

(a) 3D meshing (b) 2D meshing

Fig. 3 Meshing

3 Results and Discussions

3.1 Velocity Vectors

Figure 4 shows the distribution of velocity vectors in the test section. The considered planes are defined by z=0 and y=0. According to these results, it's clear that the velocity vectors reach its maximum values on the collector after the door and the collector. Around the water turbine, a rotating movement of the fluid has been observed. The recirculation zone of the fluid remains away from the turbine. Therefore, energy is transmitted to the turbine movement.

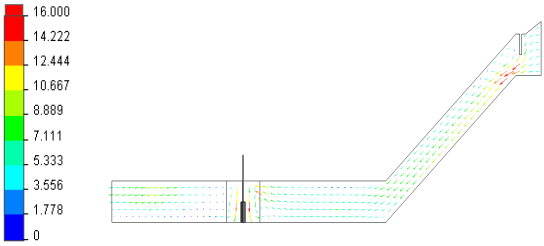

(a) Longitudinal section plane defined by z=0

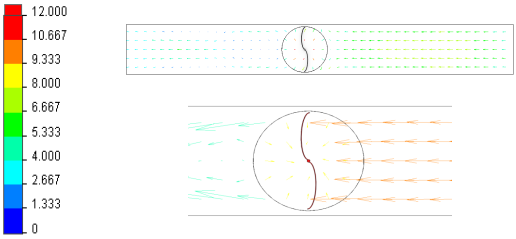

(b) Longitudinal section plane defined by y=0

Fig. 4 Distribution of the velocity vectors

3.2 Average Velocity

Figure 5 shows the distribution of the average velocity throughout the test section equipped by the water turbine. In the collector, the maximal value is always located in the vicinity of the down wall and before the door. The phenomenon of symmetry in the rotating part is apparent in these results. Also, it has been noted that the velocity at the pallet sides is very high and reaches V=16 $m.s^{-1}$. On the turbine downstream, the velocity is very low.

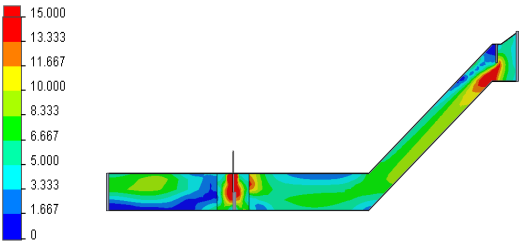

(a) Longitudinal section plane defined by z=0

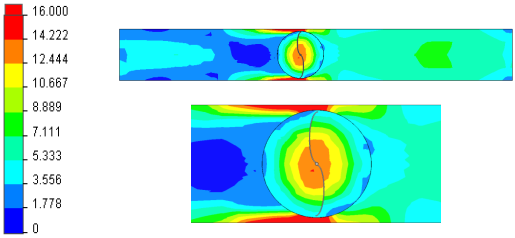

(b) Longitudinal section plane defined by y=0

Fig. 5 Distribution of the average velocity

3.3 Static Pressure

Figure 6 shows the distribution of the static pressure in the test section equipped by the water turbine. According to these results, a considerable increase of static pressure, reaching 2.7 bar, has been observed. In the vicinity of the turbine, compression and depression zones appeared. In the longitudinal section plane defined by z=0, it has been noted that the pressure increases slightly in the first part of the test section. It decreases rapidly in the turbine downstream until the atmospheric pressure, measured in the outlet section. Near the convex pallets, a compression zone has been observed. This can be explained by the rotation of the turbine. In the longitudinal section y=0 and near the pallets. A decrease of the static pressure has been noted from the maximum value on the turbine upstream to the minimum value on the turbine downstream.

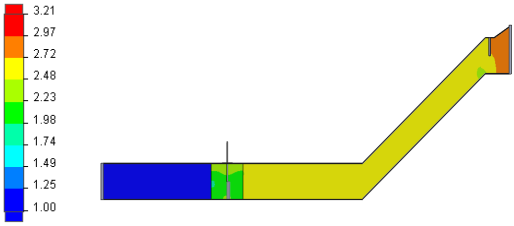

(a) Longitudinal section plane defined by z=0

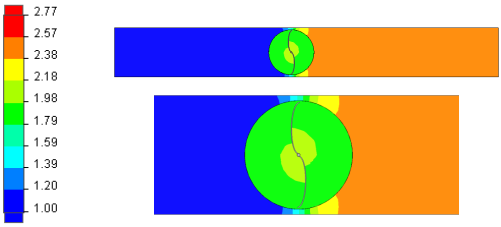

(b) Longitudinal section plane defined by y=0

Fig. 6 Distribution of the Static pressure

3.4 Dynamic Pressure

Figure 7 illustrates the distribution of the dynamic pressure in the test section equipped by the water turbine. According to these results, it has been noted that the dynamic pressure depends essentially on the fluid speed. The maximum value is obtained in the vicinity of the door and the rotating part. The symmetry phenomenon is well described in these results. The compressed areas are located in the rotating zone and near the door.

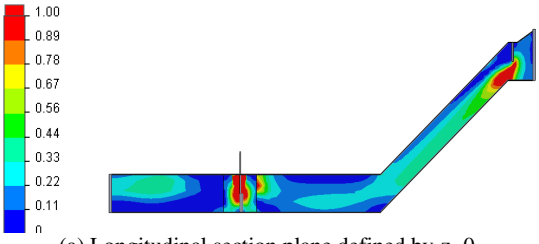

(a) Longitudinal section plane defined by z=0

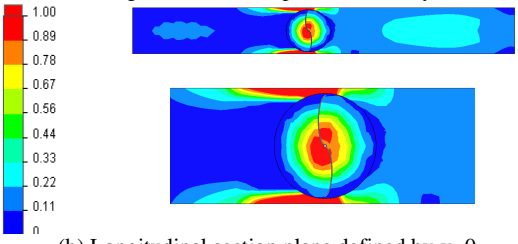

(b) Longitudinal section plane defined by y=0

Fig. 7 Distribution of the dynamic pressure

3.5 Turbulent Kinetic Energy

Figure 8 shows the distribution of the turbulent kinetic energy over the entire test section equipped by the water turbine. According to these results, it has been noted that the turbulent kinetic energy is always important in the collector chamber in the vicinity of the door. Indeed, the turbulent kinetic energy is very weak in the turbine compartment. In the turbine downstream, the turbulent kinetic energy increases. This fact is confirmed in the longitudinal section plane defined by y=0.

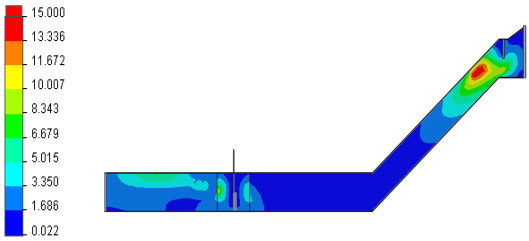

(a) Longitudinal section plane defined by z=0

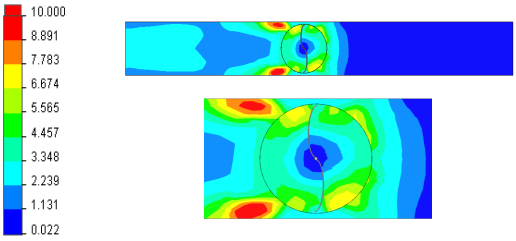

(b) Longitudinal section plane defined by y=0

Fig. 8 Distribution of the turbulent kinetic energy

3.6 Turbulent Dissipation Rate

Figure 9 shows the distribution of the dissipation rate of the turbulent kinetic energy in the test section equipped by the water turbine. According to these results, it has been noted that the dissipation rate is located in the vicinity of the door and near the pallets in the rotating zone. This fact is due to the transformation of the turbulent kinetic energy into heat.

3.7 Turbulent Viscosity

Figure 10 shows the distribution of the turbulent viscosity throughout the test section equipped by the water turbine. According to these results, it has been noted that the turbulent viscosity is very important in the collector compartment and in the turbine downstream. This fact is confirmed in the longitudinal section plane defined by y=0.

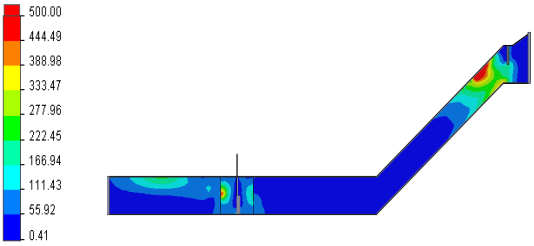

(a) Longitudinal section plane defined by z=0

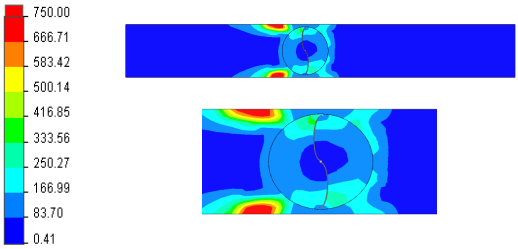

(b) Longitudinal section plane defined by y=0

Fig. 9 Distribution of the turbulent dissipation rate

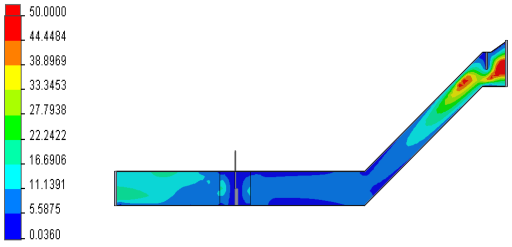

(a) Longitudinal section plane defined by z=0

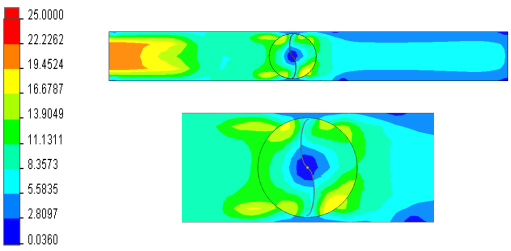

(b) Longitudinal section plane defined by y=0

Fig. 10 Distribution of the turbulent viscosity

4 Conclusion

In this study, a computational fluid dynamic investigation was developed to present the hydrodynamic characteristics around a vertical axis water turbine. Particularly, the distribution of the velocity fields, the pressure and the turbulent

characteristics was presented in different longitudinal planes of the test section. According to these results, it has been noted that the water turbine choice has a direct effect on the flow characteristics. In the future, we propose to develop an experimental investigation to study the global characteristics of the water turbine. These results will be used to validate the numerical results developed by the computational Fluid Dynamic simulation.

References

Driss, Z., Abid, M.S.: Use of the Navier-Stokes Equations to Study of the Flow Generated by Turbines Impellers. In: Navier-Stokes Equations: Properties, Description and Applications, ch. 3, pp. 51–138. Nova Science Publishers (2012)

Evans, A., Strezov, V., Evans, T.J.: Assessment of sustainability indicators for renewable energy technologies. Renewable and Sustainable Energy Reviews 13(5), 1082–1088 (2009)

Jebaraj, S., Iniyan, S.: A review of energy models. Renewable and Sustainable Energy Reviews 10(4), 281–311 (2006)

Strupczewskim, A.: Accident risks in nuclear-power plants. Applied Energy 75(1-2), 79–86 (2003)

Skoglund, A., Leijon, M., Rehn, A., Lindahl, M., Waters, R.: On the physics of power, energy and economics of renewable electric energy sources-Part II. Renewable Energy 35(8), 1735–1740 (2010)

Vine, E.: Breaking down the silos: the integration of energy efficiency, renewable energy, demand response and climate change. Energy Efficiency 1, 49–63 (2008)

Numerical Coupled Modeling of Water Hammer in Quasi-rigid Thin Pipes

Abdelaziz Ghodhbani and Ezzeddine Hadj-Taïeb

Applied Fluid Mechanical,
Proceedings Engineering and Environment,
Department of Mechanical Engineering,
National School of Engineers of Sfax,
Sfax, Tunisia
abdelaziz.ghodhbani1@gmail.com,
ezed.hadj@enis.rnu.tn

Abstract. The water hammer coupled model called « FSI four-equation model » describes the axial dynamic behavior of liquid-filled pipes against a water hammer. Dynamic coupling type, boundary conditions and initial conditions define the model. The MOC, frequently used for numerical computation is often based on linear interpolation. However, this method remains inadequate in some practical cases. For more precision, one uses the wave speeds correction method. This paper gives comparison between different methods used for the water hammer coupled model calculation in quasi-rigid pipes using the MOC. Calculation codes implemented on *Matlab* are applied to Hadj Taïeb experiment. They show that the wave speeds correction method and the linear time interpolation method converge to the same solution.

Keywords: water hammer, quasi-rigid pipes, fluid-structure interaction (FSI), method of characteristic (MOC), linear interpolation, wave speeds correction.

1 Introduction

Hydraulic systems are still affected by water hammer that can be caused by valve closing, pump stopping or any incident that can block the liquid flow. The determination of the safety components such as water tank air pressure, flywheel pumps and valve ventilation has long been part of the state of the art. For each pipe threatened, it should perform an analysis of water hammer to accurately calculate four variables: pressure (p) and velocity (V) in the liquid, speed axial ($\dot{u}$) and axial stress (σ) in the pipe.

Software based on the MOC is frequently used by manufacturers. The MOC applies well to the classical model, and also coupled model. For solving coupled models, the MOC is based on two main methods:

M. Haddar et al. (Eds.): *Design and Modeling of Mechanical Systems*, LNME, pp. 253–264.
DOI: 10.1007/978-3-642-37143-1_31

- Linear interpolation: it is carried either on the space or on the time.
- Wave speeds correction: the ratio of characteristic directions is either integer or rational.

The wave speeds correction method assuming the wave speeds ratio (n) to integer number was used by Schwarz (1978), Wiggert et al. (1985, 1987), Burmann et al. (1987), Burmann and Thielen (1988a, b) and others. This strong assumption was relieved by Tijsseling (1993), Tijsseling et al. (1996), and Bergant and Tijsseling (2001) by allowing the wave speed ratio (n) to be rational number at the expense of refined computational grids.

In this work, an algorithm for finding the solution of the wave speeds correction using rational ratio (n) is described. To minimize the numerical dispersion and damping, the algorithm doesn't use any interpolation. The phase error introduced is as small as the rational number is correct.

2 Theory

The water hammer phenomenon is usually explained by considering an ideal reservoir-pipe-valve system in which a steady flow with velocity V_0 is stopped by an instantaneous valve closure (see Fig. 1).

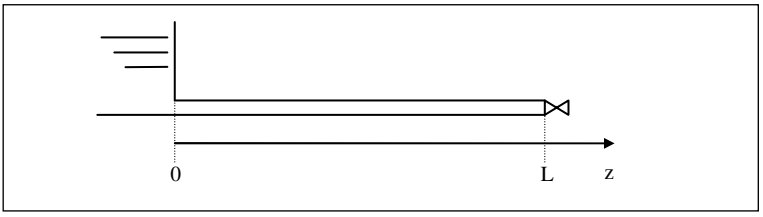

Fig. 1 Ideal reservoir-pipe-valve system

2.1 Assumptions

The one-dimensional model is valid for straight thin-walled pipe of circular- cross section. The pipe wall material is homogeneous, isotropic, linearly elastic and subjected to small deformations. The resistance to radial motion by inertia, bending stiffness and shear deformation is ignored. The contained liquid is Newtonian with homogeneous, isotropic and linearly elastic properties.

2.2 FSI-Four Equation Model

The equations for conservation of mass and momentum are derived for the liquid and the structure (pipe) using generalized Hooke's low. The coupling of liquid and pipe equations by means of boundary conditions on the interface and with the assumption of thin-walled pipe leads to the four basic equations. Schwartz (1978)

gives a clear derivation of the basic equation in a different way using the Timoshenko's beams theory. His approach gives the four equation (1), (2), (3), (4), for the four unknowns p, V_z, σ_z and $\dot{u}_z$:

$$\frac{\partial V_z}{\partial t}+\frac{1}{\rho_f}\frac{\partial p}{\partial z}=-\frac{fV_z|V_z|}{4R}+g\sin\gamma \tag{1}$$

$$\frac{\partial V_z}{\partial z}+\frac{1}{\rho_f {C_F}^2}\frac{\partial p}{\partial t}-2\nu\frac{\partial \dot{u}_z}{\partial z}=0 \tag{2}$$

$$\frac{\partial \dot{u}_z}{\partial t}-\frac{{C_p}^2}{E}\frac{\partial \sigma_z}{\partial z}=\frac{f\rho_f RV_z|V_z|}{4\rho_p(2R+e)e}+g\sin\gamma \tag{3}$$

$$\frac{\nu R}{Ee}\frac{\partial p}{\partial t}+\frac{\partial \dot{u}_z}{\partial z}-\frac{1}{E}\frac{\partial \sigma_z}{\partial t}=0 \tag{4}$$

In which, C_F , C_p , e , E , f , g , R , ρ_f , ρ_p , ν and γ are respectively wave propagation speed in the fluid (liquid), wave propagation speed in the pipe wall, pipe wall thickness, Young's modulus of elasticity of the pipe's material, Darcy-Weisbach friction coefficient, gravitational acceleration, inner radius of the pipe, fluid mass density, pipe wall mass density, Poisson coefficient, elevation angle of pipe ;

The wave speeds C_F and C_p are: $C_F=\left[\rho_f\left(\frac{1}{K}+\frac{2(1-\nu^2)R}{Ee}\right)\right]^{-1/2}$; $C_p=\left(\frac{E}{\rho_p}\right)^{1/2}$ where K is the liquid bulk modulus.

The four-equation model (1)-(4) is solved numerically by the MOC. Matrix transformations [2] leads to four characteristic directions λ_1 , λ_2 , λ_3 , λ_4 which represent the propagation speeds of axial waves in liquid-filled pipe:

$$\lambda_1=\frac{1}{\sqrt{2}}\left[q^2-\left(q^4-4{C_p}^2{C_F}^2\right)^{1/2}\right]^{1/2}=+\tilde{C}_F \tag{5}$$

$$\lambda_2=-\lambda_1=-\tilde{C}_F \tag{6}$$

$$\lambda_3=\frac{1}{\sqrt{2}}\left[q^2+\left(q^4-4{C_p}^2{C_F}^2\right)^{1/2}\right]^{1/2}=+\tilde{C}_p \tag{7}$$

$$\lambda_4 = -\lambda_3 = -\tilde{C}_p \tag{8}$$

Where $q^2 = \left(1 + 2\nu^2 \frac{\rho_f}{\rho_p}\frac{R}{e}\right) C_F{}^2 + C_p{}^2$

The four compatibility equations developed from system (1)-(4) are numerically integrated along the characteristic directions using Euler method. Hence, solving four unknowns at a point P needs four earlier points with known variables. The wave speeds correction (adjustment) method adjusts wave speeds in such a way that the four earlier points belong to computational grid.

Initial conditions are those of steady-state (V_0 and p_{res} are respectively the steady-state flow velocity and the pressure at the reservoir):

$$V = V_0 \tag{9}$$

$$p = p_{res} - \left(\frac{f\rho_f V_0 |V_0|}{4R} - \rho_f g \sin\gamma\right) z \tag{10}$$

$$\dot{u}_z = 0 \tag{11}$$

$$\sigma_z = \frac{\nu R^2 p_{rés}}{(2R+e)e} - \left(\rho_f g \sin\gamma + \frac{fR\rho_f V_0^2}{4e(2R+e)}\right) z \tag{12}$$

Boundary conditions at the reservoir (Fig. 1) are:

$$p = p_{rés} \tag{13}$$

$$\dot{u}_z = 0 \tag{14}$$

At the valve, boundary conditions describe the instantaneous closure of a free valve:

$$V_z = \dot{u}_z \tag{15}$$

$$A_f p - A_p \sigma_z = m_v \ddot{u}_z \tag{16}$$

Where A_f and A_p represent, respectively inner and pipe wall cross-section areas, m_v is the mass of the valve. Equation (16) derives from dynamic equilibrium of the valve. The acceleration $\ddot{u}_z$ can be approximated with the trapezoidal rule. Thus, the inertia effect of the valve depends on the value of m_v and the time step Δt.

3 Algorithm

This section is the aim of the paper. The algorithm proposed doesn't need any interpolations, The rational number n is: $n = \dfrac{\tilde{C}_p}{\tilde{C}_F} = \dfrac{b}{a}$, ($a$, b are integers).

To start calculation, the initial state is refined in two manners. Points obtained by refinement are used only in step 1 (Fig. 2) and step 2 (Fig. 3). A regular computational grid is used in three steps, the space steps Δz, Δz_a and Δz_b are relied by the following equation: $\Delta z = a\Delta z_a = b\Delta z_b$.

In the whole computational grid, the time step Δt satisfies the equation (17):

$$\Delta t = \frac{\Delta z}{b\left|\pm\tilde{C}_F\right|} = \frac{\Delta z}{a\left|\pm\tilde{C}_p\right|} \tag{17}$$

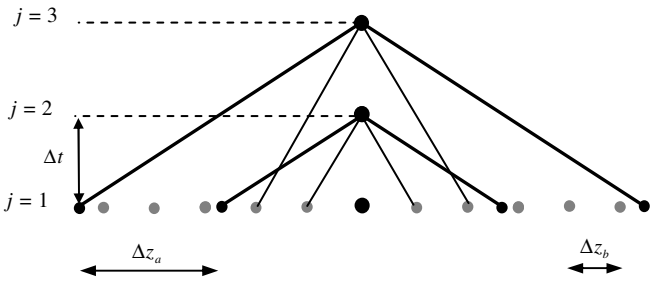

Fig. 2 Computational grid for step 1 ($2 \le j \le a+1$)

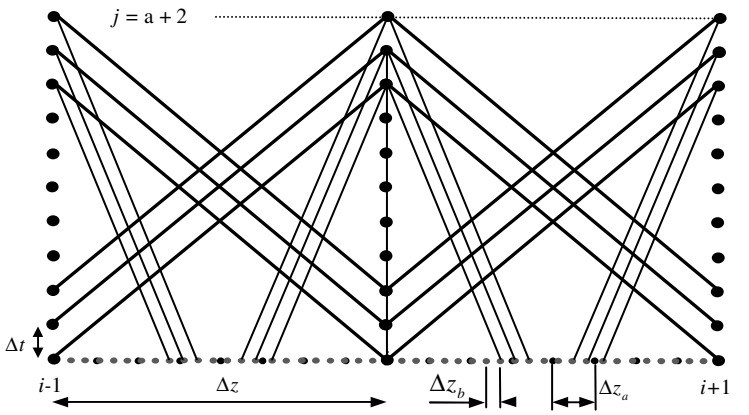

Fig. 3 Computational grid for step 2 ($a+2 \le j \le b$)

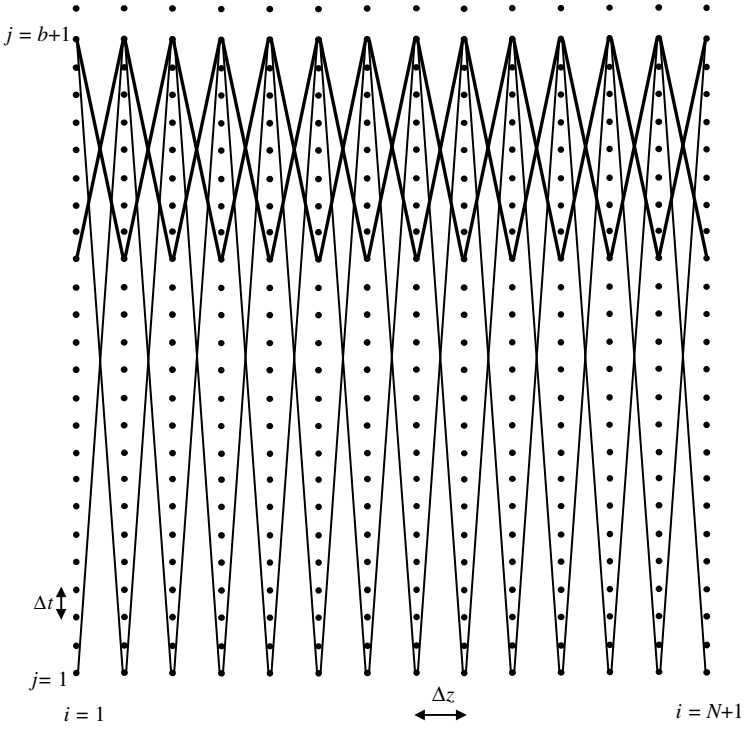

Fig. 4 Computational grid for step 3 ($j \geq b+1$)

4 Hadj Taïeb Experiment

Hadj Taïeb (1973) presented valuable experimental results in straight copper pipe with a free instantaneous valve. Experiment parameters are defined in table 1:

Table 1 Hadj Taïeb experiment

Parameters	Value
Inner diameter of the pipe	D=19,6 *mm*
Length of the pipe	L=35,7 *m*
Pipe wall thickness	e=1 *mm*
Young's modulus of elasticity	E=1,05 10^{11} N/m^2
Liquid bulk modulus	K=2,03 10^9 N/m^2
Fluid mass density	ρ_f=1000 Kg/m^3
Pipe wall mass density	ρ_f=8900 Kg/m^3
Darcy-Weisbach friction coefficient	f=0.03

5 Results

The Hadj Taïeb experiment is simulated in case of water hammer without cavitation (V_0=0,095 *m/s*). FSI is considered through Poisson coupling ($\nu = 0,5$). According to the Hadj Taïeb parameters, the wave speeds ratio (n) is near to 2,8766. This irrational number is replaced by the rational one: 23/8. The rational value is obtained, with an error of 10^{-5} by adjusting the pipe wall mass density (8910 instead of 8900). The computational grid is exactly as described in section 3. The modification of mass density causes only a negligible phase error.

Pressure history diagram (Fig. 5) shows the good agreement between time interpolation method and wave speeds correction method, whereas, space interpolation method presents some numeric damping.

The agreement between the three methods is good for the precursor wave propagation (Fig. 6). The water hammer wave is travelling at $\tilde{C}_F$, whereas the precursor wave is travelling at $\tilde{C}_p$.

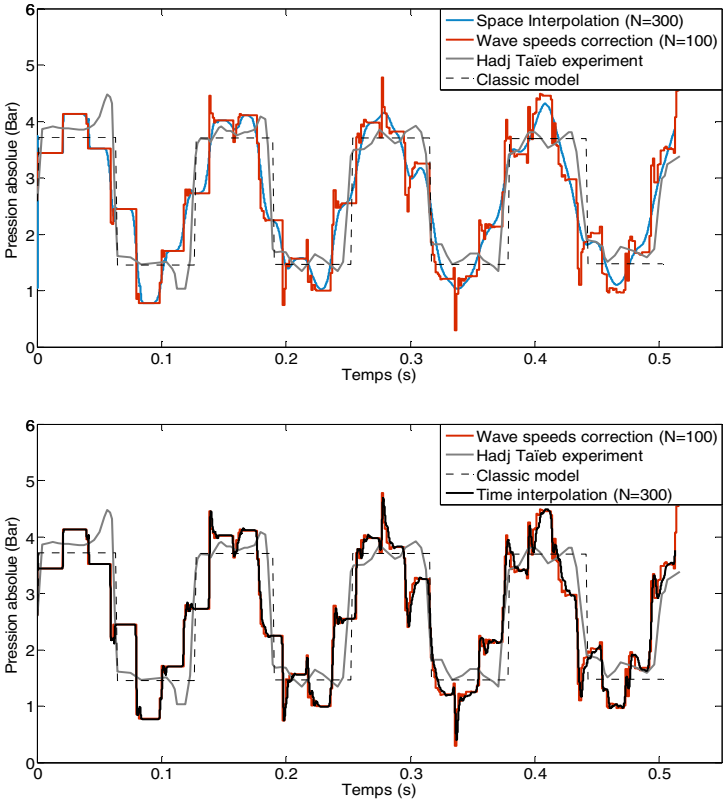

Fig. 5 Pressure at the valve

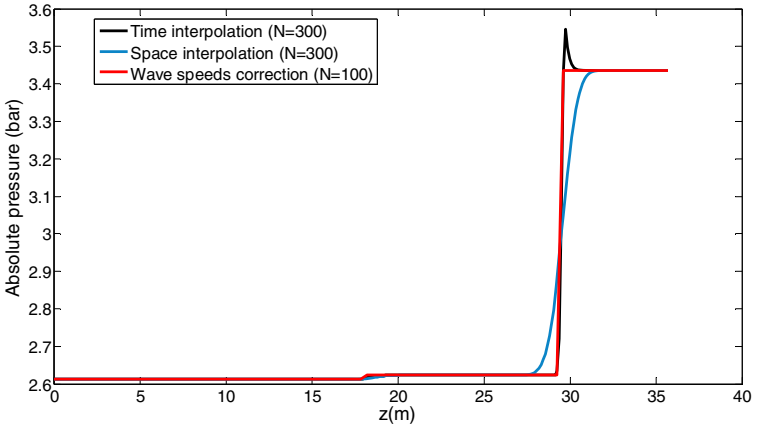

Fig. 6 Water hammer and precursor waves at time t=1/4 period of stress wave

6 Conclusion

The Hadj Taïeb experiment in quasi-rigid thin pipes in case of water hammer without cavitation is numerically simulated by the MOC. The algorithm proposed for the wave speeds correction method is simple and useful for simulation of any hydraulic problem. Any interpolations are necessary which minimize the time of calculation comparatively with other algorithms.

Codes implemented in *Matlab* show that the time interpolation method and wave speeds correction method are in good agreement either for absolute pressure history at the valve or precursor wave at the beginning of transient flow.

Disagreements shown between numerical and experimental results may be attributed to the sampling step problem of the measuring instrument (some pressure values cannot be detected) and to the definition of boundary conditions.

In other works, the algorithm can be tested for pipes with junction coupling and in case of water hammer with distributed cavitation.

Acknowledgements. The authors gratefully acknowledge the helpful comments and suggestions of the reviewers, which have improved the presentation. They also thank for the financial supports provided by the MFAGPE Laboratory.

References

Ghidawi, M.S., et al.: A review of water hammer theory and practice. Applied Mechanics Reviews 58, 49–76 (2005)

Hadj-Taïeb, E.: Ecoulement transitoires dans les conduits déformables avec cavitation de vapeur et dégazage de l'air dissous. Thèse d'Etat, Faculté des Sciences de Tunis (1999)

Tijsseling, A.S.: Exact solution of linear hyperbolic four-equation system in axial liquid-pipe vibration. Journal of Fluids and Structures 18, 179–196 (2003)

Tijsseling, A.S.: Fluid structure interaction in case of waterhammer with cavitation. PhD Thesis, Delft University of Technology, Faculty of Civil Engineering, Communication on Hydraulic and Geotechnical Engineering, Report No. 93-6, Delft, The Netherland (1993) ISSN 0169-6548

Tijsseling, A.S., et al.: Skalak's extended theory of water hammer. Journal of Sound and Vibration 310, 718–728 (2007)

Appendix

The algorithm developed for wave speeds correction method is implemented in *Matlab 2009*. The code can be used for any hydraulic problem. First, calculate real (often irrational) value of the wave speeds ratio n. Second, the rational number defined by two integers a and b is found. Finally, mass densities are changed in such a way that the ratio n is equal to the rational number ($n=b/a$).

The program is organized as follows:

1) Introduce all data: experiment parameters, integers a, b and N, wave, etc.
2) Define constants used for matrices and vectors:

$$\Sigma_F = \frac{2\nu\tilde{C}_F^{\,2}}{C_p^{\,2} - \tilde{C}_F^{\,2}}$$

$$\Sigma_p = \frac{\nu\rho_f R}{Ee}\frac{C_F^{\,2}\tilde{C}_p^{\,2}}{C_F^{\,2} - \tilde{C}_p^{\,2}}$$

$$k_{F1} = \left(\Sigma_F + 1\right) g \sin\gamma$$

$$k_{F2} = f\left(\frac{\Sigma_F \rho_f R}{4\rho_p\left(2R+e\right)e} - \frac{1}{4R}\right)$$

$$k_{p1} = \left(1+\left(1-2\nu\right)\Sigma_p\right) g sin\gamma$$

$$k_{p2} = f\left(\frac{\left(1-2\nu\Sigma_p\right)\rho_f R}{4\rho_p\left(2R+e\right)e} - \frac{\Sigma_p}{4R}\right)$$

3) Define matrices used for transient flow calculation

$\mathbf{M_0}$: matrix used to calculate boundary points at the reservoir

$$\mathbf{M_0} = \begin{bmatrix} 0 & 1 & 0 & 0 \\ 1 & -\tilde{C}_F\left(\frac{1}{\rho_f C_F^{\,2}} + \frac{\Sigma_F \nu R}{Ee}\right) & \Sigma_F & \frac{\Sigma_F \tilde{C}_F}{E} \\ 0 & 0 & 1 & 0 \\ \Sigma_p & -\tilde{C}_p\left(\frac{\Sigma_p}{\rho_f C_F^{\,2}} + \frac{\nu R}{Ee}\right) & 1-2\nu\Sigma_p & \frac{\tilde{C}_p}{E} \end{bmatrix}$$

$\mathbf{M_i}$: matrix used to calculate interior points

$$\mathbf{M_i} = \begin{bmatrix} 1 & \tilde{C}_F\left(\frac{1}{\rho_f C_F^{\,2}} + \frac{\Sigma_F \nu R}{Ee}\right) & \Sigma_F & -\frac{\Sigma_F \tilde{C}_F}{E} \\ 1 & -\tilde{C}_F\left(\frac{1}{\rho_f C_F^{\,2}} + \frac{\Sigma_F \nu R}{Ee}\right) & \Sigma_F & \frac{\Sigma_F \tilde{C}_F}{E} \\ \Sigma_p & \tilde{C}_p\left(\frac{\Sigma_p}{\rho_f C_F^{\,2}} + \frac{\nu R}{Ee}\right) & 1-2\nu\Sigma_p & -\frac{\tilde{C}_p}{E} \\ \Sigma_p & -\tilde{C}_p\left(\frac{\Sigma_p}{\rho_f C_F^{\,2}} + \frac{\nu R}{Ee}\right) & 1-2\nu\Sigma_p & \frac{\tilde{C}_p}{E} \end{bmatrix}$$

$\mathbf{M_L}$: matrix used to calculate boundary points at the valve

$$\mathbf{M_L} = \begin{bmatrix} 1 & \tilde{C}_F\left(\frac{1}{\rho_f C_F^{\,2}} + \frac{\Sigma_F \nu R}{Ee}\right) & \Sigma_F & -\frac{\Sigma_F \tilde{C}_F}{E} \\ 1 & 0 & -1 & 0 \\ \Sigma_p & \tilde{C}_p\left(\frac{\Sigma_p}{\rho_f C_F^{\,2}} + \frac{\nu R}{Ee}\right) & 1-2\nu\Sigma_p & -\frac{\tilde{C}_p}{E} \\ 0 & -A_f & \frac{m_v}{\Delta t} & A_p \end{bmatrix}$$

4) Calculate steady-state displacement at the valve:

$$u_z\Big|_{N+1}^{1} = -\frac{L^2}{2E}\left(\frac{\rho_f f R V_{z0}{}^2}{4e(2R+e)}(1-\nu)+\rho_f g\sin\gamma\left(1+\frac{\nu R^2}{(2R+e)e}\right)\right)$$

5) Calculate steady-state variables with main computational grid and refinement computational grid according to equations (9)-(12).
6) Calculate transient flow

1st step:

T=0;
j1=1;
For t=dt:dt:a*dt
T=[T,t];
j1=j1+1 ;

Interior points:

For i=2:N

$$\mathbf{Y_{i1}} = \begin{bmatrix} V_{zb}\Big|_{b(i-1)-j+2}^{1} & V_{zb}\Big|_{b(i-1)+j}^{1} & V_{za}\Big|_{a(i-1)-j+2}^{1} & V_{za}\Big|_{a(i-1)+j}^{1} \\ p_b\Big|_{b(i-1)-j+2}^{1} & p_b\Big|_{b(i-1)+j}^{1} & p_a\Big|_{a(i-1)-j+2}^{1} & p_a\Big|_{a(i-1)+j}^{1} \\ \dot{u}_{zb}\Big|_{b(i-1)-j+2}^{1} & \dot{u}_{zb}\Big|_{b(i-1)+j}^{1} & \dot{u}_{za}\Big|_{a(i-1)-j+2}^{1} & \dot{u}_{za}\Big|_{a(i-1)+j}^{1} \\ \sigma_{zb}\Big|_{b(i-1)-j+2}^{1} & \sigma_{zb}\Big|_{b(i-1)+j}^{1} & \sigma_{za}\Big|_{a(i-1)-j+2}^{1} & \sigma_{za}\Big|_{a(i-1)+j}^{1} \end{bmatrix}$$

$$\mathbf{N_{i1}} = \mathbf{M_i}\,\mathbf{Y_{i1}}$$

$\mathbf{n_{i1}} = diag(\mathbf{N_{i1}})$; the function (diag) writes a vector by a matrix diagonal.

$$\mathbf{k_{i1}} = (j-1)\Delta t\begin{bmatrix} k_{F1}+k_{F2}V_{zb}\Big|_{b(i-1)-j+2}^{1}\Big|V_{zb}\Big|_{b(i-1)-j+2}^{1}\Big| \\ k_{F1}+k_{F2}V_{zb}\Big|_{b(i-1)+j}^{1}\Big|V_{zb}\Big|_{b(i-1)+j}^{1}\Big| \\ k_{p1}+k_{p2}V_{za}\Big|_{a(i-1)-j+2}^{1}\Big|V_{za}\Big|_{a(i-1)-j+2}^{1}\Big| \\ k_{p1}+k_{p2}V_{za}\Big|_{a(i-1)+j}^{1}\Big|V_{za}\Big|_{a(i-1)+j}^{1}\Big| \end{bmatrix}$$

$$\mathbf{s_{i1}} = \mathbf{n_{i1}} + \mathbf{k_{i1}}$$

$\mathbf{M_i y} = \mathbf{s_{i1}}$; $\mathbf{y}$ is the unknown vector: $\mathbf{y} = \left[V_z\Big|_i^j ; p\Big|_i^j ; \dot{u}_z\Big|_i^j ; \sigma_z\Big|_i^j\right]$

end

Boundaries

Boundary points are calculated as described for interior points by writing new vectors $\mathbf{s_{01}}$ and $\mathbf{s_{L1}}$.

Unknown vectors $\mathbf{y_0}$ at the reservoir and $\mathbf{y_L}$ at the valve are:

$$\mathbf{y_{01}} = \left[V_z \Big|_1^j ; p \Big|_1^j ; \dot{u}_z \Big|_1^j ; \sigma_z \Big|_1^j \right]$$

$$\mathbf{y_{L1}} = \left[V_z \Big|_{N+1}^j ; p \Big|_{N+1}^j ; \dot{u}_z \Big|_{N+1}^j ; \sigma_z \Big|_{N+1}^j \right]$$

They are obtained by solving the equations:

$$\mathbf{M_0 y_0 = s_{01}}$$

$$\mathbf{M_L y_L = s_{L1}}$$

Save data in matrices defined at the beginning.

Calculate displacement at the valve.

end

Finally, Step 2 and step 3 are calculated as described in step 1, according to computational grids presented in figures 3 and 4.

Energetic Analyses of a NH_3-NaSCN Absorption Machine Operating at Three Pressure Levels

Ridha Ben Iffa, Lakdar Kairouani, and Nahla Bouaziz

UR EE, ENIT, BP37, le Belvédère 1002, Tunisie
r.iffa@yahoo.fr,
lakdar_kairouani@yahoo.fr,
nahlabouaziz@yahoo.fr

Abstract. This study proposes a refrigeration cycle operating on a compression-absorption cycle. This instalation can improve the performance of an absorption refrigeration machine energy consuming low exergy value. This installation uses the NH_3-NaSCN as refrigerant. In addition this cycle is working at three pressure levels, the absorber is operated at an intermediate pressure (Pint) between the pressures, P_{EV} and P_{CD}, for temperatures of evaporation and condensation, respectively (-10°C, 40°C). The machine operates at a temperature of generator T_{GE} = 53 ° C and presents a COP of 0.60. For the same conditions the single stage machine presents a COP of not more than 0.55 at a generator temperature of 140 ° C.

Keywords: Absorptions, COP, evaporator, refrigerant, NH_3 - NaSCN.

Abbreviations: COP, Coefficient of performance; **f,** circulation ratio; **h,** specific enthalpy (J/kg); $\dot{m}$,mass flow rate(kg/s); **P,** pressure (bar, Pa); $\dot{Q}$ heat-transfer rate (W); **T,** temperature (K, °C); **x,** mass fraction. **Subscripts: AB,** Absorber; **CD,** condenser; **COM,** compressor; **EV,** evaporator; **GE,** generator; **η,** efficiency (%).

1 Introduction

Absorption machines have several advantages such as protecting the environment and the nature, this type of refrigerating machine does not use CFCs fluids (chlorofluorocarbons), which attack the ozone layer (Kang et al.2000 ;Boer et al.1987 ;Göktun 2000 ; Laouir et al. 2002), besides they are quiet compared to vapor compression machines (Riffat and Guoquan 2004).

There are several models of absorption machines, can be found by a simple compound machines floor that is to say a single absorber, an evaporator, a condenser and a single generator, which are the conventional absorption machine. This machine is working between two pressure levels (PEV evaporator pressure and PCD condenser pressure) has been the subject of several studies (Alvares and Trepp 1987; Misra et al. 2002; Mumah et al. 1994 ; Kouremenos 1985; Hulten and Berntsson 2002; Selahattin 1999).

M. Haddar et al. (Eds.): *Design and Modeling of Mechanical Systems*, LNME, pp. 265–272.
DOI: 10.1007/978-3-642-37143-1_32

Other models are constituted by different stages with different associations between the system components; they worked at three pressure levels (Saghiruddin and Siddiqui 2001; Bouaziz et al.2011; Charia et al.1991 ; Kumar 1993 ; Sun 1998). There is a wide range of torque that can be used for the refrigerating machine such us NH3/H2O, NH3/NaSCN and NH3/LiNO3 (Sun 1998 ; Rodakis and Antonopoulos 1995; Linghui and Junjie 2010; Kairouani et al. 2005).

2 Modeling System

Fig.1 shows the system analyzed. This machine is composed of an evaporator, an absorber, a generator, a condenser and a compressor which functions: bring the vapor leaving the evaporator to an intermediate pressure ($\mathbf{P_{AB}}$).

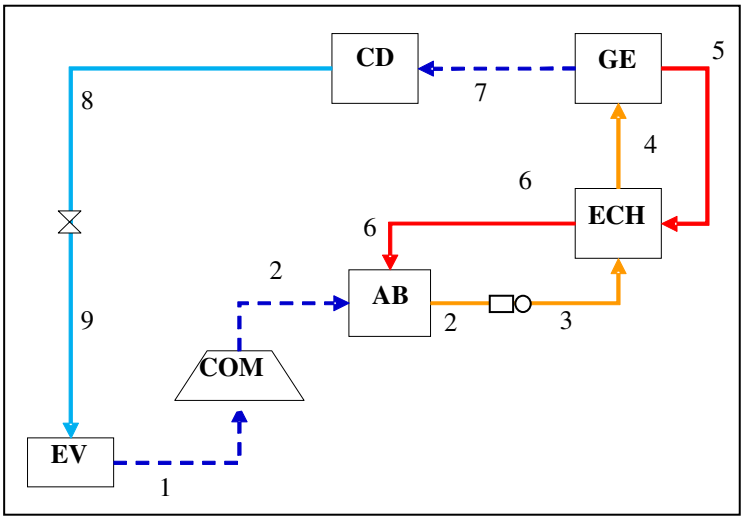

Fig. 1 Absorption system

2.1 The Generator GE

The refrigerant-rich solution **(4)** receives the quantity of heat $\mathbf{Q_{GE}}$ at a temperature $\mathbf{T_{GE}}$ causing refrigerant vaporization portion of dissolved in the solution. This phenomenon called desorption. At the output of the generator, we obtain a refrigerant vapor **(7)** and a refrigerant-depleted solution **(5)**.

2.2 The Condenser CD

The condenser is a component similar to that of vapor compression machines. This is the temperature of the fluid colporteur eating the condenser who fixes the

condensation temperature $\mathbf{T_{CD}}$ and therefore the pressure overall desorber /condenser. The condensation of the refrigerant requires the rejection of the heat of condensation $\mathbf{Q_{CD}}$ to the temperature $\mathbf{T_{CD}}$.

2.3 The Evaporator EV

At the outlet of the condenser **(8)**, the liquid suffers a lamination through the expansion valve **(9)**, and then evaporate taking the heat $\mathbf{Q_{EV}}$ to the fluid or to the enclosure to cool. The evaporation temperature and consequently the pressure in the evaporator-absorber assembly is fixed by the temperature of the cold source $\mathbf{T_{EV}}$.

2.4 The Absorber AB

The vapor from the compressor **(2)** enhances the solution in the absorber. This is called absorption. The heat $\mathbf{Q_{AB}}$ released by this exothermic is removed by a heat transfer fluid at the temperature $\mathbf{T_{AB}}$. At the exit of the absorber **(3)**, we obtain a solution enriched with refrigerant.

2.5 The Compressor

At the outlet of the evaporator **(1)** the compressed vapor by a compressor to the absorber **(3)**.

It has three levels of pressure:

- Low pressure ($\mathbf{BP=P_{EV}}$)
- Medium pressure ($\mathbf{MP=P_{AB}}$)
- High pressure ($\mathbf{HP=P_{CD}=P_{GE}}$)

Energy balance and mass

The circulation ratio is the flow rate of the rich solution permits to generate a one kg of NH_3 of the generator.

$$f = \frac{1 - x_5}{x_4 - x_5} \tag{0}$$

We perform the energy balances in each system component, exchanging heat or work with the external environment. Neglecting the rectifier, we obtain:

$$\dot{m}_6 = \dot{m}_7 = \dot{m}_{NH3} \tag{1}$$

$$T_7 = T_{CD} \tag{2}$$

$$h_7 = h(T_{CD}) \tag{3}$$

$$P_7 = P(T_{CD}) = P_{CD} \tag{4}$$

$$\dot{Q}_{CD} = \dot{m}_{NH3} \cdot (h_6 - h_7) \tag{5}$$

$$\dot{m}_8 = \dot{m}_7 = \dot{m}_{NH3} \tag{6}$$

$$T_1 = T_{EV} \tag{7}$$

$$h_8 = h_7, \; h_1 = h(T_{EV}) \tag{8}$$

$$P_8 = P_1 = P(T_{EV}) = P_{EV} \tag{9}$$

$$\dot{Q}_{EV} = \dot{m}_{NH3} \, (h_1 - h_8) \tag{10}$$

$$\dot{m}_4 = \dot{m}_6 + \dot{m}_5 \tag{11}$$

$$P_6 = P_5 = P_4 = P_{CD} \tag{12}$$

$$T_6 = T(x_4, P_{CD}), T_5 = T_{GE} \tag{13}$$

$$x_5 = x(T_5, P_{CD}), \; x_4 = x_5 + \Delta x \tag{14}$$

$$h_6 = h(x_4, P_{CD}), h_5 = h(x_5, P_{CD}) \tag{15}$$

$$\dot{Q}_{GE} = \dot{m}_{NH3}(h_6 + (f - 1) \cdot h_5 - f \cdot h_4) \tag{16}$$

To determine the power of the latter, we will make the following assumption:

At the outlet of the evaporator EV ammonia vapor is treated as an ideal gas, so we have:

$$T_1 \times P_1^{(k-1)/k} = T_2 \times P_2^{(k-1)/k} \tag{17}$$

In an ideal case (adiabatic process frictionless), it consumes a power:

$$\dot{Q}_{is} = cp_{NH3} \times (T_2 - T_1) \tag{18}$$

Considering the isentropic efficiency, the real power is defined as follows:

$$\dot{Q}_{réel} = \frac{\dot{Q}_{is}}{\eta_{is}} \tag{19}$$

With:

$$\dot{Q}_{réel} = h_2 - h_1 \tag{20}$$

Therefore it can be deduced from (19) and (20) the value of the steam enthalpy at the compressor outlet:

$$h_2 = h_{1p} + \frac{\dot{Q}_{is}}{\eta_{is}} \tag{21}$$

The term performance is determined as follows (Kairouani et al. 2005):

$$\eta_{is} = 0.874 - 0.0135 \cdot \tau \tag{22}$$

$$\tau = \frac{P_2}{P_1} \tag{23}$$

$$\dot{m}_2 = \dot{m}_3 \tag{24}$$

$$x_3 = x_2 \tag{25}$$

$$T_3 = T_{CD} \tag{26}$$

$$\dot{Q}_{AB} = \dot{m}_{NH3}(h_2 - h_3) \tag{27}$$

Calculating the coefficient of performance from equations (10) and (16):

$$COP = \frac{\dot{Q}_{Ev}}{\dot{Q}_{GE} + \dot{Q}_{COM}} ; COP = \frac{h_1 - h_2}{h_7 + (f-1).h_5 - f.h_4 + h_2 - h_1} \tag{28}$$

3 Results

3.1 COP Evolution versus T_{GE}

For a condensation temperature of 40 ° C and an evaporation temperature of -10 ° C, Fig.2, shows the coefficient of performance variation according to the temperature of generator 80 ° C to 140 ° C. We note that the conventional machine does

not work at generator temperatures below 105 °C. Under these conditions the COP reaches 0.55. In the other side the new machine works from 88 ° C, the COP is slightly higher for single stage machine.

In comparison of the conventional cycle, the new machine operates at relatively low temperature, and has a higher COP.

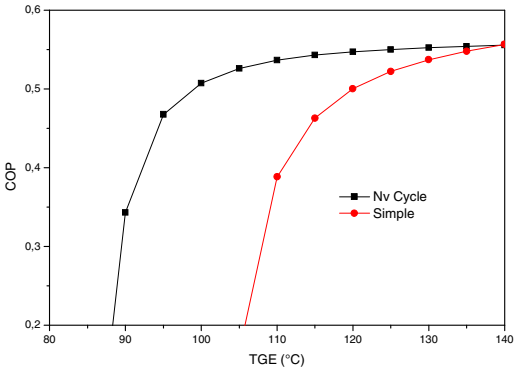

Fig. 2 COP=f (T_{GE}) with T_{EV}= -10°C and T_{CD}=40°C

3.2 COP Evolution versus T_{CD}

We keep the generator temperature and the evaporator temperature fixed respectively at 80 ° C and -5 ° C, while the temperature of condensation varies for each cycle. The analyses of Fig.3 shows that the new cycle can operate for condensing temperatures above 35 ° C, besides COP values are relatively higher than those relative to the conventional cycle.

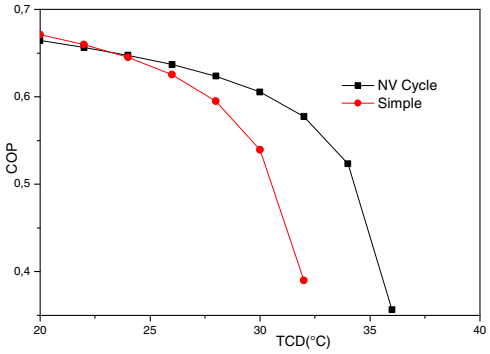

Fig. 3 COP=f (T_{CD}) with T_{EV}= -5°C and T_{GE}=80°C

We note that the present installation presents a higher COP than the conventional machine; it operates at low generator temperature and works with high condenser temperatures. On the other hand, the absorption system object of this work has an operational problem with high temperatures at the generator.

References

Kang, Y.T., Kunugi, Y., Kashiwagi, T.: Review of advanced absorption cycles: performance improvement and temperature lift enhancement. Int. J. Refrig. 23, 388–401 (2000)

Boer, D., Valles, M., Coronas, A.: Performance of double effect absorption compression cycles for air–conditioning using methanol–TEGDME and TFE–TEGDME systems as working pairs. Int. J. Refrig. 21, 542–555 (1998)

Göktun, S.: Performance analysis of a heat engine driven combined vapor compression-absorption-ejector refrigerator. Energy Convers. Mgmt. 41, 1885–1895 (2000)

Laouir, A., Legoff, P., Hornt, J.M.: Cycle de frigopmpes à absorption en cascades matérielles–détermination du nombre d'étages optimal pour le mélange ammoniac–eau. Int. J. Refrig. 25, 136–148 (2002)

Riffat, S.B., Qiu, G.: Comparative investigation of thermoelectric air-conditioners versus vapour compression and absorption air-conditioners. App. Th. Eng. 24, 1979–1993 (2004)

Alvares, S.G., Trepp, C.: simulation of solar driven aqua-ammonia absorption refrigeration system. Int. J. Refrig. 10, 40–49 (1987)

Misra, R.D., Sahoo, P.K., Gupta, A.: Application of the exergetic cost theory to the LiBr/H2O vapour absorption system. Energy 27, 1009–1025 (2002)

Mumah, S.N., Adefila, S.S., Arinze, E.A.: First law thermodynamic evaluation and simulation of ammonia-water absorption heat pump systems. Energy Convers. Mgmt. 35, 737–750 (1994)

Kouremenos, D.A.: A tutorial on reversed NH3/H2O absorption cycles for applications. Solar Energy 34, 101–115 (1985)

Hulten, M., Berntsson, T.: The compression/ absorption heat pump cycle-conceptual design improvements and comparisons with the compression cycle. Int. J. Refrig. 25, 487–497 (2002)

Göktun, S.: Optimal performance of an irreversible, heat engine-driven combined vapour compression and absorption refrigerator. Applied Energy 62, 67–79 (1999)

Saghiruddin, M., Siddiqui, A.: Economic analysis of two stage dual fluid absorption cycle for Optimizing generator temperatures. Energy Conversion and Management 42, 407–437 (2001)

Bouaziz, N., Ben Iffa, R., Kairouani, L.: Performance of a water ammonia absorption system operating at three pressure levels. JMER 3, 120–127 (2011)

Bouaziz, N., Ben Iffa, R., Kairouani, L.: Avantage d'une configuration de machine à absorption operant à trios niveaux de pression. Mécanique & Industries 12, 103–107 (2011)

Charia, M., Pilatte, A., Bouidida, M.: Machine frigorifique à absorption (eau-ammoniac) fonctionnant avec des capteurs plans sur le site de Rabat. Rev. Int. Froid 14, 297–303 (1991)

Kumar, S.: Experimental studies of a three-pressure absorption refrigeration cycle. Rev. Int. Froid 16, 31–39 (1993)

Rodakis, E.D., Antonopoulos, K.A.: Thermodynamic cycle, correlations and nomograph for NH3-NaSCN absorption refrigération systems. Heat Recovery Systems & CHP 15, 591–599 (1995)

Zhu, L., Gu, J.: Second law-based thermodynamic analysis of ammonia/sodium Thiocyanate absorption system. Renewable Energy 35, 1940–1946 (2010)

Kairouani, L., Nahdi, E., Ben Iffa, R.: Thermodynamic investigation of tow stage absorption refrigeration system connected by a compressor. Am. J. App. Sc. 2(6), 1036–1041 (2005)

Numerical Study of Anti-ram of Hydraulic Lines by an Additional Viscoelastic Pipe

Lamjed Hadj-Taïeb, Sami Elaoud, and Ezzeddine Hadj-Taïeb

Laboratory of Applied Fluids Mechanics,
Process Engineering and Environmental, ENIS,
P.B. 1173, 3038 Sfax, Tunisia
{lamjed.hadjtaieb,ezed.hadj}@enis.rnu.tn
elaoudsa@yahoo.fr

Abstract. The purpose of this paper is to study numerically the effect of adding a short viscoelastic pipe in series with a main quasi-rigid pipe on water hammer phenomenon. The model takes into account the viscoelastic behaviour of the added pipe. The governing equations of such phenomenon are two coupled, non linear, hyperbolic, partial equations. The fluid pressure and velocity are considered as two principal dependant variables. The problem has been solved by the non linear method of characteristics. The obtained results show that the deformability of the additional pipe reduces the celerity of pressure waves and significantly alleviates the pressure fluctuations.

Keywords: anti-water hammer, fluid-structure interaction, viscoelastic behaviour, method of characteristics, transient flow.

1 Introduction

Hydraulic networks are subject to pressure variations in transient. These variations can be very important in some cases and can destroy these facilities.

Inside a pipe, the unexpected changes in flow regime of a fluid frequently caused by fast opening and closing of valves, sudden stopping and starting of pumps, etc., result in instantaneous pressure changes called water hammer. The intensity of water hammer is more important if the fluid is a liquid and if the variation of the flow is brutal. The need to protect the hydraulic systems against this phenomenon is necessary.

Several anti-ram devices are used to protect hydraulic systems (Frelin 2002, Wylie and Streeter 1978), such as: flywheels, relief valves, air tanks, chimneys and balance balls protection. The role of these devices is to reduce transient effects. In many cases, due to economic and technical reasons, the use of these protective devices is difficult. Then, the use of a simple, efficient and economical anti-ram device is necessary.

The idea of using a short deformable pipe in series with the main pipe as a mean of anti-water hammer already explored in the past (Grundy and Fox 1980, Massouh and Comolet 1984). However, these studies are limited to additional

M. Haddar et al. (Eds.): *Design and Modeling of Mechanical Systems*, LNME, pp. 273–280.
DOI: 10.1007/978-3-642-37143-1_33

pipes with elastic behaviour (such as rubber), and pipe with viscoelastic behavior has not been investigated.

A numerical study has been developed by (Ghilardi and Paoletti 1986) to see the possibility to lower pressure surges in a rigid pipe by in series addition of short polymeric viscoelastic pipe. The obtained results show the efficiency of this solution on the pressure surge reduction. However, this solution has not been extended to see its effect on the depression and to avoid vapour cavitation.

The objective of this work is to numerically study the protection of water facilities against the phenomenon of water hammer by the junction of a deformable segment in series with the pipe to be protected. More precisely, we will examine the role that could have a viscoelastic behavior in reducing water hammer overpressures and negative pressures (cavitation phenomenon) due to transient flows.

In this study, we proceed to develop a mathematical model through the simplified formulations for the transient flow of fluid in quasi-rigid and viscoelastic cylindrical pipes.

The characteristics method is used for the numerical solution of the obtained equations. The viscoelastic behavior of the additional pipe wall material is simulated by a generalized Kelvin-Voigt model.

Various cases are discussed to demonstrate the effectiveness of the protection of water facilities by a deformable segment and to examine the effect of some parameters on the reliability of this anti-ram.

2 Mathematical Formulations

The continuity and momentum equations that describe one-dimensional transient flow in horizontal pipe are (Wylie et al. 1993):

$$\begin{cases} \dfrac{\partial(\rho A)}{\partial t}+\dfrac{\partial(\rho A V)}{\partial x}=0 \\ \dfrac{\partial V}{\partial t}+V\dfrac{\partial V}{\partial x}+\dfrac{1}{\rho}\dfrac{\partial p}{\partial x}=-\dfrac{\lambda V|V|}{2D} \end{cases} \tag{1}$$

where ρ is the density of the fluid, λ is the coefficient of linear loss, A is the pipe cross-sectional area, D is the pipe diameter, t is the time and x is the coordinate along the pipeline axis. The two main variables are the average velocity of flow, V, and pressure of the fluid, p.

Assuming quasi-rigid pipe and using the equation of state of the liquid (Shames 1982) and Hooke's law, the system of equations (1) becomes

$$\begin{cases} \dfrac{1}{\rho C^2}\left(\dfrac{\partial p}{\partial t}+V\dfrac{\partial p}{\partial x}\right)+\dfrac{\partial V}{\partial x}=0 \\ \dfrac{\partial V}{\partial t}+V\dfrac{\partial V}{\partial x}+\dfrac{1}{\rho}\dfrac{\partial p}{\partial x}=-\dfrac{\lambda V|V|}{2D} \end{cases} \tag{2}$$

The pressure wave celerity, C, is defined by the following expression (Stuckenbruck et al. 1985):

$$C = \left(\frac{\rho}{K} + \rho \frac{cD}{Ee} \right)^{-1/2} \tag{3}$$

where K is the bulk modulus of liquid, c is the pipe constraint factor, e is the pipe-wall thickness and E is the Young's modulus of elasticity of the pipe.

For viscoelastic pipes, they have different behavior in comparaison with metal and concrete pipes. In this case, strain can be decomposed into an instantaneous elastic strain, ε_ϕ^e, and retarded strain, ε_ϕ^r:

Taking into account the relationship between the pipe cross-section A and the total circumferential strain ε_ϕ^e ($dA/d\varepsilon_\phi = 2A$), the elastic strain, the retarded strain and the state equation of a barotropic fluid, the equations system (1) becomes (Covas et al. 2005, Hadj-Taieb and Hadj-Taieb 2009):

$$\begin{cases} \dfrac{\partial p}{\partial t} + V \dfrac{\partial p}{\partial x} + \rho C^2 \dfrac{\partial V}{\partial x} + 2\rho C^2 \left(\dfrac{\partial \varepsilon_\phi^r}{\partial t} + V \dfrac{\partial \varepsilon_\phi^r}{\partial x} \right) = 0 \\ \dfrac{\partial p}{\partial x} + \rho \left(\dfrac{\partial V}{\partial t} + V \dfrac{\partial V}{\partial x} \right) + \rho \dfrac{\lambda V |V|}{2D} = 0 \end{cases} \tag{4}$$

The retarded circumferential strain is represented by a generalized Kelvin-Voigt model of n elements:

$$\varepsilon_\phi^r = \sum_{j=1}^{n} \varepsilon_{\phi,j}^r (x,t) = \sum_{j=1}^{n} \left\{ \frac{cD}{2e} \int_0^t \left[p(x, t-t') - p_0(x) \right] \frac{J_j}{\tau_j} e^{-t'/\tau_j} dt \right\} \tag{5}$$

where J is the creep compliance function described by (Covas et al. 2005):

$$J(t) = J_0 + \sum_{j=1}^{n} J_j \left(1 - e^{-t/\tau_j} \right) \tag{6}$$

in which J_0 represents the creep-compliance of the first spring, J_j is the creep-compliance of the spring of j-element and τ_j is the retardation time of the dash-pot of j-element.

The retarded strain time-derivative in equations (5) is calculated by:

$$\frac{\partial \varepsilon_\phi^r}{\partial t} = \sum_{j=1}^{n} \frac{\partial \varepsilon_{\phi,j}^r (x,t)}{\partial t} = \sum_{j=1}^{n} \left\{ \frac{cD}{2e} \frac{J_j}{\tau_j} \left[p(x,t) - p_0(x) \right] - \frac{\varepsilon_{\phi,j}^r (x,t)}{\tau_j} \right\} \tag{7}$$

3 Numerical Resolution

The application of the method of characteristics to the system of equations (2) and (4) leads to the compatibility equations along the characteristic lines defined by:

$$\frac{\mathrm{d}V}{\mathrm{d}t} \pm \frac{1}{\rho C}\frac{\mathrm{d}p}{\mathrm{d}t} + \frac{\lambda V|V|}{2D} = 0 \tag{8}$$

for a quasi-rigid pipe, and

$$\frac{\mathrm{d}p}{dt} \pm \rho C \frac{\mathrm{d}V}{dt} + 2\rho C^2 \left(\frac{\partial \varepsilon_\phi^r}{\partial t}\right) \pm \rho C \frac{\lambda V|V|}{2D} = 0 \tag{9}$$

for a viscoelastic pipe.

Using a regular computational grid, the unknown values of (V , p), at any point **P** (i , $t+\Delta t$), can be determined by knowing their values at the points **R** ($i-1$, t) and **S** ($i+1$, t) lying on the two characteristics C^+ and C^- passing through **P**. Integrating equations (8) and (9) in the $x-t$ plane along the characteristic lines between time t and $t+\Delta t$ results in two finite difference equations:

$$C^+ : V_P - V_R + \frac{1}{\rho C}(p_P - p_R) + \frac{\lambda \Delta t}{2D} V_R |V_R| = 0 \tag{10}$$

$$C^- : V_P - V_S - \frac{1}{\rho C}(p_P - p_S) + \frac{\lambda \Delta t}{2D} V_S |V_S| = 0 \tag{11}$$

$$C^+ : p_p - p_R + \rho C (V_P - V_R) + 2\rho C^2 \Delta t \left(\frac{\partial \varepsilon_\phi^r}{\partial t}\right) + \rho \frac{\lambda C \Delta t}{2D} V_R |V_R| = 0 \tag{12}$$

$$C^- : p_p - p_S - \rho C (V_P - V_S) + 2\rho C^2 \Delta t \left(\frac{\partial \varepsilon_\phi^r}{\partial t}\right) - \rho \frac{\lambda C \Delta t}{2D} V_S |V_S| = 0 \tag{13}$$

valid along $\Delta x / \Delta t = \pm C$.

4 Applications and Results

4.1 Joining a Viscoelastic Pipe

To study the effects of an additional viscoelastic pipe joined in series to a steel main pipe the example of the hydraulic system presented by figure 1 is considered. The physical dimensions and material properties of the hydraulic installation are given in Table 1. Two materials of the added pipe, which have different viscoelastic behavior, are tested: polyethylene (PE) and polyvinyl chloride (PVC). The additional pipe has a length ranging between 2 m to 20 m.

Figure 2 shows the influence of the addition of a viscoelastic pipe on the transient pressure evolution. In the case of PE and PVC additional pipe, the initial

pressure magnitude is lowered significantly compared to that of a single main pipe. In fact, the initial overpressure reaches a value of 145 m for the single main pipe, 138 m and 90 m with PE and PVC additional pipe, respectively. This can be interpreted by the effect of energy dissipation of the viscous behavior of the additional pipe material which clearly damps the pressure wave.

Figure 3 shows the pressure evolution for different lengths of the PE and PVC additional pipe. It can be seen that the longer is the additional pipe the higher is the attenuation of the pressure surges. It is clear that the PVC pipe shows a better behavior and brings to very high damping of the pressure surge even when its length is very short. However, for the two materials, from a certain value, the length of the additional pipe has no effect on the pressure attenuation.

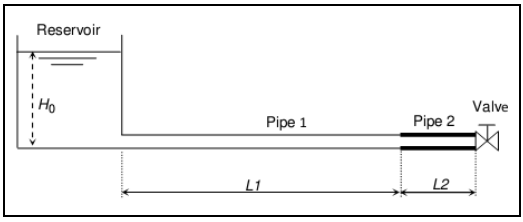

Fig. 1 Hydraulic installation scheme

Table 1 Properties of the hydraulic installation

Pipe length	$L_1 = 98\ m\ ,\ L_2 = 2\ m$
Pipe diameter	$D = 5\ cm$
Pipe thickness	$e = 3$ mm
Friction factor	$\lambda = 0.02$
Fluid density	$\rho = 1000\ \mathrm{Kg/m^3}$
Initial flow velocity	$V_{10} = 0.53\ \mathrm{m/s}$
Initial pressure	$p_{10} = 8$ bar

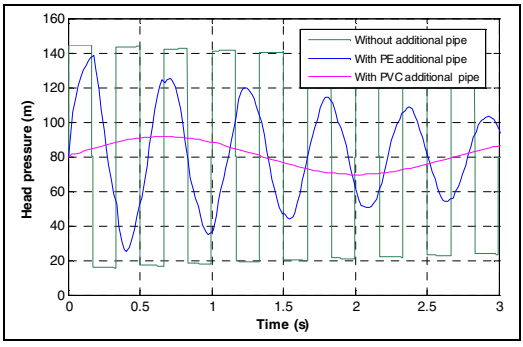

Fig. 2 Influence of adding a viscoelastic pipe on the transient pressure evolution

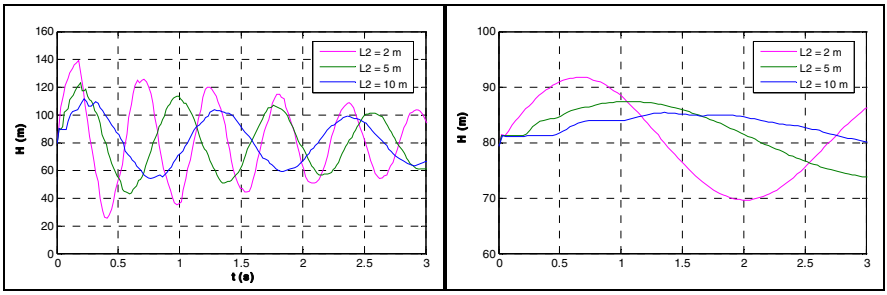

Fig. 3 Pressure evolution for different lengths of the additional pipe

4.2 Influence on Vapour Cavitation

To study the influence of adding viscoelastic pipe on vapour cavitation phenomenon numerical simulations are carried out by considering the experience of Martin (Martin 1983). In this experience water is supplied from a large header tank to a reservoir with steady-state water surface level at constant surface pressure. This is joined to quick closing valve at downstream end by a copper horizontal pipe. The transient flow is arised from the sudden closing of the valve.

Referring to Martin experiment results which are plotted in figure 4 by a dashed curve, it is clear that under transient conditions, the local liquid pressure falls below the vapour pressure p_v , and consequently vapour cavitation phenomenon occurs in some part of the pipeline.

Numerical simulation results (figure 4) show that, under the same transient conditions, adding a short viscoelastic pipe to the main pipe limits the pressure drop and the cavitation phenomenon is avoided.

It should be pointed out that results obtained by adding a PVC pipe are more consistent than those obtained by adding a PE pipe. In fact, with a PVC pipe the cavitation can be avoided even by a very short pipe (0.5 m).

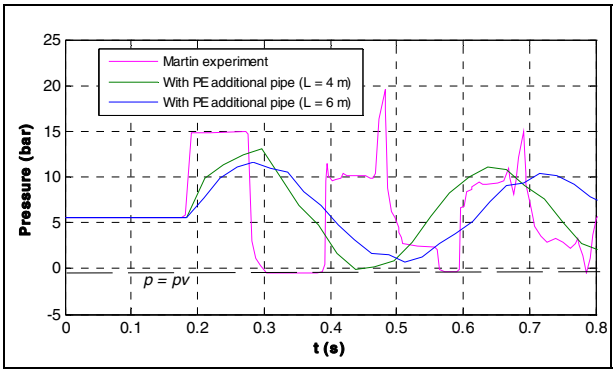

Fig. 4 Influence of adding viscoelastic pipe on vapour cavitation phenomenon

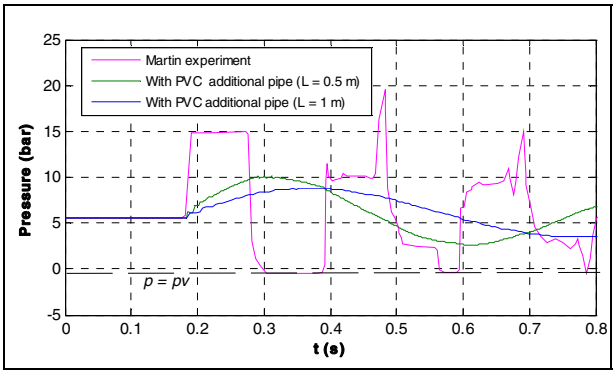

Fig. 4 (*continued*)

5 Conclusion

A numerical study of using a short viscoelastic pipe in series with a main pipe as an anti-ram is presented in this paper.

A mathematical model is developed based on the method of characteristics in which the viscoelastic behaviour of the additional pipe is simulated by a generalized Kelvin-Voigt model.

Taking into account the viscoelastic deformations has highlighted the role of the material behaviour which acts as a dissipative mechanism contributing significantly to the damping of pressure fluctuations caused by water hammer. Indeed, the introduction of the pipe wall deformability in the concept of modelling eliminated the excessive pressures encountered in the quasi-rigid behaviour.

The obtained results confirm that additional viscoelastic pipe can be useful device to attenuate the pressure surges and to avoid vapour cavitation phenomenon, of course with an optimal choice of dimensions and material characteristics.

This study also shows the effectiveness of the proposed models and the method of characteristics to give a reasonable description of the general appearance of the water hammer phenomenon in quasi-rigid and viscoelastic pipes.

References

Covas, D., Stoianov, I., Mano, J., Ramos, H., Graham, N., Maksimovic, C.: The dynamic effect of pipe-wall viscoelasticity in hydraulic transients. Part II- model development, calibration and verification. Journal of Hydraulic Research, IAHR 43(1), 56–70 (2005)

Frelin, M.: Coup de bélier, Techniques de l'Ingénieur, traité Génie mécanique. BM 4176, 1–27 (2002)

Ghilardi, P., Paoletti, A.: Additional viscoelastic pipes as pressure surges suppressors. In: 5th International Conference on Pressure Surges, Hannover, F.R. Germany (1986)

Grundy, A.K., Fox, J.A.: The effect of compressible pipe-liners on pressure transient generation. In: Pressure Surge, Paper E5, Canterbury, England, B.H.R.A. (1980)

Hadj Taieb, L., Hadj Taieb, E.: Numerical simulation of transient flow in viscoelastic pipes with vapour cavitation. International Journal of Modelling and Simulation 29(2), 206–213 (2009)

Martin, C.S.: Experimental investigation of column separation with rapid closure of downstream valve. In: Proceeding of the 4th International Conference on Pressure Surges, pp. 77–88. BHRA, Bath (1983)

Massouh, F., Comolet, R.: Etude d'un système anti-bélier en ligne. La Houille Blanche (5), 355–362 (1984)

Shames, I.H.: Mechanics of fluids, 2nd edn. McGraw-Hill Book Company, New York (1982)

Stuckenbruck, S., Wiggert, D.C., Otwell, R.S.: The influence of pipe motion on acoustic wave propagation. Transactions of the ASME 107, 518–522 (1985)

Wylie, E.B., Streeter, V.L.: Fluid Transients. McGraw-Hill, New York (1978)

Wylie, E.B., Streeter, V.L., Suo, L.: Fluid transient in systems. Prentice-Hall, Englewood Cliffs (1993)

Study of Erosion Phenomenon in the CFM56-7B Turbojet

Zohra Labed and Djamel Ghechi

Laboratory of Mechanics University of Constantine 1,
Faculty of Technology Sciences,
Campus Chaab Ersas, 25000 Constantine, Algeria
Zohra_labed@yahoo.fr,
djamelaeronautique@gmail.com

Abstract. Since the early days of aviation, the man has not stopped looking for better performance to improve the reliability of the reactor during operation. This means that it must be free all possible defects (choice of materials, choice of treatment, and choice of implementation ...).he replacement cost in him even but also the potential damage caused with the environment and the threat with the life of the human beings.

Indeed, the design of turbo machinery, complex organs, which must withstand mechanical vibration, thermal and respond to heavy exploitation. These are the fins that determine the performance of the engine. They are subject to erosion, which is a surface phenomenon associated with the removal of material caused by repeated impact with solid particles of the material. This depends on the shape, the mass, the particle velocity, hardness and toughness.

The objective of this work focuses on the characterization and identification of damage mechanisms operating in facies wear fins HP CFM56-7B engine using non destructive testing is the method of X ray. The characterization showed a fretting wear located in the upper part of the fin that increases from the 6th to the 9th stage.

Keywords: Erosion, Compressor fins HP, Non destructive testing, X ray method, CFM56-7B Turbofan.

1 Introduction

The rotating parts of aeronautical turbomachineries are made of bladed disks which enable the transfer of energy from the air to the rotor [1]. These bladed disks are especially critical parts because their dimensioning has to meet strict requirements in terms of aerodynamical performance, aeroacoustics and mechanical resistance to rotation, temperature and aerodynamical loads. Components of the object of our work are HP blades. Moreover, they are also subject to erosion, which is a surface phenomenon associated with removal of material caused by repeated impact of solid particles on the material. This damage can be either macroscopic or microscopic.

M. Haddar et al. (Eds.): *Design and Modeling of Mechanical Systems*, LNME, pp. 281–287.
DOI: 10.1007/978-3-642-37143-1_34

The objective of the work focuses on the characterization and identification of damage mechanisms that are operating in the wear facies of fins of the reactor CFM56-7B using non-destructive testing method. Based on the specific of morphology of the wear, correlations have been established, and competition between different modes of damage has been highlighted.

In turbojets double-body, the turbine consists of one or more stages (stator-rotor) at high pressure (HP) and a second at low pressure.

Fig. 1 CFM56-7B Turbofan

2 Main Components of the Turbofan CFM56-7B

A turbojet is composed mainly of the following parts (figure 1):

- Compressors: two types
  - A low-pressure compressor comprising:
  - A floor fan
  - 4 floors and BP (Low Pressure) LPC (Low Pressure Compressor) (figure 2).
  - A high pressure compressor 9 stage HP (High Pressure) HPC (High Pressure Compressor)
- Combustion chamber:
  - Ring SAC (simple) or DAC (dual and optional)
- Turbine:
  - High pressure turbine 1 stage HPT (High Pressure Turbine)
  - Low pressure turbine LPT stage 4 (Low Pressure Turbine) [2].

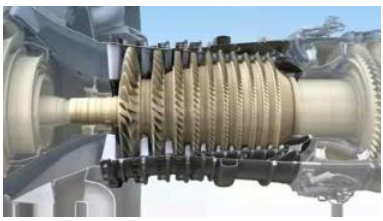

Fig. 2 Compressor

The HP turbine, whose blades are subject to the flow of combustion gases hottest room, is the most complicated in terms of keeping materials and aerodynamics. These fins are subject to several stresses as their speed of rotation, speed of fluids (Figure 3) and the pressure and temperature (that increasing or decreasing).

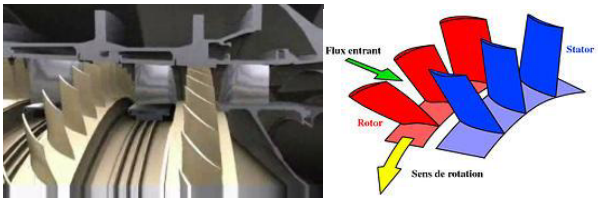

Fig. 3 Fin on disc (stator and rotor)

The diagram below shows a variety of damage (figure 4) that can undergo various components of a turbojet [3].

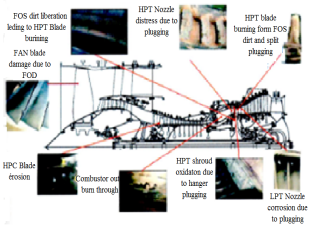

Fig. 4 Components damage reactor

3 Theory of Erosion

The erosion of materials by solid particles is a rather complex process. The shocks, between the solid particles and the surface of a material, result in the removal of material, characterized by brittle fracture. Types and sizes of cracks that form on the surface during impact are largely due to several factors: shape, mass, particle velocity, hardness and toughness of the material. When particles strike the surface at low angle of impact, the mechanism is called abrasive erosion (figure 4). When the abrasive sand strikes a surface, it rolls or slides on the surface, causing erosion by friction or cutting. Material is removed by scratching or breaking sharp edges of particles, forming small scars [4].

The components covered by this study (compressor blades) are also submitted to various constraints resulting in damage such as:

- The rupture that can be caused by shock "FOD": an external object or debris of another component;
- The erosion caused by sand or other particles in the air.

Erosion is a loss of material by impacts of particles suspended in a fluid.

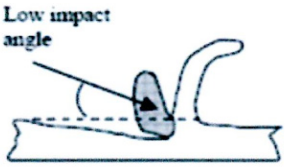

Fig. 5 Abrasive erosion

4 Factors Associated with Operating Conditions and Erosion Particle

The speed, the angle and impact of the particle are the most important parameters among all other factors, and applicable to all types of components where erosion occurs. These terms appear in the most erosion models.

The erosion rate increases with the duration of exposure to a constant value [5].

The angle of impact is defined as the angle between the surface and the path of the eroded particles, just before impact. The maximum erosion is observed between 10° and 0°, while the minimal erosion is observed around the normal to the impact.

The erosion mechanism may change depending on the characteristics of the particles. Characteristics can remain the same as the original, or change depending on operating conditions. Knowing the characteristics of the particles is very important to estimate, to reduce and to prevent erosion [6] some characteristics and particle effects are discussed here.

5 Experimental Method

The objective of this work is to detail the characteristics and the principle of technical analysis of these fins HPC CFM56-7B. In order to characterize them, we cut them and thus make samples according to the analyzes to be performed.

They have a small dimension, and are coated with a tungsten carbide at the top. It's of 6th, 7th, 8th, and 9th floor having suffered the phenomenon of erosive wear. Their wear is different at all points (figure 6).

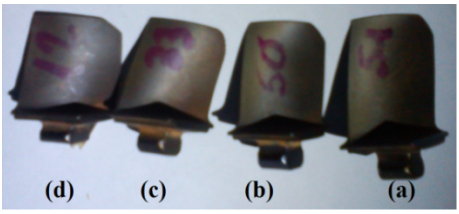

Fig. 6 Compressor fins Eroded HP: 6^{th} floor (a), 7^{th} floor (b), 8^{th} floor (c) and 9^{th} floor

We cut and prepared samples of the healthy part of the blade, for the characterization of base material: such as chemical composition, microstructure, X-ray diffraction and micro hardness tests. We are concerned with the characterization wear of facies. The characterization of damaged parts is to understand the mechanisms of damage in order to answer two questions:

How and why the injury occurred (mechanics)? For these reasons, the characterization of our samples was performed at macroscopic and microscopic scales.

We conducted a visual inspection of the surfaces of the fins shown in figure 7; we found a loss of material by erosion and a wear in the upper parts of the fins. The control by eddy current and penetrant revealed no defects.

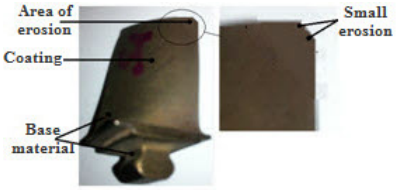

Fig. 7 Facie's wear of the 7th floor

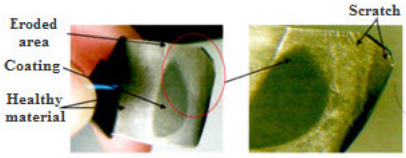

Fig. 8 Facie's wear of the 9th floor

Remember that this type of wear was found on the fins of aircraft engines which run regularly flying to southern Algeria. Therefore, we conclude that erosion is highlighted due to the nature and to metrology of sand. The Algerian desert sand (figure 9) consists of more than 90% of SiO_2 particles having an average particle size of 158 microns (figure 10).

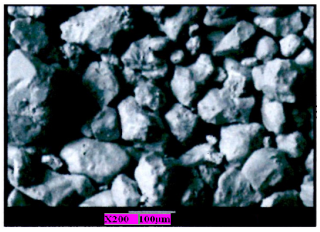

Fig. 9 SEM micrograph of sand grains in Algerian Desert

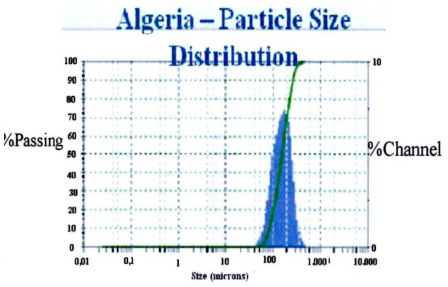

Fig. 10 Grain size of sand Algerian

On the edge's fins, we can see disappearance of a portion of the material; this phenomenon is even more pronounced in the case's fins of 9th floor (figure 11).

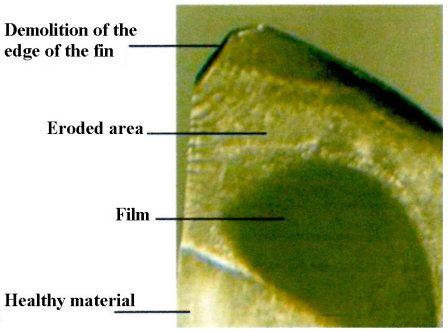

Fig. 11 Facie's wear of the 9th floor

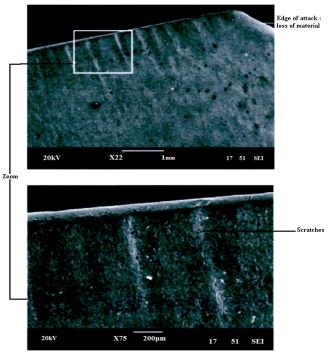

Fig. 12 SEM characterization of the area damaged by abrasive erosion of the 9th floor

In addition, the material removed by scratching, forming so a scars. We note that these scratches have an angular shape centered around the leading edge, that form may be due to the airflow (airflow loaded grain of sand).

This mechanism can be identify by fatigue wear. Indeed, according to the literature [6], that the particles hit a surface with a large angle of impact and a low speed, so the surface does not undergo plastic deformation. This surface is weakened by fatigue, and particle's detached from the surface after several impacts.

6 Conclusion

The various components of a turbojet can undergo various types of damage. Among these components, the compressor blades that have been the subject of this study, they are subject to various constraints that are causing damage, erosion caused by sand or other particles in the air.

The experimental study fins CFM56-7B turbofan, which has allowed us to see the effect of erosion.

Grained structure of heterogeneous size with the presence of deposit segregated at grain boundaries;

Porosity is likely to be caused by repeated impacts of sand grains. The dimensions of the fins may be also taking into consideration. Their size decreases from one floor to another, so at the last stage, the different constraints and impacts of sand particles will be concentrated on a surface, thus leading to greater wear.

References

[1] Technical data documentations, CFM56-7B turbofan engine (2011)
[2] Guide technique de base, d'Air Algérie (2012)
[3] Hariri, S.: Erodent particle characterization and the effect of particle size and shape on erosion. Wear (138) (1990)
[4] El Hussein, A.: Transport et stockage des dérives problématiques d'endommagement des pipes par érosion de sable et par hydrogène, Algérie (2010)
[5] Fridrici, V.: Fretting d'un alliage de titane revêt et lubrifié: application au contact aube/disque. Thèse de doctorat, Ecole Centrale de Lyon (2002)
[6] Vincent, L., Berthier, Y., Godet, M.: Testing methods in fretting: a critical appraisal. Standardization of Fretting Fatigue Test Methods and Equipment (1992)

FEA of In-Plane Shear Stresses of a Preloaded Sandwich Plate with a Viscoelastic Core: Application to the Disk Brake System

Maher Bouazizi[1], Tarek Lazghab[2], and Mohamed Soula[1]

[1] ESSTT, 5, Avenue Taha Hussein 1008 Tunis – Tunisia
bouazizi_maher@yahoo.fr,
Soulamed2003@Yahoo.fr
[2] IPEI El-Manar, P.O. Box 244, El Manar, Tunis 2092, Tunisia
lazghabt@yahoo.com

Abstract. In this work a study of the response of sandwich plates with a viscoelastic core used in brake systems to attenuate squealing noise due to friction between the disk and the pads. A finite element analysis is conducted to determine the in-plane shear stress distribution in the sandwich plate under various operating conditions. The effects of braking pressure, coefficient of friction between the disk and brake pads and angular speed of the disk on the in-plane shear stress are analyzed and compared. Results show that the coefficient of friction and braking pressure are the most influential compared to angular speed**.**

Keywords: Sandwich plate, Viscoelastic Core, Shear Stress, Finite Element Analysis, Brake system, Contact With Friction.

1 Introduction

Automotive disk brake systems produce a noise known as brake squeal. It is an undesirable phenomenon often associated with braking performance even though it has very little to do with it. One solution to mitigate brake squeal is to insert a sandwich plate behind the brake pads. The three-layer sandwich plate (metal/elastomer/metal) will dissipate the noise that would be generated from brake squeal during braking. Gacem et al. have studied the nonlinear dynamic behavior of a preloaded thin sandwich plate incorporating visco-hyperelastic layers used to attenuate noise in brake systems. Triches et al. have studied the effect of adding a sandwich plate with a viscoelastic core on brake squeal and showed this approach to be effective in reducing brake squeal occurrence. However, the sandwich plate is subjected to a combination of high shear stresses from braking friction and normal stresses from braking pressure. Under these conditions the sandwich plate may be damaged, especially during the braking phase. The sandwich plates are subjected to high shear stress and pressure due to braking. These loading conditions are not typical of sandwich plates. A large body of theoretical and experimental investigations of sandwich plate behavior from the past few decades is

M. Haddar et al. (Eds.): *Design and Modeling of Mechanical Systems*, LNME, pp. 289–296.
DOI: 10.1007/978-3-642-37143-1_35

available in. Several authors have studied the behavior of sandwich plates with a viscoelastic core. In most cases, sandwich plates are submitted to flexural loads, transverse shear in addition to in plane loading. Ramtekkar et al. studied the bending analysis of sandwich plates made of stiff face sheets and a soft core under various conditions and showed the shear stress distribution through the thickness to be discontinuous at the interface between the face sheet and the soft core. Cetkovic et al. presented the local–global analysis of laminated composite and sandwich plates using a layerwise displacement model; the effects of plate aspect ratio, side-to-thickness ratio, lamination angle schemes and degree of orthotropy on in-plane stresses, transverse shearing stresses, displacements, fundamental frequencies and critical buckling loads are shown. Reddy used the first order shear deformation theory based on the Reissner–Mindlin assumptions to study forced motions of rectangular composite plates. Pagano showed that the classical laminated plate theory gives acceptable solutions in the analysis of thin laminated composites. Choi analyzed the thermoelastic contact problem of disk brakes with frictional heat generation using the finite element method.

The analysis of preloaded sandwich plates under pure shear loading has not been treated extensively in the literature, especially for sandwich plates with a viscoelastic core. It is the objective of the current work to study the behavior of sandwich plates with a viscoelastic core used in disk brake systems. A parametric finite element study will be conducted to analyze the shear stresses in the sandwich plate under various operating conditions. The effects of the braking pressure P, the coefficient of friction μ between the pads and the disk and the angular speed ω of the disk will be considered

2 Model Description

2.1 Geometry

The simplified model of the brake system consists in a disk confined between two pads as shown in Figure 1 A viscoelastic sandwich plate is attached to the back of each pad as shown in Figure 2; it is composed of two thin steel layers and a viscoelastic core (steel/viscoelastic core/steel), their thicknesses are provided in Table 1.

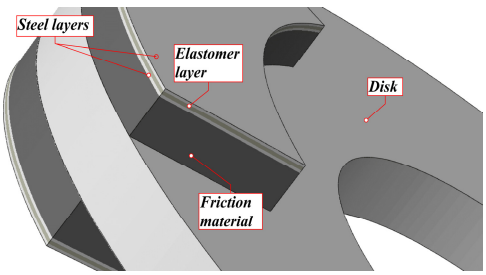

Fig. 1 Simplified model of a disk brake model

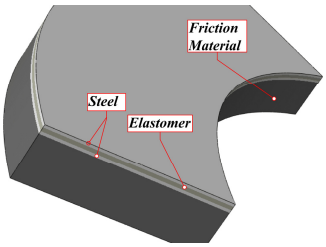

Fig. 2 Brake pad details

The geometric dimensions of the brake system are shown in Figure 3. R_D and r_D are the outer and the inner radii of the disk, respectively. R_P and r_P are the outer and the inner radii of the pad, respectively. θ is the subtended angle of the pad. e_D and e_P are the thickness of the disk and each pad, respectively. Table 1 provides a summary of the main geometric parameters of the disk brake assembly and their values.

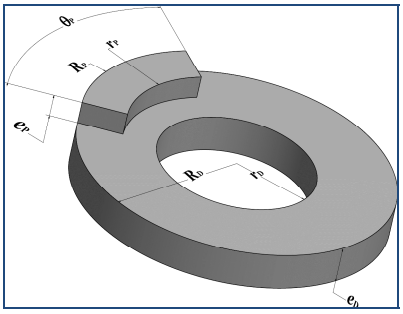

Fig. 3 Disk brake system geometric parameters

2.2 Materials

The materials used for the components of the brake system are elastic isotropic steel for the disk and external layers of the sandwich plate. The pads are made from brake shoe material essentially. The sandwich plate is made from steel layers and a viscoelastic polymer core. The relevant mechanical parameters of the materials for all these components are given in Table 2 below except for the polymer that will be discussed later

The polymer material behaves as a viscoelastic material with a shear stress relaxation modulus $G(t)$ given in terms of a Prony series as:

$$G(t) = G_0\left(1 - \sum_{i=1}^{N} g_i\left(1 - e^{-t/\tau_i}\right)\right) \tag{1}$$

Where $G_0 = G(0)$; $G_\infty = \lim_{t\to\infty} G(t)$; g_i and $\boldsymbol{\tau}_i$ are material parameters and given in Table 2 below. The Prony series data were obtained from [10].

Table 1 Geometric parameters and material properties of the disk brake components

Parameter	Unit	Disk	Pad
Young's modulus E	GPa	210	88.9
Density of disc ρ	kg/m^3	7850	7120
Poisson ratio ν	n/a	0.285	0.29
Thickness of rotor h	mm	16.0	10
Outer radius of disk R_D or R_P	mm	140	140
Inner radius of disk r_D or r_P	mm	70	100
Pad subtended angle θ	Degrees	-	62
Thickness of steel layer t_S	mm	-	0.8
Thickness of viscoelastic layer t_V	mm	-	0.4

Table 2 Prony series coefficients of the shear stress relaxation of the viscoelastic material

index i	g_i	τ_i (sec)
1	$3.9026\ 10^{-3}$	$5.1558\ 10^{-1}$
2	$9.7895\ 10^{-3}$	$1.03224\ 10^{-1}$
3	$2.0646\ 10^{-2}$	$1.7741\ 10^{-2}$
4	$5.7318\ 10^{-2}$	$3.6691\ 10^{-3}$
5	$1.3123\ 10^{-1}$	$7.2364\ 10^{-4}$
6	$2.7891\ 10^{-1}$	$1.5945\ 10^{-4}$
7	$4.9071\ 10^{-1}$	$3.1760\ 10^{-5}$
G_0 (MPa)	$9.2147\ 10^{6}$	

2.3 Finite Element Model

Mesh

A finite element model of the brake system assembly was built. It consists of two brake pads and the steel disk as shown in Figure 4. The friction material of the brake pads is modeled using C3D8R type elements (linear 8-noded continuum reduced integration brick elements with hourglass control). The sandwich plate is modeled using SC8R type elements (linear 8 noded continuum shell elements with reduced integration) for the three layers (metal/elastomer/metal). The disk is also modeled using continuum brick elements of type C3D8R. The general purpose finite element software package ABAQUS was used to conduct the simulations.

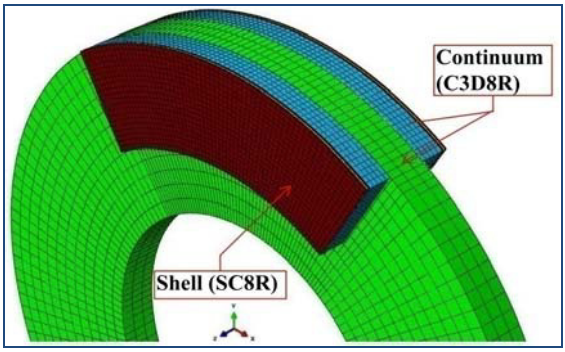

Fig. 4 Element types used in the finite element model

2.4 Parametric Study

A parametric study is conducted to analyze the behavior of the sandwich plate under various operating conditions of the disk brake system. The coefficient of friction μ, the angular speed ω and the braking pressure P are varied according to values given in Table 3 below.

Each case is identified by three subscripts (case)ijk subscript i (i= 0, 1,2) indicates the level of the coefficient of friction, subscript j (j=0, 1, 2) indicates the level angular speed and subscript k (k = 0, 1, 2) indicates the level of the braking pressure. For example in case CASE_101 corresponds to the parameter (μ = 0.40, ω = 10 rad/s, P=3 MPa) as indicated in Table 3. The parametric study will include 27 cases.

Table 3 Parameter values used for the current study

Level	0	1	2
Coefficient of friction μ	0.40	0.65	0.70
Angular speed ω (rad/s)	10	15	30
Braking pressure (MPa)	2	3	6

3 Numerical Results and Analysis

3.1 Contact Stress Distributions

The pressure distribution due to braking on the contact surface of the pad with the disk is shown for various values of the coefficient of friction in moderate (ω = 10 rad/s, P= 2 MPa) and severe braking conditions (ω = 30 rad/s, P = 6 MPa). Recall that the disk rotates in the positive z axis (see Figure 6). It can be seen that for the same value of the coefficient of friction the appearance of the contact pressure distribution is the same but the stress levels are higher for in the case of the severe

braking conditions (CASE_022, CASE_122, CASE_222). This is related directly to braking pressure. In fact the same observations could also be made about the contact shear stress in the tangential direction on the face of the brake pad in Figure 5.

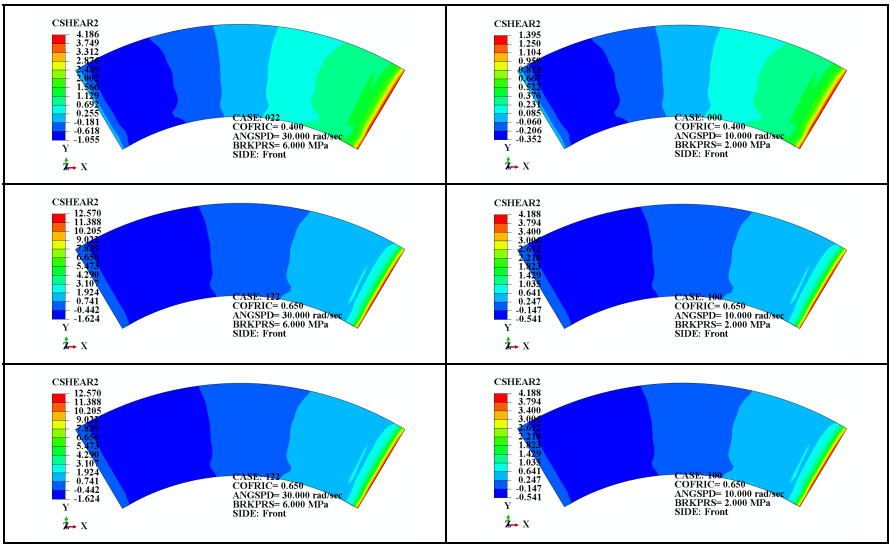

Fig. 5 Tangential contact shear stress distributions in severe and moderate conditions at several values of the coefficient of friction

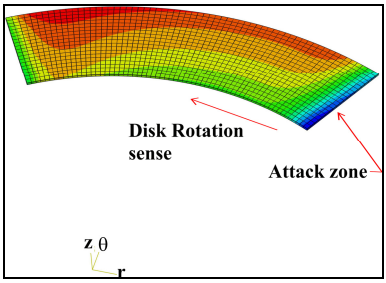

Fig. 6 Location of the attack zone in the viscoelastic core layer

3.2 Effect of Coefficient of Friction

In this study the coefficient of friction μ is varied while all other parameters are kept constant. The shear stress distribution in the viscoelastic layer will be presented; then the location of maximum in-plane shear is identified and the variation of shear stress vs. the thickness of the sandwich plate is presented at this location.

In Figure 9 are presented the shear stress distributions in the viscoelastic layer under severe and moderate braking conditions. The disk is rotating around the positive Z direction and the stresses are represented in a cylindrical coordinate system (r,θ, z) with origin at the center of the disk (see Figure 5). The shear stress distributions of the cases (*CASE_000, CASE_100, CASE_200*) correspond to moderate braking conditions (i.e. low pressure and low angular speed) whereas those corresponding to cases (*CASE_022, CASE_122, CASE_222*) are for severe braking conditions (high pressure and high angular speed). It can be seen that the shear stress distributions from both cases have the same aspect for equal values of the coefficient of friction. However, the stress levels in severe operating are approximately 3 times higher than their counterparts in the moderate operating conditions. This is again is due to the level of the braking pressure.

The shear stress maximum value increases with μ and its location drifts towards the attack zone of the pad as μ increases as shown in Figure 6 and Figure 7. The distribution of the shear stress is clearly non symmetric and depends on r and θ.

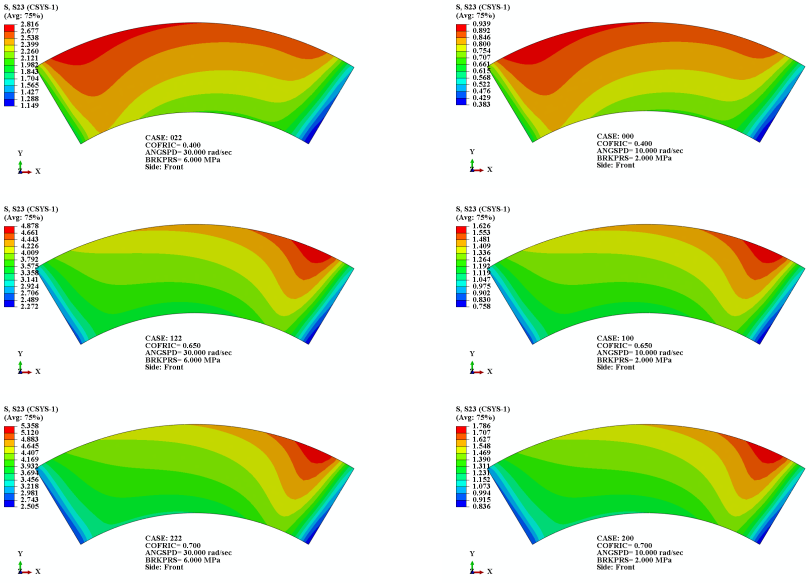

Fig. 7 The effects of coefficient of friction on shear stress in severe and moderate conditions at several values of the coefficient of friction

4 Conclusion

In this work a parametric study was conducted to determine shear stresses in the sandwich plate for various coefficients of friction, angular speed of the disk and breaking pressure. A finite element model was used to calculate the shear stresses of the model using the general purpose finite element software ABAQUS

(Karlsson).The numerical results show that the shear stresses in the viscoelastic layer of the sandwich plate are dependent on the coefficient of friction and the brake pressure and are independent of the angular speed of the disk. This is due to the assumption that the coefficient of friction is not dependent on angular speed. Variations in the coefficient of friction affect the amplitude of the shear stresses in the viscoelastic layer of the sandwich plate as well as there through the thickness distribution and the location of the maximum shear stress which drifts towards the attack zone as the coefficient of friction increases. Variations in the braking pressure affect the levels of the shear stresses without affecting their distribution. The conclusion of your paper is here.....

References

Choi, J.H., Lee, I.: Finite element analysis of transient thermoelastic behaviors in disk brakes. Wear 257(1), 47–58 (2004)

Ćetković, M., Vuksanović, D.: Bending, free vibrations and buckling of laminated composite and sandwich plates using a layerwise displacement model. Composite Structures 88(2), 219–227 (2009)

Gacem, H., Chevalier, Y., Dion, J., Soula, M., Rezgui, B.: Nonlinear dynamic behaviour of a preloaded thin sandwich plate incorporating visco-hyperelastic layers. Journal of Sound and Vibration 322(4-5), 941–953 (2009)

Herakovich, C.T.: Mechanics of composites A historical review. Mechanics Research Communications 41(0), 1–20 (2012)

Karlsson, H., Sorensen: ABAQUS v6.10: Hibbitt, Karlsson & Sorensen (2010)

Marie-Jose, P.: Comparison of Time-domain Finite Element Modelling of Viscoelastic Structures Using an Efficient Fractional Voigt-Kelvin Model Or Prony Series. McGill University (2001)

Moita, J.S., Araújo, A.L., Martins, P., Mota Soares, C.M., Mota Soares, C.A.: A finite element model for the analysis of viscoelastic sandwich structures. Computers & Structures 89(21-22), 1874–1881 (2011)

Pagano, N.J.: Exact Solutions for Rectangular Bidirectional Composites and Sandwich Plates. Journal of Composite Materials 4(1), 20–34 (1970)

Ramtekkar, G.S., Desai, Y.M., Shah, A.H.: Application of a three-dimensional mixed finite element model to the flexure of sandwich plate. Computers & Structures 81(22-23), 2183–2198 (2003)

Reddy, J.: On the solutions to forced motions of rectangular composite plates. Journal of Applied Mechanics 49, 403 (1982)

Triches Jr., M., Gerges, S., Jordan, R.: Reduction of squeal noise from disc brake systems using constrained layer damping. Journal of the Brazilian Society of Mechanical Sciences and Engineering 26(3), 340–348 (2004)

Numerical Characterization of the Mechanical Properties of a Composite Material with Metal

Lassaad Kombass[1], Fayza Ayari[2], and Mohamed Soula[3]

[1] ENIT, ESSTT, 5, Avenue Taha Hussein 1008 Tunis – Tunisia
kombass@gmail.com
[2] IPEI EL-Manar, P.O. Box 244, El Manar, Tunis 2092, Tunisia
Ayari.Fayza@Yahoo.fr
[3] ESSTT, 5, Avenue Taha Hussein 1008 Tunis – Tunisia
Soulamed2003@Yahoo.fr

Abstract. The objective of this work is to characterize a composite material (Al-Fe3O4) using micro-indentation test. A numerical method is developed via the ABAQUS software to simulate the micro-indentation test of this composite material and calculate the equivalent Young's modulus and the material hardness. Effects of the volume fraction, the inclusion size, and the load conditions during the simulation of a micro indentation test are performed Please write down your abstract here.

Keywords: Micro-indentation, metal matrix composite, Al-Fe3O4, FE analysis, Young's modulus, hardness.

1 Introduction

The powder metallurgy components are being widely used for sophisticated industrial applications. The world wide popularity of powder metallurgy lies in the ability of this technique to produce such complex shapes with exact dimensions at a very high rate production and low cost. In modern industry, development of new qualified composites is in perpetual expansion especially those with high resistant, low density and also compound composites associated to multifunctional systems . For this reason, it is very striking to use reinforced (Fe_3O_4-iron oxide) aluminum matrix composites in structural applications (automotive, aeronautics, etc.) due to their outstanding stiffness-to-weight and strength-to-weight ratios and also fatigue resistance. These materials show good thermal conductivity and wear resistance and also low thermal expansion, which makes them very high multifunctional light weight materials. Additionally, it is very attractive way to add Fe_3O_4-iron oxide reinforcing for improving the magnetic permeability of this composites and by this way, it can be obtained a good synchronization between thermal and electrical conductivities and magnetic permeability.

In this paper, a new alternative materials “aluminum–iron oxide (Fe_3O_4, naturally as the mineral magnetite) powder composite” has been developed by using a

M. Haddar et al. (Eds.): *Design and Modeling of Mechanical Systems*, LNME, pp. 297–305.
DOI: 10.1007/978-3-642-37143-1_36

microwave (in the laboratory scale) with various aspect ratios, that is iron oxide (Fe_3O_4) particle sizes and aluminum powders together were used to elaborate a MM composite. The purity level of iron oxide powders (Fe_3O_4) was found to be 99.62%. The compacts were prepared from aluminum and iron powders with various aspect ratios varying from 0.25 to 0.85. Grain size of iron oxide powders (Fe_3O_4) was reported as 2µm. This composite is new and clean and with toughness. However, the non homogeneity of the structure in this kind of materials accentuates the complexity of their numerical and analytical modeling to predict their damage during various loading process. For example, the interfaces essentially play a key role in determining mechanical and physical properties. To explore the real connection between different parameters in order to predict with high accuracy the response of the composite material under a particular loading condition, a micro scale Finite Element (FEM) model have build and parametric studies have been established to access the macroscopic material behavior. An experimental and numerical study has been established.

2 FE Model Description

Mechanical behavior of composite materials depends on different parameters, to clarify the effects of the shape, size and distribution of particles on MMC deformation behavior, we have build a Finite Element Model (FEM) based on an approximation of the microstructure by spherical distributed reinforcing particles in the metal matrix of the composite. This model is inspired from the micromechanical composition of the MMC studied material. Also, this model can provide the distribution of von Mises effective stress, strain and the maximum principal stress in the matrix and particles. The model is used to perform a comparison between experimental results and numerical results for micro indentation tests. We describe schematically the conditions of experimental tests, for micro indentation using a rigid conical indenter Figure 3, provide the geometry and mesh parameters of the two equivalent models used to analyze these experimental tests.

In this study, the effect of geometric and material parameters, such as geometric aspect ratio of the specimen and volume fraction of the reinforcing particles is considered. The volume fraction of inclusions is varied from 5% to 25% and the micro-macro transition schemes are evaluated in many cases. However, when the volume fraction increases, nearby inclusions start to interact and this affects the overall mechanical behavior, Bayraktar, Hufenbach . Simulations must then be performed on a Representative Volume Element (RVE) of the microstructure. The RVE microstructure is periodic along the 3 directions, allowing us to apply periodic boundary conditions to the external faces of the specimens. The inclusion positioning is constrained by the practical limitation of generating an acceptable FE mesh. A criterion is applied to the minimal distance between each inclusion surface and the external faces of the specimen. The volume of one particular cell inclusion is less than $1mm^3$.

The representative cells are meshed with quadratic tetrahedral. FE simulations are performed using ABAQUS (2010) and the whole volume is meshed using 4-node C3D4 (tetrahedral in ABAQUS), enabling us to better capture the strain

gradients in the matrix. The macroscopic stress predicted by the FE analysis is computed from a volume average of the stress tensor $\overline{\sigma}$ given at each integration point over the RVE of domain i :

$$\overline{\sigma} = \frac{1}{\mathrm{V(i)}} \sum_{k=1}^{N_K} \sigma_k V_k \tag{1}$$

The simplified model of the micro-indentation test consists of a conic indenter in contact with the fixed specimen as shown in Figure 1. Also Figure 2 and Figure 3 are illustrating the FE model with the RVE, the indenter and the inclusions distribution in the composite matrix.

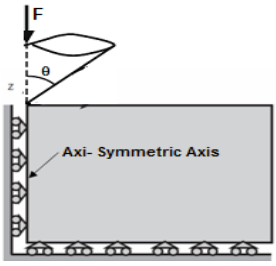

Fig. 1 Geometry of model with conical indenter

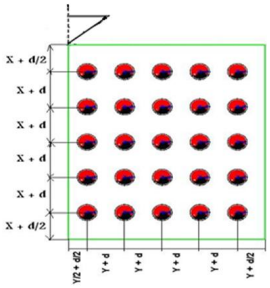

Fig. 2 Distribution of particles in the RVE

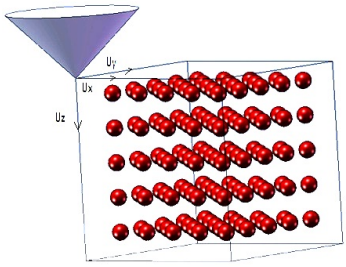

Fig. 3 RVE at 5% volume fraction with 20μm size particles and indenter with 160 μm diameter

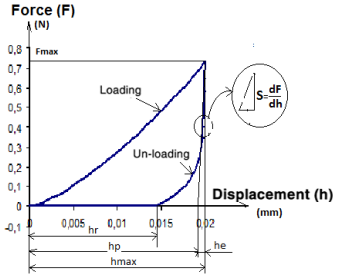

Fig. 4 Applied load vs. depth

The boundary conditions are set so that at the bottom border U_x, U_y, $U_z = 0$ and at the upper face of the specimen is imposed a negative displacement load U_y in y-direction to make via the rigid conical indenter. A static step with small step time is used to assess the gradual evolution of stresses and strains in the elements model, the equivalent reaction force is calculated and used to furnishes the maximum load, when the deformation at the contact zone riches comparable value with the considered limited experimental one.

The mechanical Al-Fe3O4 composite material properties are derived from the particles inclusions properties of the Fe3O4 and those of pure Aluminum. The inclusion material is assumed to be linearly elastic with elastic modulus Ep=250GPa and Poisson's ratio $\nu_p = 0.3$. Pure aluminum with high purity fraction is selected to be the metallic matrix with elastic modulus $E_m = 70$ GPa, Poisson's ratio $\nu_m = 0.33$

3 MMC Properties Defined within the FE Model

Elasto-plastic properties such as hardness and reduced Young's modulus of a material can be determined from the charge-discharge curve of the indentation test. The hardness can be determined from the load curve of the response to an indentation test then the reduced Young's modulus (E*) of the contact-indenter material can be determined from the discharge curve, Figure 4.

Where h_p is the pressed plastic (or contact 'h_c'), h_r is the sinking residual, h_e is the sinking spring, h_{max} is the maximum draft (maximum imposed displacement) and F_{max} the maximum contact force.

The slope of discharge S or contact stiffness response indentation is defined by:

$$S = \frac{dF}{dh} \tag{2}$$

The contact depth h_p for which the indenter and the surface are in contact is given by (W.C. Oliver & Pharr), Figure 5 and Figure 6.

$$h_p = h_{\max} - \alpha \frac{F_{\max}}{S} \tag{3}$$

Where α is a constant depending on the indenter geometry.

Material hardness H (Pa) is deduced from the applied load F_{max} (N) and the resulting deformed surface A_c (m^2).

$$H = \frac{F_{\max}}{A_c} \tag{4}$$

Where the contact area Ac determined from the contact radius $A_c = \pi a^2$.

Where :

- h_f is the depth of the residual impression,
- h_{max} is the depth from the original specimen surface at maximum load F_{max},
- h_e is the elastic displacement during unloading,
- h_a is the distance from the edge of the contact to the specimen surface at full load. Upon elastic reloading, the tip of the indenter moves through a distance he, and the eventual point of contact with the specimen surface moves through a distance h_a.

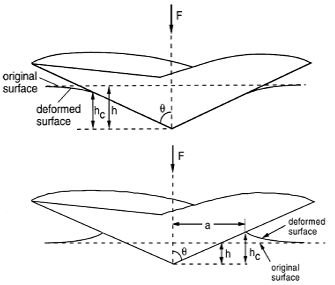

Fig. 5 Schematic illustration of conical indentation with definition of items

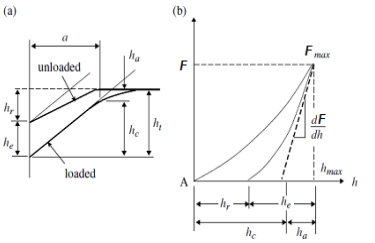

Fig. 6 (a) Schematic of indenter and specimen surface geometry at full load and full unload for conical indenter. (b) Load versus displacement for elastic-plastic loading followed by elastic unloading.

The Young's modulus of the material reduces E* can be expressed as a function of the tangent to the discharge curve S and the air contact by the "BASH" formula Ac

$$E^* = \frac{S}{2}\sqrt{\frac{\pi}{A_c}} \tag{5}$$

The Young's modulus of the composite material is calculated via the homogenization method using the model and assuming that two phases (the matrix and inclusions) are homogenous:

$$E_{composite} = \upsilon_{inclusion} E_{inclusion} + \left(1 - \upsilon_{inclusion}\right) E_{matrix} \tag{6}$$

From the value of Young's modulus determined by the micro-indentation test, we can deduce the Poisson's ratio of the composite from the homogenization method also using the relationship:

$$\frac{1}{E^*} = \frac{1-\upsilon_{matrix}^2}{E_{matrix}} = \frac{1-\upsilon_{indentor}^2}{E_{indentor}}$$

4 Results and Discussion

The numerical results of a micro-indentation aluminum matrix composite are obtained for different volume fractions, diameter of inclusions and loading conditions.

4.1 Effect of Volume Fraction of Inclusions

In this step of calculation, we set the diameter of 20μm inclusions and we imposed to the indenter displacement of 20μm. The diameter of the indenter is attached to 160 microns.

Figure 7 shows the influence of the percentage of inclusions on the force-displacement response when simulating a micro-indentation test of the composite

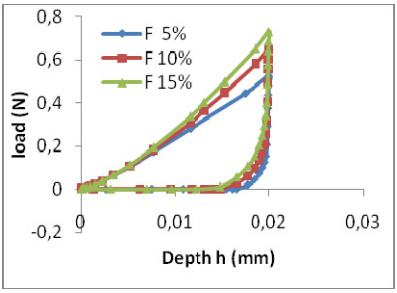

Fig. 7 Influence of the proportion of inclusions on the force-displacement response (Diameter of the inclusions is 20µm, the displacement of the indenter imposed 20µm and diameter 160µm of the indenter)

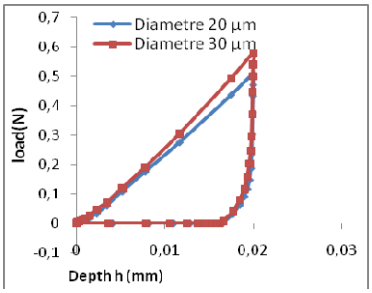

Fig. 8 Influence of the diameter of the inclusions on the force-displacement response (Diameter 160µm- displacement imposed 20µm -% Incl. 5%)

The numerical results, Figure 7 and Table 1, show that increasing of the proportion of inclusions grown the maximum force of indentation. However, the variation in the percentage of inclusions has virtually no effect on the slope of discharge (S). We also note that increasing the percentage of inclusions decreases the residual penetration (h_r). Numerical results show that increasing the percentage of inclusions can vary the total energy of deformation so the strain hardening exponent.

Table 1 shows the effect of varying the percentage of inclusions on the contact radius indenter material, the maximum force applied, the hardness, Young's modulus and yield strength of the material. From these results it is concluded that:

- The contact radius R increases with the percentage of inclusions ν_f,
- The maximum indentation force F also increases with the percentage of inclusions ν_f,
- Increasing the percentage of inclusions ν_f increased the hardness H of the composite,
- Similarly, increasing the percentage of inclusions grown the Young's modulus E* of the composite,
- The yield strength Y of the composite, it also increases with the percentage of inclusions ν_f,

Table 1 Influence of the volume fraction

ν_f	**R** (mm)	$\mathbf{F}_{max}$ (N)	**H** (MPa)	**E*** (GPa)	$\mathbf{Y}_s$ (GPa)
5%	0,0526	0,523	0,055	20,0279	0,0183
10%	0,052	0,648	0,069	20,869	0,0231
15%	0,052	0,731	0,079	20,859	0,026

4.2 *Effect of the Diameter of the Inclusions*

In this case, the diameter of the inclusions is chosen by 5% in the VER, the imposed displacement is 20 microns and the diameter of the indenter is 160 microns.

Figure 8 shows the influence of the diameter of the inclusions on the force-displacement response when simulating a micro-indentation test of the composite.

The numerical simulation results show that increasing the diameter of the inclusions grows is the maximum force of indentation. However, the variation of the diameter of inclusions did not affect the slope of discharge (S) and the residual penetration (h_r). The numerical results also show that increasing the diameter of the inclusions varies the total energy of deformation so the strain hardening exponent. Table 2 summarizes the effect of varying the diameters of inclusions on the contact radius indenter material; the maximum force applied the hardness, Young's modulus and yield strength of the material. From these results we find that

- The contact radius R decreases with the diameter inclusions (size),
- The maximum indentation force Fmax also increases with the diameter of inclusions d,
- Increasing the diameter of inclusions increased the hardness H of the composite,
- increasing the diameter of the inclusions grow is the Young's modulus E* of the composite,
- The yield strength Y_s of the composite, it also increases with the Medal of inclusions

Table 2 Influence of the diameter of the inclusions

d (µm)	R (mm)	F_{max} (N)	H(MPa)	E* (GPa)	Y_s (GPa)
20	0,050	0,523	0,066	2,202	0,022
30	0,049	0,579	0,073	2,360	0,024

4.3 *Comparative Experimental and Numerical Study*

We have achieved a comparative study between experimental results and numerical results. In fact, as it is shown by Figure 9, a good correlation is found.

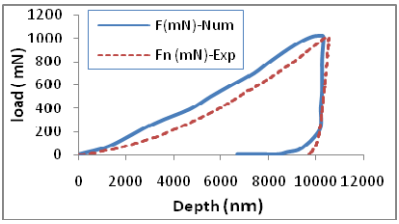

Fig. 9 Superposed experimental and numerical indentation curves

5 Conclusions

A FE model is presented to simulate the indentation of mechanical properties from a micro indentation test.

We have shown that the recently developed FE model reproduces the dependence of the indentation hardness and Young modulus of the material on the indentation depth observed in micro indentation experiments and also on volume fraction of inclusions and also on their size. A rigorous finite-element analysis of micro indentation experiments is performed and the results show very good agreement with the indentation FE data. The parameter E, H and F_{max} determined by the numerical analysis are consistent with the theoretical prediction model. This study validates the FE both as a consistent technique for mechanics and as an engineering analysis tool for advanced micro scale materials technology.

References

Adamiak, M.: Mechanical alloying for fabrication of aluminum matrix composite powders with Ti-Al intermetallics reinforcement. Journal of Achievements in Materials and Manufacturing Engineering, JAMME 31(2) (2008)

Bayraktar, E., Masounave, J., Caplain, R., Bathias, C.: Manufacturing and damage mechanisms in metal matrix composites. Journal of Achievements in Materials and Manufacturing Engineering, JAMME 31(2) (2008)

Duraes, L., Costa, B.F.O., Santos, R., Correia, A., Campos, J., Portugal, A.: Fe2O3/ aluminum thermite reaction intermediate and final products characterization. Materials Science and Engineering A 465, 199–210 (2007)

Grabowski, A., Formanek, B., Sozanska, M., Janicki, D., Nowak, M.: Laser remelting of Al-Fe-TiO powder composite on aluminium matrix. Journal of Achievements in Materials and Manufacturing Engineering, JAMME 33(1) (2009)

Hufenbach, W., Gude, M., Czulak, A., Sleziona, J., Dolata- Grosz, A., Dyzia, M.: Development of textile-reinforced carbon fibre aluminium composites manufactured with gas pressure infiltration methods. Journal of Achievements in Materials and Manufacturing Engineering, JAMME 35(2) (2009)

Mei, J., Halldearn, R.D., Xiao, P.: Mechanisms of the Aliron oxide thermite reaction. Scripta Materialia 41(5), 541–548 (1999)

Narayanasamy, R., Ramesh, T., Pandey, K.S.: Some aspects on cold forging of aluminium–iron powder metallurgy composite under triaxial stress state condition. Materials and Design 29, 891–903 (2008)

Narayanasamy, R., Pandey, K.S.: Some aspects of work hardening in sintered aluminium–iron composite preforms during cold axial forming. Journal of Materials Processing Technology 84, 136–142 (1998)

Tang, F., Anderson, I.E., Gnaupel–Herold, T., Prask, H.: Pure Al matrix composites produced by vacuum hot pressing: tensile properties and strengthening mechanisms. Materials Science and Engineering A 383, 362–373 (2004)

Oliver, W.C., Pharr, G.M.: Measurement of hardness and elastic modulus by instrumented indentation: Advances in understanding and refinements to methodology. J. Mater. Res. 19(1) (January 2004)

Yan, Y.W., Geng, L., Li, A.B.: Experimental and numerical studies of the effect of particle size on the deformation behavior of the metal matrix composites. Materials Science and Engineering: A 448(1-2), 315–325 (2007)

Ziêbowicz, B., Szewieczek, D., Dobrzañski, L.A.: New possibilities of application of composite materials with soft magnetic properties. Journal of Achievements in Materials, and Manufacturing Engineering, JAMME 20(1-2), 207–210 (2007)

Zhang, W.X., Li, L., Wang, T.J.: Interphase effect on the strengthening behavior of particle-reinforced metal matrix composites. Computational Materials Science 41(2), 145–155 (2007)

Structural Health Monitoring by Acoustic Emission of Smart Composite Laminates Embedded with Piezoelectric Sensor

Sahir Masmoudi[1], Abderrahim El Mahi[1], Saïd Turki[2], and Rachid El Guerjouma[1]

[1] LUNAM University: Maine University, Acoustic Laboratory of Maine University (LAUM) CNRS UMR 6613, Avenue Olivier Messiaen, 72085 Le Mans CEDEX 9, France
{Sahir.Masmoudi.Etu,abderrahim.elmahi, Rachid.el_Guerjouma}@univ-lemans.fr

[2] Sfax University, Sciences Faculty of Sfax, Physics Department BP1171, 3000 Sfax, Tunisia
Said.Turki@fss.rnu.tn

Abstract. The smaller sizes of current electronic devices suggest the feasibility of creating a smart composite structure using piezoelectric implant to monitor in-situ the lifetime of civil and aerospace structures. This study presents a health monitoring of composites materials integrated by piezoelectric sensors using acoustic emission (AE) technique. A series of specimens of laminates composite with and without piezoelectric implant were tested in three-point bending tests while continuously monitoring the response by the AE technique. The analysis and observation of AE signals leads to the identification of the acoustic signatures of four damage mechanisms in laminates materials. One of the major differences between the two types of materials (with and without embedded sensor) is the intense acoustic activity in the integrated material.

Keywords: Laminates, piezoelectric implant, three-point bending, acoustic emission, damage.

1 Introduction

Research activities of smart materials and structures present now a significant potential of technological innovations which can respond to the needs of many industrial sectors such as the aeronautics, the space, the energy and the civil engineering. These needs are expressed for example in reducing of vibro-acoustic levels or in improving the reliability of mechanical constructions. To achieve the optimal design of these systems and adaptive mechanical structures, new scientific and technological tools are now studied and implemented. In our days, many works (Mall and Hsu 2000, Paget et al. 2002, Ghezzo et al. 2009) have been investigated the feasibility of implantation of sensors and devices. Also they have evaluated the lifetime of smarts composites materials and they have study the damage mechanisms

M. Haddar et al. (Eds.): *Design and Modeling of Mechanical Systems*, LNME, pp. 307–314.
DOI: 10.1007/978-3-642-37143-1_37

and the mechanical behavior of materials. For example the implant of fiber-optic is studied by Measures (Measures 1992). He report on several advances and he make towards the development of fiber-optic sensors for smart structures. The piezoelectric shows a particularly good capacity to satisfy exigent applications, due to unique mechanical strength, wide frequency response range, and favorable costs (Ye et al. 2005). The piezoelectric implant is used in the fields of ultrasonic (Paget et al. 2002), electromechanical technique (Mall and Hsu 2000), noise and vibration control (Yang et al. 2005), acoustic emission (Ghezzo et al. 2009), etc. For example, Lin and Chang (Lin and Chang 2002) have developed a manufacturing method for integrating a network of distributed piezoceramic sensors onto carbon/epoxy composite structures. Their method was performed to monitor the progress of composite cure using diagnostic signals generated by the embedded piezoceramics. They demonstrated that SMART Layer does not degrade the structural integrity of the host composite structures. Also they concluded that embedded sensors can be used for structural applications without significant compromise. The control of the integrated fiber glass/epoxy composites by acoustic emission (AE) is studied by Ghezzo et al. (Ghezzo et al. 2009, 2010). Tensile tests were performed on samples while continuously monitoring their AE behavior. Results show that material properties in tensile tests are substantially the same of the material with and without integrated sensors. The embedment process causes material and geometrical discontinuities within the composite.

Acoustic emission method was used to analyze the different damage mechanisms detected in composites. AE is an efficient method to monitor, in real time, damage growth in both structural components (El Guerjouma et al. 2001). This technique represents the generation of transient ultrasonic waves due to damage development within the material under load. Any generated AE signal contains useful information on the damage mechanism. To discriminate the different damage mechanisms from the detected AE signals, many studies (Godin et al. 2005, Moevus et al. 2008) used different methods of classification. This works made it possible to identify four types of signals: A, B, C and D which correspond respectively to four damage mechanisms: matrix cracking, debonding in the fiber-matrix interface, fibers breaking and delamination.

This work presents a study of health monitoring structure of integrated laminates composite subject to three-point bending in static and creep tests. Tests applied to the specimens with and without embedded piezoelectric sensor are conducted in order to characterize the effects of introducing the sensor into the host composite material. The results of mechanical tests and AE signals collected during tests for specimens with and without integration were compared.

2 Materials and Experimental Procedure

2.1 Materials

The materials considered were manufactured in the laboratory (LAUM). they are a cross $[0_6/90_6]_S$ laminates composite fabricated by hand lay-up process from E-glass fibers of weight 300 g m^{-2} and resin epoxy of type SR1500/SD2505.

Composite plates were cured at room temperature with pressure of 30 KPa using vacuum bagging technique. The piezoelectric sensors (Fig.1-a) were embedded during the manufacturing stage, their dimensions are given in table 1.

Table 1 Dimensions of piezoelectric sensors embedded in the composite materials

Piezoelectric Sensor	Small Sensor (SS)	Large Sensor (LS)
Diameter (mm)	5	10
Thickness (mm)	0.5	1

The incorporated sensor was placed within the plies on the neutral plane of the composite, in a way to result in 45 mm from the edge of the each specimen (Fig.1-b). The composite specimens with and without sensor have been cut up using a diamond disc. The dimensions of specimens are: L = 150 mm, w = 30 mm and th = 8 mm, where L, w and th are the length, width and thickness respectively. Eventually, we obtain three types of specimens: specimen without sensor WS, specimen embedded with small sensor SS and specimen embedded with large sensor LS.

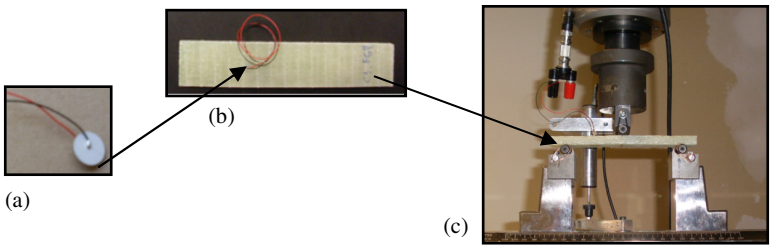

Fig. 1 a) Piezoelectric sensor, b) Integrated specimen, c) Experimental set-up of three-point bending test

2.2 Experimental Procedure

At ambient temperature, the specimens are subjected to three-point bending in static and creep until failure. Experimental tests were carried out on a standard hydraulic machine INSTRON 8801 of 10 kN capacity. The span between the outer supports was taken to 120 mm. The displacement can be measured using a linear displacement transducer (LVDT). The machine is interfaced with a dedicated computer for controlling and data acquisition. Experimental set-up is shown in figure 1-c. The specimens were tested in static three-point bending until fracture at a constant rate of 2 mm min^{-1}. The load and displacement of specimens were recorded during tests. In creep tests, the specimens are subjected to a constant load level and maintained in isotherm condition at room temperature. Then we recorded the increase displacement in time. Creep tests were done for applied load levels r (F_a/F_u) equal to 0.75, where F_a is the applied load to the specimen during the creep tests and F_u is the ultimate failure for integrated specimen in static test.

During loading, acoustic emission signals were recorded. The acquisition of the signals is carried out using the software AEWin from Euro Physical Acoustics (EPA) Corporation with a sampling rate of 5 MHz and 40 dB pre-amplification (Fig. 2-a). AE measurements are achieved by the piezoelectric sensor with a frequency range of 100 kHz-1 MHz. The AE sensor used in this study is a piezoelectric ceramic Pz 27, a detailed description of the sensors can be found in Ref. (Ferroperm catalogue). This sensor has disc form geometry. Figure 2-b shows a typical AE signal and the parameters commonly used for analysis.

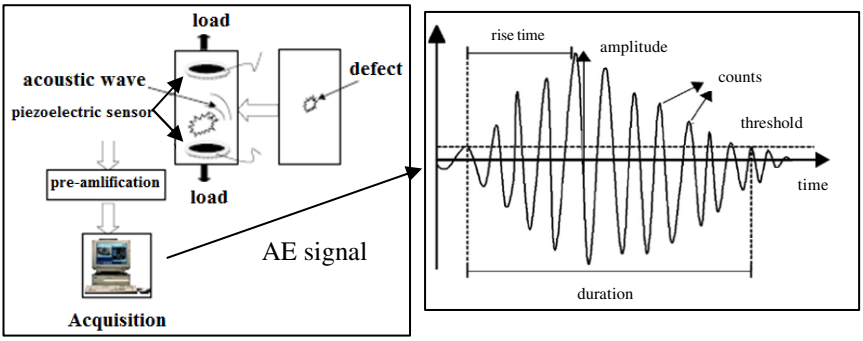

(a) (b)

Fig. 2 a) Experimental setup of acoustic emission (AE) method, b) Example of AE signal

For each AE event, several parameters are calculated by the acquisition system. These collected parameters are used as input descriptors in the proposed classification method. The five descriptors are the energy, the amplitude, the rise time, the counts and the duration of the signals. The AE signals are classified by the *k*-means method using Noesis software (2004). The *k*-means method (Likas et al. 2003) is an unsupervised pattern recognition analyses provide a multidimensional data classification. The number of classes is optimized by taking the minimum value of the factor R_{ij} (Davies and Bouldin 1979).

3 Experimental Results

3.1 Mechanical Behavior

Figure 3-a presents a comparative study of composite specimens with and without embedded sensors. This figure gives the evolution of load versus displacement for three types of specimens: WS, SS and LS. The SS specimen reaches the break after the WS specimen, while the LS specimen reaches the break before. The each load/displacement curve is divided into two zones: the first one is linear, which is elastic. It is large and allows measuring stiffness in three-point bending test. The second zone is nonlinear until the break of specimen.

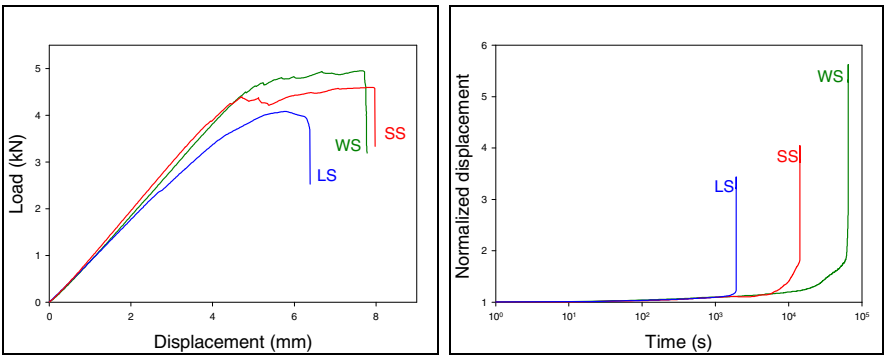

(a) (b)

Fig. 3 a) Load-displacement curves measured in static tests for WS, SS and LS specimens, b) Normalized displacement vs time in creep tests for the same type of specimens

Table 2 shows the mechanical characteristics of specimens obtained in flexural static tests. The failure load of SS specimen present a slight reduction (8%) while a reduction of 18% was observed for the LS specimen. From this result we deduced that the dimensions of the integrated sensor especially the thickness have significant influence on the material life-time and the failure load. In addition, we have noticed that the damage initiation begins away from at the sensor location, also the damage of material is away from the sensor. In the static tests, the most important result is that the material stiffness has not decreased, on the contrary, in the case of SS specimen, stiffness has increased slightly.

Table 2 Mechanical characteristics obtained in flexural static tests

Specimen	WS	SS	LS
Failure load (kN)	5	4.6	4.1
Failure displacement (mm)	7.6	7.8	6.2
stiffness (kN/mm)	0.9	0.96	0.9

The three-point bending creep tests were carried out on the identical specimens tested in static. A comparative study of composite specimens with and without embedded Pz 27 sensors is shown in figure 3-b. This figure illustrates the evolution of normalized displacement in time using a semi-logarithmic scale at load levels of $r(F_a/F_u)$ =0,75 where F_u = 3,75 kN and F_a = 5 kN. The analysis of these results shows that the integrated specimens have similar curve as that of specimen without sensor. Both integrated specimens reached the break before the material without integration. It should be noted that incorporation of sensors within composite significantly affects the material lifetime. The evolution of displacement according the time for each specimen can be divided in three distinct phases: the first one presents a slight increase of deformation which is very spread in time and represents the dominant part during test, followed by the second short zone characterized by a continuous acceleration of deformations rates which is associated to the more active damage until the final zone that represents the failure of materials.

3.2 *Identification of Damage Mechanisms by Acoustic Emission*

The acoustic signals collected during tests were classified by the *k*-means method. This analysis is achieved in order to identify the acoustic signals emitted by different type of damages, also to compare evolution of these various mechanisms in laminates material with and without embedded sensor during tests. Different damage mechanisms have been identified on fiber-matrix materials from their AE signals (Godin et al. 2005, Moevus et al. 2008). According to those previous studies, the damage mechanisms that are considered according to the collected AE signals are: matrix cracking (characterized by signals of A class), fiber-matrix debonding (B class), fibers breaking (C class) and delamination (D class). For the comparison purposes, specimens without embedded sensor were also tested. In this case, the Pz 27 is coupled on the face of the specimen using silicon grease. In this part, only results of specimens without embedded sensor (WS) and with embedded small sensor (SS) were presented.

Figure 4 shows the classification of AE signals for two types of laminates composite: WS specimen and SS specimen. This figure gives the amplitude distribution versus time. The classification of AE signals for laminates materials shows the presence of the four types of damage: A, B, C and D class. In the static tests, load was increased to failure, so the progression of damage was dependent on the increasing level of applied stress. It is worth noting that the acoustic activity of the specimens is mainly located around the amplitudes of 40-65 dB, during three quarts of the flexural test (Fig.4). After that, the amplitude distribution becomes very concentrated and very important reached until 100 dB.

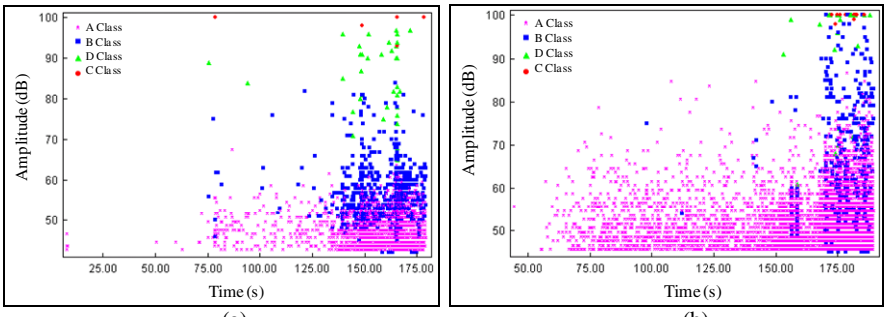

Fig. 4 Amplitude distribution versus time for cross composites in static tests: a) specimen without integration b) specimen embedded with small Pz 27 sensor

For both specimens, this visualization shows that the matrix cracking (A class) is the most important damage mechanism as it begins from the start of the test and involves much more numerous events. A class is followed by the appearance of fiber-matrix debonding (B class), delamination (D class) and fibers breaking (C class) successively. For material with embedded sensor, the events amplitude is higher and the number of cumulative AE signals is more than those observed in material without integration (Fig.4-b).

Similar to static tests, the distribution of amplitude versus time of AE signals obtained during creep tests are shown in figure 5. Also in creep tests, we have observed the presence of the four types of damage. For the comparison of embedded sensor and sensor mounted on the surface, the embedded sensor (Fig.5-b) showed a much higher sensitivity.

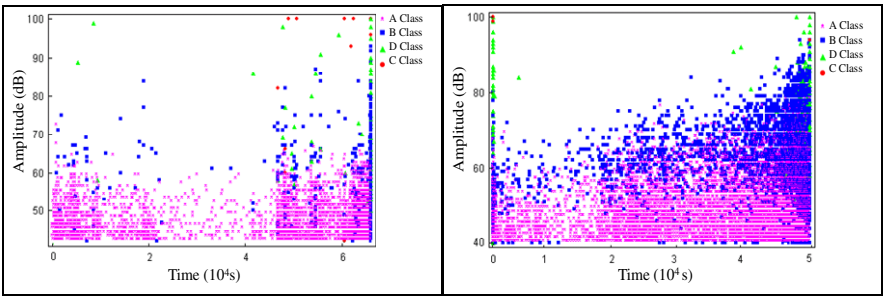

(a) (b)

Fig. 5 Amplitude distribution versus time for cross composites in creep tests: a) specimen without integration b) specimen embedded with small Pz 27 sensor

4 Conclusion

Effects of embedded piezoceramic (Pz 27) sensors on the integrity and mechanical response of the laminates composite have been presented. Three-point bending static and creep tests were performed on specimens while constantly monitored by the acoustic emission technique. The mechanical behavior of composites with and without integrated sensor shows no difference in the form. The incorporation of piezoelectric sensor influences specially the fracture load and causes low degradation of mechanical properties of material. Comparing embedded sensor to sensor mounted on the surface, the embedded sensor showed a much higher sensitivity. It was thus verified that the embedded AE sensor had great potential for AE monitoring in fiber reinforced composites structures. It is worth noting that the non-destructive monitoring of fiber reinforced composites will be enhanced when the sensors are incorporated within the composites structures.

References

Mall, S., Hsu, T.L.: Electromechanical fatigue behavior of graphite/epoxy laminate embedded with piezoelectric actuator. Smart Mater. Struct. 9, 78–84 (2000), doi:s0964-1726(00)0920767

Paget, C.A., Levin, K., Delebarre, C.: Actuation performance of embedded piezoceramic transducer in mechanically loaded composites. Smart Mater. Struct. 11, 886–891 (2002), doi:s0964-1726(02)39935-X

Ghezzo, F., Huang, Y., Nemat-Nasser, S.: Onset of resin micro-cracks in unidirectional glass fiber laminates with integrated SHM sensors: experimental results. Struct. Health Monitor 8, 477–491 (2009), doi: 1475-9217

Measures, R.M.: Smart composite structures with embedded sensors. Compos. Engin. 2, 597–618 (1992), doi:0961-9526/92

Ye, L., Lu, Y., Su, Z., Meng, G.: Functionalized composite structures for new generation airframes: a review. Compos. Sci. Technol. 65, 1436–1446 (2005), doi:10.1016/j.compscitech.2004.12.015

Yang, S.M., Hung, C.C., Chen, K.H.: Design and fabrication of a smart layer module in composite laminated structures. Smart Mater. Struct. 14, 315–320 (2005), doi:10.1088/0964-1726/14/2/003

Lin, M., Chang, F.K.: The manufacture of composite structures with a built-in network of piezoceramics. Compos. Sci. Technol. 62, 919–939 (2002), doi: S0266-3538(02)00007-6

Ghezzo, F., Starr, A.F., Smith, D.R.: Integration of networks of sensors and electronics for structural health monitoring of composite materials. Adv. Civil Eng., 1–13 (2010), doi:10.1155/2010/598458

El Guerjouma, R., Baboux, J.C., Ducret, D., et al.: Non destructive evaluation of damage and failure of fiber reinforced polymer composites using ultrasonic waves and acoustic emission. Adv. Eng. Mat. 3, 601–608 (2001), doi:10.1002/1527-2648(200108)3:8

Godin, N., Huguet, S., Gaertner, R.: Integration of the Kohonen's self-organising map and k-means algorithm for the segmentation of the AE data collected during tensile tests on cross-ply composites. NDT&E Inter. 38, 299–309 (2005), doi:10.1016/j.ndteint.2004.09.006

Moevus, M., Godin, N., R'Mili, M., et al.: Analysis of damage mechanisms and associated acoustic emission in two SiC_f/[Si–B–C] composites exhibiting different tensile behaviours. Part II: Unsupervised acoustic emission data clustering. Compos. Sci. Technol. 68, 1258–1265 (2008), doi:10.1016/j.compscitech.2007.12.001

Ferroperm Piezoceramics Catalogue, `http://www.ferroperm-piezo.com`

NOESIS software, Advanced Acoustic Emission Data Analysis Pattern Recognition and Neural Networks Software (2004)

Likas, A., Vlassis, N., Verbeek, J.: The global k-means clustering algorithm. Pat. Recog. 36, 451–461 (2003), doi: s0031-3203(02)00060-2

Davies, D.L., Bouldin, D.W.: A cluster separation measure. IEEE Trans. Patt. Anal. Mach. Int. 1, 224–227 (1979)

Vibroacoustic Analysis of Boat Propeller Using Reliability Techniques

M. Mansouri[1], B. Radi[1], and A. El Hami[2]

[1] LIMMII, FST Settat, BP : 577, Route de Casablanca, Settat, Maroc
{mansouri1969,bouchaib.radi}@yahoo.fr
[2] LMR, INSA de Rouen, BP: 8, Avenue de l'université,
76801 St. Etienne de Rouvray, France
abdelkhalak.elhami@insa-rouen.fr

Abstract. In many situations, the vibrating structures are in contact with a fluid (fluid around the hulls of a boats, reservoirs, etc), but the dynamic behaviour of the structure can be significantly modified by the presence of the fluid. Traditionally, the study of mechanical systems fluid-structure interaction is based on a deterministic approach where all the parameters used in the model are a fixed value. But it suffices to having conducted a few experimentations to realize that the limitations of such modeling. This work proposes a numerical stochastic method of the modal synthesis extended to reliability study, based on FORM and SORM approaches, for solving the large vibroacoustic problems. The method developed couples the dynamic substructuring method of type Craig and Bampton and the acoustic subdomains method based on a pressure formulation. The numerical method used takes into account the uncertainties of the input parameters of the two domains. The application of the proposed method is performed on a boat propeller immersed. This numerical study compared to an experimental study we can validate the calculation process.

Keywords: Fluid-structure interaction, reduction of model, Vibroacoustic, Numerical simulation, Modal synthesis, Reliability.

1 Introduction

The vibrating structures which are dimensioned are often in contact with a fluid (fluid around the hulls of a boats, reservoirs, heat exchangers in power plants, etc), but the dynamic behavior of the structure can be significantly modified by the presence of the fluid. The sizing must take into account the effects of fluid-structure interaction. Particularly the dynamic behavior of an elastic structure coupled to a fluid can be significantly modified through the presence of the fluid. In the vibroacoustic studies of coupled systems fluid-structure modeled by the finite element method (Sigrist 2011), (Souli and Sigrist 2009), the interest of reducing the size of the problem is obvious because we have to add all the degrees of freedom of the acoustic domain to those of the structure.

M. Haddar et al. (Eds.): *Design and Modeling of Mechanical Systems*, LNME, pp. 315–322.
DOI: 10.1007/978-3-642-37143-1_38

Traditionally, the study of mechanical systems fluid-structure interaction I based on a deterministic approach where all the parameters used in the model are a fixed value. But it suffices to having conducted a few experimentations to realize that the limitations of such modeling. Hence the need to take into accounts the uncertainty on the parameters of mechanical systems. Furthermore the knowledge of the variation of the response of a structure involving the uncertain parameters, geometry, boundary conditions, manufacturing tolerances and loads is essential in the design process. This work proposes a numerical stochastic method of the modal synthesis extended to reliability study, based on the FORM and SORM approaches, for solving the large vibroacoustic problems. The method developed couples the dynamic substructuring method of type Craig and Bampton and the acoustic subdomains method based on a pressure formulation (Craig and Bampton 1968).The numerical method used takes into account the uncertainties of the input parameters of the two domains (M. Mansouri et all. 2012). The application of the proposed method is performed on a boat propeller immersed in air and water. The numerical study is conducted using a code developed in MATLAB coupled with the finite element code ANSYS in order to evaluate the reliability of the structure. This numerical study compared to an experimental study we can validate the calculation process and the method proposed in the field of frequency analysis and reliability-study of submerged structures to build a reliable and robust model for the problems of fluid-structure interaction.

2 Vibroacoustic Problem

Front of the complexity of mechanical systems fluid-structure interaction, the classical numerical and experimental methods of the vibratory mechanical are costly, sometimes even unusable. In perfect coherence with the modular organization of large projects, the method of substructure and subdomain appears to be the most effective way to conduct the vibratory study for all fields from dynamic domains constituting the system (Treyssede and El Hami 2004). However, the application of a modal synthesis method for the vibroacoustic problem raises two crucial problems linked on the one hand to the choice of acoustic formulation and secondly the choice of method associated subdomains (El Hami et all. 1996). We consider an acoustic fluid in a rigid cavity, in contact with an elastic structure. The variables used to describe the structure Ω and the acoustic cavity F are respectively the displacement u and the pressure fluctuation p. We note ρ_f the fluid density, C the speed of sound in the fluid, and ρ_s, E and ν are respectively the density, Young's modulus and Poisson's ratio of the structure. In the sequel, the exhibitors (and indexes) s and f shall designate respectively the numbers of substructures and subdomains.

Each substructure occupies a volume noted Ω^s. Each subdomain fluid occupies a volume Ω^f. The structure Ω is composed of N^s substructures Ω^s (s = 1,..., N^s) and the acoustic fluid *F* is constituted by N^f acoustic subdomains Ω^f (f = 1,..., N^f). Into we distinguish three types of interface, defined as follows: $L^{ss'} = \Omega^s \cap \Omega^{s'}$, $L^{ff'} = \Omega^f \cap \Omega^{f'}$, $L^{sf} = \Omega^s \cap \Omega^f$.

$L^{ss'}$ denotes the interface (or junction) between the substructure Ω^s and the substructure $\Omega^{s'}$ ($L^{ss'} = \emptyset$ if these two domains are not in contact). $L^{ff'}$ represents the interface between the fluids subdomains Ω^f and $\Omega^{f'}$ ($L^{ff'} = \emptyset$ in the absence of contact between the two subdomains fluid). L^{sf} is the fluid-structure interface between the substructure Ω^s and the fluid subdomain Ω^f ($L^{ff'} = \emptyset$ if Ω^s and Ω^f are not in contact).

The finite element discretization of variational formulations structural and acoustic (Kuireghian and Zhang 1999), leads to the following algebraic form:

- For substructures

$$(K^s - \omega^2 M^s)\{u^s\} = \{F_e^s\} + \sum_{\substack{s'=1 \\ s' \neq s}}^{N^{Ss}} \{F_L^{ss'}\} \quad s=1,\ldots,N^s \tag{1}$$

where: $\{u^s\}$ the displacement vector of each sub-structure, $[M^s]$ the mass matrix of the substructure Ω^s, $[K^s]$ the stiffness matrix of the substructure Ω^s, $F_L^{SS'}$ the bonding forces and F_e^S the equivalent external forces including all excitations of type imposed displacement.

- For subdomains

$$\left(H^f - \omega^2 E^f\right)\{P^f\} = \{a_e^f\} + \sum_{\substack{f'=1 \\ f' \neq f}}^{N^f} \{a_L^{ff'}\} \quad f=1,\ldots,N^f \tag{2}$$

where : $\{p^f\}$ the acoustic pressure vector of each subdomain, $[H^f]$ the mass matrix of the fluid subdomain Ω^f, $[E^f]$ the stiffness matrix of the fluid subdomain Ω^f, $\{a^f\}$ the vector of equivalent external pressures (including exceptions inherent in frontier Γ_p^f of type imposed pressure) and $\{a_L^{ff'}\}$ the acceleration at the interface between the fluid subdomain Ω^f and the fluid subdomain $\Omega^{f'}$.

- For vibroacoustic problem

The structural and fluids degrees of freedom are grouped in a global vector:

$$\langle u \; p \rangle = \langle u^1 \; u^2 \; \ldots u^{N^s} \; p^1 \; p^2 \ldots p^{N^f} \rangle$$

Taking into account the interaction between the substructure Ω^s and the fluid subdomain Ω^f, the global matrix of fluid-structure interaction is written:

$$[L] = \begin{bmatrix} L^{11} & \cdots & L^{1N^f} \\ \vdots & \ddots & \vdots \\ L^{N^s 1} & \cdots & L^{N^s N^f} \end{bmatrix}$$

In this expression, $[L^{sf}]$ are implicitly zero when there is no interface between the sub-structure Ω^s and the fluid subdomain Ω^f. Equations (3) below can be assembled into a single equation (4):

$$\{u\} = [S][\varphi]\{w\}, \qquad \{p\} = [T][\psi]\{r\} \tag{3}$$

$$\begin{Bmatrix} u \\ p \end{Bmatrix} = [C][R] \begin{Bmatrix} w \\ r \end{Bmatrix} \tag{4}$$

where $[C] = \begin{bmatrix} S & 0 \\ 0 & T \end{bmatrix}$ and $[R] = \begin{bmatrix} \varphi & 0 \\ 0 & \psi \end{bmatrix}$.

And taking into account the compatibility conditions at the interface the last terms of equations (1 and 2) will disappear. Finally, the equation to solve of vibroacoustic problem reduced by modal synthesis without the external loads is:

$$[C]^t[R]^t\left(-\omega^2\begin{bmatrix} M & 0 \\ \rho_f L^t & E \end{bmatrix}+\begin{bmatrix} K & -L \\ 0 & H \end{bmatrix}\right)[C][R]\begin{Bmatrix} w \\ r \end{Bmatrix}=\begin{Bmatrix} 0 \\ 0 \end{Bmatrix} \tag{5}$$

3 Reliability Analysis

The first step in the analysis of the reliability is to define the design variables X_i (i=1, 2, ..., n) having a significant level of fluctuation. For each of these variables X_i (whose achievements are noted x_i), we assign a probability distribution reflecting the corresponding random. This can be achieved through statistical studies, physical findings, or lack of resources, expert advice. The quality of information is reflected in the accuracy of results. The second step is to define a number of potential failure scenarios. For each of them, a performance function G (x_i) divides the space into two regions of the variables: safety domain G (x_i)> 0 and failure domain G (x_i) ≤ 0. The boundary between these two domains is defined by G (x) = 0, called limit state function. The failure probability is given by:

$$p_f = \int_{G\leq 0} f_{X_1,\ldots,X_n}(x_1,\ldots,x_n)\,dx_1 \ldots dx_n \tag{6}$$

where $f_{X_1,\ldots,X_n}(x_1,\ldots,x_n)$ is the joint density of probability of the variables X_i. The evaluation of this integral is very costly in time of calculation, because it comes to a very small quantity and because all the necessary information on the joint density of probability is not available. And it is very rare that this integral can be studied analytically or numerically. In practice, we do not have in general the joint density of probability of the vector {X}, we must be content most often the marginal distributions for each variable X_i and some information about their correlation. In addition, the integration domain can be defined implicitly and complex according the used mechanical model. Various methods of resolution have been developed to overcome these difficulties (Radi and El Hami 2005).

Traditionally, we distinguish two main methods: the methods based on simulations such as Monte Carlo simulation and those using approximate methods such as First Order and Second Reliability Methods (FORM and SORM), these two approximation methods are based on the determination of the reliability index β, which allows to access an approximate value of probability of failure P_f (El Hami and Radi 2011). The vector of basic variables X, defined by its joint density function is transformed into a vector of centered normal variables, normalized and independent U, defined in the standard space. This transformation consists in particular to pass of random variables x_i of arbitrary marginal distributions and optionally correlated to reduced and centered normal distribution uncorrelated (independent) u_i, by the following expression:

$$u_i = T_i(x_k) = \Gamma_{ij}\phi^{-1}\left[F_{X_j}(x_j)\right] \tag{7}$$

where Γ_{ij} is the inverse of the Choleski triangularization of the correlation matrix equivalent, $F_{X_j}(x_j)$ is the distribution function of the variable x_j, ϕ^{-1} is the inverse of the Law standard Gaussian distribution. In standard space, the reliability index β is the minimum distance between the origin and the limit state function. This distance defines a point P*, said the design point (or point of failure most likely). The index β is calculated by solving an optimization problem with constraints:

$$\beta = \min\sqrt{\sum_i T_i^2(x_j)} \quad \text{u.c.} \quad G(x_j) \leq 0 \tag{8}$$

A calculation method of the transformation is available in (Kiureghian and Liu 1986), where details are given on an approximate computation of the equivalent matrix of correlation.

4 Numerical Results

Following our deterministic study applied to a boat propeller and a single blade in air and in water, we have noticed a variation of the numerical results compared to the experimental results, we have thought to extend this study to the stochastic and reliability study to take account of uncertainties in the entered variables. Figure 1 shows the finite element model of the structure. The fluid and the propeller are defined by their properties shown in the tables (1) and (2). The objective of this study is the demonstration of the interest of the proposed method. The numerical development has been realized by a code which couples MATLAB and ANSYS. The reduction's method is applied to a given simplified model of the propeller composed of four substructures and the acoustic cavity is divided into four subdomains containing each approximately the same number of elements (see Figure 1). The deterministic numerical calculations are performed on the whole structure and on the single blade and they are compared with experimental results.

Table 1 Material properties of the structure

Young's modulus [Pa]	Poisson's ratio	Density $[\mathbf{Kg.m^{-3}}]$
9.6×10^{10}	0.3	9200

Table 2 Material properties of the fluid

Density $[\mathrm{Kg.m^{-3}}]$	Speed of sound $[\mathrm{m.s^{-1}}]$
1000	1500

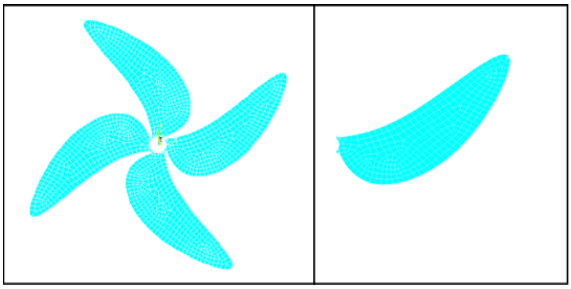

Fig. 1 Finite element model

4.1 Probabilistic Study

Front of the complexity of the problem, we have chosen to consider only the sources of uncertainties related to the material properties and we will be limited to the study of a single blade in air and in water. The choice of standard deviations and the means of random variables were chosen based on different analyzes (Mansouri et all. 2012), (Devic et all. 2001). Table (3) contains the means of random variables used in this study and the distributions laws chosen.

Table 3 Moments of the parameters of the problem and distribution laws

Parameters	Means	Standard deviation	Distribution
Young's modulus [Pa]	9.6×10^{10}	0.5×10^{10}	Gaussian
Density of structure	9200	2669.6	Uniform
Density of the fluid	1000	295.72	Uniform

In this context, the stochastic calculation was carried out using probabilistic design system. This tool is based on a calculation with Monte Carlo simulation (MC) for 100 samples and the response surface method (RSM) for 40 samples. Tables 4 and 5 show means of the natural frequencies. The first gives the finding results using the propeller blade in air and the second gives the finding results in water.

Table 4 Means of the frequencies for the propeller blade in air

Modes	ANSYS	MATLAB	MC	SD	RSM	SD
R1	74.863	73.761	72.46	12.5	73.58	15.28
R2	119.82	117.342	115.8	23.5	118.5	28.79
R3	205.58	198.819	199.6	37.1	194.7	45.36

Table 5 Means of the frequencies for the propeller blade in water

Modes	ANSYS	MATLAB	MC	SD	RSM	SD
R1	37.71	36.893	35.671	5.62	34.22	7.1
R2	67.54	66.887	66.34	11.16	67. 45	14.4
R3	126.32	124.541	124.12	25.87	121.93	27.73

4.2 Reliability Study

We have chosen to implement a direct coupling between a reliability code developed in MATLAB and ANSYS. These two codes in fact answer our needs in terms of calculation capacity and the possibility of dialogue. In this numerical study, the analysis of the reliability of the propeller in air and in water was based on an implicit limit state function G based on the first natural frequency R_1: for the propeller in air: $\mathbf{G(E,\ \rho_s) = R_1 - R_0}$, with $\boldsymbol{R_0 = 73\ Hz}$ and for the propeller in water: $\mathbf{G(E,\ \rho_s,\ \rho_f) = R_1 - R_0}$, with $\boldsymbol{R_0 = 36\ Hz}$

The mean values of random variables for this study are shown in Table (3). Tables 6 and 7 summarize the design parameters considered in the uncoupled and coupled structure for this example, and they illustrate a comparison between the results obtained from FORM and SORM approaches.

Table 6 Design parameters considered in the propeller blade in air

Parameters	FORM	SORM
Young's modulus [Pa]	8.5×10^{10}	8.5×10^{10}
Density of the structure	9030	9030
reliability index β	3.68	3.68
Probability P_f	0.083	0.012

Table 7 Design parameters considered in the propeller blade in water

Parameters	FORM	SORM
Young's modulus [Pa]	8.37×10^{10}	8.37×10^{10}
Density of the structure	8980	8980
Density of the fluid	890	890
reliability index β	3.54	3.54
Probability P_f	0.11	0.087

On the basis of preliminary deterministic study, the reliability analysis based on FORM and SORM approximate methods was conducted for the blade in air and in water. Precisely given the low values of probability of failure P_f, it seems to us more convenient to reasoning in terms of reliability index β, in order to build a trust domain of the input parameters chosen as defined in Table (3). By comparing the probabilities of failure and reliability index calculated and displayed in Tables (6) and (7) with the ranges of values of probability of failure and reliability index β corresponding accepted in various industrial sectors in particular for the marine structures ($P_f \in [10^{-2};10^{-4}]$ et $\beta \in [2.33;3.72]$), we find that there is a very important level of reliability of the blade.

5 Conclusion

The developed method in this work couples the dynamic substructuring method of type Craig and Bampton and acoustic subdomains method based on the acoustic

pressure formulation. And to take into account uncertainties related to parameters of the two domains, a reliability analysis was subsequently conducted. The used numerical method takes into account the uncertainties of input parameters such as properties of the two domains fluid and solid. The application of the proposed method is performed on a propeller boat in air and water. The numerical study is performed using a code developed which couples MATLAB and ANSYS to evaluate the reliability of the structure. The comparison of the numerical results allows us to validate jointly the process of calculation and the method proposed in the domain of frequency analysis and the reliability of submerged structures in order to build a reliable and robust model for the problems of fluid-structure interaction. The obtained results of the propellers are very encouraging. The proposed model, whose choices have been dictated by the physical phenomena involved, the deterministic results and available experimental data.

References

Sigrist, J.F.: Interaction fluide-structure: Analyse vibratoire par éléments finis. Ellipses Edition Marketing S.A. (2011)

Souli, M., Sigrist, J.F.: Interaction fluide-structure: modélisation et simulation numérique. Lavoisier (2009)

Radi, B., El Hami, A.: Reliability analysis of the metal forming process. Math. and Comp. Model. 45, 431–439 (2007)

Hami EI, Radi, B.: Fiabilité et optimisation des systèmes, théorie et application, cours et exercices corrigés. Ellipses, Technosup. (2011)

Der Kiureghian, A., Liu, P.L.: Structural reliability under incomplete probability Information. J. of Eng. Mech. ASCE 112(1), 85–104 (1986)

Treyssede, F., El Hami, A.: Une méthode couplée de sous-structuration dynamique/sous-domaines acoustiques pour des problèmes d'interactions fluide-structure de grande taille. In: XIVe Colloque Vibrations Chocs et Bruits, Juin 16-18 (2004)

Craig, R.R., Bampton, M.C.C.: Coupling of substructures for dynamic analyses. A.I.A.A. Journal 6, 1313–1319 (1968)

Der Kuireghian, A., Zhang, Y.: Space-variant finite element reliability analysis. Comp. Methods in Appl. Mech. (1999)

Mansouri, M., Radi, B., El Hami, A.: Reliability-Based Design Optimization for the analysis of Vibro-Acoustic Problems, application to a solid elastic 3D immersed in water. In: CST 2012, Croatia 4-7 (2012)

El Hami, A., Radi, B.: Some decomposition methods in the analysis of repetitive structures. Comp. and Str. 58(5), 973–980 (1996)

Devic, C., Sigrist, J.F., Lainé, C., Baneat, P.: Etude modale numérique et expérimentale d'une hélice marine (2001)

Pressure Waves in Homogeneous Gas-Liquid Mixture Flows in Deformable Pipelines

Elaoud Sami and Hadj-Taïeb Ezzeddine

Laboratory of Applied Fluids Mechanics, Process and Environment Engineering, ENIS, P.O. Box, W, 3038 Sfax-Tunisia
elaoudsa@yahoo.fr, Ezed.Hadj@enis.rnu.tn

Abstract. To predict pressure waves in homogeneous gas-liquid mixtures in elastic flexible pipes, a mathematical model based on the gas-fluid mass ratio is presented. The density of the fluid is defined by an average of both fluid components. A relationship between the pressure and the cross-section of the pipe is developed taking into account the fluid-structure interaction. The two constitutive equations, conservation of mass and momentum, yield a set of partial differential equations which are solved by the irregular grid method characteristics method. The obtained results show that the pressure wave propagation is significantly influenced by the fluid compressibility and the pipe wall elasticity.

Keywords: deformable pipe, gas-liquid flow, method of characteristics.

1 Introduction

The propagation of pressure waves in two-phase flows occurs in several hydraulic installation systems such as nuclear , geothermal power plants and in petroleum industries. Most common studies concern the quasi-rigid pipes namely the metallic pipes where the diameter and the thickness are supposed constant. One can mention, in particular, the works of (Chaudry et al. 1990, Chammami et al. 2001, Ouyang et al. 2001). In these works, the gas-liquid mixture is supposed homogeneous. The gaseous phase is represented by the volumic rate of gas which varies with the pressure. On the other hand, in most quoted works, the elasticity of the pipes has been disregarded in front of the compressibility of the mixture. It has been shown that the presence of the gaseous phase considerably absorbed the amplitude of the pressure waves provoked by the phenomenon of water hammer. The transient flows in deformable elastic pipes such as rubber tubes, arteries (Figueroa et al.2006, Ryo et al. 2009) and visco-elastic pipes, possess some features different from those related to the rigid or quasi-rigid pipes. Some studies have been developed to examine the influence of the pipe deformation on the evolution of the pressure waves (Streeter and Wylie 1983, Bahrar et al. 1998, Chen and Liang 2007). However, these studies concern liquid flows only.

In this paper, we study the transient flow of gas-liquid mixtures through elastic pipelines and observe the influence of different values of gas mass fraction and

M. Haddar et al. (Eds.): *Design and Modeling of Mechanical Systems*, LNME, pp. 323–330.
DOI: 10.1007/978-3-642-37143-1_39

Young's modulus on the pressure evolution. The interaction between the pipe wall elasticity and gas mass fraction is also analyzed. The transient regime is created by the rapid closure of a downstream valve. The numerical simulation was performed by using the characteristics irregular grid method.

2 Hypothesis

The transient flow is supposed one-dimensional and concerns homogeneous gas-liquid mixture. The calculation of the pressure loss is done by analogy with incompressible permanent flows. The gas mass ratio is noted $\theta = \left[M_g / \left(M_g + M_l\right)\right]$, where M_l and M_g represent the masses of the liquid and the gas respectively. The gas density evolves according to the following isentropic law:

$$\rho_g = \rho_{g_0} \left(p / p_0\right)^{1/n} \tag{1}$$

For rubber and other substances having a Poisson's ration of about 0.5, the volume of wall material remains constant during deformation, and the wall continuity relation is (Stuckenbruck et al.1985):

$$eR = e_0 R_0 \tag{2}$$

3 Mathematical Formulation

3.1 Momentum Equations

By application of the mass conservation and momentum laws to an element of fluid between two sections of abscissa x and x+dx of the pipe, we get the following equations of continuity and motion (Streeter and Wylie 1983):

$$\frac{\partial(\rho A)}{\partial t} + \frac{\partial(\rho A V)}{\partial x} = 0 \quad \text{and} \quad \frac{\partial V}{\partial t} + V\frac{\partial V}{\partial x} + \left(\frac{1}{\rho}\right)\frac{\partial p}{\partial x} + \frac{\lambda V|V|}{2D} = 0 \tag{3}$$

where λ is the friction coefficient .

Equations (3) form a system of two non-linear partial differential equations in which the pressure *p* and the velocity *V* are considered the main variables of the flow. To numerically solve these equations, we must express the density of the mixture ρ and the section *A* of the pipe according to the fluid pressure.

3.2 Expression of the Mixture Density

The expression of the average density of the mixture is defined according to the gas mass ratio θ (Hadj-Taïeb and Lili 1999):

$$\rho = \left[\theta/\rho_g + (1-\theta)/\rho_l\right]^{-1} \tag{4}$$

3.3 Elastic Pipe Behavior Law

For highly deformable tubes, the relation between stress and strain is:

$$d\sigma_\theta = E d\varepsilon_\theta \Leftrightarrow d(pR/e) = E\, dR/R \tag{5}$$

The Young's modulus can be expressed as follows (Streeter and Wylie 1983):

$$E/E_0 = (R/R_0)^\delta \tag{6}$$

where, δ = 0 for materials with linear elastic behavior and $\delta \neq 0$ for materials with non-linear elastic behavior.

Using (2) and posing $A = \pi R^2 = \pi D^2/4$, the integration of (5) leads to:

$$p = (A_0/A)\left[(E_0 e_0/D_0)Ln(A/A_0) + p_0\right] \quad if\ \delta = 0 \tag{7}$$

$$p = (A_0/A)\left[(2E_0 e_0/\delta D_0)\left((A_0/A)^{\delta/2} - 1\right) + p_0\right] \quad if\ \delta \neq 0 \tag{8}$$

3.4 Expression of the Wave Speed

The wave speed in the fluid can be defined as (Stuckenbruck et al.1985):

$$C^2 = \left(\frac{\partial\rho}{\partial p} + \frac{\rho}{A}\frac{\partial A}{\partial p}\right)^{-1} \tag{9}$$

By considering the relations (1) and (4), the first term on the right-hand side of (9) can be written:

$$\frac{\partial\rho}{\partial p} = \rho^2\left(\frac{\theta}{\rho_g K_g} + \frac{1-\theta}{\rho_l K_l}\right) \tag{10}$$

where K_g and K_l are the compressibility of gas and liquid respectively.

Taking into account (7) and (8), and whatever be δ, the second term on the right-hand side of (9) can be written:

$$\frac{\rho}{A}\frac{\partial A}{\partial p} = \frac{\rho D_0}{E_0 e_0 F} \tag{11}$$

$$\text{where}\quad F = \left(\frac{A}{A_0}\right)^{(\delta/2)-1} - \frac{D_0}{E_0 e_0}\, p \tag{12}$$

By substitution equations (10) and (11) in equation (9), the speed of wave's equation becomes:

$$C = \left[\rho \left(\frac{\rho}{np} \frac{\theta}{\rho_g} + \frac{(1-\theta)\rho}{\rho_l K_l} + \frac{D_0}{E_0 e_0 F} \right) \right]^{-1/2} \tag{13}$$

Posing $C_r^2 = np\rho_g / \left(\theta\rho^2\right)$ and, $C_d^2 = E_0 F e_0 / \rho D_0$,we find:

$$\frac{C}{C_d} = \left[1 + \left(\frac{C_d}{C_r} \right)^2 \right]^{-1/2} \tag{14}$$

4 Numerical Resolution by the Method of Characteristics

The method of characteristics is often used to transform the governing partial differential equations into ordinary differential equations that are valid along two sets of characteristic lines (Fig. 1). Taking into equations (10) and (11), the equations of continuity and motion (3) can be written:

$$\left(\frac{C_d}{C} \right)^2 \frac{1}{A} \left(\frac{\partial A}{\partial t} + V \frac{\partial A}{\partial x} \right) + \frac{\partial V}{\partial x} = 0 \quad \text{and} \quad \frac{\partial V}{\partial t} + V \frac{\partial V}{\partial x} + \frac{C_d^2}{A} \frac{\partial A}{\partial x} + \frac{\lambda}{2D} V|V| = 0 \tag{15}$$

where V(x, t) and A(x, t) are the two dependant variables.

By the use of the characteristics method, equations are (15) are converted into four ordinary differential equations. These four equations are presented by two pairs of equations identified as C^+ and C^- (Abbott. 1966):

$$\mathrm{C}^+ \begin{cases} dV + \left(C_d^2 / C\right) dLnA = -gJdt \\ \mathrm{dx} = (V + C)dt \end{cases} \quad \text{and} \quad \mathrm{C}^- \begin{cases} dV - \left(C_d^2 / C\right) dLnA = -gJdt \\ \mathrm{dx} = (V - C)dt \end{cases} \tag{16}$$

$J = \sqrt{\pi / A}\, \lambda V|V| / 4g$ represents the pressure loss by unit of pipe length.

The unknown values of (V , A , x, t), at any point P, as shown in Fig. 1, can be determined by knowing their values at the points Q and S lying on the two characteristics passing through P and then integrating the two equations (16).

5 Applications and Results

As an application, we consider the hydraulic installation (Fig. 2) composed by a pump supplying the mixture (air-water) through a pipe to a constant level reservoir placed at the downstream end of the pipe.

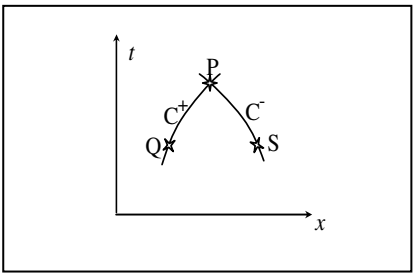

Fig. 1 Characteristic lines

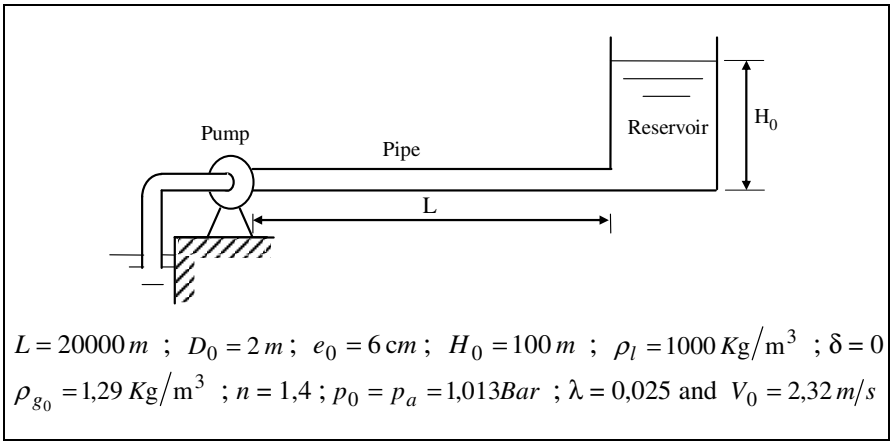

Fig. 2 Hydraulic installation

5.1 Influence of the Pipe Wall Elasticity on the Propagation of Pressure Waves

Fig. 3 represents plots of the pressure evolution as a function of time at different sections of the pipe, for $\theta = 10^{-4}$ and for different values of the Young's modulus. These plots show that the amplitude of the initial upstream depression, provoked by the sudden shut off of the pump, gets increasingly higher as long as the Young's modulus increases. These plots show too that the speed of the pressure waves decreases when the elasticity increases. In fact, it can be noted on Fig. 3, that the depression wave reaches the section x = 3L/4 after 65 s for E = 5 GPa (point A1), after 97 s for E = 1 GPa (point A2), after 128 s for E = 0.5 GPa (point A3) and after 277 s for E = 0.1 GPa (point A4).

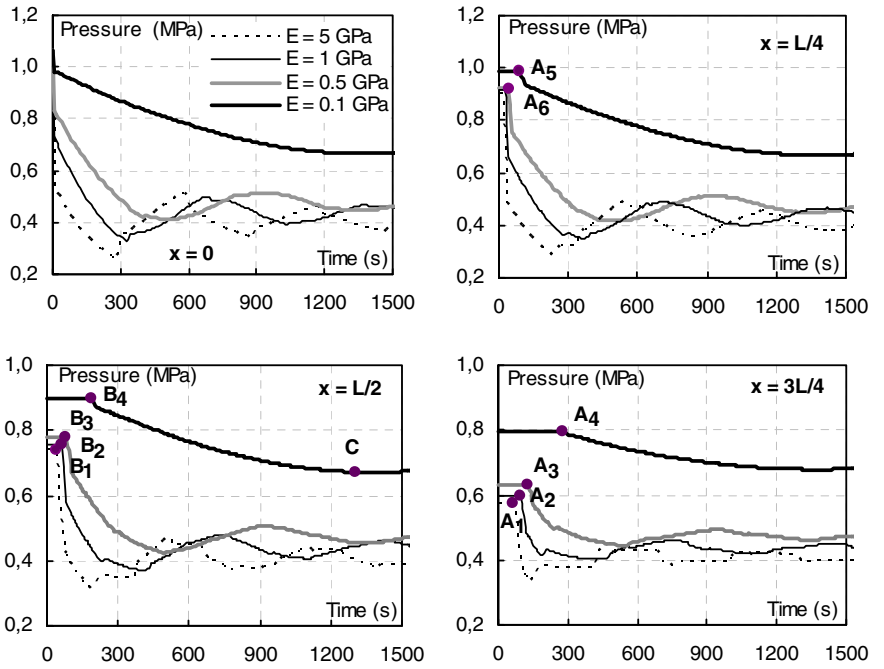

Fig. 3 Pressure evolution as function of time, at different sections of the pipe, for different values of E and for $\theta = 10^{-4}$

Furthermore, these plots show that beyond certain values of E, the speed of the pressure waves is not constant along the pipe. In fact, for E = 0,5 GPa, the pressure wave reaches the section x = L/4 (point A6) at the instant t = 36 s with an average speed of C = L/(4t)=138 m/s, while it reaches the section x =3L/4 (point A3) at the instant t = 128.s, with an average speed of 116 m/s. However, below certain values of E, the speed of waves along the pipe remains constant. In fact for E = 0,1 GPa, the pressure wave reaches the section x = L/4 (point A5) at t = 89s and it reaches the section x =3L/4 (point A4) at t = 277 s which gives an average speed in both sections equals to 55 m/s. In this case, the effect of the fluid compressibility is disregarded in front of the pipe wall elasticity. These plots show also that the restoration time of the final steady state flow is inversely proportional to the Young's modulus. In fact, it can be noted on the median section, that the final steady state for E = 0.1GPa is reached in 1100 s (point C), whereas for E = 5 GPa, E = 1 GPa and E = 0.5 GPa, the final steady state exceeds 1500 s.

5.2 Influence of Air Mass Ratio on the Pressure Evolution

Fig. 4 (a) shows the pressure evolution as a function of time for E = 2GPa and for different values of the air mass ratio θ. It can be noticed that the amplitude of fluctuations as well as the speed of these waves are inversely proportional to the

amount of gas in the mixture. Whereas, for values of E lower than 0.1GPa, the variation of the air mass fraction doesn't have any influence on the pressure waves as shown in Fig. 4 (b). In this case the pipe wall elasticity becomes preponderant and completely annihilates the effect of the fluid compressibility. The same findings can be deduced from equation (13). It's clear to see, in this equation, the interaction of the first two terms (related to θ) with the third term (related to E). In fact, for a given value of θ, when E decreases it reaches a certain value which permits to disregard the first two terms of equation (13) in front of the third term. In this case, and below this value of E, the compressibility of the fluid has no effect and the wave speed remains constant in all sections of the pipe. However, for a given value of E, the decrease of θ will lead to the increase of the wave speed and hence the pressure amplitude until θ reaches a certain value where the pipe wall elasticity becomes insignificant. In this case, the third term of equation (13) can be neglected in front of the first two terms of this equation as seen in Fig.4 (a).

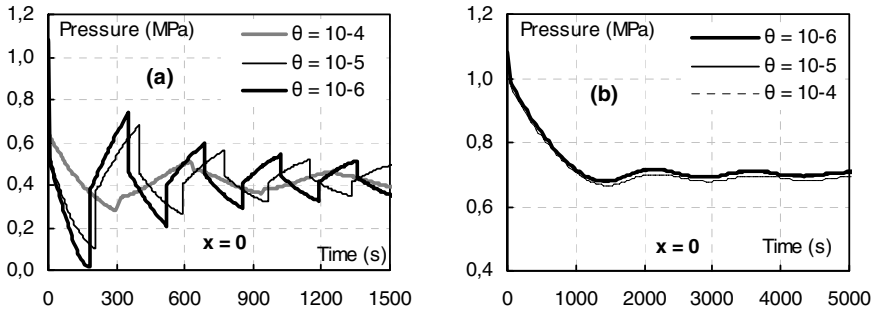

Fig. 4 Pressure evolution as function of time, at the upstream section of the pipe (x=0), for different values of θ and for E = 2 GPa (a) and for E=.0.1 GPa(b)

6 Conclusion

The numerical solution of gas-liquid mixtures transient flows in deformable pipelines caused by sudden shut-off of pumps has been presented. This problem is governed by two coupled partial differential equations of hyperbolic type. The numerical method employed is the method of characteristics. The occurrence of pressure oscillations in the different sections of the pipe was analyzed as a result of a depression wave originated by the sudden shutdown of a pump. We have analyzed the effect of the wall elasticity and the air mass fraction θ on the pressure evolution. The obtained results show that for a given value of θ, the pressure drops is proportional to Young's modulus. Furthermore it has been noted that beyond certain values of Young's modulus, θ has no influence on the pressure evolution, and beyond certain values of θ, the Young's modulus has no effect on the pressure evolution.

References

Abbott, M.B.: An Introduction to the Method of Characteristics. American Elsevier, New York (1966)

Bahrar, B., Rieutord, E., Morel, R., Zeggwah, G.: Modélisation du phénomène de coup de bélier avec prise en compte du comportement réel de la conduite. La Houille Blanche, Revue internationale de l'eau 1, 18–25 (1998)

Chammami, R., Taibi, M., Hami, M., Amar, M., Kerroum, M., Gueraoui, K., Zeggwah, G.: Influence de la nature de la paroi sur un modèle d'écoulements pulsés de fluides diphasiques. Application à la microcirculation. La Houille Blanche, Revue Internationale de l'eau 3/4, 18–23 (2001)

Chaudry, M.H., Bhallamudi, S.M., Martin, C.S., Naghash, M.: Analysis of transient in bubbly homogeneous gas-liquid mixtures. ASME, Journal of Fluids Engineering 112, 225–231 (1990)

Figueroa, C., Vignon-Clementel, I., Jansen, K., Hughes, T., Taylor, C.: A coupled momentum method for modeling blood flow in three-dimensional deformable arteries. Comput. Methods Appl. Mech. Engrg. 195, 5685–5706 (2006)

Hadj-Taïeb, E., Lili, T.: The Numerical Solution of the Transient Two-Phase Flow in Rigid Pipelines. International Journal for Numerical Methods in Fluids 29, 501–514 (1999)

Ouyang, L.B., Aziz, K.: Transient gas-liquid two-phase flow in pipes with radial influx or efflux. Journal of Petroleum Science and Engineering 30, 167–179 (2001)

Ryo, T., Oshima, M., Kobayashi, T., Takagi, K., Tezduyar, E.T.: Fluid-structure interaction modeling of blood flow and cerebral aneurysm: Significance of artery and aneurysm shapes. Comput. Methods Appl. Mech. Engrg. 198, 3613–3621 (2009)

Streeter, V.L., Wylie, E.B.: Hydraulic transients. F.E.B. Press, Ann Arbor (1983)

Chen, H., Liang, S.M.: Flow visualization of shock/water column interactions. Shock Waves Journal 17, 309–321 (2007)

Stuckenbruck, S., Wiggert, D.C., Otwell, R.S.: The influence of pipe motion on pressure wave propagation. ASME, Journal of Fluids Engineering 107, 518–522 (1985)

Intake Manifold Shape Influence on the Unsteady In-Cylinder Flow: Application on LPG Bi-fuel Engine

Mohamed Ali Jemni, Zied Driss, Gueorgui Kantchev, and Mohamed Salah Abid

Laboratory of the Electromechanical Systems, National School Engineers of Sfax, University of Sfax, BP 1173, Road Soukra, 3038 Sfax, Tunisia
{MohamedAli.Jemni,zied.driss,Gueorgui.Kantchev, MohamedSalah.Abid}@enis.rnu.tn

Abstract. The flow in the internal combustion (IC) engine intake manifold determines the flow in the cylinder prior and during the combustion. Consequently, intake-air manifolds have a major effect on engine's performances and emission pollutants. In order to achieve the best volumetric and thermal efficiency, the design of intake manifolds presents a very important objective for engines manufacturers. In this paper, the flow characteristics of air-fuel mixture flowing in various designs of manifold of IVECO 6 cylinder heavy-duty engine are studied. This engine operates with bi-fuel LPG (liquefied petroleum gas)-gasoline technology. The proposed paper aims to present a three dimensional unsteady CFD (Computational Fluid Dynamics) analysis of the flow inside the two manifold shapes. The mass flow rate of the in-cylinder charge, the velocity and the turbulent kinetic energy are investigated in order to develop a thorough understanding of the in-cylinder flow and identify the optimal manifold. The cyclic dynamic in-cylinder flow results show that the second intake manifold shape present the optimal configuration for engine charging. The comparison between simulation results and those from the literature showed a good concordance.

Keywords: Intake manifold, CFD, unsteady in-cylinder flow, bi-fuel engine.

1 Introduction

It must be obvious that the behavior of a spark ignition engine (SIE) depends to a large extent on the motions of the air-fuel and exhaust gas mixture through it. Ordinarily this motion is considered to be a steady flow; but since the flow is periodically interrupted by valves and accelerated by explosions, it is clear that each portion of the engine cycle is accompanied by vibrations of the gas concerned related to the unsteady inlet flow behavior (fig. 1). These vibrations are sometimes of very large amplitude, and may hinder or aid the performance of the engine (Philip 1938, Heywood 1988). With the use of CFD, the unsteady behavior of the intake charge can be well developed. CFD technique has become a tool for indoor

M. Haddar et al. (Eds.): *Design and Modeling of Mechanical Systems*, LNME, pp. 331–338.
DOI: 10.1007/978-3-642-37143-1_40

environment analyses since the 1970s, due to the development in computer programming and turbulence models. The parameters solved, such as flow velocity, pressure and turbulence characteristics, are crucial for designing the SIE various components, linked to the engine flow (Srebric and Chen 2002).

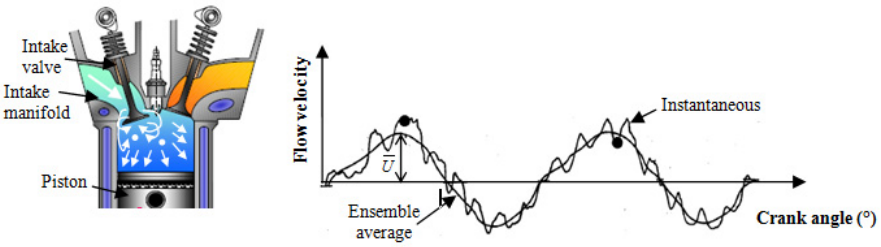

(a) Schematic of jet created by flow through the intake valve indicating its turbulent structure

(b) Schematic of velocity variation with crank angle at a fixed location in the cylinder during two consecutive cycles of an engine

Fig. 1 In-cylinder flow turbulent behavior

The use of CFD technique in the engine intake manifold is widely used by researchers in the automotive sector. Siqueira et al. (2006), are interested in evaluating numerically the pressure distribution and mass flow rate on each of the four runners during four cycles of operation, considering three different plenum geometries. Claywell et al. (2006), described the investigation of intake manifolds conceptions for a four-cylinder engine using 1D/3D coupled modeling techniques. They noted that the coupled 1D/3D methods showed that choked flow did not occur during 100% of the cycle, even at high engine speeds. Raj et al. (2013) used the CFD analysis in order to investigate the in-cylinder air motion coupled with the comparison of predicted results with the experimental results available in the literature. They concluded that a centre bowl on flat piston is found to be the best from the point of view of tumble ratio and turbulent kinetic energy which play very important role in imparting proper air motion. The aim of the present study is to investigate the unsteady in-cylinder flow through two intake manifold shapes, using FloWorks Simulation CFD code. The first manifold is adapted to the existing conventional designs (fig. 2, a). The design of the second manifold is appropriate to the natural supercharging technique, which is based on the acoustic waves behavior in the manifold runners (fig. 2, b).

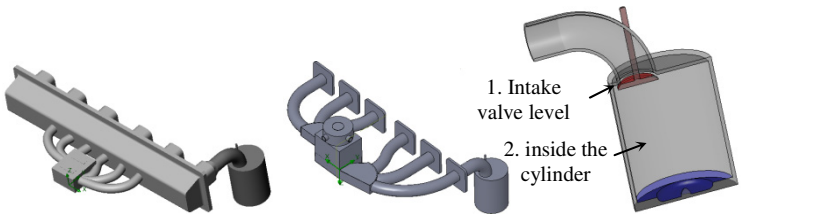

(a) Initial manifold shape (b) Second manifold shape (c) Simulation reference

Fig. 2 Intake system shapes

2 Simulation Methodology

In this study, the commonly available CFD tool FloWorks is applied. FloWorks has the advantages of importing geometry directly from a computer associated design (CAD) program such as SolidWorks. At the beginning, 3D geometry of the two manifolds is built using the SolidWorks (SW) software. The files created by SW are imported in FloWorks to build the grid for the final calculation of simulation. The CFD model is based on solving Navier-Stokes and energy equations in conjunction with the standard k-ε turbulence model.

The flow was considered incompressible, turbulent, isothermal and transient. The boundary conditions are taken as follows: at the manifold inlet we took an atmospheric pressure (≈ 1 bar), and the outlet surface of the intake manifold were changed automatically during the process, related to piston downward movement, in order to account for the opening and closing of the valves.

3 Engine Specification

The engine, on which are mounted the two manifolds, is a six-cylinder, 13.8 liter displacement, water-cooled, heavy duty, direct injection (DI), Diesel IVECO engine, installed at the authors' laboratory, which is used to power the urban bus in Sfax. It was modified to bi-fuel spark ignition engine gasoline and LPG fuelling (Jemni et al. 2011). All simulations are taken at a engine speed equal to 1500 RPM.

4 Numerical Unsteady In-Cylinder Flow Results

Results are taken in the intake valve level (flow through valve), level 1, and inside the cylinder, level 2, (fig. 2 c). The cyclic variation of the Intake valve mass flow rate of air-LPG mixer, Air-LPG mixer velocity, and turbulent kinetic energy are determined. The comparison between simulation results and those from the literature is also presented in order to validate the simulation.

4.1 Cyclic Variation of the Intake Valve Mass Flow Rate

The time evolution of the mass flow at the inlet valve (IV), through the two manifold shapes is detailed in fig. 3. Observing the two curves, we see that the closure of the valve causes a sudden drop in the flow. This latter has negative values during the first moments of the compression stroke. This behavior is explained by the influence of pressure waves reflecting on the outer surface of the valve. The return of these waves is opposite to the moving direction of the air-fuel mixture flow into the cylinder, which leads to negative amplitudes.

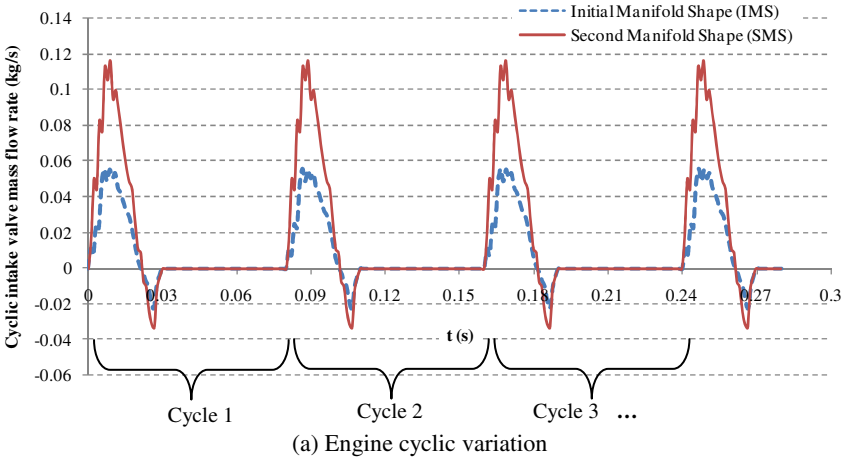

(a) Engine cyclic variation

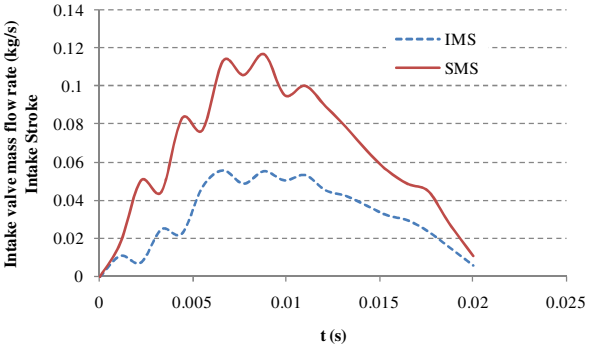

(b) Through intake strike

Fig. 3 Intake valve mass flow rate of air-LPG mixer

During the intake stroke (Fig. 3 b), there is flow oscillations whose amplitudes depend on the dynamics of the system. The parameters for these fluctuations are related to the fluid movement of the valve and the piston and the supply circuit. Comparing the instantaneous mass flow rates using the two manifolds, it is has been noted a significant difference fostering the second manifold shape (SMS). This difference appears mainly at the maximum opening of the valve. The maximum flow is equal to 0.12 kg. s^{-1} for SMS, while it does not exceed 0.06 kg. s^{-1} for the IMS.

4.2 Cyclic Variation of the Air-LPG Mixer Velocity

In Fig. 4 a, we present the cyclic variation of the in-cylinder flow velocity. Important velocity values are generated using the SMS during intake stroke, reaching maximum (134 m. s^{-1} for SMS and 65.2 m. s^{-1} for IMS) and then uncross respecting the piston movement. During the other three operating cycles of the engine,

the speed remains almost constant with some disruption. At the intake valve level, and when we confined in the intake stroke (fig. 4 b), it has been noted that there is a rapid increase in speed starting times. In arriving at the maximum, the velocity values decrease with a slower pace, and reverence the laws of the piston and opening the inlet valve. The mean difference in velocity between the two manifolds shape is 42%. Such a difference shows the influence of the manifold geometry on the cylinder charging and filling.

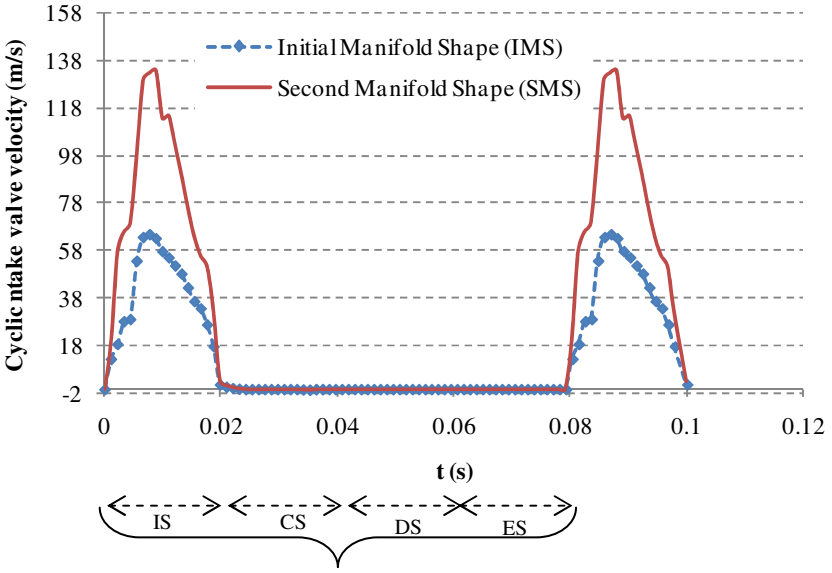

(a) Engine cyclic variation

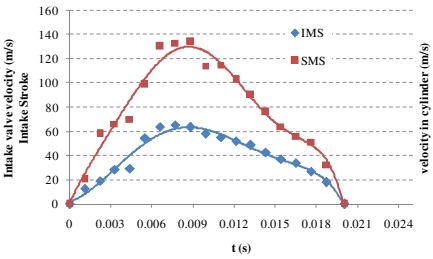

(b) Through intake strike at the IV stroke

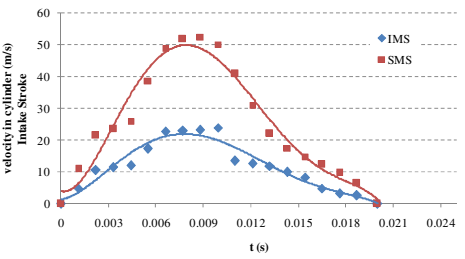

(c) Inside cylinder

Fig. 4 Air-LPG mixer velocity

Inside the combustion chamber, the velocity profiles indicate, as previously stated, the efficiency of the SMS (Fig. 4 c). The in-cylinder velocity varies from 0 to 135 m. s^{-1} for SMS and between 0 and 62 m. s^{-1} for the IMS. In addition, it has been that the difference is almost double that proves the effect of the intake manifold geometry on the in-flow velocity as well as the engine filling ratio.

The evolutions of the two curves are similar, since they are related both to the piston and intake valve movements.

4.3 *Cyclic Variation of Air-LPG Mixer Turbulent Kinetic Energy*

The turbulent kinetic energy (TKE) intensity for two manifold shapes during the engine cyclic variations and during the intake stroke can be viewed in (fig. 5 a) and (fig. 5 b) respectively. During the first moments of the aspiration stroke, the interactions between the fluid jet (air and fuel) are the most important mechanism for the production of the TKE intensity, which explains the shape of the slope of the two curves (between 0 s and 0.01 s). At t = 0.01 s, the curves reach the maximum TKE values. The abrupt fluctuation turbulence intensity (t = 0.004 s and t = 0.016 s) is due to the valve sudden opening and exhaust valve closing. In the compression stroke (stroke C) of a small negative peak has been observed. This phenomenon is explained by renewing in-flow (either waves produced in the cylinder) on the surface of the piston, thus generating a flow opposite to the movement direction.

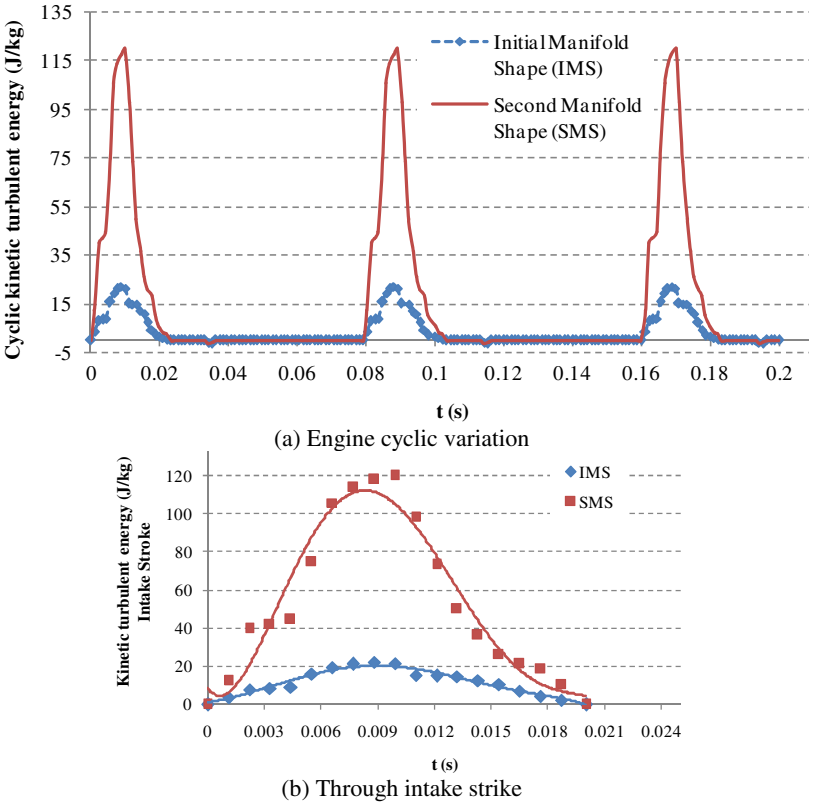

Fig. 5 Air-LPG mixer turbulent kinetic energy

Looking at fig. 5 b, it has been noted that the level of TKE intensity is higher using the SMS. This behavior is explained by the flow nature altogether directional and optimal. The difference of the intensity between the two manifolds attain up to 78%. At the end of the intake stroke, TKE values decrease slowly respecting the deceleration of the piston speed approaching to the bottom dead center (BDC).

Making an assessment on the previous results, it has been observed the effectiveness of the second manifold shape compared to the initial manifold shape.

4.4 Comparison with the Experiment Results

For the second manifold, our numerical results were compared with those found by other experimental results conducted by Mahrous et al. (2007) and Fuchs et al. (1998).

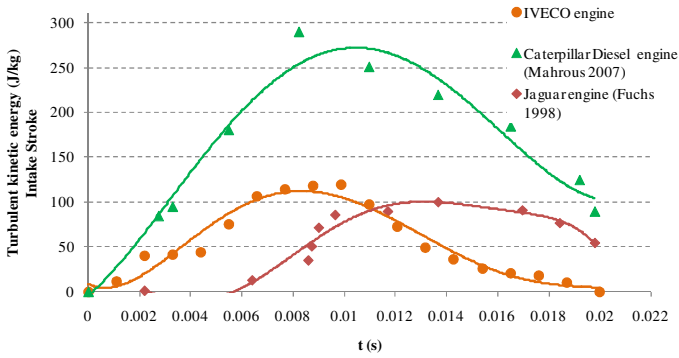

Fig. 6 Cyclic variation of the turbulent kinetic energy in the intake stroke (comparison with the literature)

Fig. 6 shows the variation of TKE during the intake stroke using three engines, our engine IVECO, Caterpillar engine and Jaguar respective with unit displacement equal to 2.3 l, 2.51 l, 2.5 l respectively. According to these results, it has been noted that almost all three cases reach their maximum turbulent kinetic energy in the interval [0.007 s, 0.013 s], which corresponds to the time of maximum piston speed for each engine. Also, it is clear that turbulence levels are more intense in the case of Caterpillar. This is due to the value of the unit cylinder displacement which is the most important. For this, when comparing the TKE between the other two engines, we find that, despite the larger Mahrous's engine unit cylinder displacement, the turbulence is more intense in our engine. This finding is clear especially in the intake first times, that is to say when the piston moves between the top dead center and the bottom dead center. This effect is achieved through the intake system adequate and reliable for the cylinder filling and reduced losses.

5 Conclusion

The present paper shows that the in-cylinder flow of air-LPG mixture through the intake valve and inside cylinder during the intake stroke, as a result of various intake manifold shapes, can be although explained using unsteady CFD investigations. The aim is to identify the most appropriate manifold configuration point of view flow characteristics. The numerical results affirm well the efficiency of the second intake manifold shape checking the good cylinder charging and filling. The comparison with the literature confirms our simulation results.

Acknowledgements. The authors would like to acknowledge supports from various organizations including Tunisian Regional Transport Company of Sfax (SORETRAS) and National School of Engineers of Sfax for their efforts and helpful technical and financial assistance.

References

Philip, M.M., Boden, R.H., Schecter, H.: Acoustic Vibrations and Internal Combustion Engine Performance. Standing Waves in the Intake Pipe System. Journal of Applied Physics 9, 16 (1938)

Srebric, J., Chen, Q.: An example of verification, validation, and reporting of indoor environment CFD analyses. ASHRAE Transactions 108(2), 185–194 (2002)

Heywood, J.B.: Internal combustion engine fundamentals. McGraw-Hill Inc. (1988)

Siqueira, C.R., Kessler, M.P., Araújo, L.A.R., Rodrigues, E.C.: Three-dimensional Transient Simulation of an Intake Manifold using CFD Technique. Society of Automotive Engineers 2006-01-2633 (2006)

Args, R., Mallikarjuna, J.M., Ganesan, V.: Energy efficient piston configuration for effective air motion – A CFD study. Applied Energy 102, 347–354 (2013)

Jemni, M.A., Kantchev, G., Abid, M.A.: Influence of intake manifold design on in cylinder flow and engine performances in a bus diesel engine converted to LPG gas fuelled, using CFD analyses and experimental investigations. Energy 36, 2701–2715 (2011)

Mahrous, A.F., Wyszynski, M.L., Wilson, T., Xu, H.M.: Computational fluid dynamics simulation of in-cylinder flows in a motored homogeneous charge compression ignition engine cylinder with variable negative valve overlapping. Proceedings of the Institution of Mechanical Engineers, Part D: Journal of Automobile Engineering 221, 1295–1304 (2007)

Fuchs, T.R., Rutland, C.J.: Intake Flow Effects on Combustion and Emissions in a Diesel Engine. SAE International, Paper Number: 980508 (1998)

Development of an Analytical and Numerical Tools for Launcher/Satellite Vibro-acoustic Prediction

Mohammed Amine Zafrane[1], Abdelmadjid Boudjemai[2], Nabil Boughanmi[1], and Mohamed El Houari Bouanane[3]

[1] Electronic Department Electrical Engineering Faculty, University of Science and Technology Oran-Mohammed Boudief, USTOMB, Algeria, P.O. Box 1505 El M'Naouar, Oran, Algeria
amine.eln@hotmail.com, boughanminabil@yahoo.com
[2] Centre of Space Techniques, Space Mechanical Division P.O. Box 13 Arzew 31200, Oran, Algeria
a_boudjemai@yahoo.fr
[3] Mechanical Engineering Faculty, Mechanical department, USTOMB, P.O. Box 1505 El M'nouar, Oran, Algeria
houaribouanane@yahoo.fr

Abstract. During flight mission, space vehicle is subjected to a severe fluctuating external-pressure loading when its rocket-propulsion system is operated in the atmosphere. Such acoustic loading and its frequency spectrum and Pogo effect, the acoustic loading results from the broad frequency-spectrum acoustic field generated by the mixing of the rocket-engine exhaust stream with the ambient atmosphere. Acoustic loads are principal source of structural vibration and internal noise during launch. This loading may be critical for vehicle components, as well as for the payload such as satellites. Coupled loads analysis (CLA) is a critical process for many high technology systems including launch vehicles and satellites. CLA predicts responses caused by major dynamic and loads events such. CLA helps to minimize risk and maximize the probability of mission success.

Keywords: satellite, coupled load analysis, launch vehicle, Acoustic.

1 Introduction

These during the launch of space vehicles there is a large external excitation generated by acoustic and structural vibration. This is due to acoustic pressure fluctuation on the vehicle fairing caused by the engine exhaust gases. This external excitation drives the fairing structure and produces large acoustic pressure fluctuations inside the fairing cavity [1]. Launcher-satellite coupled analysis is used for payload dimensioning and verifications and its important phase of the mission analysis. The prediction [2] of acoustic loading is essential to provide a

M. Haddar et al. (Eds.): *Design and Modeling of Mechanical Systems*, LNME, pp. 339–345.
DOI: 10.1007/978-3-642-37143-1_41

necessary input for the determination of vibration loads throughout the vehicle, and for the development of the vibration-test specifications and the associated dynamic design requirements which are necessary to ensure overall vehicle reliability.

Potential problems which may result from acoustic loading include:

- Malfunction of electronic and mechanical components in the vehicle from structural vibration and internal acoustic loading.
- Fatigue failure of internal component and supporting hardware.
- Fatigue of lightweight exterior structure.
- Fatigue of lightweight spacecraft structure.
- Adverse environmental conditions for vehicle occupant.

2 Sound Pressure at the Surface of Cylinder due to Incident Plane Wave

To invest the acoustic loading on a rocket fairing structure [3], it is important to predict and analyzed the sound pressure at the surface of cylinder of infinite length. To predict the overall external sound pressure, it is necessary to consider the pressure due to both incident and scattered waves, the later occur due to the reflection of waves from the surface. As shown in figure 1.

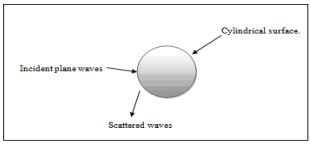

Fig. 1 Geometry of the cylindrical external problems

The total external sound pressure at the surface of a cylinder is the superposition of these two waves:

Incident sound pressure denoted by P^i and scattered sound pressure denoted by P^s.

Theoretical investigations of the external acoustic loading at the surface of a cylinder can be found in previously reported work [6-10].

2.1 The Total Sound Pressure

The total sound pressure at surface of a cylinder due to both incident and scattered waves can be calculated by sampling adding equation (4) and (5) as following (Morse, 1936; Morse&Ingard, 1986):

$$P^{Total} = -P^0 \sum_{m=0}^{M-1} A_m \cos\left(m\Phi_i\right) H_m\left(ka\right) + P^0 \sum_{m=0}^{M-1} \varepsilon_m i^m \cos\left(m\Phi_i\right) J_m\left(ka\right) \qquad (1)$$

The total sound pressure as a function of azimuth angle, rayon (a) and frequencies on the cylinder is represented in the figures 2, 3 and 4.

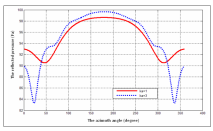

Fig. 2 Total sound pressure as a function of azimuthally angle at the surface of a cylinder of radius a, for values of ka= 1 and 3. [Reference pressure 20 micro P and incident pressure magnitude P0=1Pa].

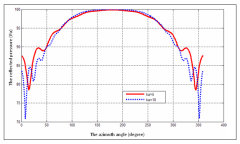

Fig. 3 Total sound pressure as a function of azimuthally angle at the surface of a cylinder of radius a, for values of ka= 5 and 10. [Reference pressure 20 micro P and incident pressure magnitude P0=1Pa].

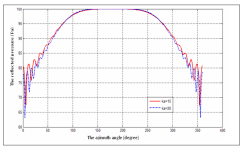

Fig. 4 Total sound pressure as a function of azimuthally angle at the surface of a cylinder of radius a, for values of ka= 15 and 20.[Reference pressure 20 micro P and incident pressure magnitude P0=1Pa].

The total Sound pressure fluctuations as a function of azimuthally angle at the surface of a cylinder for various values of Ka are shown clearly in the Cartesian figures 3 to 5 respectively. From these results is can be seen that the total sound pressure amplitude is relatively varying at the front (phi=180) of the cylinder and varies more aggressively at the back (phi=0). It is also interesting to see that the sound pressure fluctuations increase at the back of the cylinder as the value of Ka increase. The reason is that when Ka increase, the interference pattern between the two diffracted waves travelling around the two sides of the cylinder becomes more complex and this increase the scattered sound pressure fluctuations at the back of the cylinder (see figures scatted).

3 Coupled Load Analysis

In flight missions, launch vehicles are subjected to various broadband loads. In terms of acoustic solicitation, critical instants during a rocket launching, such

lift-off and transonic flight. These excitations expose the launcher's upper parts to extreme pressure loadings. During lift-off, the jet noise generated is reflected by launch platform and re-injected into the payload compartment, can damage sensitive parts of the payload (figure5), destroying the satellite mission and wasting considerable amount of money. [4 and 5]

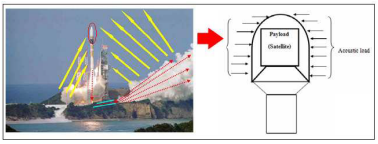

Fig. 5 Position of the satellite at lift-off

Table 1 Title of the table

Geometry	**Dimension in cm**
Max diameter	175.1
height	308.9

Figure 6 show the configuration of the parabolic fairing.

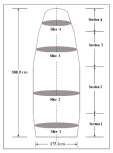

Fig. 6 The fairing form

The response of the fairing or the total acoustic pressure for different values of the frequency is shown in the figures 07, 08 and 09.

The table (2), shows the various values of ka for a frequency f = 50 Hz

Table 2 The values of ka for f=50 Hz

Slice	***Position z (m)***	***Ka***
Slice 1	0.76	1.305952760067850e+000
Slice 2	211.3	1.150699634745099e+000
Slice 3	254.7	7.853981633974483e-001
Slice 4	287.4	3.561689345639592e-001

The total sound pressure level for a frequency f= 50Hz on the fairing is given in Figure 07.

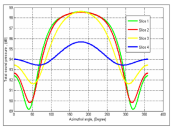

Fig. 7 The repartition of acoustic at the fairing at f=50 Hz

For a frequency f=80 Hz, The following table (3), shows the various values of ka.

Table 3 The values of ka for f=80 Hz

Slice	Position z(m)	Ka
Slice 1	0.76	2.089524416108560e+000
Slice 2	211.3	1.841119415592158e+000
Slice 3	254.7	1.256637061435917e+000
Slice 4	287.4	5.698702953023346e-001

The total sound pressure level presented on the fairing is given in Figure 08.

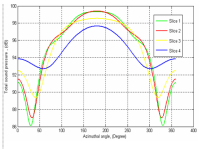

Fig. 8 The repartition of acoustic at the fairing at f=80 Hz.

For a frequency f=125 Hz, The following table (4), shows the various values of ka.

Table 4 The values of ka for f=125 Hz

Slice	Position z(m)	Ka
Slice 1	0.76	3.264881900169625e+000
Slice 2	211.3	2.876749086862747e+000
Slice 3	254.7	1.963495408493621e+000
Slice 4	287.4	8.904223364098978e-001

The total sound pressure level presented on the fairing is given in Figure 09.

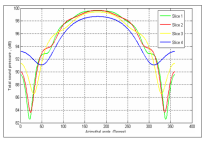

Fig. 9 The repartition of acoustic at the fairing at f=125 Hz

This study was done on a parabolic fairing. To generalize the application, we developed a graphical user interface allows selection of the faring shape and evaluate the acoustic spectrum for a frequency range determined.

The figure (10) represents the homepage.

Fig. 10 The Launch/Satellite coupled Graphical User Interface

Figure (11) shows the results of the segmentation of the fairing and the distribution of acoustic for each segment for the first four frequencies:

- F1= 50 Hz
- F2= 63 Hz
- F3= 100 Hz
- F4= 125 Hz

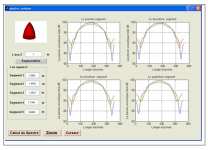

Fig. 11 Segmentation and calculation of the acoustic spectrum

4 Conclusions

It is a question in this study of developing a tool making it possible to better characterize the excitations applied to the small launchers, and of the vibroacpustic prediction using of the suitable methods.

As first step the results obtained concerning the acoustic pressure in the generic launcher are satisfactory as for the satellite casting/launcher, the algorithms genetics are very effective for the dimensioning of the fairing under different constraints

References

Pirk, R., Desmet, W., Plumers, B., Sac, P., Goes, C.S.: Vibro-acoustic analysis of the Brazilian vehicle satellite launcher (VLS) fairing

Pellisseti, M.F., Faransen, S.H.J.A., Calvi, A., Kreis, A., Schueller, G.I., Michel: Stochastic Launcher-Satellite Coupled Dynamic Analysis. Journal of Spacecraft and Rocket 43(6) (November-December 2006)

Morshed, M.M.M.: Investigation of External Acoustic Loading on a launch vehicle fairing during Lift-off. Ph.D. Dissertation, Scoolof Mechanical Engineering, the university of Adelaide, SA, Australia (2008)

Zaafrane, M.A., Boudjemai, A., Boughanmi, N., Bouanane, M.H.: Optimisation Multidisciplinaire par Algorithmes Génétiques du Couplage Satellite-Lanceur. In: Colloque International "Modélisation Stochastique et Statistique (MSS 2010)", Novembre 21-23. USTHB, Algeria (2010)

NASA TECHNICAL STANDAR Payload Vibroacoustic test criteria.NASA-STD-7001, June 21 (1996)

Potter, R.C.: Correlation Patterns of the Acoustic Pressure Fluctuations on the S-IC Vehicle Due to the Exhaust Noise ofthe Test and Launch Stand, Wyle Labs, Report WR 66-15, Contract NAS8-20073-1 (1966)

Fuller, C.R.: Analytical Model for Investigation of Interior Noise in Aircraft with Multiple Propellers Including Synchrophasing. Journal of Sound and Vibration 109(1), 141–156 (1986)

Fuller, C.R.: Free-field Correction Factor for Spherical Acoustic Waves Impinging on Cylin-ders. American Institute of Aeronautics and Astronautics (AIAA) 27(12), 1722–1726 (1989)

Junger, C.M., Feit, D.: Sound Structure and Their Interaction, ch. 10. MIT Press (1993)

Gardonio, P., Ferguson, N.S., Fahy, F.J.: A Modal Expansion Analysis of Noise Transmission Through Circular Cylindrical Shell Structures with Blocking Masses. Journal of Sound and Vibration 244(2), 259–297 (2001)

Multi-leaks Detection and Sizing in Viscoelastic Pipeline System

Ayed Lazhar, Lamjed Hadj-Taïeb, and Ezzeddine Hadj-Taïeb

Laboratory of Applied fluids Mechanics and Modeling,
ENIS P.O. Box 1173, 3038 Sfax, Tunisia
{hlzed,lamjed_hadjtaieb}@yahoo.fr,
Ezed.Hadj@enis.rnu.tn

Abstract. This paper presents a technique for detecting and locating several leaks in a single viscoelastic pipe by means of transient analysis. The system studied is a reservoir-pipe-valve one. The viscoelastic behavior of the pipe wall material is modeled by a generalized Kelvin-Voigt model. To determine the leak location the mathematical formulation has been solved by the characteristics method. The method uses transient pressure waves initiated by the sudden closure of a down-stream shut-off valve. The computed results describe the influence of the multi-leaks on pressure time-history and the effect of leaks locations on the pressure signal behavior. The results show that the method of characteristics is for great importance to model and simulate the affect of multi-leaks on transient pressure. Sensitivity of the proposed method on the location of the leak is determined in the case: two or three leaks. The effects of Young's modulus are also investigated.

Keywords: transient flow; pressure wave; viscoelastic pipe; leak detection; leak location.

1 Introduction

Water losses were identified from the beginning of the twentieth century. Research has shown that most of the losses are related to leaks which are the result of aging distribution networks that can be easily corroded and destroyed by intense mechanical stress. In recent years important strategies for reducing leakage are investigated and better leak detection technologies are enhanced (Andrew F. Colombo a Pedro Lee b Bryan W. Karney 2009).

Investigations of water losses were led by lai in 1991 and continued until now. These surveys have reported that water losses vary between 9% in Germany and 43% in Malaysia.

In addition to the amount of water lost leaks are costly in terms of energy consumption (Colombo A.F. Karney B.W. 2002). In U.S.America Research has shown that about 5 - 10 billion KWH of power were wasted on the water lost through leakage (AWWA. 2003).

M. Haddar et al. (Eds.): *Design and Modeling of Mechanical Systems*, LNME, pp. 347–354.
DOI: 10.1007/978-3-642-37143-1_42

Several techniques have been proposed for the detection of leaks in water systems such as acoustic technique (Babbitt 1920), electromagnetic techniques (Atherton et al. 2000), tracer gas injection (Furness and van Reet 1998; Black 1992). These techniques cannot be applied in all flow conditions or for any configurations of the transport systems and have a variable and expensive cost. The well studied system is a reservoir-pipe-valve system (Brunone 2001; Didia.C 2004-2005; Hadj-Taïeb et al 2012; …). In all these works authors use transient methods to detect leaks. Some of them use frequency analysis and others use the time-analysis of hydraulic transient in pipe flow.

The impact of a leak on the pressure evolution of a single pipeline system in the time domain is a well researched area and it was found in previous studies that a leak imposes a sudden pressure drop and other effects that depend on mechanical behaviour of the pipeline-system.

Single leak detection is a well studied area either in concrete pipes or in viscoelastic ones but not multi-leaks-detection.

In the present work in order to overmaster the singularity of the multi-leak detection problem, we propose the conception of a novel technique based on the method of characteristics. The model is extended to include the various leak positions and their effects on the head pressure at the end section of a reservoir pipe valve system with viscoelastic behaviour. The technique here proposed for leak detection belongs to the class of the Transient Analysis Methods. It uses the analysis of the time pressure history for locating and sizing leaks (Brunone 1999; Brunone and Ferrante 1999; Covas 2004 2005).

A leak as a singularity has several effects on the resultant pressure graph. The main effect is when the initial pressure wave reaches the leak. It will produce a reflection which can be seen when it arrives back at the section where the pressure wave has been created (Brunone and Ferrante 2001; Didia.C et al 2005; Hadj-Taïeb et al 2012). This effect is used as a tool for multi-leaks location and sizing.

The proposed numerical model of the 'water-hammer' for flow dynamic in viscoelastic pipeline with several leaks, based on the characteristic method, is presented in section 2. Simulation results are shown in section 3 and finally some conclusions and perspectives are given in section 4.

2 Numerical Scheme of Water Hammer in Viscoelastic Pipe

The simplified one-dimensional continuity and momentum equations that describe transient flow in elastic pipe are given in (Covas et al 2004 and Hadj-Taïeb et al 2012). These equations are transformed into a system of ordinary differential equations and solved by the method of characteristics (MOC).

A grid of characteristics is established in order to accomplish an orderly computer solution. The pipe of length L is initially subdivided into J *segment of pipes* every part of pipe have a length L_k discritized into equal N_k space-steps $\Delta x = L_k / N_k$.

So, and the compatibility equations are:

$$Q_{k,Pi} - Q_{k,i-1} + \frac{gA}{C}\left(H_{k,Pi} - H_{k,i-1}\right) + \frac{\lambda}{2DA} Q_{k,i-1}\left|Q_{k,i-1}\right|\Delta t + 2CA\Delta t\left(\frac{\partial \varepsilon_r^{\phi}}{\partial t}\right)_{k,i-1} = 0 \quad (1)$$

along the positive characteristic line ($dx/dt = +C$) and

$$Q_{k,Pi} - Q_{k,i+1} - \frac{gA}{C}\left(H_{k,Pi} - H_{k,i+1}\right) + \frac{\lambda}{2DA} Q_{k,i+1}\left|Q_{k,i+1}\right|\Delta t - 2CA\Delta t\left(\frac{\partial \varepsilon_r^{\phi}}{\partial t}\right)_{k,i+1} = 0 \quad (2)$$

along the negative characteristic line ($dx/dt = -C$).

The head pressure at the leak section is numerically obtained by equation (3)

$$H_{Pk} = \left[\left(-C_d A_{\ell k}\sqrt{2g} + \sqrt{\Delta_k}\right)\Big/\left(4\frac{gA}{C}\right)\right]^2 \quad (3)$$

$$\Delta_k = \left(C_d A_{\ell k}\sqrt{2g}\right)^2 - 8\frac{gA}{C}\left[\left(Q_{k+1,2} - Q_{k,N_k}\right) - \frac{\lambda\Delta t}{2DA}\left(Q_{k+1,2}\left|Q_{k+1,2}\right| - Q_{k,N_k}\left|Q_{k,N_k}\right|\right)\right.$$
$$\left. - \frac{gA}{C}\left(H_{k+1,2} + H_{k,N_k}\right) + 2CA\Delta t\left(\left(\frac{\partial \varepsilon_r^{\phi}}{\partial t}\right)_{k,Nk} + \left(\frac{\partial \varepsilon_r^{\phi}}{\partial t}\right)_{k+1,2}\right)\right] \quad (4)$$

where, C is the elastic wave speed estimated by (Covas et al 2004-2005).

3 Application and Results

To locate the leak by the transient flow analysis of incompressible flow supply system, we consider a polyethylene pipe of 0.0506 m in diameter and 277 m long. This pipe is connected to a constant pressure reservoir at the upstream end. At the downstream end, we consider a rapid closure valve.

We assume a flow rate $Q_0 = 1.008\ .10^{-3}\ m^3 s^{-1}$ and an absolute head pressure $H_0 = 44\ m$. The fluid is water with a density $\rho_0 = 1000\ Kgm^{-3}$ .The properties of the fluid system used in the calculations are similar to those of the system studied in (Hadj-Taïeb et al 2012). The K^{th} leak is located at X_K from the reservoir (upstream end of the system). In this paper to make easy the analysis of different figures, the colours shading of table-lines are similar to those of the figures legend.

Figures 1 and 2 and the enlargement of fig.2 (fig.3) are plotted at the downstream end section of the pipe that is just upstream of the valve. The pipe is supposed to be intact or respectively with two or three leaks.

The pressure wave caused by the instantaneous closing of the valve is propagated from the incident site through the hydraulic system. This wave full of energy is reflected every time it encounters a singularity. First time in Figs. 1 and 2 the

friction is considered equal to zero to separate the effect of several leaks from the friction effect on the temporal spectrum of pressure.

In fig.1 and if the pipe contains two leaks respectively located at $L_1 ; L_1 + L_2$ from the reservoir. Counting from the reservoir the so called first leak is that the closest to the tank. In fig. 1 this leak is located at different positions $(L_1 = 8L/10; L/5; L/5)$ and the second one is located at $L_1 + L_2$ from the tank where $L_2 \in \{L/10; L/6; 3L/5\}$.

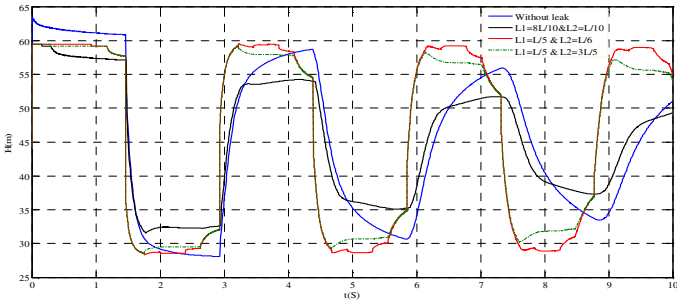

Fig. 1 Head pressure time-evolution at the end section of a reservoir-pipe-valve system with two leaks

By analyzing fig. 1 one can observe that when a sudden pressure surge is induced in a pipe system it introduces changes in the hydraulic transient event propagation.

One can easily observe the effects of the two leaks separately since the discharges of the two leaks are the same in fig. 1 and they vary like an orifice with constant opening degree. They induce two reflected waves. When they reach the closed valve each of these two waves undergoes a total reflection. Hence the shapes of the head pressure curves vary with the leaks locations indeed fig.1 shows this effect. When the leaks are close to the valve the head pressure decrease is more accelerated than the case when they are located far from the valve.

Figs. 1 and 2 show that in pressurized pipe with constant flow rate when there is an instantaneous or fast change in flow conditions the presence of leak induces a sudden pressure decrease that occurs at the travelling time $t_{\ell k}$ of the transient to the k^{th} leak and to return to the source. So end the location of the k^{th} leak can be estimated based on this travelling time by equation (5) (Hadj-Taïeb et al 2012).

$$X_k = L - \frac{\Delta t_{\ell k} C}{2} \tag{5}$$

where X_k is the distance to the k^{th} leak from the upstream end section (the reservoir).

The leak location uncertainty is estimated referring to equation (6)

$$\varepsilon_{lock} = \frac{= \overline{C\Delta t_{\ell k}} - C\Delta t_{\ell k}}{\overline{C\Delta t_{\ell k}}} \quad wherek\ is\ the\ leak\ order \tag{6}$$

Figs. 1 and 2 represent respectively two cases studied, the first is for the occurrence of two leaks and the second figure is plotted in the case of three leaks occurring in the same flow conditions. Fig.1 shows the head pressure time- evolution at the end section of an elastic pipe system $(\lambda=0)$. By analyzing the pressure time-evolution, in reduced scale: $(t\in[0\,,1.463s])$ and by applying equation (5), table 1 summarized the estimation of two leaks locations.

Table 1 Calculation of leaks locations from numerical simulation (case of two leaks)

$t_0(s)$	$\Delta t_{\ell 1}(s)$	$\Delta t_{\ell 2}(s)$	$X_1(m)$	$X_2(m)$
1.463	0.1522	0.3043	248.188	219.396
1.463	0.9277	1.171	101.386	55.33
1.463	0.2926	1.171	221.61	55.33

Figure 2 presents the time variation of piezometric head for three leaks located respectively from the tank at $(L_1, L_1+L_2, L_1+L_2+L_3)$ where, $L_1\in\{L/4, L/3, L/5\}$, $L_2=L/4$ and $L_3=L/4$. In this studied case the friction coefficient is equal to zero, so end the effect of three leaks on piezometric head at the end section of a viscoelastic pipe system is presented. The enlargement of fig.2 (fig.3) presents the piezometric head time-evolution when the leaks flows are equal $(Q_{\ell 0k}=0.1Q_0)$ *where* $k\in\{1,2,3\}$.

This figure shows that for the second and third leak the leaks pressure drops are equal but for the first leak there is a clear increase of leak pressure drop with the decrease of the distance of the leak from the downstream (valve).

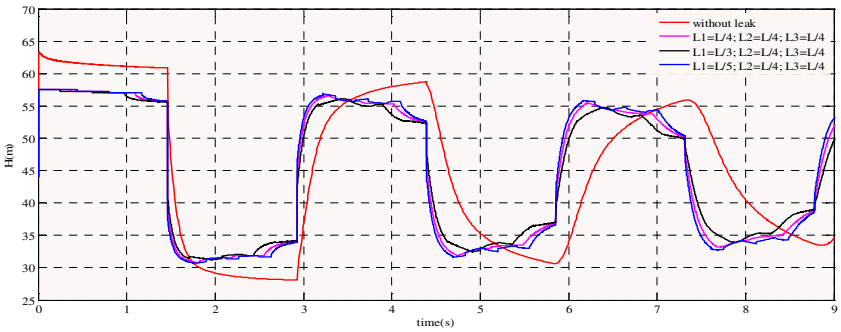

Fig. 2 Head pressure time-evolution at the end section of a reservoir-pipe-valve system with three leaks

By analyzing fig.3 and applying the equation (5), table 2 shows the locations of three leaks occurring in the same pipe system and in the same condition of flow monitoring.

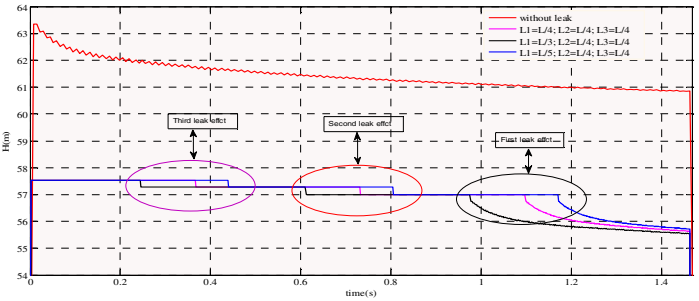

Fig. 3 Enlargement of figure 2

Table 2 Calculation of leaks locations from numerical simulation (case of three leaks)

$t_0(s)$	$\Delta t_{\ell 1}(s)$	$\Delta t_{\ell 2}(s)$	$\Delta t_{\ell 3}(s)$	$X_1(m)$	$X_2(m)$	$X_3(m)$
1.463	0.3658	0.7331	1.1	207.8	138.5	68.77
1.463	0.2463	0.6121	0.977	230.37	161.13	91.98
1.463	0.4404	0.8077	1.172	193.63	124.1	55.14

The leaks locations uncertainties calculated by applying equation (6), are given by table 3 and they are less than 1%, so they are acceptable (Brunone et al 2001).

Table 3 Calculation of leaks locations uncertainties from numerical simulation

Case of three leaks			Case of two leaks	
$\varepsilon_{1Loc}(\%)$	$\varepsilon_{2Loc}(\%)$	$\varepsilon_{3Loc}(\%)$	$\varepsilon_{1Loc}(\%)$	$\varepsilon_{2Loc}(\%)$
0.025	0	0.069	0.45	1
0.2	0.28	0.39	0.18	0.126
0.14	0.44	0.47	0.00451	0.126

Figure 4 shows the effect of the elastic strain in pressure history at the end section of pipeline system with three leaks located in the same locations and for different values of Young's modulus. This figure shows that for frictionless flow there's no change in the leaks locations but an important result can be shown, which is the impact of the elasticity of the pipe system on the pressure drop due to the pressure wave reflected by the leak, indeed if the Young's modulus is increasing the amplitude of the pressure drop due to the wave reflected by the leakage decreases, this can make no detectable the leak closer to the valve (fig.4).

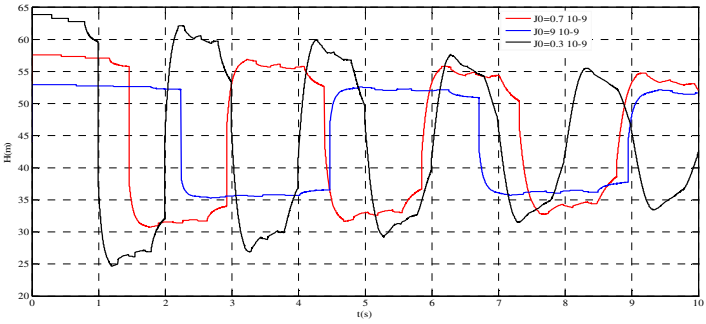

Fig. 4 Young's modulus influence on the head pressure at the downstream of a reservoir-pipe-valve- system with three leaks

4 Conclusion

This paper can be included in the research activity focused on the possibility of locating more than two leaks in viscoelastic pipe. Precisely it is pointed out the effect of several leaks on the pressure signal both in terms of the reflected pressure wave and the damping of the extreme values of the pressure. The effect of one leak may appear separately from another which facilitates the application of the proposed method. The pressure curves at the downstream end of a viscoelastic–pipeline-system with several leaks near the tank are in phase advance with respect to those in which the leaks are near the valve. The numerical simulation results show that the pressure wave is damped rapidly in the case where different leaks are near the valve yet these same results have shown that the leakage-effects on which this technique is based are present in all cases. For several leaks in viscoelastic pipe-system the results show that the leaks pressure drops are smaller for the leaks farer away from downstream. This conclusion makes relevant the application of this technique and its development to achieve the goal of real-time location of several leaks in piping viscoelastic systems.

This study leads to the use of a high technique in locating several leaks occurring in viscoelastic pipe system.

References

American Water Works Association, Leaks in Water Distribution Systems: A Tecnical/Economic Overview. AWWA, Denver (1987)

Atherton, D., Morton, K., Mergelas, B.: Detecting breaks in prestressing pipe wire. Journal of AWWA 92(7), 50–56 (2000)

AWWA Water Loss Control Committee, Applying worldwide BMPs in water loss control. Journal of AWWA 95(8), 65–79 (2003)

Babbitt, H.E.: The detection of leaks in underground pipes. Journal of AWWA 7, 589–595 (1920)

Brothers, K.J.: Water leakage and sustainable supply-truth or consequences? Journal of AWWA 93(4), 150–152 (2001)

Brunone, B., Golia, U.M., Greco, M.: Some remarks on the momentum equation for fast transients. In: Cabrera, E., Fanelli, M. (eds.) Proc. Int. Meeting on Hydraulic Transients and Water Column Separation, vol. 209, pp. 201–209 (1991)

Brunone, B.: Detecting leaks in pressurized pipes by means of transients. International Journal of Hydraulic Research 39, 539–547 (2001)

Colombo, A.F., Lee, P., Karney, B.W.: A selective literature review of transient-based leak detection methods. J. Hydro.-Environ. Res. 2, 212–227 (2009)

Covas, D., Stoianov, I., Mano, J., Ramos, H., Graham, N., Maksimovic, C.: The dynamic effect of pipe-wall viscoelasticity in hydraulic transients Part I – Experimental analysis and creep characterization. J. Hydraul. Res. 42, 516–530 (2004)

Covas, D., Stoianov, I., Mano, J., Ramos, H., Graham, N., Maksimovic, C.: The dynamic effect of pipe-wall viscoelasticity in hydraulic transients Part II – Model development calibration and verification. J. Hydraul. Res. 43, 56–70 (2005)

Ferrante, M., Brunone, B.: Pipe system diagnosis and leak detection by unsteady-state tests 1 Harmonic analysis. Adv. Water Resour. 26, 95–105 (2003a)

Ferrante, M., Brunone, B.: Pipe system diagnosis and leak detection by unsteady-state tests 2 Wavelet analysis. Adv. Water Resource 26, 107–116 (2003b)

Hadj-Taieb, L., Ayed, L., Hadj-Taieb, E.: Leak detection in viscoelastic pipe by means of transient. In: Conditioning Monitoring Machines in Non Stationary Operations, pp. 69–79. Springer (2012)

Lai, C.C.: Unaccounted for water and the economics of leak detection. Water Supply 9(3,4), IR1-1–IR1-8 (1991)

Mechanical Behaviour and Damage Evaluation by Acoustic Emission of Sandwich Structure

Imen Ben Ammar[1,2], Chafik Karra[2], Abderrahim El Mahi[1], Rachid El Guerjouma[1], and Mohamed Haddar[2]

[1] LUNAM University, Maine University, <CNRS UMR 6613>, Acoustic Laboratory of Maine University (LAUM), Avenue Olivier Messiaen, 72085 Le Mans CEDEX 9, France
{Imen.ben_ammar.etu,Abderrahim.elmahi, Rachid.el_Guerjouma}@univ-lemans.fr
http://www.univ-lemans.fr/fr/index.html

[2] Research Unit of Mechanics, Modeling and Manufacturing (U2MP), National School of Engineers of Sfax (ENIS), <Code: 05/UR/11-13>, BP 1173-3038 Sfax, Tunisia
chafik.karra@ipeis.rnu.tn, mohamed.haddar@enis.rnu.tn
http://www.u2mp.org/

Abstract. The aim of the present study is to investigate the mechanical behaviour of sandwich structure under static 4-bending loading. Two type of sandwich structures constituting with the $[0/90_2/0]_s$ cross-ply laminates as skins and with PVC closed-cell as foams which are differing in their densities: 60 and 100 kg m^{-3}, were considered. The effects of the foam densities on the mechanical behaviour of composites under loading were studied. This work is also interested in identifying and characterizing the local damage in the composites with the use of acoustic emission method (AE). The damage investigation in those materials is reached by the analysis of acoustic emission signals collected from static 4-point bending tests. A cluster analysis of AE data is achieved and the resulting clusters are correlated to the damage mechanism of specimens under loading tests.

Keywords: Sandwichs, 4-point bending, acoustic emission, static behaviour.

1 Introduction

Sandwich composite materials are increasingly being used in a variety of industrial applications such as, marine, automobile industry, aeronautics, aerospace etc. They are more advantageous compared to the other traditional metallic materials that they are characterized by their lightness, their Corrosion resistance, their simplicity of implementation, their insulation, their resistance to fatigue, their hardness and their flexibility. They are characterized by high rigidity, a high flexural strength and a low surface density.

(Farooq 2003) studied the mechanical behaviour of sandwich structure under static and dynamic loadings. The sandwichs panels are constituted by two skins of

M. Haddar et al. (Eds.): *Design and Modeling of Mechanical Systems*, LNME, pp. 355–363.
DOI: 10.1007/978-3-642-37143-1_43

glass fibres/epoxy and core of different foam thicknesses and densities. The testing procedures of this study include static and fatigue testing of cores in compression, indentation, shear and three-point bending tests and skins in flexural tests. The experimental studies are compared to the results obtained by the sandwich beam theory. This comparison carried out a good agreement between the two results. They showed also that the foams play an important role in the performance of sandwich composites in different loading environments. The bending and shear modulus increase with increasing core density. However, the bending modulus decreases with increasing core thickness. They studied also the mechanical behaviour on the fatigue of sandwich composites. The results of these investigations have highlighted the influence of many parameters (frequency of applied load, stress ratio, stress level, thickness of the core, density of the core materials and failure criteria in fatigue testing) on the performance of sandwich composites.

(M. Assarar 2007) studied the mechanical behaviour of sandwich and laminate structures under static 3-point bending tests. The distance between supports was 100 to 800 mm, for the different types of sandwiches which are constituted by two skins of glass fibres/epoxy and core of different foam thicknesses (60, 80 and 200 kg m^{-3}). They showed that the behaviour of a sandwich beam with lower density (60 and 80 kg m^{-3}) was linear at the beginning of the test, then it become non linear and when the distance between support decreases, the non-linear zone of the curve become shorter.

(R. Berbaoui et al. 2009) identified by acoustic emission method (AE) and analyzed the damage mechanism of a polymer concrete under an important load for a long time. The concrete specimens were subjected to 3-point bending tests and creep. Multivariate statistical analysis of collected signals was performed during the creep tests by a method of classification, composed by of Fuzzy C-mean and PCA methods. They showed the appearance of three types of damage which are cracking of the resin matrix signed by an acoustic signatures, their amplitudes were between 42 and 60 dB, the second mode of damage was the interfacial decohesion signed by a burst, their amplitudes were between 50 and 90 dB, the last mode of damage correspond to the break of aggregates signed by an acoustic signature their amplitudes were between 95 and 100 dB which appeared at the end of the test.

The aim of the present work is to analyse the mechanical behaviour of sandwich structure under static 4-bending tests. The effects of foam densities on the mechanical behaviour are studied in the first part. In the second part of this work, we use the acoustic emission method to identify and characterize the local damage in the different sandwich structures under static 4-bending buckling tests.

2 Materials and Methods

The materials considered in the analysis are sandwich structures which are prepared, in the Lab. LAUM (Acoustics Laboratory of the University of Maine, France).

Sandwich materials were constructed with the $[0/90_2/0]_s$ cross-ply laminates as skins and with PVC closed-cell foams supplied in panels of thickness of 20 mm. Two foams were considered differing in their densities: 60 and 100 kg m^{-3}. The layers of the cross-ply laminates of the skins were constituted of the unidirectional layers.

The four-point bending tests are performed using an Instron 8500 Digital Servo hydraulic testing system. The specimen dimensions are 22 mm × 40 mm × 300 mm, as shown in Fig. 1.

The sandwich material was supplied by the same manufacturer to avoid the variation during the fabrication and cutting of panels that could affect the behaviour of the samples during the static testing (Bezazi A and al. 2007). Four Point Bending (4PB) flexural testing was performed to specimens. In static tests, the specimens were loaded at a constant rate of 1 mm mn^{-1}.

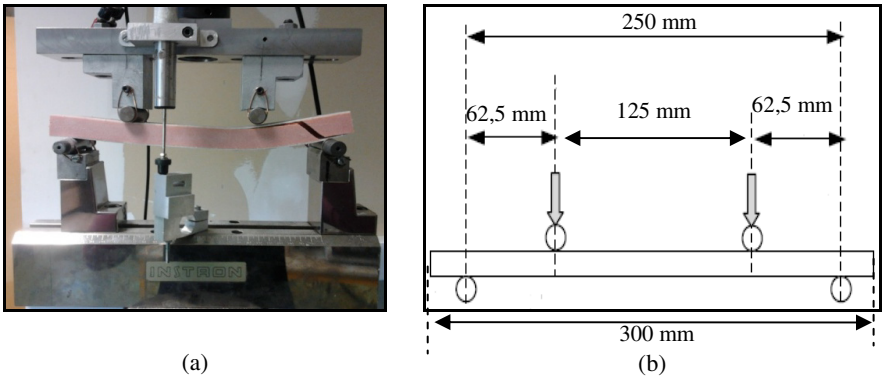

Fig. 1 Experimental four point bending set up and dimensions

The ultrasonic waves are recorded by the using of two channel data acquisition system from Euro Physical Acoustics (EPA) corporation with a sampling rate of 5MHz and a 40 dB pre-amplification. AE measurements are achieved by using two piezoelectric sensors with a frequency range 100 kHz–1 MHz, placed on the faces and the core of the specimens with silicon grease (Berbaoui B et al. 2009), as shown in the figure 2. The amplitude of the threshold was equal to 38 dB. The amplitude distribution covers the range 0–100 dB (0 dB corresponds to 1 mV for the transducer output).

The calibration of each test uses a pencil lead break procedure in order to generate repeatable AE signals. Several time-based descriptors are calculated by the acquisition system for each AE event: the amplitude, the energy, the duration, the rise time, the number of times the amplitude of the event goes beyond the given amplitude threshold (called counts), as shown in the figure 3.

These collected parameters are used as input descriptors in the proposed classification method (Arora A and Tangri K 1981) and (Marec A 2008).

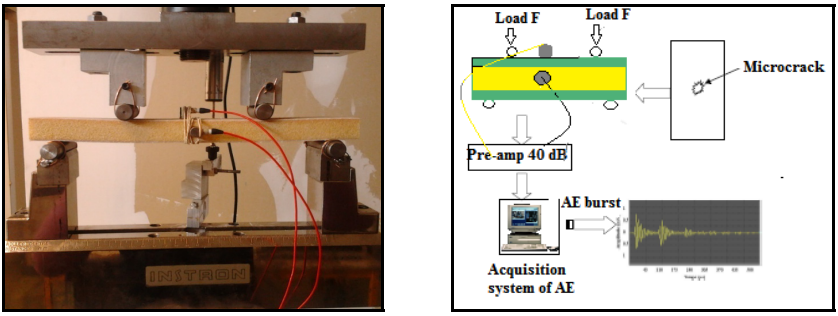

Fig. 2 Experimental set up of acoustic emission method

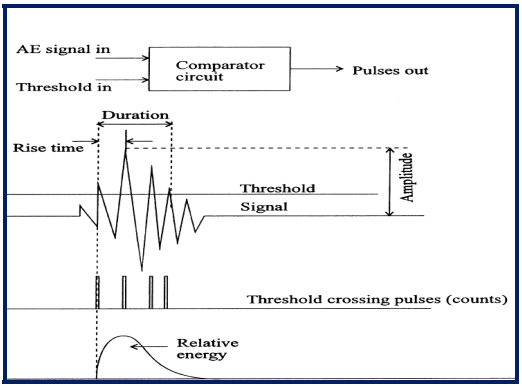

Fig. 3 Characteristic of a bust type of acoustic emission

In addition, once the automatic classification is realized with the fuzzy C-means clustering method, we use the PCA to visualize the clusters of data into a two-dimension subspace. This method requires the identification of damage mechanisms in the materials as each cluster corresponds to different damage mechanism which are illustrated in the table 1 (Shafiq B and Quispitupa A 2006) and (Quispitupa A et al. 2004).

Table 1 Characteristics of types of signals

Damage	Core damage	Interface failure	Resin cracking	Fiber rupture
Rise time	Average	Short	Short	Slow
Amplitude	~45-60	~60-80	~80-90	Above 90
Energy	0-25	3-219	88-374	347-13568

3 Mechanical Behaviour of Sandwich Structure

Four point bending tests have been performed repeatedly on all specimens. Three to five specimens were tested statically to failure. Static tests were performed in

4-point bending under displacement control in which sandwich specimens were loaded up to failure at a constant rate of 1 mm mn^{-1}. Values for F_u (ultimate failure load), d_u (ultimate failure displacement), and stiffness for each sandwich specimen were obtained from these tests. An average value of stiffness and fracture characteristics of five specimens were selected.

Static tests were performed to obtain strength and stiffness data. Figure 4 shows load-displacement curves in static tests for sandwich structures differentiated by the foams 60 and 100 kg m^{-3}.

Three regions are showed by this curve. The first region is primary region of compressive behaviour of skin laminates. This region initially corresponds to reversible linear behaviour and initiation, progression and development of transverse cracking in 90° plies of the skin, as observed in flexural testing of skins. The second region exhibits the compressive behaviour of core due to bending of the top skin and leads to non-linear behaviour of load-displacement curve that is mostly dependent on the properties of core. In the third region, with the further increase in load, there is initiation and development of delamination between skin and core which leads to the fracture of the skin and it corresponds to the propagation of the crack until final collapse.

The characteristics of the sandwich structures deduced from the static tests are reported in Table 2.

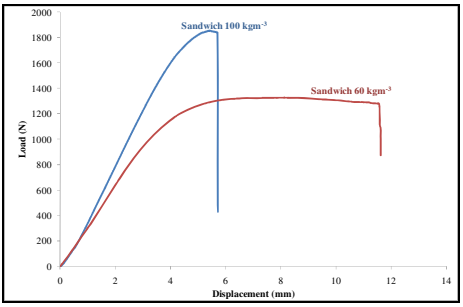

Fig. 4 Load-displacement curves in static four point bending tests

Table 2 Mechanical properties of sandwich structures in static 4-point bending tests

Foam	Rigidity (kNmm^{-1})	Critical load (kN)	Critical displacement (mm)
60 kg m^{-3}	0.31	1.11	11.6
100 kg m^{-3}	0.45	1.75	5.6

4 Acoustic Emission of Sandwich Structures

An external load level of 90 and 100% of the static failure load applied to the sandwich structure results a several damage mechanism observed with a

microscopic scale. In this study, those composite materials are damaged with static four-point bending tests.

4.1 Load Level of 90%

The same descriptors are used to compose the patterns of the sandwich structures under a level load equal to 90% of the static failure load.

The figures 5 and 6 show respectively the amplitude distribution and the time dependency of the different damage types. The number of clusters set for classifying the data is two for the sandwich structure with densities foam 60 kg m^{-3} and three for the sandwiches with a densities foam 100 kg m^{-3}.

For the sandwich with a densities foam 60 kg m^{-3}, figure 5 shows that the amplitude of the cluster 1 of the hits is in the range from 35–50 dB and the amplitude of cluster 2 cover the range 60-64 dB. For the sandwich with densities foam 100 kg m^{-3}, the amplitude of cluster 1 is in the range from 35–60 dB and the amplitude of the cluster 2 cover the range 70–80 Db. Finally the amplitude of the cluster 3 is in the range from 90–100 dB.

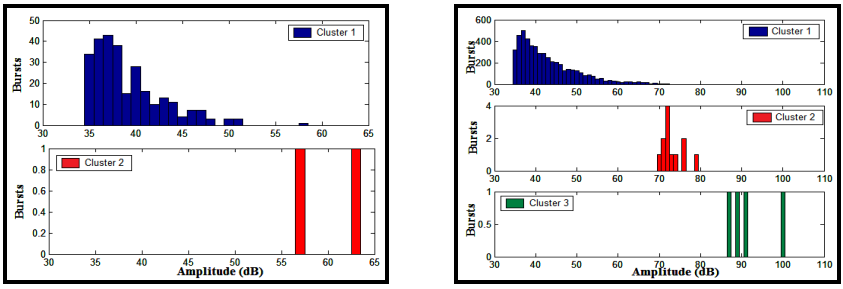

(a) (b)

Fig. 5 AE Amplitude distribution of each class obtained by classification for sandwich structures composite under 90% of the ultimate static load in: (a) densities 60 kg m^{-3} (b) densities 100 kg m^{-3}

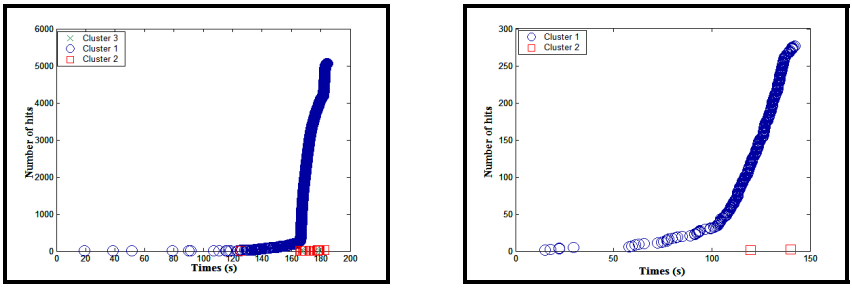

(a) (b)

Fig. 6 Time dependency of the identified damage types under 90% to ultimate static load in sandwich with foam their densities (a) 60 kg m^{-3} and (b) 100 kg m^{-3}

The time dependency of the different damage types (fig. 6) shows that the core damage are the most important mechanism of the sandwich specimens which start at the beginning of the test, whereas the failure begins from the starting of the experiment and are less numerous than the core damage. At the end of the tests of the sandwich with densities foam 100 kg m^{-3}, a few signals represent a break in the fiber which is absent in sandwich with densities foam 60 kg m^{-3}.

4.2 Load Level of 100%

Figure 7 shows the amplitude distribution of each class obtained by classification for sandwich under 100% of the ultimate static load in the case of two types of sandwich differing in their foam densities 60 and 100 kg m^{-3}.

In order to identify the evolution of each damage mechanism with time, the clustering method is applied to sandwich materials. The same descriptors are used to compose the patterns. The number of clusters set for classifying the data is four.

The first cluster has the lowest amplitudes, such as the burst amplitudes for the sandwich with foam 60 kg m^{-3} (sandwich 1) corresponding to 30–46 dB. However, it corresponds to 36–60 dB for sandwich with foam 100 kg m^{-3} (sandwich 2). Therefore, this cluster is representative of core damage.

For the second cluster, the amplitude distribution covers the range 68–80 dB for the sandwich 1 and it corresponds to 70–80 dB for the sandwich 2 typically indicating the interfaces failure.

In the third cluster, the amplitude distribution covers the range 80–89 dB for the sandwich 1 and it corresponds to 89 dB for the sandwich 2 typically indicating a resin cracking.

Finally, the last cluster the amplitude distribution for the sandwich 1 and 2 it corresponds above 90 dB and typically indicating a fiber rupture.

The time dependency of the different damage type shows that the core damage is the most important damage mechanisms for the two types of sandwich which starts at the beginning of the test. The second type of damage was the interface

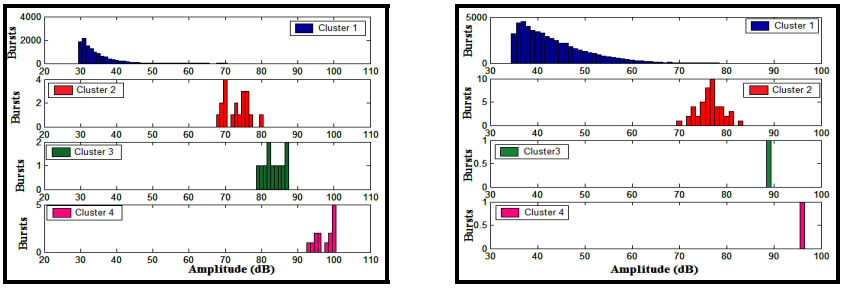

Fig. 7 AE Amplitude distribution of each class obtained by classification for sandwich structures composite under 100% of the ultimate static load in: (a) densities 60 kg m^{-3} (b) densities 100 kg m^{-3}

failure, which is smaller than the resin cracking (the third type of damage). At the end of the tests on specimens, few signals are detected which represent a breakage of the fiber. This is a very important result showing that the damage mechanisms don't have the same dynamic as indicated in the figure 8.

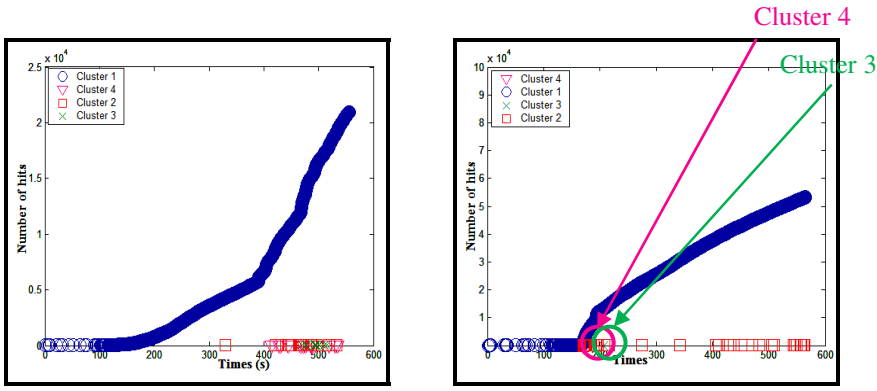

Fig. 8 Time dependency of the identified damage types under 100% to ultimate static load in sandwich with foam their densities (a) 60 kg m^{-3} and (b) 100 kg m^{-3}

5 Conclusion

The aim of this work is to investigate the mechanical behaviour of sandwich structures under static tests. Two types of sandwich structures which are differentiated by the densities of their foam were considered. .This study has shown that the rigidity of the sandwiches increase with increasing core density.

The classification carried out with the temporal descriptors allowed us to identify the different modes of damage that appeared on the specimens during the tests of 4-point bending in static under loading levels of 90% and 100% of the static failure load. The resulting clusters clearly identify the damage mechanisms of two types of sandwiches which depend on the densities of their foam.

References

Journal Article

Berbaoui, R., El Mahi, A.: Guerjouma, R (2009) Analyse par émission acoustique de l'endommagement et de la rupture du béton polymère en fluage. Manuscrit auteur, publié dans JNC 16, Toulouse, France (2009)

Shafiq, B.: A Fatigue characteristics of foam core sandwich composites. International Journal of Fatigue 28, 96–102 (2006)

Quispitupa, A., Shafiq, B., Just, F., Serrano, D.: Acoustic emission based tensile characteristics of sandwich composites. Composites: Part B 35, 563–571 (2004)

Arora, A., Tangri, K.: Acoustic emission: a means of measuring crack growth at elevated temperatures. Exp. Mech. 21(7), 261–267 (1981)

Bezazi, A., El Mahi, A., Berthelot, J.-M.: Experimental analysis of behavior and damage of sandwich composite materials in three-point bending. Part 1. Static tests and stiffness degradation at failure studies. Strength of Material 39(2), 170–177 (2007)

Marec, A., Thomas, J.-H., El Guerjouma, R.: Damage characterization of polymer-based composite materials: Multivariable analysis and wavelet transform for clustering acoustic emission data. Mechanical Systems and Signal Processing 22(6), 1441–1464 (2008)

Book

Farooq, K.: Comportement mécanique des composites sandwichs en statique et fatigue cyclique. Thèse de doctorat, Université du Maine, Le Mans (2003)

Assarar, M.: Étude expérimentale et modélisation du comportement dynamique des composites stratfiés et sandwichs. Thèse de doctorat, Université du Maine, Le Mans (2007)

Marec, A.: Contrôle de santé des matériaux hétérogènes par émission acoustique et acoustique non linéaire : Discrimination des mécanismes d'endommagement et estimation de la durée de vie restante. Thèse de doctorat, Université du Maine, Le Mans (2008)

CFD Modeling of the High Efficiency Rotor Separator in Cement Grinding Circuit

Guizani Rim[1,*], Mokni Inès[1], Mhiri Hatem[1], and Philippe Bournot[2]

[1] Thermal and Thermodynamic Unit of Industrial Processes (UTTPI),
National School of Engineers of Monastir (ENIM),
Av. Ibn ElJazzar, 5019 Monastir, Tunisia
{guizani_rim,mokni_ines}@yahoo.fr,
hatem.mhiri@enim.rnu.tn
[2] IRPHE, UNIMECA, 60 rue Juliot Curie,
Technopole de Château-Gombert,
13453 Marseille Cedex 13, France
bournot@univmed.fr

Abstract. This paper presents a numerical study of the gas-solid flow in the high efficiency rotor separator. The industrial CFD code (Fluent) is used for modeling the high turbulent fluid flow field and predicting the pressure drop inside the high efficiency separator. The DPM model is used to estimate the selectivity curve of the cyclone separator. Some factors which affect the performance of dynamic separator were identified. As well, this study aimed to highlight the limitations and difficulties that may be found to analyze such flow. The results proved that the RSM model better captures the phenomenon in the dynamic separator when compared with experimental results made by the Enfidha Cement plant CE. But much difficulty has been reached to achieve convergence.

Keywords: rotor separator, CFD, selectivity curve.

1 Introduction

Separators are widely used in the cement industrial plants and particularly in the grinding circuits. They are designed for selecting fine particles from coarse particles. The fine particle fraction is collected as finished product while the coarse particle is sent for supplementary grinding. The trick is to ascertain that the coarse fraction doesn't contain fine particles on one hand and, to ensure that the fine fraction doesn't contain coarse particles on the other hand. Separators can be divided into two groups: static separators or cyclones and dynamic separators or high efficiency separators. The major difference is that static separators don't have rotating elements while for the dynamic separator, a cylindrical rotor is necessary for the separation.

* Corresponding author.

M. Haddar et al. (Eds.): *Design and Modeling of Mechanical Systems*, LNME, pp. 365–372.
DOI: 10.1007/978-3-642-37143-1_44

In the past, extensive research has been focused on static separator however little was on dynamic separators. An experimental and a numerical studies of Jinyu Jiao et al (2006) [1] were made on a dynamic cyclone. They noted that the rotational classifier position and the ratio of the classifier opening area to the inlet area have significant impact on the separation efficiency of the dynamic cyclone. A further study made by Jinyu Jiao et al (2008) [2] on a rotor dynamic cyclone shows that the inlet gas velocity affects the separation efficiency depending on rotor rotational speeds. Recently a numerical simulation with the Fluent software is made by Qiang Huang et al (2012) [3]. In this study Qiang Huang et al concluded that a turbo air classifier with positively bowed guide blades produce smaller cut size and a higher classification precision than with straight guide blades.

Computational fluid dynamics (CFD) has become an important tool in the study of the flow field and the efficiency curve of dynamic separators in order to make design improvements. But a comprehension of the flow field inside the device is also needed.

In this paper, we will try to simulate the flow field in a dynamic separator where conditions are simulated using the Fluent software. In this study, we used the Reynolds Stress Model (RSM) with a multiple reference frame approach (MRF) and the discrete phase model (DPM) availables in Fluent to describe the gas-solid flow in the SEPOL third generation separator and also to predict its performance. Efficiency curve and pressure drops are then compared with experimental results provided by the Enfidha Cement plant “CE”.

2 Operating Principles of the High Efficiency Separator

The dynamic cyclone installed in the grinding circuit of Enfidha Cement and studied is equipped with four fine collection cyclones. The central material feed ensures uniform material distribution in the upper covering of the cage rotor. The separating air stream is generated by an external fan and fed into the separating chamber through a spiral inlet. The volume of separating air entering into the different height sectors of the separating chamber can be adapted to the conditions by means of adjusting flaps. The particulate matter is separated into fine and coarse fractions in the separating chamber due to the action of gravitational and airflow forces. Rotor blades prevent coarse material from entering the interior of the rotor. The coarse material drops into the cone and is returned to the grinding process. The fines are carried by the separating air into the interior of the rotor, are absorbed downward and then transported to the cyclones. The clean air stream returns to the fan.

A general view of the studied dynamic separator and its different components is shown in fig. 1. The rotation direction, the rotor blades and the setting of the fixed blades are shown in fig. 2.

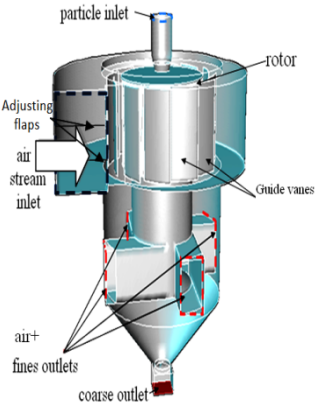

Fig. 1 A general view of the studied dynamic separator

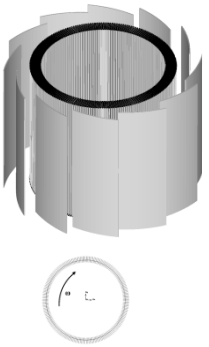

Fig. 2 Diagram of the rotor blades and the rotation direction

3 Simulation Conditions

The computational grid consisted of 991320 computational cells. We tried to build a hexahedral mesh in the maximum volume to achieve better results. The choice of the grid is too delicate to predict the complex flow field inside the studied geometry. A fine-grid simulation is needed to capture all the physical phenomena in the huge separator with 4040mm in diameter. However, a full-field simulation with a sufficiently fine grid needs very long computational times to get adequately resolved solution. Grid refinements tests are done so that we could be sure that the solution is not grid dependant.

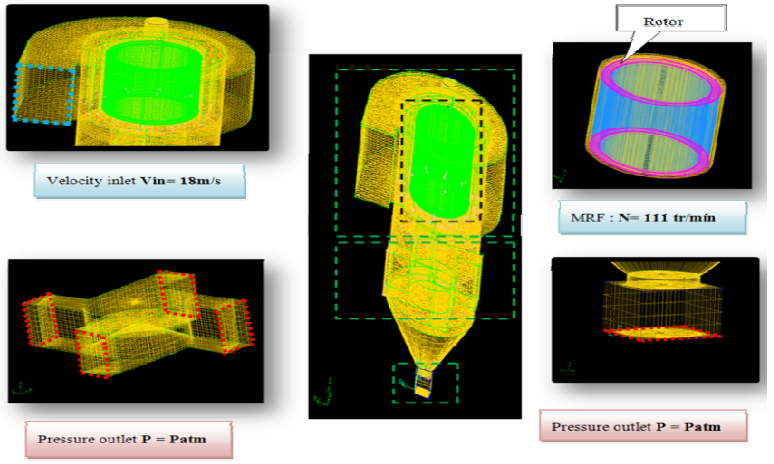

Fig. 3 CFD grid of the dynamic separator and boundary conditions

Fig. 3 shows an overview of the separator grid, the boundary conditions and the rotary part grid called (MRF) generated on Fluent. A "velocity inlet" boundary condition was used for gas flow inlet for an air flow rate of 200000 m^3/h. The "pressure outlet" condition is chosen in the solid and gas exits. No slip condition was used in wall boundary, and near wall treatment was standard wall function. The simulation was conducted at a rotor cage rotary speed of 111 r/min. Cement particles density is 1190 Kg/m3. They are injected from the mass flow inlet surface. The coupled calculation of the discrete phase with the continuous gas phase is adopted. The rotor cage has an outer diameter of 2740 mm and a height of 1900mm.

4 Model Description

To predict the flow pattern and the performance of the dynamic separator, unsteady CFD simulations were performed. In this study, a three dimensional simulations is carried out for the gas-solid separator. Multiple Reference Frame (MRF) approach is used to simulate the interaction between the moving rotor and the stationary surrounding parts. The (RSM) model is used to describe the anisotropic turbulence in the separator. For an incompressible flow, the governing equations can be written as follows [4]:

$$\frac{\partial \overline{U}\,\mathrm{i}}{\partial x_i} = 0 \tag{1}$$

$$\rho \frac{\partial \overline{U}\,\mathrm{i}}{\partial t} + \rho \overline{U}\, j \frac{\partial \overline{U}\,\mathrm{i}}{\partial x_j} = -\frac{\partial \bar{P}}{\partial x_i} + \frac{\partial}{\partial x_j}\left(\mu \frac{\partial \overline{U}\,\mathrm{i}}{\partial x_j} - \rho \overline{u'_\iota u'_J}\right) \tag{2}$$

Where the velocity components are decomposed into the mean $\overline{\mathrm{U}}\,\mathrm{i}$ and fluctuating $\mathrm{u'}_\mathrm{i}$ velocities which are related as given by:

$$Ui = \overline{U}\,\mathrm{i} + \mathrm{u'}_\mathrm{i} \tag{3}$$

Decomposing the variables in Navier Stokes equations yields an additional term Rij= $\overline{\mathrm{u'_\iota u'_J}}$ to the momentum equation. This term is called the Reynolds stress tensor. It includes the turbulence closure, which must be modeled to close (2).

4.1 Turbulence Model RSM

Transport equations of the Reynolds stresses terms (Rij= $\overline{\mathrm{u'_\iota u'_J}}$) are written as:

$$\frac{\partial R_{ij}}{\partial t} + C_{ij} = P_{ij} + \left(D_{T,ij} + D_{L,ij}\right) - \varepsilon_{ij} + \phi_{ij} \tag{4}$$

Where C_{ij}, P_{ij} , D_{ij} ,ε_{ij} , ϕ_{ij} *et* Gij are respectively: the convective transport term, the stress production term, the diffusion term, the dissipation term, the pressure

strain term and the buoyancy production term. The RSM model requires the following empirical constants [4]:

$$C_{\mu} = 0.09,\ C_{\varepsilon 1} = 1.44,\ C_{\varepsilon 2} = 1.92,\ \sigma_{\varepsilon} = 1,\ \sigma_{k} = 0.82.$$

4.2 Discrete Phase Model DPM

The motion of a particle is described by the stochastic Lagrangian multiphase flow model. Its trajectory is obtained by integrating the particle force balance. There are many forces that act on a particle in cyclone separator as centrifugal force, drag force and gravity force. Thus, the particle motion equation can be written as follows [4]:

$$\frac{\partial \vec{u}_p}{\partial t} = F_D\left(\vec{u} - \overrightarrow{u_p}\right) + \frac{\vec{g}\left(\rho_p - \rho\right)}{\rho_p} + \frac{\vec{F}}{\rho_p} \tag{5}$$

F is a source term which expresses the presence of an additional force. $F_D\left(\vec{u} - \overrightarrow{u_p}\right)$ is the drag force per unit particle mass and $F_D$is given by [4]:

$$F_D = \frac{18\,\mu}{\rho_p\, d_p^2} \frac{C_D Re_p}{24} \tag{6}$$

Where $$\mathrm{Re_p} = \frac{\rho \mathrm{d_p}(\vec{u} - \overrightarrow{u_p})}{\mu} \tag{7}$$

C_D, ρ, ρ_p, μ et dp are respectively the drag coefficient, the fluid density, the particle density, the molecular viscosity of the fluid and the particle diameter.

4.3 Multiple Reference Frame Model MRF

The MRF model is a steady state approximation where the fluid zone in the rotor is modeled in a rotating frame of reference and the surrounding zones are simulated in a stationary frame.

To transform the fluid velocities from stationary to rotating frames, the following relation is used [4].

$$\overrightarrow{v_r} = \vec{v} - \overrightarrow{u_r} \tag{8}$$

Where $$\overrightarrow{u_r} = \vec{\omega} * \vec{r} \tag{9}$$

$\overrightarrow{v_r}$ is the velocity relative to the rotating frame, $\vec{v}$ is the absolute velocity and $\overrightarrow{u_r}$ the whirl velocity. $\vec{\omega}$ is the angular velocity and $\vec{r}$ is the position vector to the rotating frame.

Solving the equations of motion in the rotating frame results in additional acceleration terms in the momentum equation [4].

$$\frac{\partial \rho}{\partial t} + \nabla . \rho\, \overrightarrow{v_r} = 0 \tag{10}$$

$$\frac{\partial}{\partial t}(\rho\,\vec{v}) + \nabla.(\rho\,\overrightarrow{v_r}\,\vec{v}) + \rho(\vec{\omega} * \vec{v}) = -\nabla p + \nabla\overline{\overline{\tau}}_r + \vec{F} \quad (11)$$

Where $\overline{\overline{\tau}}_r$ is the viscous stress. The Coriolis and centripetal accelerations are included in the momentum equation with the term $(\vec{\omega} * \vec{v})$.

5 Simulation predictions and Discussion

5.1 Separator Performance

The main performance characteristics to be considered in the design of dynamic air classifier separators are the pressure drop and the separation efficiency. The pressure drop across cyclone air classifier is a significant characteristic since it is directly related to the operating costs. The pressure drop over a cyclone separator can be calculated as the difference of static pressure between the inlet and outlet.

The values of the pressure drops computed across the dynamic separator are listed in table 1 and then compared with experimental results provided by the CE plant. The comparison shows that the developed models underestimate the pressure drop in the rotor separator.

Separator efficiency can also be illustrated by the selectivity or the tromp curve. This curve has a fished-hook shape showing for each grain size what percentage of the separator feed is selected as fines (left side of the curve) or retained as grits (right side of the curve). The main characteristics of the curve are its inclination of the quasi linear portion called "Imperfection" and the distance of the horizontal axis of the lowest point (τ) called bypass [5]. For a dynamic air classifier separator, high selectivity means a steeper curve and a smaller bypass.

The numerical and experimental selectivity curves calculated of the studied dynamic separator are shown in fig. 4.

From this figure, it can be seen that the experimental and numerical curves are close for particle size less than 20µm and they are almost the same for particle size greater than 20µm. This difference can be the result of electrostatic force between particles that FLUENT doesn't take account of it. From this figure, we can also note that the experimental by-pass is a little bit high.

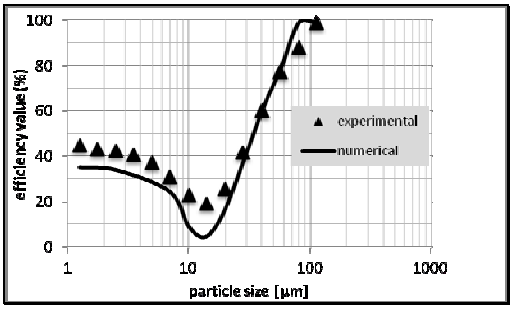

Fig. 4 Experimental and numerical selectivity curves of the studied dynamic separator

Table 1 The experimental and numerical pressure drop of the dynamic separator

	outlet 1	outlet 2	outlet 3	outlet 4
Exp ΔP[Pa]	1426	1642	1529	1625
CFD ΔP[Pa]	1403.6	1407.0	1404.6	1406.5

5.2 Streamlines in the Dynamic Separator

Fig. 5 describes clearly the flow path lines projected onto the plane (x=0) in the dynamic separator. From this figure, we can locate a lot of recirculation flows. We also note that the flow pattern from the separation zone to the exit fines tubes is characteristic of severe flow recirculation which takes the form of axisymmetric bubbles. This phenomenon is called the vortex breakdown which is clearly observed closer the vortex axis of the rotary cyclone.

The vortex breakdown has been found detrimental in cyclone separators [6-7].

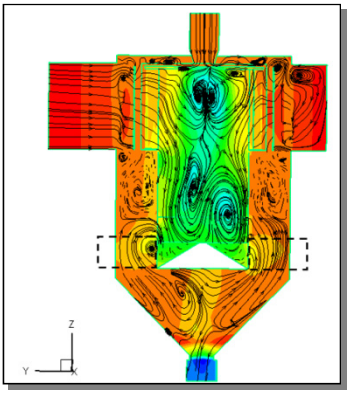

Fig. 5 Pathlines and secondary flows in the dynamic separator

6 Conclusion

In this work, CFD numerical simulations of the flow field have been performed on the gas-solid dynamic separator.

The results prove that the turbulence RSM and the stochastic Lagrangian DPM models with the Multiple Reference Frame can predict flow pattern qualitatively correct and better captures the essential features of the swirling flow in the rotary cyclone.

The calculated pressure drop and the selectivity curve of the dynamic separator are compared to experimental measurements given by Enfidha Cement industry. In general results are in good agreements. But better results can be found if we used other multiphase model as the Eulerian model that takes account of the interactions between particles but powerful computer codes are required.

Secondary recirculation flows and bubble breakdown phenomenon is can be observed by CFD simulation and locating these flows can be an important factor for the improvement of separator conception.

References

[1] Jiao, J., Zheng, Y., Sun, G., Wang, J.: Study of the separation effi-ciency and the flow field of a dynamic cyclone. Separation and Purification Technology 49, 157–166 (2006)
[2] Jiao, J., Zheng, Y., Wang, J., Sun, G.: Experimental and numerical investigations of a dynamic cyclone with a rotary impeller. Chemical Engineering and Processing 47, 1861–1866 (2008)
[3] Huang, Q., Liu, J., Yu, Y.: Turbo air classifier guide vane improvement and inner flow field numerical simulation. Powder Technology, 226 (2012)
[4] FLUENT 6.3, Documentation. User's Guide Fluent.Inc (2001)
[5] Herrmann, C.: Increased Cement Grinding Efficiency by Using High Efficiency Separators. IEEE Transactions on Industry Applications IA-22(2) (1986)
[6] Lucca-Negro, O., O'Doherty, T.: Vortex breakdown: a review. Progress in Energy and Combustion Science 27, 431–481, 434 (2001)
[7] Keller, J.J.: On the interpretation of vortex breakdown. Phys. Fluids 7 (1995)

Waterhammer in Flexible Pipes

Othman Damak and Ezzeddine Hadj-Taïeb

L.R. Applied Fluid Mechanics,
Process Engineering and Environmental, ENIS,
P.O. Box 1173, 3038 Sfax, Tunisia
othman.damak@yahoo.fr,
Ezed.Hadj@enis.rnu.tn

Abstract. Consideration is given in this paper to the numerical solution of the transient flow in highly flexible pipes such as rubber tubing and arterial system. The transient regime is provoked by the waterhammer phenomenon. A mathematical model constituted of continuity and motion equations is presented. In this model, the tube wall is assumed to be elastic and the compressibility of the liquid is neglected. To take into account the fluid-structure interaction, a nonlinear relationship between the pressure and the cross-section area of the pipe is developed. A system of two nonlinear partial differential equations of hyperbolic type is formulated. The irregular grid characteristics method is applied to solve this system. The numerical developed algorithm permits to get indications on the evolution of the pressure waves due to a valve fast closing at the downstream end of the flexible pipe. Computation results show that the pressure wave propagation is significantly influenced by the pipe wall elasticity.

Keywords: wave pressure, flexible pipe, fluid-structure interaction, method of characteristics.

1 Introduction

For a long time, transient flows in elastic piping systems have received a lot of interest to predict the pressure fluctuations provoked by the waterhammer phenomenon. The circumstances where these pressure fluctuations appear are numerous, such as the case of voluntary disturbances (rapid valve-closure) or the case of accidental disturbances (sudden pump-failure, pipeline ruptures…). The most widely of the previous investigation has considered the pipe to be quasi-rigid, such as metallic pipes, with constant diameters and thicknesses (Bergeron 1949, Streeter and Wylie 1967).

Recent investigations, by many authors, have examined the pipe's flexibility effect on the pressure wave propagation in deformable elastic pipes such as rubber hoses and arteries. These transients possess some properties which are different from those related to the rigid or quasi-rigid pipes. In such flexible systems the fluid is considered incompressible relative to the elastic properties of the tube wall material. We can quote the studies of (Rooz et al. 1982) and (Porenta et al 1986).

M. Haddar et al. (Eds.): *Design and Modeling of Mechanical Systems*, LNME, pp. 373–380.
DOI: 10.1007/978-3-642-37143-1_45

They have presented an uncoupled mathematical model for radial deformable pipes, constituted by two equation system, where the pipe wall axial motion has been neglected. The dynamic fluid pressure and the radial deformation of the pipe wall were then separately calculated. (Stuckenbruck and Wiggert, 1986 and Karra et al. 2007) have investigated the problem of an elastic flexible-tubing model in witch Poisson coupling takes place between the pipe wall and the liquid. They developed an interactive elastic tube model in which the dynamic fluid pressure causes circumferential and axial motion of the tube wall. A four-equations system has been formulated which accounts for wave propagations in both the wall and the liquid. In all previous studies, unsteady flows are generated by gradual changes in flow conditions when a tube is subjected, at the inlet, to a periodic flow excitation. The problem of transient flows in flexible pipes provoked by sudden valve-closures has not been examined. The purpose of this study is to show the influence of the nonlinear elastic behaviour of the pipe wall on the propagation of the pressure wave generated by the waterhammer phenomenon. A mathematical model, of two nonlinear partial differential equations of hyperbolic type, in which the liquid compressibility is neglected against the pipe wall deformability, is investigated. Since the governing equations of such flow are nonlinear, the solution can be obtained only by some approximate numerical techniques. The characteristics grid method, based on the pipe cross area, is applied. Numerical results obtained by this numerical technique are presented for different values of the exponent used for nonlinear elastic-wall equation.

2 Mathematical Formulation

By application of the mass conservation and momentum laws to an element of fluid between two sections of abscissa x and x+dx of the pipe, we get the following equations of continuity and of motion (Wylie et al. 1993):

$$\frac{\partial A}{\partial t}+\frac{\partial VA}{\partial x}=0 \tag{1}$$

$$\frac{\partial V}{\partial t}+V\frac{\partial V}{\partial x}+\frac{1}{\rho_l}\frac{\partial p}{\partial x}+\frac{\lambda V|V|}{2D}=0 \tag{2}$$

where λ is the coefficient of friction.

Equations (1) and (2) form a system of two nonlinear partial differential equations of hyperbolic type in which the pressure p and the velocity V, are considered being the main variables of the flow. To solve numerically these equations, the cross section $A=\pi D^2/4$ of the pipe is expressed in term of the fluid pressure as following:

$$p=(A_0/A)[(E_0e_0/D_0)Ln(A/A_0)+p_0] \quad if\ \delta=0 \tag{3}$$

$$p = (A_0/A)\left[(2E_0e_0/\delta D_0)\left((A_0/A)^{\delta/2} - 1\right) + p_0\right] \quad if\ \delta \neq 0 \tag{4}$$

where e is the thickness of the tube and $R = D/2$ is its radius. The module of Young in nonlinear elasticity obeys the relation (Streeter and Wylie, 1967):

$$E/E_0 = (R/R_0)^{\delta} \tag{5}$$

where $\delta = 0$ for the materials with linear elastic behaviour and $\delta \neq 0$ for the materials with nonlinear elastic behaviour.

According to (Stuckenbruck et al. 1985), the celerity of the pressure waves in the fluid can be defined by the expression:

$$C = \sqrt{\frac{E_0 e_0 F}{\rho_l D_0}} \tag{6}$$

with, whatever be the value of δ ($\delta = 0$ or $\delta \neq 0$):

$$F = \left(\frac{A}{A_0}\right)^{(\delta/2)-1} - \frac{D_0}{E_0 e_0} p \quad \text{and} \quad \frac{\partial p}{\partial A} = \frac{1}{A}\frac{E_0 e_0 F}{D_0} \tag{7}$$

The theory of characteristics is applied to transform the system of partial differential equations (3) and (4) into a system of ordinary differential equations that will be integrated numerically on curved characteristic lines (Hadj-Taïeb and Lili 1999).

3 Applications and Results

Considering the flow of a liquid achieved through the hydraulic device of the figure 1. The characteristics of the device are given on table 1.

3.1 Initial and Boundary Conditions

In the case of deformable pipes, the initial conditions are obtained by annulling the terms of $\partial/\partial t$ and by solving the obtained differential equation using the method of Runge-Kutta.

The initial steady state flows of the different numerical tests associated to this application are first determined. Results show that for the used value of E_0, the initial steady state flow depends on δ.

The transient flow is created by a downstream sudden closing $V(L, t) = 0$, $\forall\ t > 0$ and a constant upstream pressure $p(0,t) = p[A(0)]$, $\forall\ t > 0$.

Table 1 Characteristics of the pipe

$L = 1m$	$H_0 = 1.07m$	$\nu = 0.5$
$D_0 = 1.8cm$	$V_0 = 0.8\,m/s$	$E_0 = 2.2210^6\,Pa$
$e_0 = 1mm$	$\lambda = 0.02$	$\rho_l = 1000\,Kg/m^3$

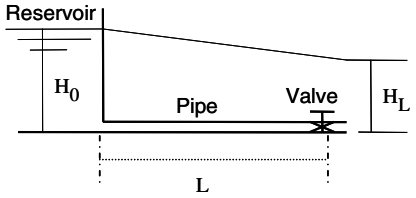

Fig. 1 Hydraulic and geometric proprieties of the installation

3.2 Influence of the Pipe Wall Elasticity on the Propagation of Pressure Waves

The characteristics grid and the evolution of pressure waves, for sudden shutoff of all flow at the downstream end of the pipe, are presented for $\delta = 10;20;30;40;50$ on figure 2 to 6. These figures show the computed pressure curves at some cross sections of the pipe (x=L/4, x=L/2, x=3L/4, x=L). The results reproduce perfectly the physical phenomena concerning the reflection of these waves on the two pipe extremities: the upstream constant level tank and the downstream closed valve. After the sudden valve closure, a positive pressure wave travels along the steady state pressure gradient until it reaches the upstream end of the pipe. A region of overpressure is developed for some time depending on the value of δ. The pressure wave is reflected as a depression when it reaches the constant level tank. The negative reflected pressure wave, traveling from the upstream end of the pipe, causes pressure to drop. Going back down the pipe, the front of the depressive wave becomes more and more spread. As the waves are damped by wall friction, the depression is less important than the first waterhammer amplitude. The negative pressure wave reaches the downstream closed end, where it reflects and causes more depression. That is, it intensifies. The process is repeated until the pressure fluctuations are damped at the final steady state pressure. In effect, as shown on figures 2 and 3, for the values $\delta = 10$ and $\delta = 20$, the sudden valve closure provokes a pressure wave with abrupt front. It is possible to see that the use of small values of δ smoothes the reflected pressure waves. This can be explained by the fact that for these values, the pipe becomes more elastic, which increases its capacity to attenuate the pressure fluctuations. For relatively big values of δ, the over-pressures become severe provoking shock waves to occur as shown in figures 4, 5 and 6.

The figure 4 represents the evolution of the pressure waves and the characteristic lines in the domain x-t, for a more important value of the pipe wall elasticity exponent ($\delta = 30$). Some oscillations appear in the pressure curves probably due to numerical instabilities. The running together of the grid lines indicate the existence of shocks which are transmitted along the pipe and generate some shifts in the pressure curves and the characteristic lines.

The results of figures 5 and 6 show, for the values $\delta = 40$ and $\delta = 50$, a strong set of reflections from both upstream and downstream boundaries. As long as the final steady-state has not been established the behavior of characteristic

paths in the compression region differs from those of the depression one. For the relatively great values of δ the running together of the grid lines indicate the existence of shocks which are transmitted along the pipe. In this case, internal boundary conditions have been employed in the characteristics method.

The phenomena of wave front spreading, of wave front steepening and wave shock inception are well represented in the different characteristics diagrams. However, it is clear that the characteristics method results in too many oscillations and does not give smooth results.

The amplitudes of the pressure-head variation, using the method of characteristics, are shown in figure 7. The results obtained for the exponent $(\delta = 10, 20, 30, 40, 50)$ are at the downstream end ($x = L$) and the middle ($x = L/2$) of the pipe. The accuracy of this method is acceptable particularly for the little values of δ. In this figure, the effect of the variation of δ on pressure wave

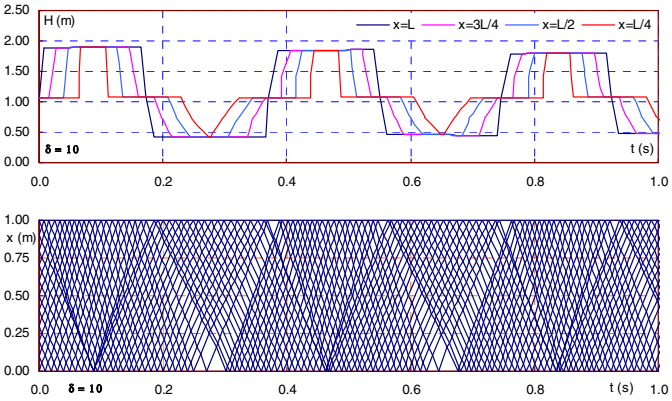

Fig. 2 Evolution of the pressure waves along the characteristic lines for $\delta = 10$

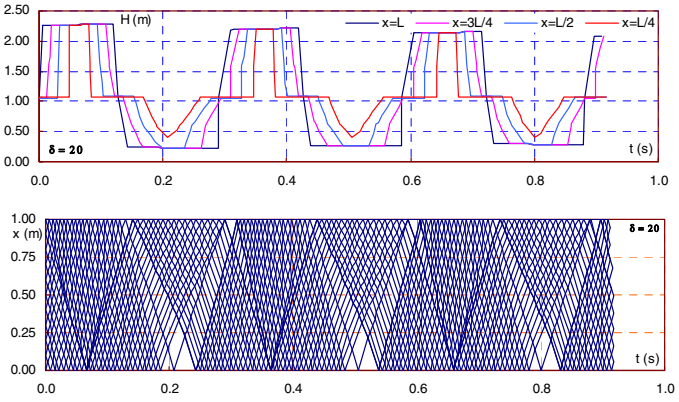

Fig. 3 Evolution of the pressure waves along the characteristic lines for $\delta = 20$

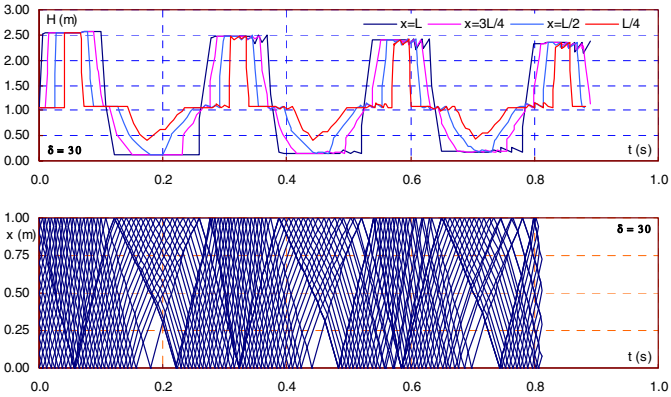

Fig. 4 Evolution of the pressure waves along the characteristic lines $\delta = 30$

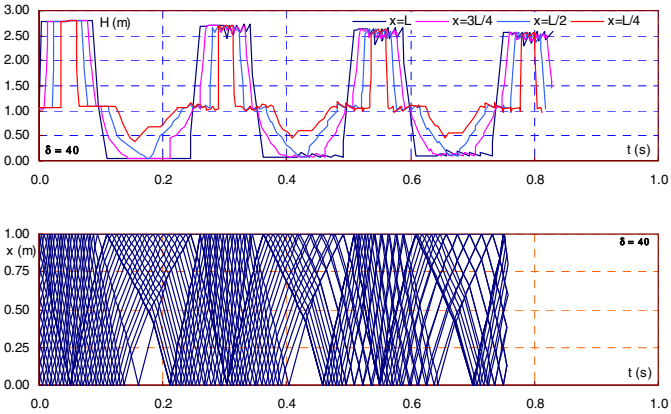

Fig. 5 Evolution of the pressure waves along the characteristic lines $\delta = 40$

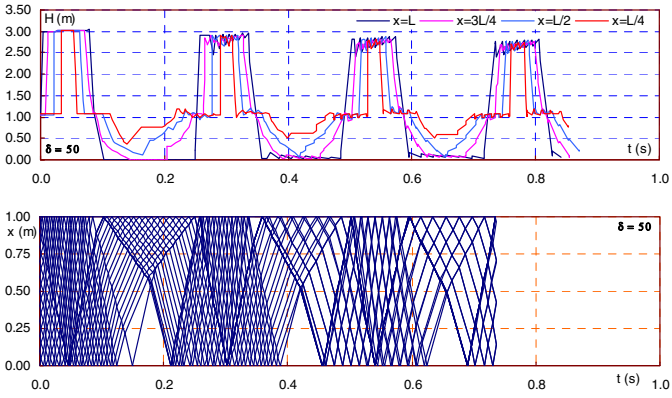

Fig. 6 Evolution of the pressure waves along the characteristic lines $\delta = 50$

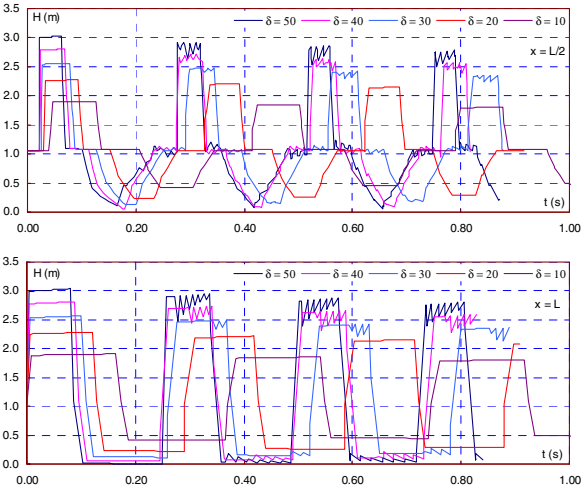

Fig. 7 Influence of the pipe wall elasticity on the pressure waves due to the watehammer

evolutions is very clear. We notice that the amplitude and the celerity of these pressure waves vary with the value of the pipe wall elasticity exponent. Moreover, it can be noted that the celerity of the pressure waves decreases when the elasticity increases. In effect and as an example, referring to the tracing relative to the section $x = L/2$, we note that the pressure wave front reaches this section more and more rapidly when the exponent δ increases.

4 Conclusion

The numerical solution of the transient flows in deformable pipelines provoked by the waterhammer phenomenon has been presented in this paper. This problem is governed by a coupled system of two nonlinear partial differential equations of hyperbolic type. The mathematical model presented in this paper takes into account the influence of the pipe elasticity on the transient flow. The numerical method employed is the method of curved characteristic

The study shows that the evolution of the pressure in time and in space is related to the dynamic behavior of the pipe wall. The pipe deformation has an important effect on the damping of the disturbances and the pressure waves generated by the waterhammer. Despite this method is less computer cost, supplementary equations are however necessary in computing the pressure head magnitudes at the shock wave front.

The characteristics method allows making the shock inception visible in the x, t plane, but it requires the use of interpolation method to compute the pressure head evolution at any interior section of the pipe. Nevertheless these interpolations have no effects on the numerical solution precision and the characteristic lines evolution.

References

Bergeron, L.: Du coup de bélier en hydraulique en coup de foudre en électricité, Dunod, Paris (1049)

Streeter, V.L., Wylie, E.B.: Hydraulic transients. McGraw Book Company, New York (1967)

Rooz, D., Young, F., Rogge, T.R.: A Finite-Element Simulation of Pulsatile Flow in Flexible Obstructed Tubes. ASME Journal of Biomechanical Engineering 104, 161–167 (1982)

Porenta, G., Young, D.F., Rogge, T.R.: A Finite-Element Model of Blood Flow in Arteries Including Taper, Branches and Obstructions. ASME Journal of Biomechanical Engineering 108, 119–124 (1986)

Stuckenbruck, S., Wiggert, D.C.: Unsteady flow through flexible tubing with coupled axial wall motion. In: 5th International Conference on Pressure Surges Hannover Germany, September 11-17 (1986)

Karra, C., Abid, S., Hadj Taieb, E.: Finite Element Analysis of a Fluid Structure Interaction in Flexible Pipeline. African Journal of Science and Technology (AJST) Science and Engineering Series 8, 63–70 (2007)

Wylie, E.B., Streeter, V.L., Suo, L.: Fluid transients in system. Prentice Hall, New Jersey (1993)

Stuckenbruck, S., Wiggert, D.C., Otwell, R.S.: The influence of pipe motion on acoustic wave propagation. Transactions of the ASME 107, 518–522 (1985)

Hadj-Taïeb, E., Lili: The numerical solution of the transient two-phase flow in rigid pipelines. International Journal for Numerical Methods in Fluids 29, 501–514 (1999)

Numerical Analysis of Fluid Flow and Heat Transfer within Grooved Flat Mini Heat Pipes

Jed Mansouri, Samah Maalej,
Mohamed Sassi, and Mohamed Chaker Zaghdoudi

Laboratoire Matériaux, Mesures et Applications (MMA) – INSAT –
Centre Urbain Nord BP N° 676 – 1080 Tunis, Tunisia
{jadmansouri,mohsassi}@yahoo.fr,
{chaker.zaghdoudi,samah.maalej}@insat.rnu.tn

Abstract. A Theoretical study is carried out in order to verify the Mini Heat Pipe (MHP) concept for cooling high power dissipation electronic components and determines the potential advantages of constructing mini channels as an integrated part of a Flat Mini Heat Pipe (FMHP). Hence, a detailed mathematical model of a FMHP with axial microchannels is developed in which the fluid flow is considered along with the heat and mass transfer processes during evaporation and condensation. The model is based on the equations for the mass, momentum and energy conservation, which are written for the evaporator, adiabatic, and condenser zones. The model can predict the maximum heat transfer capacity, the optimal fluid mass, and the flow and thermal parameters along the FMHP.

Keywords: Flat Mini Heat Pipes, Microchannels, Electronics Cooling, Fluid Analysis, Thermal Analysis.

Nomenclature

A	Constant in Eq. (23), Section, m²	L_a	Adiabatic length, m
C_p	Specific heat, J/kg.K	L_{as}	Dry zone length, m
d	Side of the microchannel, m	L_b	Blocked length, m
D_g	Groove height, m	l_c	Condenser width, m
D_h	Hydraulic diameter, m	L_c	Condenser length, m
f	Friction factor	l_e	Evaporator width, m
g	Gravity acceleration, m/s²	L_e	Evaporator length, m
h	Heat transfer coefficient, W/m².K	L_t	FMHP overall length, m
Ja*	Modified Jacob number	$\dot{m}$	Mass flow rate, kg/s
k	Poiseuille number	m_1	Constant in equation (23)
l	Width, m	m_2	Constant in equation (23)
La	Laplace constant, m	m_3	Constant in equation (23)

M. Haddar et al. (Eds.): *Design and Modeling of Mechanical Systems*, LNME, pp. 381–394.
DOI: 10.1007/978-3-642-37143-1_46

N_g	Number of grooves
Nu	Nüsselt number
P	Pressure, N/m²
Pr	Prandtl number
Q	Heat flux, W/m²
Q	Heat transfer rate, W
Q_a	Axial heat flux rate, W
Q_c	Heat flux rate transferred by conduction, W
Q_{conv}	Heat flux rate transferred by convection, W
r_c	Radius of curvature, m
Re	Reynolds number
S	Heat transfer area in the evaporator or condenser zone, m²
S_g	Groove spacing, m
t	Thickness, m
T	Temperature, °C
T_f	Film temperature, °C
T_{sf}	Heat sink temperature, °C
T_{sat}	Saturation temperature, °C
T_w	Wall temperature, °C
V_e	Liquid or vapor velocity, m/s
w	Axial velocity, m/s
W	FMHP width, m
W_g	Groove width, m
z	Coordinate, m

Greek Symbols

α	Contact angle, °
β	Tilt angle, °
Δh_v	Latent heat of vaporization, J/kg
λ	Thermal conductivity, W/m.K
μ	Dynamic viscosity, kg/m.s
ρ	Density, kg/m^3
σ	Surface tension, N/m
τ	Shear stress, N/m²
θ	Angle defined in Eq. (13), °

Subscripts and superscripts

a	Adiabatic
c	Condenser, Curvature
ev	Evaporator
f	Film
il	Interfacial (liquid side)
iv	Interfacial (vapor side)
l	Liquid
lw	Liquid-Wall
max	Maximum
min	Minimum
sat	Saturation
sf	Heat sink
v	Vapor
vw	Vapor-Wall
w	Wall

1 Introduction

Flat Mini Heat pipes (FMHPs) represent promising solutions for electronic equipment cooling (Groll et al. 1998, Mansouri et al. 2011a, 2011b, Maalej et al. 2011a, 2011b, Zaghdoudi and Sarno 2001, Zaghdoudi et al. 2003, 2004a, 2004b, 2011a,.2011b, 2011c, 2011d). Heat pipes are sealed systems whose transfer capacity depends mainly on the fluid and the capillary structure. Several capillary structures are developed in order to meet specific thermal needs. They are constituted either by an integrated structure of microchannels or microgrooves machined in the internal wall of the heat pipe, or by porous structures made of wire screens or sintered powders. According to specific conditions, composed capillary structures can be integrated into heat pipes.

Despite the advances in FMHP designs, most of them, especially those including grooves, reveal only the functionality during horizontal operation, with few FMHPs successfully demonstrating adverse-gravity or acceleration functionality.

These studies show that the manufacture of FMHPs that maintain the same performance for all orientations is a problem yet to be overcome.

For FMHPs constituted of an integrated capillary structure including microchannels of different shapes and associated in network, the theoretical approach consists of studying the flow and the heat transfer in isolated microchannels. From the FMHP models (Khrustalev and Faghri 1995, Faghri and Khrustalev 1997, Khrustalev and Faghri 1999, Lefèvre et al. 2003, Launay et al. 2004, Tzanova et al. 2004, Angelov et al. 2005, Shi et al. 2006, Do et al. 2008, Do and Jang 2010), the following main conclusions can be outlined:

- An increase of the heat load decreases the evaporator thermal resistance and increases the condenser thermal resistance due to the change in the longitudinal meniscus distribution along the FMHP.
- Shear stresses at the liquid-vapor interface are significantly non-uniform, decreasing towards the center of the liquid-vapor meniscus. This non uniformity increases with the curvature of the liquid-vapor interface.
- The effect of the vapor flow on the liquid flow in the grooves decreases with curvature of the liquid-vapor interface.
- Frictional vapor-liquid interaction significantly affects the thermal performance of the FMHP with axial grooves, and shapes of the liquid and vapor cross-sectional areas should be precisely accounted for when calculating the friction factor-Reynolds number products.
- At the evaporator, heat is mainly transferred in the short thin film region, where the liquid is very close to the wall. Thus, to improve heat transfer, the microregion number in a FMHP cross section must be as high as possible.
- For triangular microchannels, the heat transfer rate is rather limited by the large pressure drops in the corners; nevertheless, the vapor pressure drops are not negligible.
- The thermal resistance of the vapor phase is more important than the transversal thermal resistance in the liquid film and the wall. Thus, increasing the triangular cross-section allows the increase of the liquid and vapor flow cross sections, and consequently the increase of the capillary limit and the reduction of the vapor thermal resistance.

Table 1 lists the main theoretical studies published in the literature on flat mini heat pipes. This list does not include studies on flat heat spreaders with a principle operation a little bit different from that of the FMHPs. The table gives also the shape of the microchannels which constitutes the capillary structure. As it is indicated the main shapes used as capillary structures are triangular, rectangular or trapezoidal.

The present study deals with the development of model of a FMHP to be used for cooling high power dissipation electronic components. A mathematical model of a FMHP with axial rectangular microchannels is developed in which the fluid flow is considered along with the heat and mass transfer processes during evaporation and condensation. The numerical simulation results are presented regarding the thickness distribution of the liquid film in a microchannel, the liquid and vapor pressures and velocities as well as the wall temperatures along the FMHP.

Table 1 Overview of the main theoretical studies on flat mini heat pipes

Author	Capillary Structure
Khrustalev and Faghri (1995)	Rectangular axial grooves
Faghri and Khrustalev (1997)	Rectangular axial grooves
Khrustalev and Faghri (1999)	Rectangular axial grooves
Lefevre et al. (2003)	Rectangular and trapezoidal axial grooves
Launay et al. (2004)	Triangular axial grooves
Tzanova et al. (2004)	Rectangular axial grooves
Angelov et al. (2005)	Rectangular axial grooves
Shi et al. (2006)	Rectangular axial grooves
Do et al. (2008)	Rectangular axial grooves
Do and Jang (2010)	Rectangular axial grooves

2 FMHP Modeling

A sketch of the studied FMHP is illustrated by Fig. 1. It is composed of 47 square axial microchannels. The overall dimensions of the FMHP are 100 mm length, 50 mm width, and 3 mm thickness. The main geometrical parameters are listed in table 2. It is filled with water by means an automatic filling apparatus which is developed especially for this application.

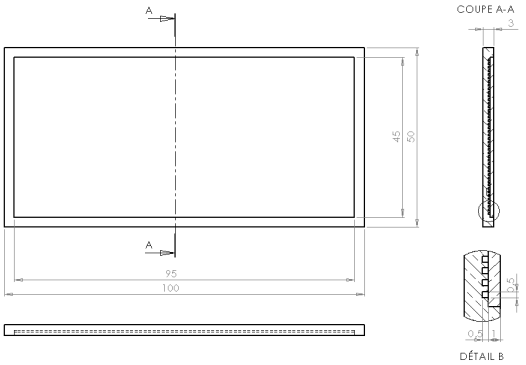

Fig. 1 Sketch of the FMHP

Table 2 Main geometrical parameters of the FMHP

FMHP width, W	50 mm
FMHP overall length, L_t	100 mm
FMHP thickness, t	3 mm
Microchannel height, D_g	0.5 mm
Microchannel width W_g	0.5 mm
Microchannel spacing S_g	1 mm
Overall width of the microchannels	45 mm
Overall length of the microchannels	95 mm
Number of the microchannels, N_g	47

The liquid accumulates in the corners and forms four meniscuses (Fig. 2). Their curvature radius, r_c, is related to the difference of pressure, between vapor and liquid phase, by the Laplace-Young equation. In the evaporator and adiabatic zones, the curvature radius, in the parallel direction of the microchannel axis, is lower than the one perpendicular to this axis. Therefore, the meniscus is described by only one curvature radius. In a given section, r_c is supposed constant. The axial evolution of r_c is obtained by the differential of the Laplace-Young equation. The part of wall that is not in contact with the liquid is supposed dry and adiabatic. In the condenser, the liquid flows toward the microchannel corners. There is a transverse pressure gradient, and a transverse curvature radius variation of the meniscus. The distribution of the liquid along a microchannel is presented in Fig. 2.

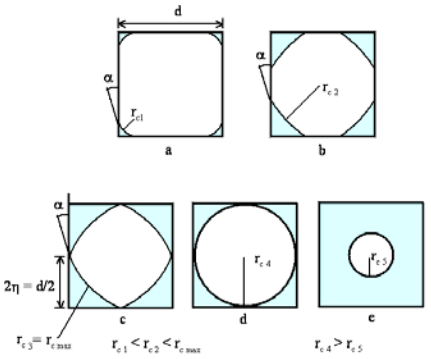

Fig. 2 Evolution of the curvature radius of the liquid-vapor interface along a microchannel

The microchannel is divided into several elementary volumes of length, dz, for which, we consider the Laplace-Young equation, and the conservation equations written for the liquid and vapor phases as it follows:

Laplace-Young equation

$$\frac{dP_v}{dz} - \frac{dP_l}{dz} = -\frac{\sigma}{r_c^2}\frac{dr_c}{dz} \tag{1}$$

Liquid and vapor mass conservation

$$\frac{d\left(\rho_l\, w_l\, A_l\right)}{dz} = \frac{1}{\Delta h_v}\frac{dQ}{dz} \tag{2}$$

$$\frac{d\left(\rho_v\, w_v\, A_v\right)}{dz} = -\frac{1}{\Delta h_v}\frac{dQ}{dz} \tag{3}$$

Liquid and vapor momentum conservation

$$\rho_l \frac{d(A_l w_l^2)}{dz}dz = \frac{d(A_l P_l)}{dz}dz + A_{il}\left|\tau_{il}\right| + A_{lw}\left|\tau_{lw}\right| - \rho_l\, g\, A_l \sin\beta\, dz \tag{4}$$

$$\rho_v \frac{d(A_v w_v^2)}{dz} dz = -\frac{d(A_v P_v)}{dz} dz - |\tau_{il}| A_{il} - |\tau_{vw}| A_{vw} - \rho_v g A_v \sin\beta \, dz \tag{5}$$

Energy conservation

$$\lambda_w \frac{\partial^2 T_w}{\partial z^2} - \frac{h}{t_w}(T_w - T_{sat}) = -\frac{1}{l \times t_w} \frac{dQ}{dz} \tag{6}$$

The quantity dQ/dz in equations (2), (3), and (6) represents the heat flux rate variations along the elementary volume in the evaporator and condenser zones, which affects the variations of the liquid and vapor mass flow rates as it is indicated by equations (2) and (3). So, if the axial heat flux rate distribution along the microchannel is given by

$$Q = \begin{cases} Q_a \, z/L_e & 0 \le z \le L_e \\ Q_a & L_e < z < L_e + L_a \\ Q_a \left(1 + \dfrac{L_e + L_a - z}{L_c - L_b}\right) & L_e + L_a \le z \le L_t - L_b \end{cases} \tag{7}$$

we get a linear flow mass rate variations along the microchannel.

The liquid and vapor passage sections, A_l, and A_v, the interfacial area, A_{il}, the contact areas of the phases with the wall, A_{lp} and A_{vp}, are expressed using the contact angle and the interface curvature radius by

$$A_l = 4 * r_c^2 \left(\sin^2\theta - \theta + \frac{\sin 2\theta}{2}\right) \tag{8}$$

$$A_v = d^2 - A_l \tag{9}$$

$$A_{il} = 8 \times \theta \times r_c \times dz \tag{10}$$

$$A_{lw} = \frac{16}{\sqrt{2}} r_c \sin\theta \, dz \tag{11}$$

$$A_{vw} = \left(4 \times d - \frac{16}{\sqrt{2}} r_c \sin\theta\right) dz \tag{12}$$

$$\theta = \frac{\pi}{4} - \alpha \tag{13}$$

The liquid-wall and the vapor-wall shear stresses are expressed as

$$\tau_{lw} = \frac{1}{2}\rho_l w_l^2 f_l\,,\quad f_l = \frac{k_l}{R_{e_l}}\,;\quad R_{el} = \frac{\rho_l w_l D_{hlw}}{\mu_l} \tag{14}$$

$$\tau_{vw} = \frac{1}{2}\rho_v w_v^2 f_v\,, f_v = \frac{k_v}{R_{ev}}\quad,\quad R_{ev} = \frac{\rho_v w_v D_{hvw}}{\mu_v} \tag{15}$$

Where k_l and k_v are the Poiseuille numbers, and D_{hlw} and D_{hvw} are the liquid-wall and the vapor-wall hydraulic diameters, respectively.

The hydraulic diameters and the shear stresses in (14) and (15) are expressed as follows

$$D_{hlw} = \frac{\sqrt{2}\times r_c\left(\sin^2\theta - \theta + \frac{\sin 2\theta}{2}\right)}{\sin\theta} \tag{16}$$

$$D_{hvw} = \frac{d^2 - 4r_c^2\left(\sin^2\theta - \theta + \frac{\sin 2\theta}{2}\right)}{d - \frac{4}{\sqrt{2}}\sin\theta\times r_c} \tag{17}$$

$$\tau_{lw} = \frac{1}{2}\frac{k_l w_l \mu_l \sin\theta}{2\sqrt{2}\left(\sin^2\theta - \theta + \frac{\sin\theta}{2}\right)r_c} \tag{18}$$

$$\tau_{vw} = \frac{k_v w_v \mu_v\left(d - \left(\frac{4}{\sqrt{2}}\sin\theta\right)r_c\right)}{2\left(d^2 - 4r_c^2\left(\sin^2\theta - \theta + \frac{\sin\theta}{2}\right)\right)} \tag{19}$$

The liquid-vapor shear stress is calculated by assuming that the liquid is immobile since its velocity is considered to be negligible when compared to the vapor velocity ($w_l << w_v$). Hence, we have

$$\tau_{il} = \frac{1}{2}\frac{\rho_v w_v^2 k_v}{R_{eiv}}\quad R_{eiv} = \frac{\rho_v |w_v| D_{hiv}}{\mu_v} \tag{20}$$

where D_{hiv} is the hydraulic diameter of the liquid-vapor interface. The expressions of D_{hiv} and τ_{iv} are

$$D_{hi} = \frac{d^2 - 4r_c^2\left(\sin^2\theta - \theta + \frac{\sin 2\theta}{2}\right)}{2\ \theta\ r_c} \tag{21}$$

$$\tau_{il} = \frac{k_v \theta \; r_c w_v \mu_v}{d^2 - 4r_c^2 \left(sin^2 \theta - \theta + \frac{sin\, 2\theta}{2} \right)} \tag{22}$$

In (6), h represents the heat transfer coefficient in the evaporator, adiabatic and condenser sections. For these zones, the heat transfer coefficients are determined from the experimental results [12]. Hence, the heat transfer coefficients can be calculated by

$$Nu = A\, Re^{m1}\; Pr^{m2}\; Ja*^{m3} \tag{23}$$

A, m_1, m_2, and m_3 are constants, which are determined from the experimental results. For the evaporation heat transfer, (23) is calculated by taking the liquid physical properties at the saturation temperature and the vapor physical properties at the film temperature ($T_f = (T_{sat}+T_w)/2$). For condensation heat transfer, the liquid and vapor physical properties are determined by considering the film and saturation temperatures, respectively.

Nu, Re, Pr, and Ja* are the Nusselt, Reynolds, Prandtl and modified Jackob dimensionless numbers, respectively. They are defined as follows:

$$Re = \frac{\rho_l V_e \; La}{\mu_l} = \frac{\dot{m}}{\mu_l \; S} = \frac{Q}{\mu_l \; S \;\; \Delta h_v} = \frac{q}{\mu_l \; \Delta h_v} \tag{24}$$

where V_e is the liquid or the vapor velocity. μ_l is the liquid dynamic viscosity, and Δh_v is the latent heat. S is the heat transfer area in the evaporator ($l_e \times L_e$) or condenser section ($l_c \times L_c$), Q is the heat flux rate, and q is the heat flux transferred in the evaporator or the condenser zone.

$$La = \sqrt{\frac{\sigma}{(\rho_l - \rho_v) g}} \tag{25}$$

where σ is the liquid surface tension. ρ_l and ρ_v are the liquid and vapor densities, respectively. g is the gravity acceleration.

$$Pr = \frac{\mu_l C_{pl}}{\lambda_l} \tag{26}$$

where C_{pl} is the liquid specific heat, and λ_l is the liquid thermal conductivity.

$$Nu \;\; = \frac{h \; La}{\lambda_l} \tag{27}$$

where h is the heat transfer coefficient in the evaporator or condenser section.

$$Ja* = \frac{\rho_l}{\rho_v} \frac{C_{pl} \; T_{sat}}{\Delta h_v} \tag{28}$$

The constants of (23) are determined from the experimental data by a linear regression analysis, for the evaporation and the condensation phenomena. It is found that the heat transfer law proposed by (23), the experimental results are well correlated when considering A = 902, m_1 = 0.825, m_2 = 0.333, m_3 = -0.999, and m_4 = -0.020, for the evaporation phenomenon, and A = 2.165×10^{-12}, m_1 = 1.001, m_2 = -0.032, m_3 = 2.644, and m_4 = 1.907, for the condensation phenomenon. For the evaporation heat transfer coefficient, it was found that the deviation from the experimental results is ± 20 % (Zaghdoudi et al. 2011c), and for the condensation heat transfer coefficient, the deviation from the experimental results is ± 10 %.

The equations (1-6) constitute a system of six first order differential, nonlinear, and coupled equations. The six unknown parameters are: r_c, w_l, w_v, P_l, P_v, and T_w. The integration starts in the beginning of the evaporator (z = 0) and ends in the condenser extremity ($z = L_t - L_b$), where L_b is the length of the condenser flooding zone. The boundary conditions for the adiabatic zone are the calculated solutions for the evaporator end. In z = 0, we use the following boundary conditions:

$$\begin{cases} r_c\big|^{0} = r_{cmin} & (a) \\ w_l\big|^{0} = w_v\big|^{0} = 0 & (b) \\ P_v\big|^{0} = P_{sat}(T_v) & (c) \\ P_l\big|^{0} = P_v - \dfrac{\sigma}{r_{cmin}} & (d) \end{cases} \tag{29}$$

The solution is performed along the microchannel if r_c is higher than r_{cmin}. The coordinate for which this condition is verified, is noted L_{as} and corresponds to the microchannel dry zone length. Beyond this zone, the liquid doesn't flow anymore. Solution is stopped when $r_c = r_{cmax}$, which is determined using the following reasoning: the liquid film meets the wall with a constant contact angle. Thus, the curvature radius increases as we progress toward the condenser (Figs. 2a and 2b). When the liquid film contact points meet, the wall is not anymore in direct contact with vapor. In this case, the liquid configuration should correspond to Fig. 18c, but actually, the continuity in the liquid-vapor interface shape imposes the profile represented on Fig. 2d. In this case, the curvature radius is maximal. Then, in the condenser, the meniscus curvature radius decreases as the liquid thickness increases (Fig. 2e). The transferred maximum power, so called capillary limit, is determined if the junction of the four meniscuses starts precisely in the beginning of the condenser.

3 Numerical Results and Analysis

In this analysis, we study a FMHP with the dimensions which are indicated in Table 2. The capillary structure is composed of microchannels as it is represented by the sketch of Fig. 1. The working fluid is water and the heat sink temperature is

equal to 40 °C. The conditions of simulation are such as L_e = 20 mm, L_a = 35 mm et L_c = 45 mm, and the introduced mass of water is equal to the optimal fill charge.

The variations of the curvature radius r_c are represented in Fig. 3. In the evaporator, because of the recession of the meniscus in the channel corners and the great difference of pressure between the two phases, the interfacial curvature radius is very small on the evaporator extremity. It is also noticed that the interfacial curvature radius decreases in the evaporator section when the heat flux rate increases. However, it increases in the condenser section. Indeed, when the heat input power increases, the liquid and vapor pressure losses increase, and the capillary pressure become insufficient to overcome the pressure losses. Hence, the evaporator becomes starved of liquid, and the condenser is blocked with the liquid in excess.

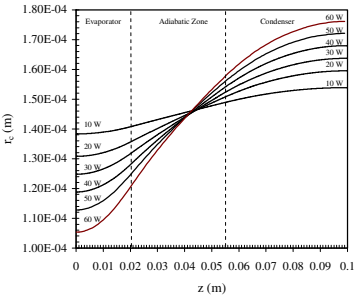

Fig. 3 Variations of the curvature radius r_c of the meniscus

The evolution of the liquid and vapor pressures along the microchannel is given in Figs. 4 and 5. We note that the vapor pressure gradient along the microchannel is weak. It is due to the size and the shape of the microchannel that don't generate a very important vapor pressure drop. For the liquid, the velocity increase is important near of the evaporator extremity, which generates an important liquid pressure drop.

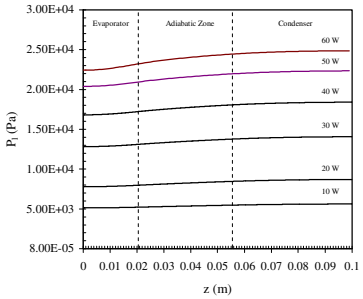

Fig. 4 Variations of the liquid pressure P_l

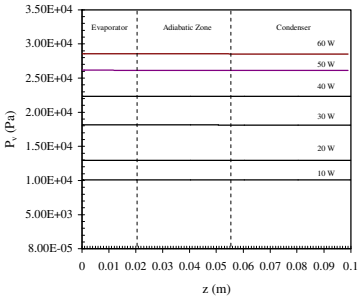

Fig. 5 Variations of the vapor pressure P_v

Figure 6 presents the evolution of the liquid phase velocity along a microchannel. In the evaporator section, as the liquid passage section decreases, the liquid velocity increases considerably. On other hand, since the liquid passage section increases along the microchannel (adiabatic and condenser sections), the liquid velocity decreases to reach zero at the final extremity of the condenser. In the evaporator, the vapor phase velocity increases since the vapor passage section decreases. In the adiabatic zone, it continues to grow with the reduction of the section of vapor passage. Then, when the condensation appears, it decreases, and it is equal to zero on the extremity of the condenser (Fig. 7). We can note also that the vapor velocities are higher than those of the liquid phase. This confirms the hypothesis of the model which considers a laminar flow for the liquid phase with weak interfacial stresses.

The variations of the wall temperature along the FMHP are reported in Fig. 8. In the evaporator section, the wall temperature decreases since an intensive evaporation appears due the presence of a thin liquid film in the corners. In the adiabatic section, the wall temperature is equal to the saturation temperature corresponding

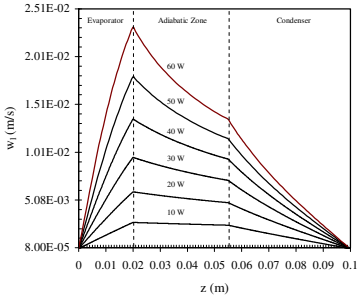

Fig. 6 The liquid phase velocity distribution

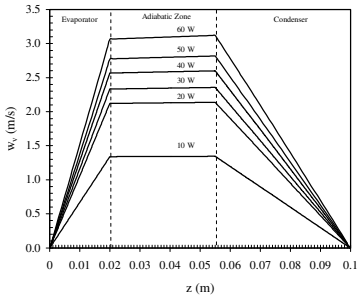

Fig. 7 The vapor phase velocity distribution

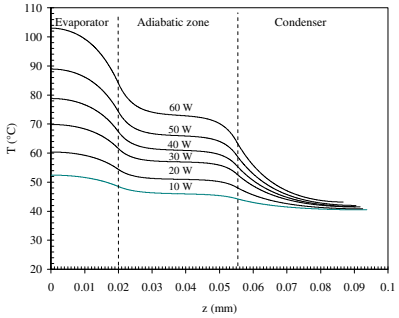

Fig. 8 Variations of the FMHP wall temperature

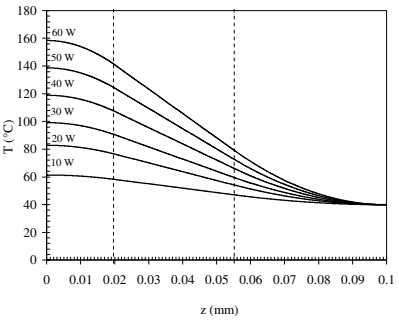

Fig. 9 Variations of the copper plate wall temperature

to the vapor pressure. In the condenser section, the wall temperature decreases. The variations of the wall temperature along a copper plate having the same dimensions as the FMHP are shown in Fig. 9. By comparing the temperature distributions obtained in Figs 8 and 9, it is demonstrated that the maximum values of the temperatures which are reached in both cases (FMHP and copper plate), indicate the efficiency of the FMHP in reducing the hot spots that could be generated for high heat inputs.

Fig. 10 shows the variations of the heat flux rate transferred by conduction, Q_c, along the FMHP, for different imposed heat inputs. For a given heat input, in the evaporator section, Q_c increases. However, in the adiabatic zone, it decreases rapidly to nearly zero and then increases sharply. In the condenser zone, Q_c decreases and reaches zero at the FMHP extremity. Fig. 11 shows the variations of the heat flux rate, Q_{conv}, transferred by convection. We can note that Q_{conv} is higher than Q_c. It increases in the evaporator zone and decreases in the condenser zone. However, in the adiabatic zone, Q_{conv} increases firstly to reach a value which is nearly equal to the axial heat input, Q_a, and then decreases. Note that the summation of the heat flux rates transferred by conduction and convection Q_c and Q_{conv} is equal to the axial heat flux rate, Q_a (Fig. 12). It increases linearly in the evaporator zone, it remains constant in the adiabatic section, and it decreases in the condenser zone.

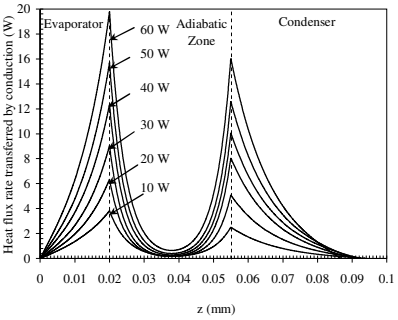

Fig. 10 Variations of the heat flux rate transferred by conduction

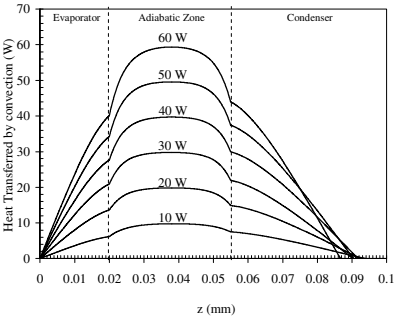

Fig. 11 Variations of the heat flux rate transferred by convection

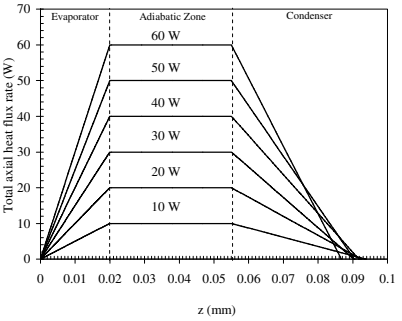

Fig. 12 Variations of the total heat flux rate

4 Conclusion

Based on the mass conservation, momentum conservation, energy conservation, and Laplace-Young equations, a one dimensional numerical model is developed to simulate the liquid-vapor flow as well as the heat transfer in a FMHP constituted by microchannels. The model takes into account interfacial effects, the interfacial radius of curvature, and the heat transfer in both the evaporator and condenser zones. The resulting coupled ordinary differential equations are solved numerically to yield interfacial radius of curvature, pressure, velocity, temperature distribution as a function of axial distance along the FMHP, for different heat inputs. It is clear from these results that incorporating such FMHP as part of high integrated electronic packages can significantly improve the performance and reliability of electronic devices, by increasing the effective thermal conductivity, decreasing the temperature gradients and reducing the intensity and the number of localized hot spots.

References

Angelov, G., Tzanova, S., Avenas, Y., Ivanova, M., Takov, T., Schaeffer, C., Kamenova, L.: Modeling of Heat Spreaders for Cooling Power and Mobile Electronic Devices. In: 36th Power Electronics Specialists Conference (PESC 2005), Recife, Brazil, June 12-15, pp. 1080–1086 (2005)

Do, K.H., Kim, S.J., Garimella, S.V.: A Mathematical Model for Analyzing the Thermal Characteristics of a Flat Micro Heat Pipe with a Grooved Wick. International Journal Heat and Mass Transfer 51, 4637–4650 (2008)

Do, K.H., Jang, S.P.: Effect of Nanofluids on the Thermal Performance of a Flat Micro Heat Pipe with a Rectangular Grooved Wick. International Journal of Heat and Mass Transfer 53, 2183–2192 (2010)

Faghri, A., Khrustalev, D.: Advances in Modeling of Enhanced Flat Miniature Heat Pipes with Capillary Grooves. Journal of Enhanced Heat Transfer 4, 99–109 (1997)

Groll, M., Schneider, M., Sartre, V., Zaghdoudi, M.C., Lallemand, M.: Thermal Control of Electronic Equipment by Heat Pipes. Revue Générale de Thermique 37, 323–352 (1998)

Khrustlev, D., Faghri, A.: Thermal Characteristics of Conventional and Flat Miniature Axially Grooved Heat Pipes. Journal of Heat Transfer 117, 1048–1054 (1995)

Faghri, A., Khrustalev, D.: Advances in Modeling of Enhanced Flat Miniature Heat Pipes with Capillary Grooves. Journal of Enhanced Heat Transfer 4, 99–109 (1997)

Khrustlev, D., Faghri, A.: Coupled Liquid and Vapor Flow in Miniature Passages with Micro Grooves. Journal of Heat Transfer 121, 729–733 (1999)

Launay, S., Sartre, V., Lallemand, M.: Hydrodynamic and Thermal Study of a Water-Filled Micro Heat Pipe Array. Journal of Thermophysics and Heat Transfer 18, 358–363 (2004)

Lefèvre, F., Revellin, R., Lallemand, M.: Theoretical Analysis of Two-Phase Heat Spreaders with Different Cross-section Micro Grooves. In: 7th International Heat Pipe Symposium, Jeju Island, South Korea, October 12-16, pp. 97–102 (2003)

Maalej, S., Mansouri, J., Zaghdoudi, M.C.: Experimental and Theoretical Analysis on Enhanced Flat Miniature Heat Pipes With Axial Capillary Grooves and Screen Meshes. International Review of Mechanical Engineering (IREME) 5, 180–195 (2011a)

Maalej, S., Mansouri, J., Sassi, M.B.H., Zaghdoudi, M.C.: Theoretical and Experimental Study on the Thermal Performance of Flat Miniature Heat Pipes including Rectangular Grooves. International Review of Mechanical Engineering (IREME) Special Issue on Heat Transfer 5, 265–277 (2011b)

Mansouri, J., Maalej, S., Sassi, M.B.H., Zaghdoudi, M.C.: Experimental Study on the Thermal Performance of Enhanced Flat Miniature Heat Pipes. International Review of Mechanical Engineering (IREME) 5, 196–208 (2011a)

Mansouri, J., Maalej, S., Sassi, M.B.H., Zaghdoudi, M.C.: Theoretical Investigation on the Thermal Performance of Two-Phase Heat Spreaders including Parallel Microchannels. International Review of Modeling and Simulations (IREMOS) 4, 364–379 (2011b)

Shi, P.Z., Chua, K.M., Wong, S.C.K., Tan, Y.M.: Design and Performance Optimization of Miniature Heat Pipe in LTCC. Journal of Physics: Conference Series 34, 142–147 (2006)

Tzanova, S., Ivanova, M., Avenas, Y., Schaeffer, C.: Analytical Investigation of Flat Silicon Micro Heat Spreaders. In: 39th IAS Annual Meeting Conference Record of the 2004 IEEE on Industry Applications Conference, October 3-7, vol. 4, pp. 2296–2302 (2004)

Zaghdoudi, M.C., Sarno, C.: Investigation on the Effects of Body Force Environment on Flat Heat Pipes. J. Thermophysics and Heat Transfer 15, 384–394 (2001)

Zaghdoudi, M.C., Tantolin, C., Godet, C.: Heat Pipes for Efficient Cooling. Power Electronics Europe 1, 15–21 (2003)

Zaghdoudi, M.C., Tantolin, C., Godet, C.: Use of Heat Pipes Cooling Systems in Electronics Industry. Electronics Cooling 10, 12–20 (2004a)

Zaghdoudi, M.C., Tantolin, C., Godet, C.: Experimental and Theoretical Analysis on Enhanced Flat Miniature Heat Pipes with Axial Grooves. Journal of Thermophysics and Heat Transfer 18, 330–347 (2004b)

Zaghdoudi, M.C., Tantolin, C., Sarno, C.: Experimental Investigation on the Use of Flat Mini Heat Pipes For Avionics Electronic Modules Cooling. International Review of Mechanical Engineering (IREME) 5, 770–783 (2011a)

Zaghdoudi, M.C., Tantolin, C., Sarno, C.: Acceleration and Vibration Effects on the Thermal Performance of a Two-phase Heat Spreader with Embedded Flat Mini Heat Pipe. International Review of Aerospace Engineering (IREASE) 4, 109–121 (2011b)

Zaghdoudi, M.C., Maalej, S., Mansouri, J., Sassi, M.B.H.: Flat Miniature Heat Pipes for Electronics Cooling: State of the Art, Experimental and Theoretical Analysis. International Journal of Engineering and Applied Sciences 7, 166–189 (2011c)

Zaghdoudi, M.C., Tantolin, C., Sarno, C.: Use of Flat Mini Heat Pipes for the Thermal Management of High Dissipative Electronic Packages for Avionic Equipments. International Review of Mechanical Engineering (IREME) 5, 843–855 (2011d)

Part IV
Modelling and Analysis of Materials and Structures

Micropolar Models of Architectured Materials from Discrete Homogenization: Case of Textile Monolayers

Ibrahim Goda[1], Mohamed Assidi[2], and Jean-François Ganghoffer[1]

[1] LEMTA, Université de Lorraine,
Nancy, France
ibrahim.goda9@etu.univ-lorraine.fr,
jean-francois.Ganghoffer@univ-lorraine.fr
[2] CRP Henri Tudor, Luxemburg,
Luxemburg
Mohamed.assidi@tudor.lu

Abstract. A general methodology for the determination of the effective behavior of architectured materials endowed with a discrete structure at the microscopic scale is presented. It relies on the discrete homogenization method to derive the effective mechanical properties from the topology of the material and the properties of the micro constituents. This methodology is presently applied to textile monolayers modelled as a network of undulated and interwoven beams representing the yarns in the fabric. The initially discrete fabric architecture is represented at the mesoscopic level by an anisotropic micropolar effective continuum. The effective mechanical properties are validated by FE simulations performed over a representative unit cell.

Keywords: textiles, effective mechanical properties, discrete homogenization, micropolar model, flexural rigidities.

1 Introduction

Over the past decade, considerable attention has been devoted to textile composites and especially woven fabrics, which are now used as structural components in construction mechanics and especially aerospace engineering. These structures have many advantages over unidirectional fiber reinforced composites, such as enhanced dimensional stability over a large range of temperatures, more balanced properties in the fabric plane, and better impact resistance. The multi-scale nature of the fabric (macro-scale), composed of yarns (meso-scale), themselves composed of fibers (micro-scale) leads to a complex mechanical behavior, see (Assidi et al. 2011) for a review of the existing modeling strategies. The present contribution addresses the issue of the prediction of the mechanical behavior of different woven fabric architectures from the discrete homogenization.

M. Haddar et al. (Eds.): *Design and Modeling of Mechanical Systems*, LNME, pp. 397–404.
DOI: 10.1007/978-3-642-37143-1_47

2 Discrete Homogenization of Fabrics and Effective Properties of an Equivalent Anisotropic Micropolar Continuum

The topology of the fabric with the unit cell for plain weave and twill consists of warp and weft with an initial crimp (Fig. 1 and Fig. 2 respectively). The contact between warp and weft is accounted for by vertical connecting beams.

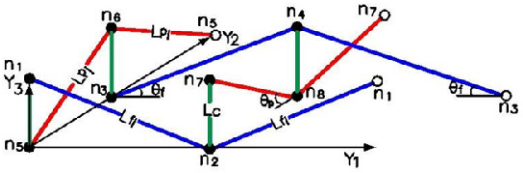

Fig. 1 Representative unit cell for plain weave

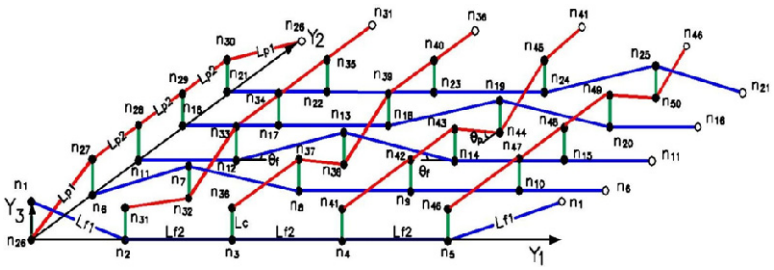

Fig. 2 Representative unit cell for twill

The main novelty advocated in the present work is the substitution of the initially discrete material by an equivalent continuous Cosserat solid. The proposed method (discrete homogenization) allows evaluating the effective classical and micropolar elastic constants. Such a technique is exploited to compute the macroscopic elastic properties of fabric by taking into account axial, transverse shearing, flexural and torsional deformations of the yarns building the fabrics. The consideration of couple stresses interpreted as moments enables to compute the flexural rigidities of textile monolayers, which is a challenging task considering their small thickness. The homogenized constitutive law relates stress to strain measures and as a second part couple stresses to curvatures, as explained next.

The homogenization method assumes that all physical quantities vary at both local and global scales, and that those quantities are periodic with respect to the local scale, due to the periodicity of the existing microstructure. As the woven fabrics have a periodic structure based on an identified RVE, it is possible to apply the asymptotic expansion homogenization method. Due to the discreteness of the

fabric architecture, we chose to apply the discrete asymptotic homogenization method proposed in (Caillerie et al. 2006; Raoult et al. 2008; Dos Reis and Ganghoffer 2012), to calculate the effective behavior of such periodic lattices. More precisely, we substitute to the initially discrete fabric structure a micropolar effective continuum endowed with translational and rotational degrees of freedom. Micropolar elasticity incorporates local rotations of material points in addition to displacements in the kinematic description; as a consequence, the material can transmit both Cauchy stresses and couple stresses. The method allows presently the treatment of elementary cells, including internal nodes; it is based on the asymptotic development of the kinematic and static variables under consideration, at an arbitrary order a priori. The method relies on the connectivity of the beam lattice within the representative unit cell, the constitutive model of the microbeams, and the equilibrium of forces and moments at each node of the lattice. We consider presently a Timoshenko beam model, accounting for transverse shear within the yarns, which is a realistic model when yarns are made of several filaments.

From a technical point of view, two geometrical parameters need an asymptotic expansion, namely the beam length $l^{\varepsilon b}$ and beam radius $r^{\varepsilon b}$. Similarly, the nodal displacement $u^{\varepsilon n}=(u_x, u_y, u_z)$, and the nodal microrotation $\phi^{\varepsilon n}=(\phi_x, \phi_y, \phi_z)$ defined at the origin and extremity of each beam are the kinematic variables that need an asymptotic expansion. For a large enough fabric structure, the ratio of the elementary cell length to the macroscopic fabric length constitutes a small parameter $\varepsilon=l/L$, versus which all geometrical and kinematic variables are expanded.

The general form of the constitutive equations can presently be identified from the expressions of the homogenized stress and couple stress tensors, built from the dyadic product of identified stress vector S^{i} and couple stress vector μ^{i}, as

$$\begin{aligned}
\sigma &= \frac{1}{g}\mathrm{S}^{\mathrm{i}} \otimes \frac{\partial \mathrm{R}}{\partial \lambda^{\mathrm{i}}} = \frac{1}{g}\left(\mathrm{S}_1^{\mathrm{i}} + \varepsilon \mathrm{S}_2^{\mathrm{i}}\right) \otimes \frac{\partial \mathrm{R}}{\partial \lambda^{\mathrm{i}}} = \underbrace{\frac{1}{g}\mathrm{S}_1^{\mathrm{i}} \otimes \frac{\partial \mathrm{R}}{\partial \lambda^{\mathrm{i}}}}_{[E]\{\epsilon\}} + \underbrace{\frac{1}{g}\varepsilon \mathrm{S}_2^{\mathrm{i}} \otimes \frac{\partial \mathrm{R}}{\partial \lambda^{\mathrm{i}}}}_{[B]\{\chi\}} \\
\mathrm{m} &= \frac{1}{g}\mu^{\mathrm{i}} \otimes \frac{\partial \mathrm{R}}{\partial \lambda^{\mathrm{i}}} = \frac{1}{g}\left(\varepsilon \mu_1^{\mathrm{i}} + \varepsilon^2 \mu_2^{\mathrm{i}}\right) \otimes \frac{\partial \mathrm{R}}{\partial \lambda^{\mathrm{i}}} = \underbrace{\frac{1}{g}\varepsilon \mu_1^{\mathrm{i}} \otimes \frac{\partial \mathrm{R}}{\partial \lambda^{\mathrm{i}}}}_{[B]\{\epsilon\}} + \underbrace{\frac{1}{g}\varepsilon^2 \mu_2^{\mathrm{i}} \otimes \frac{\partial \mathrm{R}}{\partial \lambda^{\mathrm{i}}}}_{[K]\{\chi\}}
\end{aligned} \tag{1}$$

with $\boldsymbol{g}$ the Jacobian of the transformation from Cartesian to curvilinear coordinates (they act as Lagrangian coordinates at continuum level) and $\mathbf{R}$ the position vector of any material point in the effective continuum. For periodical uniform structures endowed with a central symmetry, the stiffness coefficients are invariant under a coordinate inversion, implying that the vectors μ_1^{i} and $\mathrm{S}_2^{\mathrm{i}}$ in previous expressions should vanish; the stress and couple stress vectors then simplify to

$$
\begin{aligned}
\mathrm{S}^i = \mathrm{S}_1^i = \sum_{b\in B_R} & \left(\frac{\pi E_s \left(r^b\right)^2}{L^b} \left(e_x.\Delta \mathrm{U}_1^{\mathrm{b}}\right) e_x + \left(\frac{3\pi E_s \left(r^b\right)^4}{\left(L^b\right)^3 \left(1+\dfrac{3E_s\left(r^b\right)^2}{G_s k_s \left(L^b\right)^2}\right)} \left(e_y.\Delta \mathrm{U}_1^{\mathrm{b}} - \frac{L^b}{2}\left(e_z.\left(\phi_0^{O_{R(b)}} + \phi_0^{E_{R(b)}}\right)\right)\right) e_y \right. \right. \\
& \left. \left. + \left(\frac{3\pi E_s \left(r^b\right)^4}{\left(L^b\right)^3 \left(1+\dfrac{3E_s\left(r^b\right)^2}{G_s k_s \left(L^b\right)^2}\right)} \left(e_z.\Delta \mathrm{U}_1^{\mathrm{b}} + \frac{L^b}{2}\left(e_y.\left(\phi_0^{O_{R(b)}} + \phi_0^{E_{R(b)}}\right)\right)\right) e_z \right) \right) \delta^{ib} \\
& = \sum_{b\in B_R} \left(F_{x1}^b e_x + F_{y1}^b e_y + F_{z1}^b e_z \right)
\end{aligned}
\tag{2}
$$

$$
\begin{aligned}
\mu^{\mathrm{i}} = \mu_2^{\mathrm{i}} = \sum_{b\in B_R} & \left(\left(\frac{\pi G_s \left(r^b\right)^4}{2L^b} \left(e_x.\left(\phi_1^{E_{R(b)}} - \phi_1^{O_{R(b)}} + \frac{\partial \phi_0}{\partial \lambda^i}\delta^{ib} \right)\right) e_x \right. \right. \\
& \left. \left. + \frac{\pi E_s \left(r^b\right)^4}{4L^b} \left(\left(e_y.\left(\phi_1^{E_{R(b)}} - \phi_1^{O_{R(b)}} + \frac{\partial \phi_0}{\partial \lambda^i}\delta^{ib} \right)\right) e_y + \left(e_z.\left(\phi_1^{E_{R(b)}} - \phi_1^{O_{R(b)}} + \frac{\partial \phi_0}{\partial \lambda^i}\delta^{ib} \right)\right) e_z \right) \right) \delta^{ib} \\
& = \sum_{b\in B_R} \left(M_{2x}^{E(b)} e_x + \frac{1}{2}\left(M_{2y}^{E(b)} - M_{2y}^{O(b)}\right) e_y + \frac{1}{2}\left(M_{2z}^{E(b)} - M_{2z}^{O(b)}\right) e_z \right) \delta^{ib}
\end{aligned}
$$

with F_{x1}^b, F_{y1}^b, F_{z1}^b, M_{2x}^n, M_{2y}^n, and M_{2z}^n respectively, the first order normal and transverse efforts and the second order moment. Those expressions still involve the unknown displacements u_1^n, u_2^n and rotations ϕ_0^n, ϕ_1^n, which are determined for all nodes by solving the equilibrium equations. The previously identified continuum constitutive equations are those of a micropolar linear (in general anisotropic) elastic solid are given by

$$
\sigma_{ij} = E_{ijkl}\epsilon_{kl} + B_{ijkl}\chi_{kl},\ m_{ij} = B_{klij}\epsilon_{kl} + K_{ijkl}\chi_{kl} \quad (i,j,k,l = x,y,z) \tag{3}
$$

where E_{ijkl}, B_{ijkl} and K_{ijkl} are the micropolar fourth rank stiffness tensor; the assumption of centrosymmetrical lattices correspond at the continuum level to the vanishing of the pseudo-tensor with coefficients B_{ijkl} . Two characteristic bending lengths of the anisotropic micropolar continuum are calculated from the effective rigidities, for plain weave and twill successively.

$$
l_{c1} = \sqrt{\frac{K_{55}^{\mu}}{2\left(K_{33}^s + K_{34}^s\right)}} = 0.23 \text{ mm} \qquad l_{c2} = \sqrt{\frac{K_{66}^{\mu}}{2\left(K_{43}^s + K_{44}^s\right)}} = 0.31 \text{ mm}
$$

$$
l_{c1} = \sqrt{\frac{K_{55}^{\mu}}{2\left(K_{33}^s + K_{34}^s\right)}} = 0.33 \text{ mm}\ l_{c2} = \sqrt{\frac{K_{66}^{\mu}}{2\left(K_{43}^s + K_{44}^s\right)}} = 0.48 \text{ mm}
$$

The geometrical parameters of the fiber tows are chosen as follows:

Table 1 Configuration parameters of plain weave and twill fabrics

Weft	L_{f1} = 0.618 mm	L_{f2} = 0.487 mm	θ_f =40°	d_f = 0.27 mm
Warp	L_{p1} = 0.56 mm	L_{p2} = 0.41 mm	θ_p =40°	d_p = 0.25 mm

The mechanical properties of the warp and weft made of PES are given in Table 2; those properties are given to the beams of the respective lattices of plain weave and twill (Fig. 1 and 2 respectively).

Table 2 Elastic properties of weft and warp yarns

Weft	E_{sf}=1889 MPa	G_{sf}=756 MPa	v_f=0.25
Warp	E_{sp}=13853 Mpa	G_{sp}= 5541 Mpa	v_p =0.25

Relying on the previous geometrical and material data, the tensile, flexural, and torsional rigidities of the beam segments building the fabric lattice are defined:

Tensile rigidities: $$k_{lf} = \frac{E_{sf} A_f}{L_f} \quad , \quad k_{lp} = \frac{E_{sp} A_p}{L_p} \quad , \quad k_{lc} = \frac{E_{sc} A_c}{L_c} \quad .$$

Flexural rigidities: $$k_{tf} = \frac{12 E_{sf} I_f}{\left(L_f\right)^3} , \quad k_{tp} = \frac{12 E_{sp} I_p}{\left(L_p\right)^3} \quad , \quad k_{tc} = \frac{12 E_{sc} I_c}{\left(L_c\right)^3} .$$

Torsional rigidities: $$k_{rf} = \frac{G_{sf} J_f}{L_f} \quad , \quad k_{rp} = \frac{G_{sp} J_p}{L_p} , \quad k_{rc} = \frac{G_{sc} J_c}{L_c} .$$

In order to assess the effect of rotational degrees of freedom at the macroscopic scale, a beam incorporating a periodically distributed textile mesostructure and submitted to pure bending is considered (Fig. 3).

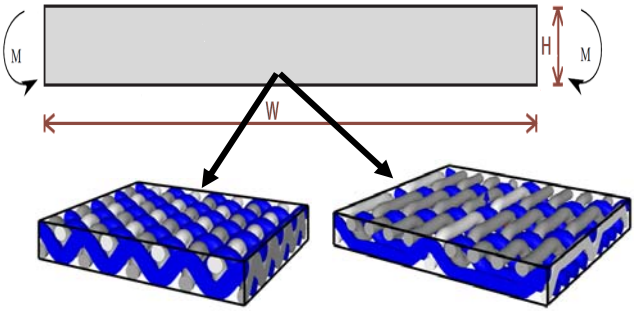

Fig. 3 Geometrical parameters of a micropolar beam subjected to a pure bending moment

The bending stiffnesses K_{xz}^{μ} and K_{yz}^{μ} of the macrobeam are defined from the simplified equilibrium equation of an anisotropic micropolar beam submitted to a uniform bending moment *M*, as

$$\underbrace{\left(E_x^* I_z^* + K_{55}^{\mu} H\right)}_{K_{xz}^{\mu}} \frac{\partial \phi_z}{\partial x} = -M \qquad \underbrace{\left(E_y^* I_z^* + K_{66}^{\mu} H\right)}_{K_{yz}^{\mu}} \frac{\partial \phi_z}{\partial y} = -M \tag{4}$$

with E_x^* and E_y^* the effective homogenized moduli of the macroscopic equivalent beam, I_z^* the quadratic moment of the macroscopic beam along the z-direction, given by $I_z^* = \frac{H^3}{12}$, and K_{55}^{μ}, K_{66}^{μ} the homogenized micropolar moduli corresponding to the couple stresses m_{xz} and m_{yz}. The effective properties of the (homogenized) macroscopic beam allow calculating the classical and micropolar rigidities. We adopt the thickness of fabrics as the macroscopic parameter, here chosen as H=0.52 mm. The gain in flexural rigidity due to the micropolar effect for a microstructured beam is quantified by the parameter $\%g_r = \frac{K^{\mu} - K^c}{K^c} \times 100$. Important gains in bending stiffness are obtained (Table 3) in comparison to a beam made of a Cauchy type continuum material for both types of fabric.

Table 3 Bending stiffness of a beam with a microstructure of plain weave and twill

	Plain weave	Twill
E_x^* (MPa)	139.40	186.90
E_y^* (MPa)	287.70	330.50
K_{55}^{μ} (N)	1.84	4.63
K_{66}^{μ} (N)	7.50	15.84
K_{xz}^{μ} (N.mm)	2.58	4.59
K_{xz}^{c} (N.mm)	1.63	2.19
$\%gr_{xz}$	58.30	109.60
K_{yz}^{μ} (N.mm)	7.27	12.10
K_{yz}^{c} (N.mm)	3.37	3.87
$\%gr_{yz}$	115.73	212.70

Micropolar effects appear to be important for those fabrics; the gain in rigidity gr_{xz} is 58.30% for plain weave compared to 109.60% for twill, and gr_{yz} is 115.73% for plain weave versus 212.70% for twill. Hence, such monolayers exhibit quite interesting bending mechanical properties.

3 Validation by FE Simulations

In order to validate the homogenized moduli, the total strain energy stored in the unit cell is equated with the energy of an equivalent homogeneous continuum, which is obtained by the prescribed strain/stress fields. In the elastic regime, the macroscopic behavior of a unit cell relates the effective stress tensor $\tilde{\sigma}_{ij}$ to the effective strain $\tilde{\epsilon}_{ij}$ by the homogenized, stiffness matrix K^s as

$$\tilde{\sigma}_{ij} = K^s \tilde{\epsilon}_{ij} \tag{5}$$

where $\tilde{\sigma}_{ij} = \frac{1}{V}\int_V \sigma_{ij} dV$ and $\tilde{\epsilon}_{ij} = \frac{1}{V}\int_V \epsilon_{ij} dV$

Table 4 provides a complete and detailed description of the geometrical parameters used to construct the FE and discrete homogenization models.

Table 4 Configuration parameters of plain weave and twill fabrics

	Plain weave	Twill
L_{f1} *(mm)*	0.60	0.60
L_{f2}*(mm)*	--	0.48
L_{p1} *(mm)*	0.52	0.52
L_{p2} *(mm)*	--	0.42
θ_f *(Deg)*	*36*	*36*
θ_p *(Deg)*	38	38
d_f *(mm)*	0.27	0.27
d_p *(mm)*	0.25	0.25

Using periodic boundary conditions over a unit cell (Fig. 4), one is able to evaluate the components of the stiffness tensor for the unit cell.

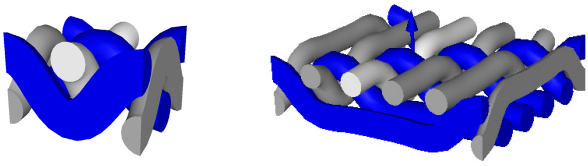

Fig. 4 Representative unit cells for the FE determination of effective moduli

A relatively good agreement has been obtained between the effective properties determined from discrete homogenization and those computed numerically (Table 5). the observed differences are at most of 20%, and are due to the approximation of the geometrical representation of the yarn trajectories by piecewise straight lines with sharp corners at the crossover points; in finite element simulations, the curvilinear trajectories of the yarns (the middle line) in the 3D model have been identified using Bezier splines (thus having a smooth radius of curvature).

Table 5 Effective elastic constants of plain weave and twill

	Discrete homogenization		Finite element simulation	
	Plain weave	Twill	Plain weave	Twill
K_{11}^{s} (MPa)	180	230	150	203
K_{12}^{s} (MPa)	55	88	51	85
K_{22}^{s} (MPa)	344	420	433	545
K_{66}^{s} (MPa)	10	11	12.5	8.5
E_{x}^{*} (MPa)	171	211	144	192
E_{y}^{*} (MPa)	327	386	415	529
ν_{xy}^{*}	0.16	0.20	0.12	0.16
ν_{yx}^{*}	0.31	0.38	0.34	0.42

4 Conclusion

The proposed homogenization technique proves efficient from a numerical point of view, and has been implemented in a dedicated code; the effective mechanical properties are determined from the topology of the fabric and the mechanical properties of the yarns. The representation of yarns could be improved by considering a more elaborate model of yarns, accounting especially for transverse compressibility. The proposed discrete homogenization technique will be extended to textile multilayers and to a nonlinear effective behavior.

References

Assidi, M., Ben Boubaker, B., Ganghoffer, J.F.: Equivalent properties of monolayer fabric from mesoscopic modelling strategies. Int. J. Solids Struct. 48, 2920–2930 (2011)

Ben Boubaker, B., Haussy, B., Ganghoffer, J.F.: Consideration of the yarn-yarn interactions in meso/macro discrete model of the fabric. Part I: Single Yarn Behavior, Mechanics Research Communications 34, 359–370, Part II: Woven Fabric Under Uniaxial and Biaxial Extension. Mechanics Research Comminucations 34, 371–378 (2007)

Caillerie, D., Mourad, A., Raoult, A.: Discrete homogenization in graphene sheet modeling. J. Elast. 84, 33–68 (2006)

Raoult, A., Caillerie, D., Mourad, A.: Elastic lattices: equilibrium, invariant laws and homogenization. Ann. Univ. Ferrara 54, 297–318 (2008)

Dos Reis, F., Ganghoffer, J.F.: Equivalent mechanical properties of auxetic lattices from discrete homogenization. Comput. Mater. Sci. 51, 314–321 (2012)

Inspection Time Optimization for a Cracked Component Based on a Reliability Approach

Maher Eltaief[1], Chokri Bouraoui[1], and Alaa Chateauneuf[2]

[1] Laboratoire de Génie Mécanique, Ecole Nationale d'Ingénieurs de Monastir, 5019 Monastir, Tunisie, Université de Monastir
eltaiefmaher@yahoo.fr
[2] Poly Tech Clermont Ferrant, Université Blaise Pascal, BP 63000 Clermont-Fd, France

Abstract. The Fatigue Crack Growth (FCG) requires the monitoring of the evolution of the length of the crack during the lifespan of the component. Maintenance inspections are needed to ensure the survival of the component. Depending on the inspections results a maintenance policy is implemented. Based on an economic study and using a dynamic method the optimal time is determined for a single and two inspections. Generalization of this method is presented for the multiple inspections. In order to illustrate and validate this method two applications are carried out: the first one is general and the second one is applied to the crack growth in mixed mode.

Keywords: reliability, optimization, inspection time, crack growth, mixed mode.

1 Introduction

In classic analytic crack method all the mechanical and geometrical properties such as the initial crack size, the load, the material properties and the crack growth parameters are supposed to be deterministic. This is leads to have a very conservative behavior. However and due to the randomness of these properties, the FCG is naturally considered as a random process and requires an appropriate inspection program in order to prevent the failure and to improve the maintenance strategies (Nechvall et al. 2010). During the lifespan of these mechanical components, inspections are required in order to decide which kind of maintenance is needed. Several methods are used to define a maintenance optimal inspection program; several authors choose an optimal maintenance time according to a fixed Probability of Failure (P_f). Others use an optimal maintenance program based on the minimum value of the P_f in order to ensure the required security (Han 1999). In an economic point of view, the optimal maintenance program is defined by minimizing the total cost function (Laggoune et al. 2009). In these studies results of previous inspections of maintenance are not taken into account.

In the present work a new formulation of the cost function in the case of a single inspection based on the decision tree is developed where the results of

M. Haddar et al. (Eds.): *Design and Modeling of Mechanical Systems*, LNME, pp. 405–413.
DOI: 10.1007/978-3-642-37143-1_48

previous inspections of maintenance are taken into account. This formulation is treated in a sequential mode starting from the initial crack process. The method is then generalized to the case of two and multiple inspections.

2 Computation of Crack Growth Rate

FCG is described by different empirical expressions. The most used one is of the Paris law (Paris et Erdogan 1963) witch represents the crack length growth ratio as a function of a loading cycle's number:

$$\frac{da}{dN} = C.\left(\Delta K_{Iéq}\right)^{m} \tag{1}$$

Where a is the crack length, N is the number of loading cycles, C and m are materials parameters $\Delta K_{Iéq}$ is the stress intensity factor range corresponding to the mixed mode (Eltaief et al. 2012).

The lifespan of fatigue may be calculated by integrating the equation (1):

$$N_f = \int_{a_0}^{a_c} \frac{da}{C.\left(\Delta K_{Iéq}\right)^{m}} \tag{2}$$

Where a_0 and a_c are the initial and critical crack lengths respectively.

3 Reliability Assessment

The reliability assessment requires defining the failure criterion of the structure. Which is represented by a limit state function G(X) expressed in terms of uncertain parameters X such as $G(X) > 0$ is the field of safety and $G(X) < 0$ represents the failure domain. The P_f is given by, where $f_x(x_i)$ is a joint probability function:

$$P_f = \int_{G(X)\leq 0} f_X(x_1, x_2, \dots \dots, x_n)\, dx_1, dx_2, \dots dx_n = \Pr(G(\{x\}) < 0) \tag{3}$$

In general the information relative to the probability density function is not available. The computation of the P_f by the equation (3) is very difficult. For this reason, the approximation methods FORM/SORM were developed (Yan et al. 1999). The P_f is then estimated by the FORM approximation as:

$$P_f = \emptyset(-\beta\ ) \tag{4}$$

Where Ø is cumulative distribution function of the standard normal random variable and β is the Reliability Index (RI) determined Rackwitz-Fiessler algorithm.

4 Updating the Reliability Based on Inspection Results

The safety margin corresponding to inspection event is denoted by M_i. During inspections, two types of results could be reported: the crack is detected or not detected.

The updated P_f for the case of crack detection $P_{f,up}^{d}$ could be easily calculated by the Bayesian approach (Jiao and Moan 1990) as:

$$P_{f,up}^{d} = P(G(X) \leq 0 | M_i \leq 0) = \frac{P(G(X) \leq 0 \cap M_i \leq 0)}{P(M_i \leq 0)} \quad (5)$$

$\overline{M_i}\overline{M_i}$ is denoted to be the complementary of the crack detection event M_i.

By using the total probability theorem (Jiao and Moan 1990), the updated P_f for the case of no crack detection $P_{f,up}^{nd}$ is:

$$P_{f,up}^{nd} = P\left(G(X) \leq 0 \middle| \overline{M_i} \leq 0\right) = \frac{P(G(X) \leq 0) - P(G(X) \leq 0 | M_i \leq 0)P(M_i \leq 0)}{1 - P(M_i \leq 0)} \quad (6)$$

5 Inspection Optimization Based on Total Cost Minimization

Based on global cost function minimization, the optimal time inspection for a cracked component submitted to a fatigue loading is carried out. Failure and inspections costs relative to each inspection are introduced in the global cost function. The following assumptions are adopted:

- The inspection is realized without reparation.
- The lifespan T_f, the failure cost (C_f) and the inspection cost (C_I) are known.

In this study, a dynamic method is used treating the problem in a sequential way starting with the initial crack. Based on the decision tree for the case of a single inspection, a total cost between t=0 and t_1 time of the first inspection is defined, leading to determine the date $t_{1optimal}$ of the first inspection for which the total cost is minimal.

For the case of two inspections, the total cost between $t_{1optimal}$ and t_2 time of the second inspection is defined. By minimizing this total cost, $t_{2optimal}$ is determined corresponding to the optimal time of the second inspection and on and on for the case of the multiple inspection.

5.1 Case of a Single Inspection

The figure 1 illustrates the decision tree in the case of single inspection realized at the time t_1 with $0<t_1<T_f$.

Based on the decision tree, we can identify two types of cost:

- $C_F(t_1)$: the expected cost of failure in the interval $[0,t_1]$ with $0 < t_1 < T_f$
- $C_I(t_1)$: the inspection cost realized at the time t_1

In the interval $[0,t_1]$, and affecting the probability of occurrence of each event, the total cost is defined as follows:

$$C_T(t_1) = \frac{C_F(t_1) + C_I(t_1)}{t_1} = \frac{C_f . P_f(t_1) + C_i . (1 - P_f(t_1))}{t_1} \quad (7)$$

Where $P_f(t_1)$ is the P_f at the time t_1. The date $t_{1optimal}$ of the first inspection corresponding to $C_T(t_{1optimal})$ minimal.

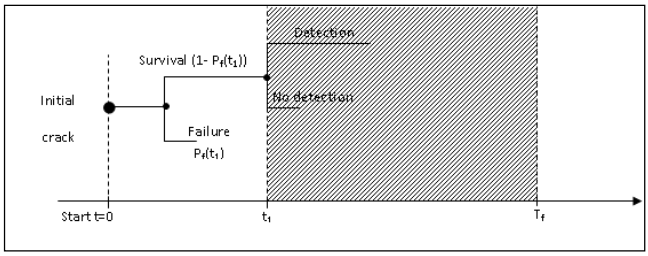

Fig. 1 The decision tree in the case of a single inspection

5.2 Case of Two Inspections

As in the case of a single inspection, two different costs are defined:

- $C_F(t_{1optimal}, t_2)$: the expected cost of failure in the interval $[t_{1optimal}, t_2]$.
- $C_I(t_{1optimal}, t_2)$: the inspection cost realized at the time t_2.

In the interval $[t_{1optimal}, t_2]$, the total cost in the case of the second inspection is defined as follows:

$$C_T(t_{1optimal}, t_2) = \frac{C_F(t_{1optimal}, t_2) + C_I(t_{1optimal}, t_2)}{t_2 - t_{1optimal}} \tag{8}$$

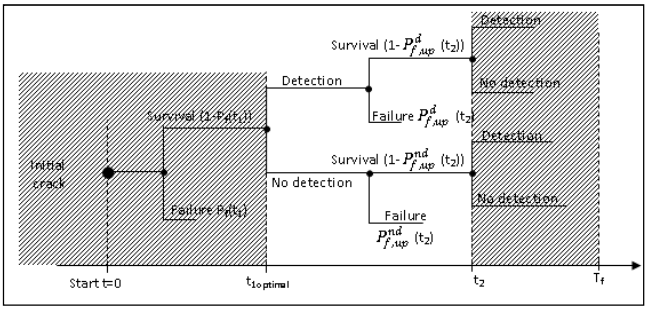

Fig. 2 The decision tree in the case of two inspections

The result of the first inspection at the time $t_{1optimal}$ gives two cases see figure 1:

Case 1

If the crack is detected and affecting the probability of occurrence of each event, the total cost in the interval $[t_{1optimal}, t_2]$ becomes:

$$C_T(t_{1optimal}, t_2) = \frac{C_f.P^d_{f,up}(t_{1optimal},t_2)+C_i.(1-P^d_{f,up}(t_{1optimal},t_2))}{t_2-t_{1optimal}} \tag{9}$$

Where $P^d_{f,up}(t_{1optimal}, t_2)$ is the $P^d_{f,up}$ between the time $t_{1optimal}$ and t_2.

Case 2

If the crack is not detected, we have:

$$C_T(t_{1optimal}, t_2) = \frac{C_f.P_{f,up}^{nd}(t_{1optimal},t_2)+C_i.\left(1-P_{f,up}^{nd}(t_{1optimal},t_2)\right)}{t_2-t_{1optimal}} \quad (10)$$

Where $P_{f,up}^{nd}(t_{1optimal}, t_2)$ is $P_{f,up}^{nd}$ between the time $t_{1optimal}$ and t_2.

5.3 Case of Multiple Inspections

The total cost of the n^{th} inspection is defined as follows:

$$C_T(t_{(n-1\ optimal)}, t_n) = \frac{C_F(t_{(n-1)optimal}, t_n) + C_I(t_{(n-1)optimal}, t_n)}{t_n - t_{(n-1)\ optimal}} \quad (11)$$

Where $C_F(t_{(n-1)optimal},t_n)$ is the expected cost of failure in the interval $[t_{(n-1)optimal}, t_n]$ and $C_I(t_{(n-1)optimal},t_n)$ is the inspection cost realized at the time t_n.

5.4 Flowchart of Computing the Optimal Inspection Time

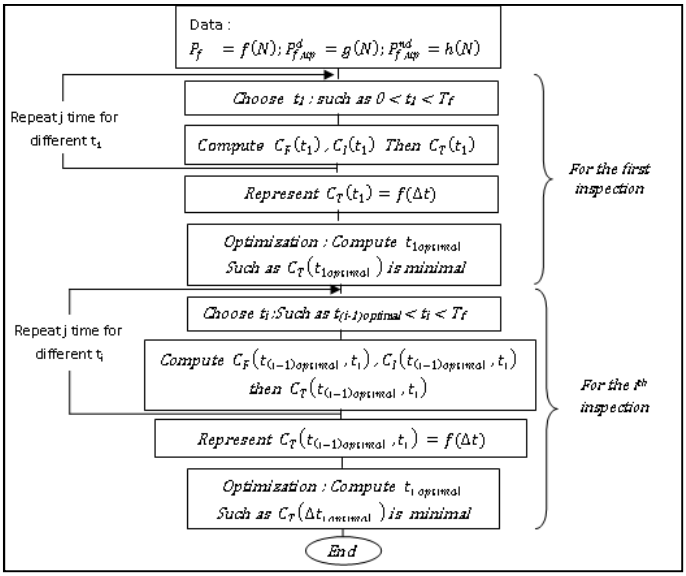

Fig. 3 Flowchart of computing the optimal inspection time

6 Application of the Method

6.1 Application 1: General Application for Illustrating the Method

In this application, the P_f and the $P_{f,up}^{d}$ are assumed to follows weibull distribution and are written as follows:

$$P_f = 1 - e^{-(\frac{t}{\gamma})^{\beta}} \quad \text{and} \quad P_{f,up}^{d} = 1 - e^{-(\frac{t}{\gamma})^{\beta-\alpha}}$$

$$\gamma = 10^6 \text{ cycles}, \ \beta = 2 \ , \ \alpha = 5.10^{-1} \text{ et } r = 0.001$$

The cost function of the first inspection is determined by applying Eq (7) for a time t_1 in the interval $[0,T_f]$. This methodology is well explained in the flowchart in the figure 3.

The figure 4 shows the evolution of the total cost of the first inspection versus the variation of the time inspection Δt. The figure 4 shows that, the optimal inspection time of the first inspection $t_{1optimal}$ reflecting the minimum cost is estimated to $t_{1optimal} = 3{,}25.10^4$ cycles.

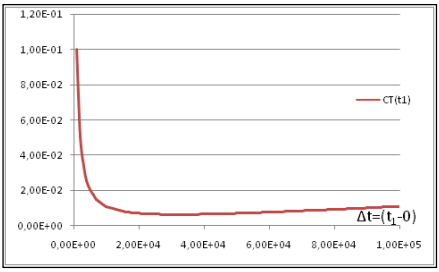

Fig. 4 Evolution of the total cost versus Δt (first inspection)

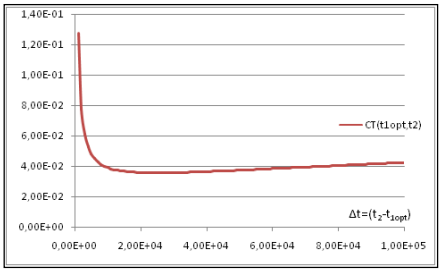

Fig. 5 Evolution of the total cost versus Δt (second inspection)

In order to determine the optimal inspection time of the second inspection $t_{2optimal}$, Eq (8) and Eq (9) are applied for different t_2. The figure 5 shows the evolution of the total cost of the second inspection versus Δt. We note that the optimal inspection time of the second inspection $t_{2optimal}$ is:

$$\left(t_2 - t_{1optimal}\right)_{optimal} = t_{2optimal} - t_{1optimal} = 2{,}55.10^4 \text{cycles}$$

$$where\ as \quad t_{1optimal} = 3{,}25.10^4 \text{cycles} \quad then \quad t_{2optimal} = 5{,}8.10^4 \text{cycles}$$

6.2 Application 2: Case of Crack Growth in Mixed Mode

A rectangular plate of length 2L=100 mm and of width 2W=50 mm is considered, it contains a crack rectilinear central of length 2W=50 mm and disposed at an angle β=30° loaded with a constant amplitude cyclic stress σ. The nature of random parameters and their scattering values are given in the table 1.

Table 1 Data FCG characteristics

Parameters	Law	average	Coefficient of variation
a_0 (m)	normale	$2.1\ 10^{-4}$	3%
a_c (m)	normale	$5.5\ 10^{-4}$	3%
C (m/cycle/(MPa.m$^{0.5}$)^m)	log-normale	$6.8\ 10^{-12}$	10%
a_d (m)	normale	$4.5\ 10^{-4}$	3%
m	deterministic	3	-
(MPa)	deterministic	75	-

Figure 6 shows the evolution of the P_f and $P_{f,up}^{d}$ versus the cycle's number after an inspection operation in the case of crack detection. We note that the crack detection accelerates the increase of P_f, consequently a disaster cost, which would have happened due to the failure is gained.

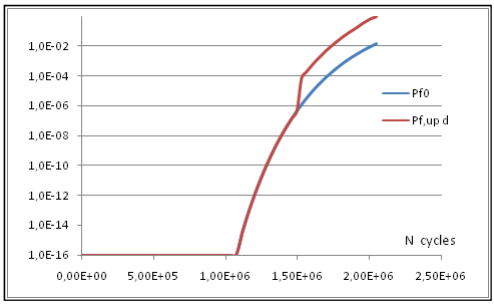

Fig. 6 Evolution of P_f and $P_{f,up}^{d}$ versus the cycle's number

The figure 7 shows the evolution of the total cost of the first inspection depending on Δt. By analyzing this curve, the optimal inspection time of the first inspection is $t_{1optimal} = 1{,}6.10^6$ cycles.

The figure 8 shows the evolution of the total cost of the second inspection depending on the Δt. By analyzing this curve, the optimal inspection time of the second inspection $t_{2optimal}$ is:

$$\left(t_2 - t_{1optimal}\right)_{optimal} = t_{2optimal} - t_{1optimal} = 1{,}6.\,10^5 \text{cycles}$$

Where as $t_{1optimal} = 1{,}6.\,10^6 \text{cycles}$ $then$ $t_{2optimal} = 1{,}96.\,10^6 \text{cycles}$.

Figure 9 shows the evolution of the total cost of the first and the second inspection depending on the Δt. From this figure we see that the Δt optimal corresponding to the second inspection decreases relative to that of the first inspection. This result is physically coherent since the crack growth increases first slowly then increases exponentially until the rupture.

For the case of multiple inspections if Δt optimal is very low, the maintenance program should be changed from inspection to replacement or repair. In this case we can deduce the maximum number of inspections to be performed.

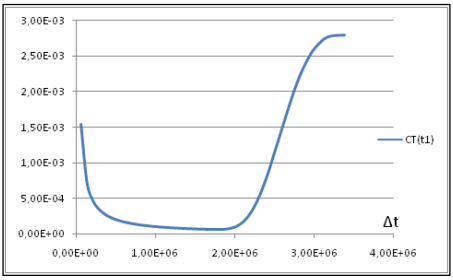

Fig. 7 Evolution of the total cost versus Δt (first inspection)

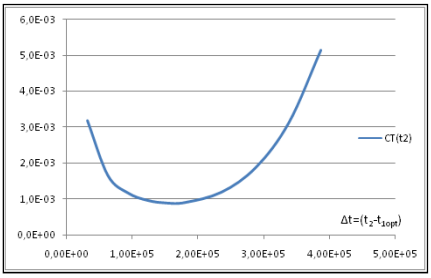

Fig. 8 Evolution of the total cost versus Δt (second inspection)

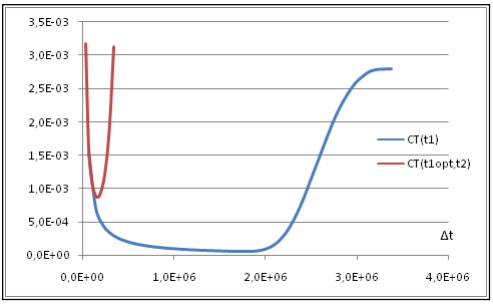

Fig. 9 Evolution of the total cost of the first and the second inspection

7 Conclusion

In this study we have proposed a general approach integrating the coupling of fatigue-reliability and its application to the fatigue crack growth. Based on the Rackwitz-Fiessler algorithm and the Bayesian approach, the failure probability and the updated failure probability are determined using the FORM method. Taking into account the results of previous inspections and based on the approach of minimizing the total cost, an optimal maintenance schedule is implemented. A sequential approach starting by the initial crack is applied to build the total cost function. Two applications have been presented to show the efficiency of this approach. The first one is general and based on the model of weibull and the second one is applied to the fatigue crack growth in a mixed mode.

References

Journal Article

Nechval, N., Nechval, K., Purgailis, M., Strelchonok, V.: lanning Inspections in the Case of Damage Tolerance Approach to Service of Fatigued Aircraft Structures. International Journal of Performability Engineering (July 2010)

Jiao, G., Moan, T.: Methods of reliability model updating through additional events. Struc. Safe. 9, 139–153 (1990)

Han, P.H.: Inspection and maintenance planning of pipeline under external corrosion considering generation of new defects. Struct. Saf. (2), 203–222 (1999)

Laggoune, R., Chateauneuf, A., Aissani, D.: Opportunistic policy for optimal preventive maintenance of a multi-component system in continuous operating units. Comput. Chem. Eng. (33), 1499–1510 (2009)

Paris, P.C., Erdogan, F.: A critical analysis of crack propagation laws. J. Basic Eng. 85, 528–534 (1963)

Chang, J., Xu, J.Q., Mutoh, J.: A general mixed-mode brittle fracture criterion for cracked materials. Engng. Fract. Mech. 73, 1249–1263 (2006)

Yan-Gang, Z., Tetsuro, O.: A general procedure for first/second-order reliability method (FORM/SORM). Struct. Saf. 95, 95–112 (1999)

Eltaief, M., et al.: Toward optimal updating time inspection based on reliability approach of fatigue crack propagation. Applied Mechanics and Materials 146, 96–111 (2012)

Fatigue Behavior of Aluminum Alloys Requested by a Simple Overload: Environment Influence

Mohamed Mazari[1], Wahiba Bendaho[1], Chahinez Gafour[1], Mohamed Benguediab[1], and Nara Ranganathan[2]

[1] Laboratory of Materials and Reactive Systems,
Djillali Liabes University, BP 89,
Larbi Ben M'hidi 22000 Sidi Bel Abbes, Algeria
mazari_m@yahoo.fr
[2] Laboratory of Mechanics and Rheology,
F. Rabelais University of Tours, France
narayanaswami.ranganathan@univ-tours.fr

Abstract. In this study we were interested in the behavior of two aluminum alloys (2024 T351 and 7075 T7351) requested by a simple overload with an aim of determining the number of cycles of delay of each one and of comparing their behavior various environments (air and vacuum).For that, we carried out fatigue tests stopped by a simple overload with a rate of overload $\tau = 2$ and reports/ratios of loads R=0,1 and R=0,5.The results obtained show that the number of cycles of delay of alloy 2024 T351 is higher than that of the alloy 7075 T7351 and that the number of cycles of delay is more significant in the vacuum than with the air for two materials.This observation will lead us to make a judicious choice as for the industrial use (aeronautical) of two materials.

Keywords: fatigue, overload, aluminum alloy, a number of cycles of delay.

1 Introduction

The influence of the spontaneous load change on fatigue crack behavior in a structure is a natural phenomenon which suddenly appears. For this reason several authors such as Schijve [1], Von Euw and Al.[2], Wei and Al [3] and Bathias [4] were interested to overloads phenomenon and they defined some governing factors of this phenomenon.

Among these factors are:

- ΔKpic : amplitude of the stress intensity factor corresponding to the overload in [MPa.m$^{1/2}$] ;
- Nd : number of delay cycles ;
- a_d: crack length disturbed by the overload in [m].

some authors tried to explain other aspects relating to the overloads they show that 2024 T351 alloy for a overload rate τ the delay decreases if the load ratio R

M. Haddar et al. (Eds.): *Design and Modeling of Mechanical Systems*, LNME, pp. 415–421.
DOI: 10.1007/978-3-642-37143-1_49

increases, for Ri > 0 and for $\tau = 2$, the crack can be blocked definitively [5] . In the field of negative charge ratios (Ri < 0) and for a given overload rate, the delay decreases when the load ratio R increases [6].

2 Experimental Conditions

2.1 Materials

In this study, we used two high-strength aluminum alloys which chemical properties and the mechanical characteristics are given, respectively, in tables 1 and 2.

Table 1 Chemical properties

Elements%	**Si**	**Fe**	**Cu**	**Mn**	**Mg**	**Cr**
2024 T351	0.10	0.22	4.46	0.66	1.50	0.01
7075 T7351	0.70	0.16	1.52	0.04	2.55	0.20

Table 2 Mechanical characteristics

Material	$\sigma_{0.2}$ (MPa)	σ_R (MPa)	A (%)	K	n
2024 T351	318	524	12.8	652	0.104
7075 T7351	470	539	11.7	960.5	0.051

2.2 Specimens

All the tests were carried out on CTX specimen with:

- For 2024 T351, X = 75mm, B= 10 and 4 mm, the geometry of some specimen was modified by N. anganathan to be able to take opening measurements vertically of the axis of loading (picture 1)
- For 7075series, X = 38,4 mm, B=12mm

The general configuration of specimens is given in figure 1.

For this geometry, the stress intensity factor K is given by:

$$K = \frac{p}{B\sqrt{w}} f\left(\frac{a}{w}\right) \quad (1)$$

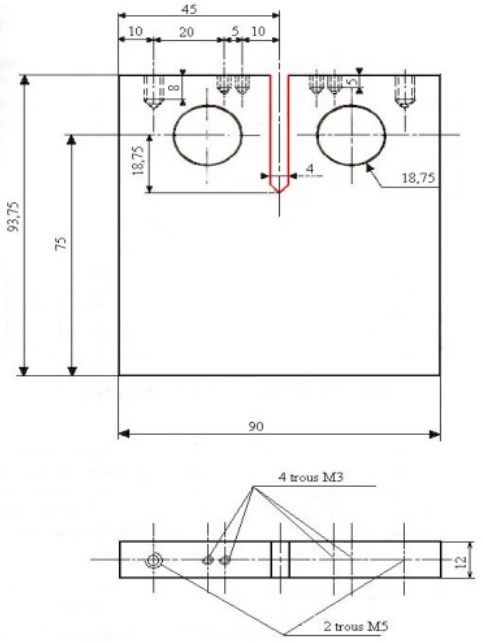

Fig. 1 Specimen geometry

Where P: is the applied load (N)
B: specimen thickness (mm)
W: spicemen width (mm)

Two compliance functions $f\left(\frac{a}{w}\right)$ were used and are given by:

- **For** $0{,}3 < \frac{a}{w} < 0{,}7$

$$f\left(\frac{a}{w}\right) = 29{,}6\left(\frac{a}{w}\right)^{\frac{1}{2}} - 185{,}5\left(\frac{a}{w}\right)^{\frac{3}{2}} + \ldots \quad (2)$$

- **For** $0{,}2 < \frac{a}{w} < 0{,}3$

$$f\left(\frac{a}{w}\right) = 4{,}55 - 40{,}32\left(\frac{a}{w}\right) + 414{,}7\left(\frac{a}{w}\right)^{2} - \cdots \quad (3)$$

- **For** $\frac{a}{w} > 0{,}3$ the equations (2) and (3) give appreciably the same results.

This function was established by Newman [86].

3 Results and Discussions

3.1 Delay Curves

We observed three types of delay:

a) Immediate Delay

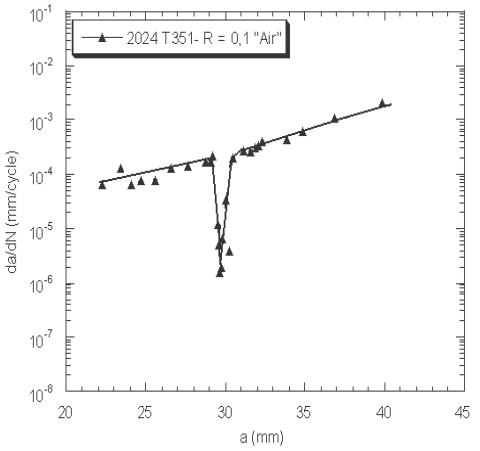

Fig. 2 Immediate delay (R=0.1 under Air)

b) Differed Delay

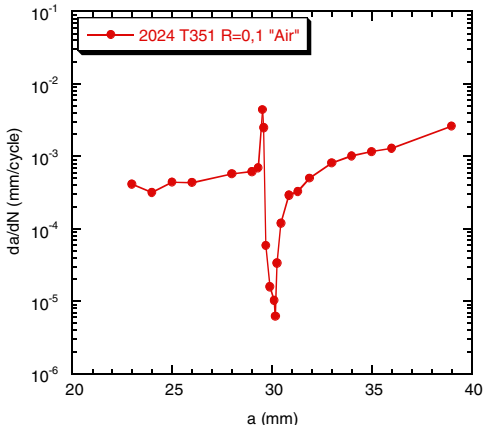

Fig. 3 Differed delay (R=0.1 under Air)

c) Blocking

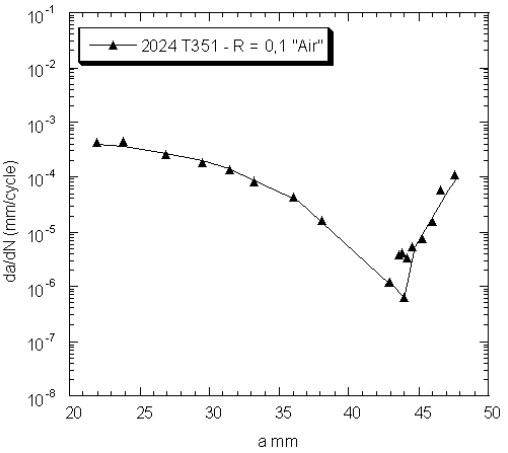

Fig. 4 Blocking (R=0.1 under Air)

3.2 Evolution of the Number of Delay Cycle

To characterize the effect of material, of the report/ratio of load and the environment, we presented the evolution of the number of cycle affected N_d by the overload according to the amplitude of the stress intensity factor ΔK.

a) Material and Load Ratio Effect

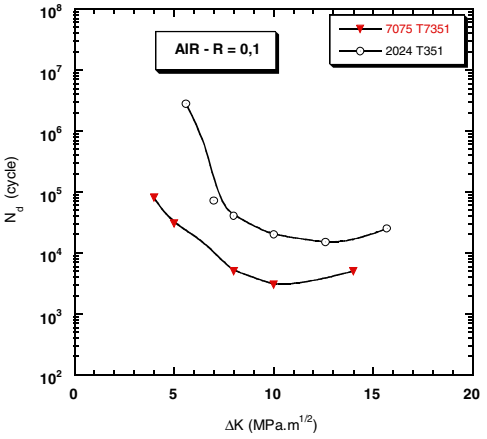

Fig. 5 Evolution of delay cycle N_d according to ΔK for R=0.1 under Air

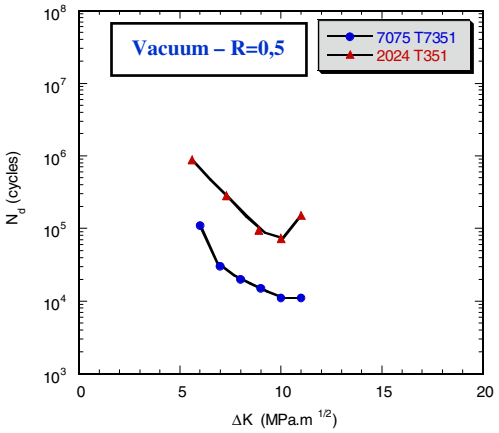

Fig. 6 Evolution of delay cycle N_d according toΔK for R=0.5 under Vacuum

We note that:

- The delay propagation is more important in R=0,1 than in R=0,5;
- The two materials present, overall, the same shape of U as what was observed by Vecchio & Al [7] and Ranganathan & Al [5].

b) Environment Influence

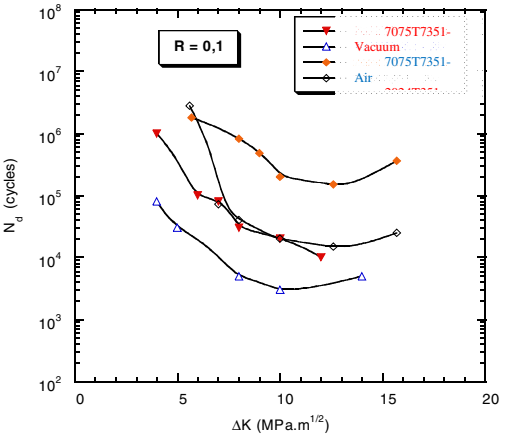

Fig. 7 Evolution of delay cycle N_d according to ΔK for R=0.1 and R=0.5 under Air and vacuum for 2 materials

4 Conclusion

In this study we highlighted the number of delay cycles due to the effect of a simple overload.

We studied the material effect, the load ratio effect and the environment influence. We noted that overall the two materials take the same form out of U. The 7075T7351alloy present a delay ten times weaker than 2024T351 for $7 < \Delta K < 14$ MPa$\sqrt{m}$ with R = 0,1 and for $7 < \Delta K < 10$ MPa$\sqrt{m}$ with R = 0,5.

This behavior can be explained by the fact that the 2024T351 alloy presents a strong cyclic consolidation and that for low values of ΔK the crack tends to deviate of its axis of propagation after the application of the overload.

The delay under vacuum is more important than under air for two studied materials with R=0, 1.

References

[1] Schijve: Prediction Methods for Fatigue Crack Growth in Aircraft Material. ASTM STP 700, 3 (1979)
[2] Von Euw, E.F.J., et al.: Stress Analysis and Growth of Cracks: Proceedings of the 1971 National Symposium on Fracture Mechanics: Part 1. ASTM STP 513, 230 (1972)
[3] Wei, R.P.: Load interaction effects on fatigue crack growth. NASA CR, 2239 (1973)
[4] Bathias, C.: Effects of overload on fatigue crack growth in some aluminium alloys. In: International Conference of Mechanical Behavior of Materials, Boston, pp. 16–20 (1976)
[5] Ranganathan, et al.: Overload Effects in Aluminum Alloys: Influence of Plasticity and Environment. Journal of ASTM International 1(10) (2004)
[6] Stephens, R.I., et al.: ASTM STP 595, 27 (1976)
[7] Vecchio, R.S., et al.: Fat. of Eng. Matls and St. 7, 181 (1984)

Optimization Based Simulation of Self-expanding Nitinol Stent

Mohamed Azaouzi[1], Nadhir Lebaal[2], Ahmed Makradi[1], and Salim Belouettar[1]

[1] Advanced Material and Structure Department,
Public Research Centre Henri Tudor,
66 rue de Luxembourg,
L-4002 Esch-sur-Alzette, Luxembourg
mohamed.azaouzi@tuor.lu
[2] Department of Mechanical Engineering,
Université de Technologie de Belfort-Monbéliard,
F-90010 Belfort, France
nadhir.lebaal@utbm.fr

Abstract. Self-expanding Nitinol (nickel-titanium alloy) stents are tubular, often mesh like structure, which are expanded inside a diseased artery segment to restore blood flow and keep the vessel open following angioplasty. The super-elastic and shape memory properties of Nitinol reduce the risk of damage to the stent, both during delivery into the body and due to accidents while in operation. However, as Nitinol stents are subjected to a long-term cyclic pulsating load due to the heart beating (typically 4×10^7 cycles/year) fatigue fracture may occur. One of the major design requirements in medical implants is the device lifetime or, in engineering terms, fatigue life. The objective of this paper is to optimize the stent design by reducing the strain amplitude and mean strain over the stent, which are generated by the cyclic pulsating load. An optimization based simulation methodology was developed in order to improve the fatigue endurance of the stent. The design optimization approach is based on the Response Surface Method (RSM), which is used in conjunction with Kriging interpolation and Sequential Quadratic Programming (SQP) algorithm.

Keywords: Nitinol stent, shape memory, finite element analysis, numerical simulation, design optimization.

1 Introduction

Self-expanding stents are mesh-like tube structures made of a nickel-titanium alloy (Nitinol). Nitinol materials for stents offer superior implant characteristics due to their superelastic and shape memory properties (Morgan 2004). Because of these properties, self-expanding Nitinol stents are being used widely to treat occlusions in endovascular arterial lumens. Nitinol stent has proven to reduce the extent of arterial recoil and restenosis. However, as the stent is subjected to a

M. Haddar et al. (Eds.): *Design and Modeling of Mechanical Systems*, LNME, pp. 423–430.
DOI: 10.1007/978-3-642-37143-1_50

long-term cyclic pulsating loads due to the heart beating (typically 4×10^7 cycles/year), fatigue fracture may occur (Pelton el al. 2008). Nitinol stents should be designed to withstand at least 400 million cycles, which is equivalent to 10 years of cyclic fatigue. The fatigue endurance is a major design requirement which could be achieved by optimizing the stent design and manufacturing process. While extensive work has been done recently to evaluate the structural behavior of self-expanding Nitinol stent using FEA, little attention has been focused on the numerical shape optimization of this medical device, because of the complex material behavior and loading conditions. In this paper an optimization strategy based on FEA has been developed. The response surface methodology is used here in order to find the optimal stent design using numerical simulations. The RSM (Azaouzi and Lebaal 2012) has the advantage to reduce the cost of design and analysis by approximating a complex model. This approximation is conducted knowing the results of FEA calculated at some points in the design space sampled using the Design of Experiment (DOE) methods (Dean and Voss 1999). The response of the objective function to each data point in the design space is evaluated through the approximation model. Then, a response surface for each objective function is constructed using Kriging interpolation (Kaymaz 2005) from the set of FEA results. Nevertheless, an accurate approximation of the objective function and an appropriate selection regarding the DOE are necessary to guarantee a quick convergence to the optimal solution. The FEA was performed in order to study the fatigue behavior of a given stent design. Numerical simulations of the stent deployment and pulsating load were conducted using Abaqus© Finite Element (FE) code (Abaqus standard 2011). Since the pattern repeats itself symmetrically, a reduced model based on a "V-shaped" strut was considered, in order to provide insight into the strain amplitude and mean strain which are generated by the cyclic pulsating load due to the heart beating.

2 Numerical Modeling

A self-expanding Nitinol stent based on the design of SMART control stent manufactured by Cordis© Corporation is selected for the FEA and optimization. The stent is composed of a series of V-shaped struts in circumferential rows which are connected by bridges (Figure 1a). The typical dimensions of a strut are as follow: length L =3mm, width W=0.2mm and thickness T=0.2mm. The manufacturing process of Nitinol stents starts from a thin tube in which a pattern is micromachined. The FE model is built from this machined tube. The stent is expanded to its nominal dimensions, typically at a diameter much larger than the original tube diameter. The stent is then annealed to provide its new unloaded configuration. It is then crimped from the outside and inserted into a delivery system (usually a system of catheter). Once inside the blood vessel, the delivery system pushes the stent out of its containment, self-expanding to exert radial forces on the blood vessel.

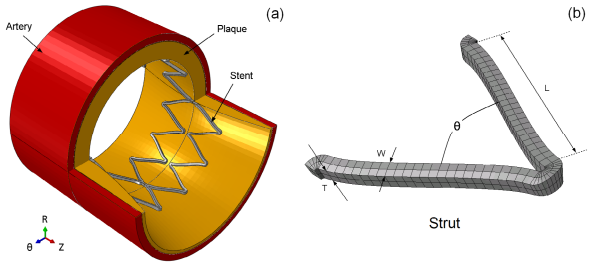

Fig. 1 Numerical modeling of the stent and artery

2.1 Analysis Procedure

Both the manufacturing process, which includes expansion, annealing and crimping of the self-expanding stent, and the subsequent deployment followed by one cycle pulsating load of the stent were modeled using Abaqus©/standard FE code. Symmetrical boundary conditions are applied to maintain symmetrical deformation. The cylinder used to expand and crimp the stent is considered rigid. A radial displacement was imposed for the expansion ($+U_r$) and crimping ($-U_r$) simulations respectively. Then, the same radial displacement is imposed on the outer cylinder in the opposite direction ($+U_r$) for the self-expansion simulation. As the first pulse cycle is considered to provide the worst-case stress-strain condition, a radial sinusoidal displacement (U_r) was applied to the stent in order to simulate the pulsating load due to the heart beating. The cyclic change in the artery diameter is defined by the percent of compliance C expressed as follow:

$$C = \frac{D_s - D_d}{D_d}(\%) \tag{1}$$

where: D_s and D_d are respectively the artery diameter at the systolic and diastolic pulse pressure.

The cyclic radial displacement is defined by the following equation:

$$U_r = U_r^0 \, sin(2\pi.t) \;\text{ with }\; U_r^0 = C.D_d = D_s - D_d \text{ and } \; 0 \le t \le 1 \tag{2}$$

The contact interactions between the cylinder and stent as well as the stent and plaque were modeled with the penalty method and a pure master-slave formulation. The contact between the plaque and artery is assumed to be tied. The penalty method was used because it prevents the chattering behavior that might occur due to the differences in mass densities between the stent and the plaque tissue during contact. A Coulomb friction coefficient of 0.1 was used to model the contact interaction.

Solid linear hexahedron FE was used in order to capture the local peak stress and strain. The hexahedron FE is the best candidate for the FEA of stent models because it provides good balance between accuracy and efficiency. As stents are loaded dominantly in bending, the fully-integrated quadratic hexahedron element with twenty nodes was selected (C3D20). This FE does not suffer from

hourglassing and has integration points closer to the surface. The C3D20 FE provides good estimate on the peak stress even with the coarsest mesh. The plaque and artery were meshed with a fully-integrated linear hexahedron element that is denoted in Abaqus by C3D8. The cylinder is meshed with quadratic shell FE. Mesh convergence were performed to strike a balance between solution accuracy and efficiency. The average FE size of the strut, artery and plaque are respectively: 0.05, 0.2 and 0.15mm.

2.2 Material Behavior Modeling

The behavior of Nitinol is extremely complex, as can be seen from its uniaxial behavior shown in Figure 2. The key characteristic of Nitinol is its superelastic material behavior, making it an extremely flexible metal alloy that can undergo very large deformations without losing the ability to recover its original shape upon unloading. At rest, the material presents itself in an austenite phase. When loaded beyond a certain stress, the austenite phase transforms into martensite phase. The transformation produces a substantial amount of strain, which on unloading is reversible. Since the transformation strains are large (of the order of 6%) compared to elastic strains in typical metals, the material is said to be superelastic. Further loading beyond superelastic limit reveals plastic behavior in martensite phase. The constitutive model used in this paper is based on the generalized plasticity theory. It models the superelastic behavior of Nitinol, where any strain increment is decomposed into a linear elastic part, and into a stress induced transformation part (Auricchio et al 1997).

The hyperelastic constitutive model used to describe the atherosclerotic plaque behavior in the vessel is based on the Moony-Rivlin hyperelastic constitutive theory which has been demonstrated to be appropriate for the modeling of tissue behaviors (Lally and Prendergast 2003). The mechanical behavior of the artery was modeled using a homogeneous, isotropic and hyper-elastic constitutive model material (Holzapfel et al 2004). This model has been found to adequately describe the non-linear stress-strain relationship of hyperelastic arterial tissue.

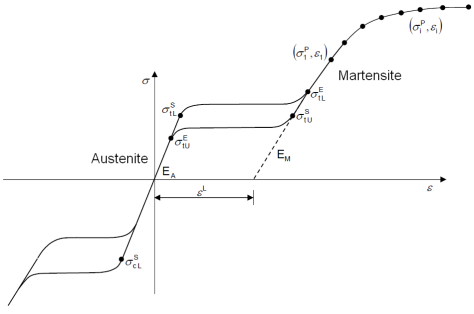

Fig. 2 Mechanical behavior of Nitinol alloy

3 Stent Design Optimization

The objective of optimization presented herein, is to improve the fatigue resistance (avoid fracture) of the stent by minimizing the strut volume without decreasing significantly its radial stiffness (maintain the wall vessel). The optimization problem is highly non-linear with non linear constraint and three design variables to be optimized (length, thickness and width of the strut). The optimization problem consists in determining an optimal stent design by minimizing the strut volume, while avoiding that the radial force decreases below a critical value (2N), and at the same time avoiding that the strain amplitude increases more than 0.4% (Nitinol stents have a constant fatigue life with strain amplitude below 0.4% (Pelton et al. 2008)). These two design requirements are translated respectively by two constraint functions g_1 and g_2. Thus, the optimization problem can be formulated as follow:

$$\text{Minimize } J(x) = V(x)/V_0$$
$$\text{such that } g_1(x) \leq 0 \text{ and } g_2(x) \leq 0 \text{ with } x^l \leq x \leq x^u \tag{3}$$

where: $J(x)$ is the normalized objective function, $V(x)$ is the volume of the strut at iteration *k*, V_0 is the initial strut volume and x is the vector of design variables. This vector is bounded by $\boldsymbol{x}^l$ and $\boldsymbol{x}^u$ which respectively represent lower and upper limits: $\boldsymbol{x}^l$ = (2.5, 0.1, 0.1) and $\boldsymbol{x}^u$ = (5, 0.3, 0.3).

The first constraint functions can be expressed as follow:

$$g_1(x) = (F_c - F)/F_c \tag{4}$$

where: F_c is the critical radial force (F_c = 2N) and F is the radial force calculated at the iteration k.

The second constraint function has the following expression:

$$g_2(x) = (\Delta\varepsilon_{max} - \Delta\varepsilon^c_{max})/\Delta\varepsilon^c_{max} \text{ With } \Delta\varepsilon_{max} = max\left|(\varepsilon^i_s - \varepsilon^i_d)/2\right| \tag{5}$$

where: $\Delta\varepsilon^c_{max}$ is the critical strain amplitude, $\Delta\varepsilon_{max}$ is the maximum amplitude strain calculated at the iteration k and ε^i_s, ε^i_d are the equivalent strains calculated at the integration point of each FE respectively at the systolic and diastolic pulse pressure.

To search for the optimum parameters with low computational time and with a good accuracy, the RSM is adopted and coupled with an auto adaptive strategy of the research space. The RSM consists in the construction of an approximate expression of the objective function starting from a limited number of evaluations of the real function. In order to obtain a good approximation, Kriging interpolation has been used to approximate the response surface in an explicit form according to the design variables of optimization. In this method, the approximation is

computed by using the evaluation points based on a composite DOE (Dean and Voss 1999). Once the objective function is built, the SQP algorithm is used to obtain the optimal approximate solution which respects the imposed constraints. More details about the optimization procedure may be found in (Azaouzi and Lebaal 2012).

4 Numerical Results

FEA of the in vivo pulsatile loading of the Nitinol stent was conducted considering strain-based approach, which provides insight into the mechanisms of fatigue behavior to predict lifetime. Strain-based approach was used because the in vivo pulsatile conditions in the stent are considered to be under displacement control. After the stent deployment, an artery compliance of 5% was assumed in order to simulate the pulsating load. The numerical results corresponding to the pulsatile loading is illustrated in Figure 3. In order to illustrate in an illuminating way the deformation filed within the strut, strains amplitude ($\Delta\varepsilon = |\varepsilon_s - \varepsilon_d|/2$) are represented as a function of mean strains ($\varepsilon_{mean} = (\varepsilon_s + \varepsilon_d)/2$) which are calculated over the strut. $\Delta\varepsilon$ and ε_{mean} are calculated at every integration point of each solid FE using a Python script which was implemented specially for the post-processing of numerical results. Each point in the diagrams represents a couple of $\Delta\varepsilon$ and ε_{mean} that were calculated at the integration point of the hexahedron FE.

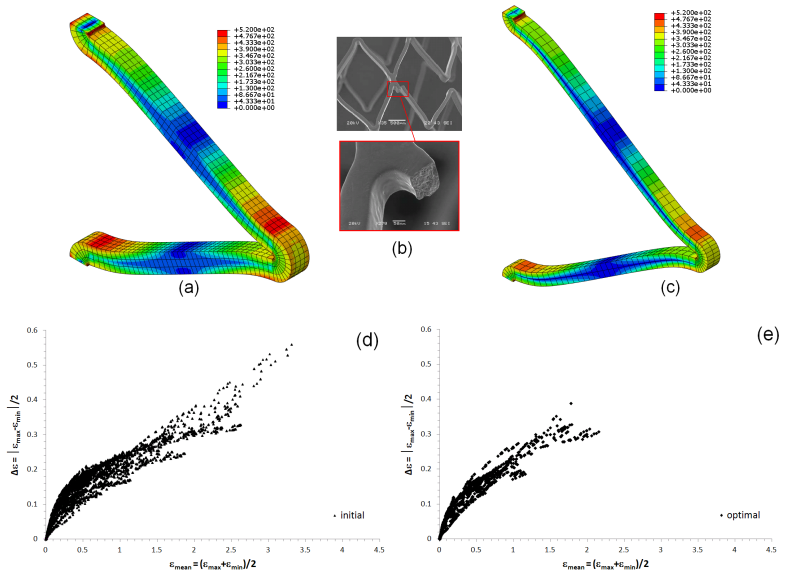

Fig. 3 Equivalent strain before and after optimization

Figure 3 shows the relationship between strut dimensions and equivalent strains that are generated by the pulsating load. As could be noticed, the strut dimensions have an impact on $\Delta\varepsilon$ and ε_{mean} and consequently the fatigue lifetime of Nitinol stents. The strain distribution illustrated in Figure 3 gives an idea about the significance of the optimized design parameters (L, W and T) that improve the fatigue behavior of Nitinol stents. It can be noticed that $\Delta\varepsilon$ and ε_{mean} were decreased significantly and the limitation on the strain amplitude was fulfilled. Figure 3c illustrates the equivalent stress distribution over the strut after optimization. The equivalent stress located in the tip regions of the bridges was reduced by about 100MPa. This result demonstrates the effectiveness of the optimization approach and the improvement of the fatigue resistance of the stent.

5 Conclusion

An optimization methodology has been performed for self-expanding Nitinol stent design, based on Kriging interpolation and combined with constraint gradient based method (SQP). The numerical algorithm shows its suitability and robustness as a tool for solving non linear optimization problem, by taking into account high nonlinearities of the FEA such as (super elasticity, large deformation and contact interaction). The relationship between strut dimensions and fatigue life of Nitionl stent was demonstrated in this paper using FEA. It has been shown that strains amplitude and mean strains which are generated by the pulsating load after stent deployment may be decreased by minimizing the strut volume. In addition, it has been demonstrated that optimization of the strut cross-section and length increase fatigue lifetime of Nitinol stent. The FEA presented herein was performed for a typical oversizing and pulsatile loading conditions. However, further stenting conditions should be considered such as patient's anatomy, artery shape and location.

Acknowledgements. This work has been supported by the National Research Funding of Luxembourg (FNR) via the project DeStenEE, C09/MS/09.

References

Morgan, N.B.: Medical shape memory alloy applications– the market and its products. Materials Science & Engineering A 378, 19–23 (2004)

Pelton, A.R., Schroeder, V., Mitchell, M.R., Gong, X.Y., Barney, M., Robertson, S.W.: Fatigue and durability of Nitinol stents. Journal of the Mechanical Behavior of Biomedical Materials, 153–164 (2008)

Azaouzi, M., Lebaal, N.: Tool path optimization for single point incremental sheet forming using response surface method. Simulation Modeling Practice and Theory 24, 49–58 (2012)

Dean, A., Voss, D.: Design and Analysis of Experiments. Springer, New York (1999)

Kaymaz, I.: Application of Kriging method to structural reliability problems. Struct. Safety 27, 133–151 (2005)

Abaqus standard, Version 6.12, Dassault systems (2011), `http://www.simulia.com`

Auricchio, F., Taylor, R.L., Lubliner, J.: Shape memory alloys: macromodelling and numerical simulations of the superelastic behavior. Computer Methods in Applied Mechanics and Engineering 146, 281–312 (1997)

Lally, C., Prendergast, P.J.: An investigation into the applicability of a Mooney-Rivlin constitutive equation for modeling vascular tissue in cardiovascular stenting procedures. In: Proceedings of the International Congress on Computational Biomechanics, Zaragoza, Spain, pp. 542–550 (2003)

Holzapfel, G.A., Sommer, G., Regitnig, P.: Anisotropic Mechanical Properties of tissue components in Human Atherosclerotic plaques. Journal of Biomechanical Engineering 126, 657–665 (2004)

Anisotropic Damage Model with Unilateral Effect and Sliding Friction for Brittle Materials

Abdelkibir Benelfellah[1], Arnaud Frachon[1], Micheal Gratton[1], Micheal Caliez[1], and Didier Picart[2]

[1] Loire valley University, ENI Val de Loire,
Laboratoire de Mécanique et Rhéologie,
B.P.3410, 41034 Blois Cedex, France
benelfellah@univ-tours.fr
[2] CEA, DAM, Le Ripault, F-37260 Monts, France
didier.picart@cea.fr

Abstract. The opening-closing effect of the microcracks is a kinematic phenomenon usually modeled using a set of damage variables. The influence of microcracks must be taken into account depending on their opening or closing state, which results in different elasticity for the same level of damage. In this work, the volumetric, deviatoric and tangential model denoted as V-D-T is chosen and modified by introducing the opening-closing effect into the free energy. This model is coupled with a sliding-friction mechanism of the microcrack lips when the latter are closed. Simulations of compression tests with confinements are presented to validate the model.

Keywords: Anisotropic damage, Microcracking, Degradation, Induced anisotropy, Constitutive modeling, microplane model.

1 Introduction

Brittle materials are characterized by asymmetric behavior in tension and compression and dependence of damage evolution to confinement pressure (influence of microcracks reclosing). The effectiveness of damage was modeled by using two damage variables to separate the opening and closing states (Ladeveze *et al* 1994). Other authors had introduced a set of variables or dependent parameters, often inspired by micromechanisms, such as the blocked energy by closed defects ((Boursin *et al* 1996), (Chaboche and Maire 1997)), parameter tensor of fourth order (Halm and Dragon 2002), open-cracks ratio (Baste *et al* 1989) and the opening mode cracks concept (Thionnet and Renard 1999) (Thionnet 2010), etc. A microplane model is chosen in this study for modeling the unilateral effect and sliding- friction mechanism. Microplane models were introduced in 1938 (Taylor 1938) and applied to metal plasticity (Batdorf and Budiansky 1949) or to brittle materials such as concrete, ceramics, rocks, ice, etc (Bazant and Oh 1983), (Bazant and Gambarova 1984), (Bazant and Oh 1985), (Beghini *et al* 2007), (Carol *et al* 2001) (Carol and Willam 1996) and (Kuhl *et al* 2001). Particularly, the

M. Haddar et al. (Eds.): *Design and Modeling of Mechanical Systems*, LNME, pp. 431–438.
DOI: 10.1007/978-3-642-37143-1_51

volumetric-deviatoric-tangential model (denoted V-D-T) is chosen due to (1) its flexibility and (2) the possibility to decouple each effect (Carol *et al* 2001). The "macroscopic" strain tensor is projected on a set of fixed planes called "microplanes". In this article, space is discretized into 42 angular sectors to describe isotropy providing a good compromise between accuracy and computation speed (Bazant and Oh 1985). The constitutive law proposed at the microplane level enables unilateral and sliding-friction effects to be taken into account. The "macroscopic" stress is determined using the principle of virtual work, through an integral of the "microplane" stress over the entire solid angle.

2 Formulation of the Constitutive Model

The model is based on a free energy potential defined at each microplane whose angular integral corresponds to the total free energy, given by:

$$\Psi^{mac} = \frac{3}{4\pi}\int_{\Omega} \Psi^{mic}(\mathbf{t}_{\varepsilon}, q)\, d\Omega \tag{1}$$

where $\mathbf{t}_{\varepsilon}$ is the vector resulting from the strain tensor projection into each microplane with normal $\mathbf{n}$ (see below Eq.3). q is any dissipative variable such as damage, sliding-friction, etc. The macroscopic stress is defined as the derivative of the free energy with respect to the macroscopic strain tensor, *i.e*:

$$\sigma = \frac{\partial[\rho_0 \Psi^{mac}]}{\partial \varepsilon} = \frac{3}{4\pi}\int_{\Omega} \frac{\partial[\rho_0 \Psi^{mic}]}{\partial \mathbf{t}_{\varepsilon}} \cdot \frac{\partial \mathbf{t}_{\varepsilon}}{\partial \varepsilon}\, d\Omega \tag{2}$$

where ρ_0 denotes the mass per unit volume. In this paper, strain tensor is decomposed into its volumetric, deviatoric and tangential parts using the following relations:

$$\mathbf{t}_{\varepsilon} = \varepsilon.\mathbf{n} \quad , \quad \varepsilon_V = \mathbf{V} : \varepsilon \quad , \quad \varepsilon_D = \mathbf{D} : \varepsilon \quad , \quad \varepsilon_T = \mathbf{T} : \varepsilon \tag{3}$$

$$\mathbf{V} = \frac{1}{3}\delta \quad , \quad \mathbf{D} = \mathbf{n} \otimes \mathbf{n} - \frac{1}{3}\delta \quad , \quad \mathbf{T} = \mathbf{n}.\mathbf{I} - \mathbf{n} \otimes \mathbf{n} \otimes \mathbf{n} \tag{4}$$

where δ is the second order identity tensor and $\mathbf{I}$ is the fourth order identity tensor. The second term of Eq.2 leads to:

$$\sigma = \frac{3}{4\pi}\int_{\Omega} \{\sigma_V.\mathbf{V} + \sigma_D.\mathbf{D} + \sigma_T.\mathbf{T}\}\, d\Omega \tag{5}$$

The state laws define each stress associated with a given projection as given by:

$$\sigma_V := \frac{\partial[\rho_0 \Psi^{mic}]}{\partial \varepsilon_V} \quad , \quad \sigma_D := \frac{\partial[\rho_0 \Psi^{mic}]}{\partial \varepsilon_D} \quad , \quad \sigma_T := \frac{\partial[\rho_0 \Psi^{mic}]}{\partial \varepsilon_T} \tag{6}$$

The free energy of the V-D-T model for anisotropic damage proposed by Carol *et al* (Carol *et al* 2001) is modified in this article. Two dissipative phenomena (damage and sliding-friction) are introduced in the model as in the discrete approach (Bargellini *et al.* 2008). Anisotropic damage is defined using (1) the volumetric, deviatoric and tangential damage variables d_V, d_D and d_T respectively as well as (2) their effectiveness using three functions $\alpha_V(X_V)$, $\alpha_D(X_D)$ and $\alpha_T(X_T)$. X_V, X_D and X_T are random variables to control the effectiveness depending on the state (open or close) of the microcracks. These functions cancel the damage effect for closed-microcracks. A tangential inelastic strain variable ε_T^p is introduced to model sliding with friction between the lips of closed-microcracks. Thus, the free energy across a microplane can be written in the following form:

$$\begin{aligned}\Psi^{mic} &= \frac{1}{2}k_V\left(1-\alpha_V\left(X_V\right)d_V\right)\varepsilon_V^2 + \frac{1}{2}\mu_D\left(1-\alpha_D\left(X_D\right)d_D\right)\varepsilon_D^2 \\ &+ \frac{1}{2}\mu_T\left[\left(1-d_T\right)\varepsilon_T\cdot\varepsilon_T + \left(1-\alpha_T\left(X_T\right)\right)d_T\left(\varepsilon_T-\varepsilon_T^p\right)\cdot\left(\varepsilon_T-\varepsilon_T^p\right)\right]\end{aligned} \tag{7}$$

where k_V, μ_D and μ_T are defined as the volumetric, deviatoric and tangential moduli, respectively. These moduli are connected to the usual elastic moduli k and μ by the following relation:

$$k_V = 3k \quad , \quad \frac{2}{5}\mu_D + \frac{3}{5}\mu_T = 2\mu \tag{8}$$

The main difficulty of this anisotropic damage model is to avoid dissipation at open/close transition and stiffness recovery. The following points were checked:

1. Two of the effectiveness variables are based on their related strain component, *i.e.* $\alpha_V(\varepsilon_V)$ and $\alpha_D(\varepsilon_D)$.
2. The continuity of the stress-strain response is verified at the open/close transition. A continuous function is chosen allowing progressive closure of microcracks without dissipation.
3. The state of microcrack is managed by the strain normal to the microcracks, ε_N, and not using the tangential strain vector, ε_T. To ensure continuity of the stress-strain response and no dissipation, a Heaviside's function (denoted *H*) is chosen for the tangential effectiveness function α_T and the sliding-friction variable ε_T^p is initialized to ε_T at the open/close transition.

3 Evolution Laws

The damage variables are driven by their thermodynamic force F^{d_i} (*i*=*V*, *D* or *T*) given by:

$$d_i(F^{d_i}) = \max\left(d_0, 1-\exp\left(-\left[\frac{F^{d_i}}{a_i}\right]\right)\right) \text{ with } 0 \le d_i \le 1 \tag{9}$$

where a_i is a parameter and d_0 is the initial damage. The forces are given by differentiating the free energy with respect to damage, *i.e*:

$$F^{d_V} = \frac{1}{2}k_V\varepsilon_V^2 \ , \ F^{d_D} = \frac{1}{2}\mu_D\varepsilon_D^2 \ , \ F^{d_T} = \frac{1}{2}\mu_T\left(\varepsilon_T^T\cdot\varepsilon_T + \alpha_T\left(\varepsilon_T - \varepsilon_T^P\right)^2\right) \tag{10}$$

For a progressive unilateral effect in volumetric and deviatoric parts, the following functions are used:

$$\alpha_i\left(\varepsilon_i\right) = \frac{\eta_1}{2}\left(1+\tanh\left(\eta_2\varepsilon_i + \eta_3\right)\right) \tag{11}$$

where η_1, η_2 and η_3 are the same three parameters for $\alpha_V\left(\varepsilon_V\right)$ and $\alpha_D\left(\varepsilon_D\right)$. The damage effectiveness on the tangential parts is driven by normal strain as follow:

$$\alpha_T\left(\varepsilon_N\right) = H\left(-\left(\varepsilon_V + \varepsilon_D\right)\right) \tag{12}$$

For the sake of simplicity, sliding-friction evolution law is restricted to a Drucker-Prager yield criterion. Thermodynamic force associated to the internal friction variable ε_T^p is given by:

$$\mathbf{F}_T^P = -\frac{\partial\Psi_T}{\partial\varepsilon_T^p} = \frac{1}{2}H(-\varepsilon_N)d_T\mu_T\left(\varepsilon_T - \varepsilon_T^p\right) \tag{13}$$

The existence of a sliding-friction criterion is postulated and defined as:

$$f\left(\mathbf{F}_T^P\right) = \mathbf{F}_T^P + r\left(\mathbf{F}_V + \mathbf{F}_D\right) \tag{14}$$

where $\mathbf{F}_V$ and $\mathbf{F}_D$ are the volumetric and deviatoric component stress respectively in microplane. Note that the sliding-friction criterion is built with an associated thermodynamic force $\mathbf{F}_T^P$ and the volumetric and deviatoric stress.

4 Numerical Simulation of Compression Tests

The most important phenomena for brittle material are the anisotropic damage effectiveness and confinement pressure dependence. In this section, numerical simulations of some experiments are presented to verify the performance of the V-D-T model. Compression experiments with different confining pressure (0, 5 and 10 MPa) were done on an explosive aggregate (Le *et al.* 2010). The damageable elastic behavior of these experimental data is obtained by removing stress relaxation and irreversible strain. In a high confined pressure tests the damage is supposed

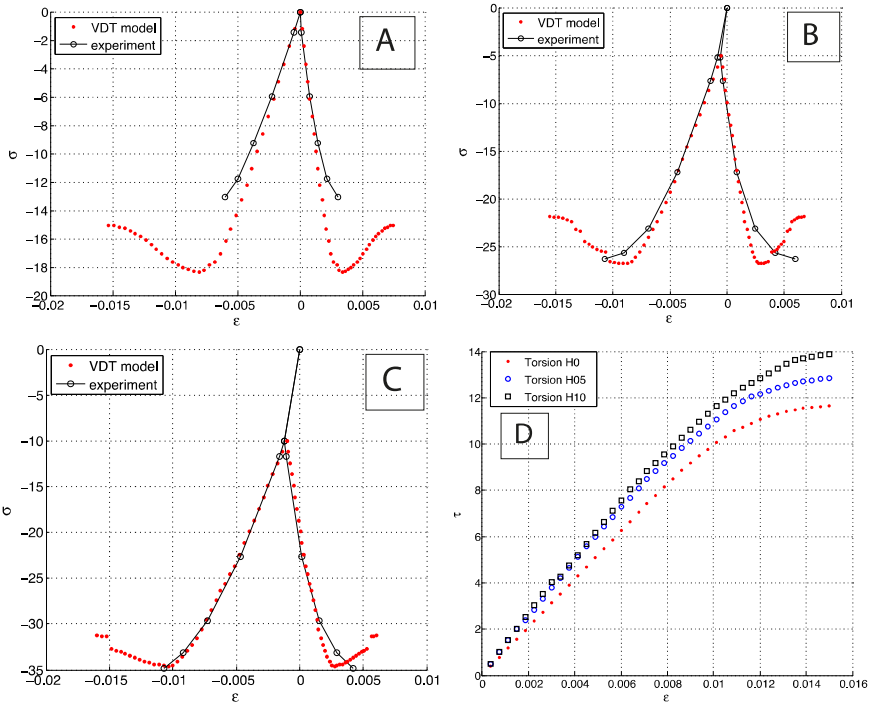

Fig. 1 Compression and torsion tests with 0, 5 and 10 MPa of confinement for aggregate material. A to C: experiments (black line) versus simulations (red line). D: simulations

being not effective. This results the bulk and shear moduli are equal to k=3335 MPa and μ=1538 MPa, respectively. The experimental results given on figure 1 lead to choose the others elastic parameters: Initial damage value ($a_V = a_D = a_T = 0.035$) and the following effectiveness and damage parameters $\eta_1 = 1$, $\eta_2 = 10^5$, $\eta_3 = 0$, $a_V = a_D = a_T = 0.035$MPa, and $r = 0.55$were used.

Figure 1A shows the stress-strain response of a compression test without confinement. Firstly, a linear response is observed, the elastic limit being about -6 MPa followed by a non-linearity due to material damage and frictional sliding dissipation. This non-linearity is less pronounced on the simulation. Afterwards, the computed axial stress reaches a value of -18 MPa, while the maximum experimental value of axial stress is -13 MPa. Lastly, the computed curve results from the competition between two antinomic mechanisms: the softening damage and the stiffening effectiveness. In the directions of normal positive projected strain, the damage reaches its maximum value.

Figure 1B gives the stress-strain response to a compressive test with a 5 MPa pressure confinement. The computed stress is consistent with experimental data and the peak in the stress-train curve is estimated quite well.

The stress-strain response obtained with 10 MPa pressure confinement is given on figure 1C. The proposed model predicts the maximum stress quite well. The damage law must evolve to reinforce the non-linearity of the stress-strain response for unconfined conditions.

Figure 1D shows the stress strain responses for torsion conditions with various confinements (0,5 and 10MPa). An initial dependence of the shear modulus on the confining pressure is observed. This difference is taken into account by damage effectiveness and friction sliding.

Figure 2 shows an asymmetric behavior between compression and tension. The initial slope in tension test is lower than in compression as could be expected for a previously damage material. The maximum stress is equal to 13 MPa (respectively 18 MPa) in tension (resp. in compression) when the material described in (Gratton et al. 2009) exhibits a 3 to 5 MPa maximum stress in tension. Damage due to tensile conditions is thus underestimated. The evolution of the damage must be amplified for positive normal strains.

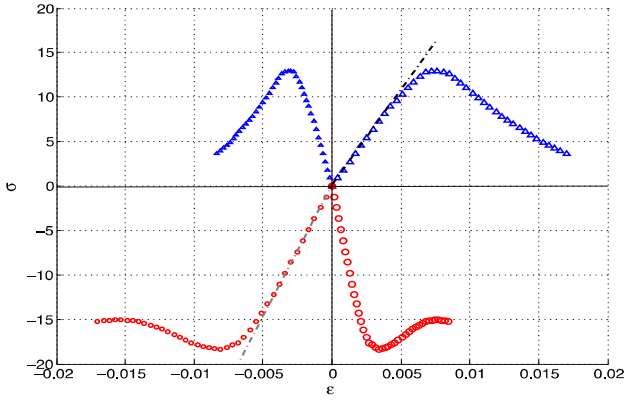

Fig. 2 Computing of simple compression and tension test for aggregate material

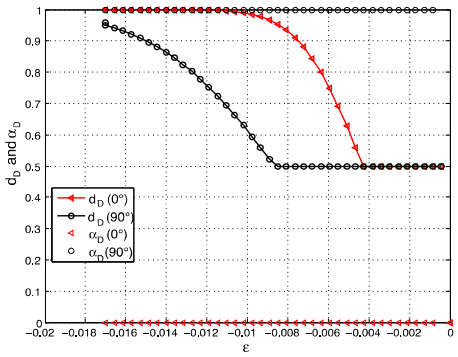

Fig. 3 Numerical evolution of the deviatoric damage and unilateral effectiveness for two microplanes with respect to longitudinal strain during an unconfined compression test

Figure 3 shows the deviatoric damage and its effectiveness evolutions with respect to the longitudinal strain during an unconfined compression test to show the interaction between damage and effectiveness. For the plane which normal is in the longitudinal direction (0°), the damage increases but the effectiveness cancels its influence. In the transverse direction (90°), the damage is completely active due to a high value for α.

5 Conclusion

A V-D-T model has been improved by the introduction of the damage effectiveness and frictional sliding mechanisms between closed microcracks lips. This constitutive law respects the thermodynamics requirements. Based on phenomenological evolution laws for the damage variables and related effectiveness, the simulations of unconfined compressive experiments show a reasonably good accordance. A different maximum stress is obtained for compressive or tensile loading conditions and the shear response shows a dependence on the confinement. Compared to classical constitutive models, this model provides an easier way to describe the coupling between sliding-friction and induced anisotropic damage. The way effectiveness functions in the model cancel the damage effects in the other directions where the strain is mainly negative needs to be further developed. Further studies will be devoted to the damage evolution laws to improve the response whatever the loading path. One proposal is to determine two sets of parameters, one in tension to accelerate the damage evolution and another one in compression to reduce this evolution. The second proposal is to combine the normal and tangential strain values in the thermodynamic forces to influence the damages evolutions. Finally, the model will implement in a finite element code for engineering applications.

References

(Ladeveze et al. 1994) Ladeveze, P., Gasser, A., Allix, O.: Damage Mechanisms Modeling for Ceramic Composites. J. Eng. Mater. Technol. 116, 331–336 (1994), doi:10.1115/1.2904296

(Boursin et al. 1996) Boursin, A., Chaboche, J.L., Roudolf, F.: Mécanique de l'endommagement avec conditions unilatérales et stockage d'énergie élastique. C. R. Acad. Sci. Paris Série II, 369–376 (1996)

(Chaboche and Maire 1997) Chaboche, J.L., Maire, J.F.: A new formulation of continuum damage mechanics (CDM) for composite materials. Aerospace Science and Technology 1(4), 247–257 (1997), doi:10.1016/S1270-9638(97)90035-3

(Halm and Dragon 2002) Halm, D., Dragon, A., Charles, Y.: A modular damage model for quasi-brittle solids - interaction between initial and induced anisotropy. Archive of Applied Mechanics 72, 498–510 (2002), doi:10.1007/s00419-002-0226-9

(Baste et al. 1989) Baste, S., Guerjouma, R.E., Alain, G.: Mesure de l'endom-magement anisotrope d'un composite céramique-céramique par une méthode ultrasonore. Rev. Phys. Appl. (Paris) 24, 721–731 (1989), doi:10.1051/rphysap:01989002407072100

(Thionnet and Renard 1999) Thionnet, A., Renard, J.: Modelling unilateral damage effect in strongly anisotropic materials by the introduction of the loading mode in damage mechanics. International Journal of Solids and Structures 36, 4269–4287 (1999), doi:10.1016/S0020-7683(98)00192-9

(Thionnet 2010) Thionnet, A.: From Fracture to Damage Mechanics: A behavior law for microcracked composites using the concept of Crack Opening Mode. Composite Struct. 92, 780–794 (2010), doi:10.1016/j.compstruct.2009.08.047

(Taylor 1938) Taylor, G.I.: Plastic strain in metals. Journal Institute of Metals 62, 307–324 (1938)

(Batdorf and Budiansky 1949) Batdorf, S.B., Budiansky, B.: A mathematical theory of plasticity based on the concept of slip, volume Technical Note No. 1871. National Advisory Committee for Aeronautics (1949)

(Bazant and Oh 1983) Bazant, Z.P., Oh, B.H.: Deformation of Cracked Net-Reinforced Concrete Walls. Journal of Structural Engineering 109, 93–108 (1983)

(Bazant and Gambarova 1984) Bazant, Z.P., Gambarova, P.G.: Crack Shear in Concrete: Crack Band Microplane Model. Journal of Structural Engineering 110, 2015–2035 (1984)

(Bazant and Oh 1985) Bazant, Z.P., Oh, B.H.: Microplane Model for Progres-sive Fracture of Concrete and Rock. Journal of Engineering Mechanics 111, 559–582 (1985)

(Beghini et al. 2007) Beghini, A., Bazant, Z.P., Zhou, Y., Gouirand, O., Caner, F.C.: Microplane model M5 for multiaxial behavior and fracture of fiber-reinforced concrete. Journal of Engineering Mechanics-ASCE 133, 66–75 (2007)

(Carol et al. 2001) Carol, I., Jiràsek, M., Bazant, Z.: A thermodynamically consistent approach to microplane theory. Part I. Free energy and consistent microplane stresses. International Journal of Solids and Structures 38, 2921–2931 (2001), doi:10.1016/S0020-7683(00)00212-2

(Carol and Willam 1996) Carol, I., Willam, K.: Spurious energy dissipation/ generation in stiffness recovery models for elastic degradation and damage. International Journal of Solids and Structures 33(20-22), 2939–2957 (1996), doi:10.1016/0020-7683(95)00254-5

(Kuhl et al. 2001) Kuhl, E., Steinmann, P., Carol, I.: A thermodynamically consistent approach to microplane theory. part II. dissipation and inelastic constitutive modeling. International Journal of Solids and Structures 38(17), 2933–2952 (2001), doi:10.1016/S0020-7683(00)00213-4

(Bargellini et al. 2008) Bargellini, R., Halm, D., Dragon, A.: Modelling of quasi-brittle behaviour: a discrete approach coupling anisotropic damage growth and frictional sliding. European Journal of Mechanics - A/Solids 27, 564–581 (2008), doi:10.1016/j.euromechsol.2007.11.003

(Gratton et al. 2009) Gratton, M., Gontier, C., Allah, S.R.F., Bouchou, A., Picart, D.: Mechanical characterisation of a viscoplastic material sensitive to hydro-static pressure. European Journal of Mechanics - A/Solids 28, 935–947 (2009), doi:10.1016/j.euromechsol.2009.03.002

(Le et al. 2010) Le, V., Gratton, M., Caliez, M., Frachon, A., Picart, D.: Experimental mechanical characterization of plastic-bonded explosives. Journal of Materials Science 45, 5802–5813 (2010), doi:10.1007/s10853-010-4655-5

Creep Effect on the J-Integral around a Crack Tip in a Cracked Nonlinear Viscoelastic Plate of PVC

Fethi Gmir[1,3], Abdessattar Aloui[1,2], and Mohamed Haddar[1]

[1] Unit of Mechanic, Modelisation and Production (U2MP) ENIS, Tunisia
[2] Higher Institute of Applied Sciences and Technology Gabes, Tunisia
[3] Higher Institute of Industrial System Gabes, Tunisia
{Fethi.gmir,Abdessattar.Aloui}@issatgb.rnu.tn
Mohamad.haddar@enis.rnu.tn

Abstract. The J-integral method, developed by Rice in 1968, assesses the energy release rate in the case of a linear or nonlinear elastic material. This energy was recorded for the formulation of cracks criteria failure and instability. The present work focuses on the study of the evolution of this integral in the case of a nonlinear viscoelastic material when it undergoes creep under constant stress. An analytical approach and a numerical simulation, based on the finite element method, have been developed for determining the rate of energy release. The analytical approach is based on the stress field and intensity factors in the vicinity of the crack tip located on a PVC plate, taking into account the nonlinear viscoelastic behavior of this material. The comparison between analytical and numerical results shows a good agreement.

Keywords: Viscoelastic materials, creep, crack, J- integral.

1 Introduction

The J-integral of Rice [1] is usually used in quasi-static fracture to characterize the energy release rate associated with crack growth. The integral contour subject has received considerable attention because of its many interesting features in the mechanics applications fracture. These integrals have the distinction of being equivalent to the rate of energy release, and to be independent of the chosen integration contour.

In this context, several authors have used J-integral to evaluate the restoration energy rate in mechanics crack. Rice and Rosengren [2] showed that J-integral uniquely characterizes crack tip stresses and strains in non-linear materials. Kobayashi et al. [3] used finite element analysis to determine numerically Rice's J-integral values in centrally notched plates of steel. Courtin et al. [4] applied the crack opening displacement extrapolation method and the J-integral approach in 2D and 3D ABAQUS finite element models. Nevertheless, since the knowledge of the field near the crack tip is not required in the energetic method, the J-integral calculations seem to be a good technique to deal with the fatigue growth of

M. Haddar et al. (Eds.): *Design and Modeling of Mechanical Systems*, LNME, pp. 439–446.
DOI: 10.1007/978-3-642-37143-1_52

general cracks. Rajaram et al. [5] presented an approach to obtain fracture mechanics singularity strength (J, K1, etc.) along a 3D crack-front using tetrahedral elements. Hocine et al. [6] determined the energy parameter J for rubber-like materials. Owen and Fawkes [7] developed many numerical methods using finite element analysis to obtain stress intensity tractor (SIF) values.

Dubois et al. [8] conducted experimental and numerical validation for the viscoelastic creep under the environmental effects. In fracture mechanics, Chen and Shield [9] developed the M-integral between the effects of mixed mode in the case of stationary cracks. In addition, Moutou Pitti et al. [10] have generalized this integral to be independent on orthotropic structure.

Schapery [11] has developed methods for the analysis of deformation and fracture for quasi-static visco-class backgrounds elastics nonlinear and illustrated typical applications of these methods. The J-integral and the restoration energy rate, are applied in the case of non-linear elastic environments.

In this context, the J-integral is extended to the case of nonlinear viscoelastic materials, and allows to integrate the stress and displacement field at the crack tip.

2. Theoretical Investigation

The flow of energy passing through a closed contour surrounding the crack tip was calculated by J. R. Rice [1] as an integral over this contour, denoted by J. This integral is independent of the chosen contour. To simplify the calculation we can choose a circular contour of radius r (Fig. 1). The J-integral can be written as:

$$J = \int_{\Gamma} \left(W dy(\vec{x},\vec{y}) - T_i \frac{\partial u_i}{\partial x} ds \right) \tag{1}$$

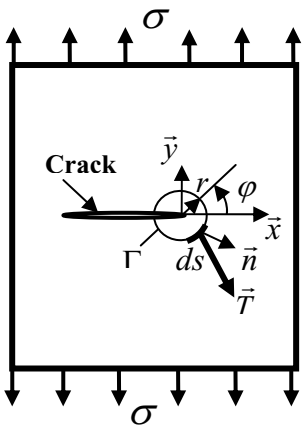

Fig. 1 Crack tip surrounded by a circular contour

$\vec{T}$ is the stress vector applied to the contour element

$\vec{n}$ is the unit vector normal to the contour element ds.

T_i are the components of the stress vector on the contour Γ, verifying the following boundary conditions:

$$T_i = \sigma_{ij} n_j \tag{2}$$

with

$$n_x = \frac{dy}{ds} \qquad \text{and} \qquad n_y = \frac{dx}{ds}$$

u_i is the displacement of the contour Γ following the direction i.

W represents the specific strain energy.

We have:

$$dx = -r \sin\varphi \, d\varphi \qquad dy = r \cos\varphi \, d\varphi \tag{3}$$

During the viscoelastic material creep under constant stress ($\sigma_{ij} = cte$), specific energy can be decomposed into an initial part W_0 independent of time and a second part ΔW_t representing the effect of creep on that energy. We have:

$$W = \int_0^{\varepsilon_{ij0}} \sigma_{ij} d\varepsilon_{ij} + \int_0^t \sigma_{ij} \dot{\varepsilon}_{ij} dt \tag{4}$$

By decomposing the movement u_{it} of contour Γ an initial displacement contour u_{i0} and displacement Δu_{it} of creep of the material, with: $u_{it} = u_{i0} + \Delta u_{it}$,
we obtain :

$$J = \int_\Gamma (W_0 dy - T_i \frac{\partial u_{i0}}{\partial x} ds) + \int_\Gamma (\Delta W_t dy - T_i \frac{\partial \Delta u_{it}}{\partial x} ds) \tag{5}$$

with :

$$W_0 = \int_0^{\varepsilon_{ij0}} \sigma_{ij} d\varepsilon_{ij} \tag{6}$$

$$\Delta W_t = \int_0^t \sigma_{ij} \dot{\varepsilon}_{ij} dt \tag{7}$$

The J-integral is decomposed in two parts, first part J_0, which is independent on time and describes the state of initial loading, with the moment of the beginning of creep material and a second part J_t, which represents the effect of creep on this integral.

$$J_0 = \int_\Gamma (W_0 dy - T_i \frac{\partial u_{i0}}{\partial x} ds) \tag{8}$$

$$J_t = \int_{\Gamma} (\Delta W_t dy - T_i \frac{\partial \Delta u_{it}}{\partial x} ds) \tag{9}$$

The flow of energy per unit time is defined in a region surrounded by the contour Γ by:

$$\dot{J}_t = \int_{\Gamma} (\Delta \dot{W}_t dy - T_i \frac{\partial \Delta \dot{u}_{it}}{\partial x} ds) \tag{10}$$

With the boundary conditions (2) and let us note that $\Delta \dot{W}_t = \sigma_{ij} \dot{\varepsilon}_{ij}$ in the case of creep under constant stress σ_{ij}, we obtain then:

$$\dot{J}_t = \int_{\Gamma} \sigma_{ij} (\dot{\varepsilon}_{ij} dy - \frac{\partial \Delta \dot{u}_{it}}{\partial x} dx_i) \tag{11}$$

In the vicinity of the crack tip the fields of the stresses, displacements and strains can be written as follows:

- The stresses field:

$$\sigma_x = \frac{K_I}{\sqrt{2\pi r}} \left[\cos \frac{\varphi}{2} (1 - \sin \frac{\varphi}{2} \sin \frac{3\varphi}{2}) \right] \tag{12.a}$$

$$\sigma_y = \frac{K_I}{\sqrt{2\pi r}} \left[\cos \frac{\varphi}{2} (1 + \sin \frac{\varphi}{2} \sin \frac{3\varphi}{2}) \right] \tag{12.b}$$

$$\tau_{xy} = \frac{K_I}{\sqrt{2\pi r}} \cos \frac{\varphi}{2} \sin \frac{\varphi}{2} \cos \frac{3\varphi}{2} \tag{12.c}$$

- The displacements field:

$$u_{xt} = K_I (1+\nu) D(\sigma, t) \sqrt{\frac{r}{2\pi}} \cos \frac{\varphi}{2} (\kappa - \cos \varphi) \tag{13.a}$$

$$u_{yt} = K_I (1+\nu) D(\sigma, t) \sqrt{\frac{r}{2\pi}} \sin \frac{\varphi}{2} (\kappa - \cos \varphi) \tag{13.b}$$

- The strain field:

$$\varepsilon_x = \frac{K_I (1+\nu) D(\sigma, t)}{\sqrt{2\pi r}} \cos \frac{\varphi}{2} \left[\frac{1}{2} (\kappa - 1) - \sin \frac{\varphi}{2} \sin \frac{3\varphi}{2} \right] \tag{14.a}$$

$$\varepsilon_y = \frac{K_I (1+\nu) D(\sigma, t)}{\sqrt{2\pi r}} \cos \frac{\varphi}{2} \left[\frac{1}{2} (\kappa - 1) + \sin \frac{\varphi}{2} \sin \frac{3\varphi}{2} \right] \tag{14.b}$$

$$\gamma_{xy} = \frac{K_I (1+\nu) D(\sigma, t)}{\sqrt{2\pi r}} \cos \frac{\varphi}{2} \sin \frac{\varphi}{2} \cos \frac{3\varphi}{2} \tag{14.c}$$

Where:

$\kappa = \frac{3-\nu}{1+\nu}$ is the Kolossov factor for a plane stress loading and ν is the Poisson's ratio. $K_I = \sigma\sqrt{\pi a}\,Y$ account for the intensity stresses factor, Y being a correction factor , which depends on the crack geometry. In this study we supposed that the Poisson's ratio remains constant since it is about an isothermal transformation, in more material is considered isotropic. The flexibility module of the material $D(\sigma,t)$, which depends on the applied stress and time.

Using the expression of the flexibility material module developed for the case of creep under constant stress:

$$D(\sigma,t) = \left[g_0 D_0 + g(\sigma)\sum_{i=1}^{n} D_i\left(1-e^{\frac{-t}{\tau_i}}\right) \right] \tag{15}$$

Where g_0 and $g(\sigma)$ are nonlinearity factors, given starting from the simple creep tests under constant stresses. D_0 and D_i are material flexibility coefficients.

For a plane state of stresses, we can write:

$$\sigma_{ij}\dot{\varepsilon}_{ij} = \sigma_x\dot{\varepsilon}_x + \sigma_y\dot{\varepsilon}_y + \tau_{xy}\dot{\gamma}_{xy} \tag{16}$$

$$\sigma_{ij}\frac{\partial \Delta\dot{u}_{it}}{\partial x}dx_i = \left(\sigma_x + \tau_{xy}\right)\frac{\partial \Delta\dot{u}_{xt}}{\partial x}dx + \left(\sigma_y + \tau_{xy}\right)\frac{\partial \Delta\dot{u}_{yt}}{\partial x}dy \tag{17}$$

we can also show that the operator $\frac{\partial}{\partial x}$ can be written according to the polar coordinates (r,φ) following form:

$$\frac{\partial}{\partial x} = \cos\varphi\frac{\partial}{\partial r} - \frac{\sin\varphi}{r}\frac{\partial}{\partial \varphi} \tag{18}$$

We determine thus $\dot{J}_t$ with the relation (11), then we calculates J with the following equation:

$$J = J_0 + \int_0^t \dot{J}dt \tag{19}$$

We get :

$$J = \frac{\kappa+1}{4}K_I^2(1+\nu)g_0D_0 + \frac{3\kappa+1}{8}K_I^2(1+\nu)g(\sigma)\sum_{i=1}^{n} D_i\left(1-e^{\frac{-t}{\tau_i}}\right) \tag{20}$$

For the PVC case, the nonlinearity factors g_0 and $g(\sigma)$ are illustrated in fig. 2. These factors are computed from experimental creep data obtained by creep tests on PVC specimens [12].

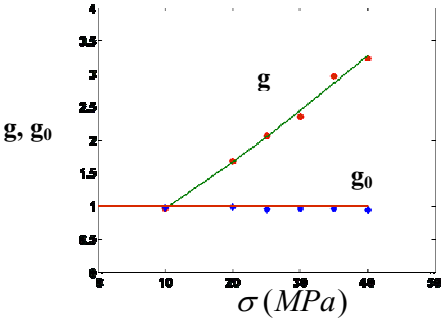

Fig. 2 Nonlinear Factors according to the stress

3 Analytical and Numerical Results

As an example, we consider a PVC cracked plate with the dimensions $l \times b = 150\,mm \times 40\,mm$. The length of the central crack is $2a = 10\,mm$.

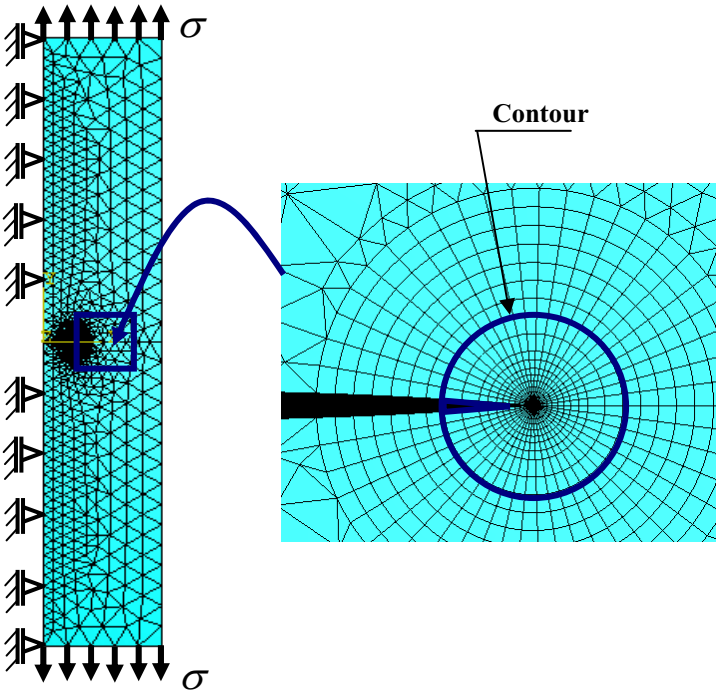

Fig. 3 Discretization around the crack tip

For this case, we have [13]:

$$K_I = \sigma\sqrt{\pi a}\,\frac{1-0.5\frac{a}{b}+0.37\left(\frac{a}{b}\right)^2-0.044\left(\frac{a}{b}\right)^3}{\sqrt{1-\frac{a}{b}}} \tag{21}$$

We use the finite element code ABAQUS, to simulate the PVC plate behavior numerically. To exploit the symmetry of the problem (figure 3), of the half-plate dimensions are 150 mm × 20 mm × 4 mm, and that of the fissure 5mm×0.4mm.

The half-plate is meshed with 1976 of triangular thin shell elements of type STRI 65 to 6 nodes. In order to improve calculation convergence and to lead to more precise results, a fine and radiant mesh of type S8R5 to 8 nodes is applied around the crack tip.

ABAQUS will compute the terms in the Prony series automatically from a given set of normalized shear creep compliance data, which can be derived by adding the instantaneous compliance to the curve data and dividing by the instantaneous compliance. The Poisson's ratio of the plate is assumed to remain unchanged over time.

The analytical and numerical results are illustrated in figure 4.

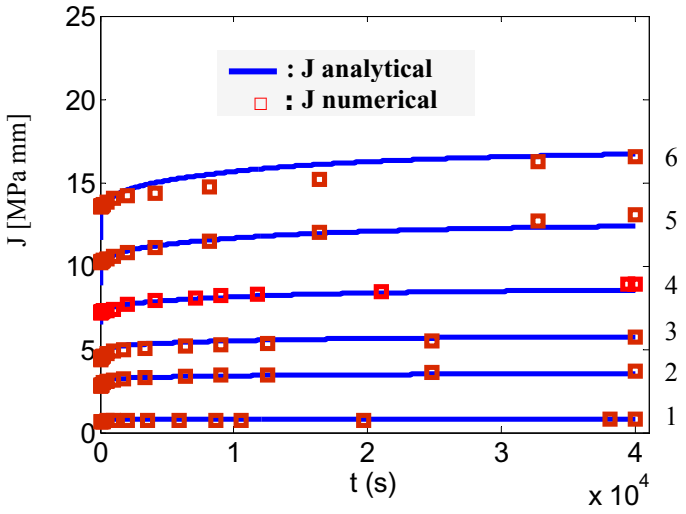

Fig. 4 Creep Effect on J-integral

1 : σ_1 = 10 MPa , 2 : σ_2 = 20 MPa , 3 : σ_3 = 25 MPa ,

4 : σ_4 = 30 MPa , 5 : σ_5 = 35 MPa, 6: σ_6 = 40 MPa

4 Conclusion

In this work, we have determine the energy release rate or J contour integral in a cracked plate of viscoelastic material having a nonlinear behavior, undergoing creep under constant stress. A theoretical study has been developed to describe the effect of creep of the material on this integral.

The analytical solution of J-integral calculated near the crack tip was compared with that determined numerically using the computer code ABAQUS. The numerical solution based on estimates of contour is fairly accurate and robust, even with a fairly coarse mesh, because the integral is taken on a field of elements surrounding the crack front.

Excellent agreement is found between the analytical and numerical results.

References

[1] Rice, J.R.: A path independent integral and the approximate analysis of strain concentration by notches and cracks. J. of Applied Mechanics 35, 379–385 (1968)

[2] Rice, J.R., Rosengren, G.F.: Plane strain deformation near a crack tip in a power law hardening material. J. Mech. Phys. Solids 16, 1–12 (1968)

[3] Kobayashi, A.S., Chiu, S.T., Beeuwkes, R.: A numerical and experimental investigation on the use of J-integral. J. Appl. Mech. 15, 293–305 (1973)

[4] Courtina, S., Gardina, C., Bezinea, G.: Advantages of the J-integral approach for calculating stress intensity factors when using the commercial finite element software ABAQUS. Eng. F. Mech. 72, 2174–2185 (2005)

[5] Rajaram, H., Socrate, S., Parks, D.M.: Application of domain integral methods using tetrahedral elements to the determination of stress intensity factors. Eng. Fract. Mech. 66(5), 455–482 (2000)

[6] Ait Hocine, N., Nait Abdelaziz, M., Ghfiri, H., Mesmacque, G.: Evaluation of the energy parameter J on rubber-like materials: comparison between experimental and numerical results. Eng. Fract. Mech. 55(6), 919–933 (1996)

[7] Owen, D.R.J., Fawkes, A.: J Engineering fracture mechanics: numerical methods and applications, Pineridge, Swansea, UK (1983)

[8] Dubois, F., Randriambololona, H., Petit, C.: Creep in wood under variable climate condition: numerical modelling and experimental validation. Mech. Time-Depend Mater. 9, 173–202 (2005)

[9] Chen, F.M.K., Shield, R.T.: Conservation laws in elasticity of J -integral type. J. Appl. Mech. Phys. 28, 1–22 (1977)

[10] Moutou Pitti, R., Dubois, F.: Mixed mode fracture separation in viscoelastic orthotropic media: numerical and analytical approach by the Mθv. Int. J. Fract. 145, 181–193 (2007)

[11] Schapery, R.A.: Correspondence principles and a generalized J integral for large deformation and fracture analysis of viscoelastic media, Mechanics & Materials Center, Civil Engineering Department, Texas A&M University, College Station, TX 77843,USA (1984)

[12] Gmir, F., Aloui, A., Haddar, M.: A nonlinear creep of PVC under dynamic loading. In: Deuxième Congrès Tunisien de Mécanique COTUM: Sousse – Tunisie, Mars 19-21 (2012)

[13] Sähn, S., Göldner, H.: Bruch- und Beurteilungskriterien in der Festigkeitsle-hre. VEB Fachbuchverlag Leipzig (1989)

Worn Surface Characteristics of a Friction Material during Braking Simulation Test

Amira Sellami[1], Mohamed Kchaou[1,2], Riadh Elleuch[1], Harpreet Singh[3], and Ming Zeng[4]

[1] Univ Sfax ENIS – LASEM - BP 3038 Sfax –Tunisia
riadh.elleuch@gnet.tn
[2] Univ Sousse – ISSATS – BP 4003 Sousse - Tunisia
[3] School of Mechanical, Materials and Energy Engineering, Indian Institute of Technology Ropar, Roopnagar-140001 (Punjab) - India
[4] Engineering Research Center of Nano-Geomaterials of Ministry of Education, China University of Geosciences, Wuhan 430074, P.R. China

Abstract. In this study, the chemical and microstructural changes occurring during braking simulation tests at the surface of a commercial brake lining material were investigated by scanning electron microscopy equipped with an energy-dispersive X-ray spectrometer (X-EDS). It could be shown that patches of a third body material develop, comprising a compositional mix of all constituents of the pad and iron oxides from the disk. The majorities of particles rich in carbon which appeared dark grey remained totally or partially uncovered and did not form preferential supports of secondary plate development. It was observed that filler mineral powders, such as barite ($BaSO_4$) and calcium carbonate, which are friable particles, easily wear and generate an important part of third body rich in C, Ca, Ba and Fe elements. Rockwool fibres and shots contributed to the formation of the bearing surface by forming primary support of development of flat plates. The major wear mechanism was delamination of filler particles from the organic binder, supported by local degradation of the phenolic resin during asperity heating.

Keywords: brake lining material, friction test, delamination of filler, flat plates.

1 Introduction

Automobile brake system consists of metallic brake disc and brake pads in order to maintain a steady friction coefficient. Brake pad helps in transferring kinetic energy into heat during the application of brake to stop or slow-down a moving automobile by friction. This material is usually fabricated from a phenolic resin binder with addition of more than 10 ingredients (Kumar et al 2010), (Fei et al 2010), (Sallit et al 2004), (Ingo et al 1998) The lining materials must present a good combination of mechanical properties such as a high hardness, compressive strength, good resistance to severe temperatures, should maintain a relatively high, stable and reliable friction coefficient at wide range of braking conditions, temperature, humidity, presence of dirt and water spraying from the road and should have excellent thermal properties, which interact to accurate the pad performance under braking.

M. Haddar et al. (Eds.): *Design and Modeling of Mechanical Systems*, LNME, pp. 447–452.
DOI: 10.1007/978-3-642-37143-1_53

Generally it is assumed that third body layers develop during interactions of a tribology couple, which differ in composition from both the mating parts of the couple. These layers may develop as a result of tribo-oxidation of metallic surfaces in contact and the compacting of the debris generated during attrition (Wirth et al.1994). When a friction material pad slides against a gray cast iron rotor, the rotor and pad friction surfaces undergo microstructural and chemical changes (Jacko 1978). Many researchers (Osterle and Bettge 2004) and (Jang 2001) have focused on the structure and the role of this third body and the mechanisms occurring in the contact. Wirth et al (1994) reported the formation of films containing $BaSO_4$, which is a frequently used as filler for brake pads. Eriksson (2000) confirmed that iron oxide as a major constituent of surface films of brake pads and discs.

The motivation for the present work is to investigate the tribologically induced changes in the surface of a commercial brake lining material under friction testing. The results will be correlated with micro- and macroscopical properties.

2 Experimental Procedure

The base composition of the friction material used in this study is given in Table 1. This material contains the most important ingredients which are commonly used in a conventional brake material. Cylindrical pads with a diameter of 14 mm and a height of 16 mm were pressed against a rotating steel disk. Normal and tangential forces as well as the mean surface temperature of the disk were monitored during the test. The continuous braking simulation was performed at a constant speed of 9 m/s with a normal load of 277 N for 1h 20 min.

Several microscopic and spectroscopic techniques were applied for characterizing the surface, the superficial zones and the wear debris of the pads after braking test. A scanning electron microscope (SEM) equipped with an energy-dispersive X-ray spectrometer (X-EDS) was used to reveal topography and to identify the different constituents of the pad material. Fig. 1 shows a SEM observation using scanning electron microscopy of the friction material. It reveals the presence of ingredients of various types, natures and in various combinations and amounts that sizes range from 50 µm to more than 0.5 mm. EDS results compiled in Table 2 show that the large bright areas are metallic fillers (brass), black rich in carbon, whereas the agglomerates of mineral particles are grey in color.

Table 1 Composition of the brake pad in wt %

Ingredients	Composition
Binder	14.2
Organic fillers	1.8
Mineral Fillers	20.2
Organic particles	44.6
Mineral particles	17.6
Metallic fillers	1.6

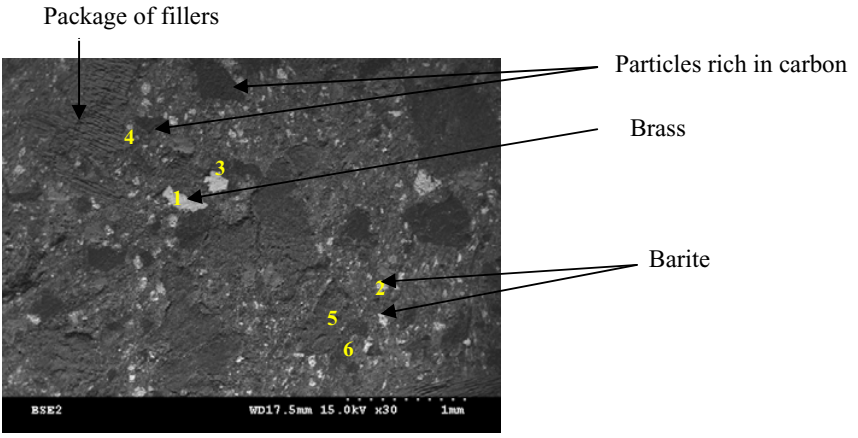

Fig. 1 SEM observation of the pad before the friction test with localization of the six zones subjected to the EDS analysis

Table 2 Compositions in weight % of the six zones from Fig. 1

	C	O	Al	Si	S	Cl	K	Ca	Cu	Zn	Br	Ba
pt1	20	02	-	-	01	-	-	-	41	32	-	03
pt2	13	17	01	02	11	-	-	0.86	-	-	-	53
pt3	08	01	-	-	-	-	-	-	51	39	-	-
pt4	65	23	01	01	01	01	-	0.95	-	-	-	05
pt5	63	12	-	01	05	01	01	0.74	-	04	-	10
pt6	64	12	-	01	01	01	01	2.41	-	-	07	09

3 Results

By the end of the friction test, the temperature of the organic matrix composite got increased by more than 400°C, which led to the degradation of the phenolic resin, as has also been reported by Bark and Moran (1979). That is why it is important to study the correlation between chemical and tribological mechanisms occurring in the contact by taking into account of the third body (Fig. 2a). This third body has been found to be mainly consisting of oxides of iron (Fig. 3a), which perhaps are formed by the elements getting involved from the pad under shape powder layers and flat plates formed by compacting and shearing of the powder in the contact. Fig.2 shows the presence of flat plates (plateau), imprints of loose particles and powder layers. Moreover, the EDS analysis showed the presence of elements of mineral constituents such as Si, Al, Mg and Ca (Fig. 2a). The third-body formed on the worn surface of this mineral particle is characterized by the presence of element from the disc (Fe). As shown in (Fig 2a and b), the size of the compacted flat plates of third-body ranges from 50 to 150 µm. The loose particles (Fig. 2b and d) are therefore acting as support to the flat plates of the third body, which are

formed by accumulation and compaction of third-body powder layers (Fig. 2a, c and h). This constitutes one of the possible mechanisms involved in the formation and expansion of the flat plates, as has also been suggested by Desplanques et al (2009). The growth of the flat plates leads to the covering of the mineral particles as could be observed in Fig. 2f. The EDS data (Fig. 3b and d) confirms this result, as a matter of fact, the presence of Si, Mg, Al, Ca, Ba and Fe coming from the disc show that the third body flat plates are formed on the mineral particles.

The EDS of zone 3 (Fig. 3c) shows the presence of third body powder layer on a mineral filler due to the presence of Mg, Al and Ca, and a little amount of Fe (Fig. 2f). There is a significant presence of filler in zone 3. Subsequently, the coalescence of neighboring plates leads to the increase in size of flat plates, which can cover mineral particles.

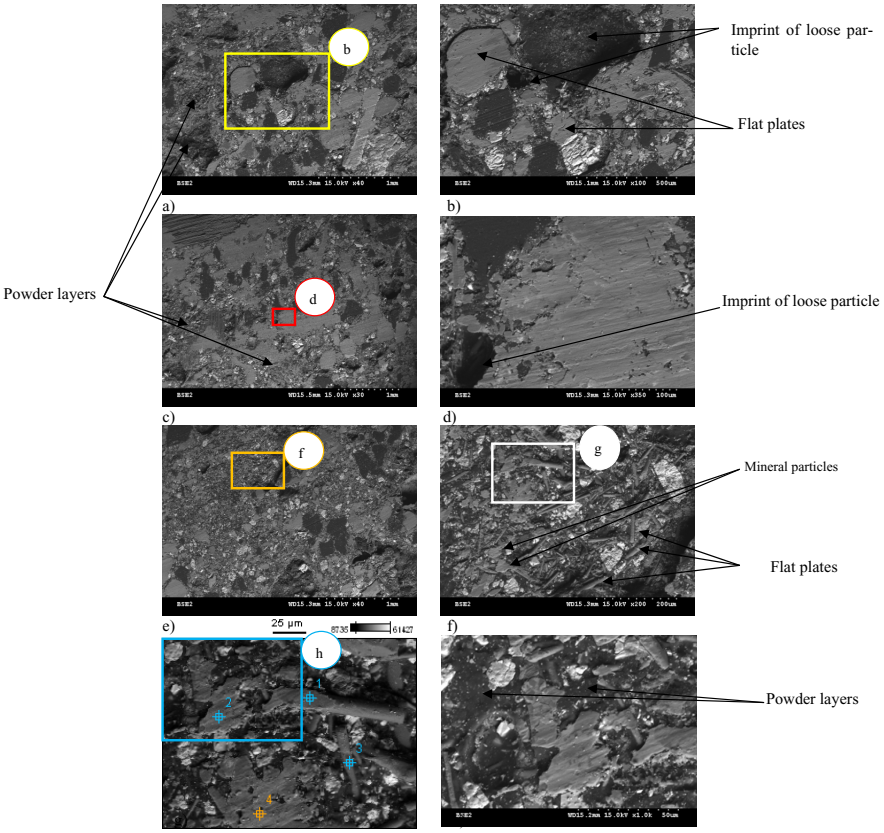

Fig. 2 SEM observations of the pad after the friction test (a-c-e) scale 1mm(b-d-f-h) scale 500-100-200 and 50 µm(g) scale 25 µm with localization of the four zones subjected to the X-EDS analysis

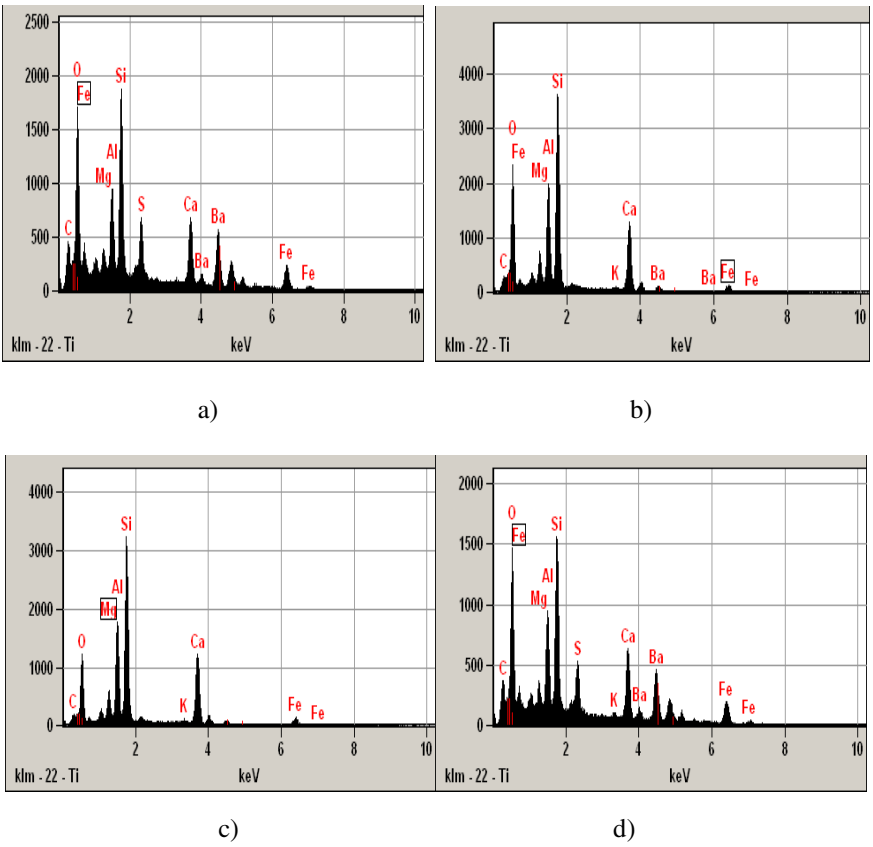

Fig. 3 X-EDS analysis of zones located on Fig.1: a) zone1: Thin film of third-body on a mineral particle; b) zone 2 third-body flat plates formed on a mineral particle; c)zone 3 third body powder layer; d)zone 4 third-body flat plates formed on a mineral particle

Oriented parallel to the sliding plane or slightly inclined in the matrix, fibres emerge from the rubbed surface, appearing mostly uncovered with compacted third body (Fig.2f). They do not form primary plates or do not serve as support for the formation of plates of third body. They seem to act as obstacles to extension of the bearing plate regardless of their orientation relative to the direction of sliding.

4 Conclusion

During the braking process, the friction in the contact disc-pad gives rise to tribological issues characterized by flat plates (plateau) of the third body, which assure the accommodation of speed. This investigation can facilitate further understanding of the process of formation of flat plates of third body, their process of growth accumulated upstream to fibers, which are compacted in the contact to form new flat plates. Moreover, the powder layers responsible for the formation of plates are

generated by detachment of material and delamination of fillers from the pad. Finally, examination of the microstructure can be of interest to detect a relationship between the microstructure and the tribological evolution. However, among the difficulties to improve performance related to the understanding of relationships between microstructure, properties and braking behavior, is the complexity of the industrial formulation such as that studied in this paper.

Acknowledgements. The authors gratefully acknowledge the Tunisian Ministry of Higher Education and Scientific Research for their continuous support of research at the Laboratory of Electro-Mechanical Systems of Sfax. Special thanks to STUGA Society (Tunisia) for providing us the brake lining samples.

References

Kumar, M., Bijwe, J.: Studies on reduced scale tribometer to investigate the effects of metal additives on friction coefficient – Temperature sensitivity in brake materials. Wear 269(11-12, 28), 838–846 (2010)

Fei, J., Li, H.J., Fu, Y.W., Qi, L.H., Zhang, Y.L.: Effect of phenolic resin content on performance of carbon fiber reinforced paper-based friction material. Wear 269, 534–540 (2010)

Ingo, G.M., D'Uffizi, M., Falso, G., Bultrini, G., Padeletti, G.: Thermal and microchemical investigation of automotive brake pad wear residues. Thermochimica Acta 418(1-2, 15), 61–68 (2004)

Sallit, I., Richard, C., Adam, R., Robbe-Valloire, F.: Characterization methodology of a tribological couple: metal matrix composites/brake pads. Mater. Characterization 40, 169–188 (1998)

Wirth, A., Eggleston, D., Whitaker, R.: A Fundamental tribochemical study of the third body layer formed during automotive friction baking. Wear 179, 75–81 (1994)

Jacko, M.G.: Physical and chemical changes of organic disc pads in service. Wear 46, 163–175 (1978)

Osterle, W., Bettge, D.: Comparison of methods for the characterization of brake pad surfaces. Prakt Metallogr 41, 494–505 (2004)

Jang, H., Lee, J., Fash, J.W.: Compositional effects of the brake friction material on creep groan phenomena. Wear 251, 1477–1483 (2001)

Eriksson, M.: Friction and contact phenomena of disc brakes related to squeal. PhD thesis, Uppsala University, Acta Universitatis Upsaliensis (2000) ISBN 91- 5544716-3

Bark, L.S., Moran, D., Percival, S.J.: Inorganic and organic changes during friction material performance. Wear 53, 107–119 (1979)

Desplanques, Y., Degallaix, G.: Interactions between Third-Body Flows and L calisation Phenomena during Railway High-Energy Stop Braking. SAE Interntional Journal of Passenger Cars - Mechanical Systems 1, 1267–1275 (2009)

Multi-scale Anisotropic Approach for Modeling Woven Fabric Composite

Abderraouf Gherissi[1], Amine Ammar[2], Fethi Abbassi[1], and Ali Zghal[1]

[1] URMSSDT- ESST Tunis, 5 Avenue Taha Hussein,
BP, 56, Bâb Manara, 1008 Tunisia
abderraouf.gherissi@ensam.eu,
fethi.abbassi@ipeib.rnu.tn,
ali.zghal@esstt.rnu.tn
[2] ENSAM Arts et Métiers Paris-Tech d'Angers,
2 boulevard du Ronceray BP 93525,
49035 Angers cedex 01 France
amine.ammar@ensam.eu

Abstract. In the present work, we resolve the multiscale modeling problem of woven composite; we take into account the texture of woven fabric. The anisotropic muliscale modeling was creating under Abaqus and Matlab software. We was developed the texture to avoid yarn's interpenetration and to organize intersection between warp and weft. The fabric behavior it's governing by the orientation of yarns below mechanical charge. The influence of fabric shear will be revealed. The macro modeling step is done on an Abaqus explicit code. The shear angle exceeds the locking angle in the extreme fabric's shear zones will be presented; simulation results and experimental test will be confront. And we will prove that the anisotropic approach can be suitable for simulate woven fabric composite.

Keywords: multi-scale modeling, anisotropic approach, fabric 2D/2.5D, Composite forming and Finite element analysis.

1 Introduction

The woven fabric composites were made in high performance applications such as in the automobile industry, aircraft industry and in aerospace structural mechanism, where most advantageous design and performance are presented. The woven composite forming by resin injection on the pre-formed reinforcing (RTM) or by using pre-impregnated composite thermoplastic matrices (CFRTP) have a necessity to develop a preliminary expensive forming process. This simulation gives a precious guide, where it is necessary for the elaboration of pieces and for forming process; moreover it's a benefit for the calculi time and substituent a big part of experimental process. This predictive character can be seen through the work of many authors by various methods. Same authors they consider a macro hyperelastic or hypoelastic models for the fabric (see Dong et al 2001 [1], Thijie et al 2007

M. Haddar et al. (Eds.): *Design and Modeling of Mechanical Systems*, LNME, pp. 453–460.
DOI: 10.1007/978-3-642-37143-1_54

[2], Aimene et al 2010 [3], Khan et al 2010 [4]). Others take into account a continuous mesocopic approaches (see reviews by Badel et al 2008 [8], Badel et al 2009 [9], Boisse et al 2006 [10], Hamila et al 2009 [11]). Even the forming of these composites is among the most studied processes (see P.Boisse et al [10], P.Badel et al [9], P.Boisse et al [12]). They apply a hypoelastic model for fiber; take into account the fiber direction and the transverse compaction by a non-linear elastic fiber's behavior and simulate the fabric with using shell elements. Others authors used a discrete models (see the work of Zhou et al 2004 [5], Ben Boubaker et al 2007 [6], Miao et al 2008 [7]), they develop a judicious discrete models, but it spend a lot of development of beam and spring elements to implicated a forming process.

All of previous exposed works avoids using anisotropic model, since they considered that cannot be suitable to modeling woven composite, especially forming process .The present study revolted this challenge, and introduced the anisotropic behavior in the meso scale step. The resolution have four difficulties: The first delicate aspect concerns the mechanical behavior of the yarns. The second problem relates to discrete geometric model of the yarns; the third difficulty concerns the anisotropic simulation for the meso-scale modeling, the yarns contacts and boundary conditions. The fourth problem concerns the mico-meso and meso-macro path. Especially it must strictly conserve the mechanical behavior information of the first simulation scale.

2 Multiscale Modeling Procedure

The methodology of anisotropic multi-scale simulation of woven composites is an approach micro, meso and macro scale. In order to develop a micro-meso scale analysis of such woven composite, it is necessary to know the weaving fabric characteristic and the yarn's profile. Our study is based on experimental analysis under binocular microscope. The mesoscopic observations on binocular was made after cross-cuts of the material, following different directions, the observations allow to have the dimensions and shapes of the yarns, and the weave and the number of plies, see Figure 1. Observations and statistical calculations allowed us to extract the dimensional parameters of fabric. To resolve this problem, our solution was to develop a simple interpolation in weaving (such as Bezier spline or natural cubic spline curve), after meshing we correct the problem of interpenetration between wefts and warps. We have programmed the anisotropic continue approach by using MATLAB. The follow diagram in the fig .2 clarifies the procedure:

For the contact problem we have taken the suggest of P.Badel et al [13], where they propose: while the shear angles reaches large values, lateral contacts will be very complex and the shear rigidity of the reinforcement is a consequence of lateral compression of the yarns; and the orthotropic hypoelastic or elastic constituve equation have used at finite strains, where the stress rate with respect to a rotated frame.

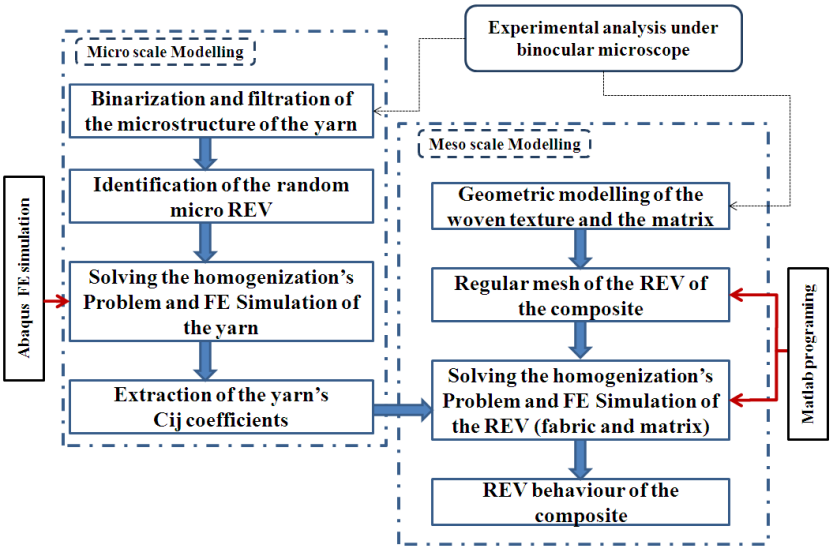

Fig. 1 Methodology of Micro/Meso scale Modeling of woven composites

2.1 Constrictive Equations of Micro Scale Modeling Step

In order to predict the micro scale elastic constants of the yarn we have calculate the elastic stiffness matrixes. Computing the stresses within the matrix, the fibers, and the interface of the matrix-fibers. We considering the fibers it are surrounding by the matrix and we assumed the matrix and fibers are linearly elastic and the fibers are infinitely long. We have use one of three different approaches, that are developed in previous work see [14], to determine the elastic constants for the composite material based on micromechanics demarche. Here we will use the random numerical model.

The volume fraction relation can be shown as follow:

$$V\,f + V\,m = 1 \tag{1}$$

Where: V_f and Vm are respectively volume fraction of the fibers in the REV of the yarn and the volume fraction of the polymer matrix.

The simple rule-of-mixtures model gives that the young modulus in the principal fibers direction can be written as:

$$E_l = E_1^f V\,f + E_m V_m \tag{2}$$

$$\frac{1}{E_2} = \frac{V^f}{E_2^f} + \frac{V^m}{E^m} \tag{3}$$

The Poisson's ratio:

$$\nu_{12} = \nu_{12}^f V^f + \nu^m V^m \tag{4}$$

The shear modulus

$$\frac{1}{\mathrm{G}_{12}}\ \frac{\mathrm{V}^{\mathrm{f}}}{G_{12}^{f}}+\ \frac{\mathrm{V}^{\mathrm{m}}}{\mathrm{G}^{\mathrm{m}}} \tag{5}$$

While the simple rule-of-mixtures models used above give perfect results for E1 and ν12, the results obtained for E2 and G12 do not agree well with finite element analysis and elasticity theory results. Then, we need to modify the simple rule-of-mixtures models shown above: for E2, we have the following modified rule-of-mixtures formula [15]:

$$\frac{1}{E_2}=\frac{\frac{\mathrm{V}^{\mathrm{f}}}{E_2^{f}}+\frac{\eta \mathrm{V}^{\mathrm{m}}}{\mathrm{E}^{\mathrm{m}}}}{\mathrm{V}^{f}+\eta \mathrm{V}^{m}} \tag{6}$$

Where η is the stress-partitioning factor (related to the stress σ_2). This factor satisfies the relation $0 < \eta < 1$ and is usually taken between 0.4 and 0.6. Another alternative rule-of-mixtures formula for E2 is given by [15]:

$$\frac{1}{E_2}=\frac{\eta^{f}\mathrm{V}^{f}}{E_2^{f}}+\ \frac{\eta^{m}\mathrm{V}^{m}}{\mathrm{E}^{\mathrm{m}}} \tag{7}$$

Where the factors ηf and ηm are given by [15]:

$$\eta^{f}\ =\frac{\mathrm{E}_1^{f}\ \mathrm{V}^{\mathrm{f}}+[\left(1-\nu_{12}^{f}\ \nu_{21}^{f}\right)E^{m}+\nu^{m}\ \nu_{21}^{f}\ \mathrm{E}_1^{f}\ ]\mathrm{V}^{\mathrm{m}}}{\mathrm{E}_1^{f}\ \mathrm{V}^{\mathrm{f}}+E^{m}\mathrm{V}^{\mathrm{m}}} \tag{8}$$

$$\eta^{m}\ =\frac{\left[\left(1-\nu^{m^2}\right)\mathrm{E}_1^{f}-\left(1-\nu^{m}\ \nu_{12}^{f}\right)E^{m}\ \right]\mathrm{V}^{\mathrm{f}}+E^{m}\mathrm{V}^{\mathrm{m}}}{\mathrm{E}_1^{f}\ \mathrm{V}^{\mathrm{f}}+E^{m}\mathrm{V}^{\mathrm{m}}} \tag{9}$$

The above substitute model for E2 gives accurate results and is used whenever the modified rule-of-mixtures model of (9) cannot be applied, i.e. when the factor η is not known. The altered rule-of-mixtures model for G12 is given by the following formula [15]:

$$\frac{1}{\mathrm{G}_{12}}=\frac{\frac{\mathrm{V}^{\mathrm{f}}}{G_{12}^{f}}+\frac{\eta'\mathrm{V}^{\mathrm{m}}}{\mathrm{G}^{\mathrm{m}}}}{\mathrm{V}^{\mathrm{f}}+\eta'\mathrm{V}^{\mathrm{m}}} \tag{10}$$

Where η' is the shear stress-partitioning factor. Annotation that η' gratifies the relation $0 < \eta' < 1$ but using $\eta' = 0.6$ gives results that link with the elasticity result. As a final point, the elasticity result gives the following formulation for G12 [15]:

$$\mathrm{G}_{12}=\mathrm{G}^{\mathrm{m}}[\frac{[(\mathrm{G}^{\mathrm{m}}+\mathrm{G}_{12}^{\mathrm{f}})-\mathrm{V}^{\mathrm{f}}(\mathrm{G}^{\mathrm{m}}-G_{12}^{f})]}{[(\mathrm{G}^{\mathrm{m}}+\mathrm{G}_{12}^{\mathrm{f}})+\mathrm{V}^{\mathrm{f}}(\mathrm{G}^{\mathrm{m}}-G_{12}^{f})]}] \tag{11}$$

The adapted FE method consists in applying three simple traction loads following the three main axes (1, 2 and 3) and three simple shear loads in the directions 2-3, 1-2 and 2-3 see fig.2:

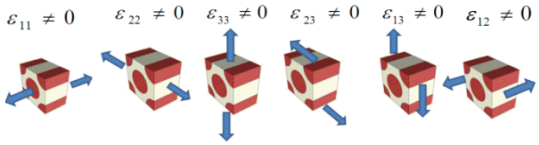

Fig. 2 The six different cases to be solved for the homogenized elastic properties of RVE

The imposing deformation loads in the principal directions coincide with the axes of symmetry of the cell, which is to say of the form:

$$\underline{\underline{E}} = E_{11}\,\underline{e}_1 \otimes \underline{e}_1 + E_{22}\,\underline{e}_2 \otimes \underline{e}_2 + E_{33}\underline{e}_3 \otimes \underline{e}_3 \tag{12}$$

We imposed a macroscopic simple share deformation of the form:

$$\underline{\underline{E}} = E_{ij}/2\,(\underline{e}_i \otimes \underline{e}_j + \underline{e}_j \otimes \underline{e}_i) \tag{13}$$

An imposed macroscopic displacement is used to calculate the $C_{ijkl}^{\hom}$ coefficients; we have taken into account that the yarn represents an orthotropic characteristic.

2.2 *Constrictive Equations of Meso Scale Modeling Step*

At first it is necessary to resolve the change in cross sections along yarns at the inter-section weft and Warp and then it is required to approximate the yarn's profile by Bezier curves or natural cubic splines. The intersection zone between weft and warp will create interpenetration and will result an error in the contact's yarns zones and in the FE simulation. For this case we have develop a geometric models for woven fabric under Matlab software, this step it is primarily for the meso anisotropic model. In order to resolve the meso scale modeling step, the idea consists to create the transition between references R and R', referring to the passage matrix [P]; several studies have developed the passage matrix method see [16, 17]. The orientation of each yarn will be considered; geometric references related to each yarn and one reference linked to the entire RVE must be taken into consideration, especially yarns that will change orientation by increasing the applied shear load. The REV vectors of the composite it show in the figure 6. Then we calculate the transition matrix [P], which is expressed as follows:

$$[p]=\begin{bmatrix} P_{11} & P_{12} & P_{13} \\ P_{12} & P_{22} & P_{23} \\ P_{13} & P_{23} & P_{33} \end{bmatrix} \tag{14}$$

In each yarn points « i » the local material reference is R (xi,yi,zi) see fig.3.

The R' reference it 'is for Global RVE: the global reference is R' (X', Y', Z') see fig.3. We can write the stress tensor or deformation tensor in the new reference through the following relations:

$$\{\sigma'\} = \{M_\sigma\}\{\sigma\} \tag{15}$$

$$\{\epsilon'\} = \{M_\epsilon\}\{\epsilon\} \tag{16}$$

Where:

$$\{M_\sigma\} = \begin{Bmatrix} [D_1] & 2[A] \\ [B] & [D_2] \end{Bmatrix} \text{ and } \{M_\epsilon\} = \begin{Bmatrix} [D_1] & [A] \\ 2[B] & [D_2] \end{Bmatrix} \tag{17}$$

Where:

$$[A] = \begin{bmatrix} P_{21}P_{31} & P_{11}P_{31} & P_{11}P_{21} \\ P_{22}P_{32} & P_{12}P_{32} & P_{12}P_{22} \\ P_{23}P_{33} & P_{13}P_{33} & P_{13}P_{23} \end{bmatrix} \tag{18}$$

$$[B] = \begin{bmatrix} P_{12}P_{13} & P_{22}P_{23} & P_{32}P_{33} \\ P_{11}P_{13} & P_{21}P_{23} & P_{31}P_{33} \\ P_{11}P_{12} & P_{21}P_{22} & P_{31}P_{32} \end{bmatrix} \tag{19}$$

$$[D_1] = \begin{bmatrix} P_{11}^2 & P_{21}^2 & P_{31}^2 \\ P_{12}^2 & P_{22}^2 & P_{32}^2 \\ P_{13}^2 & P_{23}^2 & P_{33}^2 \end{bmatrix} \tag{20}$$

$$[D_2] = \begin{bmatrix} P_{22}P_{33} + P_{32}P_{23} & P_{12}P_{33} + P_{32}P_{13} & P_{12}P_{23} + P_{22}P_{13} \\ P_{21}P_{33} + P_{31}P_{23} & P_{11}P_{33} + P_{31}P_{13} & P_{11}P_{23} + P_{21}P_{13} \\ P_{21}P_{32} + P_{31}P_{22} & P_{11}P_{32} + P_{31}P_{12} & P_{11}P_{22} + P_{21}P_{12} \end{bmatrix} \tag{21}$$

For anisotropic fabric material, the stiffness matrix C was written in the base (x, y, z) as a function of the matrix C 'is already established in the base (x', y ', z'):

$$\{C\} = \{M_\epsilon\}\{C'\}\{M_\epsilon\}^t \tag{22}$$

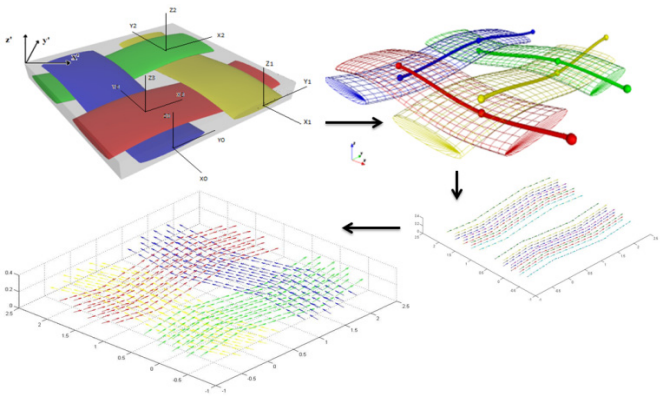

Fig. 3 The approach of the meso scale modeling under Matlab software

3 Evaluation of the Anisotropic Multi-scale Approach

To evaluate the implemented approach, we have tested the G1151 fabric which is a 2.5 D interlock fabric from Hexcel Company. We tested the material under Hemispherical forming test and compared with Abaqus explicit simulation. The results presented in the fig. 4 clearly show that the shear angle exceeds the locking angle in same fabric's zones between simulation results and experimental test, when it justifies quantitatively the numerical approach.

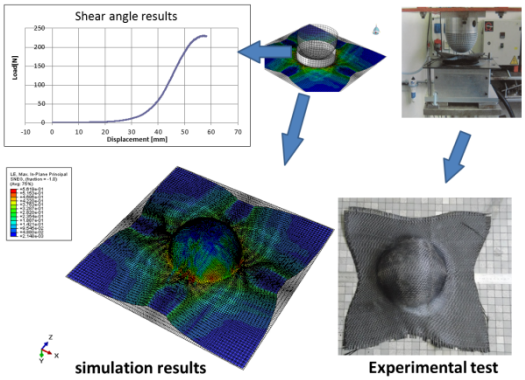

Fig.4 Experimental test versus numerical simulation approach for woven fabric G1151

4 Conclusion

The present investigation was developing the anisotropic multi-scale modeling. We could link scales of modeling; the geometric development in Matlab has reduced the modeling complexity related to the yarn interpolation and weft -warp intersection and yarns crossing and matrix and interpenetration. The meso-scale modeling approach developed in this paper shows that can be applied others fabrics by using the same process. For 2D fabric (for example satin and taffeta) and 2.5D and 3D fabric (for example interlock).Clearly showed the contribution of the mode of weaving on the elastic behavior of the composite and the forming process. Several methods exist and principally differ according to our approach see ([5], [6], [7], [9] and [12]). This study represents a contribution to solving the complex problem of woven composites at the meso scale and the implementation of multi-scale procedure. At an advanced stage has been provided to generalize the method for other woven fabric composites observed in experimental studies often forming of woven composite.

Acknowledgements. This work is partially supported by URMSSDT- ESST Tunis.

References

[1] Dong, L., Lekakou, C., Bader, M.G.: Processing of composites: Simulations of the draping of fabrics with updated material behaviour law. Journal of Composite Materials 35, 138–163 (2001)
[2] Ten Thije, R.H.W., Akkerman, R., Huetink, J.: Large deformation simulation of anisotropic material using an updated Lagrangian finite element method. Comput. Meth. Appl. Mech. Eng. 196, 3141–3150 (2007)
[3] Aimène, Y., Vidal-Sallé, E., Hagège, B., Sidoroff, F., Boisse, P.: A hyperelastic approach for composite reinforcement large deformation analysis. Journal of Composite Materials 44(1) (2010)
[4] Khan, M., Mabrouki, T., Vidal-Sallé, E., Boisse, P.: Numerical and experimental analyses of woven composite reinforcement forming using a hypoelastic behaviour. Application to the double dome benchmark. Journal of Materials Processing Technology 210, 378–388 (2010)
[5] Zhou, G., Sun, X., Wang, Y.: Multi-chain digital element analysis in textile mechanics. Composites Science and Technology 64, 239–244 (2004)
[6] Ben Boubaker, B., Haussy, B., Ganghoffer, J.F.: Discrete models of woven structures. Macroscopic approach. Composites Part B 38, 498–505 (2007)
[7] Miao, Y., Zhou, E., Wang, Y., Cheeseman, B.A.: Mechanics of textile composites: Micro-geometry. Composites Science and Technology 68, 1671–1678 (2008)
[8] Badel, P., Vidal-Salle, E., Maire, E., Boisse, P.: Simulation and tomography analyzis of textile composite reinforcement deformation at the mesoscopic scale. Composites Science and Technology 68, 2433–2440 (2008)
[9] Badel, P., Gauthier, S., Vidal-Salle, E., Boisse, P.: Rate constitutive equations for computational analyses of textile composite reinforce ment mechanical behaviour during forming. Composites: Part A 40, 997–1007 (2009)
[10] Boisse, P., Zouari, B., Daniel, J.L.: Importance of in-Plane Shear Rigidity in Finite Element Analyses of Woven Fabric Composite Preforming. Composites part A 37-12, 2201–2212 (2006)
[11] Hamila, N., Boisse, P., Sabourin, F., Brunet, M.: A semi-discrete shell finite element for textile composite reinforcement forming simulation. Int. J. Numerical Methods in Engineering 79, 1443–1466 (2009)
[12] Boisse, P., Zouari, B., Gassert, A.: A mesoscopic approach for the simulation of woven fibre forming. Composites Science and Technology 65, 429–436 (2005)
[13] Badel, P., Vidal-Sallé, E., Boisse, P.: Computational determination of in-plaine shear mechanical behaviour of textile composite reinforcements. Coputational Materials Science 40, 439–448 (2007)
[14] Abbassi, F., Gherissi, A., Zghal, A., Mistou, S., Alexis, J.: Micro-scale modeling of carbon-fiber reinforced thermoplastic materials. Applied Mechanics and Materials 146, 1–11 (2012)
[15] Voyiadjis, G.Z., Kattan, P.I.: Mechanics of Composite Materials with MATLAB. Springer, Heidelberg (2005)
[16] Chevalier, Y. (s.d.). Comportements élastique et viscoélastique des composites. Techniques de l'Ingénieur A 7 750
[17] Xue, P., Peng, X., Cao, J.: A non-orthogonal constitutive model for characterizing woven composites. Composites: Part A 34, 183–193 (2003)

Optimization of Single Point Incremental Forming of Sheet Metal with Isotropic and Combined Hardening Behavior

Arfa Henia, Bahloul Riadh, and Hédi Belhadjsalah

Laboratoire de Génie Mécanique (LGM),
Ecole Nationale d'Ingénieurs de Monastir (ENIM),
Université de Monastir,
Avenue Ibn Eljazzar, 5019 Monastir
{henia_arfa,bahloul_riadh}@yahoo.fr,
hedi.belhadjsalah@enim.rnu.tn

Abstract. Incremental forming is a progressive sheet metal forming process characterized by large displacements, large localized strains, low cost and time saving. The aim of this work is to optimize the single point incremental forming process combining Box-Behnken design of experiments, response surface methods and genetic algorithms. The forming of truncated cones in aluminum was studied with the finite element codes Abaqus\implicit. We use two hardening laws (isotropic and combined hardening models) for modeling the incremental forming process. A comparison between two approaches results is made.

Keywords: SPIF, Finite element modeling, Optimisation, Design of experiments, Response surface methodology, Genetic algorithm.

1 Introduction

Incremental forming is characterized by a simple tool which imposes a local plastic deformation on sheet in a progressive way (J.R. Duflou and al 2007). Figure 1 presents a configuration of the single point incremental forming. During the numerical simulations of single point incremental forming, we integrated an isotropic hardening behavior. Except that the process is characterized by the cyclic aspect due to the tool displacement characteristic. Within this framework, the analysis of the distribution of the stresses measured of an element shows the cyclic aspect of the process (H Arfa. and al 2011). The materials generally used are aluminum alloys. As well, the type of hardening behavior has an importance during the unfolding the process of single point incremental forming. Indeed a better approach with the criterion of plasticity will give a better numerical prediction of the final sheet thickness. Figure 1 present the principle of single point incremental forming.

M. Haddar et al. (Eds.): *Design and Modeling of Mechanical Systems*, LNME, pp. 461–468.
DOI: 10.1007/978-3-642-37143-1_55

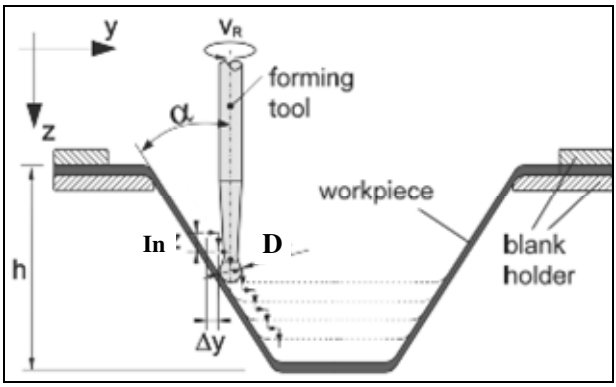

Fig. 1 Principle of SPIF

An analysis of the way of loading highlighted the importance of the cyclic phenomenon of incremental forming (H Arfa. and al 2011). In this paper, a first step is taken to present numerical configuration of SPIF. For numerical results, response surfaces are developed for two approaches of hardening behavior. An optimization procedure is based by graphical response surfaces methodology (RSM). By determining a mathematical relationship of second order between the response of the forming problem and the variables that affect the response, we propose to find the optimum solutions defined by the minimum values of sheet thinning.

2 Numerical Modeling of SPIF

The Single Point Incremental Sheet Forming (SPIF) process allows producing complex three dimensional shapes from Computer Aided Design (CAD) models without specially designed forming tools. In our study, The Finite Element (FE) study focuses on the SPIF process based on a unidirectional tool path strategy of contours and step downs to obtain truncated cones. Different process parameters are considered. The numerical simulation of SPIF has been done with the numerical code Abaqus\Implicit. The tool is modeled as a rigid surface. Figure 2.a presents the initial position of the tool. Quadrilateral shell elements with 4 nodes and 6 degrees of freedom per node (S4R) and five Gaussian reduced integration points through the thickness direction were used. Two hardening behaviors are considered: isotropic and combined hardening law expressed respectively as:

$$\overline{\sigma} = k(\varepsilon_0 + \varepsilon_p)^n \tag{1}$$

$$\sigma_y = \sigma_0 + k_v(1 - \exp(-n_v \varepsilon_{eq})) \tag{2}$$

The hardening parameters obtained by the inverse method from the classical and indent tests are for this model given in Table 2.

Table 1 Isotropic hardening parameters for SPIF (P.A.F. Martins and al 2008)

AA 3003	Value
K (MPa)	184
ε_0 (MPa)	0.00196
n	0.224

Table 2 Mixed isotropic-kinematic hardening parameters for SPIF, determined by inverse method, from (C Henrard, 2009)

AA 3103	Value
σ_0 (MPa)	20
Kv (MPa)	89
nv	22.5

Figures 2.a and 2.b show the deformed shape of thickness distribution respectively for isotropic and combined hardening law for cones with 50° wall angle, 1.2mm initial thickness, 10mm tool diameter and 0.5mm vertical increment.

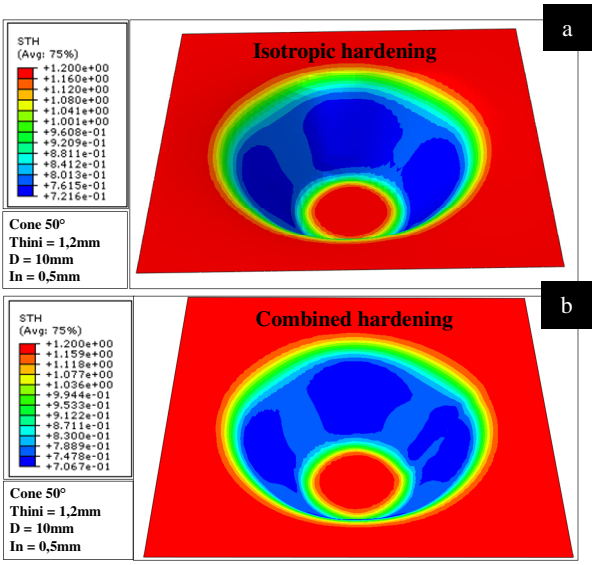

Fig. 2 Schematic of FEA simulations a) iso-values of the final sheet thickness for isotropic hardening b) iso-values of the final sheet thickness for combined haredening

For seeing more the differences between two hardenings laws approaches, we will present in the next part a design of numerical experiment.

3 Optimization Results Obtained Using the GA and the Global Approach Based on RSM

Statistical design of experimentation under response surface methodology (RSM) reduces the cost of experimentation and a collection of statistical and regression techniques provide information about the main and interaction effect among the selected variables (Weuster-Botz, 2000), forming limit diagrams have been built by using a Box–Behnken design of experiments and response surfaces method based on the two criteria: maximum forming angle and effective strains (Ham and Jeswiet, 2007). Dimensional Accuracy of Single Point Incremental Forming (SPIF) such as the sheet rate thinning is studied with the use of a Box-Behnken design analysis (H.Arfa, 2012). Four factors are varied and they are material thickness, wall angle, tool size, and incremental step size.

Table 3 Factors identification

Name	Description	Inferior born (-1)	Middle (0)	Superior born (1)
α (°)	Wall angle	50	60	70
D (mm)	Punch diameter	10	17.5	25
Th_{ini} (mm)	Initial thickness	0.85	1.425	2
In (mm)	Step size	0.5	1.25	2

The Box-Behnken design can analyses four factors in three levels in a total number of 27 numerical simulation runs performed. It is used to determine the effect of process parameters on the considered responses, and also it can be employed to develop mathematical models connecting the response to the various factors conducing to the optimization of SPIF process. The levels of screened significant variables were further optimized by the application of GA to a RSM based quadratic model. Interaction effects of significant medium variables are also investigated in the present work. Mathematical modeling is integrated with statistical experimentation techniques for better interpretation of results and experimental errors. We will pass in the following part to response surfaces methodology corresponding to the thinning rate for isotropic and combined hardening.

3.1 Response Surface Methodology: RSM

RSM is the regression method exploring the relationships between several explanatory variables and one or more response variables. The method was first introduced by Box and Wilson (G. E. P.Box, and K. B. Wilson, 1951). The RSM constitutes the second shutter of the experimental designs method. This technique aims at determining in a quantitative way the variations of the response function. Modeling of the objective function of the response can also be used as a basis in search for optimal conditions. Figures 3a and 3b are surface representations of the predicted thinning rate respectively for isotropic and combined hardening. A second order quadratic mathematical model was developed to predict the influence

of various variables on the thinning rate (%) and reduced to four variables for GA based optimization. The response surface equation for four variables adopted in the present case is of the following form: (3).

$$Th_{rate} = \beta_0 + \beta_1\alpha + \beta_2 D + \beta_3 Epini + \beta_4 In + \beta_5\alpha^2 + \beta_6 D^2 + \beta_7 Epini^2 + \beta_8 In^2 + \beta_9\alpha.Epini + \beta_{10}\alpha.In + \beta_{11}\alpha.D + \beta_{12} Epini.In + \beta_{13} Epini.D + \beta_{14} In.D \quad (3)$$

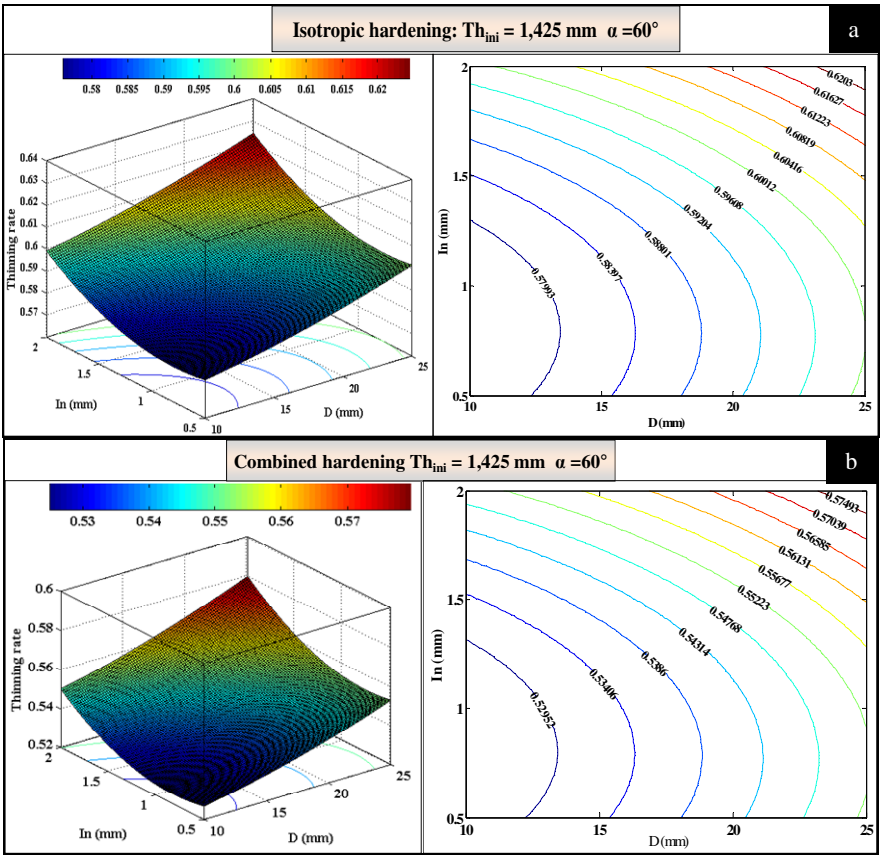

Fig. 3 Responses surface of thinning rate a) isotropic hardening b) combined hardening

The preceding figures show that the increase in the tool diameter and the vertical increment size inferred an amplification of the thinning rate of sheet. The results show that the sheet thinning evolves in a nonlinear way according to the considered parameters and that is more sensitive to the vertical step size than to the punch diameter. These results are verified for the two approaches of hardening law. Moreover the thinning rate of a combined hardening law is less than witch of isotropic hardening law.

3.2 *Optimization Results Obtained Using the GA and the Global Approach*

A MATLAB based programs were developed in this work. An optimization problem is formulated based on the genetic algorithm and is proposed and applied to find the optimum solutions. In this paragraph, we will present with genetic algorithm in case of 60° wall inclination angle corresponding to combined hardening law with 1.425mm initial thickness. A variation of the wall angle is elaborated with the aim of seeing the difference between parameters of optimisation according to this factor.

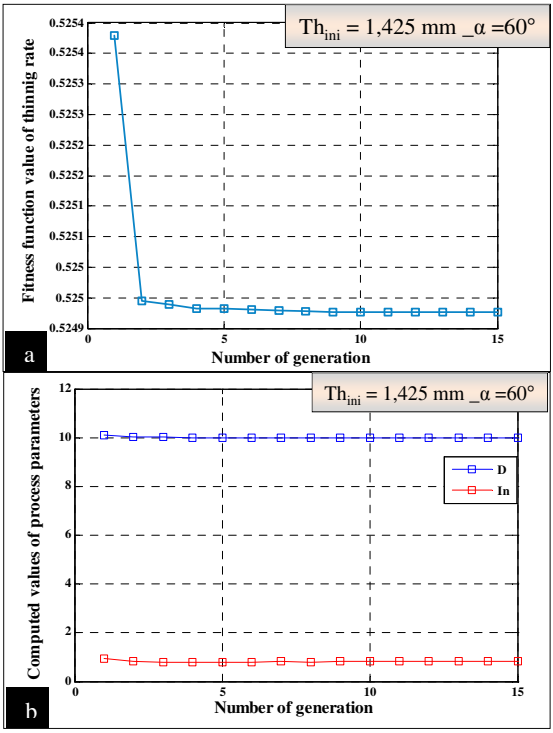

Fig. 4 Optimasation results a) Convergence history of thinning rate objective function b) process parameters

The genetic algorithm optimization was performed for a search population size of 300 individuals. The results for optimum thinning rate are shown in figure 4.a. The optimum value for the thinning rate is about 52.50% based on GA. The objective function of thinning rate is converged after 15 iterations (Figure 4). The optimal design parameters are 10mm for the tool diameter and 0.815mm the vertical step size. In tables 4 and 5, we will present an optimization results summary for cones with 50°, 60° and 70° wall angles with a fixed initial thickness 1.425mm respectively for isotropic and combined hardening law.

Table 4 Optimisation results summary for isotropic hardening

Objective functions	Thinning rate for part with 50° wall angle		Thinning rate for part with 60° wall angle		Thinning rate for part with 70° wall angle	
Optimization methods	Global approach	Genetic algorithm	Global approach	Genetic algorithm	Global approach	Genetic algorithm
Global minimum	43.81%	43.81%	57.59%	57.59%	66.63%	69.68%
D_opt	10	10	10	10	10	10
In_opt	0.5300	0.5303	0.800	0.7992	1.0700	1.0681

Table 5 Optimisation results summary for combined hardening

Objective functions	Thinning rate for part with 50° wall angle		Thinning rate for part with 60° wall angle		Thinning rate for part with 70° wall angle	
Optimization methods	Global approach	Genetic algorithm	Global approach	Genetic algorithm	Global approach	Genetic algorithm
Global minimum	37.05%	37.05%	52.50%	52.50%	66.08%	66.08%
D_opt	10	10	10	10	10	10
In_opt	0.5450	0.5452	0.8150	0.8144	1.0850	1.0838

Tables 4 and 5 involve that the thinning rate increases considerably with the increase of the wall angle. Thinning rate pass from 43.81% to 66.63% and 37.05% to 66.08% respectively for isotropic and combined hardening law. The optimum tool diameter is remaining equal to 10mm for 50, 60 and 70° wall angle in all considered cases. As well as, the results corresponding to the optimisation by general approach are very close to those of genetic algorithm in the two example of hardening law. Except that the thinning rate given by an isotropic hardening law is more important than that given by combined hardening.

4 Conclusion

Genetic programming is a greater technique because it provides the architect with the explicit expression of an approximation function containing design variables proven to have a significant impact on the objective performance measure. A Box-Behnken design has been applied to screen the four most significant variables with response on thinning rate. Wall angle, tool diameter, vertical increment and initial thickness have been found to be the most significant variables and theirs values have been further optimized by Genetic Algorithm based Response surface methodology. The numerical results of thinning rate response obtained by using a genetic algorithm (GA) are very close to the computed values founded by global approach which is considered as reference method. This is verified for isotropic and combined hardening law approaches.

References

Arfa, H., Riadh, B., Hédi, B.H.S.: (CMSM–2011) Etude paramétrique du formage incrémental mono-point

Arfa, H., Riadh, B., Hédi, B.H.S.: (Cotume 2012), Optimisation du formage incrémental par la technique des surfaces de réponse

Box, G.E.P., Wilson, K.B.: On the experimental attainment of optimum conditions. Journal of the Royal Statistical Society, Series B 13, 1–45 (1951)

Henrard, C., Bouffioux, C., Eyckens, P., Sol, H., Duflou, J., Van Houtte, P., Van Bael, A., Habraken, A.M.: Forming Forces in Single Point Incremental Forming, Prediction by Finite Element Simulations, Validation and Sensitivity. Submitted to Computational Mechanics (2009)

Duflou, J.R., Tunçkol, Y., Szekeres, A., Vanherck, P.: Experimental study on force measurements for single point incremental forming. J. Mater. Process. Technol. 189, 65–72 (2007)

Ham, M., Jeswiet, J.: Single point incremental forming limits using a Box-Behnken design of experiment. Key. Eng. Mater., 344629–344636 (2007)

Martins, P.A.F., Bay, N., Skjoedt, M., Silva, M.B.: Theory of single point incremental forming. Ann. CIRP - Manuf. Technol. 57, 247–252 (2008)

Weuster-Botz, D.: Experimental design for fermentation media development: Statistical design of global random search. Journal of Bioscience and Bioengineering 90, 473–483 (2000)

Ply Orientations Effect in the Fracture Toughness of Mixed Mode Delamination in E-Glass/Polyester Woven Fabrics

Emna Triki[1], Bassem Zouari[2], Abdesslam Jarraya[1], and Fakhreddine Dammak[2]

[1] U2MP, National Engineering School of Sfax,
B.P.W1173-3038, Sfax, Tunisia
emna_triki@yahoo.fr,
abdessalem.jarraya@enis.rnu.tn
[2] UDSM, National Engineering School of Sfax,
B.P. W1173-3038, Sfax,Tunisia
bzouari@yahoo.com,
Fakhreddine.Dammak@enis.rnu.tn

Abstract. The aim of this work is to study the influence of ply orientation on the fracture toughness of thick E-glass/polyester woven fabric composites laminates. Two different types of laminates were fabricated with different ply orientations: (i) balanced: plain weave (taffetas T) and (ii) unbalanced: 4-hardness satin weave (S). Experiments were conducted using standards delamination tests under mixed mode loading using MMF tests under static conditions. The experimental results have been expressed in terms of total strain energy release rate and R-curves. We remark that the critical fracture toughness depends on the ply orientations and its maximum value is reached for a ply orientation +45°/-45°.

Keywords: E-glass/polyester, Woven fabrics, Delamination, MMF, R-curve.

1 Introduction

Glass/polyester laminates are widely used in a large variety of marine applications including sporting equipment and military structures. This is because of their light weight and competitive prices. One of the most harmful damage mechanisms in the glass reinforced structures is delamination. It is dependent on both the material (fibre, weave structure and matrix) and the manner in which the specimen is loaded; pure mode I (Double Cantilever Beam DCB test (ASTM D5528)) or pure mode II (End Notch Flexure ENF and End Load Split ELS test (Blackman et al. 2006, Brunner et al. 2008)), as well as any combination of both (Mixed Mode Bending MMB test and Mixed Mode Flexion MMF test (Benzeggah et al. 1989, Davies 1987)). Delamination resistance and their susceptibility to growth are normally characterized using fracture mechanics theory and the critical strain energy release rate parameter known as the interlaminar fracture toughness (G_c). Therefore, interlaminar delamination is prone to appear and propagate if the energy release rate applied to the system equals the critical energy release rate.

M. Haddar et al. (Eds.): *Design and Modeling of Mechanical Systems*, LNME, pp. 469–476.
DOI: 10.1007/978-3-642-37143-1_56

Numerous studies have been devoted to the analysis of delamination in unidirectional laminates in which the plies are unidirectional (ASTM D5528, Hiley 2000). Really composite structures are generally multidirectional (Hiley 2000, Hashemi et al. 1990). However, various studies were already reported on the mode II fracture (Choi et al. 1999, Andersons and König 2004) and in mixed-mode I+II fracture (Kotaki and Hamada 1997, Solar and Belzunce 1989). Some others researchers have investigated delamination in woven fabric composites (Xu et al. 2010, Duplessis et al. 2010).

The present study is mainly concerned with thick glass/polyester woven fabric composites with two weaving conditions: (i) balanced fabric: plain weave and (ii) unbalanced: 4-hardness satin weave. The experimental method used was Mixed-Mode Flexure MMF test which was carried in order to investigate the effect of weave structure and ply orientations on the crack growth behavior.

2 Material System and Specimen Description

The studied composite materials are made with polyester resins reinforced with E-glass fibres. Two main types of fibre reinforcement are used: 4-harness satin weave (S), plain weave (taffetas T). Two types of materials are used in this study: balanced and unbalanced woven plies, the first is composed of 12 layers taffetas stacked alternately with different ply orientation $[0°/90°]_{12}$, $[+45°/-45°]_{12}$ and $[90°/0°]_{12}$,the second is composed of 8 layers satin weave stacked alternately with different ply orientation $[0°/90°]_8$, $[+45°/-45°]_8$ and $[90°/0°]_8$. The delamination initiator consisted of a polypropylene thin sheet (30 μm thickness) inserted during layup at the mid-plane of the plate. Table 1 shows the constituent materials of the composite laminates.

Table 1 Constituent materials of composite laminates

Material	Type	
Reinforcement	E-woven roving glass fibre	
	4-harness satin weave ,	plain weave (taffetas)
	fabric areal density: 600 $g.m^{-2}$	400 $g.m^{-2}$
	volume fraction V_f=31%	
Matrix	Orthophthalic polyester resin	
	Peroxide Catalyst : MEKPO –M50 catalyst (1.5% of matrix volume)	

The composites laminates were fabricated in the form of panels of 300 x 250 mm with a thickness of 8 mm by mean of a molding system. Specimens types used for experiment have the following dimensions: nominal width b= 30 mm, total length L=140 mm (from the load line to the clamp), nominal thickness ($2h$) were 8 mm and the initial crack length was a_0=80 mm (Fig. 1).

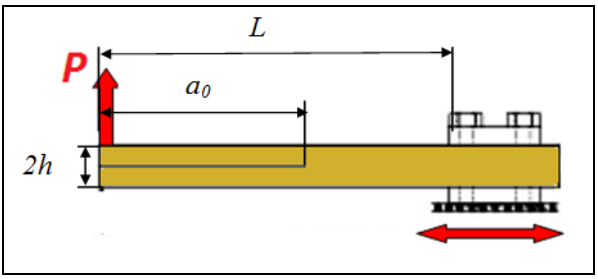

Fig. 1 Specimen in MMF configuration

The elastic properties of the studied materials, E_{11}, E_{22}, G_{12}, and ν_{12}, were determined from traction tests on specific samples , and they are given in table 2.

Table 2 Interface properties for Glass/polyester

Material	E_{11} (GPa)	E_{22} (GPa)	G_{12} (GPa)	ν_{12}
Satin	21,21	15,74	7,16	0,12
Taffetas	17,3	17,3	7,52	0,15

3 Experimental Set-Up and Testing Procedure

The mixed mode flexure MMF test is depicted schematically in Fig. 1. In this test, only one arm of the specimens is loaded while the other is free (Fig. 2).

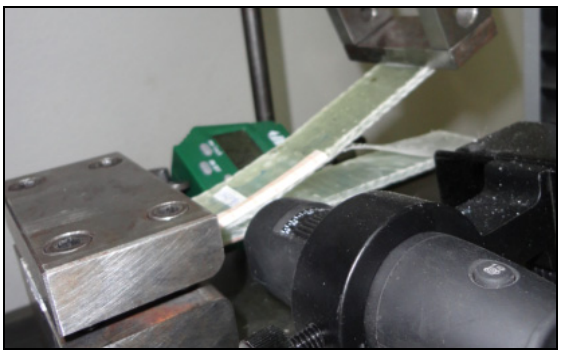

Fig. 2 MMF tests in the deformed configuration

The tests were performed using computer-controlled testing machine at 2 mm/min constant displacement rate which respect the standards recommends; rate between 1 and 5 mm/min. The displacement of the upper cross-head is saved with the corresponding load in the computer by means of UTMII Software.

Insize camera microscope system is used to follow crack propagation. The edges of the specimens are marked 1 mm apart from each other to detect a non-uniform crack front resulting from non-uniform loading. During tests specimens are clamped in a support that can slide in the longitudinal direction (Fig. 3).

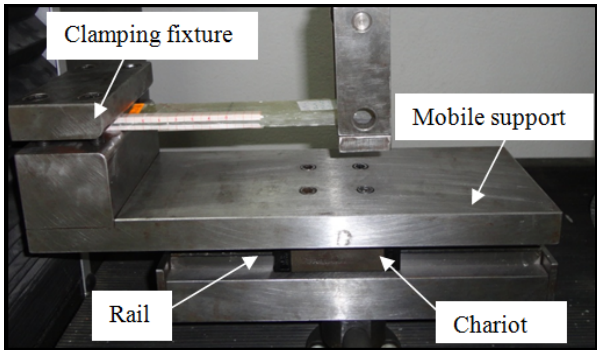

Fig. 3 Photography of the MMF clamping fixtures used in the experiments

4 Results and Discussion

Fig. 4 and Fig. 5 show the load displacement curves from the MMF tests for balanced and unbalanced woven fabrics.

It revealed initially a linear behavior after which the crack initiate, and then the crack propagate. Crack initiation of the remaining specimens was detected by an audible crack after which the two woven fabrics showed a gradual force drop.

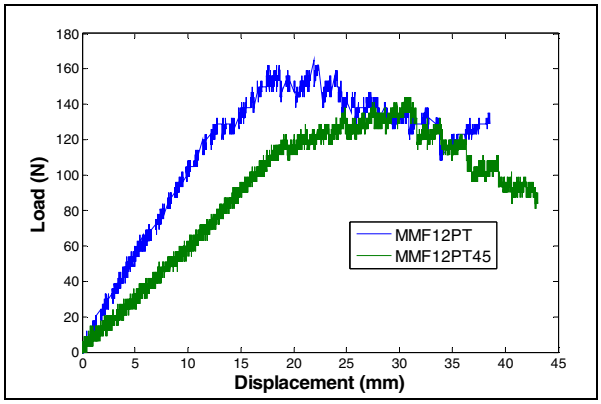

Fig. 4 Load displacement curves for balanced specimens

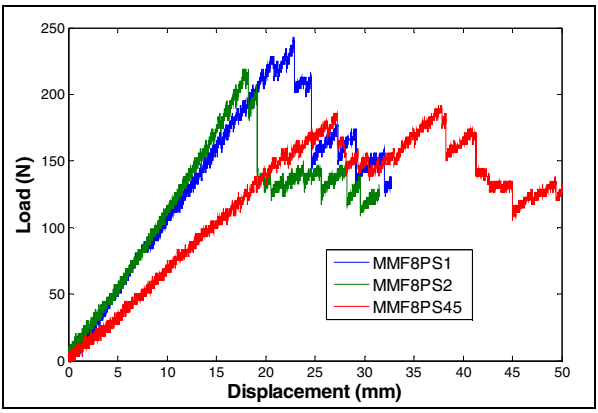

Fig. 5 Load displacement curves for unbalanced specimens

Critical energy release rate G_{tc} is the main parameter that can be used to assess damage process in composite structures after delamination event. However, the fracture toughness G_{tc} can be defined as the critical value of energy allowing crack propagation which can be calculated from load-displacement curves.

According to the Modified Beam Theory (MBT), the mode I and mode II energy release rate components as functions of the applied load can be obtained as (Williams 1989).

$$G_I = \frac{3P^2\left(a+\chi_I h\right)^2}{b^2 E_{11} h^3} \tag{1}$$

$$G_{II} = \frac{9P^2\left(a+\chi_{II} h\right)^2}{4b^2 E_{11} h^3} \tag{2}$$

Where P is the applied load, a is the instantaneous crack length, b is the width, $2h$ is the nominal thickness, E_{11} is the elastic module of the material and χ_I and χ_{II} are the correction crack length factors which can be calculated as (Kinloch et al. 1993) and (Robinson and Hodgkinson 2000).

In practice, it is preferable to evaluate the fracture toughness by the propagation value because the initiation value of the fracture toughness depend on the starter film thickness and with the location of the edge of the film in woven fabrics composites For this experiment, the fracture toughness will be presented by the mean propagation value. Data points from fracture toughness experiments were used to construct a delamination resistance curve (R-curve) illustrated in Fig. 6 and Fig. 7, which present the evolution of fracture toughness (G_I) versus crack length (a), where G_I is the sum of G_I and G_{II}.

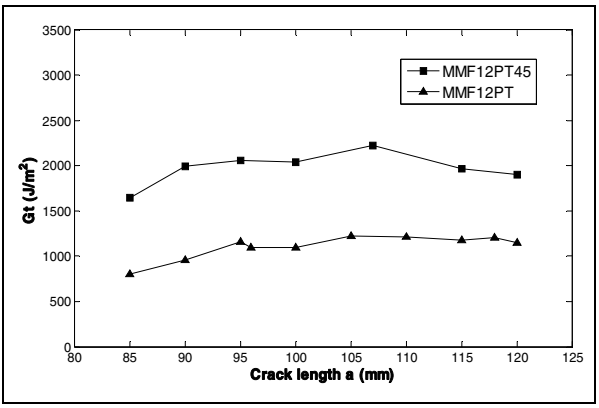

Fig. 6 R-curves for balanced specimens

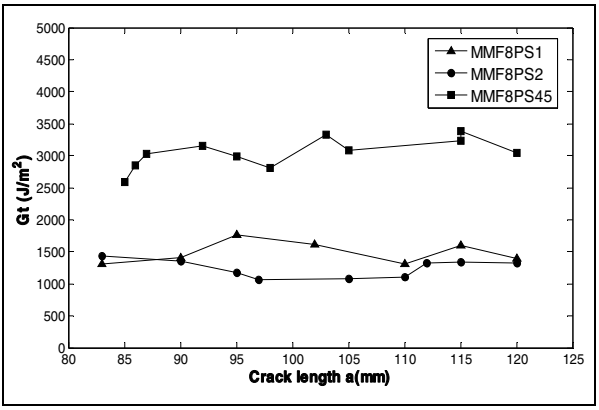

Fig. 7 R-curves for unbalanced specimens

From the MMF test results, the total energy release rate G_{tc} is given by the mean value which is indicated in table 3.

Table 3 Mean values of total energy release rate for satin and taffetas interfaces

G_t (J/m^2)	0°/90°	90°/0°	+45°/-45°
Satin	1573	1319	3227
Taffetas	1170	1170	2092

The critical total energy release rate G_{tc} values are nearly the same for 0°/90° and 90°/0° ply orientation in balanced and unbalanced specimens, but for +45°/-45° ply orientation the two materials present a resistance to delamination more important than the cases of 0°/90°or 90°/0°. This difference is more important for

the satin reinforcement than the taffetas. When the interply angle, θ, was varied from 0° to 90°, the mixed mode fracture toughness exhibited significant sensitivity. The mean interlaminar fracture toughness values are presented in Fig. 8. We remarked that at +45°/-45° ply orientation, the G_t values was about the twice that of 0°/90°or 90°/0° for the two types of woven fabrics.

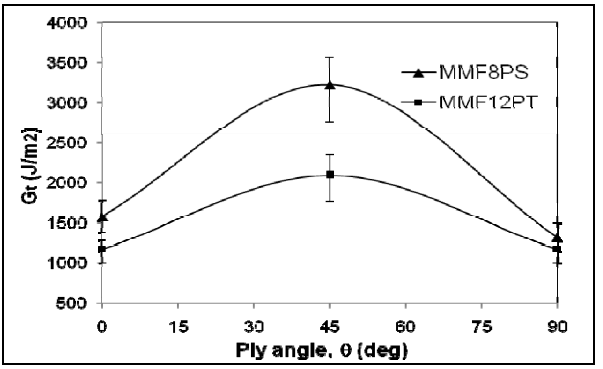

Fig. 8 The evolution of fracture toughness with ply orientation

The empirical functions reflecting the evolution of the total energy release rate are as follow:

$$G_t = -0.325\theta^2 + 29.25\theta + 1170 \quad \text{for balanced specimens} \tag{3}$$

$$G_t = -0.99\theta^2 + 89.88\theta + 1559 \quad \text{for unbalanced specimens} \tag{4}$$

5 Conclusion

The influence of weave structure and ply orientations on the crack growth behavior has been investigated in balanced and unbalanced thick E-glass/polyester woven fabric composite laminates. An experimental study has been carried out on the unbalanced woven fabrics: 4-harness satin wave and balanced woven fabrics: Taffetas under mixed mode l+II delamination tests (MMF tests). These tests have enabled the growth of intralaminar cracks, and the initiation of interlaminar damage on these types of woven fabrics taking into account the influence of ply orientation. The results suggest that the two woven fabrics show very similar G_t values for 90°/0° and 0°/90° ply orientations. For the two woven fabrics in 45°/-45° orientation, the fracture toughness is more important than the cases of 0°/90° and 90°/0°. So the woven fabrics exhibited significant sensitivity to ply orientation.

References

ASTM D5528. Test method for mode I interlaminar fracture toughness of unidirectional Fiber-Reinforced Polymer Matrix Composites. Annual Book of ASTM Standards ; 15.03. ASTM Int., W. Conshohocken, PA

Blackman, B.R.K., Brunner, A.J., Williams, J.G.: Mode II fracture testing of composites: a new look at an old problem. Eng. Fract. Mech. 73, 2443–2455 (2006)

Brunner, A.J., Blackman, B.R.K., Davies, P.: A status report on delamination resistance testing of polymer-matrix composites. Eng. Fract. Mech. 75, 2779–2794 (2008)

Benzeggah, M.L., Gong, X.J., Roedlandt, J.M.: A mixed mode delamination specimen and its finite element analysis. In: ICCM7 China 210 (1989)

Davies, P.: Comportement en délaminage des matériaux composites à matrice thermoplastiques. Dissertation, UTC (1987)

Hiley, M.J.: Delamination between multi-directional ply interfaces in carbon-epoxy composites under static and fatigue loading. In: Williams, J., Oxford, P.A. (eds.) Fract. Polym. Compos. Adhes., vol. 27, pp. 61–72 (2000)

Hashemi, S., Kinloch, A.J., Williams, J.G.: The effects of geometry rate and temperature on the mode I mode II and mixed-mode I/II interlaminar fracture of carbon-fibre poly (ether keton) composites. J. Compos. Mater. 24, 918–956 (1990)

Choi, N.S., Kinloch, A.J., Willims, J.G.: Delamination fracture of multidirectional carbon-fiber/epoxy composites under mode I, mode II and mixed mode I/II loading. J. Compos. Mater. 33, 73–100 (1999)

Andersons, J., König, M.: Dependence of fracture toughness of composite laminates on interface ply orientations and delamination growth direction. Compos. Sci. Technol. 64, 2139–2152 (2004)

Kotaki, M., Hamada, H.: Effect of interfacial properties and weave structure on mode I interlaminar fracture behavior of glass satin woven fabric composites. Comp. Part A 28A, 257–266 (1997)

Solar, M.A., Belzunce, F.J.: Fracture toughness and R-curves of glass fibre reinforced polyester. Compos. 20(2), 120–124 (1989)

Xu, Y., Zhang, W., Bassir, D.: Stress analysis of multi-phase and multi-layer plain weave composite structure using global/local approach. Compos. Struct. 92, 1143–1154 (2010)

Duplessis, et al.: Intralaminar and interlaminar damage in quasi-unidirectional stratified composite structures: Experimental analysis. Compos. Sci. Technol. 70, 1504–1512 (2010)

Williams, J.G.: Fracture mechanics of anisotropic materials. Application of Fracture Mechanics to Composite Materials 6, 3–38 (1989)

Kinloch, A.J., Wang, Y., Williams, J.G., Yayla, P.: The mixed mode delamination of fiber composite materials. Compos. Sci. Technol. 47, 225–237 (1993)

Robinson, P., Hodgkinson, J.M.: Interlaminar fracture toughness. In: Hodgkinson, J.M. (ed.) Mechanical Testing of Advanced Fiber Composites, pp. 170–210. Woodhead Publishing, Cambridge (2000)

Experimental Implementation of the Multipoint Hydroforming Process

Naceur Selmi and Hédi Belhadjsalah

Mechanical Engineering Laboratory (LGM),
National Engineering School of Monastir (ENIM),
University of Monastir, Avenue Ibn El Jazzar 5019 Monastir, Tunisia
naselmi2002@yahoo.fr,
hedi.belhadjsalah@enim.rnu.tn.mail

Abstract. The process of flexible hydroforming is a combination be-tween the hydroforming and the multipoint flexible forming, which allows a synergy of the advantages of two processes. On one hand, the hydroforming process allows a contribution in the flexibility by replacing one of two shaping tools by a fluid, on the other hand, the multipoint flexible forming, allows modifying freely the final shape with its reconfigurable tool, constituted by a matrices of adjustable punch elements. This innovative process presents a potential interest by accumulating at once the advantages of hydro-forming and flexible multipoint hydroforming. The purpose of this paper is to present the process review and its experimental implementation to highlight the contribution in flexibility and to validate the feasibility of the multipoint flexible hydroforming and its ability to produce of complex metal sheet part with improved quality.

Keywords: Hydroforming, Multipoint, Flexibility, Sheet metal forming.

1 Introduction

Advanced industries are called to produce lighter and more complex sheet met-al constituents with improved structural strength, and thinner profiles, with improved quality, as well as lower tooling costs, more polyvalent and resourceful forming tools, especially for industries with small or medium lot-size and with great varieties (aerospace industry, shipbuilding).

To satisfy these requirements, several innovative and flexible processes had been developed these last decades, among these processes, the hydroforming and the multipoint flexible forming are the processes which carry most of interests. The hydroforming process is attractive compared with conventional solid die forming processes, the basic advantage consist to suppress one of two forming tools (punch or die), which is replaced by hydraulic pressure.

An increasing interest was observed for the hydroforming process, various versions, were progressively proposed, for the production of lighter structures and complex forms

The multi-point flexible forming (MPF) is another recent flexible technique for manufacturing three-dimensional sheet metal parts. In this process, the sheet metal

M. Haddar et al. (Eds.): *Design and Modeling of Mechanical Systems*, LNME, pp. 477–484.
DOI: 10.1007/978-3-642-37143-1_57

can be formed between a pair of opposed matrices of punch elements in-stead of the conventional fixed shape die sets. The punches elements are con-trolled simply, by adjusting the height of the elements of both upper and the lower matrices, different curved surfaces can be created (figure 1). By using this technolgy, production of parts with different geometries will be possible just by using one same die set that lead to great saving in time and manufacturing cost specially in the field of small batch or single production.

Various versions of multipoint flexible forming were elaborated particularly in the naval and aerospace field, the investigations of Robert C. SCHWARZ [1], Ming-Zhe Li [2], [3], Yan [4], Zhong-Yi [5] and Hwang [6], concerned the flexible multipoint forming and its adequacy for a production of lighter structures and complex forms. However in multipoint processes, the direct contact between the blank and punch elements generates a severe dimpling on the final part. The insertion of elastomeric sheets (interpolator), between dies and blank, has been an efficient solution to attenuate dimpling severities [7, 8, 9, and 10].

Multipoint sandwich flexible forming (MPSF) (figure 2), has been another in-innovative version of the multipoint forming in this process, the movable multipoint die is substituted by a stack of elastomeric sheets, and one thick die sheet is inserted between lower multipoint die and interpolator to re-duce dimples [7, 8, 9], but it is often necessary to adapt the shape of this stack to the depth of the part to be produced.

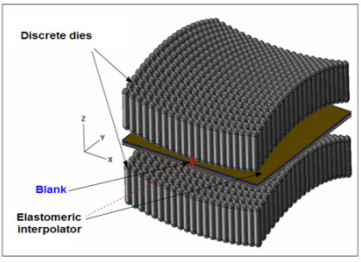

Fig. 1 Multipoint forming process

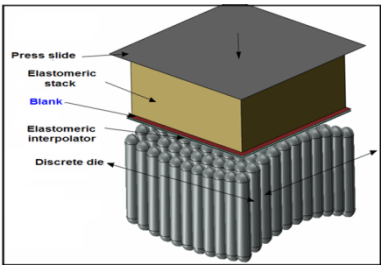

Fig. 2 Multipoint sandwich flexible forming (MPSF)

2 Presentation of the Process

The multipoint flexible hydroforming (MPFH), object of this paper, is an original process which combines the hydroforming and the multipoint flexible forming, to obtain a synergy of the advantages of both processes. It allows to keep the whole flexibility of the basic multipoint flexible forming (with two multipoint discrete dies), by using uniquely one multipoint die to perform completely the final part shape, the second multipoint die is advantageously substituted by the fluid pressure, which can be applied via an elastomeric membrane (Figure 3).

2.1 Testing Set Up of the Multipoint Flexible Hydroforming

To prove the feasibility and to carry out a valuable experimental investigation of the multipoint flexible hydroforming, an experimental prototype was designed and realized. The testing assembly of the process includes three basic parts.

The hydroforming pressure, produced in the upper module, is applied, via the elastomeric medium, to the metal sheet workpiece, located at the middle module, to be conformed to the shape of the multipoint die (fig.4) in the lower module.

The upper fluid cell module constitute the hydroforming tool; it performs the first aspect of process flexibility the second one is performed by the reconfigurable multipoint forming die in the lower module.

During the forming phase of the metal sheet between the last two forming modules, upper's or highest punch elements extremities, entering firstly in contact with formed sheet, produce extremely concentrated pressure that usually initiates forming dimples in the contacted sheet. To attenuate dimpling phenomena, the formed sheet is separated from multipoint tool by a medium sheets stack generally called interpolators. Through the thicknesses of sheet stack, localized high pressures are rearranged, the maximum of concentrated loading is moved from worked piece interface to that of interpolator stack, and local pressure loading is then better distributed at the worked sheet interface.

The basic object of relocation of the concentrated contact loading is to moderate severities of the load boundary conditions that lead to better regularity and less dimpling of final part profile.

Considering the phenomena complexity, of multiple interactions between multi-point tools, interpolators and work piece for the multipoint flexible hydroforming process, analysis are focused, in recent investigations[12,13,14], on the most influent parameters on the quality of the final product. It emerges essentially, that an increase of the punch elements density, the thicknesses of the initial blank and the interpolator, improve the final part quality. The object of this paper consist to prove the feasibility and to carry out a valuable experimental investigations of the multipoint flexible hydroforming, and to highlight the ability of this process in flexibility and quality upgrading of final product.

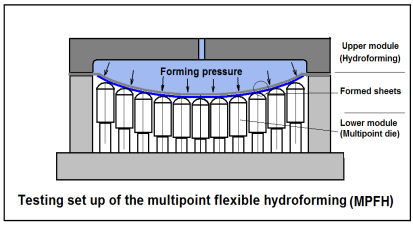

Fig. 3 Multipoint flexible hydroforming process

Fig. 4 Multipoint die set up for (MPFH)

3 Finite Element Analysis

ABAQUS/Explicit was used for Finite element analysis of the multipoint flexible hydroforming process presented in figure 5; the final part shape to be formed was a double curved shell with different depth, the shape function of desired final shape can be written in Cartesian coordinate system as follows:

$$z(x,y) = \sum_i \sum_j a_{ij}.(x^i.y^j). \quad (1)$$

For examples:

$$z = a.(x^2 + y^2): \text{Parabolic shape.} \quad (2)$$

The discrete die size was 100 mm x 100 mm, the density of punch elements setting was (11x11 and 21x21), many cases of blank and interpolator sheet thicknesses was used for analysis. The sheet stack (interpolator and blank) are simply positioned directly on the punch element matrix, as seen in figure 5, with free edges conditions. The shape function (Analytical field) law can be settled before forming step of the process (fixed multipoint method) or progressively modified, throughout the forming process (progressive method). The fluid pressure was applied on the upper side of the blank in a linear smooth load path. The elasto-plastic material model was used for deformable steel sheets (Stainless steel material (E = 210 000 Mpa, v =0.3) with strain-stress curve presented in figure 6. The Mooney–Rivlin hyperelastic material model was used to elastomeric interpolators, this model was built from the uni-axial test data presented in figure 7 from the reference [7]. Dynamic/explicit method was used for the simulation, the deformable shell parts instances (blank and interpolator) are meshed in S4R elements, the rigid instances (punch element matrix etc.) are meshed in elements R3D4. Coulomb law was used with friction coefficient of 0.1 for general contact interaction between constituents of the model.

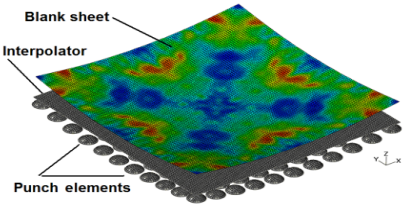

Fig. 5 Geometry model of Multipoint flexible hydroforming process

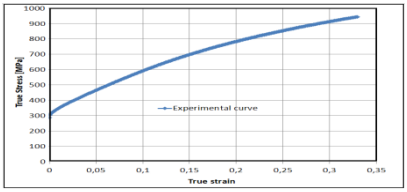

Fig. 6 Stress–strain curve of Stainless steel

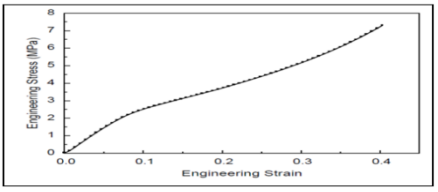

Fig. 7 Uniaxial data of hyperelastic material

4 Results Discussions

4.1 Effect of the Process Parameters

4.1.1 Effect of the Sheet Thicknesses

The effect of blank thickness can be observed from the simulation results (Fig. 8), for lower thickness, all surface of final part is severely dimpled and the increase of thickness reduces dimpling and improves the profile regularity and the surface quality. This effect is confirmed by experimental way (fig. 9), by producing many doubly curved parabolic (shape part eq.(2)) for aluminum alloy sheet part produced, severe dimpling effect is observed for thin sheet (0.5 mm) with irregular profile and buckled edges, for relatively thicker sheet (2mm) successful sheet part is obtained with more regular profile with no significant dimples.

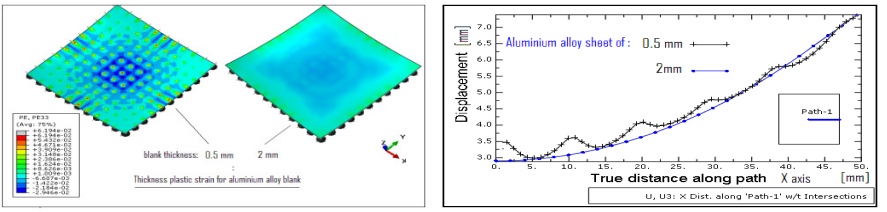

Fig. 8 Dimples: Effect of blank thickness

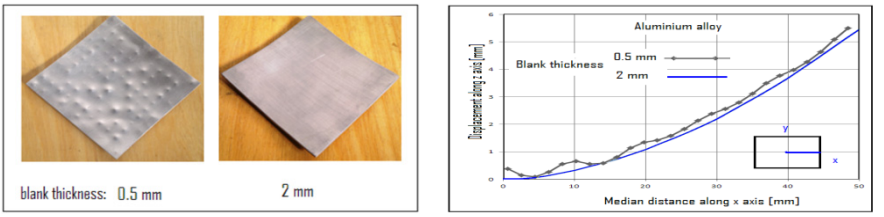

Fig. 9 Dimples: Effect of blank thickness (experimental results for 0.5mm and 2mm)

4.1.2 Punch Elements Density

Basic set up of multipoint die with 121 punch elements (11x11) was used for simulation and experimental investigations carried out in this work, buckling phenomena on the median edges of formed blank are occurred for the 1mm initial blank and 1mm elastomeric interpolator thicknesses, the increasing of punch density to 441 punch elements (21x21) (figure 10) reduces buckling, residual stresses and improves profile regularity of final product, but increases largely the complexity of multipoint tool adjusting.

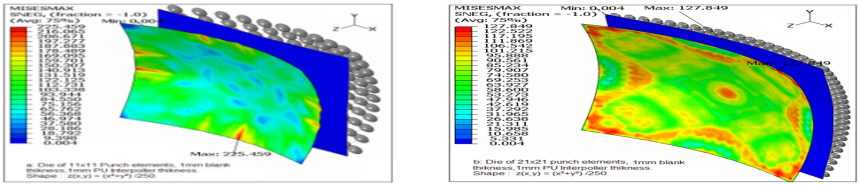

Fig. 10 Dimples and edge buckling: Effect of punches density

5 Interest of the Metallic Die Sheet

The motivation here is to highlight ability of specific set up of the process, in flexibility and quality upgrading of final product, especially for thinner metal sheet. In this new version we will insert a metallic thick die sheet (fig.11), instead of the elastomeric interpolator conventionally inserted between multipoint die and blank side, the combination of both methods can be considered also.

As illustrated in last results (figure 8 and 9), it was observed, more regular profiles and less sensitivity to edge buckling and dimpling, for thicker blanks. In other terms, for a given deep and punch density, thin blank is more sensitive for edge buckling and dimpling, it have tendency to flow around punch tip curvatures, and elastomeric interpolator have not sufficient stiffness to filter punch contact singularities. The basic idea is to move the boundary conditions severities, from soft elastomeric to thick and stiff metallic medium, that acts as a stiff interpolator filter towards contact singularities and improves ability to form a thin shell final part as seen in simulations results (fig.12).This method is validated by experimental way as illustrated in (fig.13), the aluminum alloy final product of 0.5mm is severely dimpled (without or with elastomeric interpolator), with 2 mm aluminum die sheet, better quality of outer edges and suppression of dimples are obtained fig . This confirm that a using of metallic die sheet medium is largely more relevant for thinner sheet product than increasing of punches density or elastomeric thickness

The stainless steel final products of (without or with elastomeric interpolator of 4 mm thickness,) are significantly dimpled and buckled at the outer regions), better quality of outer edges and suppression of dimples are obtained with an aluminum alloy die sheet medium of 2mm (fig.14).

Instead of request of costly increased number of punches for relatively thinner blank, the use of metallic sheet media is better and efficient way to eliminate significantly dimpling and edge buckling with reasonable density of punch elements.

The metallic sheet medium can be considered as a fast rigid die, formed (in situ) by the multipoint hydroforming tools, only in one step, it can be used for many thin shell formed parts, the shape can be readjusted to take in account the spring back or to reuse it another final part shape. The metallic medium die can be made in low cost steel or aluminum alloy for weightiness consideration.

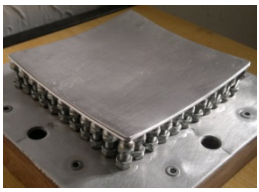

Fig. 11 MPFH with metallic medium

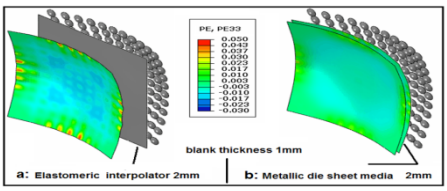

Fig. 12 a: Elastomeric interpolator, b: Metallic media

Fig. 13 Aluminum alloy products: left: elastomeric interpolator, right: metallic media

Fig. 14 Stainless steel product: left: With elastomeric interpolator, b: With metallic media

6 Conclusions

The multipoint flexible hydroforming process (MPFH) combines adequately the hydroforming and multipoint flexible forming processes, to obtain a synergy of the advantages of both processes. The feasibility of the process is validated by the prototype designed and realized by authors and the results of preliminary experimental works are in good agreement with previous numerical analysis of the process, successful doubly curved shell product was obtained by the process.

This process is an accurate and low cost technology with great saving in time manufacturing especially in the field of fast prototyping, small batch or single production.

Using of metallic sheet media is more efficient way to eliminate dimpling and edge buckling and to extend flexible multipoint hydroforming quality for thin sheet products with reasonable density of punch elements, the result is resourceful process with reduced number of components.

References

[1] Schwarz, R.C., Nardiello, J., Paparazian, J.M.: Suppression of dimpling in sheet metal parts formed on discrete tooling. In: Recent Advances in Experimental Mechanics, pp. 757–768. Kluwer Academic Publishers (2002)

[2] Li, M.-Z., Liu, Y., Su, S., Li, G.: Multi-point forming: A flexible manufacturing method for a 3-d surface sheet. Journal of Materials Processing Technology 87, 277–280 (1999)

[3] Li, M.-Z., Cai, Z.-Y., Liu, C.-G.: Flexible manufacturing of sheet metal parts based on digitized-die. Robotics and Computer-Integrated Manufacturing 23, 107–115 (2007)

[4] Yan, A.-M., Klappka, I.: Spring-back in stretch forming process of aero-nautic panel production by finite element simulation. Int. J. Mater. Form., (suppl. 1) 201–204 (2008)

[5] Cai, Z., Li, M.: Optimum path forming technique for sheet metal and its realization in multi-point forming. Journal of Materials Processing Technology 110, 136–141 (2001)

[6] Hwang, S.Y., Lee, J.H., Yang, Y.S., Yoo, M.J.: Springback adjustment for multi-point forming of thick plates in shipbuilding. Computer-Aided Design 42, 1001–1012 (2010)

[7] Zhang, Q., Dean, T.A., Wang, Z.R.: Numerical simulation of defor-mation in multi-point sandwich forming. International Journal of Machine Tools & Manufacture 46, 699–707 (2006a)

[8] Zhang, Q., Wang, Z.R., Deana, T.A.: Multi-point sandwich forming of a spherical sector with tool-shape compensation. Journal of Materials Processing Technology 194, 74–80 (2007b)

[9] Zhang, Q., Wang, Z.R., Dean, T.A.: The mechanics of multi-point sandwich forming. International Journal of Machine Tools & Manufacture 48, 1495–1503 (2008c)

[10] Cai, Z.-Y., Wanga, S.-H., Li, M.-Z.: Numerical investi-gation of multi-point forming process for sheet metal: wrinkling, dimpling and springback. Int. J. Adv. Manuf. Technol. 37, 927–936 (2008)

[11] Cai, Z.-Y., Wang, S.-H., Xu, X.-D., Li, M.-Z.: Numeri-cal simulation for the multi-point stretch forming process of sheet metal. Journal of Materials Processing Technology 209, 396–407 (2009)

[12] Selmi, N., BelHadj Salah, H.: Simulation numérique de l'hydroformage à matrice flexible. In: 7éme Journées Scientifiques en Mécanique et Matériaux JSTMM 2010, Hammamet, November 26-27 (2010)

[13] Selmi, N., Bel Hadj Salah, H.: Hydroformage flexible multipoint: Aptitudes aux formes complexes. In: CMSM 2011, Sousse, Mai 31-Juin 1 (2011)

[14] Selmi, N., Bel Hadj Salah, H.: Flexible multipoint hydroforming using metallic sheet medium. In: Second Tunisian Congress of Mechanics, Sousse-Tunisia, March 19-21 (Cotume 2012)

Surface Integrity after Orthogonal Cutting of Aeronautical Aluminum Alloy 7075-T651

Al-Adel Zouhayar, Ben Moussa Naoufel,Yahyaoui Houda, and Sidhom Habib

Mechanical, Material and Processes Laboratory (LR99ES05),
ESSTT, 5, Avenue Taha Hussein 1008,
University of Tunis, Tunis, Tunisia
zouha26@gmail.com

Abstract. In this study, an experimental approach has been developed to predict plastic strain and residual stresses resulting from turning in orthogonal cutting configuration of aeronautical aluminum alloy AA7075-T651. This approach consists in the variation of cutting parameters which are depth of cut and cutting speed to reveal their effect on the micro-hardness, plastic strain and residual stresses. The plastic strain gradient has been obtained by an experimental micro-hardness-strain relationship using a specific tensile sample.

Keywords: Plastic strain, orthogonal cutting, AA7075-T651, residual stress.

1 Introduction

The cutting of aluminum alloys has recently acknowledged appreciable interest owing to their ample application in aerospace and automotive industry (Halley et al. 1999) due to their performance (lightness, good thermal conductivity, high mechanical characteristics…).

For this reason, it is important to study the tool-material interactions under machining conditions which can modify the properties of near surface layers which affect operating performance of workpieces. The workpieces characteristics can be controlled by cutting parameters variation. Many studies have been conducted to inspect the relationships between machining process parameters and surface integrity (residual stresses, plastic strain, phase transformation, work hardening…). However, the effects of machining parameters on the surface characteristics were rarely studied for the case of AA7075-T651 alloy. Campbell et al. (Campbell et al. 2006) studied the microstructural characteristics of AA7075-T651 chips and work pieces produced by orthogonal cutting under different cutting speed (360, 540 and 720 m/min). They found that the cutting speed increases the thickness of deformed layers results in a softening of the machined work piece. However, the effect of machining parameters on residual stresses and plastic strain were not considered. Considering the lack of results it is important to study the effect of machining parameters on the distribution of residual stresses, plastic strain and microhardness in the orthogonal cutting configuration for the 7075-T651 alloy.

M. Haddar et al. (Eds.): *Design and Modeling of Mechanical Systems*, LNME, pp. 485–492.
DOI: 10.1007/978-3-642-37143-1_58

2 Material and Experimental Procedure

2.1 Material

The aluminum alloy AA7075-T651 is an Al-Zn-Mg-Cu precipitation strengthened commercial alloy. T651 tempering process includes solution treatment, stretching and artificially ageing of the material at 120°C for 24h (Park and Ardell 1983).

The sequence of strengthening precipitation for the Al-Zn-Mg alloy is the following:

$$\text{SSS} \rightarrow \text{Guinier-Preston (GP) zones} \rightarrow \eta'(\text{MgZn2}) \rightarrow \eta(\text{MgZn2})$$

The η phase is an incoherent intermediate precipate and has a hexagonal crystal structure, while the η' phase is semi coherent (Thomas and Nutting 1959).

In this experiment, the samples used for cutting tests are disks with a thickness of 15 mm obtained from a bar of AA7075-T651with a diameter of 80 mm.

The mechanical properties, obtained by simple tensile test and the standard chemical composition of the material are given in Tables 1 and 2.

Table 1 Mechanical properties

Parameters	Value
Ultimate tensile stress	622MPa
Yield tensile stress	520MPa
Young's modulus	73GPa
Elongation (%)	9.6
Hardness	180Hv

Table 2 Chemical composition

Si	Fe	Cu	Mn	Mg	Cr	Zn	Ti	Al
0.08	0.17	1.4	0.03	2.7	0.19	6.1	0.2	The rest

2.2 Experimental Set-Up

The orthogonal cutting tests were conducted on a numerical controlled lathe (RealMeca T400), equipped with a piezzo-electric transducer-based type dynamometer type Kistler 9257B (figure 1), using an uncoated carbide tools with a rake angle γ of 0°, a clearance angle α of 7° and a cutting edge radius Rn of 20µm.

The orthogonal cutting tests have been conducted under different cutting speed and depth of cut (Table 3). The cutting and thrust forces measured experimentally for all test conditions are listed in Table 3.

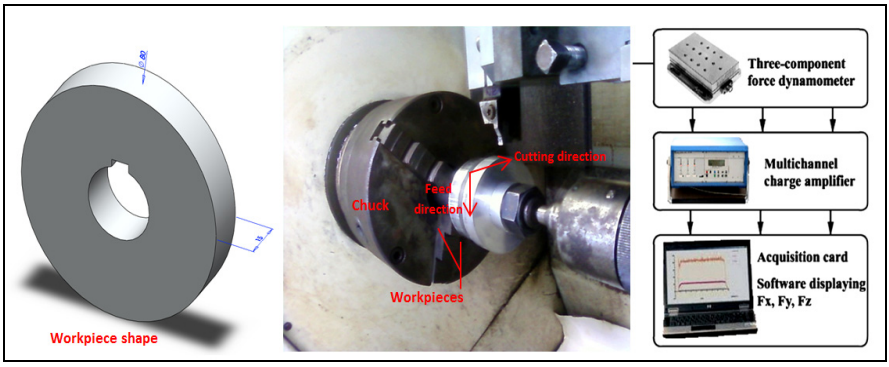

Fig. 1 Experimental setup used for orthogonal turning and cutting force measurement

Table 3 Experimental test conditions

Conditions	1	2	3	4	5	6	7	8	9	10	11	12
Cutting speed (m/min)	200	450	700	950	200	450	700	950	200	450	700	950
Depth of cut (mm)	0.15	0.15	0.15	0.15	0.25	0.25	0.25	0.25	0.35	0.35	0.35	0.35
Cutting force (N)	750	700	630	520	1080	890	620	470	1410	890	580	460
Thrust force (N)	420	380	350	320	520	400	325	290	585	395	310	285

3 Evaluation of the Machined Surface Properties

3.1 Work Hardening

A Shimadzu HMV2000 micro hardness tester is used to quantify the cold work hardening by measuring the variation of micro hardness generated by orthogonal cutting for all cutting condition. The applied force and duration of indentation are 100 gf and 15 s, respectively. Each indentation was well spaced to avert interference between each of them (approximately thirty indentations were done along the profile).

3.2 Microhardness-Plastic Strain Relationship

In order to find a correlation between the micro hardness and the equivalent plastic strain, a specific tensile sample was used. The utility of this specimen is his capability to offers different levels of plastic strain values along the calibrated area at the end of one tensile test. The method used to determine the dimensions of the specific tensile sample is detailed in [Article].

The sample was obtained by milling from the same bar used for cutting tests and electro polished by layers of 50 mm until reaching a homogeneous

micro-hardness of 180 Hv. Before the tensile test, a grid was electro-graved on the tensile sample. The grid's dimensions before and after tensile test were observed by optical microscope and used to calculate the equivalent plastic strain evolution in calibrated zone. After tensile test, the micro hardness in each zone of tensile sample was measured. The level of micro hardness at each point was performed by averaging five measurements.

3.3 Residual Stresses Measurements

In order to evaluate the distribution of residual stresses generated by orthogonal cutting, the hole drilling method was used. This method allows determining the levels of axial and circumferential residual stresses at each depth of machined layer by only one measurement.

4 Results

4.1 Cutting Forces

Both cutting forces and thrust forces increases with increasing of the depth of cut; However they decreases when the cutting speed increase. This is can be explained by the elevation of heat generated in the cutting region due to the increase of the cutting speed.

4.2 Micro Hardness

Micro hardness measurements for all cutting conditions show a decreased hardness at the surface like the example shown on the Figure 4, which gradually increased with distance from the machined surface. Fig.5 shows the effect of machining parameters on the depth of the affected layer.

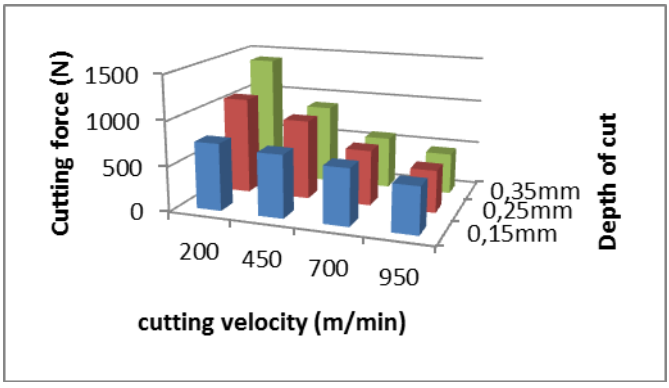

Fig. 2 Effect of machining parameters on the cutting force

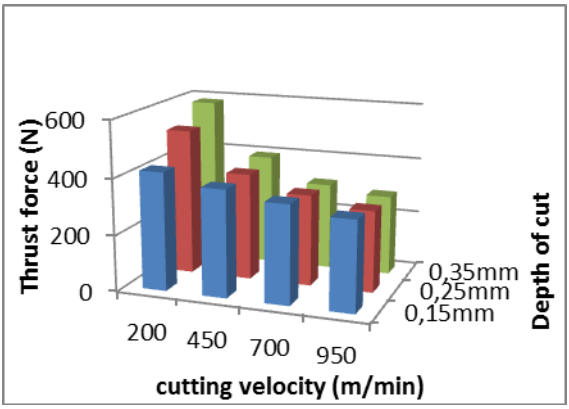

Fig. 3 Effect of machining parameters on the Thrust force

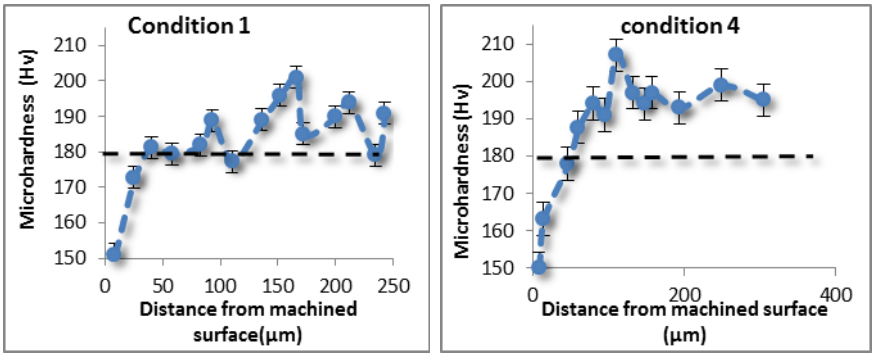

Fig. 4 Examples of microhardness profiles of 7075-T651 alloy

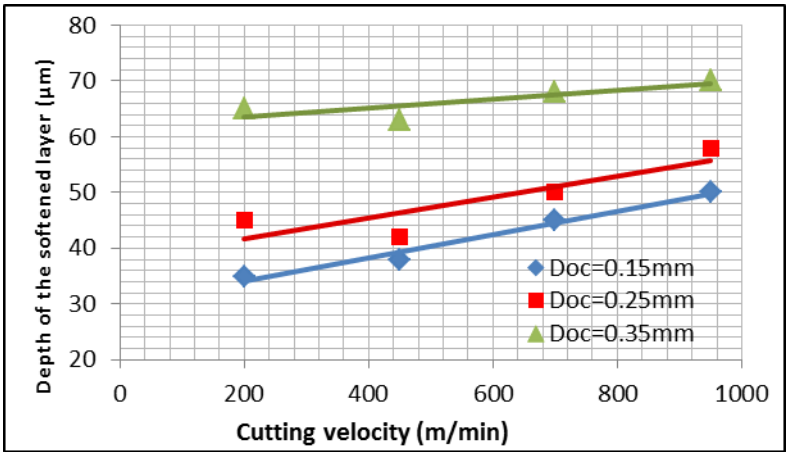

Fig. 5 Effect of machining parameters on the depth of the softened layer

4.3 Plastic Strain

As explained previously, the specific tensile specimen was used to identify a relationship between microhardness and plastic strain for the 7075-T651 alloy (Fig.6). This relationship was used to convert all microhardness measurements of the machining workpieces in plastic strain.

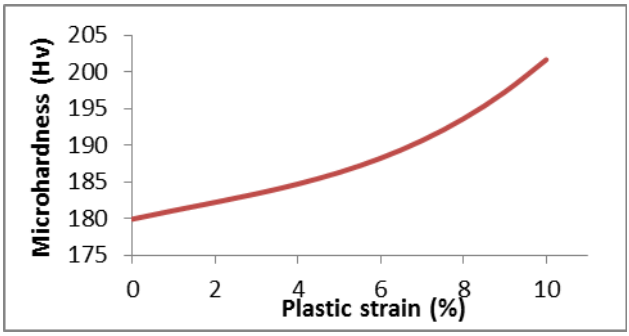

Fig. 6 Microhardness/plastic strain correspondence of the 7075-T651 alloy

Table 4 shows the value of the maximal plastic strain generated by orthogonal cutting. The maximum plastic (εp^{Max}) strain increases with the cutting velocity (Vc) and decreases with the depth of cut (Doc).

Table 4 Maximum plastic strain

Test	1	2	3	4	5	6	7	8	9	10	11	12
εp^{Max} (%)	10	10.04	10.67	11.5	9.18	9.63	10.67	10.04	9.3	3.7	9.65	7.55

4.4 Residual Stresses

To evaluate the effect of the cutting velocity on the distribution of residual stresses (axial and circumferential), three levels of cutting speed are fixed for a depth of cut equal to 0.35 mm. The measurements shows for the three cutting speed (450 m/min, 700 m/min and 950 m/min), the circumferential residual stresses are positive in the surface; however the axial residual stresses are compressive.

These results are in agreement with the incompatibility of plastic strain generated by orthogonal cutting.

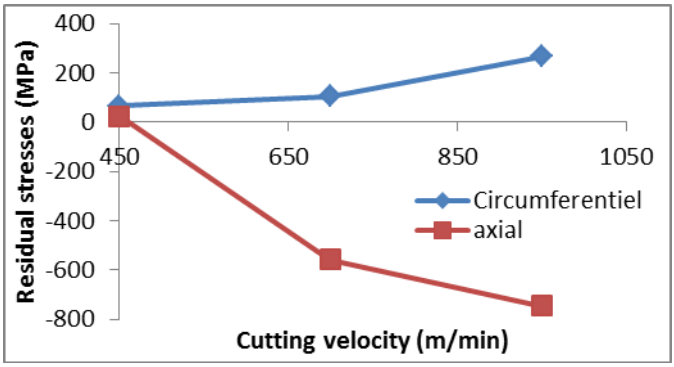

Fig. 7 Effect of the cutting velocity on the distribution of residual stresses

5 Conclusion

The machining of the 7075-T651 alloy induces a softening on the subsurface layer. The depth of this softened layer increases with both cutting velocity and depth of cut. The softening generated by the machining process can be explained by the microstructural changes of the 7075-T651 alloy, the heat generation in cutting region induces a coalescence of $MgZn_2$ precipitates and a restoration by annihilation of dislocations. A micrographic observation can confirm these phenomena. This softening of the machined surface affects the plastic strain and the distribution of residual stresses generated by orthogonal cutting.

The principal results of this experimental study are the following:

- The cutting forces (cutting force and thrust force) decreased with cutting speed and feed (depth of cut);
- The machining (case of orthogonal cutting) induces a softened layer in the superficial layers of the aluminum alloy AA7075-T651;
- The depth of the softened layer increases by increasing the cutting speed and feed;
- The results of residual stresses confirm the softening introduced in the surface layers by turning in the configuration of orthogonal cutting of the aluminum alloy 7075-T651.

Acknowledgements. The authors gratefully acknowledge the helpful comments and suggestions of the reviewers, which have improved the presentation.

References

(Halley et al. 1999) Halley, J., Helvey, A., Smith, K.S., Winfough, W.R.: Proceedings of the 1999 ASME Design Engineering Technical Conference, DETC99/VIB-8057 (1999)

(Campbell et al. 2006) Campbell, C.E., Bendersky, L.A., Boettinger, W.J., Ivester, R.: Microstructural characterization of Al-7075-T651 chips and work pieces produced by high-speed machining. Materials Science and Engineering: A 430(1-2, 25), 15–26 (2006), doi:10.1016/j.msea.2006.04.122, ISSN 0921-5093

(Park et Ardell 1983) Park, J.K., Ardell, A.J.: Metall. Trans. A 14, 1957–1965 (1983)

(Thomas and Nutting 1959) Thomas, G., Nutting, J.: J. Inst. Met. 87, 81–90 (1959)

Buckling of Laminated Composite Shells of Pipe Cracks

Benyahia Hamza and Ouinas Djamel

Laboratory of Numerical Modeling
and Experimental Mechanics Phenomena,
University Ibn Badis Mostaganem
BP 188 27000 Algeria
h_benyha@yahoo.fr,
douinas@netcourrier.com

Abstract. The behavior of composite cracked pipes under the effect of buckling is explored by performing a linear buckling analysis using the finite element method. The pipe is pressed under compression in the presence of cracks longitudinal, radial and inclined relative to the horizontal. The results indicate that increasing the radius of the pipe conduit to the reduction of buckling parameter and the maximum values are obtained for the lowest fiber orientations. The maximum stresses are obtained for the radius of 400mm. Moreover, the increase in the number of plies in composite pipe leads to the increase of the parameter buckling. The size of the crack, its orientation and position in the pipe are identified.

Keywords: Buckling, and crack pipe, Concentration of constraints, Finite Element Analysis.

1 Introduction

International competition and the evolution of the means of production in the engineering industry results impose increasingly high where new technologies and composite materials are key points for success [1]. Composite materials are widely used in industrial applications and are both in the field of transport (aviation, aerospace, marine, rail ...) and in the hydraulic field as they achieve performance than conventional materials can not provide [2].

The transition metal materials for composite materials generates significant costs but it is actually an investment in the medium and long term. The inhomogeneity and anisotropy of composite damage mechanisms make their more numerous and more complex. Composites are obtained by blending different elementary constituents with different macroscopic behaviors. The choice of these components can improve the performance of the final material, to meet a specific need (lightweight, stress resistance, good resistance to fatigue ...). In a composite

M. Haddar et al. (Eds.): *Design and Modeling of Mechanical Systems*, LNME, pp. 493–501.
DOI: 10.1007/978-3-642-37143-1_59

structure, we can see damage appear consists of micro-debonding and micro-cracks, fold-outs, breaks fibers and matrices, debonding of the interface ....

The search operation on the buckling of pipes into the broader context of "smart" materials and composite structures, is interested in, especially, the laminated composite structures (cylindrical shells) whose behavior is varied so sensitive mechanical stress, which could not be achieved with conventional materials pipes structures have a tendency to buckle under the application of axial loading. Buckling is defined as the sudden deformation (structural collapse) that occurs when the energy (axial) deformation of the membrane stored by the structure is converted into bending energy without changing external forces. Buckling can also occur before the failure of the material due to stresses. It can occur on the entire structure or locally [4].

Buckling of pipes is a sensitive phenomena can occur at any time, but how detected?

2 Presentation of the Problem of Buckling

The layered composite material of a pipe contains a discontinuous phase reinforcing stiffest and stronger than the continuous phase of the matrix. Its mechanical properties result essentially from:

- The nature of the constituents and their properties.
- The reinforcement geometry (shape, slenderness ratio), distribution (allocation, orientation), and its concentration (volume or mass).

The search for new composite materials more efficient for space applications, aeronautics and hydraulics caused in recent years, a growing interest on the part of industry. Often asked more and more manufacturers of pipes increased their resistance to stress thermal and mechanical properties to which they are subjected during commissioning (buckling, impact, abrasion, cracks, breaks) [3]. In this paper, we are interested in the linear analysis by the finite element method to improve the behavior of these materials, the trend is on the one hand, to adopt the solicitation under compression in the presence of cracks and on the other hand the thickness and fiber orientation of the pipe.

One of the advantages of laminates is the ability to orient the fibers in directions adapted to the stresses imposed on the structure. The design of a laminate structure thus requires the choice of materials, orientations of the fibers and the arrangement of the folds (folds of stacking sequence given of inclination).

3 Geometric Models of Pipe

3.1 Pipe without Crack

In this model, we consider a cylindrical shell laminated composite (***AS4/PEEK***) with 12 plies $(\theta/-\theta)_{12}$, the thickness of plies ep = 0.127mm and length H = 6000mm. the usefulness of this study is to see the effect of the fiber orientation of the composite and the variation in the diameter of the buckling coefficient.

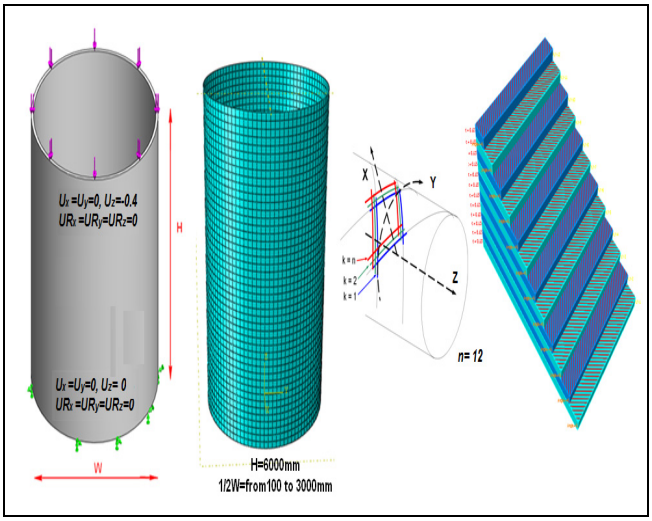

Fig. 1 Geometrical model, mesh and number of plies of a pipe

The pipe is subjected to compression in the direction perpendicular to the interface under the applied stress. In a first approach we consider the geometric model of the pipe without cracking (Fig. 1). In the second, it provides for the existence of a crack in deferent sizes and positions (Fig. 2).

Table 1 Mechanical characteristics of the material

Properties	*E1(MPa)*	*E2(MPa)*	*ν12*	*G12(MPa)*	*G13(MPa)*	*G23(MPa)*
AS4/PEEK	234000	14000	0.2	2750	2750	5600

In the calculation we used the commercial code ABAQUS finite element 6.11. We used 14 850 quadrilateral elements with a refined mesh near the crack as shown in (Fig.2). The resolution was made in a state of plane stress. The mechanical properties of the material studied are shown in Table 1.

3.2 *Pipe with Crack*

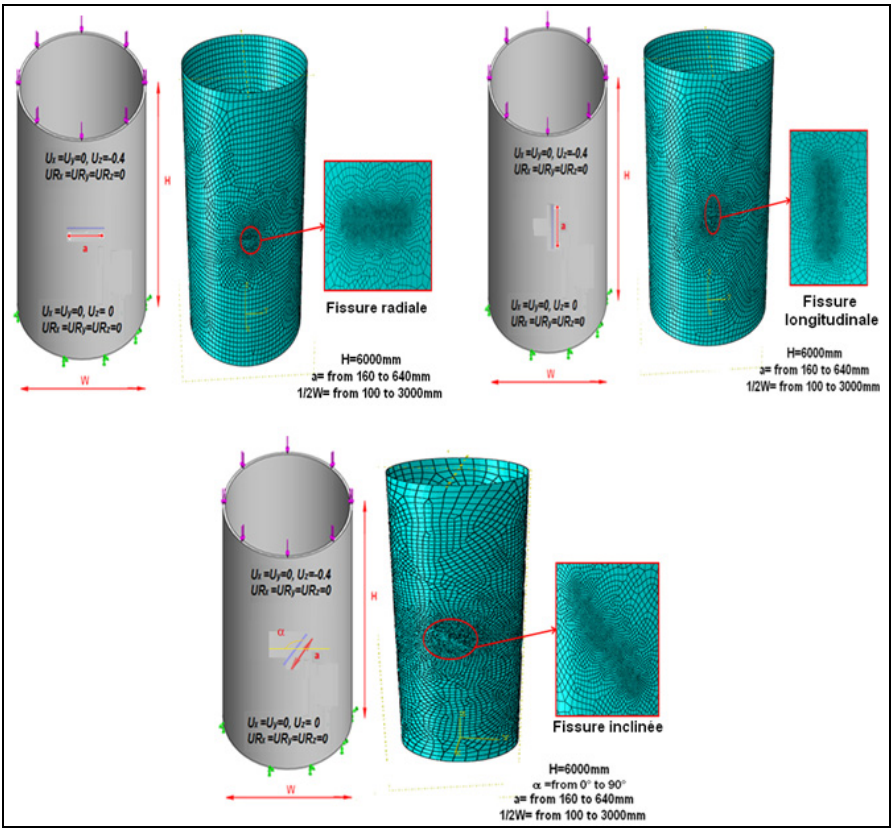

Fig. 2 Geometric model and the mesh pipe with crack

4 Influence of Fibre Orientation on the Coefficient and Buckling Stress Von Mises

The Fig.3 shows the variation of coefficient λ as a function of the fiber orientation θ of the composite material for different diameters of pipe. It is clear that the increase of the radius of pipe leading to the buckling coefficient reduction.

And the maximum values are obtained by the lowest fiber orientation in a range varying from 0 ° to 20°.

The constraint augment progressively with the increase of the radius of pipe up to a peak recorded at R = 400mm, beyond this value, the stress decreases Fig. 4.

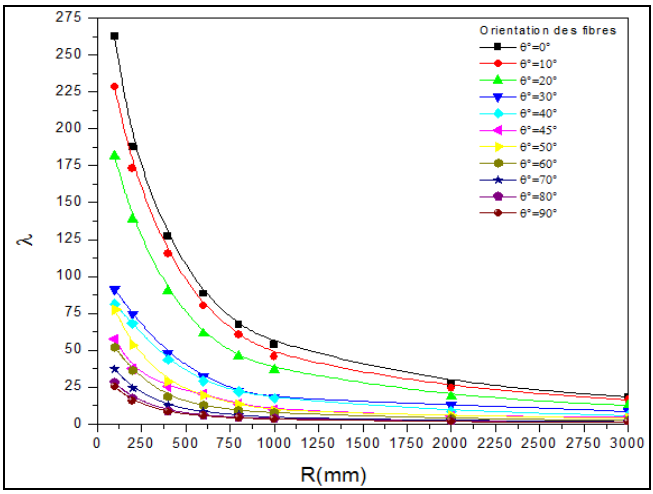

Fig. 3 Effect of the fiber orientation : (θ/–θ):λ ∱(R)

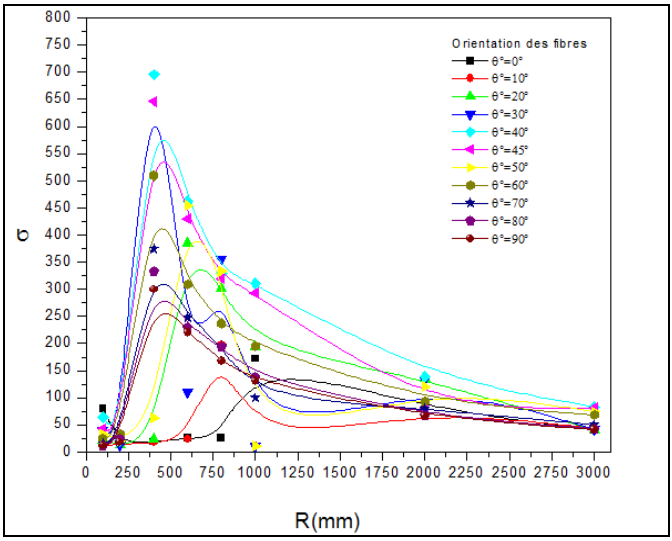

Fig. 4 Effect of the fiber orientation : (θ/-θ):σ ∱(R)

5 Effect of Pipe Diameter on the Coefficient of Buckling λ∱(θ)

The Fig. 5 shows the development of the buckling coefficient regardless of the diameter of the pipe, we see a decrease in λ with the increase of the angle of orientation of the fibers. Except for the angle $\theta = 0°$ is a noticeable stabilization of buckling coefficient λ up to 40 °, beyond this value λ decreases.

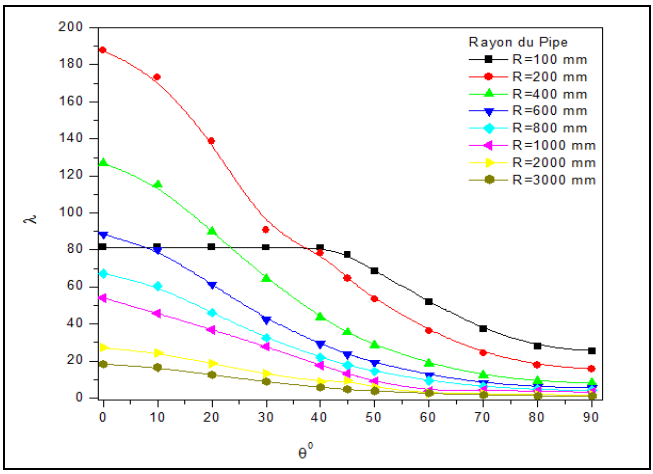

Fig. 5 Effect of variation in the diameter: λ = (θ)

Similarly, the constraint augment is reached maximum values important in increasing the radius R = 400mm pipe up, beyond this value, the stress decreases Fig. 6.

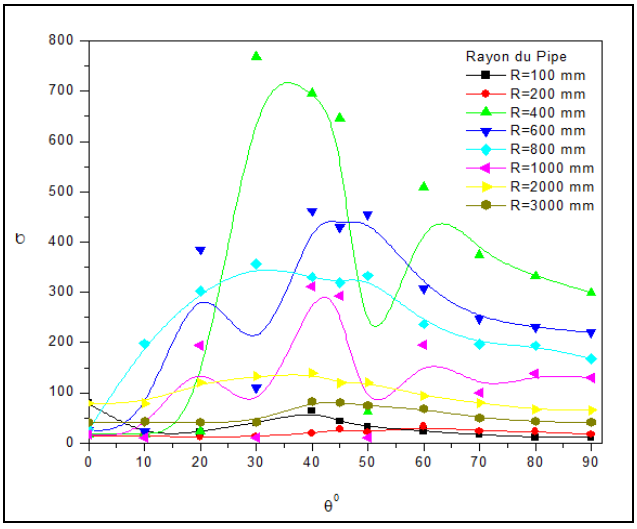

Fig. 6 Effect of variation in the diameter: σ = (θ)

6 Effect of the Number of Plies

It is found that the growth of the number of plies increases the value of the buckling coefficient λ. In addition the increase of fiber orientation $(\theta/-\theta)$ causes decrease **λ** Fig. 7.

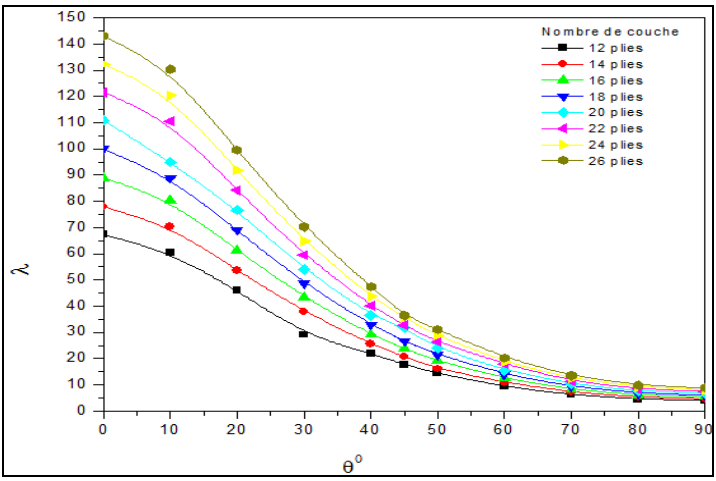

Fig. 7 Effect of varying the number of layer: λ ∱ (ep)

The Pic. 8, we showed the effect of fiber orientation on the expansion of the number of layers, the constraint increases rapidly to a maximum value between 20 ° and 45 °.

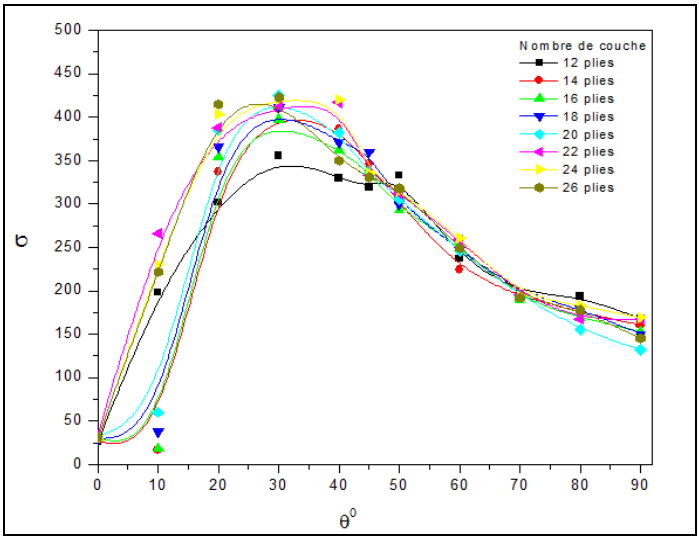

Fig. 8 Effect of varying the number of layer: σ ∱ (ep)

7 Effect of Crack on λ

It is to note that λ decreases Quasis-linearly with the increase of the fiber orientation. This decrease is greater with the importance of the size of the crack, and the value of λ is inversely proportional to the growth of the diameter of pipe.

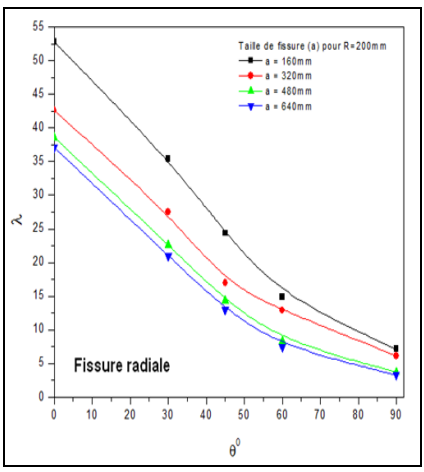

(A)

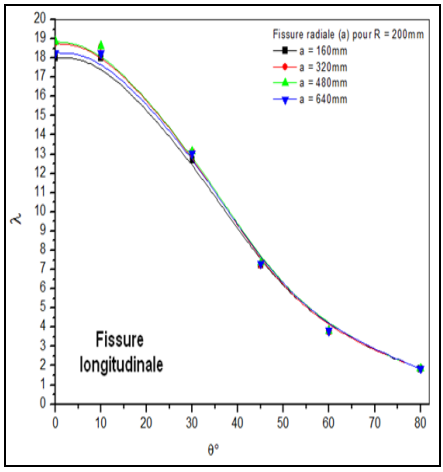

(B)

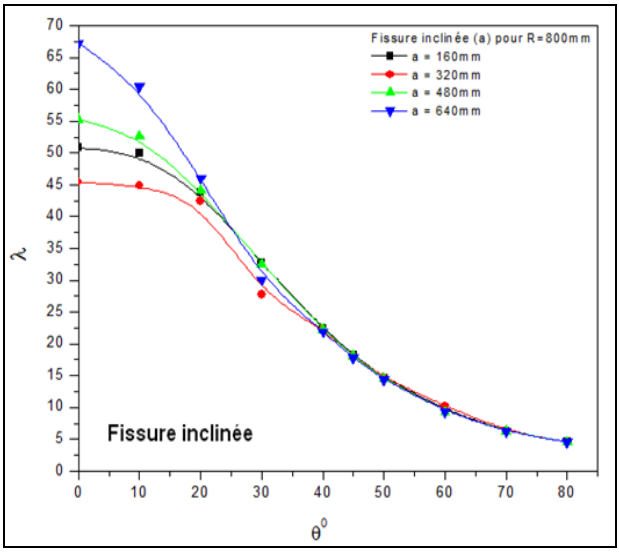

(C)

Fig. 9 (A),(B)and(C) Effect of crack

8 Conclusion

The holding of composite structures subjected to a compressive loading is a feature dimensioning the extent of the rupture properties in compression are generally much lower than in tension (especially in the direction of reinforcement).

The study was lead by using the calculation code (ABAQUS), with the latter we determined the parameter buckling in laminated composite pipe under the influence of a variety of stress.

The overall results indicate:

- The critical buckling load reaches maximum values important when the fibers are oriented at 45 °. The minimum values are obtained when the fibers are oriented in the range of 50 ° to 90 °.
- The increase in the radius of the pipe leading to the decrease of the parameter buckling and maximum values are obtained for the lowest fiber orientations.
- The maximum stresses are obtained for the radius of 400 mm.
- In addition, the increase in the number of plies of composite pipe leads to the increase of the buckling parameter.

The compressive strength is currently a feature difficult to measure experimentally and to assumed.

References

[1] Vaziri, A.: On the buckling of cracked composite cylindrical shells under axial compression. Compos. Struct. 80, 152–158 (2007)

[2] Cailletaud, G., Tijani, M., Cantournet, S., Corte, L., el Arem, S., Forest, S., Herve-Luanco, E., Maziere, M., Proudhon, H., Ryckelynck, D.: Mécanique Des Matériaux Solides, 2 (Mars 2011)

[3] Kweon, J.H., Jung, J.W., Kim, T.H., Choi, J.H., Kim, D.H.: Failure of carbon composite-toaluminum joints with combined mechanical fastening and adhesive bonding. Compos. Struct. 75, 192–198 (2006)

[4] Vellaichamy, S., Prakash, B.G., Brun, S.: Optimum design of cutouts in laminated composite structures. Computers and Structures 37, 241–246 (1990)

Effect of Cooling on Mechanical Properties and Residual Stresses in Aluminium AA2017 Friction Stir Welds

Hassen Bouzaiene, Mahfoudh Ayadi, and Ali Zghal

UR-MSSDT(99-UR11-46)-ESSTT, Tunisia
Bouzaiene.hassen@yahoo.fr,
{mahfoudh.ayadi,Ali.zghal}@esstt.rnu.tn

Abstract. Friction stir welding (FSW) is a relatively new joining technique particularly for aluminium alloys that are difficult to fusion weld. The most common applications are aircraft structures where the cost and weight can be reduced by using new joining techniques instead of riveting. The paper has investigated the effect of cooling on the distribution of residual stresses in friction stir welding of AA2017 aluminium alloy. An attempt has been made to examines the possibility to modify the residual stress state in the joint by applying cooling fluid during FSW processes. The results show that the magnitude of the tensile stress can be reduced significantly in the weld region and we can produce compressive stresses which can be beneficial e.g. for reducing crack propagation speed.

Keywords: Friction Stir Welding, Welding parameters, Residual stresses, Cooling.

1 Introduction

Friction stir welding (FSW) is initially invented and patented at the Welding Institute, Cambridge, United Kingdom (TWI) in 1991 (W.M. Thomas et Al. 1991) to improve welded joint quality of aluminium alloys. It is a continuous and autogenously process. It makes use of a rotating tool pin moving along the joint interface and a tool shoulder applying a severe plastic deformation. The mechanical resistance of the FSW joint is usually characterized by macrostructure, residual stress, tensile strength properties and fracture surface which are evaluated and correlated with the welding parameters.

The existence of high value of residual stress exerts a significant effect on the postweld mechanical properties, particularly the fatigue properties (Mishraa et Al. 2005). Therefore, it is of practical importance to investigate the residual stress distribution in the FSW welds.

In the recent past, Some research articles have been developed on residual stresses occurring in FSW processes with particular reference on aluminium alloys (Donne et Al. 2001) (Peel et Al. 2003) (Weifeng Xu et Al. 2011). They are

M. Haddar et al. (Eds.): *Design and Modeling of Mechanical Systems*, LNME, pp. 503–507.
DOI: 10.1007/978-3-642-37143-1_60

interested in the study of residual stress distribution under various operating parameters of the process such as tool rotation rate, traverse speed and the tool geometry.

This investigation revealed several results. First, the residual stresses in all the FSW welds were quite low compared to those generated during fusion welding. Second, longitudinal (parallel to welding direction) residual stresses were tensile and transverse (normal to welding direction) residual stresses were compressive. Third, longitudinal residual stress exhibited a ‘‘M’’-like distribution across the weld. Fourth, large-diameter tool widened the M-shaped residual stress distribution. Fifth, peak tensile residual stress was observed at the edge of the tool shoulder.

However, a few research activities (Staron et Al. 2002) have been interested to the influence of other operating parameters like cooling on the distribution of residual stresses in the FSW welds. The present paper examines the possibility to modify the residual stress state in the joint by applying cooling fluid during FSW processes.

2 Experimental

The material used in this study was a 6 mm thick AA2017-T451 rolled plate. The butt joints were made using a 7.5 kW powered universal mill (Momac model) with 5 to 1700 r/min and welding feed rate ranging from 16 to 1080 mm/min. the plate was cut and machined into rectangular welding samples of 160 mm×80 mm. Welding test was performed using two samples in butt-configuration, in contact along their larger edge, fixed on a metal frame which was clamped on the machine milling table as shown in figure 1. The clamping device is designed and manufactured in the laboratory.

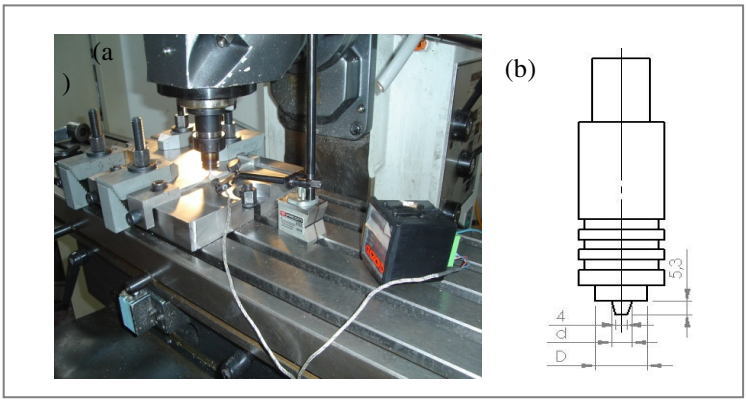

Fig. 1 (a) The clamping devices and (b) The welding tool shape

As far as the utilized tool is regarded, it is made from a high-alloy steel with a tool shoulder diameter (Dsh=18mm) and a threaded conical pin M6x1 with the following geometrical characteristics: largest diameter D=6mm, small diameter d=4mm and height h= 5.3mm. The tilt angle of the tool was 3° relative to the axis Z of the machine. Two different rotational speeds (N) (910rpm and 1280rpm) and Two different welding speeds (S) (67mm/min and 86mm/min) were used to fabricate the joints. Some welding operations were performed under cooling using soluble oil Hocut 558 with a varied flow rate (Q=4L/min). At the end of the welding cycle, a dwell time, flowing between the removal of the tool and loosening of the joint parts, was fixed at about 10 minutes. These welding parameters that used to fabricate the joints are presented in the table 1.

Table 1 The Welding parameters

Sample No.	N [rpm]	S [mm/min]	D_{sh} [mm]	cooling
4	910	67	18	Without
2	910	86	18	Without
3	1280	86	18	Without
16	1280	86	18	Q=4L/min

The measurements of residual stresses in all the studied samples was performed using the technique of X-ray diffraction. These measurements are performed in the LASMIS laboratory of the university of Technology of Troyes (UTT- France). They are carried with a Seifert XRD 3003 PTS diffractometer. Figure 2 explains the residual stress measurement locations and the orientation of the associated reference frame.

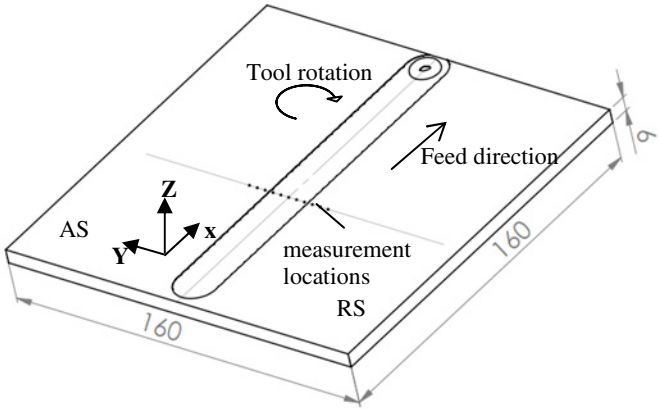

Fig. 2 Schematic of the weld dimensions and residual stress measurement locations

3 Results

The Figure 3 shows that, by applying a coolant, the magnitude of the tensile longitudinal residual stresses can be significantly reduced and became compressive. As well, transversal residual stresses distribution changes and the compressive peak value reaches about -100MPa.

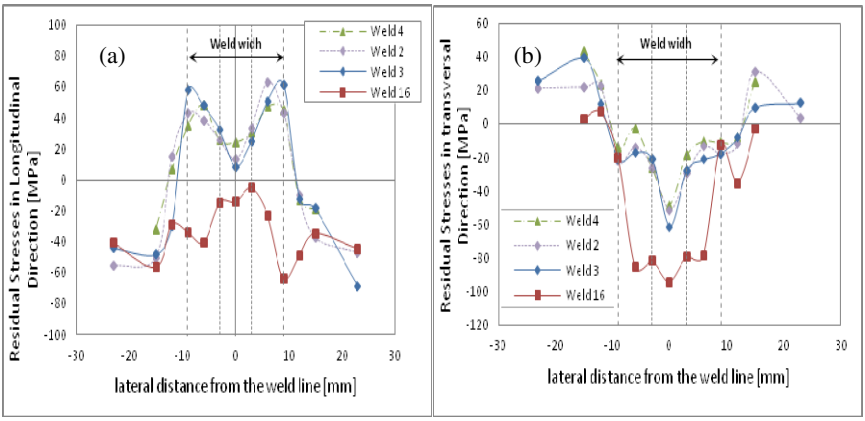

Fig. 3 Residual stress in (a) longitudinal and (b) transversal direction

4 Conclusions

In this investigation an attempt has been made to study the effect of cooling on the on the distribution of residual stresses in Friction Stir Welding of AA2017 aluminium alloy. From this investigation, the following important conclusions are derived:

(i) There is no significant relationship between the variation of FSW processing conditions (rotational speed and welding speed) and the residual stress distribution in both longitudinal and transversal direction.

(ii) The results show that, applying a coolant, during friction stir welding can significantly reduce tensile residual stresses in the weld region and produce compressive stresses which can be beneficial e.g. for reducing crack propagation speed.

(iii) The convective heat transfer coefficient has great importance and impact on the distribution of residual stresses in the FSW process.

Acknowledgements. The authors are grateful to Bruno GUELORGET for technical assistance and acknowledge Prof. Manuel FRANCOIS for his helpful discussions. They wish to thank the whole lab group LASMIS (laboratory of the university of Technology of Troyes UTT- France) for their useful advice and hospitality.

References

Thomas, W.M., Nicholas, E.D., Needham, J.C., Murch, M.G., Temple-Smith, P., Dawes, C.J.: Friction Stir Butt Welding, PCT/GB92/ 02203 (1991)

Mishraa, R.S., Ma, Z.Y.: Friction stir welding and processing. Materials Science and Engineering R 50, 1–78 (2005)

Dale Donne, C., Lima, E., Wegener, J., Pyzalla, A., Buslaps, T.: Investigations on Residual Stresses in Friction Stir Welds. In: 3rd International Symposium on Friction Stir Welding, Kobe, Japan (2001)

Peel, M., Steuwer, A., Preuss, M., Withers, P.J.: Microstructure, mechanical properties and residual stresses as a function of welding speed in aluminum AA5083 friction stir welds. Acta Mater. 51(16), 4791–4801 (2003)

Xu, W., Liu, J., Zhu, H.: Analysis of residual stresses in thick aluminum friction stir welded butt joints. Materials and Design 32, 2000–2005 (2011)

Staron, P., Koçak, M., Williams, S.: Residual stresses in friction stir welded Al sheets. Appl. Phys. A 74(suppl.), S1161–S1162 (2002)

Experimental and Numerical Study of Polypropylene Composite Reinforced with Jute Fibers

Ahcene Mokhtari and Mohand Ould Ouali

Laboratoire Elaboration et Caractérisation des Matériaux et Modélisation,
Université Mouloud MAMMERI de Tizi-Ouzou,
BP 17 RP, 15000 Tizi-Ouzou
mokh.ahcene@yahoo.fr,
m_ouldouali@mail.ummto.dz

Abstract. This paper is devoted to the study of the mechanical response of polypropylene (PP) thermoplastic composite reinforced with jute fibers. In order to use these composites in structural applications it is necessary to understand the mechanisms governing their mechanical behavior and damage. For this purpose, we have fabricated two kinds of PP/jute laminates: $[0°/90°]_{2S}$ and $[+45/-45°]_{2S}$ with the fibers direction, using the molding technique under compression. The mechanical properties of the material are then characterized by tensile and compressive tests. The numerical part of this work concerns the incorporation of the Matzenmiller, Lubliner, and Taylor (MLT) damage model to take into account the post-elastic-peak and the post-peak strain softening responses observed in the the PP/jute composite. This is possible by using formulation with two criterions. The 3D constitutive law has been implemented into the finite code Abaqus using an explicit scheme. In order to assess the capability of this model to describe the material behavior, comparisons are made between numerical and experimental results. Excellent agreements are found between numerical predictions and experimental observations. The model also captures correctly the zones where damage occurs in the two kinds of laminates.

Keywords: PP/jute, mechanical behavior, damage, laminate, modeling.

1 Introduction

Composite thermoplastic (PP) reinforced with natural fibers are mainly used in industrial transport [1]. The use of these composites materials, made of natural fibers, have for objective the substitution of the synthetic fibers like glass fibers [2]. Exotic fibers are attractive because of their low-cost, their high strength, their stiffness and their less impact on the environment in comparison to the other fibers [3-9]. This work is concerned by jute fibers which are incorporated into a polypropylene matrix containing up to 50 vol% fibers. In this study we are particularly interested on the study of mechanical behavior and damage of this composite.

M. Haddar et al. (Eds.): *Design and Modeling of Mechanical Systems*, LNME, pp. 509–516.
DOI: 10.1007/978-3-642-37143-1_61

The modeling approach adopted assumes that the material degradation occurs within two steps. The first one is due the formation discontinuities in the matrix. The second is happen before total failure of the composite. A model is proposed and implemented in order to describe the mechanical response until total material failure. For this purpose we make use of a formulation with two criterions.

2 Material and Experiment

2.1 Material

The material adopted in this study is a polypropylene (PP) thermoplastic composite reinforced with jute fibers (PP/jute). Two stacking sequences of laminates are fabricated: [0°/90°]2S, [+45/-45°]2S, with the angle referred to the longitudinal direction as shown in figure 1. The laminates [0°/90°]2S are used for the material characterization in the orthotropic directions, while the [+45/-45°]2S lamina are used to identify the material shear response. All the specimens are fabricated by the technique of molding by compression.

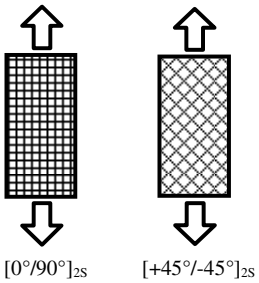

Fig. 1 Schematization of the two laminates kinds: $[0°/90°]_{2S}$ and $[+45/-45°]_{2S}$

2.2 Fabrication Process

In this study, the matrix is a polypropylene (PP) resin with a density of 0.89 g/cm3; the jute fibers with a density of 1.46 g/m3 are employed as reinforcement. The PP/jute composites are realized by the technique of molding under compression. This technique consists on putting the grains of polypropylene and the jute fibers oriented in the desired direction in a mold and to apply a constant pressure. During this thermal compression, the mould is heated over the fusion point temperature. After what the composite is kept at the ambient temperature of 25 °C during 48h before the mechanical testing.

2.3 Tensile Test

The mechanical properties of PP/jute composite materials have been investigated on an IBERTEST testing machine with a load-cell of 10 KN. The tests are

displacement-controlled with a speed of 2mm/min. According to ISO-527-5 standard, the dimensions of the [0°/90°] laminates are 250 mm in length and 25 mm in width and the dimensions of the [+45°/45°] laminates are 250 mm of length and 25 mm of width according to ISO 3518 standard. The tensile tests of this second kind of laminates correspond to shear loeading for the jute fibers. The mechanical properties of PP/jute composite obtained during tensile tests are listed in Table 1.

Table 1 Mechanical properties of Jute/PP composite

Properties	$E_1(MPa)$	$E_2(MPa)$	$G_{12}(MPa)$	ν_{12}
Value	1912	1878	979.8	0.27

At a certain strain stage, [0°/90°] laminates exhibit a non-linear behavior until maximal stress, then softening is observed until final material failure The non-linear part of the curve indicates that significant loss of rigidity occurs in the material due to formation of micro-cracks. The responses of [+45°/45°] laminates to tensile loading is linear until it reaches onset of damage. The material seems to be not significantly damaged. After this post-elastic peak, micro-cracks appear and increase causing loss of rigidity and final failure occurs suddenly.

3 Numerical Modeling

Commonly, composite materials don't exhibit significant plastic deformation. So, the damageable constitutive laws used to describe the progressive damage of such material are elastic-brittle. In the case of thermoplastic composites reinforced by fibers, three zones can be distinguished. The first one is the elastic undamaged zone. The second begins where a decrease of the rigidity appears. It concerns the nucleation, generally in the matrix, of first discontinuities. However during this stage, the linear or non-linear macroscopic composite response still less affected by this damage: the curve continue to increase and material deformation needs higher stresses levels to be achieved. The last zone corresponds to the material softening before total failure of the reinforced composite. Formation and evolution of microcracks (surfaces discontinuities) and cavities (volume discontinuities) are observed during this stage. Initially, the material behavior of the laminates is assumed elastic orthotropic: and can be modeled using the relation

$$\{\varepsilon\} = [E]\{\sigma\} \tag{1}$$

Where $[E]$ is the classical compliance matrix defined using the original elasticity constants of the undamaged laminate E_i, ν_{ij} and G_{ij}. When significant damage occurs in the material, this matrix should include variables taking into effect the decrease or the loss of the material rigidity. Consequently, the $[E]$ can be rewritten:

$$[E]=\begin{bmatrix} \frac{1}{(1-d_{11\text{-}k})E_1} & \frac{-\nu_{21}}{E_2} & \frac{-\nu_{31}}{E_3} & 0 & 0 & 0 \\ \frac{-\nu_{12}}{E_1} & \frac{1}{(1-d_{22\text{-}k})E_2} & \frac{-\nu_{32}}{E_3} & 0 & 0 & 0 \\ \frac{-\nu_{13}}{E_1} & \frac{-\nu_{23}}{E_2} & \frac{1}{(1-d_{33\text{-}k})E_3} & 0 & 0 & 0 \\ 0 & 0 & 0 & \frac{1}{(1-d_{12\text{-}k})G_{12}} & 0 & 0 \\ 0 & 0 & 0 & 0 & \frac{1}{(1-d_{23\text{-}k})G_{23}} & 0 \\ 0 & 0 & 0 & 0 & 0 & \frac{1}{(1-d_{13\text{-}k})G_{13}} \end{bmatrix} \quad (2)$$

The damage parameters $d_{ij\text{-}k}$ vary from 0 (undamaged material) to 1 (total failure) and represent the modulus reduction under different conditions. They are introduced to take into account effect of progressive material damage on the longitudinal, transverse and in-plane shear response respectively. As it will be seen later, subscribe k $(k=1,2)$ indicates either the material behavior is in the post-elastic zone $(k=1)$ or in the softening zone $(k=2)$.

The (MLT) [14] damage model is adopted to characterize the damage onset and the material hardening. So, the damage evolution law is done in the case of [0°/90°] laminates by

$$d_{ij-k}=1-\exp\left[-\frac{-\ln\beta_{ij}}{e}\left(\frac{E_{ij}\varepsilon_{ij}}{\sigma_f}\right)^m\right] \quad with\ \beta_{ij}=\frac{\varepsilon_f}{\sigma_f}E_{ij} \quad (3)$$

σ_f is the maximal stress, its corresponds to the onset of the total material failure, ε_f is the strain corresponding to σ_f. The m parameter should be defined from the Young's modulus, the maximum stress and the corresponding strain. The damage parameters $d_{ij\text{-}1}$ describe the nonlinear material behavior observed experimentally. For [+45/-45] laminates, it is written

$$d_{ij-1}=\left(\frac{\varepsilon^q-\varepsilon^q_{\lim}}{\varepsilon^q_f-\varepsilon^q_{\lim}}\right)^{\frac{1}{n}} \quad (4)$$

The q and n material parameters represent the rigidity loss in the post-elastic curve and describe the development of the different failure modes. The rapid material failure is similar for both laminates. Generally, it corresponds to fibers failure, so the load carrying capacity of that lamina is completely loosed. The formation and propagation of macroscopic cracks cause this final failure. This physical phenomenon is modeled by introducing a second damage variable d_{ij-2} given by the following equation:

$$d_{ij-2} = \left(1 - d_{ij-1}\right)\left(\frac{\varepsilon_{ult}^{q}}{\varepsilon_{ult}^{q} - \varepsilon_{f}^{q}}\left(1 - \frac{\varepsilon_{f}^{q}}{\varepsilon^{q}}\right)\right)^{\frac{1}{n}} \tag{5}$$

ε_{ult}^{q} is the ultimate failure strain as schematized in figure 2.

The material behavior is linear before the first peak $(\varepsilon \le \varepsilon_{\lim})$. In this zone the material is assumed undamaged. So the onset of damage is governed by Raghava and al. criterion. The material failure begin when the Tsai Wu criterion

Table 2 Tensile strength of Jute/PP composite

	$[0°/90°]_{2S}$ laminates		$[+45/-45°]_{2S}$ laminates	
Properties	$\sigma_f\,(MPa)$	ε_t^{ult}	$\sigma_f\,(MPa)$	ε_t^{ult}
Value	27.17	0.019	16.62	0.033

Figures 2 and 3 show the nonlinear behavior in tensile responses of [0°/90°]2S and [+45/-45°]2S laminates. The damage variables d_{ij-1} are quite favorable to describe the damage part (non-linear curve softening) due to the effect of gradual micro-cracking formation. The damage variables d_{ij-2} are quite favorable to describe the failure part (strain-softening).

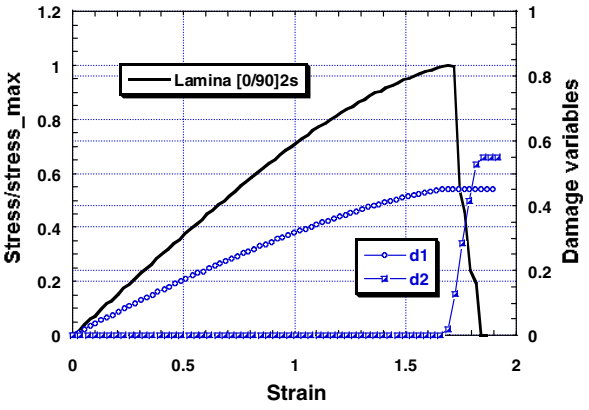

Fig. 2 Damage evaluation Model due to combined damage variables d_{ij-1} and damage variables d_{ij-2} of the lamina $[0°/90°]_{2S}$

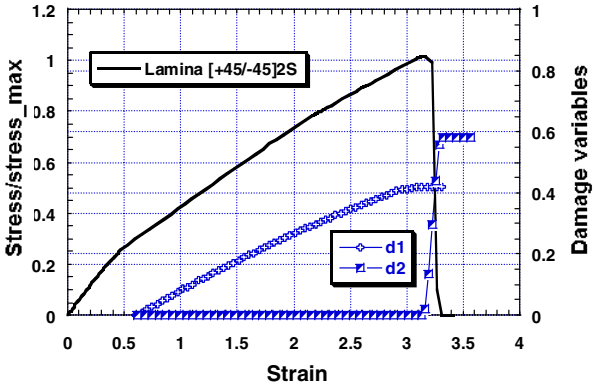

Fig. 3 Damage evaluation Model due to combined damage variables d_{ij-1} and damage variables d_{ij-2} of the lamina $[+45/-45]_{2S}$

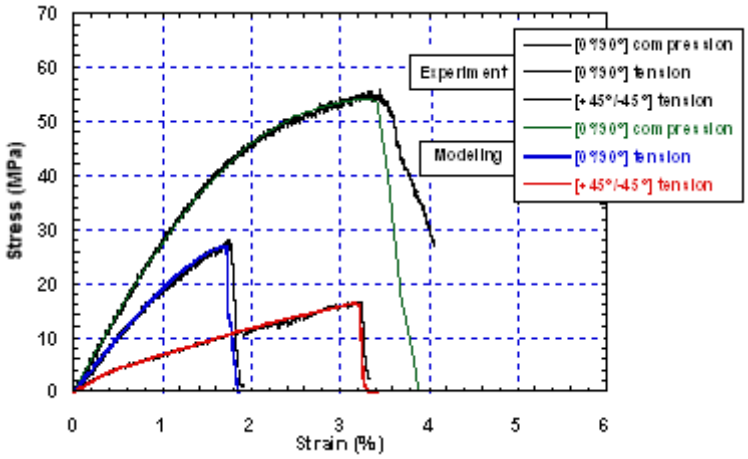

Fig. 4 A comparison between the results of these simulations and the results obtained experimentally for the tension and shear tests

4 Results and Discussions

The model proposed in the previous section has been implemented into the finite code Abaqus using an explicit scheme [20] and used to perform some simulations. Abaqus allows the implementation of user defined models using the Vectorized User MATerial (VUMAT) subroutine. The two kinds of laminates are modeled in 3D.

In order to assess the capability of this model to describe the PP/jute laminates responses, we show in the figure 4 comparison between longitudinal stresses calculated numerically and experimentally versus the strain for the [0/90]2S and [+45/-45]2S laminates. The mechanical behaviors of these specimens are different. The [+45/-45]2S laminates presented strength values lower and less rigidity than the [0/90]2S laminas. This situation can be explained by the influence of the fibers orientation on the less adhesion at the matrix/fiber interface in the case of shear loading.

5 Conclusion

The purpose of this work is twice: experimental characterization of the mechanical response of fiber-reinforced composites and formulation and assessment of a damage model describing the damage and behavior of these laminates. The material used is a polypropylene (PP) thermoplastic reinforced with jute fibers. The mechanical characterization of the two kinds of PP/jute laminates ($[0°/90°]_{2S}$ and $[+45/-45°]_{2S}$ with the fibers direction) used in the study is done by tensile and compressive tests.

The Matzenmiller, Lubliner, and Taylor (MLT) damage model is coupled to an damaged elastic law to include the failure stage (coupling damage-failure) using a formulation with two criterions. This constitutive law has been implemented into the finite code Abaqus using an explicit scheme. In order to assess the capability of this model, comparisons are made between numerical and experimental results. Excellent agreements are found between numerical predictions and experimental observations. The $[+45/-45]_{2S}$ laminates presents lower strength values and less rigidity than the $[0/90]_{2S}$ laminates. For the $[0/90]_{2S}$ laminates, cracks are germinated perpendicularly to the loading direction. $[+45/-45]_{2S}$ laminates exhibit the formation and propagation of cracks with an angle of approximately 45° with the loading direction. This crack propagation direction corresponds to the fibers orientation.

As perspectives to this work, we can propose:

- Including thermal heating generated by the material dissipation due to damage and hardening.
- Including other degradation mechanism like ageing and moisisture… and incorporate the humidity effects which play an important role in the life cycle of thermoplastic polymers.

References

[1] Mohanty, A.K., Misra, M., Dzral, L.T.: Natural fibres, biopolymères, and biocomposites. CRC Press (2005)
[2] Journal of textile Institut 96(1), 11–17 (2005)
[3] Goda, K., Cao, Y.: Research and Development of Fully Green Composites Reinforced with Natural Fibers. Journal of Solid Mechanics and Materials Engineering 1(9), 1073–1082 (2007)

[4] John, M.J., Thomas, S.: Biofibres and Biocomposites. Carbohydrates Polymers 71, 343–364 (2008)
[5] Saiful Islam, M.: The Influence of Fibre Processing and Treatments on Hemp Fibre/Epoxy and Hemp Fibre/PLA Composites. PhD Thesis –University of Waikato, Hamilton, New Zealand (2008)
[6] Satyanarayana, K.G., Arizaga, G.G.C., Wypych, F.: Biodegradable composites based on lignocellulosic fibers – an overview. Progress in Polymer Science (2008), doi:10.1016/j.progpolymsci.2008.12.002
[7] Luz, S.M., Caldeira-Pires, A., Ferrão, P.M.C.: Environmental benefits of substituting talc by sugarcane bagasse fibers as reinforcement in polypropylene composites: Ecodesign and LCA as strategy for automotive components. Resources, Conservation and Recycling 54(12), 1135–1144 (2010)
[8] Yu, L., Dean, K., Li, L.: Polymer blends and composite from renewable resources. Prog. Polym. Sci. 31, 576–602 (2006)
[9] Baley, C., Grohens, Y., Pillin, I.: Etat de l'art sur les matériaux composites biodégradables. Revue des Composites et Matériaux Avancés 14, 135–166 (2004)
[10] Philip, A.R.: Reinforced Plastics, 306 (June 1964)
[11] Wells, H., Bowen, D.H., Machphail, I., Pal, P.K.: Proceedings of the 35th Annual Technical Conference of the Reinforced Plastic and Composites Institute. Society of the Plastic Industry, Inc., New York (1980)
[12] Chawla, K.K., Bastos, A.C.: Proceedings of 3rd International Conference on the Mechanical Behaviour of Materials, Cambridge, vol. 3, p. 191. Pergamon Press (1977)
[13] Kachanov, L.: On the time to failure under creep conditions. Izv AN SSSR, Otd. Tekhn. 8, 26–31 (1958)
[14] Matzenmiller, A., Lubliner, J., Taylor, R.: A constitutive model for anisotropic damage in fiber-composites. Mechanics of Materials 20(2), 125–152 (1995)
[15] Zheng, X., et al.: Nonlinear strain rate dependent composite model for explicit finite element analysis, 71–88 (2006)
[16] SIMULIA/ABAQUS 6.10. User Manual, Abaqus Inc., Providence, RI, USA (2010)

Trip Effect on the Modeling of Thermo-mechanical Behaviour of Steels during Quenching Process

Mahmoud Yaakoubi, Mounir Kchaou, and Fakhreddine Dammak

Unit of Mechanics, Modeling and Production (U2MP),
Enis, POB W. 3038 Sfax, Tunis
mahmoud_yaakoubi@yahoo.fr,
mounir.kchaou@issatgb.rnu.tn,
fakhreddine.dammak@enis.rnu.tn

Abstract. The prediction of the residual stresses generated by heat treatment of steel parts is a complex and insufficiently controlled task due to several couplings between heat conduction, phase transformations and mechanical behaviour of material. Phase transformations during quenching induce plasticity that fairly higher than classical plasticity of multiphase material that its properties are estimated from linear law of mixture components properties. Various models were proposed to take into account of the so called transformation induced plasticity (trip) in the modeling of mechanical behavior of steel that undergoes phase transformation during quenching. In this way, two approaches for the mechanical modeling taking into account of trip are proposed. In the first approach, an increment of deformation labeled transformation induced plasticity increment is added to classic deformations increments so the plastic flow rule is modified. The second approach uses the classical thermo-elastoplastic scheme with specific evolution of yield stress of multiphase material during quenching. The validity of these approaches is discussed on the light of the results gotten from the literature.

Keywords: modeling, thermo-mechanics, quenching, TRIP, yield stress.

1 Introduction

Rapid quenching after surface heating is a heat treatment process that hardens and compresses the surface layer of the treated part thus its yield strength and fatigue resistance will be improved. Its use and its development involve difficulties to a large part of trade people. For better understanding the processes that control this practice, many studies for analyzing the phenomena intervening in the heat treatment were carried out in order to be able to predict profiles of microstructures and depth of quenching as well as stresses and residual deformations caused by the heat treatment. It's found that one of the major factors influencing the evolution of stress and deformation is the TRansformation Induced Plasticity (TRIP) (Wolff et al. 2005). This increment of plasticity appears to accommodate

M. Haddar et al. (Eds.): *Design and Modeling of Mechanical Systems*, LNME, pp. 517–522.
DOI: 10.1007/978-3-642-37143-1_62

stresses induced in the interface between parent and new phase that each one of them has its own properties. Thus, local dislocations are created in the parent phase (austenite) which has the lowest yield stress. If an external loading stress even little than the yield stress of austenite is applied during the transformation, local dislocations become permanent strains in the direction of the load at the macroscopic scale. This permanent strain is called TRIP (Moumni et al. 2011). In this study, two procedures are proposed to take into account of the TRIP effect on the heat treatment residual stresses and distortion during steel quenching. For the first procedure, a transformation induced plasticity increment is added to classic deformations increments so the plastic flow rule as well as stiffness tangent matrix is modified. The second procedure uses the classical thermo-elastoplastic scheme with specific evolution of yield stress of multiphase material during quenching. The validity of these techniques is discussed through comparison between numerical simulations and experimental results gotten from the literature (Jung et al. 2012).

2 Modeling

2.1 Approach with an Added TRIP Increment

Within the framework of the small deformations, and for a material undergoing a metallurgical transformation, the total strain is the sum of the elastic, volumetric, classical plastic and transformation induced plastic strain:

$$\Delta\boldsymbol{\varepsilon}^{t} = \Delta\boldsymbol{\varepsilon}^{e} + \Delta\boldsymbol{\varepsilon}^{v} + \Delta\boldsymbol{\varepsilon}^{p} + \Delta\boldsymbol{\varepsilon}^{pt} \tag{1}$$

- Elasticity is modeled by the law of Hooke:

$$\Delta\boldsymbol{\varepsilon}^{e} = \frac{1+\nu}{E}\Delta\boldsymbol{\sigma} - \frac{\nu}{E}\mathrm{tr}\left(\Delta\boldsymbol{\sigma}\right)\boldsymbol{\delta} \tag{2}$$

- The volumetric strain is expressed by:

$$\Delta\boldsymbol{\varepsilon}^{v} = \left(\sum_{k=1}^{5} z_k \alpha_k \Delta T + \sum_{k=1}^{4} \Delta z_k \zeta_k^{Tref}\right)\boldsymbol{\delta} \tag{3}$$

With z_k and α_k are respectively the fraction and thermal dilatation coefficient of phase k. ζ_k^{Tref} is the volume change resulted during the transformation of the austenite to phase k (or reverse) evaluated from the state of this phase at the temperature T_{ref}. Usually, T_{ref} is the room temperature or the austenitisation temperature if the austenite is thermally homogenous. Subscript k indicates the metallurgical phase (k=1: ferrite, k=2: pearlite, k=3: bainite, k=4: martensite and k=5: austenite). $\boldsymbol{\delta}$ is the Kronneker tensor.

- Classical plastic strain is calculated by using the classical theory of plasticity with the associated hardening rules. A superposition of isotropic and kinematic hardening is supposed in this modeling adopting the Chaboche theory (Lemaitre and Chaboche 1990). According to that preceded, the Von Mises yield function and the plastic strain rate tensor are defined respectively as follows:

$$f = \sigma_{eq} - \sigma_p = \left[\frac{3}{2}\xi : \xi\right]^{1/2} - \sigma_y(T) - R(p,T) \tag{4}$$

$$\dot{\boldsymbol{\varepsilon}}^p = \dot{\lambda}\frac{\partial f}{\partial \boldsymbol{\sigma}} \tag{5}$$

Where $\boldsymbol{\xi} = \mathbf{s} - \mathbf{x}$, T is the temperature, σ_{eq} is the equivalent stress, $\mathbf{s}$ is the deviatoric stress tensor, and $\mathbf{x}$ is the linear kinematic hardening tensor (back-stress); it's defined versus plastic strain tensor:

$$\dot{\mathbf{x}} = (2/3)C\ \dot{\boldsymbol{\varepsilon}}^p \tag{6}$$

With C is a material parameter. $\sigma_y(T)$ is the yield stress; R is the hardening function and $\dot{\lambda}$ is the plastic multiplier.

- The transformation induced plasticity increment is expressed by:

$$\Delta\boldsymbol{\varepsilon}^{pt} = \frac{3}{2}\Gamma(-\dot{T})\sum_{k=1}^{4}\kappa_k\varphi_k(z_k)\Delta z_k\mathbf{s} \tag{7}$$

where

$$\kappa_k = \frac{2\zeta^{Tref}}{\sigma_{y,\gamma}} \tag{8}$$

and

$$\varphi_k(z_k) = \begin{cases} -Ln(z_l)(1-z_l^2) & \text{si } z_k \le z_l \\ -Ln(z_k)(1-z_k^2) & \text{si } z_k \ge z_l \end{cases} \tag{9}$$

with

$$z_l = \frac{\sigma_{y,\gamma}}{2\zeta^{Tref}}\frac{4\mu + 3k}{9k\mu} \tag{10}$$

Where Γ is the Heaviside function, κ_k is a material parameter related to phase k; it is homogenous with stress inverse, $\sigma_{y,\gamma}$ is the yield stress of the austenite. $\varphi_k(z_k)$ expresses the transformation process dependence (Taleb et Sidoroff 2003) and $\mathbf{s}$ is the deviatoric stress tensor. μ and k are respectively shear modulus and bulk modulus of the material.

2.2 Approach with Specific Yield Stress

This approach, the transformation induced plasticity increment is omitted. So, equation (1) becomes:

$$\Delta\boldsymbol{\varepsilon}^{t} = \Delta\boldsymbol{\varepsilon}^{e} + \Delta\boldsymbol{\varepsilon}^{v} + \Delta\boldsymbol{\varepsilon}^{p} \tag{11}$$

With ε^{e}, ε^{v} and ε^{p} are the same ones cited above.

The effect of supplementary plasticity accompanying phase transformation on mechanical behaviour during quenching is taken into account through adopting a particular evolution of yield stress of the multiphase material. Indeed, we suggest that the yield stress is equal to that of the weak phase (austenite) until a threshold percentage $Ps\gamma$ of initial austenite is decomposed into cold phases. Then, yield stress is estimated using mixture linear law:

$$\sigma_{y}(T) = \sum_{k=1}^{5} z_{k}\sigma_{y,k}(T) \tag{12}$$

3 Simulation and Discussion

The FE simulation for quenching of an AISI 1045 carbon steel cylinder with 30 mm in diameter and 90 mm in length was conducted using the FE software ABAQUS linked to many user subroutines allowing the thermo-metallo-mechanical coupling analysis during heat treatment. An axisymmetric quadrilateral element was used. The initial temperature of the cylinder was assumed to be 900°C, and it's quenched with water at temperature equal to 27°C. The heat transfer coefficient varies according to surface temperature during the water quenching of a cylindrical specimen. Most of material properties such as thermal conductivity, specific heat, young modulus and plastic modulus were temperature and phase dependent. The enthalpy changes during transformations were taken into account during thermal solution. The stress-strain solution was carried out by applying the two approaches mentioned above. For the first approach, the addition of the increment TRIP to other deformations increments induces a modification on Jacobian matrix and consistency condition. When using a specific yield stress in the second approach, the threshold value $Ps\gamma$ is evaluated according to metallurgical fractions composing the aggregate. The validity of these approaches is investigated through the confrontation between the profiles of residual stresses measured on the test-tube described previously with the computation results obtained by applying these two approaches.

Figure 1a) represents the distribution of the hoop residual stresses calculated with applying the tow approaches accompanied by measured one. We can remark then that both numerical results (obtained from the added increment of TRIP and obtained through a specific material yield stress evolution) are in good agreement with experimental measures.

In the same way, figure 1 b) shows that both models can effectively predict the tendency of the axial residual stress for the case of axisymmetric model but numerical result issued from the first approach is quite more coincident with experimental measure than result obtained from the second approach. This discrepancy may be due to the adopted evaluation of the threshold percentage Psγ which requires complementary investigation.

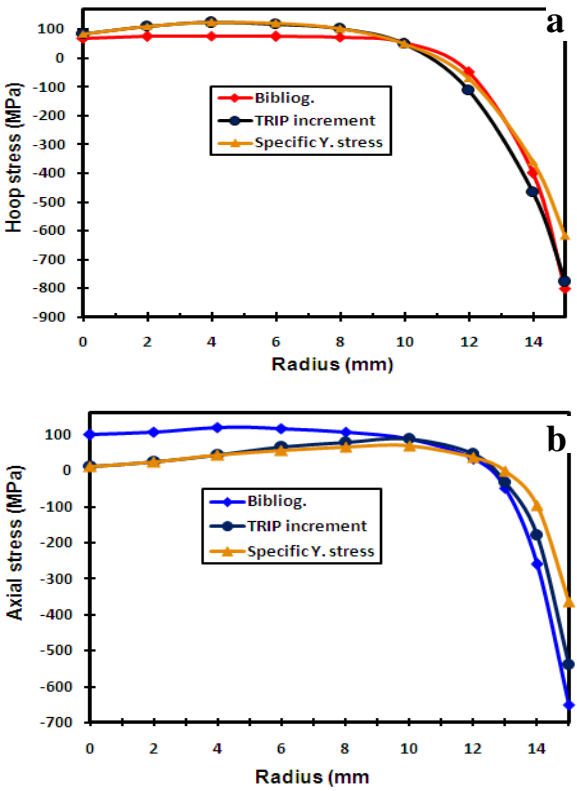

Fig. 1 Profiles of a) Hoop stress, b) Axial stress

4 Conclusion

The modeling of the effect of the transformation plasticity (TRIP) on the mechanical behavior of a steel undergoing phase transformations during the quenching process can be carried out either by evaluating the increment of TRIP and by adding it to the other increments then reformulating the yield function and the tangent matrix, or by considering that the involved material has a specific yield stress which is lower than that obtained by the linear law of mixture. Basing on experimental results ensued from the bibliography; we observed that the two methods are adequate except that the calibration of the yield stress of material requires a complementary improvement when the second approach is adopted.

Acknowledgements. The authors also gratefully acknowledge the helpful comments and suggestions of the reviewers, which have improved the presentation.

References

Wolff, M., Bohm, M., Lowisch, G., Schmidt, A.: Modelling and testing of transformation-induced plasticity and stress-dependent phase transformations in steel via simple experiments. Comput. Mater. Sci. 32, 604–610 (2005)

Moumni, Z., Roger, F., Trinh, N.T.: Theoretical and numerical modeling of the thermomechanical and metallurgical behavior of steel. Int. J. of Plasticity 27, 414–439 (2011)

Jung, M., Kang, M., Lee, Y.-K.: Theoretical Finite-element simulation of quenching incorporating improved transformation kinetics in a plain medium-carbon steel. Act. Mater. 60, 525–536 (2012)

Lemaitre, J., Chaboche, J.-L.: Mechanics of Solid Materials. Cambridge University Press, Cambridge (1990)

Taleb, L., Sidoroff, F.: A micromechanical modeling of the Greenwood–Johnson mechanism in transformation induced plasticity. Int. J. Plast. 19, 1821–1842 (2003)

Experimental Parameters Identification of Fatigue Damage Model for Short Glass Fiber Reinforced Thermoplastics GFRP

Hedi Nouri[1], Christophe Czarnota[2], and Fodil Meraghni[3]

[1] COHMAS-PSE,
King Abdullah University of Science and Technology,
Thuwal, Kingdom of Saudi Arabia
Hedi.nouri@kaust.edu.sa
[2] LEMTA, GIP-InSIC, 27 rue d'Hellieule,
88100 Saint-Dié-des-Vosges, France
[3] LEM3, Arts et Métiers ParisTech. - Metz,
4 Rue Augustin Fresnel, 57078 Metz, France

Abstract. In the present work, a new polycyclic fatigue damage model is formulated and applied for short glass fibre reinforced thermoplastics. The model is able to capture experimental trends observed for the considered composites. The damage growth description involves a set of 20 parameters in the case of a complete 3D –structure. In the current paper, it is considered the particular case of a displacement controlled fatigue tensile test involving 4 damage parameters. The present contribution is a first approach of parameter identification. It is considered a least squares sense based cost function and homogeneous fatigue tests performed on a short glass fibre reinforced polyamide. The identified set of parameters appears to be not depending on the adopted initial values. The model as the parameters determined by the minimisation algorithm, are validated on a fatigue test performed with a different loading condition.

Keywords: Short glass fiber, fatigue damage, parameters identification.

1 Introduction

The present work is a contribution to the phenomenological modeling of fatigue damage in short glass fiber reinforced thermoplastic matrix composites. In such materials, the fatigue damage kinetic occurs according to three stages: i) material softening and damage initiation ii) coalescence and propagation of micro-cracks iii) macroscopic cracks propagation and material failure, [Sedrakian et al. 2002, Van Paepegem and Degrick 2002]. Different laws have been proposed to predict the damage accumulation in unidirectional or laminated polymer matrix composites [Van Paepegem and Degrick 2002, Ye 1989]. These models do not take into account the first stage of the damage kinetic observed in short glass fiber reinforced thermoplastics. From experimental investigation it is shown that during

M. Haddar et al. (Eds.): *Design and Modeling of Mechanical Systems*, LNME, pp. 523–530.
DOI: 10.1007/978-3-642-37143-1_63

the first few hundred cycles, the damage kinetic is mainly due to the material softening depending on the applied strain level. Based on the Ladevèze and Le Dantec approach [Ladevèze and Le Dantec 1992], the proposed modeling is an attempt to extend previous works by accounting for the important stiffness reduction observed during the early stage of the damage evolution. An inverse analysis is introduced in order to determine the set of parameters introduced in the current work. It is used experimental data obtained from tension-tension fatigue tests performed on a for short glass fiber reinforced thermoplastics and a cost function written in a least squares sense. It appears that the set of parameters computed from the analysis is not depending on the initial values. The modeling with the identified parameters is accurately compared to experimental data that have not been considered for the identification.

2 New Fatigue Damage Model

To take into account the observed three damage stages, a new polycyclic fatigue damage model is formulated on the basis of the meso model proposed by Ladevèze and Le Dantec [Ladevèze and Le Dantec 1992]. According to the continuum damage mechanics, the damage is introduced as an internal state variable coupled to elastic behaviour. Assuming a thin structure where ($\sigma_{33}=0$), made of an orthotropic material, elastic moduli of the damaged material are given by:

$$\begin{aligned} E_{11} &= E_{11}^0\left(1-d_{11}\right) \\ E_{22} &= E_{22}^0\left(1-d_{22}\right) \\ G_{12} &= G_{12}^0\left(1-d_{12}\right) \\ G_{13} &= G_{13}^0\left(1-d_{13}\right) \\ G_{23} &= G_{23}^0\left(1-d_{23}\right) \end{aligned} \tag{1}$$

Where E_{11} (resp. E_{22}) is the Young's modulus in the longitudinal (resp. transverse) direction. G_{12}, G_{13} and G_{23} are the shear moduli. d_{ij} are the damage variables associated to the corresponding moduli. The superscript 0 indicates initial values measured when $d_{ij}=0$. In the case where damage is disregarded, the elastic strain energy (W_e) is given by:

$$\begin{aligned} W_e = \frac{1}{2}\frac{1}{1-\nu_{12}\nu_{21}}\Big[\Big[E_{11}^0\varepsilon_{11}+\nu_{21}E_{11}^0\varepsilon_{22}\Big]\varepsilon_{11}+\Big[\nu_{12}E_{22}^0\varepsilon_{11}+E_{22}^0\varepsilon_{22}\Big]\varepsilon_{22}\Big] \\ +G_{12}^0\gamma_{12}^2+G_{13}^0\gamma_{13}^2+G_{23}^0\gamma_{23}^2 \end{aligned} \tag{2}$$

For a damaged material, the elastic strain energy becomes dependent on the state variables d_{ij}. Then, the strain energy (W_d) of a damaged material can be computed from Eq.(2) by replacing (E_{ij}^0, G_{ij}^0) by the corresponding moduli (E_{ij}, G_{ij}) expressed in Eq. (1). One obtains:

$$
\begin{aligned}
W_d = & \frac{1}{2}\frac{1}{1-\nu_{12}\nu_{21}}\left[E_{11}^0(1-d_{11})\varepsilon_{11}\left\langle\varepsilon_{11}+\nu_{21}\varepsilon_{22}\right\rangle_+ + E_{11}^0\varepsilon_{11}\left\langle\varepsilon_{11}+\nu_{21}\varepsilon_{22}\right\rangle_-\right] \\
& + \frac{1}{2}\frac{1}{1-\nu_{12}\nu_{21}}\left[E_{22}^0(1-d_{22})\varepsilon_{22}\left\langle\varepsilon_{22}+\nu_{12}\varepsilon_{11}\right\rangle_+ + E_{22}^0\varepsilon_{22}\left\langle\varepsilon_{22}+\nu_{12}\varepsilon_{11}\right\rangle_-\right] \\
& + G_{12}^0(1-d_{12})\gamma_{12}^2 + G_{13}^0(1-d_{13})\gamma_{13}^2 + G_{23}^0(1-d_{23})\gamma_{23}^2
\end{aligned} \tag{3}
$$

Where (<A>+) and (<A>-) stand for the positive and negative parts of A, respectively. Thus, the damage affects E_{11} (resp. E_{22}) only when $\varepsilon_{11}+\nu_{21}\varepsilon_{22}$ (resp. $\varepsilon_{11}+\nu_{21}\varepsilon_{22}$) is positive. This can be explained by the following. When the material is submitted to a compressive loading, transverse matrix cracks are supposed to be closed up and do not have any effect on the damage evolution. On the opposite, during tension loading those cracks are active and contribute to the development of the damage.

The thermodynamic dual variables Y_{ij} associated to the damage variables d_{ij} are deduced from the elastic strain energy W_d of the degraded material:

$$
\begin{aligned}
Y_{11} &= -\frac{\partial W_d}{\partial d_{11}} = \frac{1}{2}\frac{1}{1-\nu_{12}\nu_{21}}E_{11}^0\varepsilon_{11}\left\langle\varepsilon_{11}+\nu_{21}\varepsilon_{22}\right\rangle_+ & Y_{12} &= -\frac{\partial W_d}{\partial d_{12}} = \frac{1}{2}G_{12}^0\gamma_{12}^2 \\
Y_{22} &= -\frac{\partial W_d}{\partial d_{22}} = \frac{1}{2}\frac{1}{1-\nu_{12}\nu_{21}}E_{22}^0\varepsilon_{22}\left\langle\varepsilon_{22}+\nu_{12}\varepsilon_{11}\right\rangle_+ & Y_{13} &= -\frac{\partial W_d}{\partial d_{13}} = \frac{1}{2}G_{13}^0\gamma_{13}^2 \\
& & Y_{23} &= -\frac{\partial W_d}{\partial d_{23}} = \frac{1}{2}G_{23}^0\gamma_{23}^2
\end{aligned} \tag{4}
$$

In the proposed modelling, the damage rate is assumed to be the sum of two components:

$$
\frac{d(d_{11})}{d(N)} = \frac{\alpha_{11}\beta_{11}}{1+\beta_{11}}\left(Y_{11}\right)^{\beta_{11}-1} + \lambda_{11}\left(Y_{11}\right)\left(e^{-(\delta_{11}N)}\right) \tag{5}
$$

$$
\frac{d(d_{22})}{d(N)} = \frac{\alpha_{22}\beta_{22}}{1+\beta_{22}}\left(Y_{22}\right)^{\beta_{22}-1} + \lambda_{22}\left(Y_{22}\right)\left(e^{-(\delta_{22}N)}\right) \tag{6}
$$

$$
\frac{d(d_{12})}{d(N)} = \frac{\alpha_{12}\beta_{12}}{1+\beta_{12}}\left(Y_{12}\right)^{\beta_{12}-1} + \lambda_{12}\left(Y_{12}\right)\left(e^{-(\delta_{12}N)}\right) \tag{7}
$$

$$
\frac{d(d_{13})}{d(N)} = \frac{\alpha_{13}\beta_{13}}{1+\beta_{13}}\left(Y_{13}\right)^{\beta_{13}-1} + \lambda_{13}\left(Y_{13}\right)\left(e^{-(\delta_{13}N)}\right) \tag{8}
$$

$$
\frac{d(d_{23})}{d(N)} = \frac{\alpha_{23}\beta_{23}}{1+\beta_{23}}\left(Y_{23}\right)^{\beta_{23}-1} + \lambda_{23}\left(Y_{23}\right)\left(e^{-(\delta_{23}N)}\right) \tag{9}
$$

The first contribution, scaled by $(Y_{ij})^{\beta ij\text{-}1}$ in Eqs. (1.5) to (1.9), is derived from the Norton dissipation potential. Note that in a previous work from Sedrakian et al [Sedrakian et al. 2002] the damage evolution is only described by this first term. The second component is introduced in order to describe the rapid stiffness

reduction occurring during cyclic loading of reinforced thermoplastics [Nouri et al 2009]. The developed model is then a complete model in the sense that the entire damage process (3 stages) could be described. The instantaneous state variables $d_{ij}(N)$ are obtained by numerical integration of Eqs. (1.5) to (1.9), with the initial conditions $d_{ij}(N=0)=d^{qs}_{ij}$. These initial values are function of the imposed displacement. In the case where the applied strain (ε^{app}_{ij}) is below a threshold value associated to the beginning of the damage process in the (i,j) direction, ($d^{qs}_{ij}=0$). From equations (1.5) to (1.9), it appears that the proposed model involves 20 parameters in the general case of a 3–D structure. Nevertheless, it should be mentioned that the model is essentially developed for thin composite structures. In that particular case, relationships governing the damage evolution are reduced to Eqs. (1.5) to (1.7) and only 12 parameters have to be identified namely, 4 parameters per damage variable. In the next section, an identification procedure is adopted to reach this goal.

3 Experimental Identification

Material damage parameters identification cannot be achieved without experimental tests involving the three stages of damage. In the present paper, we focus on longitudinal tension-tension tests leading to only a longitudinal damage d_{11}. For simplicity in the notation, d_{11} is denoted hereafter d and corresponds to the longitudinal damage in Eq. (1.5). In the same way, α, β, λ and δ substitute α_{11}, β_{11}, λ_{11} and δ_{11} in Eq. (1.5).

3.1 Experimental Procedure

We consider fatigue tests performed in tension-tension. The studied composite material is a polyamide thermoplastic reinforced short glass fibre, denoted by TP-GF hereafter. The reinforcement makes the material highly resistant to abrasion, compression, tension or bending. The specimens used in the static and fatigue tensile tests were cut from thin plates. The geometry and dimensions of the tension specimens are shown in Figure 1. Fatigue tests were strain controlled and carried out using a servo-hydraulic machine. The imposed displacement wave was sinusoidal with constant amplitude. All tests were performed at room temperature. The mechanical properties of the material have been extracted from static tension tests. Some of the properties are given in Table 1.

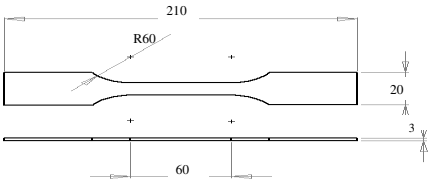

Fig. 1 Specimen used for tension tests (dimensions in mm)

Table 1 Monotonic mechanical properties of the studied material and standard deviations

Material	E^0 (MPa)	$\varepsilon_{\text{damage Threshold}}(\%)$	$\varepsilon_{\text{Rup}}(\%)$	σ_{UTS}(MPa)
TP-GF longitudinal direction	7042. (370)	0.7 (0.02)	5. (0.4)	114. (6)

Experimental cyclic tests are driven by an applied displacement, see Figure 2. It is introduced the maximum strain ε_{max} and the minimum strain ε_{min}. It is usually defined the fatigue ratio by $R=\varepsilon_{min}/\varepsilon_{max}$. Note that ε_{rup} denotes the maximum strain reached when the material fails. Three strain levels ($\varepsilon_{max}=20\%\varepsilon_{rup}$, $\varepsilon_{max}=30\%\varepsilon_{rup}$ and $\varepsilon_{max}=40\%\varepsilon_{rup}$) have been conducted using three specimens for each different levels. The ratio R remains the same for the different configuration (R=0.3). The frequency is 2Hz. Some properties are summarized in Table 2.

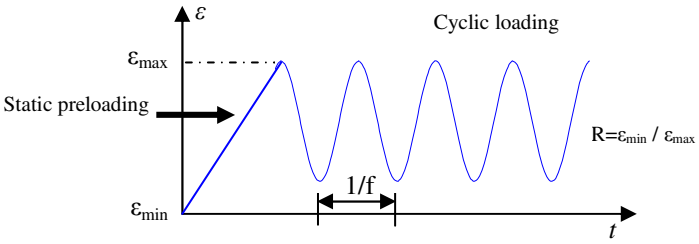

Fig. 2 Strain history obtained from an imposed displacement test. Note that the static pre-loading (up to the point F) could give rise to an initial damage representing the quasi-static damage (denoted by d_{qs} in the current work).

Table 2 Monotonic mechanical properties of fatigue test

	Test 20%	Test 30%	Test 40%
ε_{rup}	5	5	5
E^0	7600	7200	6900
d_{qs}	0.05	0.08	0.10

It is shown on Figure 3 the evolution of d versus N obtained from experimental fatigue tension-tension tests at different ε_{max} ($\varepsilon_{max}=20\%$,$\varepsilon_{max}=30\%$, $\varepsilon_{max}=40\%$). It is observed that even if data are quite scattered, an increase in ε_{max} leads to an increase in the damage rate, and an enhanced d_{qs}. This is due to a more cumulative damage occurring when the maximum strain passes from $20\%\varepsilon_{rup}$ to $30\%\varepsilon_{rup}$ to $40\%\varepsilon_{rup}$. In Figure 2, the point F defines the end of the quasi-static step. It is the highest for $\varepsilon_{max}=40\%\varepsilon_{rup}$ and the lowest for $\varepsilon_{max}=20\%\varepsilon_{rup}$. In the latter case, less damage is cumulated up to the point F, and d_{qs} is then reduced. From Eq.(1.4) with $Y_{11}=Y$, in the case of an uniaxial strain test ($\varepsilon_{22}=0$), the thermodynamic variable Y is increased when ε_{11} increases. That leads to an increase in $d(d)/d(N)$, see Eq.(1.5) with $d_{11}=d$.

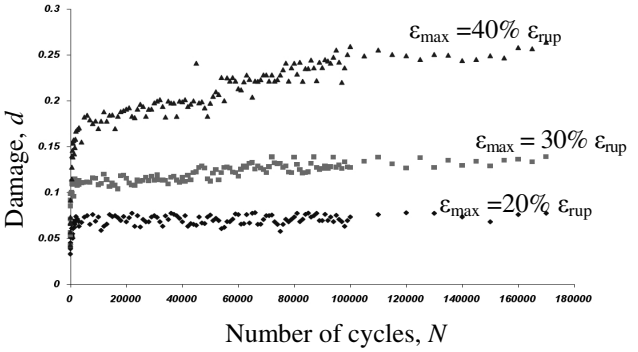

Fig. 3 Experimental results of the evolution of the damage d versus the number of cycles N. The studied composite material was subjected to tension-tension displacement controlled fatigue test. Three maximum applied strains ε_{max} were considered: 20%, 30% and 40% of the total fracture strain measured during a static tensile test. The fatigue ratio was R=0.3.

3.2 Identification of Parameters

The goal is to extract the material parameters from experimental data. An objective function representing, in the least squares sense, the difference between experimental and numerical data [Gavrus et al.1996] has been built and minimised. The cost function is written as:

$$S(\underline{P}) = \frac{\sum_{i=1}^{a}\left[d_i^{comp}(\underline{P}) - d_i^{exp}\right]^2}{\sum_{i=1}^{a}\left(d_i^{exp}\right)^2} \tag{10}$$

Where a is the number of experimental data. d_i^{exp} measures the damage in the longitudinal direction and d_i^{comp} is the computed value obtained from the modelling (Eq 1.5) with $d_{11}=d$. $\underline{P}$ is the parameter vector that contains (α, β, λ, δ).

The minimisation of the cost function is an iterative procedure. At each step, the vector $\underline{P}$ is re-estimated ($\underline{P}$ becomes $\underline{P}+\Delta\underline{P}$) and the cost function S is re-evaluated. $\Delta\underline{P}$ is computed by using a Gauss-Newton algorithm. The iterative procedure is stopped when two consecutive values of the cost function satisfy: $\left\|S(\underline{P}+\Delta\underline{P}) - S(\underline{P})\right\| < 10^{-5}$. Namely, the cost function becomes stationary. The parameters α, β, λ and δ are identified by using experimental data obtained from tests corresponding to $\varepsilon_{max}=30\%\varepsilon_{rup}$ and $\varepsilon_{max}=40\%\varepsilon_{rup}$. The comparison between experimental data used for the identification strategy and the computed damages are presented on Figure 4. Moreover, it has been assessed that the identification procedure does not depend on the initial values of α, β, λ and δ.

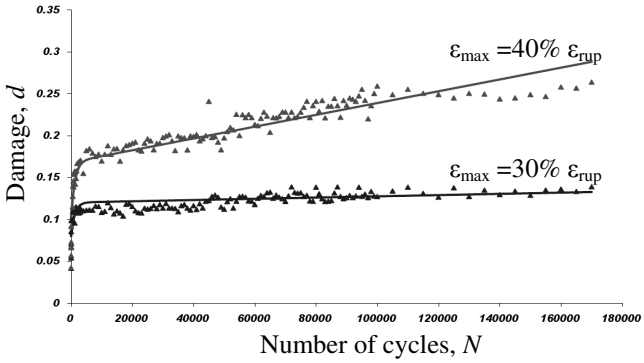

Fig. 4 Comparison between experimental and calculated damage data for two configurations (ε_{max}=30%ε_{rup} and ε_{max}=40%ε_{rup})

Finally, the set of parameters determined by the inverse procedure is validated on the experimental curve for the case where ε_{max}=20%ε_{rup}. Figure 5 shows the comparison between experimental data and numerical calculations for the parameters computed from the identification procedure.

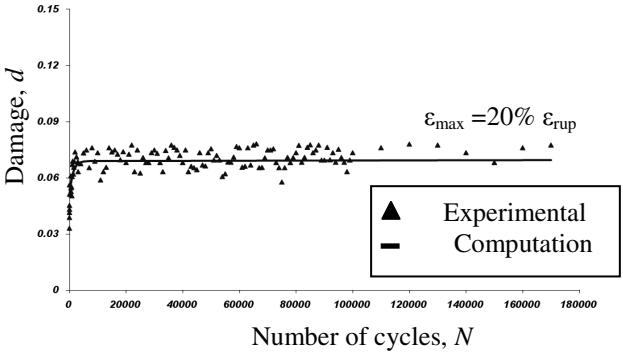

Fig. 5 Comparison between experimental and calculated damage data for ε_{max}=20% of ε_{rup}. This validates the identified set of parameters

4 Conclusion

In this work, a new cumulative fatigue damage model in short glass fibre reinforced thermoplastics is developed. These composites are characterised by an evolution of the damage in three stages. The new model is able to capture the first stage of damage specific to the composite materials with thermoplastic matrix.

This paper presents a first identification strategy: homogeneous tensile fatigue tests have been performed in the longitudinal direction. Three strain controlled fatigue tests at different levels have been carried-out to identify the four parameters

governing the evolution of the longitudinal damage. The parameters are identified by using experimental data from 2 different tests at different strain levels. The model, insensitive to the initial values, is validated on a third fatigue test.

A second identification strategy is currently ongoing. It is based on the use of optical whole-field displacement/strain measurements by digital image correlation coupled to an inverse method from one single coupon. It is worth noting that the mechanical test must give rise to heterogeneous stress/strain fields. Indeed, in this case, the constitutive parameters are expected to be all involved in the response of the specimen.

References

Sedrakian, A., Ben Zineb, T., Billoet, J.L.: Contribution of industrial composite parts to fatigue behaviour simulation. International Journal of Fatigue, 307–318 (2002)

Gagel, A., Fiedler, B., Schulte, K.: On modelling the mechanical degradation of fatigue loaded glass-fibre non-crimp fabric reinforced epoxy laminates. Composites Science and Technology 66, 657–664 (2006)

Van Paepegem, W., Degrieck, J.: A new coupled approach of residual stiffness and strength for fatigue of fibre-reinforced composites. International Journal of Fatigue 24, 747–762 (2002)

Degrieck, J., Van Paepegem, W.: Fatigue damage modeling of fibre-reinforced composite materials: Review. Applied Mechanics Review 54, 279–299 (2001)

Ye, L.: On fatigue damage accumulation and material degradation in composite materials. Composites Sciences and Technology 36, 339–350 (1989)

Ladevèze, P., Le Dantec, E.: Damage modelling of the elementary ply for laminated composites. Composites Science and Technology 43, 257–267 (1992)

Nouri, H., Meraghni, F., Lory, P.: A new thermodynamical fatigue damage model for short glass fibre reinforced thermoplastic composites. In: 16th International Conference on Composite Materials, Kyoto (July 2007)

Cooreman, S., Lecompte, D., Sol, H., Vantomme, J., Debruyne, D.: Elasto-plastic material parameter identification by inverse methods: Calculation of the sensitivity matrix. International Journal of Solids and Stuctures (November 2006)

Claire, D., Hild, F., Roux, S.: A finite element formulation to identify damage fields: the equilibrium gap method. International Journal for Numerical Methods in Engineering 61, 189–208 (2004)

Gavrus, A., Massoni, E., Chenot, J.L.: An inverse analysing a finite element model for identification of rheological parameters. Journal of Materials Processing Technology 60, 447–454 (1996)

Elasticity and Viscoelasticity of Open Cellular Material: Micromechanical Approach

Yamen Maalej[1], Mariem Imene El Ghezal[2], and Issam Doghri[2]

[1] ENIS, Mechanics,
Modeling and Production Research Unit,
B.P. 3038, Sfax, Tunisia
yamen.maalej@hotmail.com
[2] UCL, IMMC, bâtiment Euler,
4 Av. G. Lemaître B-1348,
Louvain-La-Neuve, Belgium

Abstract. Cellular materials are characterized by remarkable mechanical properties with light weight. Such materials are used in various applications mainly in energy absorption. Their microstructure are described by two major families : open and close cell foams. This paper deals with the prediction of the macroscopic behavior of open cell foams in elasticity and viscoelasticity as function of their microstructure. Firstly, we use a micromechanical model based on Cosserat homogenization framework. Secondly, Finite Element (FE) computations are performed on a unit cell subjected to periodic boundary conditions. The results are confronted to various models developped in litterature. Finaly, the linear viscoelastic behavior is deduced from elastic results by taking advantage of correspondence principle.

Keywords: Cellular materials, elasticity, viscoelasticity, homogenization, Cosserat, finite elements, LCT.

1 Introduction

The elastic and viscoelastic behavior of open cell materials was been widely studied in the litterature. They are used in diverse areas of application such as soundproofing, thermal isolation and energy absorption. Generally, cells shapes in foams (figure 1a) are idealized by regular geometric shape such as rhombic dodecahedron, tetrakaidecahedron [12], [4] and cubic cells for more simplicity [2], [9]. The mechanical behavior was achieved by homogenizing the heterogeneous structure of the material using several approaches such as the theory of beams [12], [4], [7] and the semi-empirical method with fitting parameters [2], [3]. This paper deals with the prediction of the macroscopic behavior of open cell foams in elasticity and viscoelasticity as function of their microstructure. Micromechanical model using Crosserat homogenization framework will be conducted to predict the elastic properties and extended to viscoelasticity by taking advantage of the correspondence

M. Haddar et al. (Eds.): *Design and Modeling of Mechanical Systems*, LNME, pp. 531–540.
DOI: 10.1007/978-3-642-37143-1_64

principle. Analytical model will be developped and assessed by comparing them to references results and FE computations on unit cells under periodic boundary conditions.

2 Elastic Behavior

2.1 Micromechanical Model

Several studies tried to find a link between microscopic and macroscopic properties of foams by using beam models as a scale transition [2], [12], [11], [4]. Among the unit cells used in litterature, we will focus on the model of tetrakaidecahedron cells packed in a Body Centered Cubic (BCC) lattice which is well appropriate for isotropic open cell foams. As illustrated in figure 1b, the tetrakaidecahedron cell contain six square and eight hexagonal faces. It is created by truncating the corners of a cube. Considering a coordinate system (xyz) which axes are parallel to the truncated cube axes, whereby the BCC lattice possesses cubic orthotropy and could be periodically extended in the three orthogonal directions. The Young's moduli in the lattice vector directions are equal, so only ones needs to be evaluated. In order to calculate the homogenized Young's modulus in the z direction $\bar{E}_{zz}$, a pair of tensile stress σ is applied in the z-direction as shown in figure 1c. The homogenized Young's modulus is then simply noted by $\bar{E}$. Regarding the mirror symmetry of the loading and geometry on planes dashed outlines in figure 1c, we define a representative volume element (RVE) cell bounded dy the symmetry planes (let's $(X_sY_sZ_s)$ the coordinate system of RVE cell structure).

All the struts of the tetrakaidecahedron cell are assumed to be uniform, elastic and isotropic (of Young's modulus E) beams satisfying the classical beam theory. The relative density R is defined as the density of the cellular material divided by that of the solid from which the cell walls are made :

$$R = \frac{3A}{2\sqrt{2}L^2} \tag{1}$$

where L the lenght of an edge and A its cross section area.

Our calculation are based on the general Cosserat homogenization framework presented in [8]. Each material point of the macroscopic continuum body is seen as the center of a RVE (volume V) made of a cellular material. The macroscopic stress σ_{ij} is transmitted to the cellular RVE through local forces at the RVE's boundary :

$$f_i^{(k)} = \sigma_{ij} n_j^{(k)} ds^{(k)} \tag{2}$$

where $f_i^{(k)}$ is the force acting on node (k) associated with surface area $ds^{(k)}$ and $n_j^{(k)}$ the unit vector normal to surface $ds^{(k)}$. We solve the equilibrium problem on a micromechanical scale by determining displacements. The computation

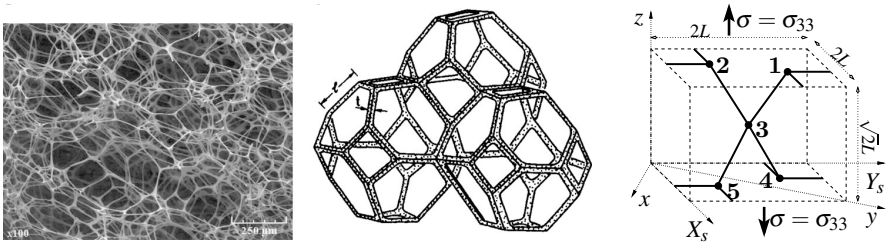

(a) (b) (c)

Fig. 1 (a) SEM of foam microstructure ; (b) Assembly of ideal tetrakaidecahedra, after Magnenet et al. [6] ; (c) RVE under tensile stress

of equivalent macroscopic deformation uses an energetic equivalence between the average external work on the discrete material sample $\bar{W}$ and the strain energy density W in the macroscopic material point :

$$\bar{W} = \frac{1}{V}\sum_k f_i^{(k)} u_i^{(k)} \quad \equiv \quad W = \frac{1}{2}\sigma_{ml}\varepsilon_{ml} \tag{3}$$

where $u_i^{(k)}$ the node displacement due to the force acting $f_i^{(k)}$ and ε_{ml} the effective macroscopic strain measure identified as :

$$\varepsilon_{ij} = \frac{1}{V}\sum_k \frac{1}{2}(n_j^{(k)} u_i^{(k)} + n_i^{(k)} u_j^{(k)})\, ds^{(k)} \tag{4}$$

Considering the symmetry of the base tetrakaidecahedra cell and sitting on a body-centered cubic (BCC) lattice (figure 1c), we define a new coordinate system (XYZ) related to the edges with unit vectors $(i,j,k)_{XYZ}$ which are related to those of the BCC lattice $(e_1,e_2,e_3)_{xyz}$ by :

$$i = e_1 \quad ; \quad j = \frac{1}{\sqrt{2}}e_2 - \frac{1}{\sqrt{2}}e_3 \quad \text{and} \quad k = \frac{1}{\sqrt{2}}e_2 + \frac{1}{\sqrt{2}}e_3 \tag{5}$$

Regarding the large web radius at the junction between edges, it will be assumed in this caculation that there is no vertex distorsion.

Using the notation of figure 1c, the effective macroscopic strain ε_{33} reads :

$$\varepsilon_{33} = \frac{1}{V}\sum_k (n_3^{(k)} u_3^{(k)}\, ds^{(k)}) \tag{6}$$

Within this tensile test, the nodes subjected to extension force $f^{(k)}$ are (1, 2, 4 and 5). We attach to each node (k) an elementary area $ds^{(k)}$ (w.r.t. the force equilibrium (2)) : $ds^{(1)} = ds^{(2)} = ds^{(4)} = ds^{(5)} = 2L^2$. Substituting in (6) and noting that the node absolute displacement are the same, the effective macroscopic strain ε_{33} leads to :

$$\varepsilon_{33} = \frac{1}{4\sqrt{2}L}(8u_3^{(1)}) \tag{7}$$

where the only displacement component $u_3^{(1)}$ needs to be determined.

Using the force equilibrium $f_3^{(1)} = \sigma_{33} n_3^{(1)} ds^{(1)} = 2\sigma L^2$ and projecting into the (XYZ) coordiante system gives :

$$f^{(1)} = {}^t(0\ ,\ 0\ ,\ 2\sigma L^2)_{xyz} = {}^t(0\ ,\ F_Y\ ,\ F_Z)_{XYZ} \quad \text{with} \quad F_Z = -F_Y = \frac{2\sigma L^2}{\sqrt{2}} \tag{8}$$

As we suppose that the rotation of node 1 relative to node 3 about the X axis is zero, it follows from equilibrium of moments that $M_X = -\frac{F_Z L}{2}$.

Making use of the principle of superposition, one may check that :

$$u^{(1)} = {}^t\left(0\ ,\ \frac{F_Y L}{AE}\ ,\ \frac{F_Z L^3}{12EI}\right)_{XYZ} \tag{9}$$

Substituting (8) in (9) and projecting into coordinate system (xyz), the displacement of node (1) in the z direction reads :

$$u_3^{(1)} = \sigma\left(\frac{L^3}{AE} + \frac{L^5}{12EI}\right) \tag{10}$$

and finaly, using (7), the homogenized Young's modulus in the z direction $\bar{E}_{zz}$ yield :

$$\bar{E} = \bar{E}_{zz} = \frac{\sigma}{\varepsilon_{33}} = \chi E \quad \text{with} \quad \chi = \frac{6\sqrt{2}I}{L^4\left(1 + \frac{12I}{AL^2}\right)} \tag{11}$$

χ is a constant depending on the geometrical microstructure parameters.

A similar work can be conducted for the homogenized Poisson's ratio :

$$\bar{\nu} = -\frac{\varepsilon_{22}}{\varepsilon_{33}} = \frac{1}{2}\frac{AL^2 - 12I}{AL^2 + 12I} \tag{12}$$

This result show explicitly the dependence of the effective mechanical properties on the foam density R, the elastic properties of the constitutive material and the edge cross section shape which is characterized by the lenght L of each edge, the cross sectional area A and the second moment of area I. For square sections with side a, $A = a^2$ and $I = a^4/12$. Using (1), the the homogenized Young's modulus (11) and Poisson's ratio (12) for square sections edge reads :

$$\bar{E} = \frac{4\sqrt{2}R^2}{9 + 12\sqrt{2}R}E \quad \text{and} \quad \bar{\nu} = \frac{3 - 4\sqrt{2}R}{6 + 8\sqrt{2}R} \tag{13}$$

It is worth noting that this result is identical to that obtained by Zhu et al. [12] using an energetic method. This result is also close to that of Li et al. [4] which used Castigliano's energy. The analysis is performed on a

tertrakaidecahedral unit cell and the expressions of Young's modulus and Poisson's ratio are respectively :

$$\begin{aligned} \bar{E} &= \frac{cR^2}{0.0787+(1.1719+1.2187k(1+\nu)cR}E \\ \bar{\nu} &= \frac{0.3421+0.2977(1+6(1+\nu)k)cR}{1+0.5955(25+26(1+\nu)k)cR} \end{aligned} \tag{14}$$

where $c = I/A^2$ and k are two geometric parameters which depend on the shape of the edge's section. For square sections, $c = 0.0833$ and $k = 1.2$.

2.2 Numerical Model

Finite element simulation are performed on a tetrakaidecahedral cell sitting on a BCC lattice. As noted in the previous section, this model represents well the open cell foam. Since the microstructure of these material is periodic along the three directions, a unit cell is sufficient to provide the information needed to compute the effective properties at the macroscopic scale provided that periodic boundary conditions are imposed [1]. Finite element simulations are therefore performed on a tetrakaidecahedral unit cell generated by Abaqus software (figure 2a). The struts are modeled by Timoshenko beam elements (Abaqus type B31) having square cross sections. The variation of the relative density is performed by adjusting the beam section.

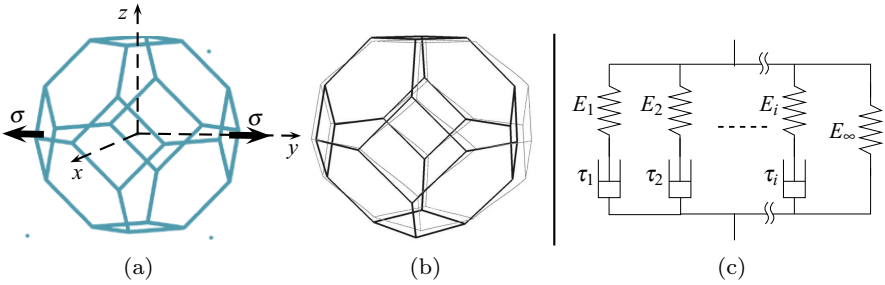

Fig. 2 (a) FE model for tetrakaidecahedral unit cell ; (b) Deformed shape under tensile test (thin lines) ; (c) Rheological model for the strut's material

In order to apply periodic boundary conditions, we placed the unit cell in a fictitious cube of dimensions L so that the six square faces of the tetrakaidecahedral unit cell are tangent to the faces of the cube (figure 2a). The origin of the coordinate system (O,x,y,z) is placed in the center of the cube. Next, we added a set of master ($M(-0.5L, -0.5L, -0.5L)$) and slave nodes (S_1, S_2 and S_3 respectively of coordinates $(0.5L, -0.5L, -0.5L)$, $(-0.5L, 0.5L, -0.5L)$ and $(-0.5L, -0.5L, 0.5L)$. Periodic boundary conditions involves the following conditions on the displacement fields u :

$$u_i(M) - u_i(S_1) = u_i(\text{nodes} \in \text{face } x = -\frac{L}{2}) - u_i(\text{nodes} \in \text{face } x = +\frac{L}{2}),\ i \in [1,3]$$
$$u_i(M) - u_i(S_2) = u_i(\text{nodes} \in \text{face } y = -\frac{L}{2}) - u_i(\text{nodes} \in \text{face } y = +\frac{L}{2}),\ i \in [1,3]$$
$$u_i(M) - u_i(S_3) = u_i(\text{nodes} \in \text{face } z = -\frac{L}{2}) - u_i(\text{nodes} \in \text{face } z = +\frac{L}{2}),\ i \in [1,3] \quad (15)$$

In order to eliminate the rigid body displacement, vector u is imposed as $u_i(M) = 0$, $i \in [1,3]$ (M is a fixed node), $u_3(S_2) = 0$ (no rotation around x), $u_1(S_3) = 0$ (no rotation around y) and $u_2(S_1) = 0$ (no rotation around z).

Due to the cubic symmetry, both the effective Young's modulus and Poisson's ratio can be derived from a tensile test applied along one of the cube axes. A displacement is applied to one of the slave nodes. The macroscopic stress tensor $\bar{\boldsymbol{\sigma}}$ is computed from the external tractions at the master and slave nodes and the strain tensor $\bar{\boldsymbol{\varepsilon}}$ from displacement components of these nodes (deformed shape under tensile test is presented in figure 2b). Furthermore, the approach is to identify the significant terms of stress $\bar{\boldsymbol{\sigma}}$ and strain $\bar{\boldsymbol{\varepsilon}}$ tensor with those of the constitutive law.

2.3 Application to Polymeric Foams

A Polyurethane (PU) open cell foam is considered as an application to compare predictions of elastic constants given by analytical (section 2.1) and FE simulation (section 2.2). The constitutive material of the solid skeleton is considered as an isotropic solid characterized by Young's modulus $E = 100\,MPa$ and Poisson's ratio $\nu = 0.45$. The variation of foam's Young's moduli and Poisson's ratio predicted by the homogenization models (equation (13) and (14)) w.r.t. relative density R (1) is plotted in figure 3, along with FE results.

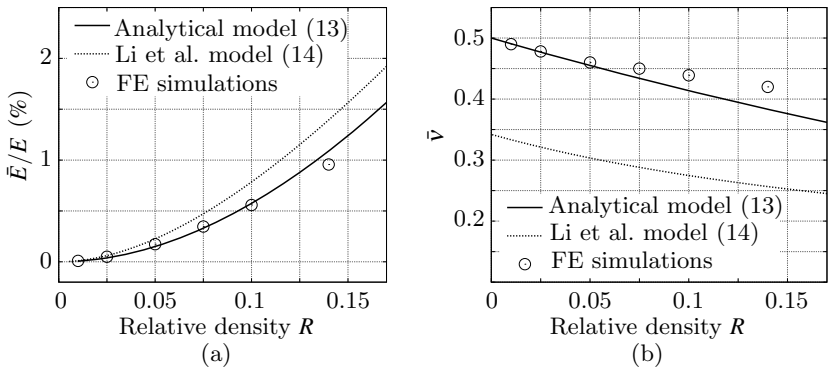

Fig. 3 Effective properties of a foam w.r.t. the relative density : (a) normalized Young's modulus, (b) Poisson's ratio

It is seen in figure 3a that at low relative densities, all predictions of Young's modulus are close. For higher densities, the model based on the Cosserat homogenization framework, which is coincides with the Zhu et al. prediction [12], gives a good agreement with FE and the difference with Li et al. predictions increases with relative density. As shown in figure 3b, despite the fact that the analytical models emanate from the same idealized microstructure (tetrakaidecahedral cell), there is an unexpected difference between the Poisson's ratios predicted by each one. For lower relative densities, Poisson's ratio predicted by Cosserat homogenization framework comes close to 0.5 and therefore, an incompressible behavior. This result agrees well with that obtained by FE simulations.

3 Viscoelastic Behavior

3.1 Analytical Model Using LCT

At small strains, open cellular materials have a linear viscoelastic response. In other words, creep strains are proportional to the stress under a constant load at any given time. Therefore, by taking advantage of the correspondance principle, we will employ the elastic solutions for solving linear viscoelastic behavior. The macroscopic viscoelastic behavior of cellular materials will be defined in terms of effective relaxation moduli and equivalently creep compliances using the microscopic ones and the geometric properties. For a homogeneous linear viscoelastic solid, the three dimensional constitutive equation is given by Boltzmann's superposition principle as follows :

$$\boldsymbol{\sigma}(t) = \int_{-\infty}^{t} \mathbb{C}(t-\tau) : \dot{\boldsymbol{\varepsilon}}(\tau) d\tau \tag{16}$$

where $\mathbb{C}(t)$ is the fourth order viscoelastic relaxation tensor and $\dot{\boldsymbol{\varepsilon}}$ is the second order strain rate tensor.

The viscoelastic strut material's stress relaxation data can be approximated by a rhelogical model constituted by a set of Maxwell elements (figure 2c). Then the relaxation Young's modulus $E_R(t)$ is given by a Prony series :

$$E_R(t) = E_\infty + \sum_{i=1}^{n} E_i \exp(-t/\tau_i) \tag{17}$$

where E_∞ the modulus at infinity and E_i those associated with relaxation times τ_i. As an application, we will use for this analysis, the experimental data obtained by Zhu and Mills [14] on solid Bulpren PU. They approaximated the relaxation Young's modulus with eight relaxation times $\tau_i = 10^{i-3}$ of moduli $E_i = 9.3$ MPa for $i = 1$ to 8 and $E_\infty = 28$ MPa.

Using the Laplace Carson Transform (LCT), the viscoelastic response can be written as the elastic solution when a change of variables is made. The

following correspondence relates the elastic constants to the relaxation functions in the Laplace Carson domain [10] : $E \leftrightarrow sE_R(s)$. Subsequently, we apply this methodology to extend the effective elastic moduli obtained in section 2.1 to linear viscoelastic behavior. Since the effective elastic moduli is linear w.r.t. the strut moduli, the application is found to be simple. As we apply the correspondance principle on elastic solution given by equation (11), we have in Laplace-Carson domain :

$$s\bar{E}_R(s) = \chi\, sE_R(s) \quad \text{with} \quad \chi = \frac{6\sqrt{2}I}{L^4(1+\frac{12I}{AL^2})} \tag{18}$$

Appling Laplace transform, (18) then yield :

$$d\bar{E}_R(t) = \chi\, dE_R(t) \quad \Longrightarrow \quad \int_0^t d\bar{E}_R(\tau) = \chi \int_0^t dE_R(\tau) \tag{19}$$

where it was assumed that the material has been stress free for times anterior to zero. Considering that $\bar{E}_R(+\infty) = \bar{E}$ and using the relationship between $\bar{E}$ and E (11), we obtain :

$$\bar{E}_R(t) = \chi E_R(t) \tag{20}$$

This means that, as well as the elastic behavior, the foam's relaxation is also linearly related by the ratio χ to the one of the constitutive solid and that it is sufficient to replace the elastic modulus by the time-dependent relaxation function. A simular result was founded by Huang and Gibson [3] who, starting from the proportionality between the elastic constants of the open cell foams and an empirical equation describing the viscoelastic behavior of solid polymer, ended with a relative creep compliance of the foam : $\bar{J}(t) = (E/\bar{E})J(t)$. Micromechanical foam model of Li et al. (14) is also generalized, by means of LCT, to linear viscoelasticity.

3.2 FE Simulation and Application to PU Foams

Similarly to the elastic analysis, we conducted FE computations on different unit cells of cellular solids. The unit cell described in section 2.2 undergoes uniaxial compression creep. The strut material obey the same relaxation law (17). The FE macroscopic relaxation modulus can be deduced using the approximation $\bar{E}_R(t) \simeq 1/\bar{J}(t)$, where $\bar{J}(t) = \bar{\varepsilon}(t)/\sigma_0$ and $\bar{\varepsilon}$ is the resulting macroscopic strain computed as detailed in section 2.2.

We report in figure 4 the different predictions of the effective relaxation modulus from different models confronted to FE computations for polymer foams having respectively 0.05 and 0.025 of relative density. As depicted in figure 4, FE results are bounded by the analytical predictions.

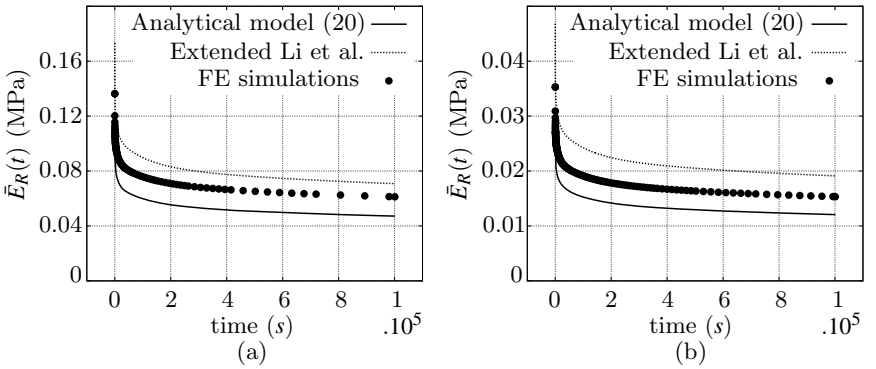

Fig. 4 Effective properties of a foam w.r.t. the relative density: (a) normalized Young's modulus, (b) Poisson's ratio

4 Conclusion

In the first part of this paper, micromechanical model using Crosserat homogenization framework was conducted to predict the properties of open cell foams. Analytical model were developped and assessed by comparing them to FE computations on unit cells under periodic boundary conditions. The macroscopic elastic behavior was found to be linearly dependent to the elastic properties of he strut material. This proportionality depends on both the shape of the edges and the relative density of the foam. For the low relative density, the analytical predictions of Young's modulus and Poisson's ratio was colse close to those of FE but small discrepancy was observed with increasing relative density particularly for the Li et al. model. In the second part, elastic solutions were extended to linear viscoelasticity using LCT. The macroscopic relaxation function follows the same proportional factor that the elastic behavior; the elasticity of the strut material is simply replaced by it's relaxation function. The analytical results have been compared with the Li et al. model (extended to viscoelasticity via LCT) and FE computations.

It is worth mentioning that while we modeled open cell cellular solids by a periodic model, the real material is random and its microstructure is more complex. The limitation of previously discussed models is that they do not account for the natural irregularities due to imperfect geometry or/and irregular arrangement of cells. This is out af the scope of the current study, for a thorough analysis of the effect of cell irregularities on the overall mechanical behavior refer for instance to [5] and [13].

References

[1] Bornert, M., Bertheau, T., Gilormini, P.: Homogénéisation en mécanique des matériaux. 1. Hermes science publication (2001)
[2] Gibson, L.J.: Biomechanics of cellular solids. J. Biomechanics 38, 377–399 (2005)
[3] Huang, J.S., Gibson, L.J.: Creep of polymer foams. J. Mech. Phys. Solids 26, 637–647 (1991)
[4] Li, K., Gao, X.L., Roy, A.K.: Micromechanics model for three-dimensional open-cell foams using a tetrakaidecahedral unit cell and castiglianos second theorem. Composites Sc. Tech. 63, 1769–1781 (2003)
[5] Li, K., Gaon, X.-L., Subhash, G.: Effets of cell shape and strut cross-sectional area variation on the elastic properties of three-dimensional open-cell foams. J. Mech. Phys. Solids 54, 783–806 (2006)
[6] Magnenet, V., Rahouadj, R., Bacher, P., Cunat, C.: Inelastic constitutive relations for foamed materials: A statistical approach and its application to open-cell melamine. Mech. Materials 40, 673–684 (2008)
[7] Mills, N.J.: Finite element models for the viscoelasticity of open-cell polyurethane foam. Cellular Polymers 25 (2006)
[8] Onck, P.R.: Cosserat modeling of cellular solids. Comptes Rendus Mécanique 330(11), 717–722 (2002)
[9] Roberts, A.P., Garboczi, E.J.: Elastic properties of random three-dimensional open cell solids. J. Mech. Phys. Solids 50, 33–55 (2002)
[10] Salençon, J.: Viscoélasticité. Presses de l'ENPC, Paris (1983)
[11] Warren, W.E., Kraynik, A.M.: Linear elastic behavior of a low-density kelvin foam with open cells. J. App. Mech. 64, 787–794 (1997)
[12] Zhu, H.X., Knott, J.F., Mills, N.J.: Analysis of the elastic properties of open cell foams with tetrakaidecahedral cells. J. Mech. Phys. Solids 45, 319–345 (1997)
[13] Zhu, H.X., Hobdell, J.R., Windle, A.H.: Effets of cell irregularity on the elastic prperties open-cell foams. Acta Mater. 48, 4893–4900 (2000)
[14] Zhu, H.X., Mills, N.J.: Modelling the creep of open cell polymer foams. Mech. Phys. Solids 47, 1437–1457 (2006)

Characterization of the Friction Coefficient and White Layer at the Tool-Chip-Workpiece Interface Using Experimental and Numerical Studies during Friction Tests of AISI 1045

Hamdi Ben Abdelali[1], Wacef Ben Salem[1], Joel Rech[2], Abdelwaheb Dogui[1], and Philippe Kapsa[2]

[1] Universté de Monastir, Laboratoire de Génie Mécanique, Avenue Ibn Al-Jazzar, 5019 Monastir, Tunisie
{hamdi.benabdelali,wacefs}@yahoo.fr, abdel.dogui@enim.rnu.tn
[2] Université de Lyon, Ecole Nationale d'Ingénieurs de Saint-Etienne, Laboratoire de Tribologie et Dynamique des Systèmes, UMR CNRS 5513, 58 Rue Jean Parot, 42023 Saint-Etienne, France
joel.rech@enise.fr, Philippe.Kapsa@ec-lyon.fr

Abstract. In this paper, a new experimental set-up able to simulate similar tribological phenomena as the ones occurring at the tool-chip-workpiece interface in metal cutting has been applied to the characterization of the tool-chip-workpiece interface during dry cutting of an AISI1045 with TiN coated carbide tools. Several friction tests have been made according to the sliding velocity. It has been shown that the apparent friction coefficient and the heat flux transmitted to the pin were strongly influenced by the sliding velocity. Metallographic studies of the machined sub-surface have been performed to understand the evolution of white layer formation. Tow phenomena have been observed: the first phenomenon is the plastic deformation from the low sliding velocity and the second phenomenon is obtained for the sliding velocity a bove of 60 m/min. White layer has been observed in this second regime. In additionally, the present paper employs the finite element method to extract local parameters around the spherical pin from experimental macroscopic measurements. A 3D ALE numerical model simulating the frictional test has been associated in order to determine the plastic strain and the contact temperature to better understand the tribological phenomena.

Keywords: Apparent friction coefficient, sliding velocity, heat flux, white layer, plastic strain, contact temperature.

1 Introduction

In order to estimate the friction coefficients at the tool-chip-workpiece interface and better understand the tribological phenomena at the tool-chip-workpiece interface, scientists consider two approaches. The first approach consists in using the

M. Haddar et al. (Eds.): *Design and Modeling of Mechanical Systems*, LNME, pp. 541–548.
DOI: 10.1007/978-3-642-37143-1_65

cutting process itself (Zemzemi et al.2007). The investigations are usually based on turning tests of a tube made of the investigated material, with a cutting tool made of the relevant substrate and coating. During tests, white bands at the surface layer of the workpiece and the chip are obtained (Poulachon et al. 2005). They are named so because, under a light microscope, they appear white on the micrographs of samples etched (or a microscope electronic scanning). The formation of white layers is the result of the increase in temperature at the tool-chip-workpiece interface and the presence of plastic deformation phenomenon (Ramesh et al. 2005). This white layer formed during machining is generally hard and brittle phase, which may cause the presence of cracks and other surface defects.

The second one consists of using bench-type tribological tests (Arrazola et al. 2008). These laboratory tests enable the control of the contact conditions and the ability to modify these conditions as desired. Several test configurations already exist. The most common test is the pin-on-disc system, which is unable to simulate the contact conditions in cutting, since the conditions (temperature, pressure) are not similar to those observed in reality as shown by (Grzesik et al. 2002). Specialists in tribology use the terminology "open tribo-system". On the contrary, in pin-on-disc systems, the pin always rubs on the same track. This configuration is labeled "closed tribo-system". Both configurations lead to fully different tribological results. So, it does not make sense to use 'closed tribo-system' in order to investigate the tribological phenomena at tool/chip/workpiece interfaces. Recently, another experimental set-up has been used successfully by (Zemzemi et al. 2009) in order to quantify the friction coefficient occurring along the tool–chip–workpiece interface. This system has been applied by (Rech et al. 2009) to characterize the frictional behavior of the couple of material involved in the present work: an AISI1045 machined by a TiN coated carbide tool. However, the tribometer was limited to sliding velocities in the range [50-250 m/min], which does not enable to qualify friction coefficient at low sliding velocities as the one occurring around to the cutting edge. (Claudin et al. 2010) has modified the tribometer in order to reach a larger range of sliding velocities [5-1000 m/min] but he was not concerned with the same couple of material.

The aim of this work is to characterize the friction coefficients during the dry machining of a AISI1045 steel with TiN coated carbide tools. This study is based on experimental and numerical studies of friction test to understand the evolution of friction coefficients and white layer formation. During the experimental test, a new version of the tribometer developed by (Claudin et al. 2010) has been used. A numerical model with the ALE approach has ben developed to simulate the friction test.

2 Experimental Approach

The influence of the sliding velocity on the apparent friction coefficient μ_{app} is plotted on Fig. 1. The apparent friction coefficient μ_{app} is then calculated as report between a normal force and tangential force.

It revealed that the apparent friction coefficient is strongly influenced by sliding velocity V_s. Three frictional regimes may be defined:

- V_s < 60 m/min (regime 1), the apparent friction coefficient is almost constant (μapp~0.54).
- 60 < V_s < 180 m/min (regime 2), the apparent friction coefficient decreases with the sliding velocity (μ_{app}=0.54→0.23).
- V_s > 180 m/min (regime 3), the apparent friction coefficient is constant (μ_{app} ~ 0.23).

The results obtained in the range 5 to 300 m/min are close to those already published by (Rech et al. 2009) using another tribometer in a narrower range of sliding velocities (50 to 250 m/min).

The tribometer provides the heat flux transmitted to the pin $Ø_{pin}$. The evolution of heat flux $Ø_{pin}$ versus the sliding velocity V_s is plotted in Fig. 2. It appears that the heat flux increases with the sliding velocity, which is coherent since more energy is dissipated in the contact. The results obtained are coherent with those found by (Rech et al. 2009).

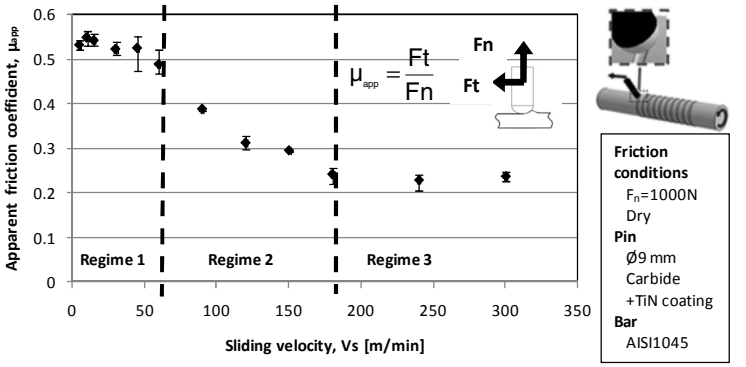

Fig. 1 Evolution of the apparent friction coefficient versus the sliding velocity

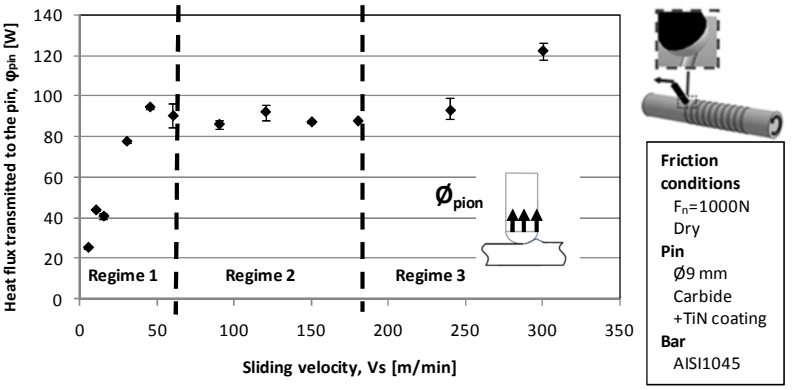

Fig. 2 Evolution of the heat flux transmitted to pins versus the sliding velocity

Three regimes can be distinguished:

- In the first regime ($V_s < 60$ m/min), the heat flux transmitted to pins $Ø_{pin}$ increases with the sliding velocity.
- In the second regime ($60 < V_s < 180$ m/min), the heat flux $Ø_{pin}$ remains almost constant.
- In the third regime ($V_s > 180$ m/min), the heat flux $Ø_{pin}$ increases with sliding velocity.

A study on a microscopic scale has been conducted to observe the microstructure of workpiece after friction tests and to understand the tribological phenomenon (evolution of apparent friction coefficient). Samples of the workpiece were taken after the passage of the pin with different sliding velocities. These samples were embedded in a cold resin, and polished and etched using a 2% Nital solution.

Once these steps are completed, microscopic observations were made on samples taken from the workpiece after friction tests with different sliding velocities. Furthermore, other observations were made samples before friction tests, show the initial state of the AISI 1045 steel. This state is compared to the other samples to better understand the transformations that can be obtained after the friction tests (Fig. 3).

Fig. 3 shows that the initial state of the steel has a ferritic-pearlitic microstructure, whereas after each friction test, it is clear that the initial state was changed. In fact, two phenomena were observed: The first obtained at low sliding velocities in which grains were crushed, (Fig. 3). This is the result of large plastic deformations. The second phenomenon is observed by increasing the friction velocity. White zones which have different color and structure comparing to the initial state of the steel are observed at the surface layer. In the machining of metals, these zones are called "White layers" (Bosheh and Mativenga 2006). Indeed, the formation of the white layer is due to the increase of temperature in the surface area of the workpiece due to the increase of the sliding velocity. The increase tendency followed by rapid cooling led to changes produced in the surface area. In this case,

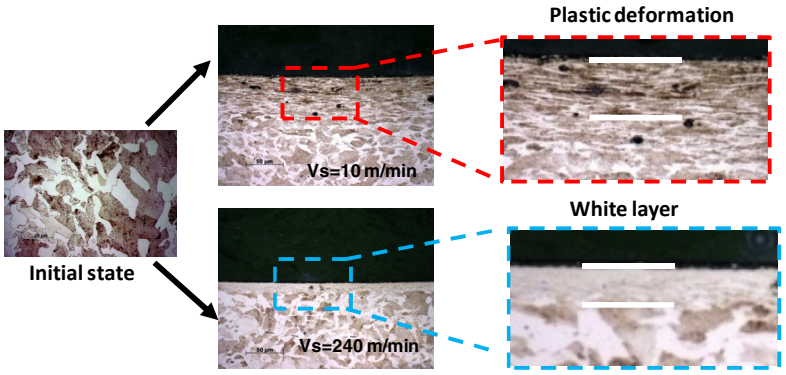

Fig. 3 Micrographs of the workpiece and the contact borders after the each friction tests

the increase of temperature also raises the possibility of chemical reactions that occur with the environment. (Han et al. 2008) found these white layers in the case of machining of AISI 1045 steel. The microstructure of the workpiece after friction test and the white layer presented in Fig. 3 are similar to those observed in the case of machining of AISI 1045 steel with a cutting tool.

3 Numerical Results

The results provided by the experimental set-up represent the macroscopic data: apparent friction coefficient μapp and heat flux transmitted to the $Ø_{pin}$. The characterization of the frictional phenomena at the tool/chip/workpiece interface necessitates focusing the analysis on the local phenomena occurring at the pin/workpiece interface using a numerical model simulating the frictional test. Description of the model is present in the work of (Ben Abdelali et al. 2012).

Fig.4 shows the evolution of the contact temperature (T) versus the workpiece depth for each macroscopic sliding velocity V_s. It appears that a maximum contact temperature increases very significantly with the sliding velocity. The maximum contact temperature is around 180°C for a sliding velocity of 5 m/min, and 1200°C for a sliding velocity of 300 m/min. While the average contact temperature determined in the previous work (Davies et al. 2003) around 160°C for a sliding velocity of 5 m/min and 940°C for a sliding velocity of 300 m/min which is relevant with maximum contact temperatures in the cutting of an AISI1045 as reported in the literature (Ceretti et al. 2007) and by (Arrozala and Ozel 2010) for the machining of other steels (AISI 4340 steel). It is also clear in Fig.4 that the temperature decreases versus the workpiece depth. As well as the workpiece depth decreases with an increasing sliding velocity.

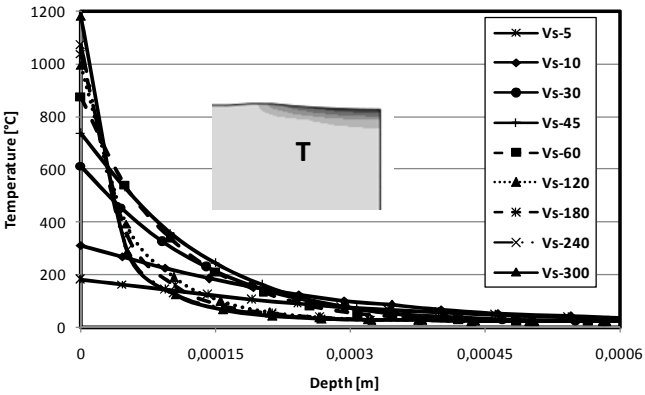

Fig. 4 Evolution of contact temperature along depth

Fig.5 shows the evolution of the equivalent plastic strain versus the workpiece depth for each sliding velocity Vs. This figure shows that the depth layer affected is almost constant, but the plastic strain is different from one sliding velocity to another. Fig.5 shows that three regimes can be distinguished:

In the first regime, for the sliding velocity Vs < 60 m/min, the equivalent plastic strain increases when the sliding velocity increases (PEEQ = 1.5 → 4.5).

In the second regime, for sliding velocity between 60 ≤ Vs ≤180 m/min, the equivalent plastic strain decreases when the sliding velocity increases (PEEQ = 4.5 → 0.55).

In the third regime, for the sliding velocity Vs > 180 m/min, the equivalent plastic strain is not affected by increasing of the sliding velocity (PEEQ ≈ 0.55).

This result is in accord with the result found by (Davim and Maranhão 2009) in the machining of steel AISI 1045 using FEM analysis. In this case, the plastic strain is in the range 0.57 to 8 at the tool-chip-workpiece interface.

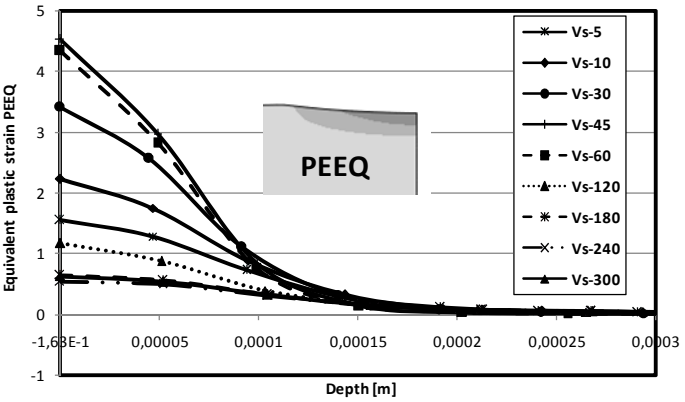

Fig. 5 Evolution of equivalent plastic strain PEEQ along depth

In this work, plastic deformation and contact temperature play a very important role in the tribological phenomena at the tool-chip-workpiece interface. Evolutions of these parameters can be divided into three regimes.

For a sliding velocity lower the 60 m/min (regime 1), we have large plastic deformations and small values of contact temperature. On the other hand, during the experimental tests the apparent friction coefficient is high (Fig.1) and layers deformed plastically have been obtained (Fig.3). This leads us to conclude that plastic deformation is most influential in tribological phenomena in this sliding velocities range.

For a sliding velocity between 60 and 180 m/min (regime 2), plastic deformation decreases and the contact temperature increases significantly as a function of the sliding velocity. During the experimental tests, the apparent friction coefficient decreases rapidly with the increasing sliding velocity (Fig.1). This decrease is due to a thermal softening caused by the rise of temperature at the contact zone. A great similarity between the contact temperature and the white layer depth is found

(Fig.5). In fact, both of them decrease when the sliding velocity increases. We can conclude that the white layer is formed due to the increase in temperature followed by the cooling with the environment and the rest of the workpiece (unheated mass). From these results, we can determine the critical temperature (minimum temperature for the formation of white layer), from these results the critical temperature is equal to 850 ° C. This leads to the fact that the contact temperature is most influential in tribological phenomena in this regime 2.

However, for a sliding velocity higher that 180 m/min (regime 3), small plastic deformations and high temperatures were obtained, in parallel decrease the experimental apparent friction coefficient is observed. These results confirm that this phenomenon is due to the thermal softening.

4 Conclusion

The work has shown that the apparent friction coefficient and heat flux transmitted to the pin are very sensitive to the sliding velocity using a new tribometer dedicated to the characterization of friction coefficients along the tool-chip-workpiece interface. During friction tests, two phenomena have been observed in superficial layers of the workpiece. We observe a plastic deformation at a lower sliding while the white layer is obtained for a higher sliding velocity. The depth and hardness of the white layer are reduced by increasing the sliding velocity. A 3D ALE numerical model, simulating the friction test, enables to extract local information from the contact area, especially the equivalent plastic strain and the average and maximum contact temperature. In this work, authors show that the relationship between the plastic stain and contact temperature with the apparent friction coefficient and white layer. These results show that the mechanical effect is dominant at a low sliding velocity and the thermal effect is dominant at a high sliding velocity in tribological phenomena.

References

Zemzemi, F., Rech, J., Ben Salem, W., Kapsa, P., Dogui, A.: Development of a friction model for the tool–chip–workpiece interface during dry machining of AISI4142 steel with TiN coated carbide cutting tools. Int. J. of Machining and Machinability of Materials (3-4), 361–367 (2007)

Poulachon, G., Albert, A., Schluraff, M., Jawahir, I.S.: An experimental investigation of work material microstructure effects on white layer formation in PCBN hard turning. International Journal of Machine Tools & Manufacture 45, 211–218 (2005)

Ramesh, A., Melkote, S.N., Allard, L.F., Riester, L., Watkins, T.R.: Analysis of white layers formed in hard turning of AISI 52100 steel. Materials Science and Engineering A 390, 88–97 (2005)

Arrazola, P.J., Ugarte, D., Domýinguez, X.: A new approach for the friction identification machining through the use of finite element modeling. Int. J. Mach. Tool. Manu. 48, 173–183 (2008)

Grzesik, W., Zalisz, Z., Nieslony, P.: Friction and wear testing of multilayer coatings on carbide substrates for dry machining applications. Surf. Coat. Technol. 155, 37–45 (2002)

Zemzemi, F., Rech, J., Ben Salem, W., Kapsa, P., Dogui, A.: Identification of a friction model at tool/chip/workpiece interfaces in dry machining of AISI4142 treated steels. J. Mater. Process. Technol. 209, 3978–3990 (2009)

Rech, J., Claudin, C., D'Eramo, E.: Identification of a friction model—Application to the context of dry cutting of an AISI 1045 annealed steel with a TiN-coated carbide tool. Tribol. Int. 42, 738–744 (2009)

Claudin, C., Mondelin, A., Rech, J., Fromentin, G.: Influence of a straight oil on friction at the tool-workmaterial interface in machining. Int. J. Mach. Tool. Manuf. 50, 681–688 (2010)

Bosheh, S.S., Mativenga, P.T.: White layer formation in hard turning of H13 tool steel at high cutting speeds using CBN tooling. Int. J. Mach. Tool. Manuf. 46, 225–233 (2006)

Han, S., Melkote, S.N., Haluska, M.S., Watkins, T.R.: White layer formation due to phase transformation in orthogonal machining of AISI 1045 annealed steel. Materials Science and Engineering A 488, 195–204 (2008)

Ben Abdelali, H., Claudin, C., Rech, J., Ben Salem, W., Kapsa, P., Dogui, A.: 2012 Experimental characterization of friction coefficients at the tool-chip-workpiece interface during dry cutting of AISI 1045. Wear 286-287, 108–115 (2012)

Bonnet, C., Valiorgue, F., Rech, J., Hamdi, H.: Improvement of the numerical modeling in orthogonal dry cutting of an AISI316L stainless steel by the introduction of a new friction model. CIRP J. of Manufacturing Science and Technology 1, 114–118 (2008)

Davies, M.A., Caoa, Q., Cooksa, A.L., Ivesterb, R.: On the measurement and prediction of temperature fields In machining AISI 1045 steel. CIRP Annals - Manufacturing Technology 52, 77–80 (2003)

Ceretti, E., Filice, L., Umbrello, D., Micari, F.: ALE Simulation of Orthogonal Cutting: a New Approach to Model Heat Transfer Phenomena at the Tool-Chip Interface. CIRP Annals - Manufacturing Technology 56(1), 69–72 (2007)

Arrazola, P.J., Ozel, T.: Investigations on the effects of friction modeling in finite element simulation of machining. Int. J. of Mechanical Sciences 52(1), 31–42 (2010)

Davim, J.P., Maranhão, C.: A study of plastic strain and plastic strain rate in machining of steel AISI 1045 using FEM analysis. Materials and Design 30, 160–165 (2009)

Ben Abdelali, H., Courbon, C., Rech, J., Ben Salem, W., Dogui, A., Kapsa, P.: Identification of a friction model at the tool-chip-workpiece interface in dry machining of a AISI 1045 steel with a TiN coated carbide tool. ASME-Journal of Tribology 133(4) (2011)

Higher Order Shear Deformation Enhanced Solid Shell Element

Jarraya Abdessalem, Hajlaoui Abdessalem,
Ben Jdidia Mounir, and Dammak Fakhreddine

Research Unit of Mechanical, Modelisation and Manufacturing Unit (U2MP),
National School of Engineers of Sfax, University of Sfax,
B.P. 1173, 3038 Sfax, Tunisia
{abdessalem.jarraya,mounir.benjdidia,
fakhreddine.dammak}@enis.rnu.tn
abdhajlaoui@gmail.com

Abstract. The paper deals with the validation of a recently proposed hexahedral solid-shell finite element for the analysis of laminated composite plates. The object of this work is to study the transverse shear as well as enhanced incompatible modes introduced to improve the in-plane deformation using the Enhanced Assumed Strain (EAS) solid shell element. The EAS three-dimensional finite element formulation presented in this paper is free from shear locking and leads to accurate results for distorted element shapes.

Keywords: Laminated composite structures, Solid-shell finite element, shear locking.

1 Introduction

Composite materials offer many advantages to structural designers. For prediction of accurate stress analysis, numerical methods have been developed for the design of these structures. As a matter of fact, nowadays many, shell elements, based on a reference surface, have been investigated and developed.

However, there is still a continuing need for more accurate values for the interlaminar normal and shear stresses, knowing that the proper modelling is non-trivial task. In recent years many studies have been devoted to understand and improve the transverse shear strain and stress distribution as outlined such the classical laminate theory (CLT) Reissner and Stavsky (1961) and Stavsky (1961) based on the Kirchhoff-Love assumptions, which can neglects the shear deformation and, as a consequence, it can lead to inaccurate results. In some works, the transverse shear strain and stress distribution are improved (Liu and Reddy (1985), Rastgaar and Aagaah (2003), Reddy (2004) and Reddy and Lee (2004)).

A large number of studies have been done to prevent volumetric locking, shear locking or thickness locking, using the enhanced assumed strain concept, namely Valente et al. (2004), de Sousa et al. (2006), Reese (2007) and Quy and

M. Haddar et al. (Eds.): *Design and Modeling of Mechanical Systems*, LNME, pp. 549–555.
DOI: 10.1007/978-3-642-37143-1_66

Matzen-miller (2008). The assumed natural strain (ANS) concept has been used as well by Hauptmann and Schweizerhof (1998), Tan and Vu-Quoc (2005), Kim et al. (2005) and Klinkel et al. (2006). The implementation of the enhanced assumed strain (EAS) and the assumed natural strain (ANS) concepts was proposed by Schwarze et al. (2011) and also by Hajlaoui et al. (2012) has implemented these two concepts in the finite element code.

The remainder of this paper in divided into five sections. Section one presents the research work in the domain of to improve the transverse shear behaviour, section two describes the fundamental formulation used. The finite element formulation is defined in section three. After that, numerical results and discussions of the finite element model are investigated in section four. Finally, some concluding remarks are analyzed and presented in section five.

2 Fundamental Formulation

The grounds of the EAS method come from the work of Simo and Rifai (1990), where the strain field is enlarged with the inclusion of additional variables, usually referred as enhancing parameters, as given by equation (1).

$$\boldsymbol{E} = \boldsymbol{E}^{c} + \tilde{\boldsymbol{E}} \tag{1}$$

Where $\boldsymbol{E}^{c}$ and $\tilde{\boldsymbol{E}}$ are respectively the compatible part and the enhanced part of the Green-Lagrange tensor. The variational basis of the finite element method with enhanced assumed strain fields is based on the well known three field Hu-Washizu principal, which, by using equation (1), takes the following forms:

$$\Pi(\boldsymbol{u}, \tilde{\boldsymbol{E}}, \boldsymbol{S}) = \int_{V} \left(\psi(\tilde{\boldsymbol{E}} + \boldsymbol{E}^{c}) - \boldsymbol{S} : \tilde{\boldsymbol{E}} \right) dV - \Pi_{ext}(\boldsymbol{u}) = 0 \tag{2}$$

$$\Pi_{ext}(\boldsymbol{u}) = \int_{V} \boldsymbol{F}_{V} . \boldsymbol{u} dV + \int_{\partial V_{f}} \boldsymbol{F}_{S} . \boldsymbol{u} dA \tag{3}$$

Where ψ is the strain energy function and $\boldsymbol{u}$ and $\boldsymbol{S}$ are the displacement and the Piola-Kirchoff stress fields respectively. Also in the equations appear the prescribed body force, $\boldsymbol{F}_{V}$, and surface traction, $\boldsymbol{F}_{S}$. Invoking the orthogonality condition:

$$\int_{V} \boldsymbol{S} : \tilde{\boldsymbol{E}} dV = 0 \tag{4}$$

reducing the number of independent variables in the original function to just two. The weake form of this modified reduced function may be obtained with the direction derivative leading to:

$$G(\boldsymbol{u}, \tilde{\boldsymbol{E}}) = \int_{V} \boldsymbol{S} : \left(\delta \boldsymbol{E}^{c} + \delta \tilde{\boldsymbol{E}} \right) dV - \int_{V} \boldsymbol{F}_{V} . \delta \boldsymbol{u} dV - \int_{\partial V_{f}} \boldsymbol{F}_{S} . \delta \boldsymbol{u} dA = 0 \tag{5}$$

This equation must be linaerized to take the following form:

$$DG.(\Delta \boldsymbol{u}, \Delta \tilde{\boldsymbol{E}}) = \int_{V} \delta \boldsymbol{E}^{c} : \mathbb{C} : \left(\Delta \boldsymbol{E}^{c} + \Delta \tilde{\boldsymbol{E}} \right) dV + \int_{V} \boldsymbol{S} : \Delta \delta \boldsymbol{E}^{c} dV + \int_{V} \delta \tilde{\boldsymbol{E}} : \mathbb{C} : \left(\Delta \boldsymbol{E}^{c} + \Delta \tilde{\boldsymbol{E}} \right) dV \tag{6}$$

3 Finite Element Formulation

The finite element is based on the eight node hexahedral solid shell element. The displacement field, with the corresponding variation and increment, is interpolated within each element domain in the following form:

$$\boldsymbol{u} = \boldsymbol{N}\boldsymbol{U}_e;\ \delta\boldsymbol{u} = \boldsymbol{N}\delta\boldsymbol{U}_e \text{ and } \Delta\boldsymbol{u} = \boldsymbol{N}\Delta\boldsymbol{U}_e, \tag{7}$$

The variation of the increment of the compatible part of the strain field can then related to the vector of nodal displacements

$$\delta\boldsymbol{E}^c = \boldsymbol{B}\delta\boldsymbol{U}_e;\ \Delta\boldsymbol{E}^c = \boldsymbol{B}\Delta\boldsymbol{U}_e, \tag{8}$$

where $\boldsymbol{B}$ is the compatible strain-displacement relations matrix. The enhanced part is related to the vector of the internal strain parameters $\boldsymbol{\alpha}$ as:

$$\tilde{\boldsymbol{E}} = \tilde{\boldsymbol{M}}\boldsymbol{\alpha};\ \delta\tilde{\boldsymbol{E}} = \tilde{\boldsymbol{M}}\,\delta\boldsymbol{\alpha};\ \Delta\tilde{\boldsymbol{E}} = \tilde{\boldsymbol{M}}\,\Delta\boldsymbol{\alpha}, \tag{9}$$

where $\tilde{\boldsymbol{M}}$ is the interpolation function matrix for the enhanced assumed strain field. The interpolation must be transferred to the global coordinates as follows:

$$\tilde{\boldsymbol{M}} = \frac{\det \boldsymbol{J}_0}{\det \boldsymbol{J}} \boldsymbol{T}_0^{-T} \tilde{\boldsymbol{M}}_{\xi}, \tag{10}$$

where $\boldsymbol{J}$ refers to the Jacobian matrix and $\boldsymbol{T}$ is the transformation tensor.

The subscript '0' means evaluation at the center of the stander element in the natural coordinates. $\tilde{\boldsymbol{M}}_{\xi}$ is the interpolation matrix for the enhanced field defined in the local frame with 5, 7, 9, 11 parameters of the compatible part given by

$$\mathbf{M}_c^{5,7,9,11} = \begin{pmatrix} \xi & 0 & 0 & 0 & 0 & 0 & 0 & 0 & 0 & \xi\eta & 0 \\ 0 & \eta & 0 & 0 & 0 & 0 & 0 & 0 & 0 & 0 & \xi\eta \\ 0 & 0 & \zeta & 0 & 0 & 0 & 0 & \xi\zeta & \eta\zeta & 0 & 0 \\ 0 & 0 & 0 & \xi & \eta & 0 & 0 & 0 & 0 & 0 & 0 \\ 0 & 0 & 0 & 0 & 0 & \frac{1}{5}-\zeta^2 & 0 & 0 & 0 & 0 & 0 \\ 0 & 0 & 0 & 0 & 0 & 0 & \frac{1}{5}-\zeta^2 & 0 & 0 & 0 & 0 \end{pmatrix}, \tag{11}$$

(5, 7, 9, 11)

After including interpolation functions for enhanced strain fileds, the linearized weak variational form is given by:

$$G + DG.(\Delta\boldsymbol{u}, \Delta\boldsymbol{\alpha}) = \begin{Bmatrix} \delta\boldsymbol{U}_e & \delta\boldsymbol{\alpha} \end{Bmatrix} \left(\begin{bmatrix} \boldsymbol{K} & \boldsymbol{L}^T \\ \boldsymbol{L} & \boldsymbol{H} \end{bmatrix} \begin{Bmatrix} \Delta\boldsymbol{U}_e \\ \Delta\boldsymbol{\alpha} \end{Bmatrix} + \begin{bmatrix} \boldsymbol{f}^{int} - \boldsymbol{f}^{ext} \\ \boldsymbol{h} \end{bmatrix} \right) = 0, \tag{12}$$

$$\boldsymbol{L} = \int_{V_e} \tilde{\boldsymbol{M}}^T \mathbb{C}\boldsymbol{B}\, dV_e ; \boldsymbol{H} = \int_{V_e} \tilde{\boldsymbol{M}}^T \mathbb{C}\tilde{\boldsymbol{M}}\, dV_e ; \boldsymbol{K} = \boldsymbol{K}_e + \boldsymbol{K}_G \tag{13}$$

$$\boldsymbol{K}_e = \int_{V_e} \boldsymbol{B}^T \mathbb{C}\boldsymbol{B}\, dV_e \tag{14}$$

$\boldsymbol{K}_G$ is the geometric stiffness matrix, such as:

$$\delta\boldsymbol{U}_e^T \boldsymbol{K}_G \Delta\boldsymbol{U}_e = \int_{V_e} \boldsymbol{S} : \Delta\delta\boldsymbol{E}^e\, dV_e \tag{15}$$

$$\boldsymbol{f}^{int} = \int_{V_e} \boldsymbol{B}^T \boldsymbol{S}\, dV_e ; \boldsymbol{f}^{ext} = \int_{V_e} \boldsymbol{N}^T \boldsymbol{F}_V dV_e + \int_{\partial V_{fe}} \boldsymbol{N}^T \boldsymbol{F}_S \mathrm{dA}; \boldsymbol{h} = \int_{V_e} \tilde{\boldsymbol{M}}^T \boldsymbol{S}\, dV_e \tag{16}$$

We use the static condensation procedure which leads to, the element stiffness matrix given by

$$\boldsymbol{K}_T = \boldsymbol{K}_e + \boldsymbol{K}_G - \boldsymbol{L}^T \boldsymbol{H}^{-1} \boldsymbol{L} \tag{17}$$

$$\boldsymbol{R}_e = \boldsymbol{L}^T \boldsymbol{H}^{-1} \boldsymbol{h} + \boldsymbol{f}^{ext} - \boldsymbol{f}^{int} \tag{18}$$

To avoid the transverse shear locking phenomena the interpolation method proposed by Dvorkin and Bathe (1984) are used. To avoid the strain locking the EAS method proposed by Betsch and Stein (1995) and extended by Klinkel et al. (1999) is adopted. Then the expression of compatible part of the Green-Lagrange tensor takes the following form:

$$\mathbf{E}^c = \mathbf{T}_S^{-T} \begin{bmatrix} \frac{1}{2}\left(g_{11} - G_{11}\right) \\ \frac{1}{2}\left(g_{22} - G_{22}\right) \\ \sum_{L=1}^{4} \frac{1}{4}\left(1+\xi_L\xi\right)\left(1+\eta_L\eta\right)\frac{1}{2}\left(g_{33}^L - G_{33}^L\right) \\ \left(g_{12} - G_{12}\right) \\ \frac{1}{2}\left[\left(1-\eta\right)\left(g_{13}^B - G_{13}^B\right) + \left(1+\eta\right)\left(g_{13}^D - G_{13}^D\right)\right] \\ \frac{1}{2}\left[\left(1-\eta\right)\left(g_{23}^A - G_{23}^A\right) + \left(1+\eta\right)\left(g_{23}^C - G_{23}^C\right)\right] \end{bmatrix} \tag{19}$$

The compatible strain-displacement relations matrix at the element level is given by:

$$\mathbf{B}_I = \begin{bmatrix} \mathbf{g}_1^T \mathrm{N}_{I,1} \\ \mathbf{g}_1^T \mathrm{N}_{I,1} \\ \sum_{L=1}^{4} \frac{1}{4}\left(1+\xi_L\xi\right)\left(1+\eta_L\eta\right)\mathbf{g}_3^T \mathrm{N}_{I,3} \\ \mathbf{g}_2^T \mathrm{N}_{I,1} + \mathbf{g}_1^T \mathrm{N}_{I,2} \\ \frac{1}{2}\left[\left(1-\eta\right)\left(\mathbf{g}_3^{B^T} \mathrm{N}_{I,1}^B + \mathbf{g}_1^{B^T} \mathrm{N}_{I,3}^B\right) + \left(1+\eta\right)\left(\mathbf{g}_3^{D^T} \mathrm{N}_{I,1}^D + \mathbf{g}_1^{D^T} \mathrm{N}_{I,3}^D\right)\right] \\ \frac{1}{2}\left[\left(1-\xi\right)\left(\mathbf{g}_3^{A^T} \mathrm{N}_{I,1}^A + \mathbf{g}_1^{A^T} \mathrm{N}_{I,3}^A\right) + \left(1+\xi\right)\left(\mathbf{g}_3^{C^T} \mathrm{N}_{I,1}^C + \mathbf{g}_1^{C^T} \mathrm{N}_{I,3}^C\right)\right] \end{bmatrix} \tag{20}$$

Where the transverse shear strains $\boldsymbol{E}_{13}^{c}$ and $\boldsymbol{E}_{23}^{c}$ are evaluated at four midpoints of the element edges A = (-1,0,0), B = (0,-1,0), C = (1,0,0), D = (0,1,0) and the thickness shear strains $\boldsymbol{E}_{33}$ is evaluated at the following four points of the reference element L_1=(-1,-1,0), L_2= (1,-1,0), L_3= (1,1,0), L_4= (-1,1,0)

From this formulation we obtain the solid shell element enhanced with 5, 7, 9 and 11 incompatible modes using the EAS and ANS (C3D8S5, C3D8C7,9,11)

4 Numerical Results and Discussion

Performance Test

To test the performance of the proposed elements in order to verify the implementation, a finesse mesh test is performed for an isotropic clamped thick beam subjected to a concentrated loading P at the tip (Fig. 1(a)).

The analytic compressive force is expressed as

$$w_{\max} = \frac{PL^3}{3EI} + \frac{PLh^2}{10GA} \tag{21}$$

with A as the area of the cross section and I as the moment of inertia.

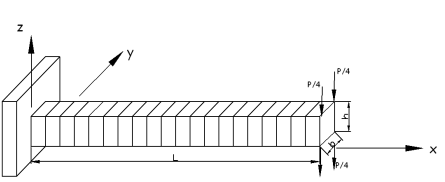

$L = 100; b = 10; h = 20; P = 4000N$

(a)

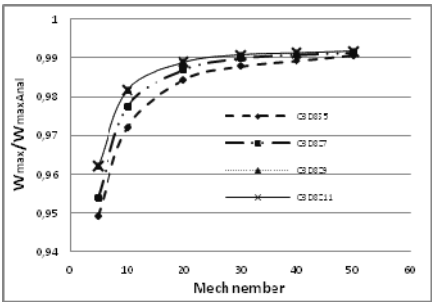

(b)

Fig. 1 Thick cantilever; $E = 100000MPa$, and $\upsilon = 0.4$

Fig. 1(b) shows the evolution of the normalized deflection (Wmax/WmaxAnal) versus the mesh finesse; one can see that the numerical solution converge toward the analytical solution for a mesh of 10 x 1 x 1 for different element solid shell.

The accuracy and the convergence of all numerical results are noted. In fact, the displacement field is in good accordance with the analytical solution. It can be emphasized that, although the C3D8C7,9,11 elements present accuracy and convergence rate comparable with the one obtained from C3D8S5 element, it's unreliable since it suffer from locking.

Transverse Shear Stress Distribution

To test the performance of the proposed elements of the transverse shear stress distribution, a test is performed for an isotropic unit cube clamped at one end subjected to a transverse shear loading at another end (fig.2 (a)).

The analytic transverse shear stress is expressed as

$$\sigma_{23} = \frac{P}{2I}\left(z^2 - \frac{h^2}{4}\right) \tag{22}$$

Fig. 2(b) shows the transverse shear stress distribution through the thickness. The present results with C3D8C7,9,11 elements have the closest results with exact solution. But the one obtained from C3D8S5 element present a constant transverse shear stress since it suffer from shear locking.

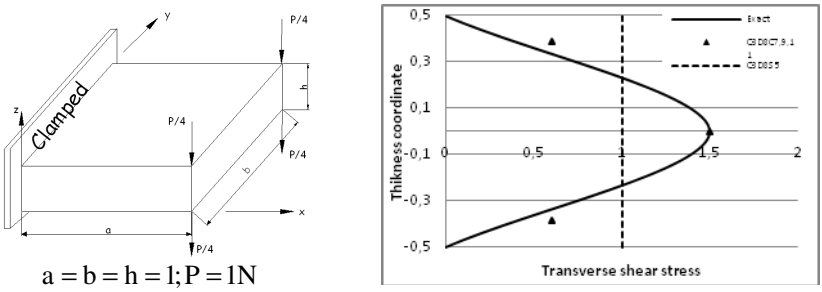

(a) (b)

Fig. 2 One-element test; $E = 1.10^7\ MPa$, and $\upsilon = 0.3$

5 Conclusions

A solid-shell finite element with an enhanced assumed strain is developed for the alleviation of shear locking. A three-dimensional finite element model taking into account thickness variation in the plan and the transverse shearing and improved by incompatible modes has been presented. The incompatible part is enriched by the enhanced assumed strain (EAS) method in order to avoid the problem of volumetric and transverse shear locking. The transverse shearing locking problem is avoided by applying the assumed natural strain (ANS) method.

References

Reissner, Stavsky, Y.: Bending and stretching of certain types of heterogeneous aelotropic elastic plates. J. Appl. Mech. 28, 402–412 (1961)

Stavsky, Y.: Bending and stretching of laminated aelotropic plates. Proc. Am. Soc. Civil Engrs. 87, 31–42 (1961)

Liu, C.F., Reddy, J.N.: A higher-order shear deformation theory of laminated elastic shells. Int. J. Eng. Sci. 23(3), 319–330 (1985)

Rastgaar Aagaah, M., Mahinfalah, M., Nakhaie Jazar, G.: Linear static analysis and finite element modeling for laminated composite plates using third order shear theory. Composite Structures 62, 27–39 (2003)

Reddy, J.N.: Mechanics of Laminated Composite Plates and Shells: Theory and Analysis, 2nd edn. CRC Press, Boca Raton (2004)

Reddy, J.N., Lee, S.J.: Vibration suppression of laminated shell structures investigated using higher order shear deformation theory. Smart Mater. Struct. 13, 1176–1194 (2004)

Fontes Valente, R.A., Alves de Sousa, R.J., Natal Jorge, R.M.: An enhanced strain 3D element for large deformation elastoplastic thin-shell applications. Comput. Mech. 34, 38–52 (2004)

Alves de Sousa, R.J., Cardoso, R.P.R., Fontes Valente, R.A., Yoon, J.-W., Gracio, J.J., Natal Jorge, R.M.: A new one- point quadrature enhanced assumed strain (EAS) solid-shell element with multiple integration points along thickness—Part II: Nonlinear applications. Int. J. Numer. Methods Engrg. 67, 160–188 (2006)

Reese, S.: A large deformation solid-shell concept based on reduced integration with hourglass stabilization. Int. J. Numer. Methods Engrg. 69, 1671–1716 (2007)

Quy, N.D., Matzenmiller, A.: A solid-shell element with enhanced assumed strains for higher order shear deformations in laminates. Tech. Mech. 28, 334–355 (2008)

Hauptmann, R., Schweizerhof, K.: A systematic development of 'solid-shell'element formulations for linear and non-linear analyses employing only displacement degrees of freedom. Int. J. Numer. Methods Engrg. 42, 49–69 (1998)

Tan, X.G., Vu-Quoc, L.: Efficient and accurate multilayer solid-shell element: non-linear materials at finite strain. Int. J. Numer. Methods Engrg. 63, 2124–2170 (2005)

Kim, K.D., Liu, G.Z., Han, S.C.: A resultant 8-node solid-shell element for geometrically nonlinear analysis. Comput. Mech. 35, 315–331 (2005)

Klinkel, S., Gruttmann, F., Wagner, W.: A robust nonlinear solid shell element based on a mixed variational formulation. Comput. Methods Appl. Mech. Engrg. 195, 179–201 (2006)

Marco, S., Vladimirov, N.I., Stefanie, R.: Sheet metal forming and springback simulation by means of a new reduced integration solid-shell finite element technology. Comput. Methods Appl. Mech. Engrg. 200, 454–476 (2011)

Hajlaoui, A., Jarraya, A., Kallel-Kamoun, I., Dammak, F.: Buckling analysis of a laminated composite plate with delaminations using the enhanced assumed strain solid shell element. Journal of Mechanical Science and Technology 26(10), 3213–3221 (2012)

Simo, J.C., Rifai, M.S.: A class of mixed assumed strain methods and the method of incompatible modes. Int. J. Numer. Meth. Eng. 29, 1595–1638 (1990)

Dvorkin, E., Bathe, K.J.: Continuum mechanics basedfour-node shell element for general nonlinear analysis. Eng. Comput. 984(1), 77–88 (1984)

Betsch, P., Stein, E.: An assumed strain approach avoiding artificial thickness straining for a nonlinear 4-node shell element. Commun. Numer. Meth. Engng. 11, 899–909 (1995)

Klinkel, S., Gruttmann, F., Wagner, W.: A robust nonlinear solid shell element based on a mixed variational formulation. Comput. Methods Appl. Mech. Engrg. 195, 179–201 (2006)

Multi-scale Modelling of Orthotropic Properties of Trabecular Bone in Nanoscale

Houda Khaterchi, Abdessalem Chamekh, and Hédi Belhadjsalah

Laboratoire de Génie Mécanique, Ecole Nationale d'Ingénieurs de Monastir, Université de Monastir, Avenue Ibn Eljazzard Monastir 5019, Tunisie
houda_enim@yahoo.fr,
hedi.belhadjsalah@enim.rnu.tn

Abstract. The bone is a hierarchically structured material with mechanical properties depending on its architecture at all scales. In this paper, a trabecular bone multiscale model based on finite element analysis was developed to link sub-nanoscopic scale (Microfibril) and nanoscopic (Fibril) to predict the orthotropic properties of bone at different structural level. To identify the orthotropic properties, we used an inverse identification algorithm. The approach shows a good efficiency in computing.

Keywords: Multi-scale modeling, Finite Element analysis, Trabecular bone, Orthotropic material.

1 Introduction

The bone is a hierarchically structured material with mechanical properties depending on its architecture at all scales. In human bodies, the bone consists of three types: Cortical bone, trabecular bone and marrow.

It has been shown that the mechanical properties of the bone vary at different structural scales (Rho et al. 1998). Therefore, in order to find the macroscopic properties of the bone, it is important to consider all of these scales. Many researchers have been investigated in this field, but the behaviour of the bone materials are modelled at different scales separately.

Structurally, bone is considered like a composite material with a complex structure. For simplicity, many studies consider an isotropic linear elastic behavior (Sansalone et al. 2010; Hambli et al. 2010; Tovar 2004). In other research, several authors simulate bone as anisotropic behavior (Martínez-Reina et al. 2009; Doblare et al. 2002; Fernandes et al. 1999; Jacobs et al. 1997; Hart and Fritton 1997).

To predict the orthotropic properties at different scales, Hamed et al. (2012) used homogenization approach. Elastic properties of trabecular bone are calculated at each structural level, from nanoscale to mesoscale. In the analysis, results from a lower level are used as inputs for a higher level. In the same way, Vaughan et al. (2012) proposed a three scale homogenisation scheme to estimate the effective properties of trabecular and cortical bone, based on finite element models.

M. Haddar et al. (Eds.): *Design and Modeling of Mechanical Systems*, LNME, pp. 557–566.
DOI: 10.1007/978-3-642-37143-1_67

We propose in this work a new approach, which is applied here to determine the orthotropic properties of the trabecular bone. The effective mechanical properties at each scale are computed from the scale immediately lower by a suitable EF model.

The first section of the study presents the structure of trabecular bone. The fundamentals of orthotropic material behavior are given in second section. In the third section, the proposed method is developed to link scales. The results are presented in section 4. Finally, conclusions of this study are given.

2 Trabecular Structure

We distinguish six levels of hierarchical organization in bone, which are outlined here with a focus on trabecular bone (as shown in Fig. 1):

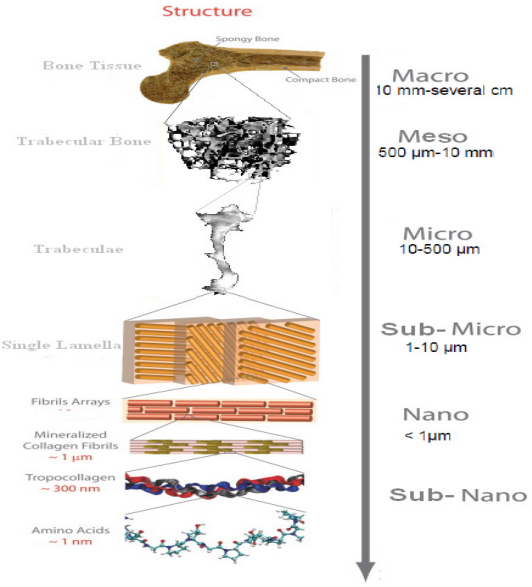

Fig. 1 Hierarchical structure of trabecular bone

1. Sub Nanostructral level: mineral and collagen are arranged in higher hierarchical levels to form the microfibrils.
2. Nanostructural level: Bone, at this level, can be considered as a multi-phase nanocomposite material consisting of microfibrils and mineral matrix.
3. Sub-microstructural level: also called a single lamella level. Mineralized fibrils are oriented in a preferential direction to form a single lamella of thickness 3 to 7 µm.
4. Microstructural level: or a single trabecula level. Several lamellae are oriented in twisted plywood patterns to form trabeculae.

5. Mesostructural level or a trabecular bone level which represents a porous network of trabeculae.
6. Macrostructural level or a whole bone level, consisting of cortical and trabecular bone types.

In this paper, we describe a multiscale approach for the characterization of mechanical properties of trabecular bone at sub-nanoscale and nanoscale.

2.1 Sub-nanostructural Level

Recent studies suggest the presence of microfibrils in fibrils, experimental works prove that all collagen-based tissues are organized into hierarchical structures, where the lowest hierarchical level consists of triple helical collagen molecules (Hulmes et al. 1995; Orgel et al. 2006; Aladin et al. 2010) and the multiscale structure was defined as triple helical collagen molecules - microfibrils - fibrils. The microfibril shown in figure 2 is a helical assembly of five tropocollagen (TC) molecules which are offset one another with an apparent periodicity of 67 nm (Barkaoui and Hambli 2012). The electron-microscopy observations show that the TC molecules are embedded in mineral matrix (figure 2).

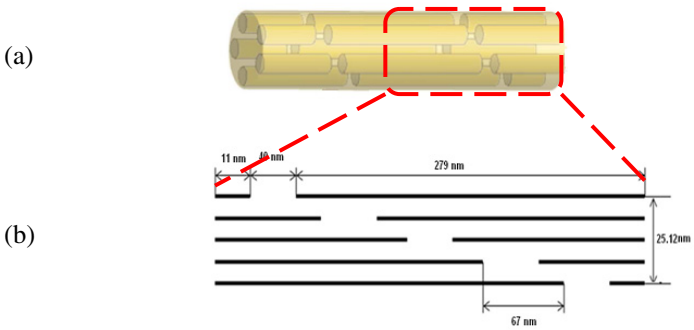

Fig. 2 Geometric model of collagen microfibril: (a) Reel 3D Microfibril, (b) unfolding in plane of the chosen portion

We assume an isotropic linear elastic behavior for both collagen and mineral. But the response is orthotropic (Khaterchi et al. 2012). The material properties used in this paper of the collagen and the mineral are summarized in Table 1.

Table 1 Geometrical parameters adopted for the microfibril (Hamed et al. 2012)

Mechanical properties	Value	
E_m	114 GPa	Young Modulus of mineral
υ_m	0.23	Poisson ratio of mineral
E_c	1.5 GPa	Young Modulus of collagen
υ_c	0.28	Poisson ratio of collagen

2.2 *Nanostructural Level*

At a higher length scale, bone is composed of fibrils which assumed as a composite with periodically distributed cylindrical inclusions of microfibrils (Hulmes et al. 1995). The microfibrils are arranged in concentric layers separated by a distance of 4 nm (Hulmes et al. 2002) and there are embedded in a matrix of mineral.

To model the nanoscale, we define a representative volume element (RVE) which describes local morphological arrangements at the fibril structure (figure 3).

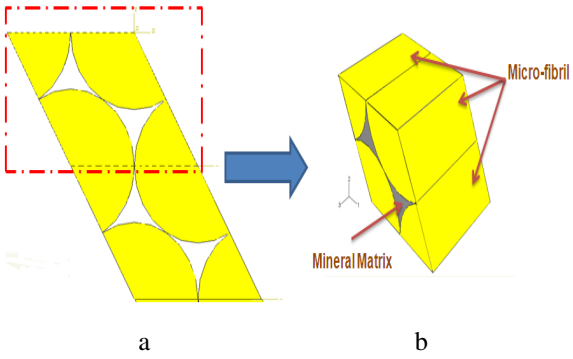

Fig. 3 Geometric model of fibril: (a) RVE of the fibril: the chosen portion, (b) FE model of fibril

We assume an isotropic linear elastic behaviour for the matrix. But the microfibril has an orthotropic behaviour. The material properties of the mineral matrix are listed in Table 1.

3 Orthotropic Material Behaviour

Many studies, for example (Ciarelli et al. 1991; Pithioux et al. 2002; Buskirk et al. 1981), show that the material properties of bone can be represented by an orthotropic material formulation. In order to model orthotropic material behaviour, the general strain-stress relation is simplified to:

$$\begin{bmatrix} \varepsilon_{11} \\ \varepsilon_{22} \\ \varepsilon_{33} \\ \varepsilon_{23} \\ \varepsilon_{13} \\ \varepsilon_{12} \end{bmatrix} = \begin{bmatrix} s_{11} & s_{12} & s_{13} & 0 & 0 & 0 \\ s_{12} & s_{22} & S_{23} & 0 & 0 & 0 \\ s_{13} & s_{23} & s_{33} & 0 & 0 & 0 \\ 0 & 0 & 0 & s_{44} & 0 & 0 \\ 0 & 0 & 0 & 0 & s_{55} & 0 \\ 0 & 0 & 0 & 0 & 0 & s_{66} \end{bmatrix} \begin{bmatrix} \sigma_{11} \\ \sigma_{22} \\ \sigma_{33} \\ \sigma_{23} \\ \sigma_{13} \\ \sigma_{12} \end{bmatrix} \quad (1)$$

The compliance matrix in Eq. (1) is formed by three orthogonal symmetry planes which characterise the orthotropic material behaviour (Malvern 1969). The symmetry of the compliance matrix means that nine constants must be given to describe orthotropic material behaviour. This can be expressed by the following relation who shows the nine components to be identified.

$$\begin{bmatrix} \varepsilon_{11} \\ \varepsilon_{22} \\ \varepsilon_{33} \\ \varepsilon_{23} \\ \varepsilon_{13} \\ \varepsilon_{12} \end{bmatrix} = \begin{bmatrix} \frac{1}{E_1} & -\frac{\upsilon_{21}}{E_2} & -\frac{\upsilon_{31}}{E_3} & 0 & 0 & 0 \\ -\frac{\upsilon_{12}}{E_1} & \frac{1}{E_2} & -\frac{\upsilon_{32}}{E_3} & 0 & 0 & 0 \\ -\frac{\upsilon_{13}}{E_1} & -\frac{\upsilon_{23}}{E_2} & \frac{1}{E_3} & 0 & 0 & 0 \\ 0 & 0 & 0 & \frac{1}{G_{23}} & 0 & 0 \\ 0 & 0 & 0 & 0 & \frac{1}{G_{13}} & 0 \\ 0 & 0 & 0 & 0 & 0 & \frac{1}{G_{12}} \end{bmatrix} \begin{bmatrix} \sigma_{11} \\ \sigma_{22} \\ \sigma_{33} \\ \sigma_{23} \\ \sigma_{13} \\ \sigma_{12} \end{bmatrix} \tag{2}$$

E_1, E_2, E_3: three Young Moduli.
G_{12}, G_{13}, G_{23}: Three shear moduli in plane12, 13 and23.
υ_{ij} : Three Poisson ratios.

Where

$$\frac{\upsilon_{21}}{E_2} = \frac{\upsilon_{12}}{E_1} \tag{3}$$

$$\frac{\upsilon_{31}}{E_3} = \frac{\upsilon_{13}}{E_1} \tag{4}$$

$$\frac{\upsilon_{32}}{E_3} = \frac{\upsilon_{23}}{E_2} \tag{5}$$

Such materials require 9 independent variables to be identified in their constitutive matrices.

4 Proposed Method

The proposed method is a simulation procedure to link different scales. From lower scale, the microfibril (sub-nanoscale) passes information to the fibril (nano-scale) in the form of mechanical properties. At the nanoscopic scale, the orthotropic properties of microfibrils (derived from the sub-nano FE result) are applied to characterize the equivalent orthotropic fibrils properties. A schematic illustration of the approach is presented in Figure 4.

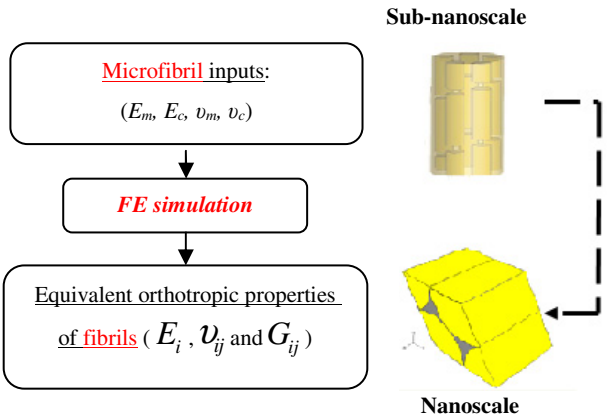

Fig. 4 Multiscale approach for bone analysis

To characterize the behaviour of the fibril, we need to compute the orthotropic properties of the microfibril. Figure 5 shows the sub-nano to nano linking scheme.

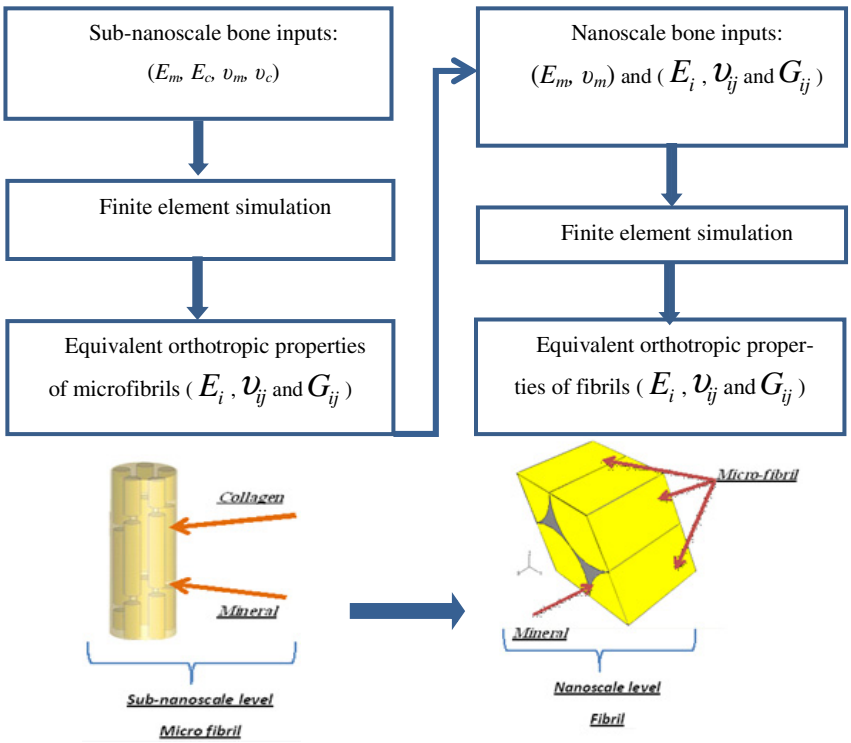

Fig. 5 Sub-nano to nano transition

4.1 Sub-nanoscale Modelling

To characterize the microfibril, we used different numerical tests (tensile and compression) and an inverse identification algorithm. This work is detailed in (Khaterchi et al. 2012).

4.2 Nanoscale Modelling

In order to compute the equivalent orthotropic fibril properties, the proposed FE model was coupled to an inverse identification algorithm. In first step, we sketched a homogeneous model representing the same geometry of the fibril. This model is used in the identification approach which consists in minimizing the difference between the predicted force-displacement curves obtained respectively by the equivalent (monophase) model and the 3D simulation using the multiphase model. To obtain the 9 orthotropic properties of the fibrils, we used the tensile and shear tests. The flowchart of the identification procedure is presented in figure 6.

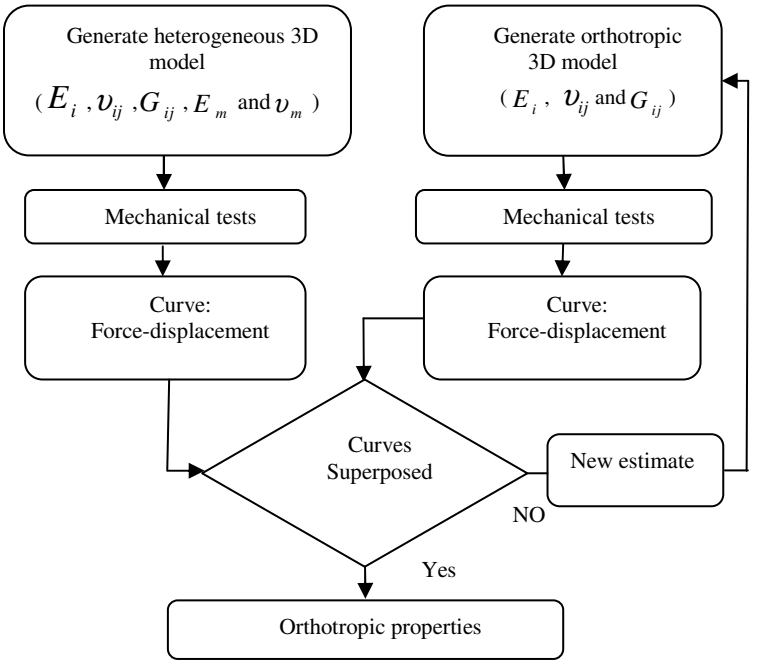

Fig. 6 Identification procedure

4.2.1 Tensile Tests

There are six parameters which can be extracted from the tensile test. These consist of axial tensile loading applied to the RVE model of fibril in 1, 2 and 3

direction to determine the axial moduli (E11, E22, E33) and the Poisson ratios (υ_{12}, υ_{23}, υ_{31}, υ_{21}, υ_{32} and υ_{13}) could be given by:

$$\upsilon_{ij} = -\frac{\overline{\varepsilon}_{jj}}{\overline{\varepsilon}_{ii}} \tag{6}$$

With i=1,2, j=2,3 and i≠j

Using eq. (3), (4) and (5), only 3 Poisson rations will be computed.

4.2.2 Shear Tests

Following a similar procedure to that describe above, the shear moduli may be determined. The shear load is applied to the RVE in 1, 2, and 3 directions to determine G_{12}, G_{13} and G_{23}.

5 Results and Discussion

First, we should valid the inverse identification algorithm shown in figure 6. We choose randomly the input properties of microfibril and we compute the orthotropic fibril parameters using tests selected. Figure 7 shows the comparison between the reaction force versus displacement of homogeneous model and the heterogeneous one. A good agreement between the two responses curves is observed. The mean square error is less than 1%.

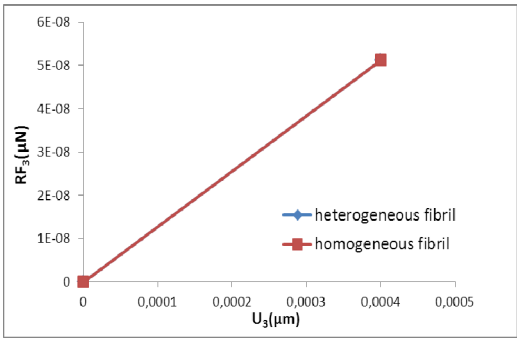

Fig. 7 Reaction force versus displacement in tensile test

To illustrate the capabilities of the approach proposed, we select one combination of mechanical properties of the microfibril; a finite element simulation is generated. First, we choose the properties of mineral and collagen listed in table 1. The method gives firstly the orthtropic properties of the microfibril, which are introduced in the higher level and secondly the properties of fibril.

Microfibril properties:

$$\begin{cases} E_1 = 33.32 \text{ GPa}; \ E_2 = 29.25 \text{ GPa}; \ E_3 = 56.27 \text{ GPa}; \\ \upsilon_{12} = 0.3; \ \upsilon_{13} = 0.14; \ \upsilon_{23} = 0.12; \\ G_{12} = 12.1 \text{GPa}; \ G_{13} = 17.75 \text{GPa}; \ G_{23} = 16.52 \text{GPa}. \end{cases}$$

Using eq. (3), (4) and (5):

$$\upsilon_{21} = 0.26; \ \upsilon_{31} = 0.23; \ \upsilon_{32} = 0.23.$$

Fibril properties:

$$\begin{cases} E_1 = 37.35 \text{ GPa}; \ E_2 = 30.73 \text{ GPa}; \ E_3 = 61.83 \text{ GPa}; \\ \upsilon_{12} = 0.3; \ \upsilon_{13} = 0.12; \ \upsilon_{23} = 0.13; \\ G_{12} = 13.29 \text{GPa}; \ G_{13} = 26.16 \text{GPa}; \ G_{23} = 21.02 \text{GPa}. \end{cases}$$

Using eq. (3), (4) and (5):

$$\upsilon_{21} = 0.24; \ \upsilon_{31} = 0.2; \ \upsilon_{32} = 0.26.$$

6 Conclusions

The aim of the present study was to link between sub-nano and nanoscale to understand the relationship of the mechanical behaviour in different scale. We propose a FE models for the microfibril and fibril. After that, we applied mechanical tests to characterise the orthotropic behaviour of bone.

The effective mechanical properties at each scale can be computed from the scale immediately lower by this proposed strategy. Moreover, it can be easily used in different scales to model the entire bone structure.

However, some other important variables including geometry and porosity were not included in the present research and will remain interesting future research topics.

References

Rho, J.Y., Kuhn-Spearing, L., Zioupos, P.: Mechanical properties and the hierarchical structure of bone. Med. Eng. Phys. 20, 92–102 (1998)

Sansalone, V., Naili, S., Bousson, V., Bergot, C., Peyrin, F., Zarka, J., Laredo, J.D., Haïat, G.: Determination of the heterogeneous anisotropic elastic properties of human femoral bone: From nanoscopic to organic scale. Journal of Biomechanics 43, 1857–1863 (2010)

Hambli, R., Katerchi, H., et al.: Multiscale methodology for bone remodelling simulation using coupled finite element and neural network computation. Biomechanics and Modeling in Mechanobiology (2010)

Tovar, A.: Bone remodeling as a hybrid cellular automaton optimization process. PhD dissertation, University of Notre Dame, Indiana (2004)

Martínez-Reina, J., García-Aznar, J.M., Domínguez, J., Doblaré, M.: A bone remodelling model including the directional activity of BMUs. Biomech. Model Mechanobiol. 8, 111–127 (2009)

Doblare, M., Garcia, J.M.: Anisotropic bone remodelling model based on a continuum damage-repair theory. J. Biomech. 35(1), 1–17 (2002)

Fernandes, P., Rodrigues, H., Jacobs, C.: A model of bone adaptation using a global optimisation criterion based on the trajectorial theory of Wolff. Comput. Methods Biomech. Biomed. Eng. 2(2), 125–138 (1999)

Jacobs, C.R., Simo, J.C., Beaupre, G.S., Carter, D.R.: Adaptive bone remodeling incorporating simultaneous density and anisotropy considerations. J. Biomech. 30(6), 603–613 (1997)

Hart, R.T., Fritton, S.P.: Introduction to finite element based simulation of functional adaptation of cancellous bone. Forma 12, 277–299 (1997)

Elham, H., Iwona, J., Andrew, Y., YikHan, L., Tadeusz: Multiscale Modeling of Elastic Properties of Trabecular Bone. J. Royal Society Interface 9(72), 1654–1673 (2012)

Vaughan, T.J., McCarthy, C.T., McNamara, L.M.: A three scale finite element investigation into the effects of tissue mineralization and lamellar organization in human cortical and trabecular bone. Journal of the Mechanical Behavior of Biomedical Materials, 50–62 (2012)

Hulmes, D.J.S., Wess, T.J., Prockop, D.J., Fratzl, P.: Radial Packing, Order, and Disorder In Collagen Fibrils. Biophysical Journal 68(5), 1661–1670 (1995)

Orgel, J.P.R.O., Irving, T.C., Miller, A., Wess, T.J.: Microfibrillar structure of type I collagen in situ. P. Natl. Acad. Sci. USA 103(24), 9001–9005 (2006)

Aladin, D.M., Cheung, K.M., Ngan, A.H., Chan, D., Leung, V.Y., Lim, C.T., Luk, K.D., Lu, W.W.: Nanostructure of collagen fibrils in human nucleus pulposus and its correlation with macroscale tissue mechanics. J. Orthop. Res. 28(4), 497–502 (2010)

Abdelwahed, B., Ridha, H.: Nanomechanical properties of mineralized collagen microfibrils based on finite elements method:biomechanical role of cross-links. Comp. Met. in Biomech. and Biomed. Eng (2012)

Khaterchi, H., Chamekh, A., BelHadjSalah, H.: Détermination des propriétés élastiques anisotropes homogènes de l'os spongieux à l'échelle nanoscopique (2012)

Hulmes, D.J.S.: Building Collagen Molecules, Fibrils, and Suprafibrillar Structures. Journal of Structural Biology 137, 2–10 (2002)

Ciarelli, M.J., Goldstein, S.A., Kuhn, J.L., et al.: Evaluation of orthogonal mechanical properties and density of human trabecular bone from the major metaphyseal regions with materials testing and computed tomography. J. Orthop. Res. 9, 674–682 (1991)

Pithioux, M., Lasaygues, P., Chabrand, P.: An alternative ultrasonic method for measuring the elastic properties of cortical bone. J. Biomech. 35, 961–968 (2002)

Buskirk, W.C., Van Ashman, R.B.: The elastic moduli of bone in mechanical properties of bone. In: Joint ASME-ASCE Conf., vol. 45, pp. 131–143 (1981)

Malvern, L.E.: Introduction to the Mechanics of a Continuous Medium. Prentice-Hall Series in Engineering of the Physical Sciences (1969)

The Use of the DIC Method to Involve the Strain Instability Occurred in an Undergoing High Shear during the ECAE Process

Romdhane Boulahia[1], Taoufik Boukharouba[1], and Jean Michelle Glaoguen[2]

[1] Laboratoire de Mécanique Avancée, Fac GPGP,
USTHB BP 32 El-Alia, Bab-Ezzouar 16111, Alger, Algérie
{Ramdane.boulahia,t.boukha}@gmail.com
[2] Bâtiment C6-205 Unité Matériaux et Transformations Bât. C6
Université Lille1 59655 Villeneuve d'Ascq France
Jean-Michel.Gloaguen@univ-lille1.fr

Abstract. Equal-channel angular extrusion (ECAE) is one of the most efficient methods of severe plastic deformation of materials used to modify texture and microstructure without reducing sample cross-section. The application of single ECAE pass to polypropylene (PP) was meticulously investigated at room temperature using a 90° die-angle tooling. Depending on extrusion conditions, PP displayed various types of plastic flow. For ram velocities beyond 4.5 mm/min, severe shear bands consisting of successive translucent and opaque bands were observed, accompanied on the top surface by more or less pronounced periodic waves. Although the application of a back-pressure significantly reduced the wave and shear-banding phenomena, slightly inhomogeneous shear deformation was still observed. Shear bands were only suppressed by decreasing extrusion velocity. Application of backpressure and/or reducing ram velocity resulted in uniform texturing along the extruded sample. Mechanical properties changes of the extruded samples due to back-pressure and extrusion velocity effects were analyzed via uniaxial tensile tests. The tensile samples displayed multiple strain localizations in shear banded materials whereas quite homogeneous deformation appeared for non-banded ones. Digital image correlation technique suitable for large deformation was used for determining the full-field strain of the tensile samples in relation to tensile strain and ECAE conditions.

Keywords: Equal channel angular extrusion, Back-pressure, Extrusion velocity.

1 Introduction

The equal channel angular extrusion process (ECAE) is a severe plastic deformation process employed to produce bulk ultra-fine grained materials with improved mechanical properties (Segal 1995, Iwahachi et al 1996). The method consists of extruding a sample through a die with two channels of equal cross-section (Fig. 1). In the crossing plane of the two channels, the sample is subjected to a large simple

M. Haddar et al. (Eds.): *Design and Modeling of Mechanical Systems*, LNME, pp. 567–574.
DOI: 10.1007/978-3-642-37143-1_68

shear strain. Considering that the sample cross-section is not modified, multipass extrusion can be performed to perform extremely large plastic strains. The homogeneity of plastic strain field is a fundamental condition to ensure homogeneity of microstructure and mechanical properties. However, depending on the specific properties of the material, the tool geometry and the process parameters, the strain state can change from the expected homogeneous simple shear to a complex inhomogeneous strain field. Various solid-state forming techniques such as forging (Saraf et al 1987), ram-extrusion (Zachariades at al 1980), die-drawing (Coates et 1999), have also been developed for improving mechanical properties of polymer bulk pieces via large plastic deformations. However, ECAE is the only one process that preserves the sample shape.

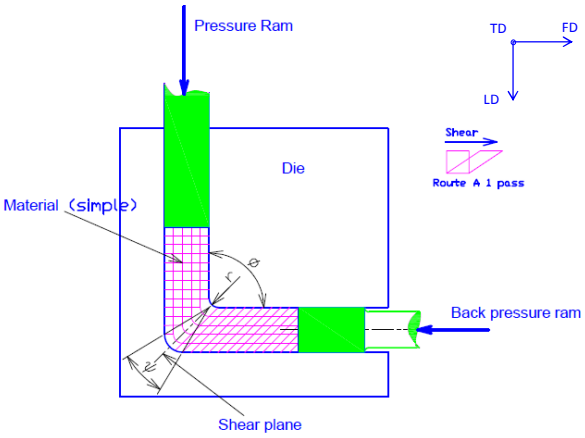

Fig. 1 Schematic illustration of a 90° ECAE die (flow direction: FD, load direction: LD, transverse direction: TD)

Severe plastic deformation methods have been the subject of intensive investigations in recent years (Azushima et al 2008). However, relatively little attention has been focused so far on polymers processed by ECAE. The technique was applied to a polymer (low density polyethylene) for the first time by (Sue and Li 1998). The morphological changes of polypropylene subjected to ECAE were examined by (Campbell and Edward 1999), (Wang et al 2011) and (Phillips et al 2006). However, neither the mechanics of the process nor the mechanical properties of the extruded material were examined. (Campbell and Edward 1999) used a constriction over the exit of the die and a ''sacrificial sample'' to create a back-pressure and to avoid the bending of the sample in the outer corner of the ECAE device.

In this paper, polypropylene samples were extruded using an experimental setup consisting of a 90° channel. Particular attention is paid to the analyses of the macroscopic flow behavior during a single ECAE pass via the load–ram displacement measurements including the effect of back-pressure and extrusion

velocity. The evolution of crystalline microstructure and mechanical properties of ECAE-processed samples is also meticulously investigated for understanding the plastic mechanisms of the process.

2 Material and Experimental Procedures

2.1 Material

The material used in this investigation is a polypropylene (PP) of weight–average molar weight of 180 kg/mol purchased from Goodfellow©. The material was supplied in the form of 10 mm thick compression-molded plates.

2.2 ECAE Experiments

ECAE experiments were conducted at room temperature (about 23°C) and under constant ram speeds in the range of 0.45–45 mm/min. Samples were cut from the as-received PP plates along the same direction. The samples were 75 mm in length with square cross-sections 10x10 mm. The ECAE die was made of stainless steel. It is schematically given in Fig. 1. An internal angle φ of 90° between the two channels, an outer corner angle ψ of 10° and an inner radius r of 2 mm were adopted. The channels had cross-sectional dimensions of 10x10mm. The ECAE tooling was adapted on an Instron© model 5800 screw testing machine. The extrusion velocity and the back-pressure are kept constant during ECAE. Before each extrusion, the die was lubricated using silicone grease. Load-ram displacement data were recorded for each extrusion.

2.3 Tensile Tests

The tensile tests were conducted on the Instron© testing machine at room temperature under a constant cross-head speed 0.75 mm/min, i.e. a nominal strain rate of 10^{-3} s^{-1}, using sample of gauge length 12.5 mm (Fig. 2.). Full-field strain measurements were achieved during tensile tests using digital image correlation (DIC) technique.

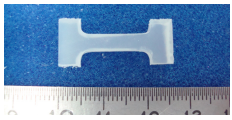

Fig. 2 Tensile samples after ECAE

2.4 DIC Procedure

DIC measurements require an artificial random speckle pattern which was generated by green dots sprayed on the surface of each sample. The random

speckle pattern was applied so that speckles do not overlap. The studied zone was illuminated by a strong white light beam. The illuminated random speckle pattern was captured during the deformation by a digital CCD camera placed in front of the sample and at a distance of 0.5 m from the sample. The images of sample surface were recorded at a frequency of 2 Hz (fig.3.). DIC method is based upon comparing images of the sample surface in the undeformed (reference) and deformed states. By this way, a Lagrangian description is performed. A step of 10 images was used for the image correlation. The zone of interest was divided into small square sub images of 64x64 pixels. The displacement vector was calculated using the corresponding sub-image pairs extracted from the reference and deformed states of the sample. By achieving the analysis on numerous sub-images, the full-field contours of displacement were obtained. The analysis was performed with Davis© software developed by Lavision©.

3 Results and Discussion

Fig. 3.b and Fig.4.b presents the deformation behaviour of PP samples at the end of the ECAE operation performed at a ram speed of 45mm/min. The strain pattern appears in a very particular manner. Without backpressure (Fig. 3b), the sample does not fill up the outer corner of the die and exhibits a wavy shape on the top surface in the exit channel: the summit of the waves is in contact with the surface of the die whereas the bottom of the waves is not. This suggests a heterogeneous strain field in the bulk which is confirmed by the occurrence of dark grey and light grey alternated stripes inclined at about 45° from FD along the sample length. The dark and light stripes in reflected light are respectively translucent and opaque in transmitted light. This means that the former ones have undergone high shear that imparted severe deformation or destruction of the spherulitic structure whereas the later ones went undeformed through the transition zone of the ECAE, keeping intact the initial light-diffusing superstructure. The fact that the sample does not fill up the outer corner of the tooling in the present study promotes the occurrence of a plastic instability accompanied with stress drop. This kind of ‘‘stick-slip’’ phenomenon, never reported in previous ECAE studies on polymers, may be due to the combined effects of the specific viscoplastic behavior of the material and the friction between the sample and the die, as a result of an unstable balance between the yield stress and the friction force.

The effects of the loading rate on the deformation behavior of PP samples at the end of the ECAE process are illustrated in Fig. 3. and 4. It is worth noting that, whatever the back-pressure value, under extrusion velocity of 0.45 mm/min, a quite uniform deformation field is obtained. In other words, the wave formation and shear bands described in previous section vanish under these loading conditions. This is again confirmed by the macroscopic response in terms of applied load–ram displacement curves as shown in Fig. 5. Moreover, without back-pressure, beyond a certain threshold, the curves exhibit a steady-state behavior. When applying a backpressure, the applied load continuously increases. To obtain a uniform deformation field, it seems therefore better to proceed under reasonably low ram velocity and by applying a back-pressure in order to avoid the

bending of the sample. In the present study, the curly shape of the summit of the waves without back-pressure (Fig. 3b) is relevant to plastic yielding confined within a limited surface layer of the material. This suggests that strong friction or stiction generates undeformed bands (light ones) with high plastic deformation close to the surface, whereas low friction generates homogeneously sheared bands (dark ones) in the channel corner. The unstable balance between the yield stress and the friction force should be responsible for the both periodic stress oscillation and the periodic banding.

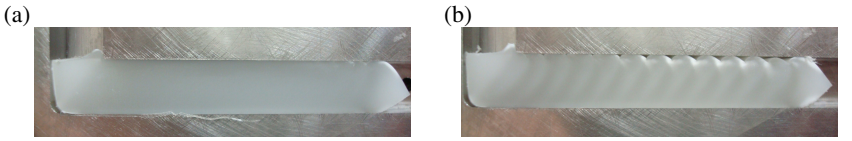

Fig. 3 Macrographs of PP samples after ECAE without back-pressure and different ram speeds: (a) 0.45 mm/min, (b) 45 mm/min

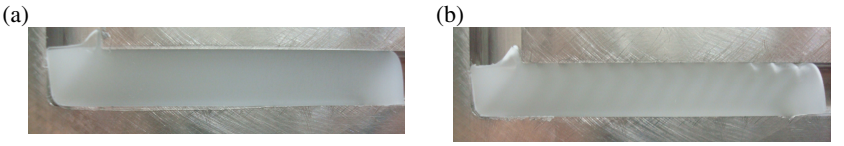

Fig. 4 Macrographs of PP samples after ECAE at a back-pressure of 900 N and different ram speeds: (a) 0.45 mm/min, (b) 45 mm/min

The effect of extrusion velocity on the stress versus strain curves (corresponding to samples extracted from the middle of the extruded material) is presented in Fig. 6. It is observed that there is a decrease in the yield stress as a function of extrusion velocity. The effect of extrusion velocity on the strain hardening can be clearly seen. Moreover, strain softening is also observed for the lower velocity. In addition, when applying back-pressure, the differences observed on the global stress level are attenuated.

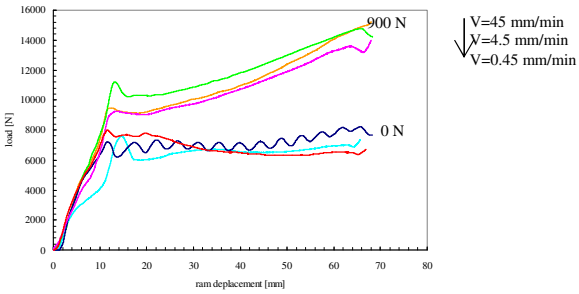

Fig. 5 Tensile stress-strain curves of PP samples before and after ECAE

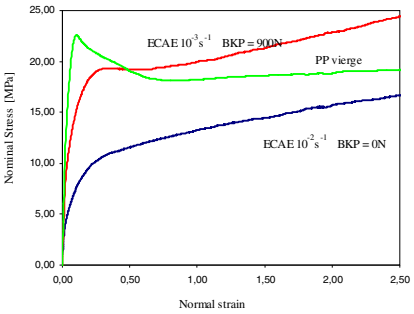

Fig. 6 Tensile stress-strain curves of PP samples after ECAE

Extrusion velocity also acts on the homogeneity of the deformation after ECAE processing. As an example, two representative tensile samples are shown for a given cross-head displacement in Fig. 7. It can be clearly seen that the sample extruded at 4.5 mm/min presents a much diffused strain instability while multiple strain localizations occur in the sample extruded at 45 mm/min. These instabilities occur in regions undergoing high shear during extrusion. The specific crystallographic texturing of these sheared bands with their (hk0) planes tilted at roughly 45° from FD is indeed highly favorable to plastic shear when applying a tensile load along FD, owing to a maximum value of the resolved shear stress. It is noteworthy that, due to this specific crystallographic configuration, the tensile yield stress for the samples extruded at 45 mm/min is far below that of the other sample extruded at 4.5 (Fig. 6). As strain increases beyond the yield point, the stress increase allows the undeformed regions to gradually proceed into plastic deformation process. Further insight into the deformation behaviour is obtained by using the DIC method. Fig. 8 presents full-field contours of true axial strain at different stages of cross-head displacement u_y: 2.5, 6.25, 10 and 12.5 mm. The strain field is shown in colour level scale. True axial strain profiles along the length of samples are given in Fig. 9. The deformation is quite homogeneous before yielding and becomes inhomogeneous after strain instabilities occur. It can be observed from these figures that strain localization occurs at relative small cross-head

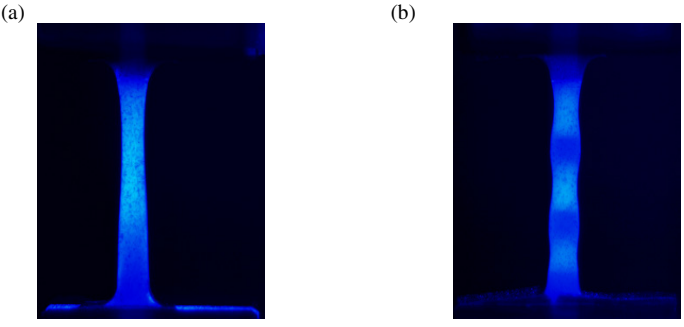

Fig. 7 PP tensile samples at a cross-head displacement of 12.5 mm after ECAE without back-pressure: (a) 4.5 mm/min, (b) 45 mm/min

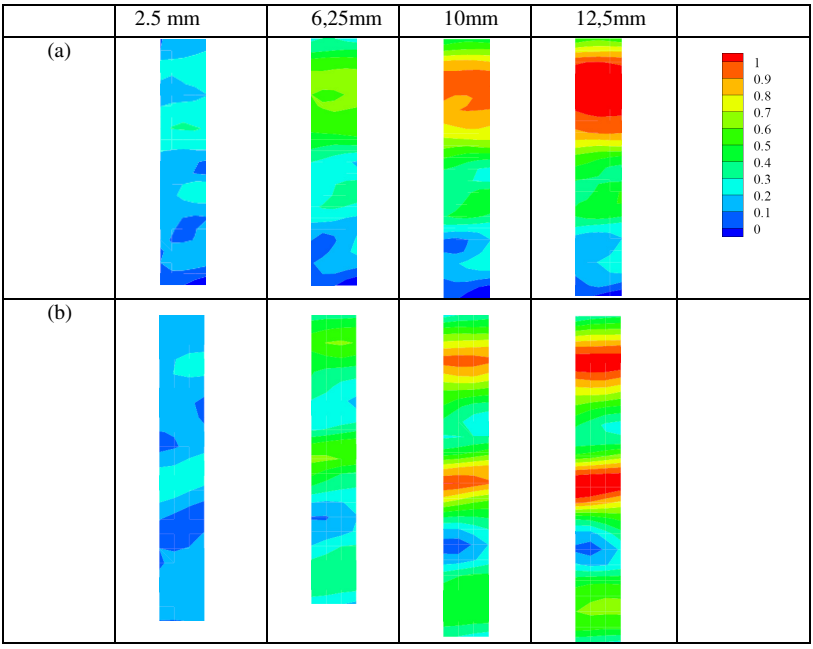

Fig. 8 Contour plots of true axial strain at different stages of cross-head displacement of a PP tensile sample after ECAE without back-pressure: (a) 4.5 mm/min, (b) 45 mm/min

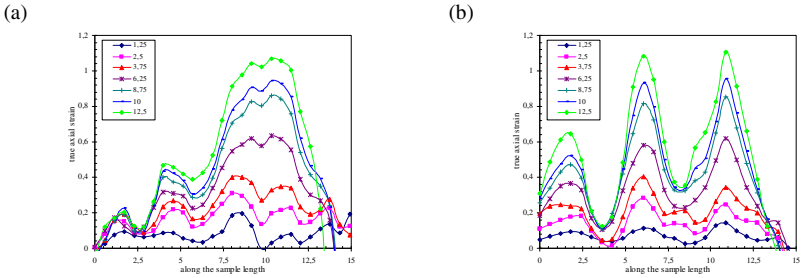

Fig. 9 True axial strain profiles along the length of a PP tensile sample after ECAE without back-pressure: (a) 4.5 mm/min, (b) 45 mm/min

displacements and increases with the increase of total displacement. The maximum local strain of the two examples is nearly comparable. However, the pattern of strain localization is completely different. Indeed, when considering multiple strain instabilities, the deformation remains nearly concentrated in the initiation zone while the instability is more diffused in the other case.

4 Conclusion

The ECAE of PP was conducted at room temperature under various extrusion velocities and back-pressure levels using a 90° die. Very particular deformation behaviours were noted. Indeed, the inhomogeneity was externally manifested by periodic shear banding and periodic waves depending on the applied back-pressure level. Low extrusion velocities appear to provide benefits with regard to flow localization. The results show that multiple strain localizations occur during uniaxial tensile testing, revealing that extrusion velocity strongly acts on the deformation homogeneity of the extruded samples. Full-field strain was measured under tensile loading using an optical strain measuring technique based upon DIC which confirms these effects.

References

Azushima, A., Kopp, R., Korhonen, A., Yang, D.Y., Micari, F., Lahoti, G.D., Groche, P., Yanagimoto, J., Tsuji, N., Rosochowski, A., Yanagida, A.: Severe plastic deformation (SPD) processes for metals. CIRP Annals - Manufacturing Technology 57, 716–735 (2008)

Coates, P.D., Ward, I.M.: Polymer 20, 1553–1560 (1979)

Campbell, B., Edward, G.: Plastics Rubb. Comp. 28, 467–475 (1999)

Phillips, A., Zhu, P.W., Edward, G.: Macromolecules 39, 5796–5803 (2006)

Saraf, R.F., Porter, R.S.: J. Rheology 31, 59–94 (1987)

Segal, V.M.: Materials processing by simple shear. Materials Science and Engineering A. 197, 157–164 (1995)

Sue, H.J., Li, C.K.Y.: J. Mater. Sci. Lett. 17, 853–856 (1998)

Wang, T., Tang, S., Chen, J.: Effects of processing route on morphology and mechanical behavior of polypropylene in equal channel angular extrusion. Journal of Applied Polymer Science 122(3), 2146–2158 (2011)

Zachariades, A.E., Mead, W.T., Porter, R.S.: Chem. Rev. 80, 351–364 (1980)

Part V
Design and Manufacturing of Mechanical Systems

Disassembly Method for Early Stages of Design

Louisa Issaoui, Maroua Kheder, Nizar Aifaoui, and Abdelmajid Benamara

LGM, ENIM, University of Monastir, Av Ibn Eljazzar 5019
Monastir, Tunisia

Abstract. Economical, useful and waste less time disassembly planning is the asset of recent research works. In spite of varied assembly and disassembly (A/D) approaches proposed in the last two decades, reducing the time of generation and optimization is still their major problem. In this paper a new approach of disassembly planning is proposed. Some criteria are early integrated in the sequence generation using a connection graph. The approach offers a reduced number of valid possibilities and allows an easy and fast optimization process. A case study is presented to prove the effectiveness of the proposed approach.

Keywords: Selective disassembly, Maintenance, Target component, Sequencing, Criterion integration, Optimization.

1 Introduction

Papers Assembly /Disassembly operations in the life cycle of a mechanical product are very important. These operations are performed not only in manufacturing, but also during product using in maintenance. They are also performed at product end of life in dismantle for disposal or for reusing. Due to A/D operation importance in mechanical product life cycle, A/D planning becomes nowadays a more and more important research issue. In particular, in product development stage and earlier than manufacturing, disassembly planning is used to judge the component or subassembly accessibility. Judgments are made in general by generating possible disassembly sequences and evaluating them for optimization. Automatic disassembly sequences generation have a growing number of applications. They are being extended to almost every industry, as Y. Tang and al [1] ensured. Tang and al gave some industrial applications as the example of BMW, the largest German car manufactory which has a dismantling plant in Orlando, Florid [2]. The US defense department has also hired military contractors to dismantle and recycle unwanted weapons [3]. Mitsubishi Electric developed an automated disassembly process, which was incorporated in integrated recycling plants for refrigerators, air conditioners, washing machines and televisions. Automatic disassembly techniques are then developed and used in the areas of automobile, electronics, aerospace, construction arms, and industrial equipment. Generally, common disassembly approaches are interested in generating disassembly sequences and optimization.

M. Haddar et al. (Eds.): *Design and Modeling of Mechanical Systems*, LNME, pp. 577–585.
DOI: 10.1007/978-3-642-37143-1_69

There are many methods adopted in this subject. A little comparison review dealing with the common and important approaches is given in this paper in section 2. The review is followed by a synthesis in. The present work, not only focuses in reducing computing time in both generation and optimization steps, but also makes automatic reasoning of the proposed approach closer to real disassembly. The disassembly planning approach is detailed in section 3. It includes the assembly analysis, the sequence generation by criteria integration, and sequences evaluation used to obtain an optimal one.

2 State of Art

2.1 Assembly/Disassembly Methodologies

Disassembly or assembly approaches proposed in the last two decades used varied methodologies. L.Wang and al [4] classified them in exact methods and meta-heuristic ones. Common exact methodologies can be summarized in three methods according to F.Demoly [5]: The separation methods and evaluation (cut set method), the tree search method, and the graph search method. Exact (or enumerative) methods such as tree search or graph search can give exactly the best result. Assembly planners usually use a cut-set algorithm, which is guaranteed to find the global optimum. But these methods are relatively slow and limited, when the number of product parts increases, because of the combinational nature of the problem.

In fact, when the number of components increases, the disassembly process becomes more complex. So, heuristic methods are developed to overcome this complexity [4]. Although these methods are efficient they do not guarantee that the global optimum will be found. They need also one or more valid sequence provided to trigger the system before starting the search. Heuristic methods, used frequently in the last decade are quick. But they may stick in local optima. To resolve these problem meta-heuristic methods such as simulating annealing, ant colony and genetic algorithm are developed. These last methods are based on generating sequences from initial proposed ones and they are able to escape local optima. During iterations new generated sequences are in continuous evolution converging to optima sequence. Initial solutions are randomly proposed. Genetic algorithm is one of the most used one among meta-heuristic methods. The majority of genetic algorithm approaches included constraint relationships and disassembling operations in chromosome as genes. But genetic researches, based on randomly initial population, failed to explain how to obtain data to construct solutions space before genetic process. They failed also to relatively reduce the solution space when the product component number increases. This may make the search process less efficient to find out an optimal solution. W.Hui and al [6] proposed a research work

converting the disassembly sequence planning problem into a searching problem on an information enhanced graph. They used a genetic algorithm to search for good disassembly solutions.

2.2 Synthesis

An Assembly disassembly exact approach offers to the user all possible subassembly combinations and all possible sequences generation even the invalid ones. These approaches transform the disassembly planning from geometric (CAD virtual manipulation) to logical manipulation, which accelerate computing. However they have limits like:

- User's skill requirement.
- Excessive user's intervention.
- Low automation level.
- Complexity problem rising with component number rising.
- Divergence of computing sequences possibilities and diagram representation.
- Some criterions can be added rather before generating to reduce the huge number of combination.
- Difficulty of applications proposed to the user and waste of time can never simplify the accessibility or disassemble judgment in product development and design.

In this present work, a new approach of disassembly planning and sequence optimization is proposed. This approach is based on an early integration of optimization criterion. This not only overcomes the complexity of combination of exact methods, but also overcomes the problem of random populations in defining solution space of meta-heuristic method. The present approach focuses on the disassembly target component and has as objectives:

- Reduction of number of possible combinational sequences.
- Avoiding random sequence generating by approaching operations to real disassembly reasoning.
- Increasing automation level.

3 Disassembly Planning Approach

The present work is an oriented target component disassembly. The disassembly is in the context of maintenance or disposal, and in the context of judgment of component position to validate design. The user selects the target component before the generation process. Some early criteria are useful to reduce computational effort and time as a fixed part criterion or component number criterion. Parts grouping in a sub-assembly can be done automatically or by the user choice. Fig. 1 depicts our approach.

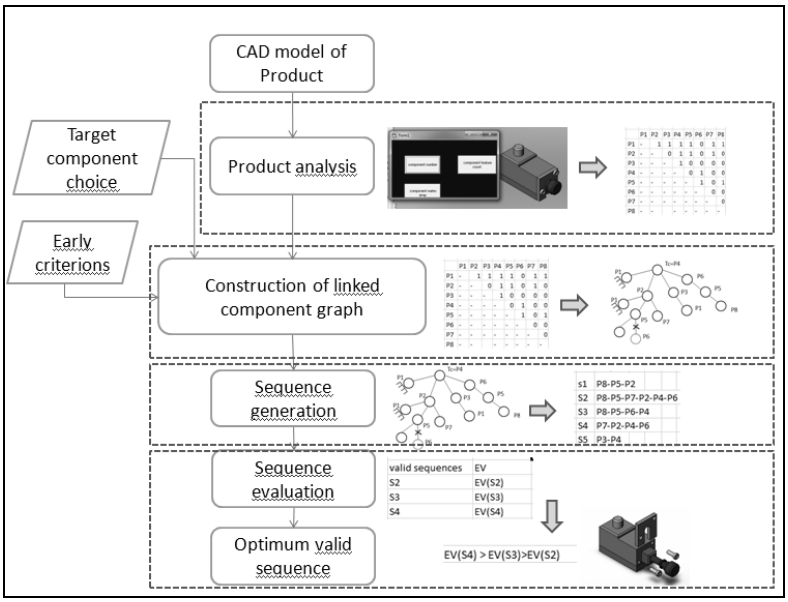

Fig. 1 Flow chart of disassembly approach

The proposed disassembly planning involves the following steps:

1) Product analysis to generate the connection matrix

Starting from a CAD model, all components of the product are enumerated. A connection matrix is constructed to identify which components are in relations. (Table1)

2) Linked component graph (LCG) construction:

From the matrix data, a linked component graph is created starting from the target component as the center node and taking into account some criterions detailed in next paragraph.

3) Generation of possible sequences:

From the LCG and starting by free component possible sequences are proposed by a search on the graph.

4) Optimization: This step is an evaluation of obtained the valid sequences using specific criteria.

3.1 Connection Analyzing and Disassembly Mobility Tests

Identifying the component relationship in the assembly is the basis of disassembly sequence generation. Component relations or connections are determined, in the present work, by analyzing assembly mates from CAD model.

Three procedures are proposed and applied in this work.

- The first is counting product component number.
- The second one is listing the component or subassembly names and constructing the assembly connection matrix Mij (table1).

Table 1 Assembly connection matrix

	P1	P2	….	Pn
P1	0	1	0	1
p	2	0	0	0
…			0	0
Pn				0

The connection matrix (table1) Mij is (n, n) symmetric matrix
Mij =1 if there is a connection between parts Pi and Pj,
else Mij = 0

- The third is collecting mate data for every component to determine the set of components in relation and the kind of geometric contact of each contact.

For each component connection information (neighbor components and connection entities) are automatically identified from mates data from CAD model. Mobility tests are then performed to check if a component is free for disassembly or not. If it is free possible disassembly directions are automatically given. Mobility is defined in this work as the component or subassembly freedom for disassembly. This is different from the link mobility of a component in an assembly in its function. In fact in, a planner link, for example, usual link freedom is defined in a three axis reference as two translations in the plan and one rotation around normal axis. However to separate parts in this case many translations are possible along all vectors belonging to an hemisphere. This hemisphere is defined by the plan of contact and its normal vector.

After analyzing stage, a list of free components is saved and a connection graph is constructed. This graph is specific to the target component. The construction is made by respecting the volume and contact number criterion. The graph starts from the target component and represents all the neighbor parts in connection with and nodes of the level before. (fig 2)

3.2 Integration of Criterions in Sequence Generation

3.2.1 Criterion Integration in the Connection Graph

Neighbor parts are the components in the product in relation with the target component TC. They are presented in the connection graph, at the first node group L1 = (g1, g2…gn). This graph, named Linked components graph (LCG) is a preparation to disassembly generation. The components in relation with TC neighbor parts are represented in the graph at next node groups as L2 = (gi1, gi2…gin). A node, belonging to LCG, is defined by last nodes address. For example an element gijk is the node in the keith branch of jeith node of the ieith node of the group L1.

Criterions are introduced in the connection graph as eliminatory tests or iterations: The graph (Fig. 2) is a set of branches. The development of a branch is stopped when the fixed part is found. This part is considered from the beginning

as the voluminous, not a candidate to be disassembled. The development of a branch in the LCG is stopped also when a part, placed in a branch developed before, is found.

Different links between TC and neighbor parts, and neighbor parts and other parts are identified automatically as described below.

P4 is connected to P2, P6, P3, and P1.
P2 is connected to P7, P5, and P1.
P6 is connected to P5.
P3 is connected to P1

The LC graph given below (fig2) takes into account the criterion of fixed part (P1). The nodes in the end of the four possible branches have contacts with other nodes. P6 exists in two branches and only one branch is developed after P6 node to respect component number criterion.

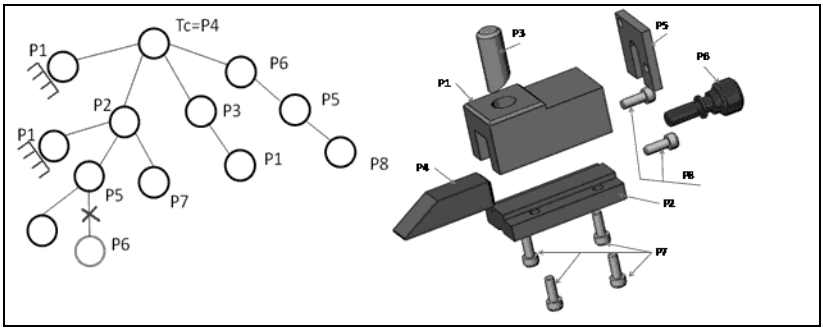

Fig. 2 LC graph of a target component TC- the burst sight of the assembly in the right

3.2.2 Criterion Integration in Sequence Generation

A set of instructions and iterations are used to generate possible sequences from the above graph. The main criterion integrated at this step is the validity criterion. It is taken into account in order to reduce computing time. Only feasible sequences are then generated and completed. This means: when generating a sequence they are defined by first parts which must be free (ready to be disassembled). The second or other next part is tested if it is free to be added to the sequence.Otherwise the generating procedure of the current sequence is stopped and another feasible sequence is searched. This can reduce the computing time and handles only feasible sequence. A validity factor Vf is assigned to the sequence. This factor has a binary value and it depends on mobility state of each element of the sequence. Each component has its own information about mobility of disassembly. This information is updated after separating the precedent component in the proposed sequence. If one or more links are broken mobility state of the component may change.

Initial value of Vf is 1.

Vf = Vf*1 if the element is free, otherwise Vf = Vf*0.

For this sample, the generation is stopped for sequences S1, S5, S6, and S7 when a blocked component is found. Valid sequences are S2, S3 and S4, as Vf keeps the value 1 until reaching the target component P4 in the sequence.

3.3 Sequence Evaluation and Optimization

3.3.1 Sequence Representation

A set of feasible and valid sequences is the result of the generation process. A sequence is characterized by the order of the component, their number, every component number, disassembly direction and orientation change, and used tools for every component. The following table represents a sequence. Tools are the user input introduced for components which are elements of only valid sequences. A component volume and disassembly direction is a data extracted automatically from analysis process. Disassembly direction of component is picked up based on geometric nature of link entities. For example a planar link has two surfaces as link entities. A surface is defined by its normal vector and a point. From these characteristics we define a mobility space: the hemisphere defined by this normal vector.

Table 2 Sequence representation

Component order of disassembly	P1	……Pi……..	Pn
Volume	V1	……...Vi…….	Vn
Disassembly direction	D1	……Di…….	Dn
Used tool	T1	……Ti…….	Tn

3.3.2 Sequence Evaluation

The sequence evaluation is based on some criterions: component number, component volume, used tool and disassembly direction.

A valorization term is assigned to every criterion as described below:

-Valorization term for used component number: p

-Volume criterion term: $\sum_{i=1}^{p} \frac{v_i}{v_t}\left(\frac{p+1-i}{p}\right)$

-Disassembly direction criterion term: $\sum_{i=1}^{p} d_i$

-Tools type and change: $\sum_{i=1}^{p} \delta_i \mu_i$

Vi is the volume of component i, Vt is the sum of p component volume,

(p+1)-i / p is a factor giving a valorization to the order of components in relation with their volumedi indicates the angle of direction change from one component to another d_i=0 for 0°, di=1 for 90°, di=2 for 180°.

δ_i =1 if there is a change of the tool , else δ_i =0.

μ_i Indicates the kind of used tool μ_i =1 for the user hand, μ_i =2 for screwdriver, μ_i =3 for mallet, μ_i =4 for press.

n is the total component number.

The following expression of four criterion terms is the evaluation function: EV (S_i): EV=2*n/ (p+αD+βT+γV)

4 Conclusion

At an early stage of product development, disassembly simulation is useful for judgment of part positions and accessibility. Designer needs this judgment to validate his proposed design. In order to develop disassembly application a new approach is proposed in this paper. This approach is based on integration of some criteria in the sequence generation step. The criteria integration is made by the construction of linked compound graph .The LC proposed graph in this paper makes the disassembly sequence generation much easier and faster. Other criteria are also used in evaluation step to propose an optimal sequence. Proposed algorithms are general and applicable for any chosen part of the product. This may be useful for a complete disassembly supported by the user intervention. The main aim of this approach is avoiding the combinatory generation of sequence and limiting the space of solutions which can be the result of genetic algorithm methods. The integration of some criteria in the sequencing process and tests of freedom (mobility for disassembly) helps to approach the virtual selective disassembly planning with reality.

The approach is implemented in the application programming interfaces (API) of SolidWorks. Opencascade development platform is also used for sequence visualization. The case study presented above shows the validity of the proposed approach.

- The proposed approach presents the following advantages:
- -Integration of the validity in the generation step. Only feasible sequences are then generated
- -Reduction of computing time, firstly because of using global reference without base transformations, and secondly because of direct determination of disassembly directions from geometric entities characteristics without link modeling.
- -Automation of different steps of disassembly process.

    - Avoiding combinatory computing by reduction of solution space. This is useful for products having a big number of components.

References

[1] Tang, Y., Chu Zhou, M., Zussman, E., Caudill, R.: Disassembly Modeling, Planning and Application. Journal of Manufacturing Systems 21(3) (2002)

[2] Grogan, P.: Auto wreckers. Biocycle 35(86) (1994)

[3] Meier, B.: Breaking down an arms buildup: Dismantling and recycling weapons, pp. Dl–D2. New York Times (late New York edition) (1993)

[4] Wang, L., Keshavarzmanesh, S., Feng, H.-Y., Buchal, R.O.: Assembly process planning and its future in collaborative manufacturing: a review. Int. J. Adv. Manuf. Technol. 41, 132–144 (2009)

[5] Demoly, F.: Conception intégrée et gestion d'informations techniques: application de l'ingénierie du produit et de sa séquence d'assemblage. Thèse de doctorat (2010)

[6] Hui, W., Dong, X., Guanghong, D.: A genetic algorithm for product disassembly sequence planning. The Department of Precision Instruments and Mechanology. Neurocomputing 71, 2720–2726 (2008)

[7] Moore, K.E., Gungor, A., Gupta, S.M.: A Petri Net Approach to Disassembly Process Planning. Journal of Computer Industrial Engineering 35(1-2), 165 (1998)

[8] Cittolin, A.: Etude de filtres universels en vue d'une détermination et d'une sélection automatique de gammes d'assemblage de produits industriels. Thèse de doctorat, Ecole Polytechnique Fédérale de Lausanne (1997)

[9] De Fazio, T., Whitney, D.: Simplified all mechanical assembly sequences. IEEE Journal of Robotics and Automation 3(6), 640–658 (1987)

[10] Bourjault, A.: Contribution d'une approche méthodologique de l'assemblage automatisé: élaboration automatique des séquences opératoires. Thèse d'Etat Université de Franche-Comté (1984)

[11] Lia, J.R., Khoob, L.P., Torb, S.B.: Generation of possible multiple components disassembly sequence for maintenance using a disassembly constraint graph. International Journal of Production Economics 102, 51–65 (2006)

[12] Rejneri, N.: Détermination et simulation des opérations d'assemblage lors de la conception de systèmes mécaniques. Thèse de doctorat (2000)

[13] Zhang, H.C., Kuo, T.C.: A graph-based approach to disassembly model for end-of-life product recycling. In: Proc. of 19th Int'l Electronics Mfg. Technology Symp., Austin, TX, pp. 247–254 (October 1996)

[14] Zhang, H.C., Kuo, T.C.: A graph-based disassembly sequence planning for EOL product recycling. In: 21st lEEE/CPMT Int'l Electronics Mfg. Technology Symp., Austin, TX, pp. 140–15 (October 1997)

[15] Dutta, D., Woo, T.C.: Algorithm for multiple disassembly and parallel assemblies. Journal of Engg. for Industry, Trans. of ASME 17, 102–109 (1995)

[16] Srinivasan, H., Gadh, R.: A geometric algorithm for single selective disassembly using the wave propagation abstraction. Computer Aided Design 30(8), 603–613 (1998a)

[17] Srinivasan, H., Gadh, R.: Complexity reduction in geometric selective disassembly using the wave propagation abstraction. In: Proc. of IEEE Int'l Conf. on Robotics & Automation, Leuven, Belgium, pp. 1478–1483 (1998)

FEM Simulation Based on CAD Model Simplification: A Comparison Study between the Hybrid Method and the Technique Using a Removing Details

Hamdi Mounir[1], Aifaoui Nizar[1], Louhichi Borhen[2], Abdelmajid Benamara[1], and Dominique Deneux[3]

[1] LGM, ENIM, University of Monastir, Av Ibn Eljazzar 5019 Monastir, Tunisia
hamdimounirtun@yahoo.fr, nizar.aifaoui@ipeim.rnu.tn, abdel.benamara@enim.rnu.tn
[2] DGPA, ÉTS, 1100, Notre-Dame Ouest, Montréal, H3C1K3, Québec, Canada
lborhen@gmail.com
[3] LAMIH-SP, Université de Valenciennes, (CNRS—Mixt Research Unit No. 8530), 59313 Valenciennes Cedex 9, France
Dominique.deneux@univ-valenciennes.fr

Abstract. The simulation process is currently used in the design and dimensioning of mechanical parts. With the progress of computer materials, the Finite Elements Method (FEM) becomes the most used approach in the simulation of mechanical behavior. The simulation process needs multiple Design-FEM loops. In order to accelerate those analysis loops, an adaptation of Computer Aided Design (CAD) model is necessary. The adaptation step consists in the simplification of the CAD model geometry by eliminating details (holes, chamfers, fillet, etc.) and faces. In this paper, a new technique of simplification of the CAD geometry is developed. This technique is a hybrid method based on a combination of the elimination details and merging faces. With this approach, the computing time is reduced by the elimination of geometric details which do not boundary conditions. An implementation of the proposed algorithm on the Open Cascade platform is also presented. The results of the hybrid method are compared with a previous publication. The reduction of the computing time and the amelioration of the result precision highlight the efficiency of the hybrid method.

Keywords: CAD model; Analysis model; simplified model; hybrid method; FEM Simulation.

1 Introduction

For a long time, design and mechanical analysis were considered two independent activities. Our research tasks aim at the improvement of the CAD models preparation's phase even before starting the mesh stage. The preparation of a CAD model consists in simplifying or cleaning the geometry by eliminating details (holes,

M. Haddar et al. (Eds.): *Design and Modeling of Mechanical Systems*, LNME, pp. 587–596.
DOI: 10.1007/978-3-642-37143-1_70

chamfer, fillet, etc), considered superfluous for the simulation (Zhu and Menq 2002). Then, these details are zones where the mesh will be automatically refined, which will generate a very important computing time without bringing more precision to the results of simulation.

The generation of an analysis model using the CAD geometry is based on some analysis assumptions. These assumptions are related to the material behavior, solicitations and the geometry definition of the part. In the bibliography, (Sun et al. 2009), (Homri et al. 2005), (Lee 2005) several research tasks were interested in the CAD geometry adaptation problems to analysis models dedicated to the mechanical analysis by the finite elements method.

Thakur et al. in (Thakur et al. 2009). In their works, they studied existing model simplification techniques that are useful from the physics based simulation and classified them broadly into four main categories based upon the type of simplification operators used in the respective techniques, i.e. surface entity, volumetric entity, explicit feature and dimensional reduction.

Belaziz et al. in (Belaziz et al. 2000), proposes an adaptation method of geometry based on the features' recognition approach. In this approach, the recognition is carried out by a morphological analysis of the CAD geometry, that's why this method is more flexible than the Dabke's method. The adapted and idealized geometry is generated by the removal of some form features considered as being non characteristic for the considered mechanical analysis.

Sheffer et al. in (Sheffer et al. 1997), develops a suppression procedure of details and "cleaning" of the CAD geometry using the principles of virtual topology. This topology is based on regrouping the faces constituting the B-Rep model in areas admitting the same characteristics of curve and dimension.

Armstrong et al. in (Armstrong et al. 1996) and Donaghy in (Donaghy et al. 1996), use the Medial Axis Transform (MAT) to carry out the adaptation and the simplification of B-Rep geometry. The MAT method builds the skeleton of a geometrical representation in order to obtain the median axis. A circle with a variable diameter sweeps the interior of the structure remaining constantly in contact, in at least 2 points with the structure. The skeleton is obtained by building the places of the center of the circle. For a 3D geometry, the circle is replaced by a sphere and the places of its center represent a surface.

Lee et al. in (Lee et al. 2004), present a method to generate progressive solid models (PSM) from feature-based models using a cellular topology-based approach. Here, cellular topology is used to generate the PSM, and then the surface entity based operators are developed to simplify the model. The main concept in this paper is to start with a feature based model as input and generate a sequence of solid models representing the underlying object with various levels of details. The intended purpose of the PSM is to stream models over a network efficiently.

Fine et al. in (Fine et al. 2000), introduced simplification operators for the Finite Element Analysis. The operators are based on the vertex removal and spherical error zone concept.

Date et al. in (Date et al. 2005), reported vertex and an edge collapse-based technique for the mesh model simplification and refinement. They defined three

metrics based on the overall geometry error, face size and face shape. The metrics are evaluated for the edges to determine their priority index for simplification.

Kim et al. in (Kim et al. 2005), reported a system for a multi-resolution feature simplification using three operators, namely wrap-around, smooth out and thinning. The method is applied to the finite element model preparation and network transmission multi-resolution modeling. The features are first recognized using rule-based techniques and then various operators are applied to suppress them. In the case of the wraparound operator, the model is considered to be wrapped by a thin plastic cover. The parts of the model hidden by the cover are considered for simplification or removal.

Foucault et al. in (Foucault et al. 2008), reported a topology simplification technique for the finite element mesh generation. The authors have developed a Mesh Constraint Topology (MCT) based on the model simplification scheme to address the sharp corner matching requirements. MCT entities are defined as composite topological entities created to suit the mesh generation requirements stated before. The MC face is a poly-surface, defined as the union of Riemannian surfaces constituting the reference model. The MC edge is a poly-curve, defined as a union of Riemannian curves constituting the reference model.

Woo et al. in (Woo 2009), presented a method that is mainly focused on the mechanical parts that will be created by machining. That is, the most simplified result of a solid model will be the solid model of stock material. Independently of user-specified design features, this method simplifies the solid model by removing the detailed geometry by using these subtractive features. If a solid model is not appropriate to be represented in terms of machining features, unnatural simplification may happen for the solid model.

Hamdi et al. in (Hamdi et al. 2009), CAD/CAE interoperability, an automatic generation of Analysis Model based on the simplification of CAD geometry is implemented using the Open Cascade platform. In this work, the simply size criteria is integrated, and in (Hamdi et al. 2010), a simplification algorithm of CAD models for a simulation by the finite element method is presented. The algorithm proposed consists in reading the B-rep model of the CAD geometry in order to identify, and then remove the details considered to be superfluous for the mechanical analysis, using two criteria of size and boundary condition.

This paper is divided in to three sections. The first one has presented a state of the art on the principal techniques used to eliminate details from the CAD geometry. In the second section, the hybrid method of simplification is proposed. In order to highlight the efficiency in the reduction of the design time and the cost of the product, an example of a mechanical part has been studied using the proposed approach, and presented in the third section.

2 Algorithm of Simplification with Hybrid Method

The proposed algorithm composed of three principal interdependent phases is represented in Fig. 1. Each phase implies overlapping stages.

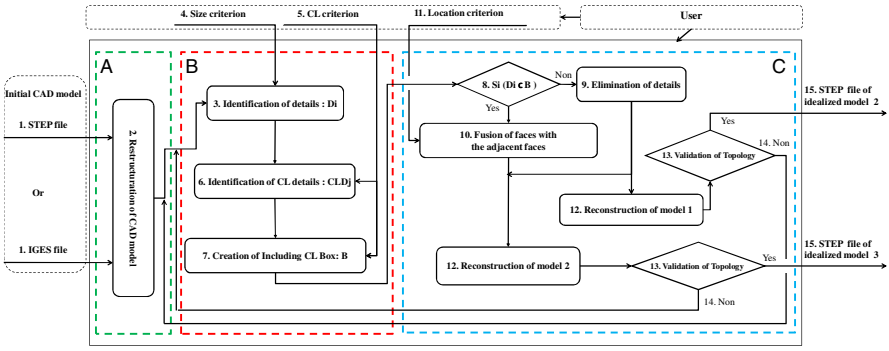

Fig. 1 Algorithm of idealization with a hybrid method

In order to be independent of the CAD/CAM systems, the proposed algorithm relies on a neutral file (Standard for Exchange of Product: STEP) to import the data of the part to be idealized. To use various tools of simulation, the idealized CAD geometry will be also stored under the same neutral format (STEP). The phase (A) of the algorithm consists in a step of pre-treatment of the CAD model. It allows restructuring the Boundary Representation (B-rep) model of the part to a data base. The structured information in this data base relates to the faces, the normal of the faces, the wires, the edges and the vertex which includes the geometry model of the part. Phase (B) consists in identifying the details candidates for simplification. That implies the implementation of algorithms of identification based on criteria (forms, sizes, function, position…). The result of this phase is a representation of Iso-zones targets for simplification. These Iso-zones are entities (edges, faces) colored according to the specificity of each face. This original vision enables the designer to visualize the least influential zones (high order of criticality) on the computation results, giving him the possibility either to interactively eliminate the entities which have a high order of criticality, or to apply the automatic algorithms of simplification. The stage (7) consists in the creation of Boundary Conditions (BC) delimited box. And the phase (C) allows the reconstruction of the simplified model. Stage (9) consists in removing the identified details, if they are outside the BC delimited box, then in rebuilding the geometric model after suppression. Stage (10) consists in the fusion of the identified details with the adjacent faces if they are inside the Box (the details represent the concentrator's stress). The result of stage (12) is an idealized CAD model whose elementary topology is validated in stage (13). At the exit of the algorithm, the designer has at his disposal an idealized model saved in the STEP format for a simulation by finite elements.

3 Data-Processing Implementation and Validation on Example

3.1 Data-Processing Implementation

The data-processing implementation of the simplification algorithm was carried out on a development's platform: 'Open Cascade'. Open Cascade is an environment dedicated to the development of 3D applications of CAD-CAM multi-platforms. This platform is available and free on Internet. It is based on a bookstore of C++ classes and tools developed and available in open source.

3.2 Example of Validation

In this section, one example of validation will allow validating the principal functionalities of the simplification algorithm. Fig. 2 presents a stair climber machine. The part "support" was selected because they have a broad variety of mechanical parts in terms of its forms, the boundary conditions, and also the details which they contain. The validation example is presented in (Hamdi et al. 2010). The CAD model simplified using the hybrid method will be compared to those published in (Hamdi et al. 2010) in which the method of detail removal is developed. The comparison is carried out on the following points:

- Number of topological entities
- Computation time
- Precision of results.

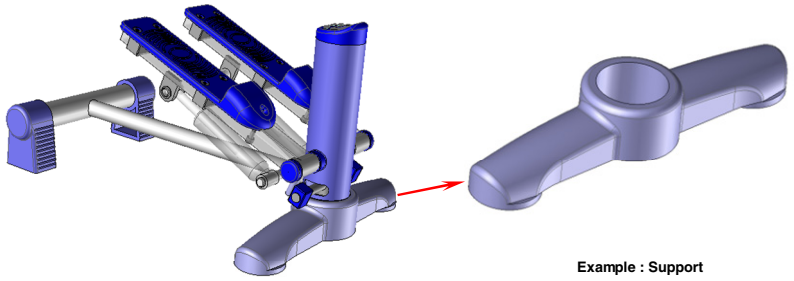

Fig. 2 Example of validation: "support of stair climber machine"

Fig. 3 presents the illustration of the principal stages to pass from a CAD model of the "support" (Fig. 3-a), to a model of analysis whose geometry is idealized (Fig. 3-k) using an hybrid method or to the second model (Fig. 3-l) using only the size criterion. A very important stage (Fig. 3-c) represents the casing by Iso-zones. These iso-zones give to the designer a very clear idea of the details candidates to the elimination by sharp colors, according to the level of criticality, details function and position (Fig. 3-d), the Boundary Conditions (BC) are defined (loading and fixing) (Fig. 3-e), this information allows to identify the BC faces (Fig. 3-f) and to create the BC box (Fig. 3-g), the (Fig. 3-h) present the region of faces that

can be fused, in (Fig. 3-i) is presented the model after the stage of details elimination, (Fig. 3-j) presents the simplified model using all the criteria (hybrid method). Finally, the simplified model was saved at a neutral format (Fig. 3-k).

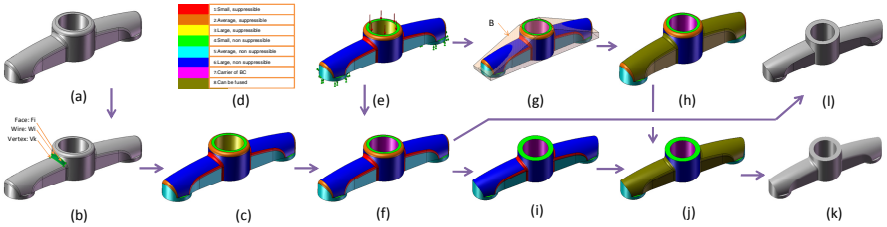

Fig. 3 Stages of CAD Model simplification using a hybrid method

Fig. 4 represents two Open Cascade windows in which are represented the idealized CAD models of the models 2, and 3. These models will be saved in 'STEP' format to be simulated by the finite element method.

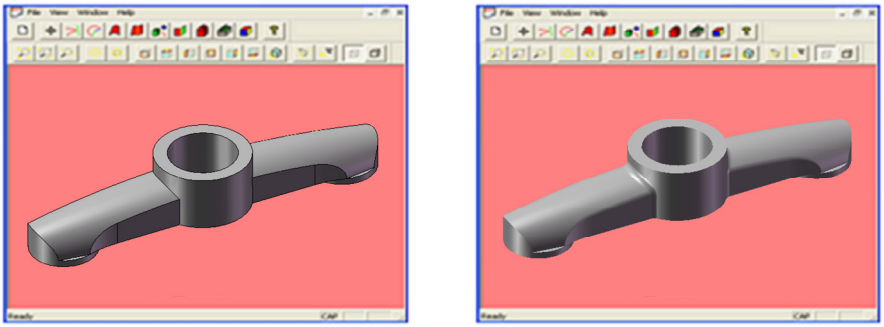

(a): Model 2: using size criterion

(b): Model 3: using hybrid method

Fig. 4 Result of the idealization algorithm implemented by OpenCascade

Table 1 represents the number of the B-rep entities of the model, before and after simplification. It has been shown that the number of entities after simplification is lower than that before simplification. That generates a reduction of the mesh and computation times of the idealized model.

Table 1 The B-rep entities before and after idealization

Models	Number of Faces	Number of Wires	Number of Edges	Number of Vertexes
Model 1	209	223	590	385
Model 2	143	156	407	268
Model 3	135	148	391	260
% of Model 2 $=\frac{\lvert n_i - n_i \rvert}{n_i} \bullet 100$	31,58%	30,05%	31,017%	30,39%
% of Model 3 $=\frac{\lvert n_i - n_i \rvert}{n_i} \bullet 100$	35,41%	33,63%	33,73%	32,47%

The graph presented in Fig. 5, shows that the hybrid method provides a gain in terms of topological entities compared to the method published in (Hamdi et al. 2010) and a gain from the initial model.

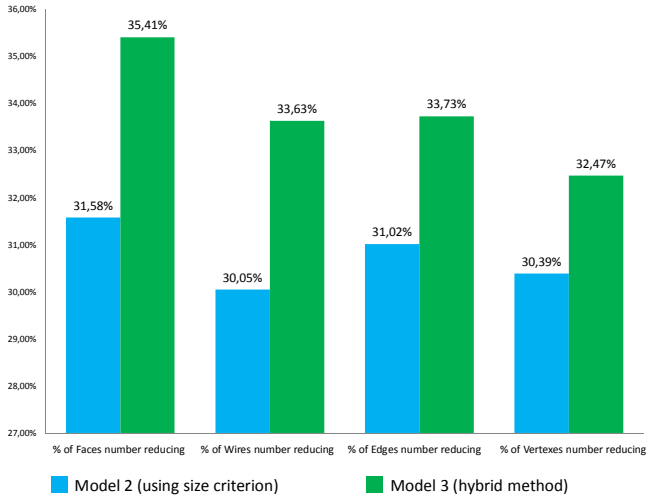

Fig. 5 Comparison between the B-rep entities of idealized model using size criterion and idealized model using hybrid method

Fig. 6 represents the computation results by the FEM simulation of the initial model, model 2 after simplification using only the size criterion (the most used criterion in the state of the art) and model 3 after simplification using the hybrid method. Figs. 6-a-1 - 6-b-1 represent respectively the states of stress and the displacements of the part before the application of the simplification algorithm. Figs. 6-a-2 - 6-b-2 respectively show the states of parts stress and displacements after simplification using only a size criterion. And Figs. 6-a-3 - 6-b-3 represent respectively the states of stress and the displacements of a simplified model after simplification using the hybrid method. For model 2, we notice that the saving time of computation is 62.5%. The error relating to the values of displacements is 2.18%, while that of the equivalent stress is 1.36%. And for model 3, it is noted that the saving of computation time is 50% and the error relating to the values of displacements is only 0.54%, while that of the equivalent stress is only 0.40%.

The graphs presented in Fig. 7, show that the hybrid method provides a gain in precision of the results more important than the method published in (Hamdi et al. 2010).

For a preliminary dimensioning analysis, the error of the first method is considered to be acceptable. If the designer aims to have a much more precise analysis in order to check the chosen dimensions, he can apply stricter criteria of simplification to dimensions of the details to be removed or to the site of the details compared to the loading using the hybrid method. This won't allow the removal of the

forms which are concentrators of the constraint. In all cases, the taking into account of the simplification link in the "design-analysis" chain brings an important saving of the computing time without any significant loss on the quality of the results. We must notice that this procedure of simplification requires a negligible execution time compared to the total simulation time.

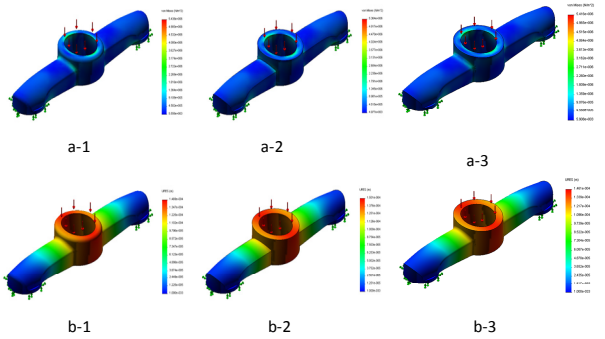

	Model 1	Model 2	Model 3
t (s)	32	12	16
C (Mpa)	5.438	5.364	5.416
d (µm)	0. 1469	0. 1501	0.1461
% t		62,5 %	50 %
% S		1,36 %	0.40 %
% d		2,18 %	0.54 %

Model 1 : Initial model
Model 2 : Simplified model (preliminary dimensioning analysis)
Model 3 : Simplified model (checking analysis)
t : simulation time
S : stress Max
d : displacement Max
% t : time percentage
% S : stress percentage
% d : displacement percentage

Fig. 6 Computation results

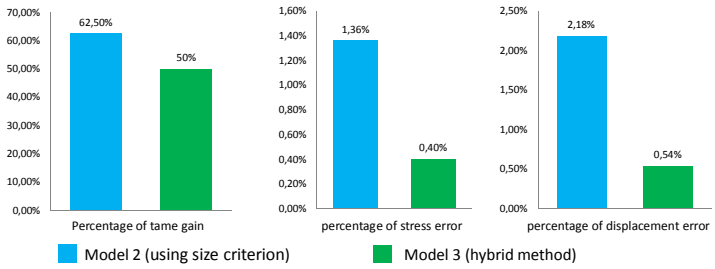

Fig. 7 Comparison between the computation results of idealized model using size criterion and idealized model using hybrid method

4 Conclusion

This study has presented a hybrid method of simplification of the CAD model. The proposed approach consists in reading the B-rep model of the CAD geometry in order to identify the details. Then, the identified details were removed or fused if they are localized in the concentrator's stress zones.

A comparison of the size's criterion method (Hamdi et al. 2010) and the hybrid method with the CAD model before simplification was conducted. The results of this comparison illustrate the major advantage of the hybrid method compared to the method based only on the size criterion since it gives a model better adapted to the need for the FEM simulation.

For a preliminary dimensioning analysis, the error of the method published in (Hamdi et al. 2010) is considered to be acceptable. If the designer aims to reach more analysis precision (in order to check the chosen dimensions), stricter simplification criteria of the dimensions are needed which is available in the hybrid method.

The simulation results presented in a treated example highlight the efficiency of the hybrid method.

The hybrid method presents the following advantages:

- In the simplification process, the input and output files are in a STEP format, which is a neutral format (used by the totality of CAD and Analysis tools and systems).
- The simplification process is based on a hybrid method, to ensure the quality of simulation the result.
- The simplification process is interactive. After treatment, the CAD part is presented by an iso-zone model, so the designer can intervene in the choice of details to be deleted using some criteria.
- The simplification process is based on a CAD model, the reconstruction process is performed without approximation.
- A hierarchic link is saved between the initial model and the adapted model, to allow a perfect CAD/Analysis integration.

To improve even more the simplification method, it can also take into account the orientation of the details compared to the loadings, this criterion will be a subject of future work.

References

Zhu, H., Menq, C.H.: B-rep model simplification by automatic fillet/round suppressing for efficient automatic feature recognition. Computer Aided Design 34(2), 109–123 (2002)

Sun, W., Ma, Q., Chen, S.: A Framework for automated finite element analysis with an ontology-based approach. Journal of Mechanical Science and Technology 23, 3209–3220 (2009)

Hamri, O., Leon, J.C., Giannini, F.: A new approach of interoperability between CAD and simulation models. TMCE 25, 245–255 (2005)

Lee, S.H.A.: CAD–CAE integration approach using feature-based multi resolution and multi-abstraction modelling techniques. Computer-Aided Design 37, 941–955 (2005)

Thakur, A., Banerjee, A.G., Gupta, S.K.: A survey of CAD model simplification techniques for physics-based simulation applications. Computer Aided Design 41, 65–80 (2009)

Belaziz, M., Bouras, A., Brun, J.M.: Morphological analysis for product design. Computer Aided Design 32(5), 377–388 (2000)

Sheffer, A., Blacker, T.D., Clustering, M.: Automated detail suppression using virtual topoly. ASME 26, 57–64 (1997)

Armstrong, C.G., Donaghy, R.J., Bridgett, S.J.: Derivation of appropriate Idealisations in Finite Element Modelling. In: The Third International Conference on Computational Structures Technology, Budapest, vol. 3, pp. 255–268 (1996)

Donaghy, R., McCune, W., Bridgett, S., Armstrong, C., Robinson, D., McKeag, R.M.: Dimensional reduction of analysis models. In: Proceeding of 5th International Meshing Roundtable, Pittsburgh, PA (1996)

Lee, J.Y., Kim, J.H., Kim, H.A.S.: Cellular topology-based approach to generating progressive solid models from feature-centric models. Computer Aided Design 36(3), 217–229 (2004)

Fine, L., Remondini, L., Leon, J.C.: Automated generation of FEA models through idealization operators. International Journal for Numerical Methods in Engineering 49(1), 83–108 (2000)

Date, H., Kanai, S., Kisinami, T., Nishigaki, I., Dohi, T.: High-Quality and Property Controlled Finite Element Mesh Generation From Triangular Meshes using the Multiresolution Technique. Journal of Computing and Information Science in Engineering 5(4), 266–276 (2005)

Kim, S., Lee, K., Hong, T., Kim, M., Jung, M., Song, Y.: An integrated approach to realize multi-resolution of B-Rep model. In: Proceedings of the ACM Symposium on Solid and Physical Modeling, Cambridge, MA, pp. 198–205 (2005)

Foucault, G., Cuillière, J.C., François, V., Léon, J.C.: Adaptation of CAD model topology for finite element analysis. Computer Aided Design 40(2), 176–196 (2008)

Woo, Y.: Automatic simplification of solid models for engineering analysis independent of modeling sequences. Journal of Mechanical Science and Technology 23, 1939–1948 (2009)

Hamdi, M., Aifaoui, N., Louhichi, B., Benamara, A.: CAD/CAE interoperability, an automatic generation of Analysis Model based on idealization of CAD geometry. In: CFM 2009, Marseille, France (2009)

Hamdi, M., Aifaoui, N., Louhichi, B., BenAmara, A.: Idealization of CAD model for a simulation by a finite element method. European Journal of Computational Mechanics 19(4), 419–439 (2010)

Tolerancing Analysis by Operations on Polytopes

Lazhar Homri, Denis Teissandier, and Alex Ballu

Univ. Bordeaux, I2M, UMR 5295, F-33400 Talence, France
{l.homri,d.teissandier,a.ballu}@i2m.u-bordeaux1.fr

Abstract. Geometric tolerancing analysis consists of simulating the behavior of a mechanical system according to geometric defects in the constituent parts. The aim is to verify system compliance in terms of the functional requirements for its expected operation. When carrying out the simulation the geometric specifications of the constituent parts and specifications of parts potentially in contact must be taken into account. One approach using polytopes consists of characterizing the specifications of the parts, the specifications of the contacts and the functional requirements of the mechanical system using sets of geometric constraints. This article describes modeling different sets of constraints manipulated by polytopes. We introduce the operations that are applied (Minkowski sum and intersection) to determine the relative position of any two surfaces of a mechanical system. Finally, tolerancing analysis of a simple mechanical system is described.

Keywords: tolerancing analysis, polytopes, Minkowski sums, intersections.

1 Introduction

In 1988 Fleming laid the foundations for a tolerancing analysis approach, based on operations on sets of geometric constraints [1]. A set of constraints characterizes all the possible positions of a surface within a tolerance zone that may be generated by offsetting the nominal model of the part [2]. Thus, the geometric variations of a part that are compliant with an ISO specification for orientation or position can be characterized [3] and [4]. Similarly, a set of constraints can characterize all relative positions of two distinct surfaces potentially in contact [1]. Fleming established the correlation between the cumulation of defect limits on parts in contact and the Minkowski sum of finite sets of geometric constraints [1]. Algorithms of Minkowski sums applied to the question of tolerancing analysis were then developed [5]. Giordano showed that modeling the relative position of two parts resulting from several potential contacts can be formalized by an intersection operation on sets of geometric constraints [6]. More generally, this approach to tolerancing consists of defining the relative position of any two surfaces of a system by intersections and Minkowski sums for sets of geometric constraints resulting from ISO specifications for the parts and specifications formulated for two parts potentially in contact [4].

M. Haddar et al. (Eds.): *Design and Modeling of Mechanical Systems*, LNME, pp. 597–604.
DOI: 10.1007/978-3-642-37143-1_71

The three main advantages of a variational approach are:

- hyperstatic systems are taken into account,
- dependencies between rotation and translation deviations of the surfaces are taken into account,
- a single interrelation between operand polytopes is necessary to characterize the relative position of two surfaces.

Historically the procedure for tolerancing analysis was based on the following physical hypotheses, which will be used in this article: no defect in form in the real surfaces, no local strain in surfaces in contact and no deformable parts. This paper describes a tolerancing analysis procedure by operations on polytopes. The first part describes determining the operand polytopes in a 3D dimension chain characterizing specifications of constituent parts and contact specifications. In the second part, operations applied in any 3D dimension chain are introduced: Minkowski sum and intersection. Finally, a simple example is given at the end of the article describing the main steps in a general tolerancing analysis procedure.

2 Definition of Operand Polytopes

The displacement limits of a surface in a tolerance zone are defined by a set of geometric constraints. The tolerance zone is arrived at by an exterior matter offset and an interior matter offset on the nominal surface. A tolerance zone can then be defined in terms of its dimension t and parameter k (where $0 \le k \le 1$) which position the tolerance zone in relation to the nominal surface.

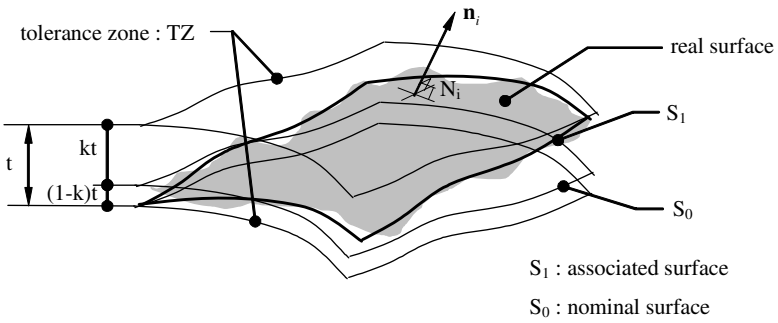

Fig. 1 Definition of a tolerance zone

For $k = 0.5$ the nominal surface is combined with the median surface of the tolerance zone, see figure 1.

Equation (1) defines the set of geometric constraints for a surface of any form [4].

$$S_1 \subseteq TZ \Leftrightarrow \forall N_i \in S_1 : (k-1).t \le \boldsymbol{\varepsilon}_{Ni}.\mathbf{n}_i \le k.t \tag{1}$$

For each point M in the Euclidean space we obtain (2) in accordance with the property of small displacement fields and equation (1).

$$\forall N_i \in S_1 : (k-1).t \le (\boldsymbol{\varepsilon}_M + \mathbf{N_i M} \wedge \boldsymbol{\rho}).\mathbf{n}_i \le k.t \tag{2}$$

Where:

- $\boldsymbol{\varepsilon}_M$: translation vector of point M of S_1, in relation to S_0,
- $\boldsymbol{\rho}$: rotation vector of S_1, in relation to S_0.

Let us define in a $(\mathbf{x}, \mathbf{y}, \mathbf{z})$ base, the projections defined in (3).

$$\boldsymbol{\varepsilon}_M \begin{bmatrix} \varepsilon_{M-x} \\ \varepsilon_{M-y} \\ \varepsilon_{M-z} \end{bmatrix}, \ \mathbf{N_i M} \begin{bmatrix} d_{\mathrm{N_i M_x}} \\ d_{\mathrm{N_i M_y}} \\ d_{\mathrm{N_i M_z}} \end{bmatrix}, \ \boldsymbol{\rho} \begin{bmatrix} \rho_x \\ \rho_y \\ \rho_z \end{bmatrix} \text{ et } \mathbf{n_i} \begin{bmatrix} n_{ix} \\ n_{iy} \\ n_{iz} \end{bmatrix} \tag{3}$$

Finally with (2) and (3), we obtain two inequations (4).

$$\left\{ \begin{array}{l} (k-1).t \le \left(n_{iy}.d_{\mathrm{N_i M_z}} - n_{iz}.d_{\mathrm{N_i M_y}}\right)\rho_x + \left(n_{iz}.d_{\mathrm{N_i M_x}} - n_{ix}.d_{\mathrm{N_i M_z}}\right)\rho_y + \left(n_{ix}.d_{\mathrm{N_i M_y}} - n_{iy}.d_{\mathrm{N_i M_x}}\right)\rho_z \\ \qquad + n_{ix}.\varepsilon_{M-x} + n_{iy}.\varepsilon_{M-y} + n_{iz}.\varepsilon_{M-z} \le k.t \end{array} \right\} \tag{4}$$

The two inequations (4) correspond to two geometric constraints defined at point N_i characterizing two half-spaces of $\mathbb{R}^6$.

Generally, for n points N_i $(1 \le i \le n)$, $2n$ half-spaces $\overline{H}_j^-$ are created $(1 \le j \le 2n)$.

A half-space $\overline{H}_j^-$ can usually be defined according to equation (5), with: $x_1 = \rho_x$, $x_2 = \rho_y$, $x_3 = \rho_z$, $x_{k4} = \varepsilon_{M-x}$, $x_{k5} = \varepsilon_{M-y}$, $x_{k6} = \varepsilon_{M-z}$

$$\overline{H}_j^- : a_{j1}.x_1 + a_{j2}.x_2 + a_{j3}.x_3.a_{j4}.x_4 + a_{j5}.x_5 + a_{j6}.x_6 \le b_j \tag{5}$$

The different coefficients a_{ji} of variables x_{ji} and the value of the second member b_j with $1 \le i \le 6$ are shown in figure 2.

The intersection of the $2n$ half-spaces $\overline{H}_j^-$ defines a polytope P, $P = \bigcap_{j=1}^{j=2n} \overline{H}_j^-$.

Figure 3 shows an example of a 3 dimension geometric polytope, written as 3-polytope, of a planar surface. This polytope is expressed at point P, the centre of the rectangular contour of the planar surface.

if j is odd:	if j is even:
$a_{j1} = -n_{(j+1)/2-y}.d_{N_{(j+1)/2}M_z} + n_{(j+1)/2-z}.d_{N_{(j+1)/2}M_y}$	$a_{j1} = n_{j/2-y}.d_{N_{j/2}M_z} - n_{j/2-z}.d_{N_{j/2}M_y}$
$a_{j2} = -n_{(j+1)/2-z}.d_{N_{(j+1)/2}M_x} + n_{(j+1)/2-x}.d_{N_{(j+1)/2}M_z}$	$a_{j2} = n_{j/2-z}.d_{N_{j/2}M_x} - n_{j/2-x}.d_{N_{j/2}M_z}$
$a_{j3} = -n_{(j+1)/2-x}.d_{N_{(j+1)/2}M_y} + n_{(j+1)/2-y}.d_{N_{(j+1)/2}M_x}$	$a_{j3} = n_{j/2-x}.d_{N_{j/2}M_y} - n_{j/2-y}.d_{N_{j/2}M_x}$
$a_{j4} = -n_{(j+1)/2-x}$	$a_{j4} = n_{j/2-x}$
$a_{j5} = -n_{(j+1)/2-y}$	$a_{j5} = n_{j/2-y}$
$a_{j6} = -n_{(j+1)/2-z}$	$a_{j6} = n_{j/2-z}$
$b_j = -k.t$	$b_j = (k-1).t$

Fig. 2 Defining the parameters of the half-space of an operand polytope

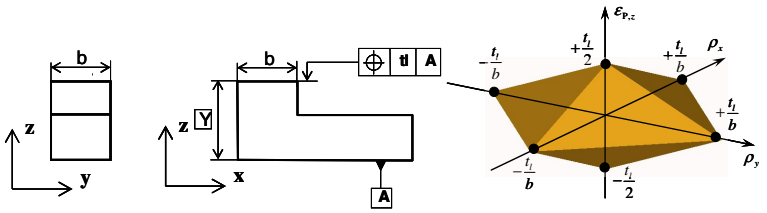

Fig. 3 Geometric 3-polytope of a planar surface with rectangular contour

Like the geometric constraints, the contact constraints are defined between two surfaces potentially in contact. Figure 4 illustrates the projection in $\mathbb{R}^3$ of the 4-polytope of a cylindrical pair joint at point P, a point midway between points A and B, with the ends of the axis of the cylinder common to both surfaces. In this case, joint clearance J is replaced by dimension t of the tolerance zone.

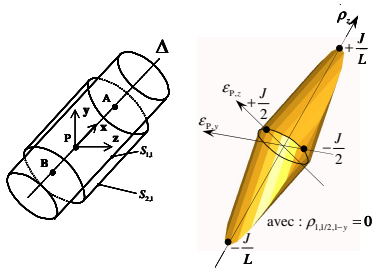

Fig. 4 Contact 4-polytope (projected in $\mathbb{R}^3$) of a cylindrical pair joint

3 Operations on Polytopes

Let us consider two *n*-polytopes $\mathcal{P}$ and $\mathcal{Q}$ defined according to equation (6).

$$\begin{aligned}\mathcal{P} &= \mathcal{P}(\mathbf{A},\mathbf{b}) = \{\mathbf{x}\in\mathbb{R}^n : \mathbf{A}.\mathbf{x}\le\mathbf{b}\} \text{ with } \mathbf{A}\in\mathbb{R}^{mp\times n} \text{ et } \mathbf{b}\in\mathbb{R}^{mp}\\ \mathcal{Q} &= \mathcal{Q}(\mathbf{C},\mathbf{d}) = \{\mathbf{x}\in\mathbb{R}^n : \mathbf{C}.\mathbf{x}\le\mathbf{d}\} \text{ with } \mathbf{C}\in\mathbb{R}^{mq\times n} \text{ et } \mathbf{d}\in\mathbb{R}^{mq}\end{aligned} \tag{6}$$

Let us define polytope $\mathcal{R}$ as the intersection of polytopes $\mathcal{P}$ and $\mathcal{Q}$:

$$\begin{aligned}&\mathcal{R}(\mathbf{E},\mathbf{f}) = \mathcal{P}\cap\mathcal{Q} = \{\mathbf{x}\in\mathbb{R}^n : \mathbf{E}.\mathbf{x}\le\mathbf{f}\}\,;\mathbf{E}\in\mathbb{R}^{(mp+mq)\times n} \text{ et } \mathbf{f}\in\mathbb{R}^{mp+mq}\\ &\text{with}: \mathbf{E}^T = \left[\mathbf{a_1},...,\mathbf{a_{mp}},\mathbf{c_1},...,\mathbf{c_{mq}}\right] \quad \text{et} \quad \mathbf{f}^T = \left[b_1,...,b_{mp},d_1,...,d_{mq}\right]\end{aligned} \tag{7}$$

Figure 5 shows the intersection of two 3-polytopes $\mathcal{P}$ and $\mathcal{Q}$.

The Minkowski sum of the two polytopes $\mathcal{P}$ and $\mathcal{Q}$ is given in the following equation:

$$\mathcal{P}+\mathcal{Q} = \mathcal{R} = \{\mathbf{r}\in\mathbb{R}^n \mid \exists\mathbf{p}\in\mathcal{P},\exists\mathbf{q}\in\mathcal{Q} : \mathbf{r}=\mathbf{p}+\mathbf{q}\} \tag{8}$$

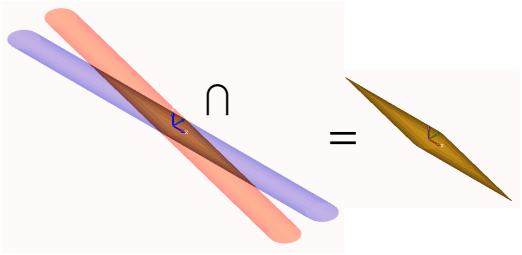

Fig. 5 Intersection of two 3-polytopes

With 1 dimension, this operation consists of adding in limited variables at intervals. This method is used in one-directional dimension chains. With 2 and 3 dimensions, the Minkowski sum consists of carrying out a sweeping operation from a reference point of one operand at the boundary of the other operand [5].

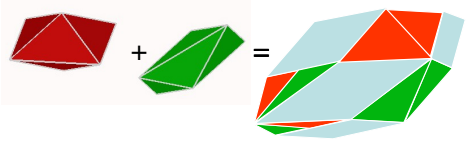

Fig. 6 Minkowski sum for two 3-polytopes

4 General Procedure for Tolerancing Analysis

Here we illustrate the general procedure for tolerancing analysis by simulating the functional condition FC expressed for the mechanism in figure 7. This mechanism consists of a rotor 1 and a stator 2. Surfaces 1,2 and 2,2 are in cylindrical pair contact according to $(B,\mathbf{x})$; surfaces 1,3 and 2,3 are in planar pair contact according to $(B,\mathbf{x})$. The contact graph is shown in figure 7 [7]. The functional condition FC requires that point A, the extremity of the axis of cylinder 1,1, is at a distance e from the axis of cylinder 2,1 in accordance with $\mathbf{y}$ such that:

$$CF : e\min \le e \le e\max \tag{9}$$

To simplify this example, we shall consider only variations in position and orientation of the surfaces in the $(B,\mathbf{x},\mathbf{y})$ plane.

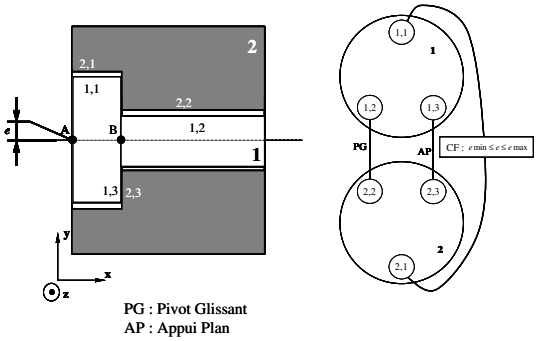

Fig. 7 Sample mechanism

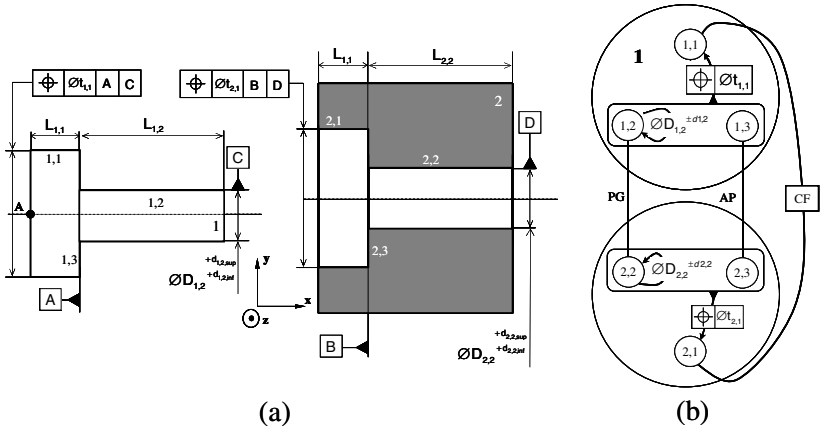

Fig. 8 ISO geometric specifications affecting FC

Figure 8a illustrates the ISO specifications for the rotor 1 and the stator 2 which are significant for the functional condition FC. Operations on the polytopes to characterize the relative position of surface 1,1 in relation to surface 2,1 at point A, are deduced from the relevant subgraph shown in figure 8b.

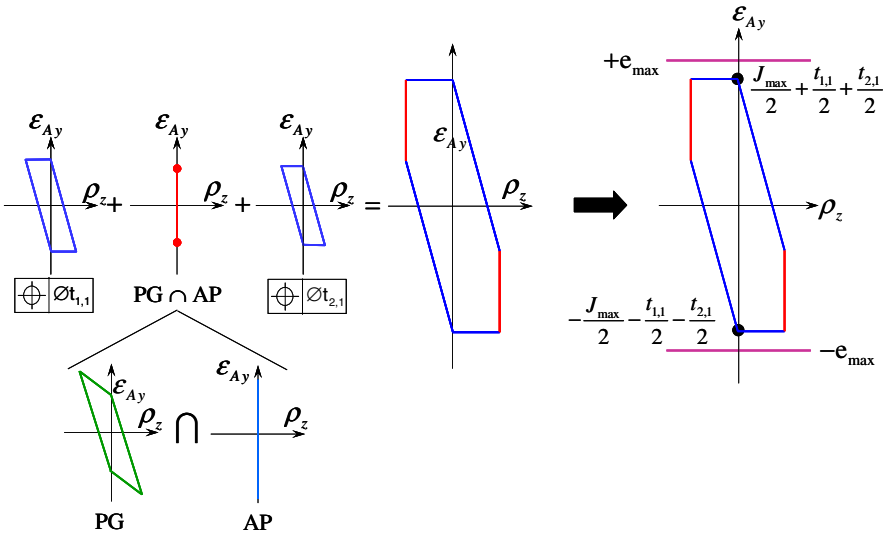

Fig. 9 Operations applied to simulate respect for functional condition FC

These operations correspond to two Minkowski sums applied to three operand polytopes. These operand polytopes correspond respectively to the specification for the location of the rotor 1, at the intersection of the contact polytopes of the cylindrical pair (PG) and the planar pair (AP) joints, and the specification for the location of the stator 2 (see figure 9).

The FC is respected by including the polytope characterizing the relative position of surfaces 1,1 and 2,1 inside the intersection of the two half-spaces that characterize the FC (see figure 9).

Equation (10) characterises respect for the FC as a function of the tolerances of the system by postulating: $J_{\max} = \left(D_{2,2} + d_{2,2}\right) - \left(D_{1,2} - d_{1,2}\right)$.

$$-\left(\frac{J_{\max}}{2} + \frac{t_{1,1}}{2} + \frac{t_{2,1}}{2}\right) \geq e\min \quad \text{and} \quad +\left(\frac{J_{\max}}{2} + \frac{t_{1,1}}{2} + \frac{t_{2,1}}{2}\right) \leq e\max \tag{10}$$

5 Conclusions and Future Developments

This article has shown how to model ISO geometric specifications for parts and contact specifications using 3D dimension chain operand polytopes. By applying Minkowski sums and intersections to the operand polytopes, the relative position

of any two surfaces of a mechanism can be determined. An application illustrates this procedure on a simple mechanism.

Operations on polytopes are currently being developed, paying particular attention not only to the basic aspects of polytopes but also to specific features inherent in geometric tolerancing. Fundamental concepts of algorithmic geometry must be adapted in order to gauge their effectiveness when applied to problems associated with tolerancing.

References

[1] Fleming, A.D.: Geometric relationships between toleranced features. Artificial Intelligence 37, 403–412 (1988)

[2] Rossignac, R., Requicha, A.A.G.: Offsetting operations in solid modelling. Computer Aided Geometric Design 3, 129–148 (1986)

[3] ISO1101, Geometrical Product Specifications (GPS), Geometrical tolerancing, Tolerances of form, orientation, location and run-out (2004)

[4] Teissandier, D., Delos, V., Couétard, Y.: Operations on polytopes: application to tolerance analysis. In: Proc. of 6th CIRP Seminar on Computer Aided Tolerancing, Enschede (Netherlands), pp. 425–433 (1999) ISBN 0-7923-5654-3

[5] Teissandier, D., Delos, V.: Algorithm to calculate the Minkowski sums of 3-polytopes based on normal fans. Computer-Aided Design 43, 1567–1576 (2011)

[6] Giordano, M., Duret, D.: Clearance Space and Deviation Space. In: Proc. of 3rd CIRP Seminar on Computer Aided Tolerancing, Cachan (France), pp. 179–196 (1993) ISBN 2-212-08779-9

[7] Ballu, A., Mathieu, L., Legoff, O.: Representation of Mechanical Assemblies and Specifications by Graphs. In: Geometric Tolerancing of Products, pp. 87–110. ISTE-WILEY (2010) ISBN 978-1-84821-118-6

The Cylinder of the Autoclave Charged with the Internal Pressure, Strengthen with a Strip Wound onto It, with Programmable Tension Realized by a Magnethoreological Structure

Marcin Bajkowski and Marek Radomski

Institut de Mechanique et Polygraphie, Ecole Polytechnique de Varsovie,
02-524 Varsovie 85 rue NarbuttaAdresse, Pologne
granada@pompy.pl, mr@wip.pw.edu.pl

Abstract. The article presents the analysis of stress distribution and the method of optimizing the construction of a cylinder where the objective function is the allowable number of working cycles. The strengthening of the cylinder with a strip was realized by programming the tension with a structure using "smart" magnethoreological fluid properties. The presented method of the strength calculation of the cylinder strengthened with the strip has been successfully used in practice during the process of constructing the isostatic presses. One example of its application is the cylinder of the isostatic press intended for hydro-extrusion of copper pipes under the pressure of 1500 MPa. The adaptation of programming the tension of the strengthening strip with the use of the structure based on MR fluids corresponds with today's market demands concerning constructions of this type.

Keywords: autoclave, strengthen, magnethoreologie.

1 Introduction

The technology of strengthening cylinders charged with internal pressure by stripes or wires wound onto them has been known for a long time. Several types of that technology have been used in the process of producing barrels and pressure vessels. However, the available literature is relatively scarce. The research on cylinders wrapped with steel strip was initiated in Badischen Anilin & Soda Fabrik in Ludwigshafen on Rhein. The technology developed then by Schierenbeck was patented in Germany in 1938. The work on this technology was also carried out in Poland by Z. Klębowski and W. Urbanowski in the '50 of the 20th century.

The '70 of the 20th century witnessed an increase in popularity of the strip strengthen cylinders, when this **t**ype of constructions began to be used in pressure chambers of isostatic presses. In the'80, further development of the technology can be observed, as well as practical use of it in cold extrusion dies (works by J. Grönbëk). A wide range of applications of the cylinders strengthened by steel stripes may be attributed to their advantages, which include, among others:

M. Haddar et al. (Eds.): *Design and Modeling of Mechanical Systems*, LNME, pp. 605–611.
DOI: 10.1007/978-3-642-37143-1_72

- the possibility of programming the stress distribution in the cylinder wall, and hence the possibility to optimize the construction considering its weight, fatigue strength, etc.
- increased operating safety due to greater strength and smaller probability of structural defects occurrence in a thin strip than in a thick-wall forging, as well as hindered crack propagation in the beam.

It is the first of the aforementioned advantages that encourages the undertaking of research on the optimization of the autoclave cylinder strengthened with a strip construction, when the objective function is the allowable number of working cycles.

The adaptation of programming the tension of the strengthening strip with the use of the structure based on MR fluids corresponds with today's market demands concerning constructions of this type.

2 Analysis of Stress Distribution

The construction of the cylinder strengthened with a strip with programmable tension realized by a magnethoreological structure is illustrated in Figure 1.

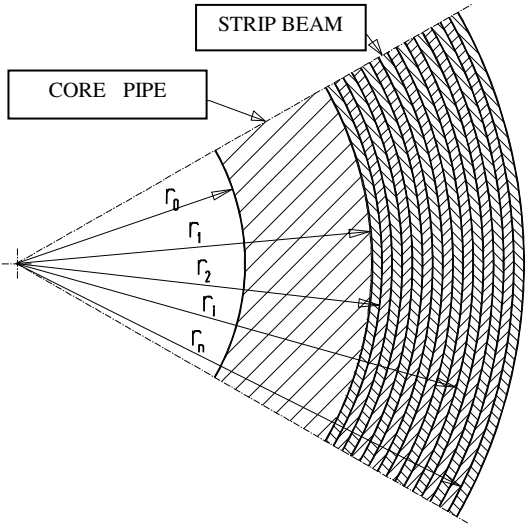

Fig. 1 Scheme of the autoclave cylinder strengthened with a strip

.

In the analysis of stress distribution the following assumption have been taken:

1. The stresses in the cylinder wall of the autoclave are superposition of the influence of the following factors:

a) the programmable beam of the strip in the process of winding, the characteristic value of which is the tensile stress of the strip occurring prior to its winding σ_T,
b) working pressure p_0, inside the cylinder of autoclave.

2. Ignored is the impact of:
   a) folding of the strip in the process of winding, the characteristic value of which is the deformation of extreme fibers of the strip σ_g,
   b) the temperature gradient, which occurs in the wall of the autoclave cylinder.

3. The materials of the core pipe of the autoclave and the strip have the same values of Young's modulus ε and the same number of Poisson ν.

4. As the strength criterion, the hypothesis H-M-H has been adopted.

5. The ratio of the thickness of the strip to the radius of the wrapped surface is smaller than 0,05.

6. Ignored has been the influence of winding the strip along the helical path, since with the small pitch, its elevation angle is close to zero (small ratio of the width of the strip to the radius of the wrapped surface).

In addition, the analysis was carried out under the assumption of plane state of stresses. With the presented assumptions there can be obtained the following formulas for the stresses in the radial and circumferential directions, the detailed derivation is in [6,7]:

for a core pipe with the internal radius r_0 and the external radius r_1 according to Lame's solutions:

$$\sigma_r(r) = \frac{p_0 - k_1^2 q}{k_1^2 - 1} - \frac{p_0 - q}{k_1^2 - 1}\frac{r_1^2}{r^2} \tag{1}$$

$$\sigma_t(r) = \frac{p_0 - k_1^2 q}{k_1^2 - 1} + \frac{p_0 - q}{k_1^2 - 1}\frac{r_1^2}{r^2} \tag{2}$$

where:

$k_1 = r_1/r_0$, and
q is the pressure on the outer surface of the pipe, caused by the pressure p_0 on the inner surface of the pipe and the tension of the wound strip;

for the area of the strip beam with the internal radius r_1 and the external radius r_n [6] :

$$\sigma_r(r) = -\frac{\sigma_T}{2}\left(1 - \frac{r_0^2}{r^2}\right)\ln\frac{k^2 - 1}{r^2/r_0^2 - 1} + \frac{p_0}{k^2 - 1}\left(1 - \frac{r_n^2}{r^2}\right) \tag{3}$$

$$\sigma_t(r) = \sigma_T\left[1-\frac{1}{2}\left(1+\frac{r_0^2}{r^2}\right)\ln\frac{k^2-1}{r^2/r_0^2-1}\right]+\frac{p_0}{k^2-1}\left(1+\frac{r_n^2}{r^2}\right) \tag{4}$$

where: $k=r_n/r_0$, and σ_T indicates stretching stress of the strip before winding it onto the pipe.

Taking into consideration the fatigue strength of the autoclave cylinder the optimal stress distribution is obtained when for any radius of a core pipe the following conditions are fulfilled: $\sigma_r(r)\leq 0$ and $\sigma_t(r)\leq 0$, which is the equivalent of:

$$\sigma_t(r=r_0)=0 \tag{5}$$

Taking into account the condition (5) in formula (2), we can determine the pressure q :

$$q=\frac{1+k_1^2}{2k_1^2}p_0 \tag{6}$$

Superposition of the radial stress on the external surface of the pipe permits to allow the required pressure p_1, which is caused by the strip beam, when the autoclave cylinder is not charged with any internal pressure, which means when $p_0=0$:

$$\sigma_{rwyp}=\sigma_{rw}+\sigma_{rp0} \tag{7}$$

where:

σ_{rwyp} - resultant stress caused by the pressure p_0 and p_1 ($\sigma_{rwyp}=-q$),
σ_{rw} - the stress caused solely by the pressure p_1 ($\sigma_{rw}=-p_1$),
σ_{rp0} - the stress caused solely by the pressure p_0, existing in the inside of a homogenous pipe with the internal radius r_0 and external radius r_n.

Therefore:

$$-q=-p_1+\frac{p_0}{k^2-1}\left(1-\frac{k^2}{k_1^2}\right) \tag{8}$$

The stress σ_T In the wound strip necessary to create the pressure p_1, can be determined after inserting (6) into (8) and comparing it with (3) and after including $r=r_1$ and $p_0=0$:

$$\sigma_T = p_0\frac{k^2+1}{k^2-1}\ln\frac{k_1^2-1}{k^2-1} \tag{9}$$

The computer analysis of stresses in the core pipe (1) and (2) and in the wound strip (3) and (4) for different values of stress σ_T determined according to (9) allowed to formulate the following conclusions:

1. The biggest substitute stress are observed in the external layer of the strengthening strip and equals:

- in the case when the cylinder of the autoclave is not charged with the working - pressure p_0 :

$$\sigma_{red} = \sigma_T \tag{10}$$

- in the case when the cylinder of the autoclave is charged with the working pressure p_0 :

$$\sigma_{red} = \sigma_T + \frac{2p_0}{k^2 - 1} \tag{11}$$

2. Load-factor of stability κ; defined as the ratio of the average stress σ_m to the stress amplitude σ_a in the working cycle of the autoclave cylinder (loading and unloading of the autoclave cylinder with the pressure p_0), increases with the increase in the reduced stress as a function of the radius in the area of beam, which makes the safety factor δ approximately constant .

3 Optimization of the Autoclave Construction

In the case of the analyzed autoclave cylinder the working cycle is characterized by the nonsymmetrical load. Assuming that the endurance test curve is approximated by the Soderberg curve, the formula of the permissible stress k_{rc} for the tensile-compression stress has the following form [8] :

$$k_{rc} = \frac{R_e(1+\kappa)}{\delta\left(\frac{R_e}{Z_{rc}}\frac{\beta}{\varepsilon} + \frac{\kappa}{\varepsilon_e}\right)} \tag{12}$$

where:

k_{rc} - permissible stress, which should be smaller than or equal the maximal stress in the cycle σ_{max};
R_e - yield point or yield strength in uniaxial tensile test;
κ - load-factor of stability defined as the ratio of the average stress σ_m to the stress amplitude σ_a in the working cycle of the autoclave cylinder;
Z_{rc} - fatigue limit for the oscillating cycle of stretching and compression (σ_m=0);
β - the notch sensitivity factor;
ε - the factor depending on the size of the object;
ε_e - factor depending on the size of the object for static loads.

Transforming the equation (12), we can examine how the load-factor of stability κ affects the value of the permissible stress k_{rc} in comparison to the yield point R_e :

$$x_{Re} = \frac{R_e}{k_{rc}} = \frac{\delta\left(R_e\beta/\varepsilon Z_{rc} + \kappa/\varepsilon_e\right)}{1+\kappa} \tag{13}$$

After inserting into (13) : δ=1,5; β=1; ε=1; ε_e=1, and approximate dependence between R_e and Z_{rc} with R_m, which for the materials used in the production of pressure vessels are, according to [9] as follows : R_e=0,85R_m and Z_{rc}=0,33R_m, the following graph, showing the course of the $x_{rc}(\kappa)$.

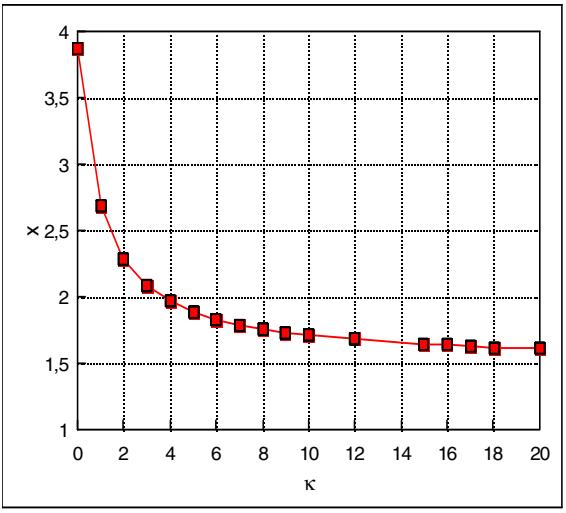

Fig. 2 The course of the $x_{rc}(\kappa)$ by (13)

This graph (Figure 2) reveals that with the increase in the load-factor of stability κ its influence on the value of the permissible stress k_{rc} decreases. In practice, it can be assumed that the increase of the value of this factor over 20 does not provide any substantial benefits.

For the analyzed autoclave cylinder the load-factor of stability κ, can be determined after taking into account (9), (10) and (11) (see [10]). The transformation of the formula received in this way leads to the following relationship for the ratio of the radiuses of the core pipe k_1 :

$$k_1 = \sqrt{1 + \frac{k^2 - 1}{\exp\left[\left(k^2 + 1\right)/\left(\kappa - 1\right)\right]}} \tag{14}$$

The ratio of the radiuses of the autoclave cylinder k can be determined as a function of load-factor of stability κ from the formulas (11) and (13) :

$$k = \sqrt{1 + \left(\kappa + 1\right)\frac{p_0 x_{\mathrm{Re}}}{R_e}} \tag{15}$$

Therefore, the equations (13), (14), (15) and (9) allow to preliminarily design the autoclave cylinder strengthened with the strip with the assumed safety factor δ while maintaining the programmable strip beam realized by the construction based on the characteristics of magnethoreological fluids.

4 Conclusion

The above presented method of calculating the endurance of autoclave cylinders strengthened with a strip with programmable tension of the beam was successfully used in practice in the production of isostatic presses. One example of its application is the cylinder of an isostatic press designed for hydro-extrusion of copper pipes under the pressure of 1500 MPa. The adaptation of programming the tension of the strengthening strip with the use of the structure based on MR fluids corresponds with today's market demands concerning constructions of this type.

References

[1] Klębowski, Z., Urbanowski, W.: Wytrzymałość płaszcza naczynia wysokociśnieniowego utworzonego z rury owiniętej wielowarstwowo taśm. Przegl. Mech. z.2, s.38–s.44 (1955)
[2] Klębowski, Z., Urbanowski, W.: Wytrzymałościowe obliczenie naczynia owijanego dla różnych wartości naciągu taśmy. Zesz. Nauk. Polit. Warszawskiej, Mechanika (5) (1958)
[3] Grönbëk, J.: Stripwinding of Tools for Bulk Metal Forming. Ph.D. Thesis, Technical Univ. of Denmark (1981)
[4] Grönbëk, J.: Stripwound Tools for Cold Forging. Wire World Int. 27 (November-December 1985)
[5] Grönbëk, J.: Design Layout of Stripwound Tools. Wire World Int. 28 (March-April 1986)
[6] Radomski, M.: Zagadnienia konstrukcji autoklawów wysokich ciśnień, maszynopis CBW PAN Unipress, Warszawa (1987)
[7] Łojkowski, W., Radomski, M.: Opracowanie założeń konstrukcji do prasowania izostatycznego na gorąco Si3N4 i SiC, sprawozdanie w ramach CPBR 2.4 cel A3.2.5 pkt 1. CBW PAN Unipress, Warszawa (1987)
[8] Kocańda, S., Szala, J.: Podstawy obliczeń zmęczeniowych. PWN, Warszawa (1985)
[9] Buchter, H.H.: Apparate und Armaturen der Chemischen Hochdrucktechnik. Springer, Berlin (1967)
[10] Łojkowski, W., Radomski, M., Rogoźnicki, W., Spólnicki, Z.: Wykonanie projektu autoklawu do prasowania izostatycznego na gorąco, punkt kontrolny nr 3, sprawozdanie w ramach CPBR 2.4. ZWC "Unipress" PAN, Warszawa (1988)

Application of the CSP Approach and the Interval Computation for the Optimal Sizing of a Compression Spring

Hassen Trabelsi[1,2], Pierre-Alain Yvars[1], Jamel Louati[2], and Mohamed Haddar[2]

[1] LISMMA, Institut Supérieur de Mécanique de Paris(SupMeca),
3 rue Fernand Hainaut 93407 Saint Ouen Cedex, France
pierre-alain.yvars@supmeca.fr
[2] U2MP, Ecole Nationale d'Ingénieurs de Sfax, Université de Sfax,
BP N 1173-3038, Sfax, Tunisie
mohamed.haddar@enis.rnu.tn

Abstract. In this present study a new design approach based on intervals calculation method and Constraint Satisfaction Problem technique «CSP approach» was discussed. It has been applied in the design of a compression spring implemented in vehicle suspension system. Compared to what is done in conventionally design, the design process proposed avoid to go through two stages of sizing (static and dynamic of design steps), since with the CSP, static and dynamic requirements can beings coupled in the same step of sizing. Also it avoids falling on the loop "design-simulate-back to the initial step in case of failure", as in the CSP all requirements imposed can be integrated from the beginning. Therefore the design parameters values of the compression spring generated by CSP verify all requirements imposed and the results simulation of the system behavior are always success and respect all constraints required. The general idea of the design process proposed consists to express the design variables by interval, integrate all different types of constraints imposed before simulation step and finally to solve the problem by CSP approach. The intervals generated by CSP represent the domains of possible values for the design variables of the system which satisfy the requirements imposed. The results obtained in this work affirmed that the suggested method is valid.

Keywords: Design, Interval computation, Constraint satisfaction problem, Compression spring, suspension system.

1 Introduction

The design activity of mechanical product systems is now immersed in a context of integrated and collaborative design. We are interested here to optimize the design approach [1-7] based on tools and methodologies using constraint satisfaction techniques [8-12]. Our approach is applied to optimize the sizing of a compression

M. Haddar et al. (Eds.): *Design and Modeling of Mechanical Systems*, LNME, pp. 613–625.
DOI: 10.1007/978-3-642-37143-1_73

spring [13-17]. Several software tools are available for sizing springs, in particular for compression springs. In most cases it is either software validation of a given size, or tools allowing very low variability specifications[13-16].

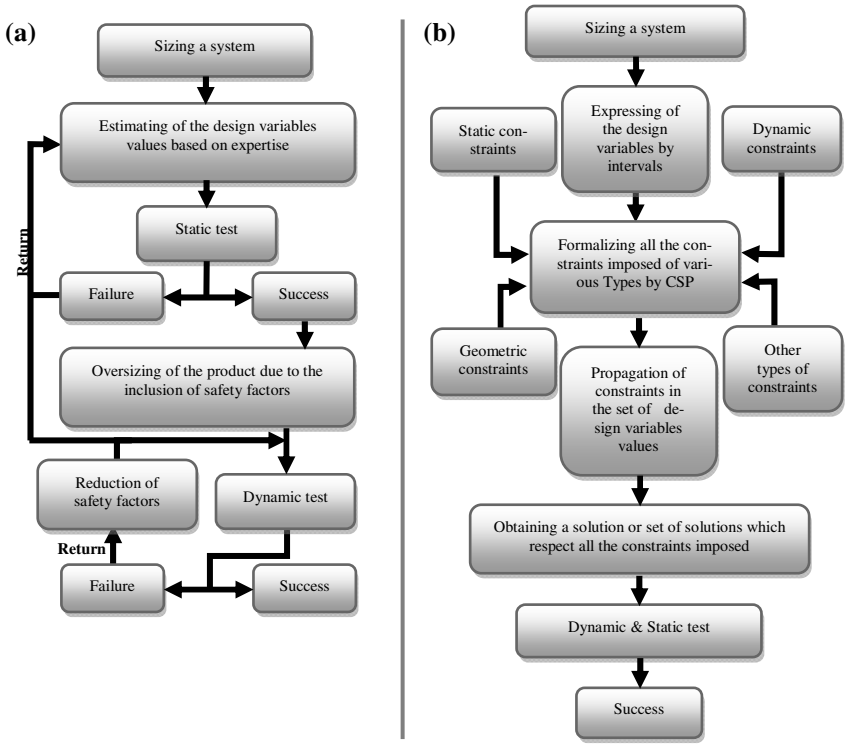

Fig. 1 Conventional process of product design vs design process based on CSP and Interval computation methods

In general the design process used in those software tools is alike the process described in Figure 1.a. In this approach we find commonly three main steps: The first one consists to estimate the design variables values based on static lows of calculation and expertise. The optimization of the choice of those values requires a lot of expertise. In the second step, the designer make static test and fixe the safety factors according the requirements imposed. The next step is to achieve the dynamic modeling then to make the dynamic test. So the designer is reflected in two situations. In the first case if the resulting behavior of the system has fulfilled the constraints imposed, the design parameters used in the simulation will be taken as a solution. In the second case if the system response does not satisfy the constraints imposed, then the designer has to change these parameters by taking into account the previous simulation and the same sizing steps must be repeated until

obtaining the optimal solution. This approach has the disadvantage that the connection between the static and dynamic design is missing and depend a lot of expertise. Also the passage through two steps of sizing (static and dynamic sizing) leads to the oversized of the spring especially when the designer took enormous safety factors after the static modeling. The designer has to go through several simulations to determine an optimal solution without being sure if the retained solution is the global optimal within the solution space. It comes from the fact that the number of simulations that can be done is limited by the time and cost constraints. To overcome in some extent those limits [16], we thought to couple the static and dynamic sizing in one step in the aim to optimize the choice of the safety factors, and to use intervals instead of fixed values in order to minimize the numbers of simulation and to obtain a set of solution instead a single solution. So to realize these goals the interval arithmetic of Moore (1966) [8] are used, and the CSP approach are integrated in a new design process described in the previous figure. In Figure 1.b we present a new design approach based on interval computation and CSP approach. This sizing process is made up of three main stages: the first step is to express design variables by intervals, here the choice of the design variables values does not require expertise but we cannot denial that expertise may reduce the calculation time. In the next step, the designer identifies the requirements that must be satisfied, express these requirements as constraints on the design variables. And then he implements all type of constraints in CSP code. Finally he spread those constraints in the intervals of design variables to frame the areas of parameter defining the product. Here the role of CSP approach comes. In fact the CSP eliminates all values of design variables that do not respect the requirements imposed. The sets of values that remain represent the set of solutions generated. This calculation was applied for the design of compression springs made by circular section rods, submitted under the action of static and dynamic forces. The paper begins with a review of the various steps of the conventional design process and the proposed new design process. Following this review, the technique used to optimize the sizing process was defined. In the third and the forth part all static and dynamic constraints of a compression spring integrated in vehicle suspension system have been described. The Section 5 was devoted to present in detail the application of the CSP approach for the sizing of the compression spring. The paper is end with a brief summary and conclusion.

2 CSP Approach

The constraint satisfaction problem [3, 6, 8-12] is a programming paradigm emerged in the 1980s for solving combinatorial problems of large sizes such as problems with planning and scheduling. This technique is extensively used to treat problems manipulating intervals and to solve mathematical problem that looks for states or objects satisfying a number of constraints. A CSP [6] is defined by a 3-tuple (X, D, C) such that:

- $X = \{x_1, x_2, x_3 \ldots, x_n\}$ is a finite set of variables which we call constraint variables with n being the integer number of variables in the problem to be solved.
- $D = \{d_1, d_2, d_3 \ldots, d_n\}$ is a finite set of variable value domains of X such that:

$$\forall\, i \in \{1,...,n\},\ x_i \in d_i \tag{1}$$

A domain should be a real interval or a set of integer values.

- $C = \{c_1, c_2, c_3 \ldots, c_p\}$ is a finite set of constraints, p being any integer number representing the number of constraints of the problem.

$$\forall\, i \in \{1,..., p\},\ \exists\, X_i \subseteq X\ /\ c_i(X_i) \tag{2}$$

Solve a CSP is the instantiation of each variable in X while addressing the whole constraints problem C, and at the same time satisfy all the constraints of the problem C. Here, a constraint is a relationship between one or more variables which limit values can take each of the variables simultaneously by the constraint. It can be any type of mathematical relationship (linear, quadratic, nonlinear, Boolean ...) covering the values of a set of variables. A solution is an assessment that satisfies all constraints. The constraint propagation is the operation which consists to apply recursively all contractors of a problem in a manner to make an exhaustive reduction of intervals. Here's an example to explain the functioning of the CSP:

Here the following continued CSP:

$$x \in [\text{-}10\ ;\ 10] \text{ and } y \in [\text{-}10\ ;\ 10]\text{; Constraints: } (C_1): y = \sin x\ ; (C_2): y = x^3; \tag{3}$$

The constraint propagation gives:

$$(C_1) \Rightarrow y \in [-10\ ;\ 10] \cap [-1\ ;\ 1],\ y \in [-1\ ;\ 1] \tag{4}$$

$$(C_2) \Rightarrow x \in [-10\ ;\ 10] \cap \sqrt[3]{[-1\ ;\ 1]},\ x \in [-1\ ;\ 1] \tag{5}$$

$$(C_1) \Rightarrow y \in [-10\ ;\ 10] \cap \sin[-1\ ;\ 1]\ \ y \in [-0.8414\ ;\ 0.8414] \tag{6}$$

$$(C_2) \Rightarrow x \in [-1\ ;\ 1] \cap \sqrt[3]{[-0.8414\ ;\ 0.8414]}\ \ x \in [-0.944\ ;\ 0.944] \tag{7}$$

The process stops and converges in the vicinity of these two intervals.

The CSP mechanisms were applied for the design of a compression spring. The purpose is to design the compression spring in any environment where it is placed. We chose the example of a compression spring integrated into a vehicle suspension. There is too many factors influence the calculation of the spring and its life, so preferably to stay in a simplified form which the spring sizing can be quickly.

3 Problem of Optimal Design of an Elastic Connection – Case of a Compression Spring

The springs are structural elements designed to maintain and store the energy and mechanical work based on the principle of the flexible deformation of the

material. They are among the components of the most heavily loaded machines and are usually used as: (Energy absorbing, Dampers in the anti-vibration protection, and Devices for control …).The purpose in this section is to determine the static design requirement of a compression spring [16-19] with round wire (Fig. 2). The design parameters [20-21] of the compression spring were classified into three types:

The variables characterizing the material: They are related to the material used. A material set, some variables are known (G, E, ρ). Others vary depending on the values of the geometric variables of the spring (Table 1).

The geometric variables: They (D_e, D_i, R, L_0, L_c, d, n, z and m) are used to define the geometry of a compression spring.

The operating variables: The spring is a component whose geometry varies significantly during use. It works between two configurations: one corresponding to the less compressed state, the second corresponding to the most compressed state. The variables defining the use of the spring are F_1, F_2, L_1, L_2 and S_h.

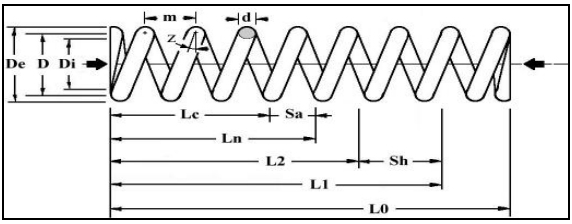

Fig. 2 Parameterizing a compression spring

3.1 Technological Relations between Design Variables

The different parameters defining the design of a compression spring are interrelated through a set of equations [21] which are detailed below.

$$D = D_e - d \quad (8) \qquad D_i = D - d \quad (9)$$

$$F_1 = R\left(L_0 - L_1\right) \quad (10) \qquad F_2 = R\left(L_0 - L_2\right) \quad (11)$$

$$F_{c\,theo} = R\left(L_0 - L_c\right) \quad (12) \qquad F_n = R\left(L_0 - L_n\right) \quad (13)$$

$$f_e = \frac{3560d}{nD^2}\sqrt{\frac{G}{\rho}} \quad (14) \qquad k = \frac{w + 0.5}{w - 0.75} \quad (15)$$

$$L_0 = m_u + \left(n_i + n_m\right)d \quad (16) \qquad L_c = d\left(n + n_i + n_m\right) \quad (17)$$

$$L_d = \pi D\left(2 + n_m + \frac{n}{\cos z}\right) \quad (18) \qquad L_n = d\left(n + n_i + n_m\right) + S_a \quad (19)$$

$$L_r = L_0 - \frac{\pi d^3 \tau_{zul}}{8DRk} \quad (20) \qquad M = \frac{\rho 10^{-3} L_d \pi d^2}{4} \quad (21)$$

$$m = \frac{L_0 - d\left(n_i + n_m\right)}{n} \quad (22) \qquad n = \frac{Gd^4}{8RD^3} \quad (23)$$

$$n_t = n + n_m + 2 \quad (24) \qquad R = \frac{Gd^4}{8nD^3} \quad (25)$$

$$s_h = L_1 - L_2 \quad (26) \qquad V_{0l0} = \frac{\pi D_e{}^2 L_0}{4000} \quad (27)$$

$$V_{0l2} = \frac{\pi D_e{}^2 L_2}{4000} \quad (28) \qquad W = 0.5\left(F_1 + F_2\right)\left(L_1 - L_2\right) \quad (29)$$

$$w = \frac{D}{d} \quad (30) \qquad \tan z = \frac{m}{\pi D} \quad (30)$$

$$\tau_{k2} = 8DR\left(L_0 - L_2\right)k / \left(\pi d^3\right) \quad (31) \qquad \tau_{kc}theo = 8DR\left(L_0 - L_c\right)k / \left(\pi d^3\right) \quad (32)$$

Also, the additional relationships such as inequalities, compatibility tables, and conditional relations were reformulate and taken into account in the design of the spring.

3.2 Choice of Compressing Spring Material

Table 1 Limits materials for compression springs

Material	***Steel DH***	***Stainless steel 302***
Limits of the manufacturer (mm)	$0.3 \le d \le 12$	$0.15 \le d \le 15$
G	81500	70000
E	206000	192000
R_m	2230 -355.94.Ln (*d*)	1919 - 255.86 Ln (*d*)
Maximum permissible stress τ_{zul} ***(% de*** R_m***)***	50	48
ρ	7.85	7.90

The type of material selected imposes values on certain parameters and a restriction on the bounds for other (Table 1). On the other hand, DIN [22] sets the application scope of these formulas for helical compression springs:

$$d \le 17 \quad (33)$$

$$D \le 200 \quad (34)$$

$$L_0 \le 630 \quad (35)$$

$$n \leq 2 \tag{36}$$

$$4 \leq w \leq 20 \tag{37}$$

The maximum static stress [23] is defined by the following equation:

$$\tau_{K2} < \tau_{Zul} \tag{38}$$

Almost all main constraint that defines the static behavior of the compression spring was included. In the next section the dynamic constraint related to the vehicle suspension system has been studied.

4 Vehicle Suspension

The suspension of vehicle is the set of elements designed to absorb shocks and ensure permanent adhesion of the wheels on the ground. The spring is one of his masterpieces. It is the element who sets the frequency of oscillation of the sprung mass and the amplitude of vertical movements. A dynamic study was made to obtain the dynamic requirements of the suspension system [24] to avoid its destruction in case of resonance. A simple model of the suspension system was treating in the following. Indeed, in Figure. 3 a suspension system of a quarter vehicles in vertical mode was exposed; it is composed by the chassis (m_2) which is connected to the wheel (m_1) by a linear spring of stiffness k_2, and in parallel with a linear viscous damper provided with a damper coefficient η. The wheel-ground contact is modeled by a linear spring of stiffness k_1 (which represents the stiffness of the tire and the rim).

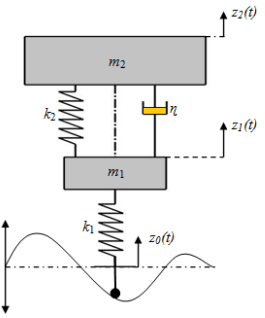

Fig. 3 Linear model of a vehicle suspension

The purpose here is to determine certain conditions under it the behavior of the system responds well and resist in case of disturbance and excitation phenomena. By applying the PFD and by the isolation of each mass, the motion equations are:

$$m_2.z_2^{\bullet\bullet} + \eta.(z_2^{\bullet} - z_1^{\bullet}) + k_2.(z_2 - z_1) = 0 \tag{39}$$

$$m_1.z_1^{\bullet\bullet} + k_1.(z_1 - z_0) = 0 \tag{40}$$

We apply the Laplace transform

$$\left(m_2.p^2+\eta.p+k_2\right)z_2-(\eta.p+k_2)z_1=0 \tag{41}$$

$$m_1.p^2.z_1+k_1.(z_1-z_0)=0\Leftrightarrow\left(m_1.p^2+k_1\right)z_1-k_1.z_0=0 \tag{42}$$

We obtain the following transfer functions:

$$z_2=\frac{\eta.p+k_2}{m_2.p^2+\eta.p+k_2}.z_1 \tag{43}$$

$$z_1=\frac{k_1}{m_1.p^2+k_1}.z_0 \tag{44}$$

The global transfer function is like the following:

$$F_t(p)=\frac{z_2}{z_0}=\frac{\left(\eta.p+k_2\right)k_1}{\left(m_2.p^2+\eta.p+k_2\right)\left(m_1.p^2+k_1\right)} \tag{45}$$

The magnitude of the transfer function is obtained simply by substituting «*p*» by «*jω*»

$$F_t(j\omega)=\frac{k_1.k_2+j.\omega.k_1.\eta}{\left(k_2-m_2.\omega^2\right)\left(k_1-m_1.\omega^2\right)+j\left(k_1-m_1.\omega^2\right).\omega\eta} \tag{46}$$

To study the stability of the suspension system return to determine the roots of the denominator (poles of the transfer function).

$$\begin{aligned}&\left(k_2-m_2.\omega^2\right)\left(k_1-m_1.\omega^2\right)+j\left(k_1-m_1.\omega^2\right).\omega\eta=0\\&\Leftrightarrow\left(k_2-m_2.\omega^2\right)\left(k_1-m_1.\omega^2\right)=0\ \text{ and }\left(k_1-m_1.\omega^2\right).\omega\eta=0\end{aligned} \tag{47}$$

So the roots of this equation are

$$\omega_{1,2}=\pm\sqrt{\frac{k_1}{m_1}} \tag{48}$$

Assume that x_{max} and x_{min} maximum and minimum displacement imposed in the requirement of the suspension system and $F(t)=F_0\sin\Omega t$ is the excitation force type sinusoidal. Then for the proper functioning of the suspension system and to avoid that the system oscillates until the destruction, it must respect the following constraints:

$$x_{\min}<x(t)<x_{\max}\quad\text{with: }|x|=\frac{F_0}{k_1}\sqrt{\frac{\left(k_1.k_2\right)^2+\left(\omega.k_1.\eta\right)^2}{\left[\left(k_2-m_2.\omega^2\right).\left(k_1-m_1.\omega^2\right)\right]^2+f_2}} \tag{49}$$

And the excitation frequency of the system is different from its natural frequency. This constraint can be expressed by the following mathematical relation:

$$\left|\Omega \pm \omega_{1,2}\right| > 0 \tag{50}$$

5 Constraint Formalization and Resolution by Interval

5.1 Definition of Design Variables and Implementation of Technological Relationships in CSP

Table 2 Constraints table

Material	*1*	*2*	*3*
E	206000	206000	192000
Coeff τ_{zul}	0.5	0.5	0.48
ρ	7.8510-6	7.8510-6	7.910-6
G	81500	81500	70000

Each design variables present in the nomenclature (view annex) of a compression spring will naturally be considered as a variable in our CSP which involve an initial range of values. They can be found in the column "initial value" in Table 4. All mathematical relations between design variables types static or dynamic described previously were implemented in CSP code using the ILOG solver library developed by IBM Company[25]. The table of valid combinations of material parameters is modeled as a table constraint. This is called global constraint representing the possible combinations of values for a set of variables constraints. Each row of a table is considered a constrained n-tuple of consistent values . For example, with Table 2, if the value of *G* must be less than 81500, lines 1 and 2 are automatically removed from the table by propagation. Only the line numbers 3 in the table remain constrained. The advantage of such constraint is to spread an event across the table. Generally all design variables of the compression spring are expressed by intervals as shown on Table 4. So it remains to propagate these constraints in the intervals of design variables to determine all possible solution of the spring sizing that satisfied the requirements imposed. All constants used in the calculation by CSP are presented in table 3.

Table 3 Constants

π	*3.14159265358979323846264338327 95*
f	0.01
m_1	25
m_2	500
k_1	200000
K_2	20000
σ	7000
Ω_e	10

5.2 Tables Implementation and Resolution by Interval

Table 4 Numerical results of the compression spring dimensions obtained by CSP

The Material parameters		
Variables	***Initials values***	***Results***
Material	{1, 2, 3}	1
G	{70000, 81500}	81500
E	{192000, 206000}	206000
R_m	[0 ; 2230]	1346.04958704917
ρ	{7.85e-06, 7.9e-06}	7.85e-06
τ_{zul}	[0, 10000]	673.024793524582
μ	[0 ; 1]	[0.263803680981595 ; 0.263803680981596]
Principal constructive parameters of the spring		
d	[0.15 ; 15]	11.9822373552438
D	[0 ; 200]	50
d_{min}	{0.15, 0.3}	0.3
d_{max}	{12, 15}	12
De	[0 ; 217]	61.9822373552438
Di	[0 ; 200]	38.0177626447563
L_0	[0 ; 630]	[300 ; 300.000003937176]
L_c	[0 ; 630]	239.644747104876
$R=k_2$	[0 ; 10000]	168
n	[2 ; 2e9]	10
n_i	[2 ; 2e9]	10
n_m	[2 ; 2e9]	0
m	[0, 315]	[18.0177626447563 ; 18.0177630992462]
z	[-π/2, π /2]	[0.114205511695686 ; 0.114205514809652]
Secondary Constructive parameters of the spring		
L_d	[0 ; +∞]	[1895.2554285776 ; 1895.25542914234]
Vol_0	[0 ; 24000]	[905.202268523842, 905.202282237354]
n_t	[4 ; 2e9]	12
w	[4 ; 20]	[4.17284339457009 ; 4.1728433945701]
f_e	[0 ; +∞]	173856.880778825
M	[0 ; +∞]	[1677.65680912714 ; 1677.65680962705]
Functional parameters of the spring		
F_1	[0 ; +∞]	[3.78982330493137 ; 3.79048475048376]
F_2	[0 ; +∞]	[4034.8317278943 ; 4034.83238933985]
L_1	[0 ; 630]	[299.977437188455 ; 299.977441118241]
L_2	[0 ; 630]	[275.983140547034 ; 275.98314447682]
S_h	[0 ; 630]	[23.9942927116351 ; 23.994300571207]
W	[0 ; +∞]	[48451.9411490427, 48451.941760955]
Vol_2	[0 ; 24000]	[832.735216325031, 832.735228182536]
Performance parameters (static rupture)		
L_r	[0 ; 630]	260.351097437785
F_c ***théo***	[0 ; +∞]	[10139.6824863809 ; 10139.6832499241]
k	[1 ; 2]	[1.3651934534846 ; 1.36519345348461]
τ_{kc}***théo***	[0 ; +∞]	[1024.50696832891 ; 1024.50704547681]
τ_{k2}	[0 ; +∞]	[8.15353582681597 ; 8.15353863417166]
Dynamic study		
Ω	[0 ; +∞]	18.3303027798234
F_0	[0 ; +∞]	4000
x_0	[0 ; +∞]	[0.0291543950465661 ; 0.0291543950465662]

The static and dynamic requirement imposed on the compression spring was coupled and implemented in CSP code according to the proposed design approach based on intervals and CSP showed in figure.2. Then after the step of constraint propagation, results in Table 4 are obtained. According to those results we notice: A drastic reduction in certain intervals and the solution for some parameters is an intervals (example: m, L_0, F_c *théo* …) and for the other parameters is just one value (example: d, d_{min}, f_e…). We notice also that the material 1 is the only who can meets the requirement imposed. So we could say that we succeed to size the compression spring with taking into account the entire static and dynamic requirement studied previously in the same time without the need to resizing the spring. This die to the fact that all the solutions generated and represented by all values (column «Results » in Table 5) of the parameters that define the possible dimensions of the spring satisfy the constraints imposed.

With the CSP the calculation was made by intervals which explain the accuracy of some values obtained. Despite the accuracy is an advantage in the CSP but it can be an inconvenient because for some parameters the value obtained is very precise witch lead to a problem in the manufacturing step (example: D_e).

We conclude, with the new design process based on CSP and interval computation we can couple more than one analysis for designing a system which provides to make an exact decision contrary to conventional design approach. Also we can determine a set of solution instead of one, thanks to mathematical operator by interval used in CSP.

6 Conclusion

From the previous study, the design optimization of a compression spring by the application of digital CSP was demonstrated. With the use of the CSP approach the static and dynamic sizing steps was coupled in the same step of sizing, also it is possible to take in account all type of constraint from the beginning a and avoid to resize the system. The optimization becomes easier since we use intervals instead of fixes values and we generate a set of solutions instead of single simulation. The computation time is interesting: in this study the simulation results are almost immediate on a computer type standard PC. To summarize, it can be claimed that the objectives and the advantages of the proposed design compared to the conventional design are verified and demonstrated. The method was applied for the design of one component of a linear system. Future research might focus on the validation of the capability of the proposed design based on CSP and intervals computation to size a full non linear system (structure + all components…) in an optimal way.

References

[1] Colton, J.S., Ouel-lette, M.P.: A form verification system for the conceptual design of complex mechanical systems. Engineering with Computers 10(1), 33–44 (1994)

[2] Hwang, H.Y., Jung, K.J., Kang, I.M., Kim, M.S., Park, S.I., Kim, J.H.: Multidisciplinary aircraft design and evaluation software integrating CAD, analysis, database, and optimization. Advances in Engineering Software 37(5), 312–326 (2006)

[3] Teorey, T.J., Yang, D., Fry, J.P.: A logical design methodology for relational databases using the extended entity relationship. ACM Comput. Surv. Model., 197–222 (1986)
[4] Philipp, G.: Component-oriented decomposition for multidisciplinary design optimization in building design. Advanced Engineering Informatics 23(1), 12–31 (2009)
[5] Song, C.Y., Lee, J., Choung, J.M.: Reliability-based design optimization of an FPSO riser support using moving least squares response surface meta-models. Ocean Engineering 38(2-3), 304–318 (2011)
[6] Yvars, P.A., Lafon, P., Zimmer, L.: Optimization of Mechanical System: Contribution of Constraint Satisfaction Method. In: Proc. of IEEE International Conference of Computers and Industrial Engineering, CIE 39, Troyes, pp. 1379–1384 (2009)
[7] Meyer, Y., Yvars, P.A.: Optimization of a passive structure for active vibration isolation: an interval-computation-and constraint-propagation-based approach. Engineering Optimization (2012), doi:10.1080/ 0305215X. 2011.652102
[8] Moore, R.E.: Interval analysis, pp. 85–103. Prentice Hall (1966)
[9] Montanari, U.: Networks of constraints: Fundamental properties and application to picture processing. Information Science (7), 95–132 (1974)
[10] Edmunds, R., Feldman, J.A., Hicks, B.J., Mullineux, G.: Constraint-based modelling and optimization to support the design of complex multi-domain engineering problems. Engineering with Computers 27(4), 319–336 (2011)
[11] Granvilliers, L., Monfroy, E., Benhamou, F.: Symbolic-Interval Cooperation in Constraint Programming. In: ISSAC 2001 Proceedings of the 2001 International Symposium on Symbolic and Algebraic Computation, pp. 150–166 (2001)
[12] Eldon, H.: Global optimization using interval analysis: The one-Dimensional Case. Journal of Optimization Theory and Application 29(4), 331–344 (2002)
[13] Kulkani, S.V., Balasubrahmanyam, K.: Optimal Design of Open Coiled Helical Springs. Journal of the Institution of Engineers (60), 7–14 (1979)
[14] Yokota, T., Taguchi, T., Gen, M.: A Solution Method for Optimal Weight Design Problem of Herical Spring Using Genetic Algorithms. Computers Ind. Engineering 33, 71–76 (1997)
[15] Deb, K., Goyal, M.: A Flexible Optimization Procedure for Mechanical Component Design Based on Genetic Adaptive Search. Journal of Mechanical Design, ASME (120), 162–164 (1998)
[16] Paredes, M., Sartor, M., Daidie, A.: Advanced assistance tool for optimal compression spring design. Engineering with Computers 21(2), 140–150 (2005)
[17] Paredes, M.: Methodology to build an assistance tool dedicated to preliminary design: application to compression springs. International Journal on Interactive Design and Manufacturing (IJIDeM) 3(4), 265–272 (2009)
[18] Spaes, J.: The Helical Springs, Applications and Calculations, Rpi – Technonathan (1989)
[19] Duchemin, M.: Metal springs - Constraints traction or compression. Engineer Technical B5431 (1985)
[20] Choné, J.: Automotive suspension springs steel. Engineer Technical BM5440 (2007)
[21] Paredes, M.: Development of tools to support the optimal design of elastic connections by spring. Doctoral thesis INSA Toulouse (2000)
[22] DIN 2008, DIN 2089-1, DIN 2089-2, Burggrafenstrate 6, postfach 11 07, 10787 Berlin, Germany (2088)

[23] Del Llano-Vizcaya, L., Rubio-Gonzalez, C., Mesmacque, G., Banderas-Hernandez, A.: Stress relief effect on fatigue and relaxation of compression springs. Materials & Design 28, 1130–1134 (2007)
[24] Suciu, C.V., Buma, S.: On the Structural Simplification, Compact and Light Design of a Vehicle Suspension, Achieved by Using a Colloidal Cylinder with a Dual Function of Absorber and Compression-Spring. In: Proceedings of the FISITA 2012 World Automotive Congress, Electrical Engineering, vol. 198, pp. 21–32 (2009)
[25] http://www-01.ibm.com/software/websphere/products/optimization/academic-initiative/

Annex

Nomenclature

D	mm	*Mean diameter of spiral turns*
De	mm	External diameter of spiral turns
Di	mm	Internal diameter of spiral turns
d	mm	Wire diameter
E	N/mm^2	Modulus of elasticity of the material
F_1	N	Spring force for the length L_1
F_2	N	Spring force for the length L_2
$F_c theo$	N	Theoretical force of the spring for L_c
f_e	Hz	Natural frequency of the spring
G	N/mm^2	Shear modulus
k	-	Coefficient of stress as a function of w
L_0	mm	Free length
L_1	mm	Spring length in charge, for force F_1
L_2	mm	Spring length in charge, for force F_2
L_c	mm	Block length
Ld	mm	Developed length
L_r	mm	Shorter length of eligible work (maximum stress)
M	g	Mass of the spring
m	mm	Step of the spring
n	-	Number of active spiral turns
n_i	-	Number of spiral turns for the extremities
n_m	-	Number of dead spiral turns
n_t	-	Total number of spiral turns
R	N/mm	Spring stiffness
R_m	N/mm^2	Minimum value of the tensile strength
S_h	mm	Course
Vol_0	cm^3	Volume envelope for L_0
Vol_2	cm^3	Volume envelope for L_2
W	Nmm	Work of the spring
w	-	Winding ratio
z	°	Winding angle
ρ	kg/dm^3	Density
τ_{k2}	N/mm^2	Constraint shear adjusted for L_2
τ_{zul}	N/mm^2	Maximal eligible constraint
v	-	Assise coefficient
μ	-	Poisson coefficient

Assembly Line Resource Assignment and Balancing Problem of Type 2

Triki Hager[1], Mellouli Ahmed[2], and Masmoudi Faouzi[1]

[1] University of Sfax, Sfax Engineering School, ENIS, U2MP, BP 1173, 3038, Sfax, Tunisia
hager_triki@yahoo.fr, faouzi.masmoudi@enis.rnu.tn
[2] University of Sousse, Sousse Engineering School, ENISo, U2MP, BP 1173, 3038, Sfax,Tunisia
ahmed.mellouli.eniso@gmail.com

Abstract. This paper presents a Multi-Objective Genetic Algorithm (MOGA) for **A**ssembly **L**ine **R**esource **A**ssignment and **B**alancing **P**roblem of type **2**(ALRABP-2). This approach minimizes both the cycle time and cost per hour of the line for a fixed number of stations to satisfy precedence constrains between tasks and compatibility constrains between resources. A modified version of Weighted Pareto-based Multi-Objective Genetic Algorithm (WPMOGA) is used to solve this problem. The effectiveness of the genetic approach has been evaluated through a set of instances randomly generated.

Keywords: balancing, assembly line, cycle time, Cost per hour, MOGA.

1 Introduction

The most difficult problem in organising mass production is usually how to get an optimal assignment of tasks to the stations so as to obtain the desired rate of production. The most famous of Assembly Line Balancing Problem (ALBP) family is the (SALB) Simple Assembly Line Balancing Problem (Baybars 1986, School 1999). Taking this problem as a base and adding other constraints and information (for example the assignment resource) to develop the ALBP, many researchers have recently proposed a more realistic framework. For example, Bukchin et al, (2000) have addressed the questions of selecting the equipment and assigning tasks to workstations to minimise total equipment costs for a pre-determined cycle time.

The problem of assignment resources to tasks can be defined as follows: For each task, we find a set of possible resource types characterised by their purchase cost, operation cost, cost of consumption and others costs, and speed of execution (processing time of the task). Many reviewers have spoken about the selection of equipments as a function of the purchase cost (Bukchin and Tzur 2000), operation cost (Hamta et al. 2011) etc. These costs of equipments or resources can be

M. Haddar et al. (Eds.): *Design and Modeling of Mechanical Systems*, LNME, pp. 627–634.
DOI: 10.1007/978-3-642-37143-1_74

grouped in a single cost, the so-called Cost per Hour *C/H*. It is calculated with the following equation (1):

$$C/H = \frac{Total\ \cos t\ of\ \ resource}{\text{Amortisation}\ \ period\ \ of\ \ resource} \tag{1}$$

On the other hand, there is the compatibility constraints between resources, which ensures that incompatible resources are allocated to different stations. For example, two resources shouldn't be allocated to the same station because their sizes exceed the available space.

This paper addresses a bi-criteria assembly line balancing: the so-called ALRABP-2 (Assembly Line Resource Assignment and Balancing Problem-2) which comprises two conflicting objective functions: minimising the cycle time *C* and minimising the resource total cost per hour *C/H* for a given number of stations *m,* considering both precedence and compatibility constraints between tasks and between resources respectively. Consequently, the accent put on:

- The allocation of the resource to each task, among the possible ones.
- The assignment of the tasks to the stations along the line such as: neither precedence nor compatibility constraint is violated.
- The total cost per hour of resources allocated to tasks is as less as possible.

The most real-life problems are optimisation problems which have multiple objectives to be considered simultaneously but the latter are usually conflicting. As a consequence, it is impossible to reach a single optimal solution for every objective. Instead, there exists the set of multiple satisfying solutions which is called "Pareto optimal" solution set (Coello et al. 2007).

In the literature, we have found a Modified Weighted Pareto-based Multi-Objective Genetic Algorithm (MWPMOGA) (Wang et al. 2012) which is characterized by the rapidity of convergence and the exactness of the search of solutions. This algorithm combines the quantitative weights with the concept of Pareto dominance to drive the MOGA towards relevant regions of the Pareto-optimal front (Wang et al. 2012). For these motives, we propose to use this powerful tool to solve an important variant of a bi-criteria decision of the assembly line problem (ARALBP-2). In this work, we propose a MWPMO to estimate the optimal Pareto front for the following two conflicting objectives: minimising the cycle time and the total cost per hour of resources. By this approach, the decision maker can select the better solution from the set of the non-dominated solutions generated by using other additional constraints such as the operator skills, budget reserved for the production line...

2 Multi-objective Genetic Algorithm (MOGA)

The MOGA used is based on MWPMOGA. The genetic process is as shown below:

2.1 Step1: Chromosome Coding

The length of the chromosome is equal to the number of tasks (n) and each gene of the chromosome defines a task (Sabuncuoglu et al. 2000). The second line of the chromosome represents the resources (R) assigned to tasks as indicated in fig. 1.

Number of task	1	8	2	9	3	4	5	6	10	7	11
Number of resource	1	2	4	3	4	2	3	4	6	5	7

Fig. 1 The chromosome

2.2 Step2: Generation of Initial Populations

The initial population cannot be randomly generated due to the presence of precedence constraints among the tasks. These constraints may lead to production of unfeasible solutions. In this paper, the method of Hamta et al, (2011) is applied to satisfy the precedence relations. One resource will be allocated to each task chromosome constructs. The choice of resources to perform a given task is made randomly from a given set of resource types that can perform this task.

2.3 Step3: Calculation of Objective Function Value

The cost per hour *C/H(k)*of chromosome *(k)* is the sum of cost per hours of all existing resources on the line. However, the cycle time *C(k)* of chromosome *(k)* is determined by the following procedure (Akpınar and MiracBayhan 2011):Tasks are assigned to workstations according to the task sequence in the chromosome as long as the predetermined cycle time is not exceeded (Akpınar and MiracBayhan 2011). Once the cycle time is exceeded at least for a model, or the compatible constraints of set of Incompatible Resource (*IR*) are not satisfied, a new station is opened for assignment and the procedure is repeated. We use the initial cycle time value which is lower bound (*LB*). It is calculated as follow:

$$LB = \max\left(\max_{1 \le i \le n} \{P_i\}, \frac{\sum_{i=1}^{n} P_i}{m} \right) \tag{2}$$

P_i= Processing time of task i by resource r which performs this task.

If the obtained number of station is higher than the given m, the cycle time C will be incremented by 1. The incrementing is repeated until the obtained number of station is equal to a given m. Fig2 illustrates the assignment of tasks to stations.

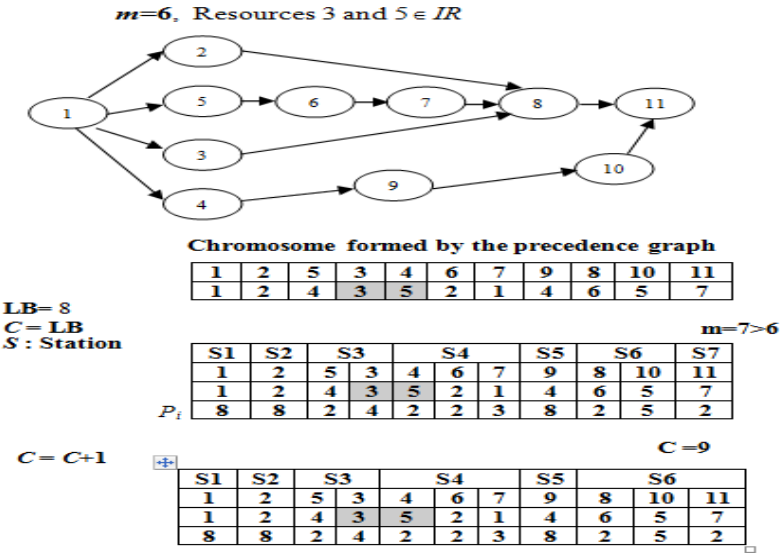

Fig. 2 The procedure of assignment of task to station

2.4 *Step4: Sorting1*

The population is sorted according to the non domination depending on objective function value of each individual (Deb et al. 2002).

2.5 *Step5: Calculation of Fitness Function Value*

The identical fitness function value for individuals at the same front will lead to identical reproduction probability for solutions at the same front (Wang et al. 2012). Fitness function is calculated as following Eq. (5)

$$F(k) = \frac{ML - L(k) + 1}{\sum_{\forall L(k)} [ML - L(k) + 1]} \tag{5}$$

F(k) () is the fitness function value of individual k
ML is the maximum front
L(k) is the front of individual k.

2.6 *Step6: Selection*

We can choose the ‘‘Roulette Wheel strategy (Holland 1975) as the selection strategy.

2.7 Step7: Crossover Operator

Two parent chromosomes will be crossover by a crossover operator. This operator crossover uses four crossover points. The four points which cut each parent into five parts (0-1, 1-2, 2-3, 3-4, 4-5), as shown in the Fig. 3, are generated randomly. This crossover operator works as follows:

- All elements from parts (0-1, 2-3, 4-5) of the first parent are copied to identical positions in the offspring 1string.
- All the elements within the parts (1-2, 3-4) of the first parent will undergo the following procedure
  - The tasks will be reordered according to the order of their appearance in the second parent vector to generate the remaining parts of offspring 1
  - The tasks will be performed by resources which belong to (P2)

The second offspring is generated by the same steps, with the parts of first parent reversed. (Apply the previous procedure in parts (0-1, 2-3, 4-5) and copying of parts (1-2, 3-4)).

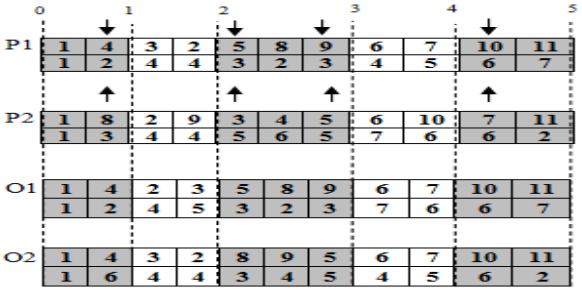

Fig. 3 Crossover operator

2.8 Step8: Mutation

The procedure consists in randomly choosing two positions within the solution string in the scramble mutation (Akpınar and MiracBayhan 2011) as shown in fig 4. These two positions have to swap places without violating the precedence constraints. Each task will be moved with her specific resource. We put fragement1 and fragement2 which are presented as follows:

- Fragment 1: all elements are placed before the first position.
- Fragment 2: all elements are placed after the first position.

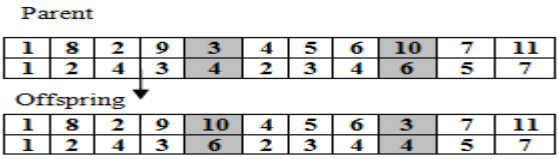

Fig. 4 Scramble mutation

With scramble mutation, only fragment1 of the parent is maintained. Fragment 2 is reconstructed randomly in a manner that ensures feasibility (Akpınar and MiracBayhan 2011).

2.9 Step9: Sorting2

Sorting of population is introduced by the following steps based on Pareto dominance definition: 1) Sorting1, 2) if there are more than 2 individuals that have the same non domination level (front), these individuals will be sorted again according to weighted value of objective function (Wang et al. 2012) as shown in Eq. (3) where $O(k)$ is the weighted value of objective function W_C and $W_{C/H}$ are weights with respect to each objective function, C_{min}, C_{max}, C/H_{min} and C/H_{max} represent the minimum and maximum values of each objective value. In order to compute the objective values with different units, normalisation method is employed. The sum of all weights is one (Wang et al. 2012) as shown in Eq(4)

$$o(k) = W_C\left(\frac{C(k)-C_{\min}}{C_{\max}-C_{\min}}\right)+W_{C/H}\left(\frac{C/H(k)-C/H_{\min}}{C/H_{\max}-C/H_{\min}}\right) \quad (3) \qquad W_C+W_{C/H}=1 \quad (4)$$

The remaining individuals will be sorted based on two previous steps. The procedure is repeated until the entire population is sorted.

2.10 Step10: Preservation Strategy for Optimal Solution

This strategy (Wang et al. 2012) is performed as the following procedure: the population of parents and offspring after evolution will be combined into one population. Then a combined population is sorted according to step9. Thereafter, we create the new population by choosing the first 50% of individuals in the combined population and rejecting the remaining 50% based on the levels.

2.11 Step11: New Generation

The population is created from previous step will become new population.

2.12 Step 12: Stopping Criteria

The stopping criterion is a predetermined number of iterations or generations. When the predetermined number of generation reaches, the MOGA will be stopped otherwise it returned to step 3 for determination the objective function value for the new population.

2.13 Step 13: Presentation of Optimal Solution (out put)

At the end of the proposed MOGA, we find the Pareto, which consists in the set of optimal solutions.

3 Results and Discussion

The effectiveness of the genetic approach has been evaluated through a set of instances randomly generated. After having these instances tested, we choose the value of GA parameter with more non-dominated solutions. The values obtained are crossover rate=100%, mutation rate=0.15, population size=100 and iteration number=100.

Figs. 5 and 6 illustrate some examples of obtained Pareto front (by the proposed MOGA). These figs show when the cycle time decreases, the cost per hour of resources rises and vice versa. Based on the proposed MOGA, we have found a big number of non-dominated solutions in a few minutes.

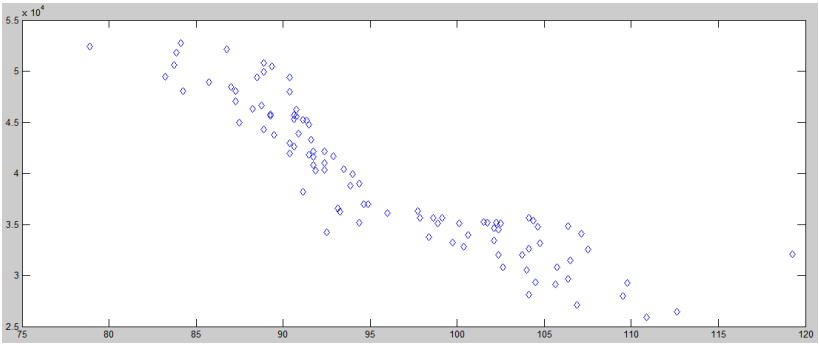

Fig. 5 The evolution of cost per hour in terms of cycle time (m=8, n=45, R=20)

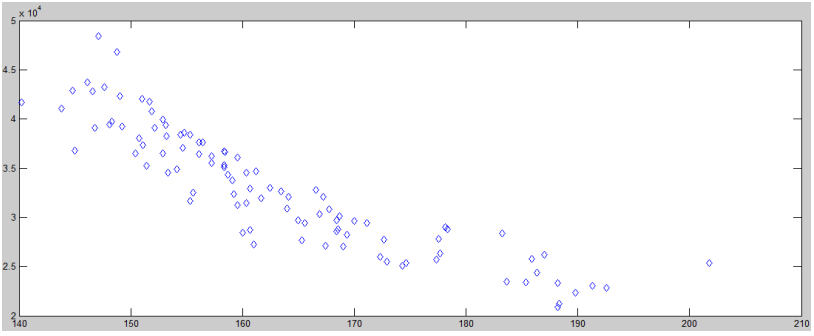

Fig. 6 The evolution of cost per hour in terms of cycle time (m=10, n=60, R=30)

4 Conclusion

This paper presents a new variant of assembly line balancing problem: the so called: ARALBP-2. The aim of this work is to minimise the cycle time *C* and the cost per hour *C/H* of resources simultaneously for a fixed number of stations *m.* To search good solution in a reasonable computing time, a modified version of

WPMOGA is developed to estimate the non dominated solutions. The effectiveness of the genetic approach has been evaluated through a set of instances randomly generated. In fact, we have found a big number of non dominated solutions for all instances. Then the decision maker has more opportunities to choose a solution that meets the best compromise between the two objectives.

References

Akpına, S., MiracBayhan, G.: A hybrid genetic algorithm for mixed model assembly line balancing problem with parallel workstations and zoning constraints. Eng. Appl. of Artificial Intel. 24, 449–457 (2011)

Baybars, I.: A survey of exact algorithms for the simple assembly line balancing problem. Manag. Sci. 21, 909–932 (1986)

Bukchin, J., Tzurm, M.: Design of flexible assembly line to minimize equipment cost. IIE Transact. 32, 585–598 (2000)

Coello, C.A.C., Aguirre, A.H., Zitzler, E.: Evolutionary multi-objective optimization. Eur. J. of Operat. Resea. 181, 1617–1619 (2007)

Deb, K., Agrawal, S., Pratap, A., Meyarivan, T.: A fast and elitist multiobjective genetic algorithm: NSGA-II. IEEE Transact. on Evolut. Comput. 6, 182–197 (2002)

Hamta, N., Fatemi Ghomi, S.M.T., Jolai, F., Bahalke, U.: Bi-criteria assembly line balancing by considering flexible operation times. Appl. Math. Model. 35, 5592–5608 (2011)

Holland, H.J.: Adaptation in natural and artificial systems. The University of Michigan Press, Ann Arbor (1975)

Sabuncuoglu, I., Erel, E., Tanyer, M.: Assembly line balancing using genetic algorithms. J. of Intel. Manufact. 11(3), 295–310 (2000)

Scholl, A.: Balancing and sequencing assembly lines, 2nd edn. Physica, Heidelberg (1999)

Wang, H.S., Che, Z.H., Chiang, C.J.: A hybrid genetic algorithm for multi-objective product plan selection problem with ASP and ALB. Exp. Syst. with Appl. 39, 5440–5450 (2012)

A Multi-objective Optimization for Multi-period Planning in Multi-item Cooperative Manufacturing Supply Chain

Wafa Ben Yahia[1,*], Naoufel Cheikhrouhou[2], Omar Ayadi[1], and Faouzi Masmoudi[1]

[1] Mechanics, Modelling and Production Research Unit,
Ecole Nationale d'Ingénieurs de Sfax (ENIS), Université de Sfax, Tunisia
Route de Sokra B.P.1173 - 3038, Sfax, Tunisia
wafa.benyahia@hotmail.fr, omar.ayadi@yahoo.fr,
faouzi.masmoudi@enis.rnu.tn

[2] Laboratory for Production Management and Processes,
Ecole Polytechnique Fédérale de Lausanne (EPFL), Switzerland
EPFL STI IGM LGPP, Station 9, CH-1015 Lausanne, Switzerland
naoufel.cheikhrouhou@epfl.ch

Abstract. Consumer goods are mainly manufactured in multiple steps often done by separate, independent production nodes, related to each others to form manufacturing supply chains (MSC). Mostly, each member of a supply chain optimizes his own local objective and accordingly, plans his operations (e.g., production, inventory, capacity planning). The purpose of this work is to improve the efficiency of production networks as a whole by developing a multi-objective optimization model for cooperative planning which aims at minimizing simultaneously the total production cost and the average inventory levels in a multi-period, multi-item environment. To solve this problem, we adopt an elitist non-dominated Sorting Genetic Algorithm (NSGA-II) to find optimal solutions. Several tests are developed to show the performance of the model.

Keywords: Multi-objective optimization model, cooperative planning, manufacturing supply chain, elitist genetic algorithm, NSGA-II.

1 Introduction

Planning operations across a supply chain (SC) is considered in the literature as a major component of supply chain management (SCM). Christopher (1998) defined the SC as "*the network of organizations that are involved, through upstream and downstream linkages, in the different processes and activities that produce value in the form of products and services in the eyes of the ultimate consumer*". In other words, a supply chain is composed of two organizations or more that are

* Corresponding author.

M. Haddar et al. (Eds.): *Design and Modeling of Mechanical Systems*, LNME, pp. 635–643.
DOI: 10.1007/978-3-642-37143-1_75

connected by materials, information and financial flows, in order to fulfil a customer request /demand. According to Stadtler (2009), planning is regarded as the activity to choose sequences and evaluate future activities for a specific decision making unit (e.g. a company).

Coordination in manufacturing supply chain (MSC) depends on the decision-making nature, which can be either centralized or decentralized. According to Holland (1995), developing a cooperative relationship is an effort to make the SC as a whole more competitive. Schneeweiss and Zimmer (2004) used hierarchical planning to coordinate between producers and suppliers in order to minimize the total cost for both partners and improve the performance of the supply chain. Dudek and Stadtler (2005, 2007), Seifert (2003), Chan and Zhang (2011) and Lyu et al. (2010) addressed the collaborative planning effectiveness in improving SC performances, by minimizing the total cost, in the case of a single objective. Kelle and Akbulut (2005) provided quantitative models that showed potential advantages of cooperation between enterprises in a SC context. They showed that cooperation minimizes the total SC cost. According to Rudberg (2004), centralized management offers better cost-effectiveness due to better coordination, possibilities of higher utilisation, and avoidance of duplication of activities. SCs coordinated on a centralized basis lead to better results, in regard to overall costs, than a SC coordinated on a decentralized basis (Axsater and Rosling, 1993; Lee and Billington, 1993; Haehling von Lanzenauer and Pilz-Glombik, 2002). Timpe and Kallrath (2000), Berning et al. (2002), and Kerschbaum et al. (2010) presented different models and algorithms for centralized master planning in chemical industry supply chains that show potential advantages of cooperation between partners in SCs. All these proposed models aimed at minimizing a total cost function which is composed of production costs, shipping costs and holding costs.

Very few works address cooperative SC from the mathematical programming perspective. Moreover, when they exist, the models are generally based on mono-objective optimization formulation. The purpose of this paper is to develop and to optimize a multi-objective model for optimal cooperative planning in MSCs in order to improve SC performances. The idea is to provide the external demand to the MSC partners in order to cooperate and generate a global optimal production plan to achieve a global goal. So the whole system is considered as one entity. To solve the multi-objective model, we adapt an elitist genetic algorithm based on the non-dominated Sorting Genetic Algorithm -II (NSGA-II).

The paper is organized as follows. In section 2 the cooperative scheme is described and formulated. The resolution methodology is presented in section 3, followed by the computational results in section 4. Finally, a conclusion and discussion of future research directions close the paper.

2 Problem Statement

This paper aims to develop an optimisation model that provides an optimal production plan for a multi-echelon manufacturing supply chain within a fixed time horizon with a finite capacity of personnel and machines. The complexity of the problem can be viewed not only from the multi-objective perspective but also in

the multi-level product complexity structure, where products are related to each others by successor and predecessor items according to the bill of materials and the sequences of operations. The demand for every finished product or semi-finished product is assumed to be known. The deadline to satisfy the customer's demand corresponds to the end of the planning horizon.

The following assumptions must be satisfied by the multi-objective optimisation problem:

- Several resources, with limited availabilities, can process several items.
- Raw materials are always available.
- Inventories at the initial period are void.
- Items can be only produced if all their predecessor components are available.
- Periodic external demand of each item is known.
- Overtime is allowed to extend fixed capacity availabilities.
- Backlogging is not allowed.
- The sequence of operations required to produce an item is fixed, and any alternative routing is prohibited.
- Inventory is calculated at the end of a time period.
- Setup time is neglected.
- External demand has to be fully met in time and quantity.

We consider a cooperative MSC, where different production sections or manufacturing plants cooperate together with the intention of generating a global optimal production plan. The manufacturing plant, which produces the final product requested by the customer, receives orders from its customers and transmits it to the other plants. Besides the inherent nature of MSC actors, these manufacturing plants share different information with each others, such as the production capacity and the production costs. Each manufacturing plant has eight working hours per day, but has different capacities and operations times. Products are transferred from a plant to the next one until reaching the last plant, where the finished products are stored to be delivered to the customer.

2.1 Planning Model

In this work, production plans are generated in order to simultaneously minimize the total production cost of the MSC and minimize the average inventory levels.

Consider the following notations:

Indexes

t	planning period, $t = 1,..., T$.
j	operation, $j = 1,. . . , J$.
r	resource, $r = 1,. . . , R$.

Set Indexes

T	set of planning periods
J	set of operations
R	set of resources
S_j	set of direct successors of operation j

Parameters

cv_j unit cost of operation j
cf_i setup cost of operation j
co_r unit cost of overtime (capacity expansion) for resource r
$D_{j,t}$ (external) demand for operation j in period t
$C_{r,t}$ Capacity of resource r in period t
$L_{j,t}$ Large constant
$a_{r,j}$ Unit requirement of resource r by operation j
$r_{j,k}$ Unit requirement of operation j by successor operation k (Depends of the manufacturing process)

Variables

C total production cost
I_{moy} average of inventory level for all operations
$x_{j,t}$ output level of operation j in period t (lot size)
$i_{j,t}$ inventory level of operation j at the end of period t
$y_{j,t}$ setup variable of operation j in period t
($y_{j,t}$=1 if product j is set up in period t; $y_{j,t}$=0 otherwise)
$o_{r,t}$ overtime of resource r in period t

Formulation

$$\text{Min } (C, I_{moy}) \tag{1}$$

$$\text{S.t} \quad C = \sum_{t=1}^{T} \sum_{j \in J} [\, (cv_j\, x_{j,t}) + (cf_j\, y_{j,t}) \,] + \sum_{t=1}^{T} \sum_{r \in R} co_r\, o_{r,t} \tag{2}$$

$$I_{moy} = \frac{1}{T} \sum_{t=1}^{T} \sum_{j \in J} i_{j,t} \tag{3}$$

$$i_{j,t-1} + x_{j,t} = D_{j,t} + \sum_{k \in Sj} r_{j,k}\, x_{k,t} + i_{j,t} \qquad \forall j \in J, \forall t \tag{4}$$

$$\sum_j a_{r,j}\, x_{j,t} \le C_{r,t} + o_{r,t} \qquad \forall r \in R, \forall t \tag{5}$$

$$x_{j,t} \le L_{j,t}\, y_{j,t} \qquad \forall j \in J, \forall t \tag{6}$$

$$x_{j,t} \ge 0, \; i_{j,t} \ge 0 \qquad \forall j \in J, \forall t \tag{7}$$

$$o_{r,t} \ge 0 \qquad \forall r \in R, \forall t \tag{8}$$

$$y_{j,t} \in \{0, 1\} \qquad \forall j \in J, \forall t \tag{9}$$

Equations (2) and (3) present the objective functions. The first criterion considered is the total production cost, which is the sum of the costs of operations, setup and overtime. The second objective considered is the average level of inventory with respect to the number of planning periods. The model output consists of the operations levels ($x_{j,t}$) (units of item j to be produced at period t), the inventory levels ($i_{j,t}$) (units of item j in the inventory at period t) for all operations considered, and the expansions of resource capacities through overtime ($o_{r,t}$) (overtime needed for resource r during the period t). The Equation (4) provides the constraints capturing the flow balance between output, inventory and consumption by external demand

or successor operations. In fact, demand has to be fulfilled at any stage and any time using the items either produced at that period or stored in previous periods. The constraints (5) represent the capacity restrictions in using the resources to produce the different items. This limitation in capacities is a representation of real-life MSC situation, where overtime can be used as a means to extend the capacity of a manufacturing plant at each period of time. Lot-sizing relationships and the choice of the items to be produced at each time period and at each plant location are expressed in (6). The constraints (7), (8) and (9) specify the domains of the different variables.

In this model, there are J*T equality constraints and (2*R*T+4*J*T) inequality constraints to satisfy.

3 Solving the Multi-objective Minimization Problem

3.1 Choice of a Resolution Method

There has been a growing interest in using genetic algorithms (GAs) to solve a variety of single as well as multi-objective problems in production and operations management. The main reason of using GAs is the high complexity of these problems that are combinatorial and NP hard (Gen and Cheng, 2000; Dimopoulos and Zalzala, 2000; Aytug et al., 2003; Altiparmak et al., 2006). Moreover, GAs show good performances in finding near-optimal solutions for multi-level lot sizing, which is the basic problem in the considered work (Dellaert and Jeunet 2000, Dellaert et al. 2000, Xie and Dong 2002, Jung et al. 2006). We adapt here a genetic algorithm to solve our problem which is NSGA-II, initially developed by Deb (2002). This algorithm is chosen for the many reasons, first the use of elitism, which shows its importance in the comparison made by Zitzler (2002) on a set of test problems. Second, according to Deb (2002), NSGA-II has a computational complexity equal to $O(MN^2)$ (M is the number of objectives and N is the population size), compared to other Multi-objective Evolutionary Algorithms (MOEAs), where the computational complexity is equal to $O(MN^3)$. In addition, NSGA-II is one of the contemporary MOEAs that demonstrated high performances and was successfully applied in various problems (Bekele and Nicklow, 2007; Hnaien et al., 2010). Finally, Deb (2002) shows the ability of NSGA-II to maintain a better spread of solutions and to converge better than two other elitist MOEAs: Pareto Archived Evolution Strategy (PAES) and Strength Pareto Evolutionary Algorithm (SPEA).

3.2 NSGA-II Description

Like any genetic algorithm, NSGA-II deals simultaneously with a set of possible solutions (called population), which allows finding Pareto fronts (set of optimal solutions with equal performances).

Initially, a random parent population P_0 is created. The population is sorted in order to provide different fronts composed of feasible solutions having the same

rank. In fact, individuals are ranked based on the concept of domination: an individual x_1 dominates another individual x_2 if the following two conditions are verified: first, all the objective functions of x_1 are not worse than *x2*, second, at least x_1 is strictly better than x_2 in one objective function. In addition, we define the parameter *crowding distance*, calculated for each individual. This parameter is calculated to estimate the density of solutions surrounding a particular individual in the population. The solution located in a lesser crowded region is selected. Selection is made using tournament between two individuals. From N parents, N new individuals (offspring) are generated in every generation by the use of the Simulated Binary Crossover (SBX) and Polynomial mutation (Deb et al., 2002 and 2001). Since elitism is introduced by comparing current population with previously found best non-dominated solutions.

4 Experimental Results

4.1 Tests Description

We consider a MSC constituted of two production plants. The demand for products is given and has to be fulfilled while facing finite capacities of personnel and machines (resources). Three types of items are produced: product 1 made from one unit of operation 1, product 2 made from one unit of operations 1 and 2, and product 3 made from one unit of operations 1, 2 and 3. The planning horizon has duration of two periods; the time period considered here is equal to one week with six working days and eight hours per day.

The genetic parameters shown in table 1 are selected after a sensitivity analysis.

Table 1 Genetic parameters

NSGA-II (parameters)	N, Population size	G, generation number	P_c, crossover probability	P_m, mutation probability	η_c, Crossover Index	η_m, Mutation Index	r, controlled elitism
Parameter values	150	1000	0.99	1/n (n=number of variables)	50	100	0.123

Two examples are studied, where the difference is the demand trend. As shown in table 2, in the first example, the external demand has an increasing pattern and in the second example it has a decreasing pattern.

Table 2 Customer demand features

	Example 1		Example 2	
Demand of	1st period	2nd period	1st period	2nd period
Product 1	20	140	90	15
Product 2	15	70	40	5
Product 3	10	70	50	5

4.2 Test Results

The development of NSGA-II and its implementation are done in C-language. The execution time does not exceed 15 minutes for all tests. The results of tests are shown in Table 3. At convergence, only one optimal solution is found and not a complete Pareto front as expected. This is due to the complexity of the problem and particularly to the flow equality constraint between MSC tiers.

For the first example the proposed solution is to produce in advance the needed products and to store them in the first period. As a consequence, there is no need to use overtime to meet the demand, since overtime is more expensive compared to nominal capacity. Besides, at the end of the planning period, the inventory level is null.

In the second example, the optimal solution provided by the algorithm is to produce the exact quantities needed to satisfy the demand of the first period. So it uses only the needed overtime in that period. Hence, there is no storage in that period. In the second period, the production quantities are higher than the demand. This explains the needs for storage of the second and the third operation at the end of the planning period, which can be considered as safety storage.

Table 3 Outputs of the developed test

	$y_{j,t}$	$x_{1,1}$	$x_{2,1}$	$x_{3,1}$	$x_{1,2}$	$x_{2,2}$	$x_{3,2}$	$o_{1,1}$	$o_{2,1}$	$o_{1,2}$	$o_{2,2}$	$i_{1,1}$	$i_{2,1}$	$i_{3,1}$	$i_{1,2}$	$i_{2,2}$	$i_{3,2}$	C	I_{moy}
Exp1	1	113	85	58	212	80	22	0	0	0	0	8	12	48	0	0	0	2669	34
Exp2	1	180	90	50	91	76	36	60	0	0	0	0	0	0	0	35	31	3130	33

5 Conclusion and Future Work

This paper proposes a cooperative planning framework for multi-tier and multi-item linear MSC. The developed bi-objective multi-period optimization model aims at minimizing the total production cost and the average inventory level, taking into account capacities and demand constraints. The proposed model shows different advantages over those discussed in the literature. In fact, compared to mono-objective models, this model considers not only costs but also inventory levels as a performance measure. Moreover, it does not consider the inventory as a cost, where an artificial extrapolation is needed, but as a performance to be minimized. The model is solved using NSGA-II coded with C language. In order to evaluate the proposed model, it can be compared to the mono-objective model developed by Dudek (2004).

For future work, we can add a constraint that forces the use of the full main capacity before using of overtime. Besides, a constraint on the storage capacity can be added to the model.

References

Altiparmak, F., Gen, M., Lin, L., Paksoy, T.: A genetic algorithm approach for multi-objective optimization of supply chain networks. Computers & Industrial Engineering 51(1), 196–215 (2006)

Axsater, S., Rosling, K.: Notes: installation vs. echelon stock policies for multilevel inventory control. Management Science 39(10), 1274–1280 (1993)

Aytug, H., Khouja, M., Vergara, F.E.: Use of genetic algorithms to solve production and operations management: a review. International Journal of Production Research 41(17), 3955–4009 (2003)

Bekele, E.G., Nicklow, J.W.: Multiobjective automatic calibration of SWAT using NSGA-II. Journal of Hydrology 341(3-4), 165–176 (2007)

Berning, G., Brandenburger, M., Gürsoy, K., Mehta, V., Tölle, F.J.: An integraed system solution for supply chain optimization in the chemical process industry. OR Spectrum 24(4), 371–402 (2002)

Chan, F.T.S., Chung, S.H.: A multi-criterion genetic algorithm for order distribution in a demand driven supply chain. International Journal of Computer Integrated Manufacturing 17(4), 339–351 (2004)

Chan, F.T.S., Zhang, T.: The impact of Collaborative Transportation Management on supply chain performance: A simulation approach. Expert Systems with Applications 38(3), 2319–2329 (2011)

Christopher, M.: Logistics and Supply Chain Management –Strategies for Reducing Cost and Improving Service, 2nd edn. Financial Times Pitman, London (1998)

Deb, K., Pratap, A., Agarwal, S., Meyarivan, T.: A Fast and Elitist Multiobjective Genetic Algorithm: NSGA-II. IEEE Transactions on Evolutionary Computation 6(2), 182–197 (2002)

Deb, K.: Multi-objective optimization using Evolutionary Algorithms. John Wiley & Sons Ltd., Singapore (2001)

Dellaert, N., Jeunet, J.: Solving large unconstrained multi-level lot-sizing problems using a hybrid genetic algorithm. International Journal of Production Research 38(5), 1083–1099 (2000)

Dellaert, N., Jeunet, J., Jonard, N.: A genetic algorithm to solve the general multi-level lot-sizing problems with time varying costs. International Journal of Production Research 68(5), 241–257 (2000)

Dimopoulos, C., Zalzala, A.M.S.: Recent developments in evolutionary computation for manufacturing optimization: problems, solutions and comparisons. IEEE Transactions on Evolutionary Computation 4(2), 93–113 (2000)

Dudek, G.: Collaborative planning in supply chains: a negotiation-based approach. Springer (2004)

Dudek, G., Stadtler, H.: Negotiations-based collaborative planning between supply chain partners. European Journal of Operational Research 163(3), 668–687 (2005)

Dudek, G., Stadtler, H.: Negotiation-based collaborative planning in divergent two-tier supply. International Journal of Production Research 45(2), 465–484 (2007)

Ertogral, K., Wu, S.D.: Auction-theoretic coordination of production planning in the supply chain. IIE Transactions 32(10), 931–940 (2000)

Haehling von Lanzenauer, C., Pilz-Glombik, K.: Coordinating supply chain decisions: an optimization model. OR Spectrum 24(1), 59–78 (2002)

Hnaien, F., Delorme, X., Dolgui, A.: Multi-objective optimization for inventory control in two-level assembly systems under uncertainty of lead times. Computers & Operations Research 37(11), 1835–1843 (2010)

Hollond, C.: Cooperative supply chain management: the impact of interorganizational information systems. The Journal of Strategic Information Systems 4(2), 117–133 (1995)

Jung, H., Song, I., Jeong, B.: Genetic algorithm-based integrated production planning considering manufacturing partners. The International Journal of Advanced Manufacturing Technology 32(5-6), 547–556 (2006)

Kelle, P., Akbulut, A.: The role of ERP tools in supply chain information sharing, cooperation, and cost optimization. International Journal of Production Economics 93-94, 41–52 (2005)

Lee, H.L., Billington, C.: Material management in decentralized supply chains. Operations Research 41(5), 835–847 (1993)

Lyu, J., Ding, J., Chen, P.S.: Coordinating replenishment mechanisms in supply chain: From the collaborative supplier and store-level retailer perspective. International Journal of Production Economics 123(1), 221–234 (2010)

Rudberg, M.: Linking competitive priorities and manufacturing networks: a manufacturing strategy perspective. Journal of Manufacturing Technology Management 6(1/2), 55–80 (2004)

Schneeweiss, C., Zimmer, K.: Hierarchical coordination mechanisms within the supply chain. European Journal of Operational Research 153(3), 687–703 (2004)

Seifert, D.: Collaborative planning, Forecasting, and Replenishment: how to create a supply chain advantage, 1st edn. AMACOM, New York (2003)

Stadtler, H.: A framework for collaborative planning and state-of-the-art. OR Spectrum 31(1), 5–30 (2009)

Timpe, C.H., Kallrath, J.: Optimal planning in large multisite production networks. European Journal of Operational Research 126(2), 422–435 (2000)

Xie, J., Dong, J.: Heuristic genetic algorithms for general capacitated lot sizing problems. Computers Mathematics with Applications 44(1-2), 263–276 (2002)

Zitzler, E., Laumanns, M., Thiele, L.: SPEA2: Improving the strength pareto evolutionary algorithm for multiobjective optimization. Computer Engineering 3242(103), 1–21 (2001)

A Feature-Based Methodology for Eco-designing Parts on Detail Phase

Raoudha Gaha[1], Abdelmajid Benamara[1], and Bernard Yannou[2]

[1] Laboratoire Genie Mecanique, Ecole Nationale d'Ingenieurs de Monastir, Universite de Monastir, Rue Ibn Aljazzar 5019 Monastir, Tunisia
raoudha.gaha@yahoo.fr, abdel.benamara@enim.rnu.tn
[2] Laboratoire Genie Industriel, Ecole Centra Paris, Grande Voie des Vignes 92290 Chatenay-Malabry, France
bernard.yannou@ecp.fr

Abstract. Today it becomes necessary for manufacturers to adopt Eco-design to guard their place in the market. Eco-designing products, is reducing their environmental impact in the early design stages throughout all stages of their life cycle (raw material extraction, manufacturing process, use, transport and end of life treatments). In the literature, many tools and methodologies were developed to simplify the environmental task to the designer by helping him reducing the environmental impact of his products. The most of these works are based in features-based modeling to extract data for realizing environmental evaluation also we found that this technology is essentially used in selecting a green machining process trough Computer Aided Process Planning (CAPP). In this paper we propose a methodology based on feature technology and on the integrations realized on CAD systems such CAD/CAL/CAPP and CAD/PLM to generate alternatives scenarios in order to choose the most ecological one till feature's selection. The environmental impact is calculated with Eco-Indicator method and shown to the designer as End-Points Indicators (Resources, Human Health, Eco-system damages) which are related to the designer's Degrees of Freedom (DoFs).

Keywords: Ecodesign, CAD, Feature technology, LCA, Scenarios.

1 Introduction

Today it becomes necessary for manufacturers to adopt Eco-design which is taking into account environmental impacts of products till design phase to guard their place in the market. In this way many researchers developed methodologies and concepts to integrate eco-design in the design process (Brezet 1997), (Janin 2000). Numerical tools are widespread used in companies, to develop products, such as Computer Aided Design (CAD) systems. Also, a large number of commercial software tools for the assessment of ecological impacts of technical systems are available such as life cycle assessment (LCA) tools. Ecological inventories of

M. Haddar et al. (Eds.): *Design and Modeling of Mechanical Systems*, LNME, pp. 645–654.
DOI: 10.1007/978-3-642-37143-1_76

processes are required to be assessed to expressive indicators. These LCA software like SimaPro, TEAM, GABi, etc. although they allow ecological assessment at a high level of detail, product data have to be introduced manually not digitally as it is required by modern product development. In the last decade, many researches were proposed to integrate ecological assessment into CAD systems. In these integrations, CAD models offered the data required by LCA (Otto 2003) and feature technology was the support for data migration (Germani 2004). All researches presented aim to data transfer between two different tools. Moreover, ecological assessment is realized on a final geometry of the part where changes on a complex component become difficult. Plus alternative scenarios assessed on final geometries which are realized on different files. Based on feature technology and works realized using this technology we propose an approach to assist designer step by step when he is choosing features. These features can involve different machining scenarios with different parameters such as selecting machine tool, cutting tool, energy consumption, etc. the offered data will allow assessing all scenarios proposed in order to present the most ecological one. In this paper, first we present a literature review of works based on CAD models for integrating CAD and LCA systems. Second, we present a state of the art of feature based modeling contribution in environmentally conscious production; also, we present the role of features based modeling in Computer Aided Process Planning (CAPP). Third, we describe our approach based on features to eco-assist designers early in the design process. Finally, we conclude about the use of feature technology in our methodology and its role in eco-design and we propose perspectives for this work.

2 Overview of Ecological Assessments on CAD Phase

To permit the integration of CAD systems and LCA software it is necessary to investigate all the product lifecycle stages from raw material, to manufacturing process, to use phase, to the end of life and transport between all phases and provide data existing in CAD models and introducing manually non-existent data in CAD system. LCA is an iterative methodology, which consists of four stages defined by standard organizations (ISO14040); goal and scope, life cycle inventories, life cycle analysis and result interpretation as shown in (figure 1).

A framework for structured data retrieval in LCA using feature technology was presented by Otto in the first time (-Otto et al 2001) and it was more developed in a second time where they introduced a framework for the integration of data from a product model and an LCI data base. Within the approach taken, efficient access to the LCI-relevant data is realized by utilizing feature technology as a means to relate with a sound semantics framework and a geometrical model linked to individual product properties (Otto 2003). Also, in (RYU et al. 2003) a feature-based CAD model is extended with explicit and implicit information in a useful manner to be adopted within an LCA system. All methods consider a CAD geometric representation as a collection of data to assess the environmental impact.

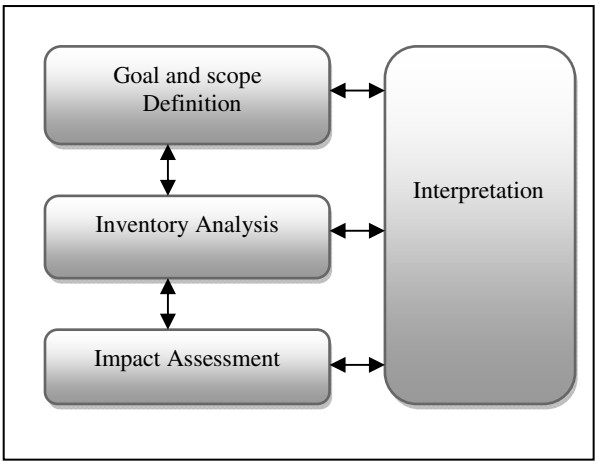

Fig. 1 LCA stages (ISO 14040)

Leibrecht thinks too, as previous works cited, that LCA tools are in discrepancy with a product modern development because each assessment require manual remodeling of product data and structural items (assemblies, parts, and features) (Figure 2) are not considered as they are used in CAD systems (Leibrecht 2005). Based on basic principles and rules that he defined for integrating ecological assessments into product models by extending directly the models and user interfaces of CAD systems, he proposed CAD-LCA integrated tool named "EcologiCAD" where no data transformation would be necessary. The lack of this solution is his dependant to the CAD system used in this work (ProEngineer).

(Marosky et al. 2007) presented the structure of an algorithm that allows a mutual transfer of data between CAD (SolidEge) and LCA tool (SimaPro), this transfer is based on extracting data from CAD model. The CAD model used is essentially a product model which consists of assemblies, sub assemblies, parts and features. In the same way (Capelli et al 2007) proposed a framework, in the first time, which is based on the analysis of the tree structure of CAD project composed of assemblies, subassemblies, parts and features (typical data representation of commercial software, i.e. ProE, SolidWork…), and consider that features, like manufacturing and production processes or geometric data, represent data associated with assembly model that can be stored in CAD files or in a specific database, if they are inserted manually by the user. In the second time this framework was developed on numerical tool "EcoCAD".

In our previous work (Gaha et al. 2011) we proposed a simple eco-design tool by integrating CAD and LCA. Geometric characteristics of a CAD model are analyzed to estimate their environmental influences during the whole phases of a product life cycle. The tool consists of a special geometric data base containing the impacts of all existing design technical solutions of a product, critical geometric features and forms concerning environmental impact are identified then

designers can select the optimal solution in terms of feasibility and ecology. However Chiu, M. C., & Chu, C. H. (2012) conclude in this work that, when required LCA data cannot be provided, the assessment result may be so far from reality, when the entire product lifecycle is concerned and designers can choose the worst alternative.

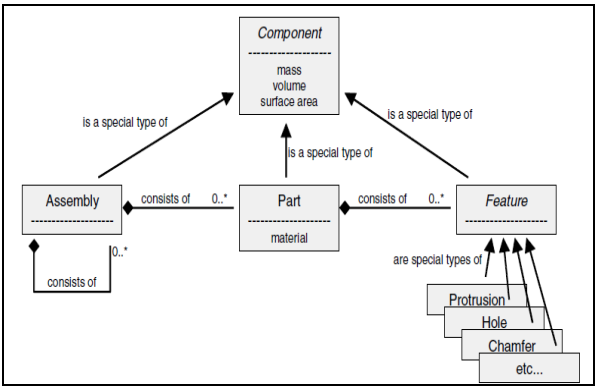

Fig. 2 Basic structure of product models (Leibrecht 2005)

As a conclusion, we found that the majority of proposed methodologies and tools for environmental assessment in CAD phase are used in post-modeling, i.e. evaluating final part. The problem appears with complex parts where modification becomes a hard act for the designer. Although its exists tools realizing environmental evaluation till features attribution such as "*SolidWorks Sustainability*", it has many disadvantages which are described in (Morbidoni 2012) essentially the LCA is practiced on material and waste streams cannot be included. This leads us to propose a methodology to help designer to see the environmental influence of his choices till the features attribution. We were based on works found in the literature which used features technology to evaluate the process planning from environmental point of view. This technology is also used in the last decade to generate automatically computer aided process plans (CAPP). In the following section we present a literature review of works using features technology for environmentally conscious process plans in the first step and we present different advantages reached by the CAD/CAM/CAPP integration using features technology.

3 Features Technology and Environmentally Conscious Process Planning: Overview

3.1 A Link between Features Based CAD/CAM/CAPP and LCI Data

Environmentally conscious production is a scope which prompted researchers to focus in, in order to provide eco-products into the market. (Sheng et al. 1995)

were interested in determining major issues for environmentally-conscious process planning. They presented comparative assessment of waste streams and computational complexity of evaluating multiple processing alternatives based on a scoring system which evaluates factors such as toxicity, carcinogenesis, irritation, flammability and reactivity. Complexity of processing alternatives is reduced through a feature-based approach, where the component environmental impact is decomposed into "micro" analyses of individual features and 'macro" analysis of feature interactions which are developed subsequently (Srinivasan, et al.1999a, 1999b).

The cradle-to-gate environmental performance can be estimated, combining geometrical and feature-based CAD/CAM data on the one hand, and life cycle inventory data related to materials and processes on the other hand (Nawata, et al. 2001) (Schmoeckel, 1999). Nawata proposed a study in which he suggests a linkage of LCI data to CAD/CAM data by application of feature modeling technology. The main objective of this study is to suggest a way to realize linkage LCI data to CAD/CAM data. LCA of mold products when machine tools are used has been conducted with varying coolant lubricants. Schmoeckel used the part information available from the CAD-system, e.g. volume, geometry and material to estimate parameters related to a selected forming process (cold extrusion) such as energy needed to form the part based on this information. The retrieve of the part information from the CAD-system was shown, as well as manner that the process is modeled in an object-oriented and obtaining of the LCI data from this process model.

An environmental analysis approach based on detailed process modeling which evaluates components from a functional design point of view was presented by (Bauer, D., and Sheng, P. 1999). (Xiaoming, X., and Yi, D. 2007), also used Feature technology to present a simplified and practical Life-Cycle Design System which analyzes life-cycle inventory (LCI) data and therefore generates life-cycle assessment (LCA) data. Then, the system can feed back the data to the design process in order to improve the machining plan.

3.2 Identifying Impactful Processes

For identifying impactful process from features attribution (Roman, F. 2005) developed a simple machine-centered environmental models and developed a framework for integrating models into various Computer Aided Process Planning (CAPP) approaches based on that previous attempts to conduct ECPP have focused on feature-based CAPP approaches only, they not considered the whole machine or auxiliary processes and they are focused on some machining operations, not the whole line or cleaning operations. In the same way (Zhao, F. et al. 2012) proposed a method which begins with an existing process plan, and then identifies impactful process steps, and associated design features, in terms of environmental impact. Alternative processes that can achieve these features are then considered to generate alternative process plans, which can be evaluated in terms of environmental and economic performance. The influence of different scenarios involved as the features attribution can generate was presented by (Taha, Z. et al. 2011). In their work they showed the effect of changing the product design parameters such as its dimensions, and basic features on the environmental impact of machining process in

terms of its energy consumption, waste produced and the chemicals and other consumables used up during the process, hence they selected the best possible product dimensions with the least environmental impact of the machining process by applying optimization methods using Genetic Algorithm and Goal Programming.

4 Proposed Approach

Our methodology consists on exploring features technology to evaluate the environmental impact of a product till the detail design phase. The influence of geometrical characteristics of a product on reducing the environmental impact was proved on previous works (Gaha et al. 2011, 2012) where the designer has a little field to act (figure 3) but an important environmental impact to reduce.

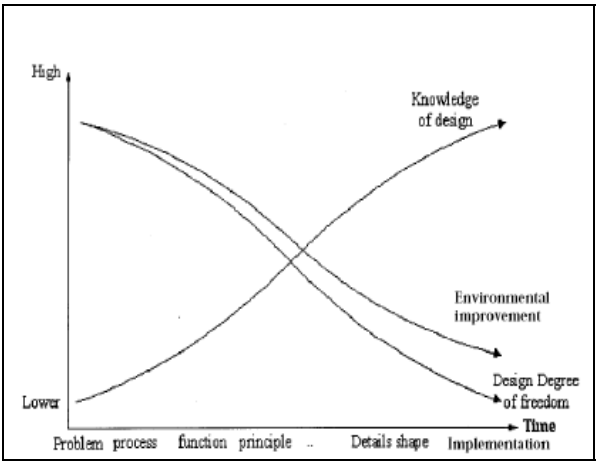

Fig. 3 Designer's acting field in the design process (Bhander et al. 2003)

From industrial designers asked and from our proper experience a number of 7 Degrees of Freedom (DoF) were determined: (Forms, Dimensions, Materials, Volumes, Production Process, Choice of « make or buy » (transport :doing locally if we have the technology) and Thermal or surface treatments). These DoFs can be used to conduct an Ecodesign since they represent feature's characteristics. The choice of DoFs implements a feature attribution. This feature is the core of a CAD model and the source of Input data to LCA systems or implemented environmental interface on CAD systems. Based on different previous works that explored feature technology on different fields, we propose an approach helping the designer to see the influence of the chosen parameters on environment.

This model consists on given designer the environmental impact of the current CAD model once a feature is attributed. The methodology presented is an algorithm that allow designer to see the environmental impact of each feature chosen in a real time and present him an optimal scenario in terms of ecology. It consists of seven steps (Figure 4).

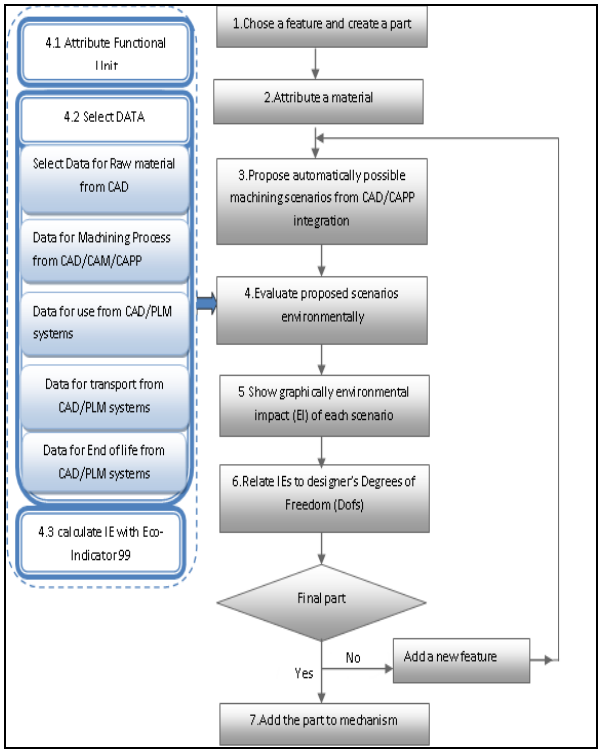

Fig. 4 Proposed methodology for Eco-designing products based on feature technology

- The first step is done by the designer in selecting a feature from CAD system data base.
- The second step, the designer attributes a material. In this step, the right material might be inexistent in CAD database, but exists in LCA database; in this case he has access to the two databases.
- The third step is based on CAD/CAM/CAPP systems. In this step there is a generation of different possible alternative machining scenarios.
- In the fourth step, environmental evaluation is realized the designer gives only the FU (we propose the FU related to the whole product) and the necessary data for realizing simple life cycle assessment (SLCA) is extracted automatically from CAD/CAM/CAPP systems and CAD/PLM systems. Data extraction is done throughout generic algorithm that we will describe in future works.
- The fifth step consists on showing graphically after an environmental impact calculus with Eco-Indicator99 method. The graphic representation is with End-points Impacts (Resources, Human Health and Eco-system damages) in a Single Score. This allows the non environmental expert designer to understand environmental impacts. This step is the final stage of a LCA according to ISO14040.

- The sixth step consists on relating IEs to DoFs with using a model of an Analytical Hierarchical Plan (AHP), which will be described also on future works.
- The seventh step is reached if the test of finishing designing part is positive; else the sixth first steps will be redone.

Here we proceed by practicing SLCA based on the work done by Morbidoni (Morbidoni 2011). The data base used is an open source self developed one.

5 Conclusion

The necessity of a simplified Ecodesign tool integrated on CAD systems is becoming more and more important in the aim to help designer to reduce the environmental impact of their products. So why, many tools were proposed in the last decade, that we presented some of them in the first section of this paper. We remarked that the majority of these tools are used to evaluate a final part which is composed of features. Today the feature technology, which is the core of detail design phase, can help generating alternative scenarios of CAPP some researchers worked on selecting the most ecological process. These works were described in the second section. From a literature review done, we proposed in the third section a feature-based methodology for eco-designing in the detail design phase by realizing an EI calculus based on Eco-Indicator 99 method from an LCI provided by integrations done on CAD systems such as CAM/CAPP and PLM. The advantages of this methodology are; first alternative scenarios proposed with their EI simply presented, second the relation with DoFs which represent the acting field of the designer and third the evaluation is done in a real time. In future works we will present the model of the generic algorithm of data extraction, and the model of process relating IEs to DoFs.

References

Journal Article

Leibrecht, S.: Fundamental Principles for CAD-based Ecological Assessments. International Journal of LCA 10(6), 436–444 (2005)

Marosky, N.: Challenges of data transfer between CAD and LCA software tools. In: 3rd International Conference on Life Cycle Management, University of Zurich at Irchel (August. 2007)

Sheng, P., Srinivasan, M., Kobayashi, S.: Multi-objective process planning in environmentally conscious manufacturing: a feature-based approach. CIRP Annals-Manufacturing Technology 44(1), 433–437 (1995)

Srinivasan, M., Sheng, P.: Feature-based process planning for environmentally conscious machining–Part 1: microplanning. Robotics and Computer-Integrated Manufacturing 15(3), 257–270 (1999a)

Srinivasan, M., Sheng, P.: Feature based process planning in environmentally conscious machining–Part 2: macroplanning. Robotics and Computer-Integrated Manufacturing 15(3), 271–281 (1999b)

Bauer, D., Sheng, P.: Integration of functional and environmental performance design decisions: A mechanical component case study. Journal of Industrial Ecology 3(4), 59–75 (1999)

Zhao, F., Murray, V.R., Ramani, K., Sutherland, J.W.: Toward the development of process plans with reduced environmental impacts. Frontiers of Mechanical Engineering 116 (2012)

Taha, Z., Sakundarini, N., Rashid, S.A.: Special Issue Section: Optimization of Product Design to Reduce Environmental Impact of Machining. IEMS 10(2), 128–133 (2011)

Bhander, G.S., Hauschild, M., McAloone, T.: Implementing Life Cycle Assessment in Product Development. Environment Progress 22(4), 255–267 (2003)

Chiu, M.C., Chu, C.H.: Review of sustainable product design from life cycle perspectives. International Journal of Precision Engineering and Manufacturing 13(7), 1259–1272 (2012)

Journal Article Only by DOI

Otto, H.E., Kimura, F., Mandorli, F., Germani, M.: Integration of CAD Models with LCA. In: Rengo, E.G. (ed.) Proceedings of the EcoDesign 2003, 3rd International Symposium on Environmentally Conscious Design and Inverse Manufacturing, pp. 155–162 (2003) ISBN 078038590X, doi:10.1109/VETECF.2003.240396

Otto, H.E., Kimura, F., Mandorli, F., Germani, M.: Integration of CAD Models with LCA. In: Rengo, E.G. (ed.) Proceedings of the EcoDesign 2003, 3rd International Symposium on Environmentally Conscious Design and Inverse Manufacturing, pp. 155–162 (2003) ISBN 078038590X, doi:10.1109/VETECF.2003.240396

Online Document (No DOI Available)

Otto, H.E., Mueller, K.G., Kimura, F.: A framework for structured data retrievalin LCA using feature technology. In: Proceedings of the EcoDesign 2001: Second International Symposium on Environmentally Conscious Desigsn and Inverse Manufacturing, pp. 250–255. IEEE (2001)

Ryu, J.Y., Kim, I., Kwon, E., Hur, T.: Simplified life cycle assessment for Ecodesign. In: Proceedings of Eco-design: Third International Symposium on Environmentally Conscious Design and Inverse Manufacturing, Tokyo, December 8-11, pp. 459–463 (2003)

Germani, M., Mandorli, F., Otto, H.E.: CAD - LCA data migration supported by-Feature technology and attributed structures. In: Proceedings of Global Conference on Sustainable Product Development and Life Cycle Engineering, pp. 379–384 (2004) ISBN 3937151214, 9783937151212

Capelli, F.: Integration of LCA and Eco-Design guideline in a virtual cad framework. In: The 13th Edition of the CIRP International Conference on Life Cycle Engineering, Leuven (2006)

Gaha, R., Benamara, A., Yannou, B.: Influence of geometrical characteristics on eco-designed products. In: Proc. of the Int. Conf. on Innovation Methods in Product Design, pp. 242–247 (2011)

Nawata, S., Aoyama, T.: Life-cycle design system for machined parts-linkage of LCI data to CAD/CAM data. In: Proceedings EcoDesign 2001: Second International Symposium on Environmentally Conscious Design and Inverse Manufacturing, pp. 299–302. IEEE (2001)

Schmoeckel, D., von Schlotheim, G.F., Wansel, A.: Evaluation of the cold extrusion production process. In: Proceedings of the EcoDesign 1999: First International Symposium on Environmentally Conscious Design and Inverse Manufacturing, pp. 414–419. IEEE (February 1999)

Xiaoming, X., Yi, D.: A Simplified and Practical Life-Cycle Design System Based on Feature-Based Modeling. In: Chinese Control Conference, CCC 2007, pp. 166–169. IEEE (July 2007) (Chinese)

Gaha, R., Benamara, A., Yannou, B.: Eco-conception d'un mitigeur de lavabo lors de la modélisation géométrique. In: Proceedings of Deuxième Congrés Tunisien de Mécanique, COTUME 2012 (Mars 2012)

Morbidoni, A., Favi, C., Germani, M.: CAD-Integrated LCA Tool: Comparison with dedicated LCA Software and Guidelines for the Improvement. Glocalized Solutions for Sustainability in Manufacturing, 569–574 (2011)

Dissertation

Janin, M.: Démarche d'éco-conception en entreprise, un enjeu: construire la coherence entre outils et processus. Phd Thesis Ensam (2000)

Brezet, J.C.: Dynamics in Ecodesign practice. UNEP Industry and Environment 20(1-2), 21–24 (1997)

Morbidoni, A.: The ecodesign issue: proposal for a new approach, methodology and tools. Phd Thesis Università Politecnica delle Marche Italia (2012)

Roman, F.: Research Overview to SRL. Environmentally Conscious Machine-based Computer Aided Process Planning. G. W. Woodruff School of Mechanical Engineering (July 2005)

The Eco-Indicator 99 – A damage oriented method for Life Cycle Assessment Impact, Methodology Report

Mates Updating of Rigid and Fully Constrained Assembly with Defects

Tlija Mehdi, Louhichi Borhen, and Abdelmajid Benamara

Mechanical Engineering Laboratory, National Engineering School of Monastir, Tunisia Av. Ibn Eljazzar, 5019 Monastir, Tunisia
tlija.mehdi@gmail.com

Abstract. Improving the numerical model requires consideration of tolerances in the CAD model. Previous research works have contributed to obtaining components on the configurations with defects from the dimensional and geometric tolerances. Nevertheless, in bottom-up design process, the assembly regeneration, with these components with defects, requires redefining assembly mates which are initially assigned to nominal assembly. Thus, this paper presents a new approach to defining realistic assembly mates in the case of rigid assembly fully constrained with joints without clearance. This method is validated though components with planar and cylindrical face.

Keywords: Assembly mates, dimensional and geometrical tolerances, CAD modeling, assembly with defects.

1 Introduction

CAD software is a virtual environment for mechanical assemblies design. These models have a digital assistance to the designer during the product life cycle: kinematic and dynamic analysis, mounting and dismounting sequences of assembly, finite elements calculation, etc. These representations are on ideal models. Indeed, the geometric and dimensional tolerances are formally represented. In other words, tolerances stack-up does not affect product geometry. Then, CAD model without tolerances affects robustness of obtained results (Tsai 2007).

In previous work we have developed models that take into account the dimensional and geometric tolerances (form defects are neglected compared to defects position and orientation) in the digital model. Indeed, realistic configurations assemblies are deducted from tolerances assigned to components. The tolerances interpretation can be performed with two hypotheses: The first hypothesis suggests that worst cases assemblies are deduced from worst cases components (Louhichi et al. 2009). While the second hypothesis calls in question the first one. The second hypothesis asserts that worst assemblies can be obtained by random components (Tlija et al. 2011). In addition, the approach allows simulating the random aspect of mounting of parts produced. In this paper, the second hypothesis is adopted.

M. Haddar et al. (Eds.): *Design and Modeling of Mechanical Systems*, LNME, pp. 655–662.
DOI: 10.1007/978-3-642-37143-1_77

2 Components with Defects

The model comprises two main sub-algorithms for the detection of random components.

2.1 Dimensional Tolerances

The first sub-algorithm takes into account the dimensional tolerances. The determination of components with defects requires research relationships between dimensions. Indeed, it is necessary to detect the n driving dimensions D_i, with VD_i values, that control the driven dimension R_j (with VR_j value). Let, therefore, the influence coefficient λ_{ij}. λ_{ij} is the ratio between the variation of the driven dimension ΔVR_j and the variation of the driving dimension ΔVD_i ($\lambda_{ij} = \Delta VD_i/\Delta VR_j$). At this stage, the problem focuses on the determination of the influence coefficient:

- Identifying relationships between dimensions by the numerical perturbation method of the model (Tlija et al. 2011): The method is based on identifying the impact of numerical change of dimension value on the CAD model. A sub-algorithm to detect the driving dimensions D_i that control the driven dimension *Rj* has been developed (figure 1 (a)).
- Determination of influence coefficient between dimensions by using the Dimensions Vectorization Model (DVM) and connected graphs technology (figure 1(b)): The automatic identification of relationships between all component dimensions is done by using a technique that is based on connected graphs (Ballu and Mathieu 1999). Indeed, these graphs are used to generate three-dimensional dimension chains. Then, the quantification of the influence between dimensions is achieved by vectorial modelling of dimensions. This method consists in representing dimensions by vectors. Then, the projection of these vectors on the reference system basis of the part allows determining the influence coefficient between dimensions.

Thus, *n* driving dimensions D_i,witch control each driven dimension RD_j, are identified. The tolerance interval t_j is discretized by a coefficient *k* (chosen by the designer according to the desired fineness). Distribution of tolerances on driving dimensions is carried out according the equation (1). VD_{ki} is the new value of D_i. t_{kj} is the k^{th} tolerance value obtained from the discretization and T_{ki} is the tolerance assigned to D_i obtained by the relation (2).

$$\text{If } \lambda_{ij} > 0 \text{ then } VD_{ki} = VD_i + T_{ki}; \text{ Else If } \lambda_{ij} < 0 \text{ then } VD_{ki} = VD_i - T_{ki}. \quad (1)$$

$$T_{ki} = |\lambda_{ij}| \, . t_{kj}/n \quad (2)$$

Components reconstruction with the new values of dimensions allows finding all configurations with defects that take into considerations dimensional tolerances.

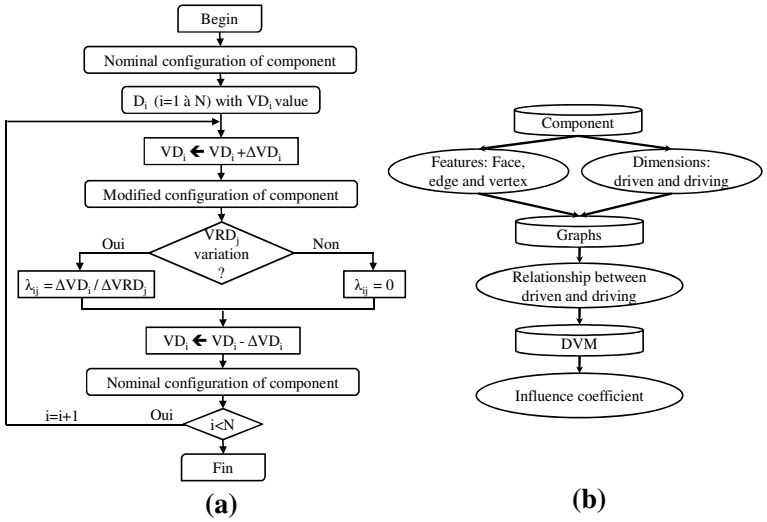

Fig. 1 Sub- algorithm for determination λ_{ij} (a) by numerical perturbation. (b) by DVM.

2.2 Geometrical Tolerances

A second sub-algorithm allows taking account geometrical tolerances. Indeed, the discretization of the tolerance zone is used to define different target configurations with defects. Then, the deviation between these two configurations (nominal configuration and configuration with defects) is defined by the deviation torsor. This tool is derived from the approach of tolerancing by SDT (small displacements torsors) (Petit and Samper 2004). Indeed, the deviation torsor of geometric element allows defining the degrees of freedom of the toleranced element. In the proposed model, the setting of the deviation between the nominal element and the element with defects is made by analogy to the parameters defined by the STD. Thus, in the numerical model, obtaining configurations with defects is achieved by the movement of the nominal element according to parameters defined above (Tlija et al. 2011). In addition, the model takes into account the requirement of maximum material (and least material) and requirement of the priority of reference systems in the CAD model. Indeed, for founding configurations with defects, the model repositions the toleranced element relative to a realistic reference. Besides, the interdependence of geometric and dimensional tolerance in the case of modifier state is respected.

3 Assembly Mates Updating

Relative positions of components are modelled in CAD software by mates. In addition, these mates must model joints between parts and satisfy functional requirements for proper functioning of the system. The positioning can be done sequentially or simultaneously. The technique of mounting components

simultaneously is insufficient in some cases (Sodhi and Turner 1994). Indeed, the solution, founded by using this technique, can be not optimal as the assembly of four bars of a picture frame. In CAD software, a primitive relations or high-level primitive relations are used for specifying assembly information. Then, the aggregation of assembly information in assembly models can be made by relational or hierarchical models. In this paper, sequential assembly technique is adopted in the proposed study.

In the numerical model, the allocation of assembly mates leads to three types of assembly: under-constrained, fully constrained and over-constrained. The first, under-constrained assembly is a system that has at least one degree of freedom. The second type of assembly does not have any relative movement between components. The last type of assembly is obtained when the assembly mates are conflicting and cannot be satisfied. Indeed, the geometric modeller cannot found a solution for positioning components with required mates. In this paper, a method of mates updating of fully constrained rigid assemblies, which joints are with contact and without clearance, is presented. In assembly with defects models, mates updating is realized by defining realistic primitive joints. These realistic joints are obtained by using coincidence mates between MGREs (Minimum Geometrical Reference Elements).

3.1 Case of Planar Faces

The mounting of nominal parts A and B (figure 2(a)) is to be performed sequentially in the following order: First, Fa2 is positioned on Fb2. Besides, maximum contact between Fa1 and Fb1 is ensured. Finally, maximum contact between Fa3 face and Fb3 is realised. These mounting requirements can be modelled, in a nominal configuration of the assembly, by three assembly mates L1, L2 and L3 (L1: Co (Fa2 & Fb2) (Coincidence between Fa2 and Fb2), L2: Co (Fa2 & Fb2) and L3: Co (Fa3 & Fb3)). In the case of a nominal assembly, the modelling of these three constraints allows to obtain a fully constrained assembly. However, this modelling is not possible in the case of configuration with defects and resulted in an over-constrained assembly.

In figure 2(a), the part B1 is one of the possible realistic configurations deduced from the part B (movement faces are magnified for better illustration): The face Fb2 submitted a rotation around the axis Yb to obtain the face F'b2. In addition, the face F'b1 is obtained by rotating of Fb1 around the axis Yb. Also, the face Fb3 is rotated around the axis Xb for obtaining the face F'b3.

The algorithm for updating assembly mates starts by applying the first mate L1 which the designer has specified first in the nominal model (L1 appears in the first order in the specification tree of the CAD software interface). The algorithm verifies that both normal of two faces are opposites. At this step, the configuration of the two components depends on their initial relative position. Thus, two configurations are mainly distinguished: C1 and C2 (figure 2(b)).

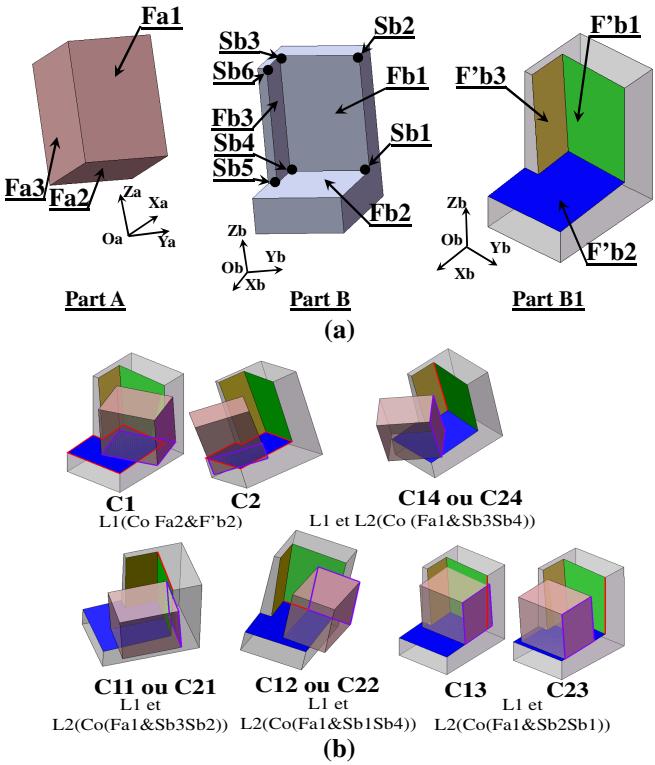

Fig. 2 (a) Parts: A, B and B1 (b) Configurations obtained with L1 or (L1 and L2)

In a second step, using the second mate L2 (Co (Fa1 & F'b1)) the system becomes over-constrained. Then, requirements must be reduced (L2: Co (Fa1 & SbiSbj (SbiSbj (i =1to 4, j=1to 4 and $i \neq j$) is an edge of F'b1). Subsequently, configurations C1i (i = 1to4) are possible and deducted from the configuration C1. Similarly, the set of configurations C2i (i = 1to4) are derived from C2. It should be noted that there is a similarity between the two sets of configurations and only the couple (C13 and C23) is different. At this stage, all configurations do not generate an assembly over-constrained, so they are kept as candidate solutions.

In a third step, using the third mate L3 (Co (F3 & F'b3) or Co (F3 & SbiSbj) with SbiSbj (i =1to 4, j=1to 4 and $i \neq j$) is an edge of F'b3) the system becomes over-constrained. Then, the mate L3 is replaced by a coincidence between F'b3 and Sa. Sa is a vertex belonging to the face F3 and is determined using a technique which is based on modelling the surface by a grid.

Determination of the tangent vertex between two faces F1 and F2 by the modelling technique of the surface by a gird: In the general case, there are two faces F1 and F2 with the respective normal N1 and N2. Let the vertices Pi and Jj respectively the four vertices that delimit F1 and F2. Let P the plane derived from F2. Both faces can have three main initial configurations (figure 3(a)):

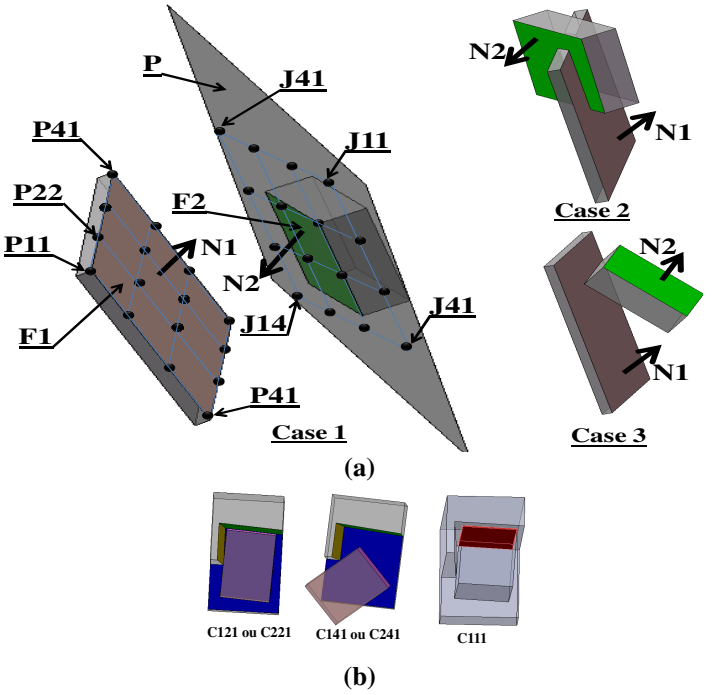

Fig. 3 (a) The three cases in 2nd step (b) Main cases in 3rd step

- Case1: If the following condition is satisfied ($\overrightarrow{N1}.\overrightarrow{N2} \prec 0$ and $\overrightarrow{PiJj}.\overrightarrow{N1} \succ 0$ for i, j = 1 to 4), then the distance d_{min} is determined (Case 1 (figure 1(a))). Initially, F1 is discretized by two parameters n and m. These two parameters are chosen according to the desired accuracy of the results. Thus, F1 is modelled by a grid of vertices P_{nm}. Then, all vertices P_{nm} are projected on P according N1 to obtain the set of vertices J_{nm}. Finally, the distance d_{min} is the minimum distance between pairs (P_{nm}, J_{nm}) provided $J_{nm} \in$ F2 (to ensure the contact). Therefore, Sa is the vertex P_{nm} such that d (P_{nm}, J_{nm}) = d_{min}.
- Case2: If the following condition is satisfied ($\overrightarrow{N1}.\overrightarrow{N2} \succ 0$), then the part A is rotated around the axis A by an angle equal to Π. So, the system becomes in the case 1.
- Case3: If the following condition is satisfied (for i, j = 1 to 4 there exists a pair (k, l) such that $\overrightarrow{PkJl}.\overrightarrow{N1} \prec 0$), then a coincident mate between the face F2 and the vertex Pk temporarily. At this stage, the model is in one of the two previous configurations (case1 or case3).

After the award of these three assembly mates, the algorithm eliminates solutions which exhibit interference (for example C111) and does not guarantee desired contacts (for example C141). The C111 is an optimal solution (figure 3(b)).

3.2 *Case of Cylindrical Faces*

The assembly of the two components of figure 4(a) is realized in three sequences in the following descending priority order: Ensure concentricity between the shaft and the bore, ensure maximum contact between the face F11 and the face F21 and ensure maximum contact between the face F12 and the face F22.

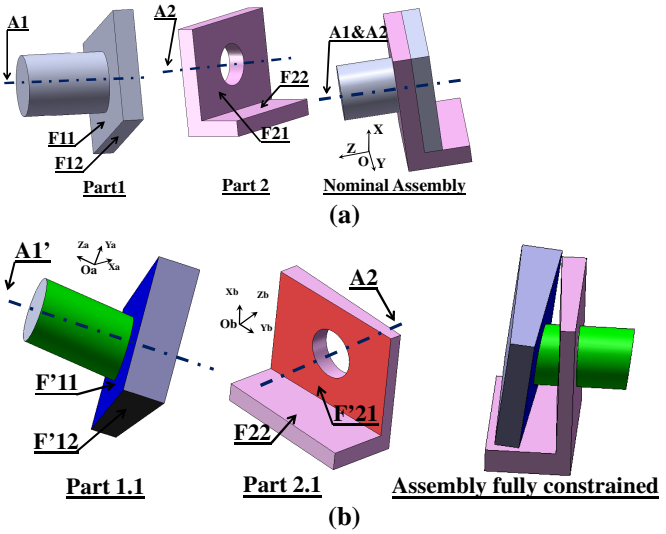

Fig. 4 (a) Nominal assembly. (b) Assembly with defects.

In nominal configuration, the designer can define three assembly mates to satisfy mounting requirements: Co (A1 & A2), Co (F12 & F22) and Co (F11 & F21).

Taking into account the tolerances assigned to each component, the two components with defects Part1.1 and part 2.1 are obtained (figure 4(b)): The axis A1' is obtained by the rotation of A1 around the axis Ya. The face F'11 is obtained by the rotation of F11 around the axis Xa and the face F'12 are derived by the rotation of F12 around the axis Za. The face F'21 is obtained by performing a rotation of F21 around the axis Xb.

Taking into consideration the mounting conditions, assembly mates L1 (Co (A1' & A2) is applied first. Besides, if a second assembly mate L2, Co (face & face), is added to the model, then the assembly becomes over-constrained. Also, if L2 (Co (face & edge)) is applied, then a fully constrained assembly is obtained. Therefore, the addition of a third assembly mate is impossible. Then, L2 is chosen as a coincidence mate between F22 and a vertex of the face F'12. This vertex is determined by the modelling technique of the face F22 by a gird described above. Using the same steps used for defining L2, L3 mate is determined to obtain an assembly fully constrained (figure 4(b)).

4 Conclusion

In this paper, a model for redefining mates of rigid assembly with defects was presented. The study is focused on the fully constrained assemblies. Joints between components of those assemblies are without clearance. The algorithm validation is performed by applying to the case of assemblies comprising contacts between the planar faces and the cylindrical faces. Updating assembly mates is achieved by satisfying mounting requirements. The model should be validated for cases under-constrained assembly and assemblies with clearances.

References

Tsai, J.-C.: Stiffness variation of compliant devices due to geometric tolerancing. In: 10th CIRP, Erlangen, Germany, March 21-23 (2007)

Louhichi, B., Tlija, M., BenAmara, A., Francois, V.: Reconstruction d'un modèle CAO à partir d'un maillage déformé - Application dans le cas de grands déplacements. Mécanique & Industries 10, 477–486 (2009)

Tlija, M., Louhichi, B., BenAmara, A.: Integration of tolerances in the mechanical product process. In: International Conference on Innovative Methods in Product Design, Venice, Italy, June 15-17 (2011)

Petit, J.-P., Samper, S.: Tolerancing analysis and functional requirement. In: Proceedings of the 5th International Conference on Integrating Design and Manufacturing in Mechanical Engineering (2004)

Ballu, A., Mathieu, L.: Choice of functional specifications using graphs within theframework of education. In: 6th CIRP Seminar on Computer Aided Tolerancing, pp. 197–206. Klumer Academic Publishers, Enshede (The Netherlands) (1999)

Sodhi, R., Turner, J.-U.: Towards modelling of assemblies for product design. Computer-Aided Design 26(2), 85–97 (1994)

Author Index